



Multi-scale characterisation of the hydro-mechanical behaviour of unsaturated sand : water retention and triaxial responses

Ghonwa Khaddour

► To cite this version:

Ghonwa Khaddour. Multi-scale characterisation of the hydro-mechanical behaviour of unsaturated sand : water retention and triaxial responses. Mechanics [physics.med-ph]. Université Grenoble Alpes, 2015. English. NNT : 2015GREAI051 . tel-01235579

HAL Id: tel-01235579

<https://theses.hal.science/tel-01235579>

Submitted on 30 Nov 2015

HAL is a multi-disciplinary open access archive for the deposit and dissemination of scientific research documents, whether they are published or not. The documents may come from teaching and research institutions in France or abroad, or from public or private research centers.

L'archive ouverte pluridisciplinaire **HAL**, est destinée au dépôt et à la diffusion de documents scientifiques de niveau recherche, publiés ou non, émanant des établissements d'enseignement et de recherche français ou étrangers, des laboratoires publics ou privés.

THÈSE

Pour obtenir le grade de

DOCTEUR DE L'UNIVERSITÉ GRENOBLE ALPES

Spécialité : **Matériaux, Mécanique, Génie Civil, Électrochimie**

Arrêté ministériel : 7 août 2006

Présentée par

Ghonwa KHADDOUR

Thèse dirigée par **Jacques DESRUES** et
codirigée par **Simon SALAGER**

préparée au sein du **Laboratoire 3SR**
dans l'**École Doctorale IMEP2**

Multi-scale characterisation of the hydro-mechanical behaviour of unsaturated sand : water retention and triaxial response

Thèse soutenue publiquement le « **13 Novembre 2015** »,
devant le jury composé de :

Monsieur, Antonio GENS

Professeur, Université de la Catalogne, (Rapporteur)

Monsieur, Bertrand FRANCOIS

Professeur, Université libre du Bruxelles, (Membre)

Monsieur, Felix Darve

Professeur, Université Joseph Fourier, Grenoble, (Membre)

Monsieur, Jean-michel PEREIRA

Chercheur, Ecole des Ponts ParisTech, (Membre)

Monsieur, Fabien CHERBLANC

Chercheur, Université de Montpellier 2, (Rapporteur)

Monsieur, Gioacchino VIGGIANI

Professeur, Université Joseph Fourier, Grenoble, (Membre)

Monsieur, Jacques DESRUES

Directeur de recherche, CNRS, Grenoble, (Directeur de thèse)

Monsieur, Simon SALAGER

Maitre de conférences, Université Joseph Fourier, Grenoble, (Co-Encadrant)



ACKNOWLEDGMENTS

Firstly, I would like to express my sincere gratitude to my advisors Jacques Desrues and Simon Salager for their continuous support, guidance, patience, motivation, encouragement and immense knowledge. I thank you also for the family-like generous care and the home feeling whenever I was in need.

I would also like to thank the rest of my thesis committee: M. Antonio Gens, M. Bertrand Francois, M. Felix Darve, M. Jean-michel Pereira, M. Fabien Cherblanc and M. Gioacchino Viggiani, for accepting to be a part of the committee to evaluate this work. I am honoured and profoundly grateful to them.

My sincere thanks go to M. Pierre Besuelle, who was an inspiration to me through these four years, and still does.

I express my warm thanks to 3SR laboratory, as a direction and members, for providing me with all the necessary facilities for the research.

Thanks to Edward Andó for sharing expertise, and his help in this thesis. Thanks to Pascal Charrier for the precious support, without which, it would not be possible to conduct this research. Thanks to Yosuke Higo (Kyoto University), Amid Hashemi (ULB) and Erika Timoshenko for the collaboration and assistance. Thanks to Jérôme Branon-Maillet, Rémi Cailletaud, Carole Reverdit, Sheherazade Mezenner, and Augustine Alessio for all the help they offered. Thanks to my fellow lab mates (one by one) for the stimulating discussions, the time we were working together, and for all the fun we have had in the last four years.

Also I thank my friends, in particular Donia Dowidar for the unceasing encouragement, support and attention. I am so grateful to have you all with me through this venture.

Last but not the least, infinite thanks to my family: my parents and my two brothers for supporting me spiritually throughout these four years, and my life in general. Thank you for all the sacrifices that you have made on my behalf. Thank you for your prayers, support and selfless care and unconditional love.

ABSTRACT

With the recent developments of full field measurements, it has become possible to do experiments on a soil specimen, and perform measurements at different scales. This progress has allowed greater understanding for all the processes that occur within the soil, and also created better environment to observe these mechanisms in 3D.

This PhD work aims to characterize water retention and hydro-mechanical behaviours of unsaturated Hostun sand at the grain scale. To achieve this goal, water retention and triaxial tests were performed and a set of experimental and image processing tools was developed and used for the two series of tests.

X-ray computed tomography set up available at 3SR Laboratory in Grenoble University was used to generate 3D images of the unsaturated soil microstructure non-destructively. A developed region growing systematic technique (trinarization technique) was used to allow the separation of the phases (i.e., grains, water and air) in the 3D images, and performing different measurements at the grain scale. Porosity and degree of saturation were measured macroscopically using the trinarized images and microscopically using a developed mapping code. The microscopic measurements were performed over an REV, whose size was determined using a developed analysis based on statistical tools. Several microscopic-discrete analyses were developed to investigate the evolution of fluid phase (water and air) with loading (suction and mechanical loading). Digital Image Correlation was performed for the two tests.

To analyze water retention behaviour of Hostun sand during drying and wetting processes, a pressure plate apparatus was developed. Suction was applied using tensiometry technique. The specimen (cylindrical $1 \times 1 \text{ cm}$) was prepared using water pluviation technique and scanned with a resolution $7.5 \mu\text{m}$. As a result, water retention curve, surface and domains were obtained and hysteresis phenomenon and soil cohesion were analyzed at the grain scale.

For the mechanical behaviour of unsaturated soils, triaxial test were performed at three conditions: saturated drained, unsaturated drained and unsaturated undrained. A triaxial apparatus that can be placed inside the x-ray cabinet was developed in order to facilitate monitoring the changes in sand microstructure and water distribution when subjecting the soil specimen to loading. The specimen (cylinder of $h \times d = 2 \times 1 \text{ cm}$) was prepared using water pluviation technique (completely saturated at the beginning of the three tests), loaded then scanned with a resolution $13 \mu\text{m}$, repeatedly till reaching 21% axial strain for the three tests.

Consequently, stress-strain curves, volumetric response and deformations measurements were obtained and deformation pattern, specimen heterogeneity, cohesion and water distribution were analyzed.

Key Words: unsaturated sand, grain scale, x-ray computed tomography, water retention behaviour, water retention domains, triaxial test, deformation, digital image correlation, water distribution, cohesion.

Résumé

Avec les récents développements des mesures de champs, il est devenu possible de réaliser des expériences sur un échantillon de sol en effectuant des mesures simultanément aux différentes échelles pertinentes : celle de l'échantillon, et celle des grains, et ceci en 3D volumique. Ces progrès ont permis une meilleure compréhension des processus qui se produisent dans le sol, en les observant au cur même des échantillons.

Cette thèse vise à caractériser les comportements de rétention d'eau et hydro-mécanique du sable d'Hostun non saturé à l'échelle du grain. Pour ce faire, des essais de rétention d'eau et des essais triaxiaux ont été effectués, qui ont nécessité le développement d'outils de traitement d'image et des montages expérimentaux spécifiques. L'installation de tomographie à rayons X du Laboratoire 3SR de l'Université de Grenoble a été utilisée pour générer des images en 3D de la microstructure du sol non saturé. Une technique de trinarisation a été mise en œuvre pour permettre la séparation des phases (les grains, l'eau et l'air) dans les images 3D, et d'effectuer différentes mesures à l'échelle du grain. La porosité et le degré de saturation ont été mesurées macroscopiquement en utilisant les images segmentées, et microscopiquement en utilisant un code de cartographie spécialement développé. Les mesures microscopiques ont été réalisées sur un volume élémentaire représentatif (VER), dont la taille a été déterminée en utilisant une analyse développée sur la base d'outils statistiques. Plusieurs analyses discrètes ont été développées pour étudier l'évolution de la phase fluide (l'eau et l'air) avec le chargement (suction, et chargement mécanique). La corrélation d'images numérique 3D volumique a été mise en œuvre systématiquement pour ces deux types d'essais.

Pour analyser le comportement de rétention d'eau du sable d'Hostun pendant les processus de séchage et de mouillage, une cellule spécifique a été développée. La suction a été appliquée en utilisant la technique de tensiométrie. L'échantillon (cylindrique $1 \times 1 \text{ cm}$) a été préparé en utilisant la technique de la pluviation sous l'eau et scanné avec une résolution de $7,5 \mu\text{m}$. La courbe de rétention d'eau, surface et les domaines hydriques ont été obtenus et le phénomène d'hystérésis et la cohésion du sol ont été analysés à l'échelle du grain.

Pour le comportement hydro-mécanique des sols non saturés, des essais triaxiaux ont été effectués sous trois conditions: saturé drainé, non saturé drainé et non saturé non drainé. Un appareil triaxial que l'on peut placer à l'intérieur de la cabine du tomographe à rayons X a été développé afin de permettre le suivi des changements dans la microstructure du sable et la distribution de l'eau lorsque l'on soumet l'échantillon à chargement mécanique. L'échantillon (cylindre de dimensions $h \times d = 2 \times 1 \text{ cm}$) a été préparé en utilisant la technique de la pluviation sous l'eau (complètement saturé au début des trois tests), amené ensuite au niveau de saturation désiré (dans le cas des essais non saturés), puis chargé par étapes successives avec scan à chaque étape avec une résolution de $13 \mu\text{m}$, jusqu'à arriver à 21% de déformation axiale pour les trois types d'essai. Les courbes contrainte-déformation, la réponse volumétrique et les déformations ont été obtenus et le profil de déformation, l'hétérogénéité de l'échantillon, la cohésion et la distribution de l'eau ont été analysés.

Mots clés: Sable non saturé, échelle du grain, rayons X, comportement de rétention d'eau, domaines de rétention d'eau, essai triaxial, corrélation d'image, déformation, distribution de l'eau, cohésion.

Contents

1	Introduction	1
1.1	Background	1
1.2	Objectives	1
1.3	Outlines of the thesis	3
2	Literature review of unsaturated soils mechanics	5
2.1	General overview	5
2.2	Water retention behaviour of unsaturated soils	5
2.2.1	Definition of unsaturated soils	5
2.2.2	Soil suction	6
2.2.3	Water Retention Curve	6
2.2.4	Influence of grain size and shape on water retention behaviour	7
2.2.5	Water Retention Surface	10
2.2.6	Hysteresis phenomenon	14
2.2.7	Water retention domains	17
2.3	Hydro-mechanical behaviour of unsaturated soils	18
2.3.1	Shear strength behaviour	19
2.3.2	Capillary cohesion	23
2.3.3	Volume change and liquid distribution	36
2.4	Summary and anticipated contribution	40
3	Experimental and data processing tools	43
3.1	General overview	43
3.2	X-ray tomography	44
3.2.1	X-ray scanner in 3SR laboratory	45
3.2.2	X-ray parameters	46
3.2.3	X-ray reconstruction	47
3.3	Trinarization	48
3.3.1	Partial thresholding	49
3.3.2	Partial Volume Effect filtering	51
3.3.3	Simultaneous phase growing	52
3.3.4	Interface filling	53
3.4	Representative Elementary Volume	54
3.4.1	REV mapping	55
3.4.2	REV analysis	56
3.4.3	Porosity and degree of saturation mapping	58
3.5	Microscopic-discrete analyses	59

3.5.1	The evolution of the number of fluid clusters with loading	59
3.5.2	The evolution of the number of fluid-fluid and solid-fluid interfaces with loading	63
3.6	Digital Image Correlation	66
3.7	Conclusion	68
4	Water Retention Behaviour	69
4.1	General overview	69
4.2	Experimental program	69
4.2.1	The material tested	69
4.2.2	The cell	70
4.2.3	Suction application technique	71
4.2.4	Specimen preparation technique	73
4.2.5	Experimental procedure	73
4.3	Water retention results	75
4.3.1	Digital Image Correlation results	75
4.3.2	Trinarization results	76
4.3.3	Macroscopic porosity and degree of saturation results	84
4.3.4	Microscopic porosity and degree of saturation results	88
4.3.5	Microscopic-discrete analyses results	101
4.4	Interpretation of water retention results	126
4.4.1	The relation between state variables $f(s, n, Sr)$	126
4.4.2	Water retention domains	133
4.4.3	Hysteresis phenomenon	136
4.4.4	Cohesion regimes	149
4.5	Conclusion	152
5	Hydro mechanical behaviour (Triaxial tests)	155
5.1	General overview	155
5.2	Material and methods	155
5.2.1	Triaxial tests	155
5.2.2	The material tested	156
5.2.3	The cell	156
5.2.4	Specimen preparation technique	156
5.2.5	Suction application technique	159
5.2.6	Experimental procedure	160
5.2.7	Loading system	164
5.2.8	Loading procedure	165
5.2.9	Experimental program	166
5.3	Triaxial tests results	168
5.3.1	Stress-Strain curve	168
5.3.2	Volumetric response	172
5.3.3	Trinarization results	173
5.3.4	Macroscopic porosity and degree of saturation results	175
5.3.5	Microscopic porosity and degree of saturation results	176
5.3.6	Microscopic-discrete analyses results	179
5.3.7	Digital Image Correlation results	187
5.4	Interpretation of triaxial tests results	197

5.4.1	The evolution of porosity and degree of saturation inside/outside the sheared zone	197
5.4.2	Cohesion and water distribution	200
5.5	Conclusion	203
6	Summary, conclusion and outlook for future work	205
6.1	Summary and conclusion	205
6.2	Outlook for future work	209
A	Trinarization results	225
A.1	Drying path D_1	226
A.2	Wetting path W_1	232
A.3	Drying path D_0	238
B	Porosity and degree of saturation mapping results	245
B.1	Porosity mapping results	246
B.1.1	Drying path D_1	247
B.1.2	Wetting path W_1	255
B.1.3	Drying path D_0	263
B.2	Degree of saturation mapping results	271
B.2.1	Drying path D_1	272
B.2.2	Wetting path W_1	280
B.2.3	Drying path D_0	288
C	Microscopic-discrete analyses results	297
C.1	Results of labelling process for water and air phases	298
C.1.1	Drying path D_1	299
C.1.2	Wetting path W_1	304
C.1.3	Drying path D_0	309
C.1.4	Results of grain size distribution and the number of grains for W_1 and D_0	314
D	Interpretation of the microscopic discrete analyses results	317
D.1	Results of the relation between state variables (s , n , S_r)	318
D.1.1	3D relation between state variables (s , n , S_r)	319
D.1.2	The relation between suction and porosity $n=f(s)$	322
D.1.3	The relation between suction and degree of saturation $S_r=f(s)$	326
D.1.4	The relation between porosity and degree of saturation $S_r=f(n)$	332
D.1.5	Frequency map results	336
E	Triaxial test results	353
E.1	Trinarization results	354
E.2	Porosity mapping results	360
E.3	Degree of saturation mapping results	367
E.4	Labelling process results	374

List of Figures

2.1	A sketch of gas, liquid and solid phases in an unsaturated soil	5
2.2	A schematic plot of water retention curve during drying process, that shows the air entry value (s_{air}) and the residual water content (Sr_0)	7
2.3	Water retention curves for different types of soil: sand, silt and clay during drying process (from Fredlund et al. (2012))	8
2.4	WRCs for the same soil type (fine sand), and same particle size (R) but different void ratio (e) in the top and WRCs for the same soil type and same void ratio but different particle sizes in the bottom (from Maaitah (2012)) .	9
2.5	WRCs of poly-dispersed granular media for a) different inter-particle distance (D_{rupt}) and b) different grain radii (R) (from Gras (2011))	10
2.6	WRCs for the same soil type but different void ratio, from Salager (2007) (top) and from Vanapalli et al. (1999) (bottom)	11
2.7	WRS for the drying path obtained by Salager et al. (2010) in terms of (a) water content and (b) degree of saturation (top) and WRS obtained by Main (2011) in terms of degree of saturation (bottom)	12
2.8	The experimental and numerical results for the relation between suction and water content projected on the plane $e=\text{constant}$ (from Salager et al. (2010))	12
2.9	The relation between water content and void ratio, projected on the plane $s=\text{constant}$ from Salager et al. (2010) (top) and the relation between Volumetric Water Content (VWC) and void ratio (e) for different ranges of suction from Plaisted (2014) (bottom)	13
2.10	The experimental and numerical results projected on the plane $Sr=\text{constant}$ (from Salager et al. (2010))	14
2.11	A sketch that illustrates hysteresis phenomenon and the scanning paths . .	15
2.12	Schematic illustration of the ink-bottle effect during (a) drying and (b) wetting (Loll et al. (2000))	16
2.13	Schematic illustration of contact angle hysteresis. A wetting fluid (left) and a non-wetting fluid (right)	16
2.14	Water retention curve and the hydraulic domains (illustrated by small sketches, bellow the curve)	18
2.15	Triaxial test results for normally consolidated saturated clay specimens in drained condition (left) and undrained condition (right) (from Bishop et al. (1957))	20
2.16	Triaxial test results for over-consolidated saturated clay specimens in drained condition (left) and undrained condition (right) (from Bishop et al. (1957))	21

2.17	Suction-controlled triaxial shear tests on dry, wetted and saturated specimens (from Uchaipichat (2010-b)). The figure shows stress-strain curves (top) and the volumetric strain (bottom) in relation with the axial strain .	22
2.18	a) Shear stress-displacement curve (τ -u) in the top, volumetric strain-displacement curve ((v/H_0) -u) in the middle and water content change-displacement curve (Δw -u) in the bottom (from Hamid et al. (2009))	24
2.19	The relation between the volumetric strain obtained macroscopically, and the largest averaged local volumetric strain obtained using VDIC (radial average) versus water content (from Bruchon et al. (2013))	24
2.20	Changes in cohesion and friction angle with suction (from Delage (2008-c))	25
2.21	a) The relation between suction and deviatoric stress b) The relation between suction and cohesion c) The relation between degree of saturation and cohesion, for silty sand soil (from Leal-Vaca et al. (2012))	26
2.22	The relation between suction and shear strength for a glacial till soil (from Gan et al. (1988))	27
2.23	The variations of the suction (ΔP) and the cohesive stress (σ_c), upon changing the liquid content (S) (from Mitarai et al. (2006))	27
2.24	Tensile strength (filled squares), critical acceleration for fluidization (open circles) of wet glass beads at different liquid contents (W). Inset: Yield stress (from Scheel et al. (2008))	29
2.25	Sections through 3D tomograms of the analyzed specimens at $W=0.02$, 0.04 and 0.11 , from left to right. Main panel: Frequencies of liquid objects as extracted from x-ray tomography data. Left axis (open symbols): Average number of capillary bridges on a sphere (triangles: fluorescence microscopy; squares: x-ray tomography). Right axis: Average number of clusters per sphere (filled symbols), and normalized volume of the largest cluster (half-filled symbols) (from Scheel et al. (2008))	30
2.26	Macroscopic cohesion (c) as a function of water content (w) for four tested granular material: sand (S), glass beads (GB_1), (GB_{45}), and (GB_{48}) (from Richefeu et al. (2008))	31
2.27	Stress-strain plot for $w=0\%$ and $w=1\%$; $\sigma=300$ Pa (left) and stress-strain plot for a dry (dashed line) and two wet samples (solid lines) with a high bond coordination number (thick line) and with two times less bonds (thin line). For the two plots, the displacements are normalized by the average particle diameter (D). In Fig 2.27-right the inset shows a zoom for small deformations (right) (from Richefeu et al. (2008))	31
2.28	The relation between capillary force (f_{cap}) and the inter-particle distance (D) during traction test at constant suction (s) for two spherical beads configuration (from Gras. (2011))	32
2.29	The relation between capillary force (f_{cap}) and the inter-particle distance (D) during traction test at different values of the radius of the bead (R) for a volume of water bridge $V=2\mu l$ (left) and different values of the volume of water bridge in μl (right) for $R=3.5mm$ (from Gras. (2011))	32
2.30	The evolution of capillary stress (σ_c) and number of liquid bonds per grain (Z) in relation with the deformation ($\varepsilon\%$) (from Gras (2011))	33

2.31	Evolution of the peak force with water content for two different values of inter-particle distances (k) (top), and for two different values of the surface tension (σ) (bottom). In Fig 2.31-top the experimental results for the evolution of the peak force with water content are shown (from Souli et al. (2012))	34
2.32	Deviatoric stress (q) and volumetric strain (ϵ_v) versus axial strain curves obtained from triaxial tests at different degrees of saturation under a constant confining pressure (10kPa): DEM (a) and MDM (b) results (from Scholtés et al. (2009))	35
2.33	Volume change measurements for silty sand soil at net normal stress a) 20kPa b) 75kPa and c) 250kPa (from Houston et al (2008))	37
2.34	Three specimens of Hostun sand loaded to failure at $\sigma_3=400$ kPa in drained condition. From left to right: dense, medium dense, loose (from Desrues (2004))	38
2.35	Snapshots of plane shear between two walls at the beginning (left), at an intermediate time (middle) and at the end of the simulation (right). Only the central part of the sample is shown and the (y) direction points into the plane. The capillary bridges are indicated by dark blue lines connecting the center of two spheres whose width is proportional to the bridge volume. It is seen that the liquid is spreading towards the top and the bottom wall (from Mani (2014))	39
2.36	The wet granulate (silicone oil colored red), after the shearing. The shear band appears brighter indicating that there is a silicon oil reduction along the shear zone (from Mani (2014))	40
3.1	X-ray scanner in 3SR Laboratory	46
3.2	Phase contrast in x-ray 8-bit reconstructed image (left) and the corresponding histogram (right)	48
3.3	Simple threshold of an image with two distinct gray values (using Image J [®])	48
3.4	Simple threshold of an image with three distinct gray values (using Image J [®]). The segmented image shows the presence of PVE and noise	49
3.5	Evolution of phase segmentation process in the developed trinarization technique. The color red represents the grains; the color green represents water; the color blue represents air and the color black for undefined regions	49
3.6	Procedure to choose the partial thresholds for each phase as the peaks of the histogram. The sand threshold (P_g), the air threshold (P_a) and the water thresholds (right- P_{w2}) and (left- P_{w1})	50
3.7	Results of partial thresholding step. Grains are represented in the color red; water is represented in color green; air is represented in color blue and the color black for undefined voxels	50
3.8	Resulted partial volume effect from partial thresholding step. PVE is represented as a sequence of water voxels around the grains. Grains are represented in the color red; water is represented in color green; air is represented in color blue and the color black for undefined voxels	51
3.9	Partial volume effect definition as a voxel shared between grain and air phases, and considered when segmenting as a water voxel	51

3.10	Standard deviation histogram and its threshold. PVE threshold filtering (V) defined as the inflexion point on the histogram	52
3.11	The result of partial volume effect filtering step. Grains are represented in the color red; water is represented in color green; air is represented in color blue and the color black for undefined voxels	52
3.12	Voxel examination in simultaneous phase growing step. The questions into the boxes are asked to a voxel neighboring a cluster of voxels already identified as belonging to a given phase; hence this voxel is candidate to be attributed to this phase in the growing process	53
3.13	The result of simultaneous phase growing step. Grains are represented in the color red; water is represented in color green; air is represented in color blue and the color black for undefined voxels	53
3.14	Evolution of phase segmentation process, including Interface filling step results. Grains are represented in the color red; water is represented in color green; air is represented in color blue and the color black for undefined voxels1	53
3.15	Evolution of the measurement of porosity as the side of the cubic sub-volume increases. This is shown for unsaturated sand specimen, with 50% degree of saturation	56
3.16	The relation between stability criteria versus the Standard deviation (left) and the peak value (right) of the corresponding sub-volume size. This is shown for unsaturated sand specimen, with 50% degree of saturation	57
3.17	Normal distribution of sub-volume size for porosity criterion $\Delta n=0.1$ (left) and for degree of saturation criterion $\Delta Sr=0.5$ (right). This is shown for unsaturated Hostun sand specimen, with around 50% degree of saturation .	58
3.18	The trinarized image of unsaturated sand (left) and porosity map in 2D with the applied grid (right). Measurement overlapping is not allowed . . .	59
3.19	Water phase processing steps: Reconstructed, trinarized, Erode-Dilate and labelling steps, respectively from left to right	61
3.20	Air phase processing steps: Reconstructed, trinarized, Erode-Dilate and labelling steps, respectively from left to right	61
3.21	Evolution of the number of water clusters with suction. This is shown for water retention test, drying path	61
3.22	Water clusters size distribution for water retention test, for $s=2.2\text{kPa}$ and $s=3\text{kPa}$	62
3.23	The relation between suction and the normalized volume of the biggest water cluster. This is shown for water retention test, drying path	63
3.24	Effective specific interfacial area calculation according to Dalla et al. (2007).	65
3.25	Solid phase processing steps: Reconstructed, trinarized, Dilate-Erode and labelling steps, respectively from left to right	65
4.1	a) SEM image of Hostun sand from Flavigny et al. (1990) b) Grain size distribution of Hostun sand from Sunyer Amat (2008)	70
4.2	Water retention cells for WRT_0 and WRT_1 and their components	71
4.3	Sketch of the arrangement used to apply the suction for WRT_0 (taken from Riedel (2011))	72
4.4	Sketch of the arrangement used to apply suction for WRT_1	72
4.5	The reference experimental WRC of Hostun sand, taken from Lins (2010) .	73

4.6	The selected points in the reference WRC, where x-ray CT scans are performed, shown in blue color for WRT ₀ and blue and red colors for WRT ₁ .	74
4.7	Digital image correlation results for WRT ₁ (D ₁ and W ₁). The two correlated states are the first state of the specimen in the drying path D ₁ (s=0kPa) and the last state of the same specimen in the wetting path W ₁ (s=0kPa)	76
4.8	Central vertical slices in the reconstructed and trinarized volumes, before and after removing the porous stone at the bottom of the specimen and the loose layer at the top of the specimen, shown for WRT ₁	77
4.9	Central vertical slices in the reconstructed and trinarized volumes, before and after removing the porous stones at the top and the bottom of the specimen, shown for WRT ₀	78
4.10	Central horizontal slices in the trinarized volumes, for all the values of suction in the drying path D ₁	80
4.11	Central vertical slices of the same azimuth in the trinarized volumes, after removing the porous stone and the upper loose layer, for all the values of suction in the drying path D ₁	80
4.12	Central horizontal slices in the trinarized volumes, for all the values of suction in the wetting path W ₁	81
4.13	Central vertical slices of the same azimuth, in the trinarized volumes, after removing the porous stone and the upper loose layer, for all the values of suction in the wetting path W ₁	81
4.14	Central horizontal slices in the trinarized volumes, for all the values of suction in the drying path D ₀	82
4.15	Central vertical slices of the same azimuth, in the trinarized volumes, after removing the upper and the bottom porous stones, for all the values of suction in the drying path D ₀	82
4.16	Water retention curve (WRC) for the three paths D ₀ , D ₁ , W ₁ , and Ref WRC	88
4.17	The chosen size of REV=140px (length of one side of the REV) compared to the grain size of Hostun sand, for the three paths D ₀ , D ₁ and W ₁	89
4.18	Central horizontal slices in the porosity map, for all the values of suction, in the drying path D ₁ . In this figure, n _{max} and n _{min} represent the maximum and the minimum porosity respectively (written below the suction value) .	90
4.19	Central vertical slices in the porosity map, of the same azimuth, for all the values of suction, in the drying path D ₁ . In this figure, n _{max} and n _{min} represent the maximum and the minimum porosity respectively (written below the suction value)	90
4.20	Central horizontal slices in the porosity map, for all the values of suction, in the drying path W ₁ . In this figure, n _{max} and n _{min} represent the maximum and the minimum porosity respectively (written below suction value)	91
4.21	Central vertical slices of the same azimuth in the porosity map, for all the values of suction in the drying path W ₁ . In this figure, n _{max} and n _{min} represent the maximum and the minimum porosity respectively (written below suction value)	91
4.22	Central horizontal slices in the porosity map, for all the values of suction, in the drying path D ₀	92

4.23	Central vertical slices of the same azimuth in the porosity map, for all the values of suction, in the drying path D_0 . In this figure, n_{\max} and n_{\min} represent the maximum and the minimum porosity respectively (written below suction value)	92
4.24	A central vertical slice in the porosity map (left), a central vertical slice in the trinarized volume (middle) and a porosity vertical profile (right) shown for $s=2\text{kPa}$, in the drying path D_1 . The mapped volume is marked by a red rectangle in the trinarized image. The yellow dashed rectangle shows the high porosity region	93
4.25	A central vertical slice in the porosity map (left), a central vertical slice in the trinarized volume (middle) and a porosity vertical profile (right) shown for $s=2\text{kPa}$, in the drying path D_0 . The mapped volume is marked by a red rectangle in the trinarized image. The yellow dashed rectangle shows the high porosity region	94
4.26	Local porosity histogram shown for $s=2\text{kPa}$ in the drying path D_1 . The mean and the most frequent (mode) porosity are marked by a red rectangle	94
4.27	Central horizontal slices in the degree of saturation map, for all the values of suction, in the drying path D_1 . In this figure, $S_{r\max}$ and $S_{r\min}$ represent the maximum and the minimum degree of saturation respectively (written below suction value)	96
4.28	Central vertical slices of the same azimuth in the degree of saturation map, for all the values of suction, in the drying path D_1 . In this figure, $S_{r\max}$ and $S_{r\min}$ represent the maximum and the minimum degree of saturation respectively (written below suction value)	96
4.29	Central horizontal slices in the degree of saturation map, for all the values of suction, in the drying path W_1 . In this figure, $S_{r\max}$ and $S_{r\min}$ represent the maximum and the minimum degree of saturation respectively (written below suction value)	97
4.30	Central vertical slices in the degree of saturation map, for all the values of suction, in the drying path W_1 . In this figure, $S_{r\max}$ and $S_{r\min}$ represent the maximum and the minimum degree of saturation respectively (written below suction value)	97
4.31	Central horizontal slices in the degree of saturation map, for all the values of suction, in the drying path D_0 . In this figure, $S_{r\max}$ and $S_{r\min}$ represent the maximum and the minimum degree of saturation respectively (written below suction value)	98
4.32	Central horizontal slices in the degree of saturation map, for all the values of suction, in the drying path D_0 . In this figure, $S_{r\max}$ and $S_{r\min}$ represent the maximum and the minimum degree of saturation respectively (written below suction value)	98
4.33	A central vertical slice in the degree of saturation map (left), a central vertical slice in the trinarized volume (middle) and a degree of saturation vertical profile (right) shown for $s=2\text{kPa}$, in the drying path D_1 . The mapped volume is marked by a red rectangle in the trinarized image. The yellow dashed rectangle shows the high degree of saturation region	100

4.34	A central vertical slice in the degree of saturation map (left), a central vertical slice in the trinarized volume (middle) and a degree of saturation vertical profile (right) shown for $s=2\text{kPa}$, in the drying path D_0 . The mapped volume is marked by a red rectangle in the trinarized image. The yellow dashed rectangle shows the high degree of saturation region	101
4.35	Central vertical slices of the same azimuth in the labelled volume of water, for all the values of suction in the drying path D_1	104
4.36	Central vertical slices of the same azimuth in the labelled volume of air, for all the values of suction in the drying path D_1	104
4.37	Central vertical slices of the same azimuth in the labelled water volume, for all the values of suction in the wetting path W_1	104
4.38	Central vertical slices of the same azimuth in the labelled air volume, for all the values of suction in the wetting path W_1	105
4.39	Central vertical slices in the water labelled volume, of the same azimuth for all the values of suction in the drying path D_0	105
4.40	Central vertical slices in the air labelled volume, of the same azimuth for all the values of suction in the drying path D_0	105
4.41	The evolution of the number of water clusters (left) and air clusters (right) with suction, for the drying path D_1	106
4.42	The evolution of the number of water clusters (left) and air clusters (right) versus suction, for the wetting path W_1	106
4.43	The evolution of the number of water clusters (left) and air clusters (right) versus suction, for the drying path D_0	106
4.44	Water clusters size distribution for all the values of suction in the drying path D_1	108
4.45	Water clusters size distribution for all the values of suction in the wetting path W_1	108
4.46	Water clusters size distribution for all the values of suction in the drying path D_0	109
4.47	Air clusters size distribution for all the values of suction in the drying path D_1	110
4.48	Air clusters size distribution for all the values of suction in the wetting path W_1	110
4.49	Air clusters size distribution for all the values of suction in the drying path D_0	111
4.50	The relation between the normalized V_{\max} for water clusters (left) and air clusters (right) versus the suction, for the drying path D_1	112
4.51	The relation between the normalized V_{\max} of water clusters (left) and air clusters (right) versus the suction, for the wetting path W_1	112
4.52	The relation between the normalized V_{\max} of water clusters (left) and air clusters (right) versus the suction, for the drying path D_0	112
4.53	The relation between the normalized effective specific interfacial area a_{wn} (calculated following the definition of Grant et al. (2007)) versus the degree of saturation, shown for D_1 , W_1 and D_0	115
4.54	A vertical slice in the labelled grain volume for a) D_1 b) W_1 and c) D_0 . . .	116
4.55	Grain size distribution for all the values of suction in the drying path D_1 .	117

4.56	The number of grains within the specimen shown for all the values of suction in the drying path D_1	117
4.57	The relation between the maximum number of grains in contact with one water cluster (Max Gw) versus the suction and the relation between the maximum number of water clusters in contact with one grain (Max Wg) versus the suction, for D_1	118
4.58	The relation between the maximum number of grains in contact with one water cluster (Max Gw) versus the suction and the relation between the maximum number of water clusters in contact with one grain (Max Wg) versus the suction, for W_1	118
4.59	The relation between the maximum number of grains in contact with one water cluster (Max Gw) versus the suction and the relation between the maximum number of water clusters in contact with one grain (Max Wg) versus the suction, for D_0	119
4.60	The relation between the maximum number of grains in contact with one air cluster (Max Ga) versus the suction and the relation between the maximum number of air clusters in contact with one grain (Max Ag) versus the suction, for D_1	120
4.61	The relation between the maximum number of grains in contact with one air cluster (Max Ga) versus the suction and the relation between the maximum number of air clusters in contact with one grain (Max Ag) versus the suction, for W_1	120
4.62	The relation between the maximum number of grains in contact with one air cluster (Max Ga) versus the suction and the relation between the maximum number of air clusters in contact with one grain (Max Ag) versus the suction, for D_0	121
4.63	The relation between the maximum number of water clusters in contact with one air cluster (Max Wa) versus the suction and the relation between the maximum number of air clusters in contact with one water cluster (Max Aw) versus the suction, for D_1	122
4.64	The relation between the maximum number of water clusters in contact with one air cluster (Max Wa) versus the suction and the relation between the maximum number of air clusters in contact with one water cluster (Max Aw) versus the suction, for W_1	122
4.65	The relation between the maximum number of water clusters in contact with one air cluster (Max Wa) versus the suction and the relation between the maximum number of air clusters in contact with one water cluster (Max Aw) versus the suction, for D_0	123
4.66	A zoom window around the intersection point between Max Wa and Max Aw curves for D_1	124
4.67	A zoom window around the intersection point between Max Wa and Max Aw curves for W_1	124
4.68	A zoom window around the intersection point between Max Wa and Max Aw curves for D_0	125
4.69	3D relation between suction, porosity and degree of saturation for the drying path D_1	127

4.70	The experimental relation between suction and porosity for two constant ranges of degree of saturation in the drying path D_1 : S_r (10–20%) and S_r (80–90%). The tendency (slope) of the relation between the suction and the microscopic porosity is presented by the two continuous lines	128
4.71	The tendency (slope) of the relation between microscopic porosity and suction, for S_r =(0–10%) (right) and S_r =(90–100%) (left) in the drying path D_1	128
4.72	The experimental relation between suction and degree of saturation for three constant ranges of porosity in the drying path D_1 : n (41–43%), n (43–45%) and n (45–47%)	130
4.73	Fitting curve for the experimental points in the relation between suction and degree of saturation for three constant ranges of porosity in the drying path D_1 : n (41–43%), n (43–45) and n (45–47%). The black dashed circles highlight air entry values s_{air} , the value of suction s_1 at which the curve reach a constant degree of saturation before the residual state, and the residual degree of saturation S_{r0}	130
4.74	The relation between average porosity of the three ranges and the three variables, s_{air} and s_1 (left) and S_{r0} (right)	130
4.75	The relation between microscopic porosity and degree of saturation for the two values of suction: $s=2\text{kPa}$ and $s=2.5\text{kPa}$ in the drying path D_1 . The tendency (slope) of the relation between microscopic porosity and degree of saturation is presented by the two continuous lines	132
4.76	The relation between microscopic porosity and degree of saturation for the two values of suction: $s=2\text{kPa}$ and $s=2.5\text{kPa}$ in the drying path D_1	132
4.77	Central horizontal (up) and vertical (bottom) slices in the trinarized volumes of $s=1.6\text{kPa}$ in the drying path D_1 (left) and $s=1.6\text{kPa}$ in the wetting path W_1 (right)	138
4.78	Central vertical slices in the: porosity map (left), trinarized volumes (middle) and degree of saturation map (right) for $s=1.6\text{kPa}$ in the drying path D_1 (up) and $s=1.6\text{kPa}$ in the wetting path W_1 (down)	139
4.79	Frequency map for $s=1.6\text{kPa}$ in the drying path D_1 (up) and $s=1.6\text{kPa}$ in the wetting path W_1 (bottom)	139
4.80	Central horizontal (up) and vertical (bottom) slices in the trinarized volumes, for $S_r \approx 30\%$ which correspond to $s=2\text{kPa}$ in the drying path D_1 (left) and $s=1.6\text{kPa}$ in the wetting path W_1 (right)	141
4.81	Central vertical slices in the: porosity map (up), trinarized volumes (middle) and degree of saturation map (bottom) for $s=2\text{kPa}$ in the drying path D_1 (left) and for $s=1.6\text{kPa}$ in the wetting path W_1 (right)	141
4.82	Frequency map for $s=2\text{kPa}$ in the drying path D_1 (up) and for $s=1.6\text{kPa}$ in the wetting path W_1 (bottom)	142
4.83	The evolution of the number of water clusters (left) and the normalized V_{max} for water clusters (right), with suction, for drying and wetting paths	143
4.84	The evolution of the number of air clusters (left) and the normalized V_{max} for air clusters (right), with suction, for drying and wetting paths	144
4.85	The evolution of the effective specific interfacial area (a_{wn}) with the degree of saturation, for drying and wetting paths	144

4.86	The evolution of the maximum number of grains per water cluster Max Gw (left) and the maximum number of water clusters per grain Max Wg (right), with suction, for drying and wetting paths	145
4.87	The evolution of the maximum number of grains per air cluster Max Ga (left) and the maximum number of air clusters per grain Max Ag (right), with suction, for drying and wetting	145
4.88	The evolution of the maximum number of air cluster per water cluster Max Aw (left) and the maximum number of water clusters per air cluster Max Wa (right), with suction, for drying and wetting	146
5.1	The whole arrangement of triaxial setup inside x-ray cabinet used to perform the three triaxial tests	157
5.2	The triaxial cell in front of x-ray source	157
5.3	A series of photographs illustrating the procedure by which a specimen is prepared in this work. In frame 1, only the lower head (piston) of the setup is seen; then in frame 2 the porous stone is placed, followed by the latex membrane (3); frame 4 and 5 illustrate the mounting of the 2-parts mould around the bottom piston end, porous stone and membrane; frame 6 and 7 show connecting the mold to the vacuum system; then in frame 8 and 9 the inside of the membrane is filled with water; between frames 9 and 10 the material is pluviated into the membrane; frame 10 shows the specimen pluviated inside the membrane followed by installing the ceramic stone at the top (11); frame 12 shows installing the upper part of the cell (the inset shows the upper piston); finally in frame 13 the upper piston is placed at the top of the specimen	158
5.4	A sketch illustrates the triaxial setup and suction system for the saturated drained test	159
5.5	A sketch illustrates the triaxial setup and suction system for the unsaturated tests (drained and undrained)	160
5.6	Triaxial loading system installed inside x-ray cabinet	164
5.7	Stress-strain curves for HN01 (SD), HN02 (UD) and HN03 (UU)	168
5.8	Stress-strain curves for HN04 (UU) and HN05 (SD)	169
5.9	Stress-strain curves for HN06 (SD), HN07 (UD) and HN08 (UU)	170
5.10	Stress-strain curves for all the performed and reference triaxial tests. In Fig 5.10-bottom, the axial stress (σ_1) is normalized by the cell pressure (σ_3) in order to exclude the influence of the different cell pressure	171
5.11	The specimen volume measurement procedure	172
5.12	The volumetric strain for the unsaturated drained test HN02 (UD) and the reference dry test HN09 (D). In the top plot, the bulk volume for HN02 (UD) is computed with respect to the initial volume of the specimen and in the bottom plot the bulk volume for HN02 (UD) is computed with respect to the volume of the specimen after applying the suction (i.e., at $\varepsilon=0\%$) . .	173
5.13	Central vertical slices of the same azimuth, in the trinarized volumes, after removing the upper and the bottom porous stones, for all the loading steps ($\varepsilon=0\%$) in the triaxial test HN02 (UD)	174
5.14	The evolution of the macroscopic porosity (up) and degree of saturation (down) with loading for the triaxial test HN02 (UD)	175

5.15	Porosity map for all the steps of loading in the unsaturated drained triaxial test HN02 (UD). In this figure, n_{\max} and n_{\min} represent the maximum and minimum microscopic porosity, respectively, shown below loading step . . .	176
5.16	Degree of saturation map for all the steps of loading in the unsaturated drained triaxial test HN02 (UD)	177
5.17	Central vertical slices in the porosity map (left), trinarized volume (middle) and degree of saturation map (right) for loading step $\varepsilon=21\%$ in triaxial test HN02 (UD)	177
5.18	Porosity vertical profile (left), central vertical slice in the trinarized volume (middle) and degree of saturation vertical profile (right) for loading step $\varepsilon=21\%$ in triaxial test HN02	178
5.19	Central vertical slices in the water labelled volume, of the same azimuth for all loading steps in the triaxial test HN02 (UD)	180
5.20	Central vertical slices in the air labelled volume, of the same azimuth for all loading steps in the triaxial test HN02 (UD)	180
5.21	The evolution of the number of water clusters (left) and air clusters (right) with loading, for the triaxial test HN02 (UD)	181
5.22	Water clusters size distribution for all loading steps in the triaxial test HN02 (UD)	182
5.23	Air clusters size distribution for all loading steps in the triaxial test HN02 (UD)	182
5.24	The evolution of the normalized V_{\max} for water clusters (left) and air clusters (right) with loading for all loading steps in the triaxial test HN02 (UD) .	183
5.25	A vertical slice in the labelled grain volume for loading step $\varepsilon=21\%$ in triaxial test HN02 (UD) (left) and the number of grains within the specimen shown for all loading steps in the triaxial test HN02 (UD)	184
5.26	Grain size distribution for all loading steps in the triaxial test HN02 (UD) .	184
5.27	The relation between the maximum number of grains in contact with one water cluster (Max Gw) versus the axial strain and the relation between the maximum number of water clusters in contact with one grain (Max Wg) versus the axial strain for the triaxial test HN02 (UD)	185
5.28	The relation between the maximum number of grains in contact with one air cluster (Max Ga) versus the axial strain and the relation between the maximum number of air clusters in contact with one grain (Max Ag) versus the axial strain, for the triaxial test HN02 (UD)	186
5.29	The relation between the maximum number of water clusters in contact with one air cluster (Max Wa) versus the axial strain and the relation between the maximum number of air clusters in contact with one water cluster (Max Aw) versus the axial strain, for the triaxial test HN02 (UD)	187
5.30	X incremental displacement field normalized by the axial strain step, for all the loading steps in the triaxial test HN02 (UD)	188
5.31	Y incremental displacement field normalized by the axial strain step, for all the loading steps in the triaxial test HN02 (UD)	188
5.32	Z incremental displacement field normalized by the axial strain step, for all the loading steps in the triaxial test HN02 (UD)	189
5.33	The rotation of the solid skeleton, for all the loading steps in the triaxial test HN02 (UD)	189

5.34	Volumetric strain field for all the loading steps in the triaxial test HN02 (UD)	190
5.35	Deviatoric (maximum shear) strain field for all the loading steps in the triaxial test HN02 (UD)	190
5.36	Central vertical slices each 10° increment, in the deviatoric strain map of the loading increment $\varepsilon=3-4.5\%$ in the triaxial test HN02 (UD)	192
5.37	Central vertical slices each 10° increment, in the deviatoric strain map of the loading increment $\varepsilon=8-10\%$ in the triaxial test HN02 (UD)	192
5.38	Central vertical slices each 10° increment, in the deviatoric strain map of the loading increment $\varepsilon=18-21\%$ in the triaxial test HN02 (UD)	192
5.39	Horizontal and vertical slices in the deviatoric strain map of the loading increment $\varepsilon=18-21\%$ in the triaxial test HN02 (UD)	193
5.40	angle= 90°	195
5.41	The cubes extracted inside and outside the sheared zone, where porosity and degree of saturation are calculated for the triaxial test HN02 (UD)	197
5.42	Porosity measurements inside and outside the sheared zone for the triaxial test HN02 (UD)	198
5.43	Degree of saturation measurements inside and outside the sheared zone for the triaxial test HN02 (UD)	198
5.44	The two cubes for which porosity and degree of saturation are measured inside and outside the sheared zone. The volume B defines the zone considered as the sheared zone for the triaxial test HN02 (UD)	199
5.45	The measurements of porosity for the cubes inside/ outside the sheared zone, the whole sheared zone (B) and the specimen (A), for the triaxial test HN02 (UD)	199
5.46	The measurements of degree of saturation for the cubes inside/ outside the sheared zone, the whole sheared zone and the specimen for the triaxial test HN02	200
5.47	Stress strain curve and the evolution of Max Wg with loading for the triaxial test HN02 (UD)	202
5.48	The experimental points and the tendency of the relation between Max Wg and the degree of saturation for HN02 (UD)	202

List of Tables

3.1	Recommended parameters for x-ray CT of unsaturated geomaterials	47
4.1	Values of the applied suction and the corresponding global expected degree of saturation for WRT_0 and WRT_1	74
4.2	Trinarization technique thresholds	76
4.3	Macroscopic porosity for WRT_0 and WRT_1 calculated using the traditional technique	85
4.4	Macroscopic porosity for D_0 , D_1 and W_1 calculated using the trinarized volumes	85
4.5	Macroscopic degree of saturation for D_0 , D_1 and W_1 calculated using the trinarized volumes	87
4.6	Mean microscopic degree of saturation extracted from the degree of saturation histogram for the three paths D_1 , W_1 and D_0	99
4.7	Water retention domains for D_1	133
4.8	Water retention domains for W_1	134
4.9	Water retention domains for D_0	135
4.10	angle=90	148
4.11	Cohesion regimes for D_1	150
4.12	Cohesion regimes for W_1	150
4.13	Cohesion regimes for D_0	151
5.1	Loading steps for the three triaxial tests performed in this work	165
5.2	angle=90	167
5.3	Mean microscopic porosity and degree of saturation for all loading steps in the triaxial test HN02	178

List of Symbols and notation

WRC	Water Retention Curve
S_{r0}	Residual water content
s	Suction
n	Porosity
W or S	Water content
S_r	Degree of saturation
e, e_0	Void ratio
Θ	Contact angle
R	Particle size
WRS	Water Retention Surface
CT	Computed Tomography
u_a	Air pressure
u_w or Δu	Water pressure
σ'	Effective stress
σ_x, σ_y and σ_z	Total stresses in x, y, z directions respectively.
σ_1, σ_3	Net major and minor normal stress, respectively
τ_{ij}	Shear stresses, where i and j can be x or y or z
I_{11}, I_{21}, I_{31}	First, second and third stress invariants of the first tensor
I_{12}, I_{22}, I_{32}	First, second and third stress invariants of the second tensor
p	Mean stress
q	One half the deviatoric stress
r	Suction
τ	Shear strength

ε	Axial strain
\acute{c}	Effective cohesion
$\acute{\phi}$	Effective angle of internal friction
ϕ^b	Friction angle associated with the matric suction stress state variable ($u_a - u_w$)
$(\sigma_n - u_a)$	Net normal stress
v_w	Flow rate of water
$k_w(u_a - u_w)$	Coefficient of permeability (hydraulic conductivity) with respect to water phase as a function of suction ($u_a - u_w$)
$\partial h / \partial y$	Hydraulic head gradient in the y-direction
ΔP	Variations of the suction
σ_c	Cohesive stress
c	cohesion
GB	Glass Beads
k	Inter-particles distance
MDM	Micro-Directional Models
DEM	Discrete Element Method
PVE	Partial volume effect
T_{min}	Minimum value in the valley of a histogram of two phases reconstructed image
T_1	Minimum value in the valley of a the histogram of air-water reconstructed image
T_2	Minimum value in the valley of a histogram of water-grain reconstructed image
P_a	Partial threshold for air
P_{w1}, P_{w2}	Partial thresholds for water
P_g	Partial threshold for grains
STD	STandard Deviation
V	Filtering threshold of STD

T_a	Tolerance threshold for air
T_{w1}, T_{w2}	Tolerance thresholds for water
T_g	Tolerance threshold for grain
REV	Representative Elementary Volume
V_v	Pore volume
V_{wt}	Pore water volume
V_t	Total volume of the specimen
px	Pixel
μm	$1\ \mu\text{m} = 0.001\text{mm}$
Δn	Stability criterion for porosity (change in porosity)
ΔS_r	Stability criterion for degree of saturation (change in degree of saturation)
Id	Identification number
DAT	File type associated primarily with ‘Data’
$V_{w\text{max}}$	Volume of the biggest water cluster
V_{wt}	Total volume of the water within the specimen
IFA	InterFacial Area
a_{wn}	Effective specific interfacial area
a_n	Air 3D area
a_s	Grains 3D area
a_w	Water 3D area
TSV	TSV file type associated primarily with ‘Tab Separated Values’
DIC	Digital Image Correlation
NCC	Normalized Correlation Coefficient
I_1, I_2	3D reference and deformed images respectively
x, y, z	Coordinates of the images
U, v, w	Integer displacement values
$\Delta x, \Delta y, \Delta z$	Displacement on X, Y and Z

WRB	Water Retention Behaviour
ρ_s	Density of soil particles (g/cm ³)
C_u	Coefficient of uniformity
e_{max}, e_{min}	Maximum and minimum void ratio
$\gamma_{max}, \gamma_{min}$	Maximum and minimum specific weight (g/cm ³)
D_{50}	The medium grain size (mm)
SEM	Scanning Electron Microscope image
WRT ₀	Water Retention Test performed by Ismael Riedel
D_0	Drying path performed by Ismael Riedel
WRT ₁	Water Retention Test performed by the author
D_1	Drying path performed by the author
W_1	Wetting path performed by the author
PMMA	PolyMethylMethAcrylate (the material of the cell)
s_0	Water pressure set as zero suction
H	The Height of water tank used in WRT ₁ to apply suction (suction in cmH ₂ O)
P	Water pressure value applied by the pressure controller
s_{air}	Air entry value
$S_{r_{exp}}$	The global degree of saturation taken from the reference curve (%)
m_s	The weight of the dry sand
V_s	Volume of the grains
N_a	Number of voxels that represent air in the trinarized images
N_w	Number of voxels that represent water in the trinarized images
N_g	Number of voxels that represent grains in the trinarized images
ΔV_w	Water volume exchange
Ref WRC	Reference water retention curve
n_{max}, n_{min}	Maximum and minimum porosity

h	Height of the specimen
d	Diameter of the specimen
V_{\max}	Volume of the biggest fluid cluster
EqD	Equivalent diameter of a sphere having the same volume as the cluster
V_{mean}	The mean volume of all air/water cluster within the specimen
$V_{w\max}$	Normalized volume of the biggest water cluster
$V_{a\max}$	Normalized volume of the biggest air cluster
V_{at}	Total volume of air within the specimen
Max Gw	Maximum number of grains per water cluster
Max Wg	Maximum number of water clusters per grain
Max Ga	Maximum number of grains per air cluster
Max Ag	The maximum number of air clusters per grain
Max Wa	Maximum number of water clusters per air cluster
Max Aw	Maximum number of air clusters per water cluster
s_1	The value of suction at which WRC reaches a constant degree of saturation before the residual state
$S_{r\max}, S_{r\min}$	The maximum and minimum degree of saturation
$\epsilon_x, \epsilon_y, \epsilon_z$	Strains over X, Y and Z

Chapter 1

Introduction

1.1 Background

Over the last two decades, major efforts have been made to analyze the influence of the presence of different pore fluids within the soil on its behaviour. Despite major achievements, the behaviour of unsaturated soils is still far from being completely understood.

Unsaturated soils are profusely found in nature, and their behaviour is different from the saturated and dry soils. The main differences between these soils are related to shear strength, stiffness as well as volume change behaviour (e.g. shrinkage, swelling, collapse). When decreasing and increasing water content, which is related to increasing and decreasing soil suction, the response of the soil changes significantly. The importance of the relation between soil suction and water content within the soil, which is represented by the so-called "water retention curve", is not only in giving insight of soil-water interaction but it is also used to estimate the shear strength and the effect of deformation with respect to the water retention capability. Some typical engineering problems of unsaturated soils are listed in the following:

- Irrigation and drainage problems in agronomy.
- Construction of dams, dikes and tunnels, slope stability and bearing capacities in construction engineering.
- Soil liquefaction in earthquakes engineering.
- Waste disposal and contaminant transport in environmental engineering.

The above given problems cannot be addressed using the conventional principles of saturated and dry soil mechanics, therefore, it was needed to understand, analyze and develop new concepts when working with unsaturated soils using proper tools, among them appropriate theoretical approaches and new testing methods with the capability of inspecting new aspects of unsaturated soils behaviour.

1.2 Objectives

The main motivation for the present research project is to achieve an improved understanding of the multi-scale complexities of the retention and hydro-mechanical behaviours of

unsaturated soils. These complexities are found at the microscopic scale (i.e., local, grain or water clusters scale) and discrete scale (i.e., phases interfaces scale) deep in the soil structure. Working at the microscopic-discrete scales allows explaining the macroscopic observations (at the soil specimen scale) related to soil behaviour, and considers the homogeneity/heterogeneity of the soil with respect to water distribution. Moreover, when analyzing the hydro-mechanical behaviour of the soil, taking into account the effects of possible changes of the mechanical loading to which the soil is subjected is a major subject. Indeed, increasing the loading might induce a change in the homogeneity/heterogeneity with respect to porosity and water distribution due to the induced deformations. These two reasons presented the necessity in this research work to investigate the retention and hydro-mechanical behaviours of the soil at the microscopic-discrete scales.

To achieve the aimed goal in this research, water retention behaviour is analyzed by determining the water retention curve and surface of Hostun sand microscopically under several initial conditions, i.e., different porosities, and different loading path directions (drying and wetting). The hydro-mechanical behaviour of saturated and unsaturated Hostun sand is investigated at different porosities and conditions (i.e., drained and undrained) through a triaxial campaign.

In order to acquire a better understanding of retention and hydro-mechanical behaviours at the microscopic-discrete scales, new experimental and image processing tools are developed. New retention and triaxial cells that allows testing relatively small Hostun sand specimens are built. Suction is applied using tensiometry. Specimens are prepared using water pluviation technique to ensure having completely saturated specimens at the beginning of the tests. An innovative mechanical loading system is used for the triaxial tests. X-ray computed tomography, is used to scan the variation in porosity and water phase distribution within the soil specimen for different values of suction and mechanical loading. A region growing segmentation technique (trinarization technique), is used to separate the three phases within the unsaturated soil specimens. Separation procedure allowed performing local measurements of porosity and degree of saturation using a developed mapping code, within a Representative Elementary Volume (REV) of a size determined using a statistical tools. Several microscopic-discrete analyses are developed to follow the evolution of fluid phase (i.e. water and air phases) with loading (i.e., suction and mechanical loading). Using the microscopic-discrete analyses, the number of fluid clusters, continuity/discontinuity of the fluid phase, the number of phases interfaces (or contacts) including the solid phase (i.e., grains) and the interfacial area (water-air surface) are defined. Digital image correlation is used to verify the presence of deformation due to suction application in retention test and to perform deformations measurements at each increment of loading in the triaxial test.

At the end, the use of former tools in this doctoral work allowed achieving the following:

- Providing appropriate equipments, tools and techniques for the multi-scale investigation and characterization of the retention and hydro-mechanical behaviours of unsaturated granular materials.
- Determining water retention curve, surface and hydraulic domains (water retention domains) for unsaturated granular materials, at different conditions (initial porosity and loading paths) and analyzing hysteresis phenomenon at the microscopic-discrete

scales.

- Determining stress- strain and volumetric response for unsaturated granular materials, at different conditions (i.e., initial porosity and drained-undrained conditions).
- Analyzing the effect of suction on water content change and on the mechanical behaviour of the unsaturated granular materials (e.g., shear strength, homogeneity/heterogeneity of water distribution, cohesion).
- Assessing the relation between the macroscopic and the microscopic-discrete behaviours of unsaturated granular materials.
- Deriving reliable experimental data that can be used for the validation, improvement and development of the constitutive equations and model parameters for numerical simulations of engineering problems.

The objective of this research project can be extended to include different engineering aspects. For example, in agricultural engineering, this work addresses a key issue related to the marked impact of machinery loading and suction variations induced by soil tillage on soil structural properties. In addition this project can be applicable to civil engineering such as seasonal wetting-drying induced deformation of natural slopes, landslides and marine structures.

1.3 Outlines of the thesis

This thesis contains six chapters. A brief description of the content of each chapter is given in the following.

After this introduction, **chapter 2** reviews the current state of knowledge concerning the experimental studies and some constitutive modelling of retention and hydro-mechanical behaviours of unsaturated soils. Additionally, chapter 2 introduces the existing gap in knowledge and outlines the expected contribution of the present study to fill this gap.

In **chapter 3**, the developed experimental and data processing tools used for the multi-scale investigation of the retention and hydro-mechanical behaviours of an unsaturated sand are introduced. X-ray tomography, trinarization technique, REV analysis, porosity and degree of saturation mapping, microscopic-discrete analyses and digital image correlation technique are presented.

Chapter 4 describes our study of water retention behaviour of unsaturated Hostun sand. The material tested, the cell, suction application technique, specimen preparation technique and the experimental procedure are discussed in this chapter. Moreover, the methods and tools introduced in chapter 3 are used to analyze retention behaviour of Hostun sand specimens. As a result, deformation is inspected for the water retention test. Local measurements of porosity and degree of saturation and water retention curve are acquired. The evolution of the number of fluid clusters, fluid phase continuity/discontinuity and contacts with suction are analyzed. The evolution of the effective interfacial specific area with the degree of saturation is checked. The relation between suction, porosity and degree of saturation (water retention surface), water retention domains, hysteresis phenomenon and soil cohesion are investigated.

Chapter 5 presents the characterization of the hydro-mechanical behaviour of unsaturated Hostun sand by means of triaxial test. The material tested, the cell, specimen preparation technique, suction application technique, the experimental procedure, loading system and procedure and the experimental program are described first. Then, the results obtained using the experimental and image processing tools presented in chapter 3 are introduced. The stress-strain curve, volumetric strain, local measurements of porosity and degree of saturation and the deformation are obtained. Moreover, the evolution of the number of fluid clusters, fluid phase continuity/discontinuity, contacts, volume change and water distribution with the mechanical loading are analyzed.

Finally, **chapter 6** summarizes the concluding remarks and proposes outlooks for further studies.

Chapter 2

Literature review of unsaturated soils mechanics

2.1 General overview

This chapter introduces the main concepts related to unsaturated soils, in the framework of this doctoral research. The water retention properties of unsaturated soils are presented in section 2.2 including unsaturated soils definition, soil suction, water retention curve, influence of grain size and shape on water retention behaviour, water retention surface, hysteresis phenomenon and water retention domains. Some typical features of the mechanical behaviour of unsaturated soils are discussed in section 2.3, including shear strength, capillary cohesion and volume change and water distribution. An attempt to describe the numerous and significant recent advances in the investigation of the behaviour of unsaturated soils, including the contributions of this research, is proposed in this chapter.

2.2 Water retention behaviour of unsaturated soils

2.2.1 Definition of unsaturated soils

Unsaturated soils consist of solid and fluid phases (i.e., liquid and gas). The solid phase represents the particles of the soil which differentiate depending on the soil type (sand, clay, silt and gravels). Fluid phase occupies the pores volume within the soil. The pores of an unsaturated soil are filled with liquid (as water) and gas (as air). Fig 2.1 shows a sketch of unsaturated soils, where the three phases: solid, liquid and gas are present.

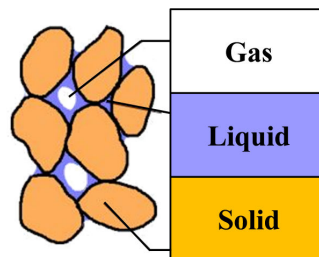


Figure 2.1: A sketch of gas, liquid and solid phases in an unsaturated soil

This research work is conducted on unsaturated granular materials where three phases: grains, water and air are present.

In the following some characteristics of unsaturated soils are presented. These characteristics distinguish the unsaturated soils from the dry soils, where the pores volume is completely filled with gas phase, and the saturated soils, where the pores volume is completely filled with liquid.

2.2.2 Soil suction

In saturated soils, water pressure is positive with respect to the atmospheric pressure and the liquid is in compression. While, in unsaturated soils, the hydrostatic water pressure is negative with respect to the atmospheric pressure and therefore the liquid is in tension. This tension, generated through the interaction of soil water and the soil matrix, is called suction and it represents the pressure difference between the soil water and the surrounding gas (see Fredlund et al. (2012, 2014)):

$$s = u_a - u_w \quad (2.1)$$

In the above relation, (s) denotes the suction, and (u_w) and (u_a) are water and air pressure, respectively. In most cases, the gas pressure is the atmospheric pressure and hence, the suction is equal to the negative water pressure.

In the vicinity of soil particles in unsaturated soils, the soil water is divided into capillary water and adsorbed water. Capillary action is a result of the water surface tension. The adsorbed water is tightly bonded to the soil particles and could be considered as a part of the solid skeleton. At equilibrium, where water flow in and out the soil is stopped, it is reasonable to assume that water has the same pressure everywhere within the soil.

Different methods can be used to apply and measure the suction, depending on the range of the demanded suction. A description of the methods for measuring and applying suction, in the laboratory or in-situ, is given by Delage et al. (2008-b) and Romero (2009). Tensiometry has been widely employed in laboratory tests to measure the soil suction (see Sreedeeep et al., 2003; Boso, 2005; Marinho et al., 2008). The tensiometer represents a significant advance towards the measurement of soil suction up to 1.5 MPa. Another technique to apply suction is the axis translation method, which can be used by imposing a positive air pressure inside the specimen and controlling the water pressure (see Eko, 2004; Vanapalli et al., 2008; Wayllace et al., 2011). This technique is used for suction range 0 to 500 kPa. The osmotic technique is used also for suction application up to 10 MPa (see Delage, 2008-a; Tang et al., 2010). The vapour equilibrium technique, allows the application of very large suctions (larger than 50 MPa), based on the control of the relative humidity of the atmosphere surrounding the specimen (see Tang et al., 2005; Blatz et al., 2009).

In this work, in order to apply and measure suction, tensiometry technique is used. The range of the demanded suction is from 0 kPa to 7 kPa (see chapter 4, section 4.2.3).

2.2.3 Water Retention Curve

Water retention curve is an important constitutive law that governs the behaviour of unsaturated soils. It represents the relation between the two state variables: soil suction (s)

and water content (w) or the degree of saturation (S_r) (see Van Genuchten, 1980; Wildenschild et al., 2004; Culligan et al., 2006; Kaestner et al., 2007).

When a saturated soil is being desaturated, air begin to enter the soil at a specific value of suction. This value is called air entry value (s_{air}), and it is defined as the suction value at which air enters the soil. When increasing the suction beyond (s_{air}), water content within the soil decreases to reach residual degree of saturation (S_{r0}) or water content. In order to extract the residual water content, suction higher than 1,000,000 kPa is needed to be applied (see Vanapalli et al., 1998). A schematic plot of water retention curve is shown in Fig 2.2. On this curve, air entry value (s_{air}) and residual water content (S_{r0}) are presented.

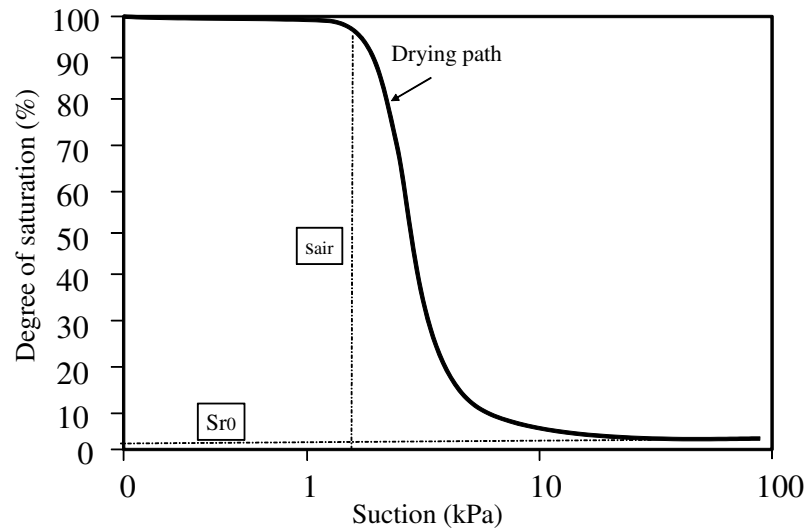


Figure 2.2: A schematic plot of water retention curve during drying process, that shows the air entry value (s_{air}) and the residual water content (S_{r0})

Different studies have been performed to obtain water retention curve experimentally (see Alla, 2009; Beddoe, 2009; Lins, 2010; Heidarian, 2012) in order to investigate the macroscopic water retention behaviour of the tested soils. Other studies have used the macroscopically obtained water retention curve to investigate the hydraulic conductivity (see Cui et al., 2008) and shear strength (see Vanapalli et al., 2000) of unsaturated soils. Numerically, different mathematical forms have been presented to obtain water retention curve based on macroscopic measurements of suction and degree of saturation (see Sun et al., 2008; Main, 2011).

2.2.4 Influence of grain size and shape on water retention behaviour

Water retention curve is not a unique property of an unsaturated soil. It differentiates macroscopically depending on the soil porosity. For different types of soil, water retention curves differ from each other depending on soil structure or arrangement of the particles as well as the porosity. For example, Fig 2.3 shows water retention curves for three different types of soil, of different porosities and structures: sand, silt and clay. In this figure, when decreasing the porosity of the soil, a shift for higher values of suction is obtained for WRC (i.e., higher value of suction is needed to desaturate clay and silt than for sand).

However, the macroscopic characteristics of the soil (e.g., porosity) are not enough to describe retention behaviour of the soil, which can be influenced by several local characteristics such as the distribution of grains and pores (see Nimmo, 2004; Dorin et al., 2011).

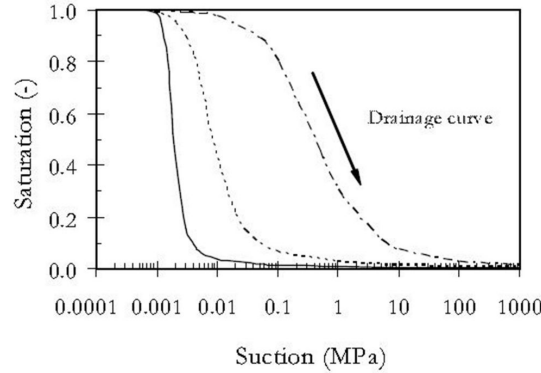


Figure 2.3: Water retention curves for different types of soil: sand, silt and clay during drying process (from Fredlund et al. (2012))

For the same soil type, different pores size and shape distribution can be obtained depending on the grain size and shape distribution which is influenced by specimen preparation technique. Consequently, different water retention behaviour can result (e.g., different water retention curves and distribution of water phase within the soil (homogeneous or heterogeneous)). The influence of particle size distribution can be seen in Fig 2.3, where clayey soil, of finer particles than sandy soil, retains water more than the sandy soil, thus higher suction is needed to desaturate the clayey soil.

When suction is applied, small pores retain water more than the big pores, thus, the big pores are desaturated before the small pores. In other words, at air entry value, relatively big pores are influenced and the residual water content is retained in the small pores. Consequently, higher air entry value (i.e., higher suction) is needed to desaturate the finer soils and higher residual water content is obtained for them.

The gradation of the soil also influences its retention ability. If the soil is poorly graded, i.e., narrow range of sizes for soil particles, lower suction is needed to be applied to desaturate the soil than for the well graded soils of wide range of sizes for soil particles (see Winfield, 2000), due to the existence of smaller pores in the well graded soils.

For the influence of particles shape, Feia et al. (2014) have investigated water retention behaviour of sub-rounded Fontainebleau sand NE34 and sub-angular Hostun sand HN34. These two materials have similar grain size distributions and mean grain sizes ($D_{50}=0.21\text{mm}$). Through drying process, Feia et al. (2014) have found that the suction needed to desaturate the sub-rounded Fontainebleau sand is higher than the suction needed to desaturate the sub-angular Hostun sand. This is due to having smaller size of the pores for the sub-rounded particles compared to the sub-angular particles, i.e., Fontainebleau sand has a D_{50} of the pore size distribution of 0.104mm while Hostun sand has a D_{50} of the pore size distribution of 0.32 mm .

The influence of grain size distribution on water retention behaviour of the soil has been analyzed also in different numerical researches. Maaitah (2012) has developed a numerical model based on experimental results to obtain WRC of unsaturated glass beads.

He obtained different WRCs for the same particle size (R) of the beads but different void ratio (e), see Fig 2.4-top. In this figure, a shift for lower suction values (or capillarity height as presented in Fig 2.4) is obtained when increasing the void ratio of the soil. However, for the same void ratio, and different particle sizes, Maaitah (2012) has showed that different WRCs can be obtained. The obtained results, presented in Fig 2.4-bottom, show that when increasing the size of the particles of the soil, a shift for lower values of suction is obtained for WRC.

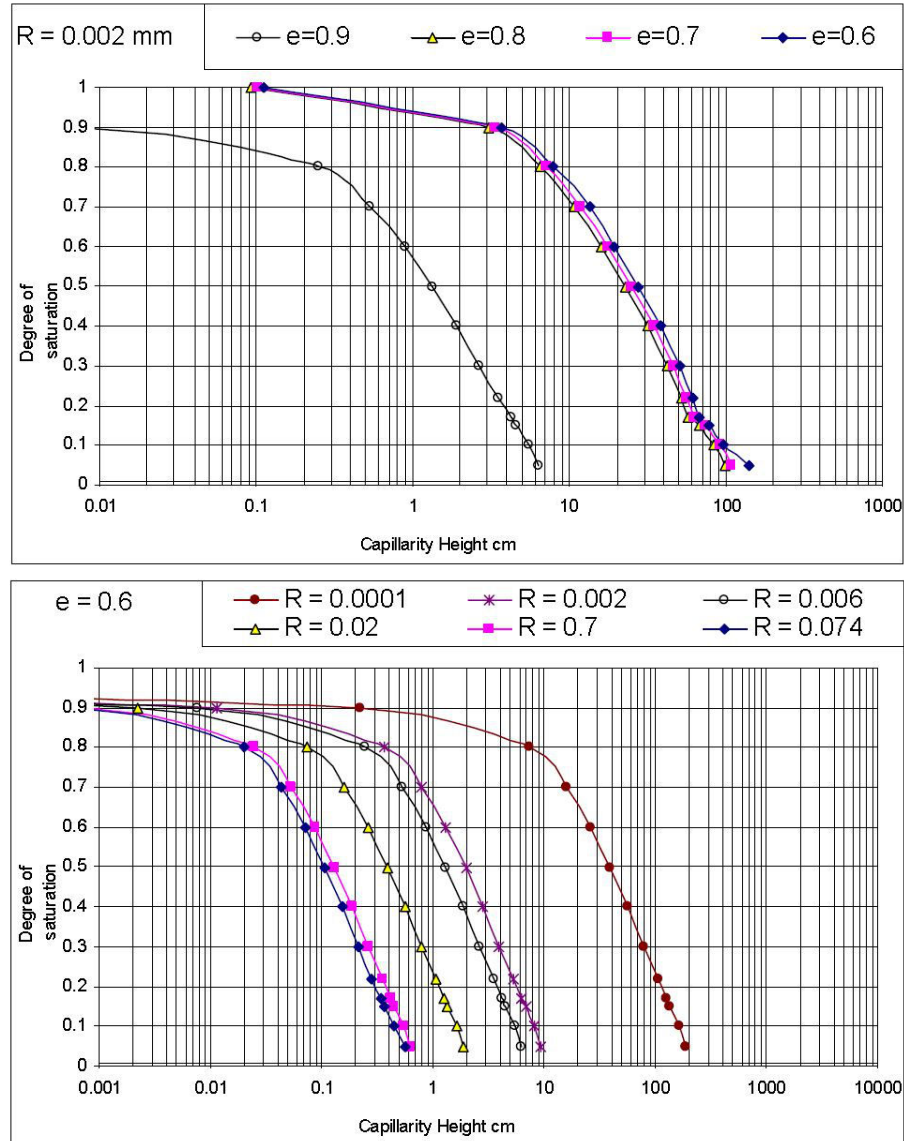


Figure 2.4: WRCs for the same soil type (fine sand), and same particle size (R) but different void ratio (e) in the top and WRCs for the same soil type and same void ratio but different particle sizes in the bottom (from Maaitah (2012))

Gras (2011) has presented water retention sensibility to rupture distance (inter-particle distance (D_{rupt})) and grain radius (R) for poly-dispersed granular media using Discrete Element Method (DEM) analysis.

The results obtained by Gras (2011), presented in Fig 2.5 show that water content increases with the decrease of the grain radius and the increase of the inter-particle distance.

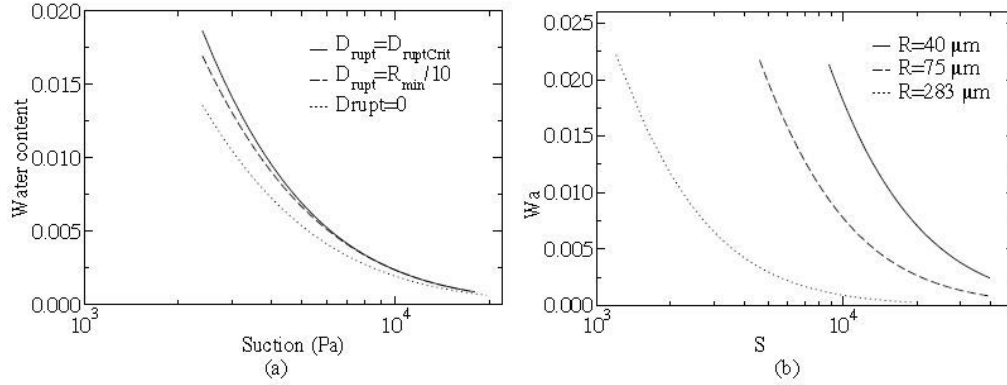


Figure 2.5: WRCs of poly-dispersed granular media for a) different inter-particle distance (D_{rupt}) and b) different grain radii (R) (from Gras (2011))

The latter observations of the influence of grain size distribution and other grain-scale characteristics of the soil on water retention behaviour of the soil have raised the necessity of working at the micro scale in this doctoral research. In order to do that, new advanced experimental methods that allow the microscopic evaluation of the structure, the physical and mechanical properties of unsaturated soils are needed to be used. In this work x-ray Computed Tomography (CT) has been used. As this technique is the main experimental tool used in this work, a detailed description of this technique including examples of its application in different fields and researches can be found in chapter 3, section 3.2.

2.2.5 Water Retention Surface

The relation between suction and degree of saturation (i.e., WRC), for the same soil type, differentiates macroscopically depending on the soil porosity (or void ratio). For example, Salager (2007) has obtained different WRCs, numerically and experimentally, for different initial void ratio (e_0) of clayey silty sand soil. Vanapalli et al. (1999) also have obtained different WRCs, experimentally, for different void ratio (e_0) of sandy clay till. The obtained results by Salager (2007) and Vanapalli et al. (1999), presented in Fig 2.6, show that when increasing the void ratio of the soil, a shift for lower values of suction is obtained for WRC. Similar results can be found in Beddoe et al. (2011).

However, most studies of water retention behaviour ignore water retention behaviour dependency on the porosity. According to Romero et al. (2008), Tarantino et al. (2008) and Wang et al. (2013) porosity can be considered as a state variable, as changes in void volume lead to changes in the degree of saturation.

In order to consider the influence of porosity on WRC, Water Retention Surface (WRS) defined as the relation between suction, porosity (or void ratio) and degree of saturation (or water content) has been investigated.

Salager et al. (2010) have investigated the relation between the three state variables: suction (s), void ratio (e) and water content (w) experimentally and analytically, for clayey silty sand in compaction tests condition. Similarly, Main (2011) has developed a numerical model in order to incorporate the influence of void ratio on water retention curve. Fig 2.7

shows water retention surface obtained by Salager et al. (2010) in terms of water content and degree of saturation, and by Main (2011) in terms of degree of saturation.

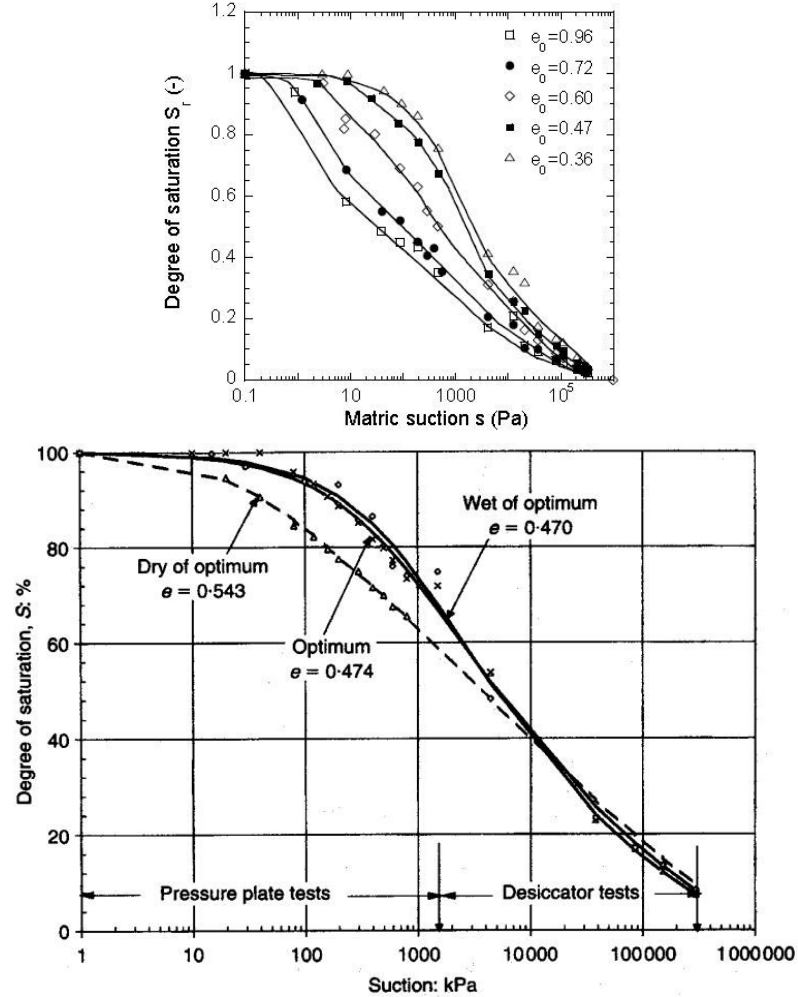


Figure 2.6: WRCs for the same soil type but different void ratio, from Salager (2007) (top) and from Vanapalli et al. (1999) (bottom)

To achieve better understanding of WRS, the relation between each two of the three state variables has been investigated and analyzed by different authors. The results for the relation between suction and water content projected on the plane $e=\text{constant}$, obtained by Salager et al. (2010) are presented in Fig 2.8.

As shown in Fig 2.8, different WRCs can be obtained for the same tested material but different void ratio. Similar results for the relation between suction and water content or degree of saturation for different void ratio are presented earlier in Fig 2.6.

For the relation between water content and void ratio at constant suction, i.e., $s=\text{constant}$, Salager et al. (2010) have found that when increasing the void ratio (e), water content within the soil (w) increases, as shown in Fig 2.9-top), and thus the degree of saturation (S_r) increases ($S_r = w \times G_s / e$, where G_s is the specific density of the solid phase).

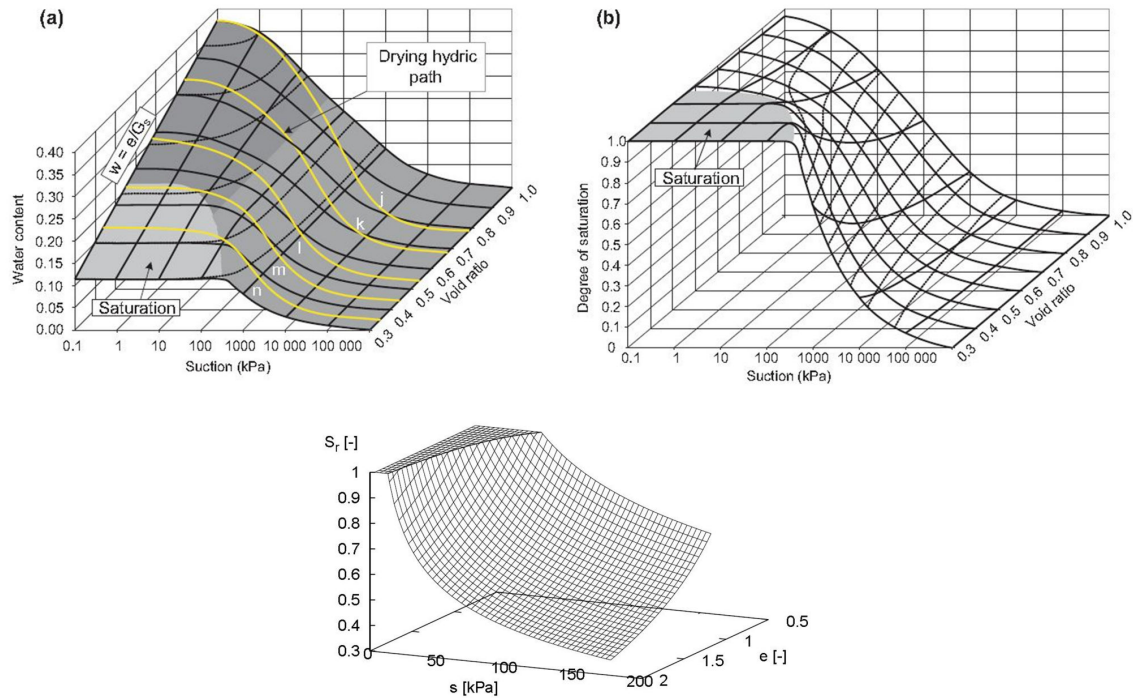


Figure 2.7: WRS for the drying path obtained by Salager et al. (2010) in terms of (a) water content and (b) degree of saturation (top) and WRS obtained by Main (2011) in terms of degree of saturation (bottom)

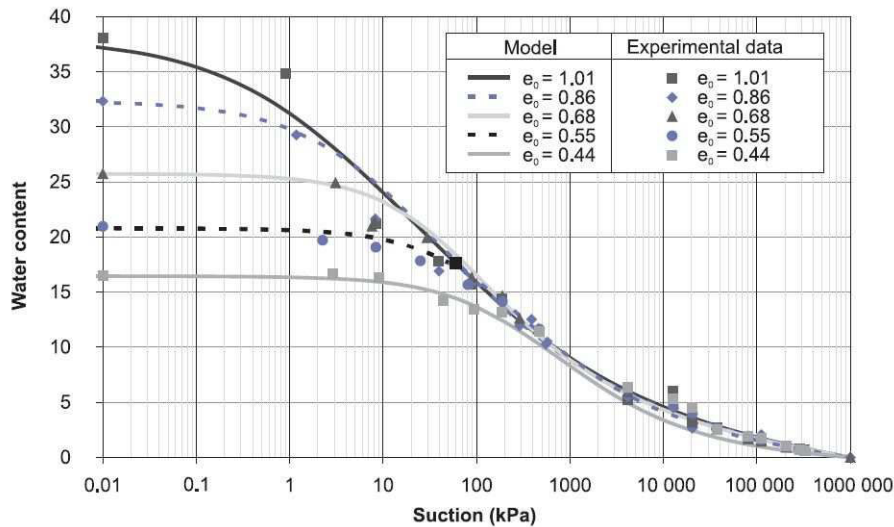


Figure 2.8: The experimental and numerical results for the relation between suction and water content projected on the plane $e=\text{constant}$ (from Salager et al. (2010))

Similarly, Plaisted (2014) has investigated experimentally the relation between Volumetric Water Content (VWC) and void ratio (e) at different ranges of suction, in wet compaction condition for a clayey soil. The results presented in Fig 2.9-bottom, shows that for high range of suction, when increasing (e), (VWC) decreases, while for the low and middle ranges of suction, the relation between (VWC) and (e) follows the same trend found by Salager et al. (2010) in Fig 2.9-top, i.e., when increasing (e), (VWC) increases.

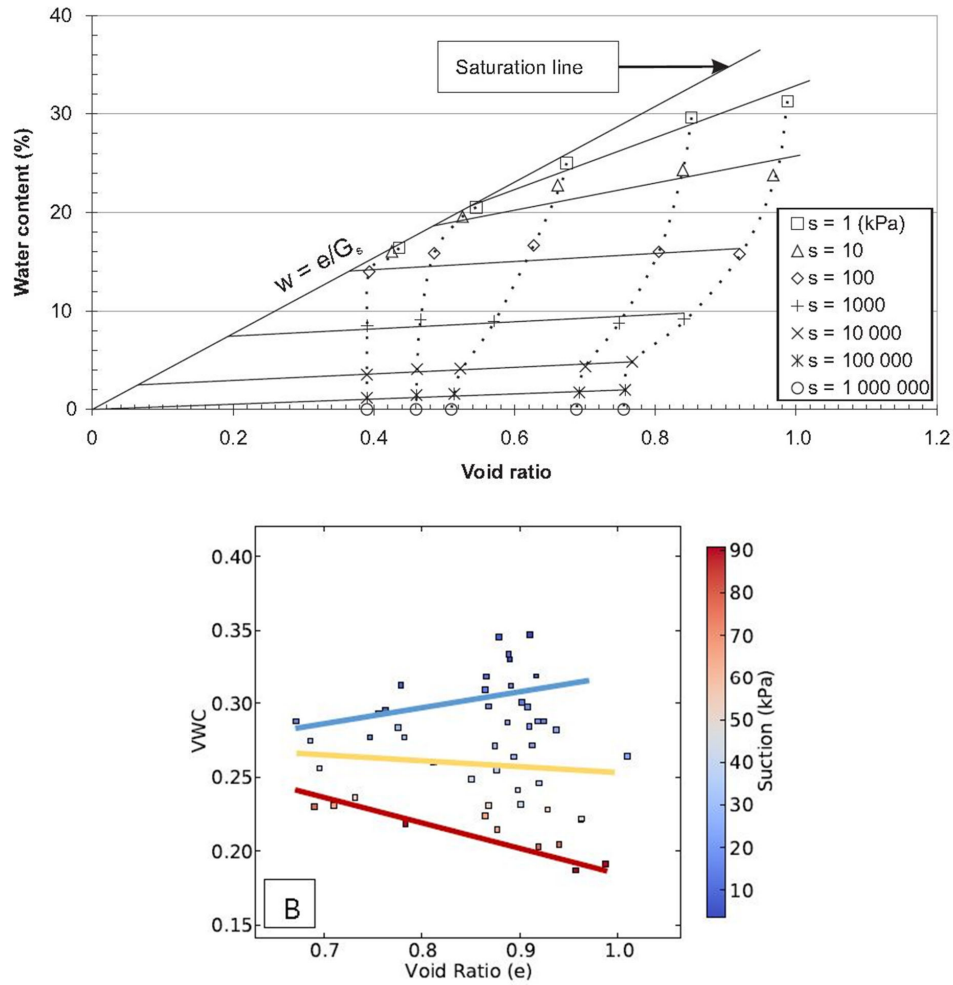


Figure 2.9: The relation between water content and void ratio, projected on the plane $s=\text{constant}$ from Salager et al. (2010) (top) and the relation between Volumetric Water Content (VWC) and void ratio (e) for different ranges of suction from Plaisted (2014) (bottom)

It is important to note that the latter results for the relation between water content and void ratio have been obtained for a drained compaction test. However, if the soil was tested in normal conditions (without compaction), the increase of porosity (or void ratio) will induce an increase in the void volume and thus the degree of saturation, which represents the ratio of water volume to void volume, will decrease (see Gallipoli (2012)).

For the relation between suction and void ratio projected on the plane $S_r=\text{constant}$, the result obtained by Salager et al. (2010) are presented in Fig 2.10. These results shows that void ratio decreases as increasing the suction (i.e., higher suction is needed to desaturate soils of lower void ratio).

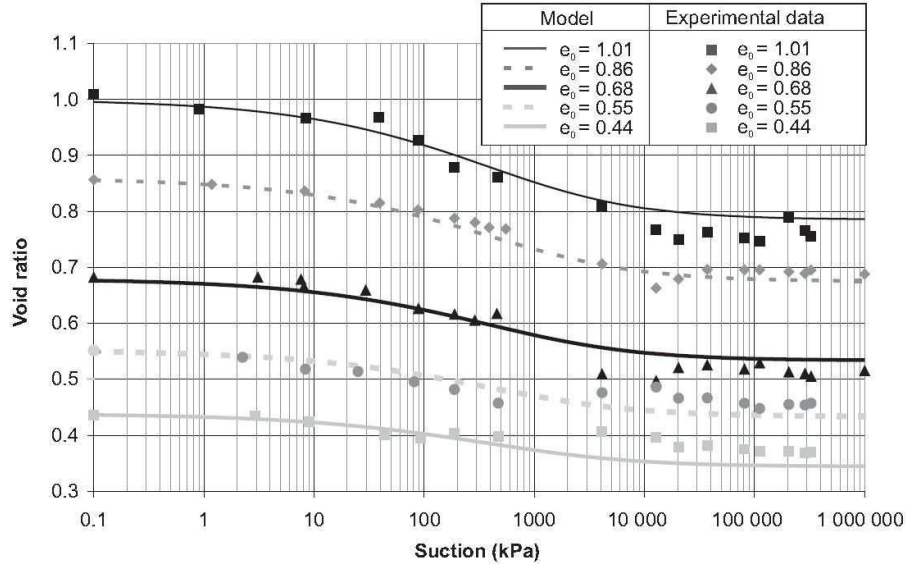


Figure 2.10: The experimental and numerical results projected on the plane $S_r = \text{constant}$ (from Salager et al. (2010))

As has been shown, all the latter presented studies have used the macroscopic measurement of suction, porosity and degree of saturation, performed for different specimens to obtain and analyze WRS. On the other hand, several studies have analyzed the influence of porosity variation on WRC, microscopically. Wildenschild et al. (2002) and Costanza-Robinson et al. (2011) have showed that the local measurements and changes of porosity can reveal water retention characteristics of partially saturated sand. Wildenschild et al. (2005) and Lu et al. (2006) had provided microscopic experimental results that describe the distribution of porosity and degree of saturation over the total volume of the studied soil specimens. Riedel et al. (2012), Kaddhour et al. (2013) and Salager et al. (2014) had investigated the relation between the local measurements of porosity and degree of saturation, performed for one soil specimen, in order to reach better understanding of WRS at the local scale (these results are to be discussed and presented later in chapter 4).

In this work, WRS is obtained and analyzed locally using the range of microscopic measurements of porosity and degree of saturation, performed for one specimen (see chapter 4, section 4.4.2). This allows incorporating the influence of grain size distribution on WRS.

2.2.6 Hysteresis phenomenon

The relation between suction and water content within the soil follows two main paths: drying path and wetting path. In drying path, a saturated soil is being desaturated, i.e., suction is increased and water content is decreased, while in wetting path, a soil of residual water content (or dry soil) is being saturated, i.e., suction is decreased and water content is increased. In between these two paths, suction value can be decreased for the drying path, or increased for the wetting path, to obtain the so called "scanning paths". When wetting a soil of residual water content, water volume increases within the soil to reach relatively high water content where most of the pores of the soil are filled with water.

However, depending on the distribution of the grains and the pores, the soil might not get completely saturated (i.e., $S_r=100\%$), due to the formation of trapped air. If the net of pores within the soil is connected by relatively big pores, pores of trapped air will not be formed. This behaviour of the soil (i.e., of not getting completely saturated when wetting), is described as hysteresis phenomenon. A sketch of this phenomenon and the scanning paths is shown in Fig 2.11.

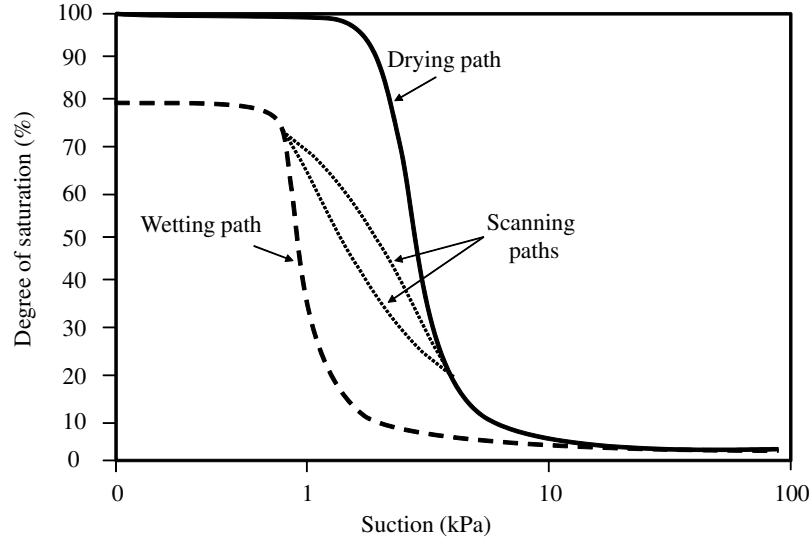


Figure 2.11: A sketch that illustrates hysteresis phenomenon and the scanning paths

Hysteresis phenomenon has been analyzed in several studies: numerically to present a water retention model capable of predicting the hysteretic response of the soil during both wetting-drying cycles (see Nimmo, 1992; Canone et al., 2008; Izady et al., 2010; Gallipoli, 2012; Lin et al., 2012; Zhou, 2013) and experimentally to achieve better understanding of this phenomenon (see Maqsoud et al., 2004; Karunarathna et al., 2010; Uchaipichat, 2010-a).

In the context of granular material, such as sand used in this study, hysteresis is attributable to combination of the ink-bottle effect and the contact angle hysteresis (see Lins (2010)). In the following, a short description of these two effects, performed schematically, is given.

Ink-Bottle effect

The ink-bottle effect is a tentative physical explanation of the fact that, the volume of water within the soil depends on the loading path, i.e., the volume of water within the soil during drying is larger than during wetting. A sketch illustrating ink-bottle effect is shown in Fig 2.12.

While water is drained from the pores (during drying), narrow necks positioned higher in the soil profile, tend to keep the water in the lower large filled with water part as shown in Fig 2.12-a. During wetting, however, narrow necks positioned lower in the soil profile, tend to keep water from flowing into the higher large pores, empty of water as depicted in Fig 2.12-b. Thus, referring to Fig 2.11, at a given suction, water content during drying will

be larger than during wetting (see Flekky et al., 2002; Maqsoud et al., 2004; Szymkiewicz, 2013). This suggests that with hysteresis, the soil has a memory of its wetting and drying history and this history influences the retention ability of the soil.

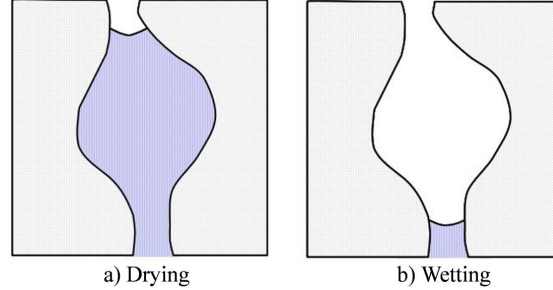


Figure 2.12: Schematic illustration of the ink-bottle effect during (a) drying and (b) wetting (Loll et al. (2000))

Contact angle

For an unsaturated soil, one of the two phases, liquid and gas, will preferentially wet the solid phase. This is decided depending on the contact angle (θ) (the angle measured through the liquid, where a liquid/gas interface meets a solid surface, as shown in Fig 2.13). The fluid for which $\theta < 90^\circ$, is said to wet the solid and is called the wetting fluid. While the fluid for which $\theta > 90^\circ$, is called non-wetting fluid. In the case of having water and air as fluid phase, water phase is considered as a wetting fluid while air is considered as non-wetting fluid, (see Zisman, 1964; Likos et al., 2002; Eral et al., 2013; Yuan et al., 2013). Fig 2.13 shows schematically the definition of contact angle for wetting and non-wetting phases, where (σ) is the surface tension (i.e., liquid-gas interfacial energy).

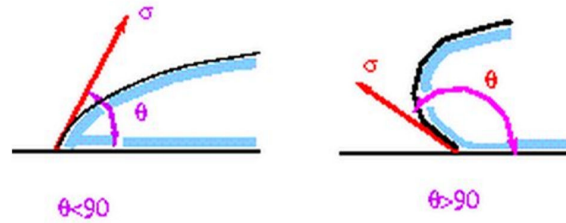


Figure 2.13: Schematic illustration of contact angle hysteresis. A wetting fluid (left) and a non-wetting fluid (right)

In the latter description of ink-bottle and contact angle effects, only schematic analyses were considered. However, to achieve better understanding of these two effects, present and active at the pore scale, a quantitative and qualitative description considering pore net characteristics need to be provided.

Some studies have presented numerical results showing the influence of inter-particle distance and solid-liquid contacts, as pore geometry characteristics, on WRC. Gan et al. (2013) have presented a particle-water discrete element based approach that captures the hysteresis of water retention during wetting and drainage at the level of pores and grains. They have found that for the tested materials with relatively mono-disperse grain size; the hysteresis of water retention arises from the dynamics of solid-liquid contact angles as

a function of local liquid volume changes. Gras (2011) has investigated the influence of contact angle and the inter-particle distance on WRC for poly-dispersed granular media using discrete element analysis. He has found that the contact angle is bigger during wetting than during the drying. Water retention increases with the decrease of the contact angle and the increase of inter-particle distance. Moreover, liquid bridges may only exist at zero inter-granular distance during wetting. As a consequence, hysteresis phenomenon presented in the decrease of water retention during wetting can be explained.

Yet, the latter presented numerical studies did not highlight the gap between the experimental and numerical results, when analyzing hysteresis phenomenon. This gap can be filled by considering the real nature of the material and its pore size and shape distribution.

In this context, this doctoral research, provides experimental measurements and qualitative characterization of hysteresis phenomenon taking into consideration the influence of pore-grain and pore-pore interaction (i.e., fluid-solid and fluid-fluid contacts respectively) and pore net connectivity (fluid phase continuity) at the grain scale.

2.2.7 Water retention domains

Water retention domains (regimes or zones) or the hydraulic domains are: the saturated domain, the funicular domain, the pendular domain, and the residual domain, see Fig 2.14. The definition of these domains and their boundaries differentiates in the literature review. Some researchers define water retention domains based on the present forces acting on water phase, such as capillary and surface tension (see Baltodano-Goulding, 2006; Cavinato, 2011). Others define water retention domains based on the continuity of fluid phase, i.e., water phase continuity retained by water films and air phase continuity (see Bastian, 1999; Brockman et al., 2004; Lins, 2010; Yadav et al., 2010; Szymkiewicz 2013).

However, none of the latter analyses has offered a clear description of fluid phase continuity at the local scale. Moreover, there is no clear description of the boundaries between these domains, at which a change in the acting force or fluid water continuity is present. In this work, the definition of water retention domain, based on fluid phase continuity is adopted. Fluid phase continuity is investigated at the grain scale to define the boundaries at which the continuity of fluid phases changes (see chapter 4, section 4.4.2).

Fig 2.14 shows water retention curve and the corresponding water retention domains, illustrated by small sketches, bellow the curve.

In the saturated state of the soil, all the pores are filled with water; water phase is continuous and soil suction is zero. Air enters the soil at air entry value, and larger pores of the soil begin to drain followed by smaller pores. In this state of the soil, which corresponds to the funicular domain, water phase is continuous and air phase is discontinuous. The pore water takes the form of clusters formed between soil particles. In the pendular domain, water continues to drain out of the soil, and water phase becomes discontinuous while air phase becomes continuous. In this domain, water exists primarily as liquid bridges between and among particles and as thin films of water around the particles. The funicular and pendular domains are the transition zone of the soil, between the saturated and residual domains, or capillary regimes, where the driving force acting on water is capillary. The amount of water in the pores in the transition zone mainly depends on the grain and pore size distribution.

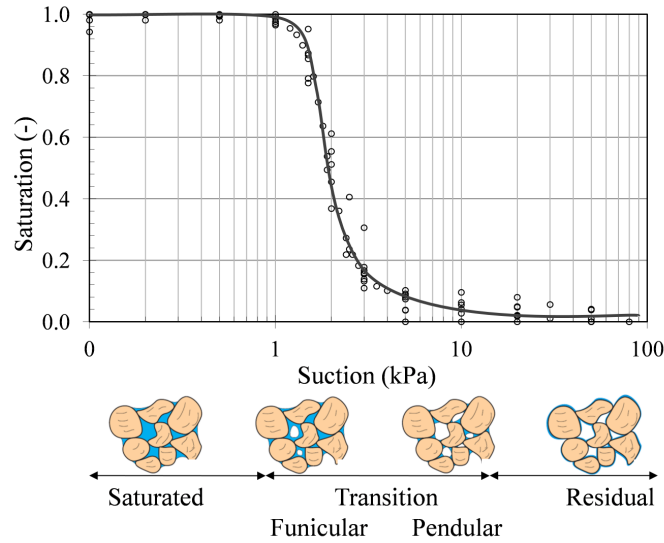


Figure 2.14: Water retention curve and the hydraulic domains (illustrated by small sketches, below the curve)

The transition zone is followed by the residual domain. In the residual zone the pore water is in the form of thin films on the soils grains. The air phase is continuous and water phase is discontinuous. Water is transported in this domain mainly by water vapour diffusion.

2.3 Hydro-mechanical behaviour of unsaturated soils

The importance of unsaturated soils in geotechnical engineering has long been recognized and efforts have been made to analyze their mechanical behaviour. The mechanical behaviour of unsaturated soils (i.e. shear strength, stiffness, bearing capacity) is strongly influenced by their water content, and respectively their suction (see Fredlund, 2014).

The influence of water content on the mechanical behaviour of the soils is reflected in their stress-strain behaviour, e.g. volume change and shear strength. As has been shown in water retention behaviour of unsaturated soils, an increase in the void ratio induces an increase in the water content within the soil. Thus, considering a deformable soil, under mechanical loading, any change in the volume of the soil, i.e., change in the void ratio, will induce a change in the water content (drained condition) or in water phase distribution (undrained condition) (see Monroy et al., 2006). The influence of water content (or suction) on the shear strength, on the other hand, is included in cohesion term in shear strength expression and suction term in the effective stress expression.

The effective stress (σ') was the primary stress state variable used to characterize saturated soils behaviour (e.g., $\sigma' = \sigma - u_w$, see Bishop et al. (1957)). For unsaturated soils, it was more difficult to characterize their behaviour because both liquid and gas phases require at least two independent stress state variables (i.e., water and air pore pressure parameters).

By the late 1960s, there was increasing awareness that the use of these two independent stress state variables would provide an approach more consistent with the principles of

continuum mechanics (see Lamb et al. (1969)). Various forms of effective stress equations that include a parameter(s) that is a material variable can be found in the literature review, e.g., $\sigma' = \sigma - \beta' u_w$, $\sigma' = (\sigma - u_a) + \chi(u_a - u_w)$, $\sigma' = (\sigma + \psi p'')$. Yet, none has proven completely successful in practice. A recent analysis discussing the conceptual principle of effective stresses of unsaturated soils, investigating and validating the generalized effective stress framework for unsaturated soils, can be found in Murthy (2002) and Nuth et al. (2008).

In 1970, unsaturated soil mechanics were considered as an extension of saturated soils mechanics. Initially, the constitutive behaviour focused primarily on the study of seepage, shear strength, and volume change problems (see Fredlund et al. (1976, 1979)). These constitutive models have been in a continuous development to include other studies such as grains contacts and cyclic loading (see Nishigaki et al., 1994; Pham, 2005; Yang et al., 2008; Nguyen et al., 2014).

The numerical, finite element and finite difference, modelling methods were used for unsaturated soils in the 1980 decade (see Papagianakis et al., 1984). The challenge was to find techniques that would ensure convergence of highly nonlinear partial differential equations of unsaturated soils mechanism (Fredlund et al., 1997; Sheng et al., 2003; Zhang et al., 2007; Sheng et al., 2008). Saturated-unsaturated seepage modelling became the first of the unsaturated soil problems to come into common engineering practice (see Lam et al., 1987; Thieu et al., 2001). Recent studies attempted to combine volume change and shear strength in the form of elastoplastic models that were an extension from research on saturated soils (see Alonso et al., 1990; Fredlund et al., 1996; Blatz, 2000). The study of contaminant transport properties, thermal soil properties, and air flow properties for unsaturated soils also took on the form of nonlinear soil property functions (Newman et al., 1997; Lim et al., 1998; Zhang et al., 2005).

The 1990 decade and beyond have become a period when the emphasis has been on the implementation of unsaturated soil mechanics into routine geotechnical engineering practice (see Terzaghi et al., 1996; Leong et al., 2001; Fredlund, 2002; Schanz et al., 2007).

In the following, some of the main characteristics of the hydro-mechanical behaviour of unsaturated soils are presented, including shear strength, capillary cohesion and volume change and liquid distribution.

2.3.1 Shear strength behaviour

Shear strength of a soil is a very important property in geotechnical analysis and dependent on the effective stress. In the classical soil mechanics, fully saturated and completely dry conditions are usually assumed in characterization of shear strength. However, the soils used for the construction of engineered structures are often unsaturated soils. For the safety of these structures, it is important to quantify the shear strength of the unsaturated soils and to also be able to quantify changes in shear strength that might occur as a result of water infiltration into the soil.

Two apparatuses commonly used to measure shear strength are: triaxial equipment and direct shear equipment. In this doctoral work, a triaxial compression apparatus is used to measure shear strength of unsaturated granular material. All the details related to the triaxial apparatus with the methodology for performing the test and interpreting the results are presented in chapter 5, section 5.2.

In a triaxial test, air and water phases can be independently maintained in an undrained or drained condition during shearing. The fluid is allowed to completely drain out from the specimen under drained conditions. The desire is to have essentially no excess pore pressure in the soil during the shearing process. In other words, the pore pressure is externally controlled at a constant value during shearing. Fluid drainage is not allowed under undrained conditions.

Changes in pore pressure during shearing may or may not be measured. It is important, however, to measure or control the pore air and pore water pressures when it is necessary to know the net normal stress and the suction at failure.

Considering a drained triaxial compression test where the soil specimen is subjected to a constant suction ($-u_w$ where $u_a=0$) and is surrounded by a constant net confining (or cell) pressure (i.e., the net minor normal stress σ_3). The specimen is failed by increasing the net axial pressure or stress (i.e., the net major normal stress σ_1). The difference between the major and minor normal stresses is commonly referred to as the deviatoric stress ($\sigma_1 - \sigma_3$) and is a measure of the shear stress developed in the soil specimen. As the soil is compressed, the deviatoric stress increases gradually until a maximum value is obtained. The applied axial stress σ_1 or the deviatoric stress can be plotted versus the axial strain ($\varepsilon\%$) and the plot is referred to as a stress-strain curve. The maximum deviatoric stress ($\sigma_1 - \sigma_3$) is an indicator of the shear strength of the soil and can be used as a failure criterion.

The hydro-mechanical behaviour of the saturated soil is explicitly analyzed in Bishop et al. (1957) and Atkinson et al. (1977). Fig 2.15 and Fig 2.16 show triaxial test results for normally consolidated and over-consolidated saturated clay specimens, respectively, obtained by Bishop et al. (1957) in drained and undrained conditions.

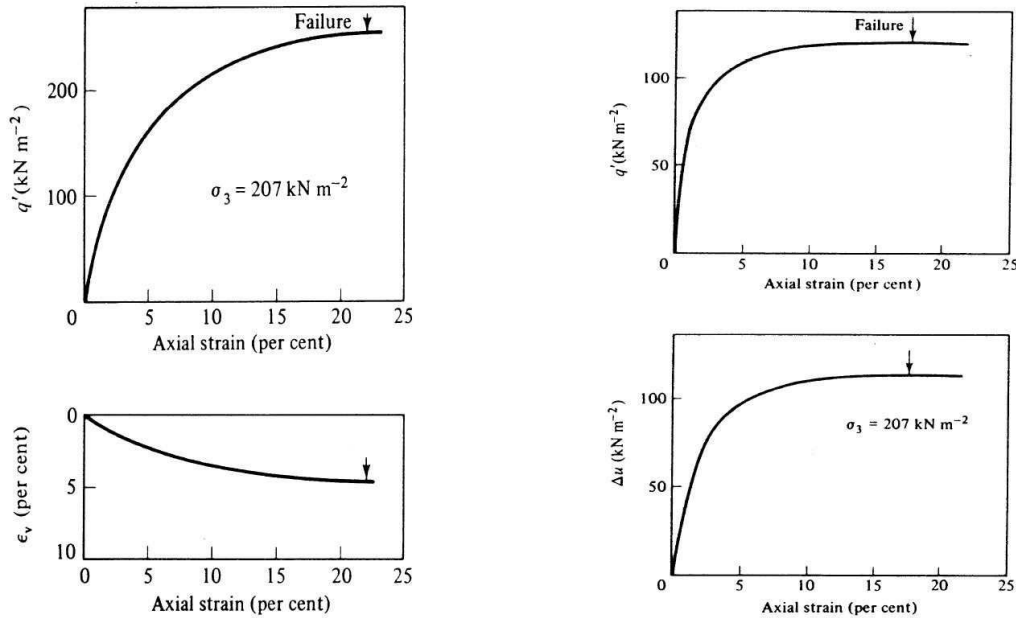


Figure 2.15: Triaxial test results for normally consolidated saturated clay specimens in drained condition (left) and undrained condition (right) (from Bishop et al. (1957))

As can be seen in the Fig 2.15 for normally consolidates specimens, the positive pore water (Δu) pressure, in the undrained test, reduces the deviatoric stress to one half of the

deviatoric stress in the case of drained test.

The over-consolidated specimen, in Fig 2.16, behaves differently from the normally consolidated specimens. The deviatoric stress reduces remarkably for the over-consolidated drained test compared to the normally consolidated drained test.

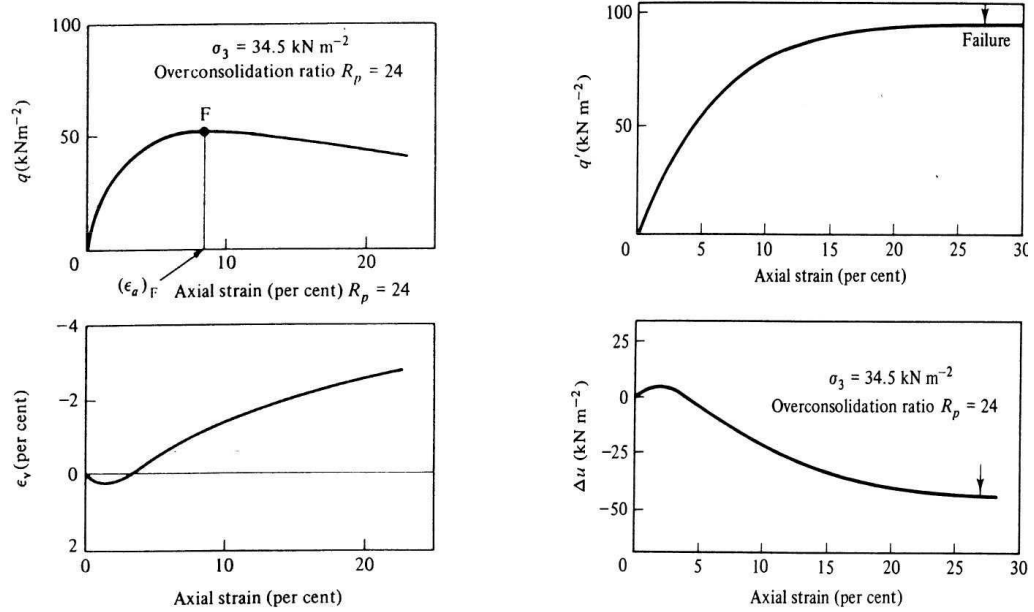


Figure 2.16: Triaxial test results for over-consolidated saturated clay specimens in drained condition (left) and undrained condition (right) (from Bishop et al. (1957))

Moreover the over-consolidated specimen contract initially then dilate strongly while the normally consolidated specimen contracts for the whole test. The over-consolidated undrained specimen behaves similarly to the normally consolidated undrained specimen (related to stress-strain curve). However pore water pressure is different for the two cases: normally and over-consolidated.

This behaviour of the four specimens shown in Fig 2.15 and Fig 2.16 shows the influence of stress history and pore water pressure on the mechanical behaviour of the soil.

For unsaturated soils, numerous shear strength tests have been conducted during the past 30 years (see Matsuoka et al., 2002; Vanapalli et al., 2002; Vanoudheusden et al., 2004; Sun et al., 2008). For example, Uchaipichat (2010-b) has conducted a triaxial test on dry, unsaturated and saturated compacted kaolin. The suction values varied from 0 to 300kPa. The experimental results, presented in Fig 2.17 show the difference between shear strength at different values of suction.

As can be seen from Fig 2.17, strain-hardening response is observed for all the tests. The deviatoric stress of the dry specimens is greater than the one obtained for the wetted (unsaturated) and saturated specimens. The volume change behaviour is contractive for all the tests.

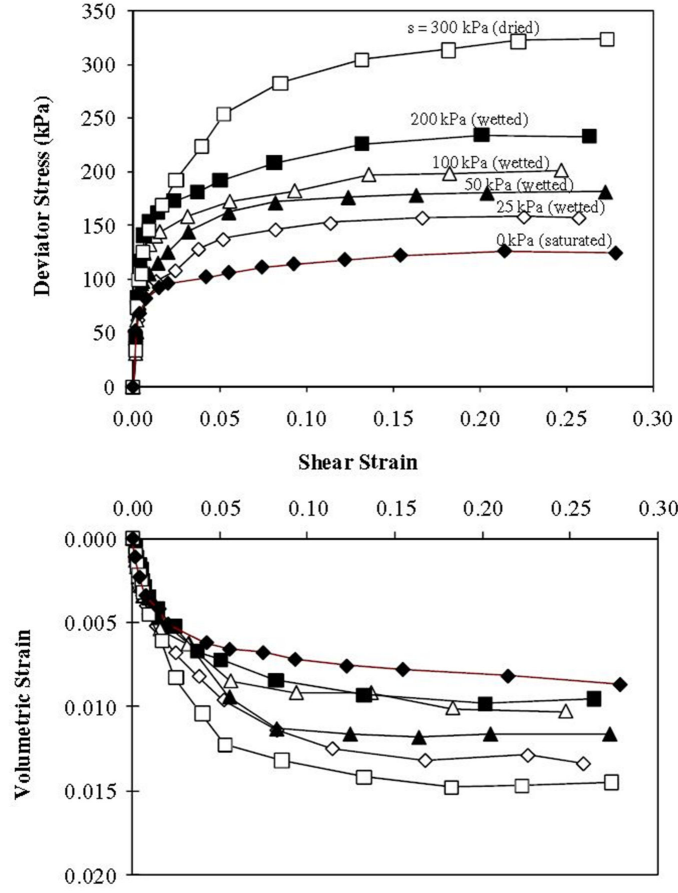


Figure 2.17: Suction-controlled triaxial shear tests on dry, wetted and saturated specimens (from Uchaipichat (2010-b)). The figure shows stress-strain curves (top) and the volumetric strain (bottom) in relation with the axial strain

The constitutive models for the shear strength of unsaturated soils can be found in different forms in the literature review. For example, according to Fredlund et al. (1979, 1993) and Wheeler (1986)), shear strength can be expressed as:

$$\tau = \acute{c} + (\sigma_n - u_a)\tan\acute{\phi} + (u_a - u_w)\tan\phi^b \quad (2.2)$$

Where \acute{c} is the effective cohesion, $\acute{\phi}$ is the effective angle of internal friction, ϕ^b is the friction angle associated with the matric suction stress state variable $(u_a - u_w)$, and $(\sigma_n - u_a)$ is the net normal stress.

Some investigations have been carried out on the relationship between the water retention curve and the shear strength of unsaturated soils, based on the idea that water retention curve provides an insight on the nature of the inter-particle contacts and stresses at various suctions (see Fredlund et al., 1996; Vanapalli et al., 1996). In terms of soil microstructure, the physical idea appears to be best adapted for sands where punctual contacts may be observed between soil particles.

2.3.2 Capillary cohesion

Capillary cohesion is the force or pressure attracting two soil particles, resulted from surface tension and pressure difference across gas-liquid interface (see Souli et al. (2008)). This cohesion may be considered essentially equal to zero, for loose sand that is either completely dry or completely saturated. For wet sand, on the other hand, capillary cohesion influences shear strength and thus soil stability (as shown section 2.3.1). This material parameter can be estimated from Mohr coulomb failure criterion (e.g., see Hoek (1990)).

In a triaxial test, the contribution of cohesion to shear strength, for unsaturated soils, is negligibly small for coarse soils or at high confining stresses. On the other hand, cohesion contribution to shear strength of fine sand is important. Therefore, many analyses have been conducted to investigate capillary cohesion and its contribution to the mechanical behaviour of unsaturated soils. These analyses can be divided into two groups: macroscopic and microscopic-discrete analyses. In the following, capillary cohesion is reviewed in the context of these two groups.

2.3.2.1 Macroscopic analyses of capillary cohesion

Traditionally, the interpretation of the relation between suction versus shear strength has been used to highlight the contribution of capillary cohesion to the mechanical behaviour of unsaturated soils. For example, Hamid et al. (2009) have investigated the influence of cohesion on shear strength by analyzing shear strength at different values of suction. In order to do that, Hamid et al. (2009) have performed a series of drained direct shear tests on unsaturated Minco silt. The results are presented in Fig 2.18, which shows shear stress-displacement curve (τ - u) in the top, volumetric strain-displacement curve ((v/H_0) - u) in the middle and water content change-displacement curve (Δw - u) in the bottom, for net normal stress 105kPa.

The results obtained by Hamid et al. (2009), presented in Fig 2.18, show that higher shear strength is obtained for the highest suction ($s=100\text{kPa}$). Similar results are found in Zakaria (1994), Khalili et al. (2007) and Nuntasarn et al. (2012).

The volumetric strain-displacement curves show that compression behaviour is observed for the three tests, followed by dilation. The amount of compression increases and dilation decreases as the net normal stress increases. However, water content changes are less obvious from test to test as compared with trends in total volume change. In these tests, Hamid et al. (2009) have observed that during shearing, there was re-arrangement sliding of soil grains resulted in the disruption and the rupture of menisci between soil grains. The disruption of menisci caused a tendency for increasing pore water pressure and decreasing suction. Due to the tendency for increasing pore water pressure, the water flowed from the specimen and water volume decreased while the specimen was shearing.

Bruchon et al. (2013) have characterized collapse phenomenon during water infiltration into partially saturated Hostun sand. During the imbibition process, the deformation of the granular skeleton caused by gravity effect was obtained using Volumetric Digital Image Correlation tools (VDIC). The results obtained are presented in Fig 2.19. In this figure, the volumetric strain obtained macroscopically, and the largest averaged local volumetric strain obtained using VDIC are plotted as a function of water content.

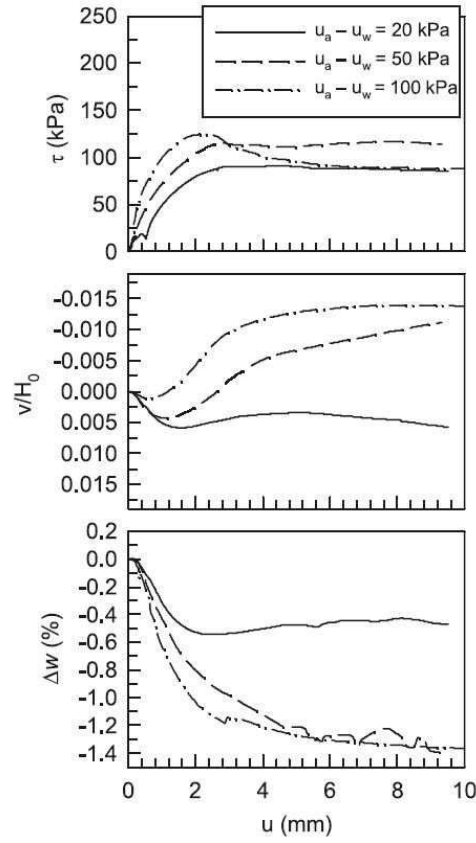


Figure 2.18: a) Shear stress-displacement curve (τ - u) in the top, volumetric strain-displacement curve ((v/H_0) - u) in the middle and water content change-displacement curve (Δw - u) in the bottom (from Hamid et al. (2009))

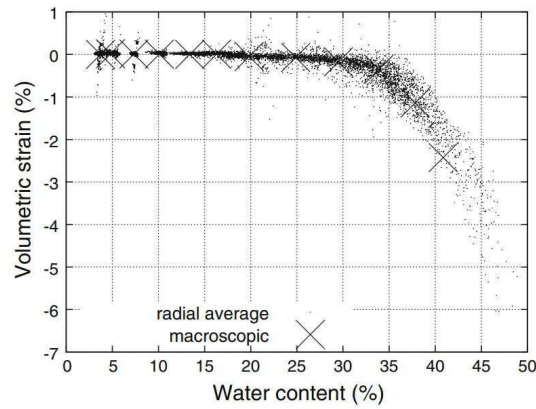


Figure 2.19: The relation between the volumetric strain obtained macroscopically, and the largest averaged local volumetric strain obtained using VDIC (radial average) versus water content (from Bruchon et al. (2013))

In this figure, it is shown that an increase of negative volume change is observed as increasing the water content. Moreover, the volume change of the specimen at local scale started at a particular water content (25%) which is coincided with the coalescence of capillary bridges between grain clusters observed using x-ray tomography.

Other investigations have used the relation between suction (or water content) versus cohesion to interpret the contribution of capillary cohesion to the mechanical behaviour of unsaturated soils (see Ho et al., 1982; Fredlund et al., 1996; Gallipoli et al., 2003; Lu et al., 2004; Lu et al., 2006; Delage, 2008-c). In these studies it was found that an increase in suction, thus a decrease in the degree of saturation, would induce an increase in capillary cohesion (see Fig 2.20 from Delage (2008)) and thus increase in the shear strength of the soil. In Fig 2.20, cohesion (right vertical axis) is plotted in relation with suction. The resulted curve is shown with rectangular empty symbols.

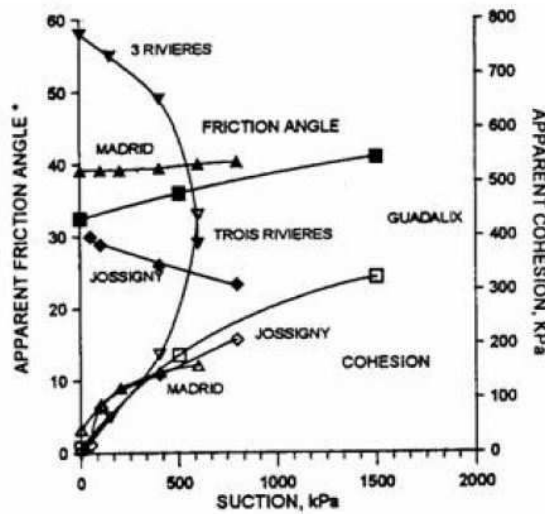


Figure 2.20: Changes in cohesion and friction angle with suction (from Delage (2008-c))

Leal-Vaca et al. (2012) have also analyzed the relation between suction and shear strength (the deviatoric stress) to obtain cohesion contribution to shear strength. They performed drained triaxial test on unsaturated silty sand, under 150kPa confinement pressure, for wetting and drying paths. Their results are presented in Fig 2.21.

Fig 2.21-a shows the relation between suction and the deviatoric stress. In this figure, the deviatoric stress is greater during drying than wetting for suction over 980kPa, while for suction lower than 980kPa this behaviour is not maintained due to the difference in water distribution within the specimen during drying and wetting processes.

In Fig 2.21-b, which shows the relation between suction and cohesion, drying path has a maximum cohesion that is greater than the one for wetting path. For both paths, cohesion change with the variation of suction is not constant (i.e., increasing the suction induces an increase in the cohesion to reach a maximum value then decreases regardless the corresponding increase in suction).

The relation between the degree of saturation and cohesion, obtained experimentally and analytically by Leal-Vaca et al. (2012), is shown in Fig 2.21-c. The results obtained by different researchers are also presented in Fig 2.21-c.

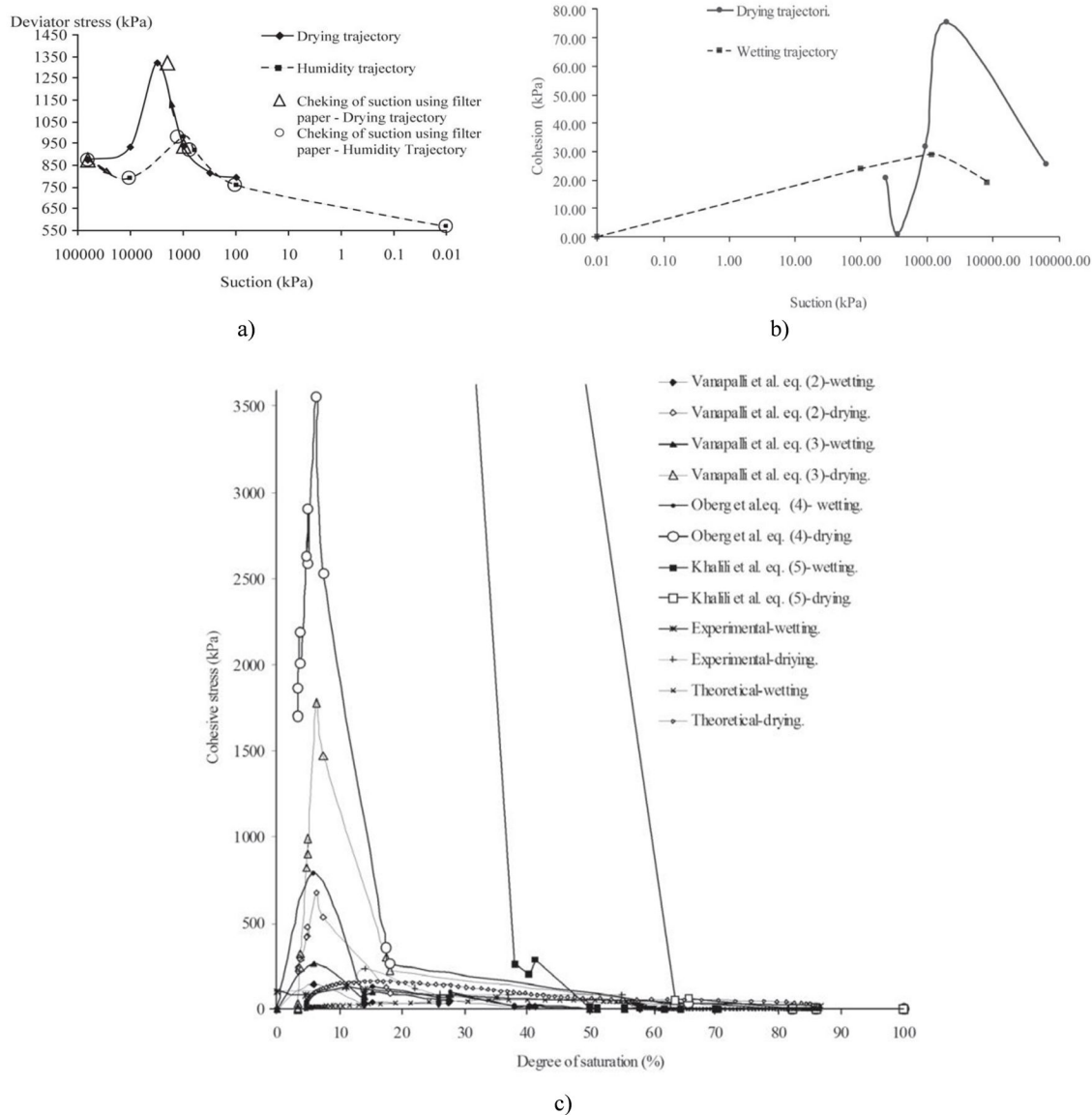


Figure 2.21: a) The relation between suction and deviatoric stress b) The relation between suction and cohesion c) The relation between degree of saturation and cohesion, for silty sand soil (from Leal-Vaca et al. (2012))

As shown in this figure, greater cohesion stress is obtained for drying path than for wetting path, from the different researchers. Increasing the degree of saturation induces an increase in the cohesion to reach a maximum value then decreases regardless the corresponding increase in degree of saturation. For dry and saturated soils, minimum cohesion is found.

Gan et al. (1988) has presented the relation between suction and shear strength, shown in Fig 2.22, for a glacial till soil (42% silt, 30% clay, and 28% sand), obtained for drained direct shear tests. The tests were performed by maintaining a constant net normal stress ($\sigma - u_a$) of approximately 72.6 kPa. The results show that shear strength increases as increasing the suction. Similar results were obtained by Vanapalli et al. (2000, 2002).

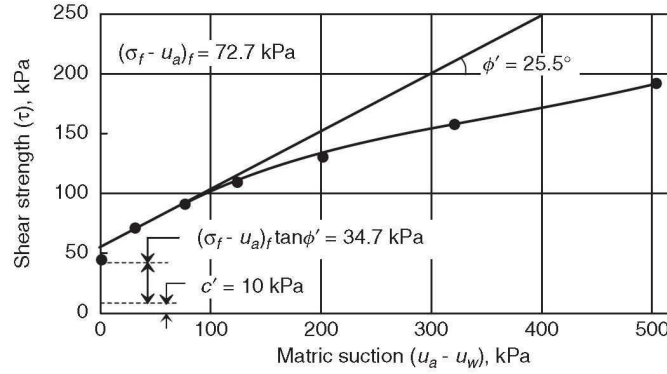


Figure 2.22: The relation between suction and shear strength for a glacial till soil (from Gan et al. (1988))

As has been presented in the latter analyses, the contribution of cohesion to the shear strength of the soil has been evaluated in the macroscopic analyses based on the relation between suction (or degree of saturation) versus shear strength (or cohesion). It has been found in these analyses that when increasing soil suction, capillary cohesion increases. However this evolution is not true for all the ranges of suction or water content. This can be shown in Mitarai et al. (2006), who have presented schematically the variations of the suction (ΔP) and the cohesive stress (σ_c), upon changing the liquid content (S) within a granular medium, as shown in Fig 2.23. In this figure, the dependency of the suction on the liquid content (i.e., WRC) is given by a red solid line while the cohesive stress versus liquid content is schematically shown by the green dashed lines. The domains: pendular, funicular and capillary are defined based on dominant force acting on the liquid phase (i.e., capillary action decreases as decreasing water content in the soil).

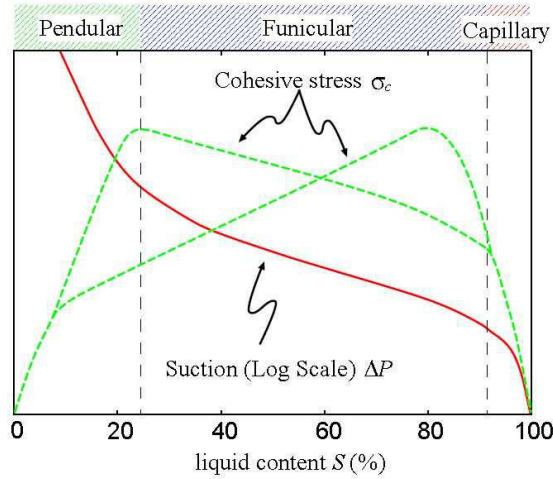


Figure 2.23: The variations of the suction (ΔP) and the cohesive stress (σ_c), upon changing the liquid content (S) (from Mitarai et al. (2006))

The overlapping dashed curves for low and high (S) are better established, while the non-overlapping intermediate curves vary significantly between experiments. The cohesive stress (σ_c) increases as adding more and more liquid to initially dry grains, shown by the positive slope, for small (S), of the (σ_c) line in the pendular state. At the opposite end,

cohesion becomes zero for completely saturated granular media ($S=100\%$), schematically shown by the green dashed line with negative slope for (S) close to 100% in the capillary state. In the funicular state, the cohesive stress (σ_c) dependency on the liquid content (S) is not clearly understood. The cohesive stress (σ_c) may either increase or decrease with (S) in the funicular state. These possible curves are shown by the green dashed lines, where both lines connect to single lines in the limits when $S=0$ and $S=100\%$. As can be seen in Fig 2.23, there would be at least one maximum of the cohesive stress at a certain liquid content, though it is not clear, a priori, where is the exact location of the peak.

From Mitarai et al. (2006)) it could be concluded that cohesion increases when decreasing suction, i.e., increasing water content in a specific range (i.e., low water content range), and when increasing the suction in high water content range. This conclusion is consistent with the macroscopic results obtained by the early presented researches, i.e., the increase of cohesion as increasing the suction in high water content range. However, as different materials have different retention behaviour and water domains, the latter range of suction corresponding to high water content range, that induces an increase in capillary cohesion, is not constant for the different materials.

In order to achieve better understanding of the relation between suction (or water content) and cohesion, the latter macroscopic observations were analyzed at the microscopic-discrete scales by several researchers. In the following, a review of these microscopic-discrete analyses is presented.

2.3.2.2 Microscopic-discrete analyses of capillary cohesion

In this section, capillary cohesion analyses performed at microscopic and discrete scales are presented. These analyses capture the local mechanisms related to grain and water volume microscopic structure and include the experimental and numerical (discrete) studies.

As stated before, the apparent cohesion unique to unsaturated soils arises from negative pore water pressure and surface tension effects occurring at the interface of the pore water, pore air, and soil particles. The contribution of pore pressure to total stress depends on the degree of saturation (and thus, suction) and pore size distribution. However, several recent analyses performed at the microscopic-discrete scales have showed that the contribution of capillary cohesion to the mechanical behaviour of soils is related also to some microscopic-discrete measurements such as the number of water bridges and clusters and the inter-particle distance. These microscopic-discrete measurements depend on the microscopic-discrete geometrical properties of the granular medium, according to Geromichalos et al. (2003).

Scheel et al. (2008) have analyzed the contribution of capillary cohesion to soil strength by investigating the influence of water content at the local scale on the mechanical properties of a glass bead pile through a wetting process and tensile strength measurements. Using x-ray tomography and Matlab[®] analysis, the statistics of volume and surface area of individual liquid clusters (defined as connected regions of liquid wetting more than two beads), the angular distance of bead contact points, as well as the number of capillary bridges and liquid clusters per bead were obtained.

The results obtained by Scheel et al. (2008) are presented in Fig 2.24. In this figure, tensile strength and cluster statistics of the wet glass beads at different liquid contents (W)

are presented. In Fig 2.24 tensile strength is shown to be increasing rapidly as increasing liquid content then tends towards a plateau after $W=0.02\%$.

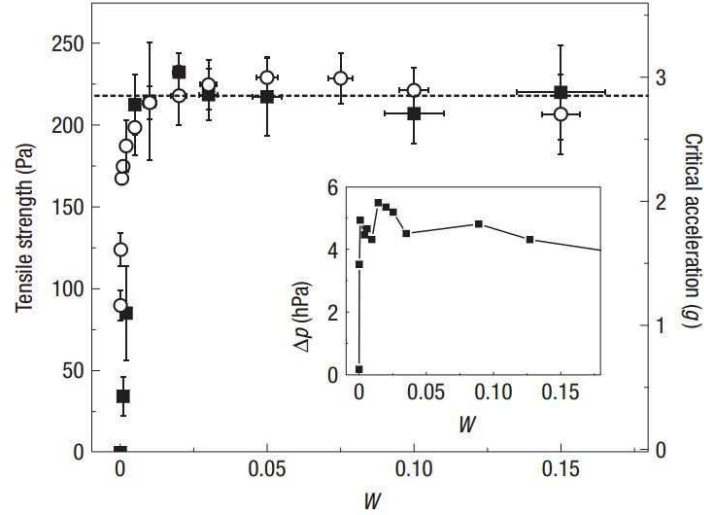


Figure 2.24: Tensile strength (filled squares), critical acceleration for fluidization (open circles) of wet glass beads at different liquid contents (W). Inset: Yield stress (from Scheel et al. (2008))

This behaviour can be related to the number of capillary bridges, as this number increases rapidly at the beginning of the test when increasing (W), as shown in Fig 2.25. However, beyond $W=0.02\%$, the number of capillary bridges per bead decreases regardless the increase in (W).

Scheel et al. (2008) have explained the small increase in tensile strength beyond $W=0.02\%$ as it can be attributed to the increase of the number of liquid clusters per bead in the range $W=0.02-0.03\%$, and to the increase of the volume fraction of the largest liquid cluster in the range ($W=0.05-0.2\%$).

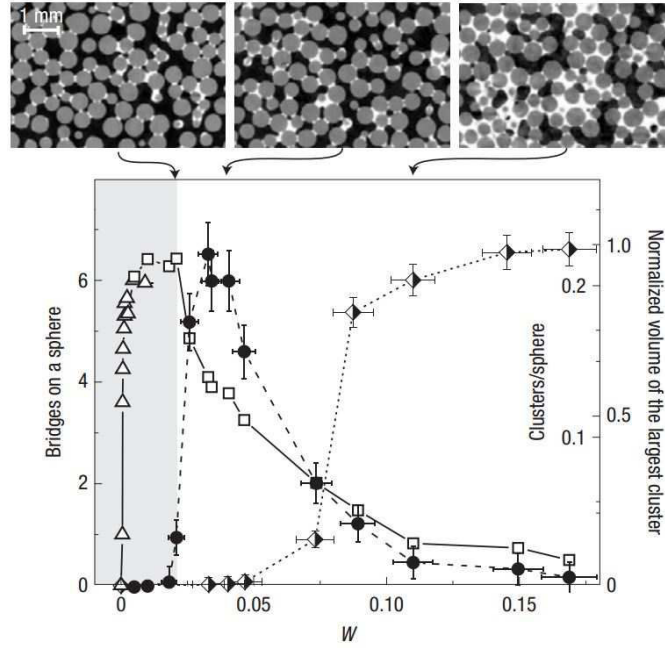


Figure 2.25: Sections through 3D tomograms of the analyzed specimens at $W=0.02, 0.04$ and 0.11 , from left to right. Main panel: Frequencies of liquid objects as extracted from x-ray tomography data. Left axis (open symbols): Average number of capillary bridges on a sphere (triangles: fluorescence microscopy; squares: x-ray tomography). Right axis: Average number of clusters per sphere (filled symbols), and normalized volume of the largest cluster (half-filled symbols) (from Scheel et al. (2008))

Richefeu et al. (2006, 2008) have investigated the contribution of capillary cohesion to the mechanical behaviour of wet sand and glass beads using a discrete element approach and simple compression experiments. The experimental results, shown in Fig 2.26, shows the macroscopic cohesion (c) as a function of water content (w) for four tested granular materials of different particle size: Sand (S): 0.16mm and Glass Beads (GB_1): 1mm , GB_{45} : 0.45mm and GB_{48} : 0.6mm). Beside the increase in cohesion (c) as increasing water content (w) in the range $w=0-5\%$ (i.e., low water content ranges), in Fig 2.26, the influence of particle size and shape is shown also. The angular sand shows higher cohesion than the spherical glass beads. Glass beads specimens G_{45} and G_{48} are of higher cohesion of GB_1 .

Numerically, Richefeu et al. (2006, 2008) have found that the shear stress (τ) for the wet glass beads of water content $w=1\%$ is higher than that for the dry material $w=0\%$, at the same vertical loading $\sigma=300\text{Pa}$, as shown in Fig 2.27-left. Moreover, they found that the bond coordinate number (i.e., number of liquid bonds) within the specimen is a decisive parameter for the overall cohesion of wet granular materials. Fig 2.27-right shows three simple compression tests for three specimens. The first specimen is dry (dashed line in the figure); the second and third specimens are wet with a high bond coordination number (thick line) and with two times less bonds (thin line).

As can be shown in the figure the two wet specimens are of a higher shear stress than the dry specimen. The specimen of two times less bonds is of a lower shear stress than the other wet specimen.

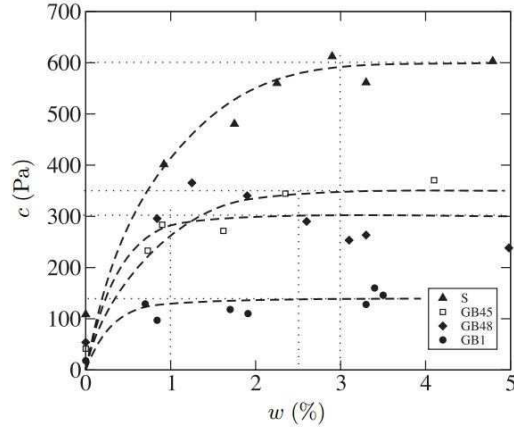


Figure 2.26: Macroscopic cohesion (c) as a function of water content (w) for four tested granular material: sand (S), glass beads (GB₁), (GB₄₅), and (GB₄₈) (from Richefeu et al. (2008))

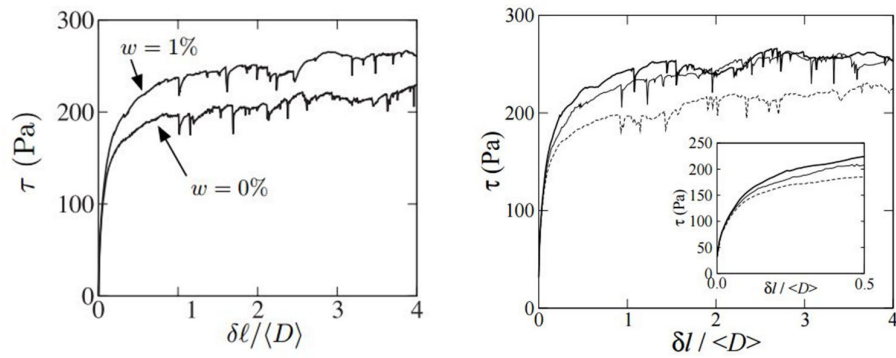


Figure 2.27: Stress-strain plot for $w=0\%$ and $w=1\%$; $\sigma=300$ Pa (left) and stress-strain plot for a dry (dashed line) and two wet samples (solid lines) with a high bond coordination number (thick line) and with two times less bonds (thin line). For the two plots, the displacements are normalized by the average particle diameter (D). In Fig 2.27-right the inset shows a zoom for small deformations (right) (from Richefeu et al. (2008))

Gras (2011) presented the relation between capillary force (f_{cap}) and inter-particle distance (D) during traction tests, for a configuration of two spherical beads of a radius $R = 5.025 \text{ mm}$. The results presented in Fig 2.28, show the former relation for different constant suction values (s) or dimensionless suction (H). As can be seen in the figure, capillary force decreases as increasing the inter-particle distance.

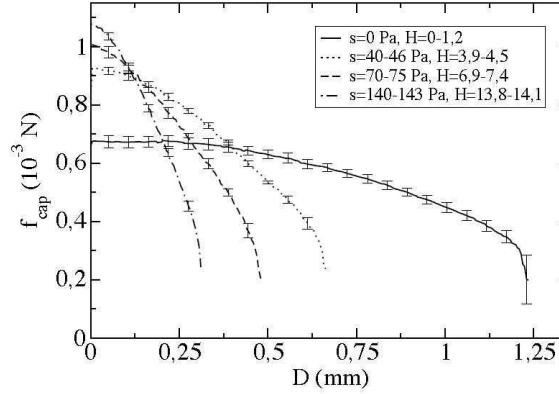


Figure 2.28: The relation between capillary force (f_{cap}) and the inter-particle distance (D) during traction test at constant suction (s) for two spherical beads configuration (from Gras. (2011))

Moreover, the inter-particle distance at which the rupture of capillary bridge takes place (rupture distance) decreases as increasing the suction and the absolute value of the slope of the curve connecting the capillary force to inter-granular distance increases with suction.

Gras (2011) has also presented the influence of the radius of the beads (R) and the volume of water bridge (V in μl), as shown in Fig 2.29. It is found that capillary force increases as increasing the size of the beads. Moreover, higher capillary force is obtained for the larger volume of water bridge at the rupture distance. At the rupture distance, a larger volume of the water bridge is obtained while at low inter-particle distance the influence of the volume of water bridge is less remarkable.

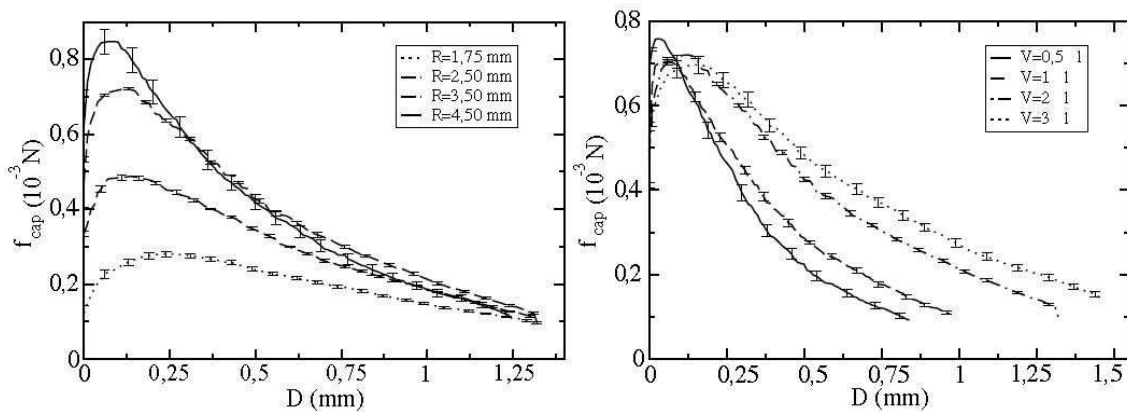


Figure 2.29: The relation between capillary force (f_{cap}) and the inter-particle distance (D) during traction test at different values of the radius of the bead (R) for a volume of water bridge $V=2\mu\text{l}$ (left) and different values of the volume of water bridge in μl (right) for $R=3.5\text{mm}$ (from Gras. (2011))

Numerically, using discrete element method, Gras (2011) has performed a simple compression tests on a specimen of poly-dispersed grains of a diameter between 0.2 and 1.2mm. The results presented in Fig 2.30 show the evolution of capillary stress (σ_c) and number of liquid bonds per grain (Z) in relation with the deformation ($\varepsilon\%$). It was found that there was a slight increase in capillary stress when decreasing the suction. Moreover, a slight decrease in the number of liquid points is observed when increasing the suction, which can be explained by the decrease of rupture distance of the liquid bonds as increasing the suction (see Fig 2.28). This reduction in the number of bridges liquid is directly related to the decrease in water content of the medium when increasing the suction.

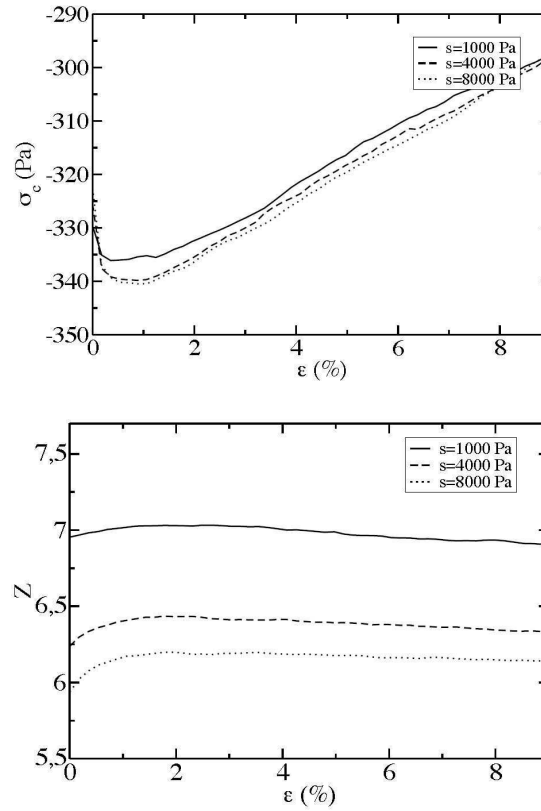


Figure 2.30: The evolution of capillary stress (σ_c) and number of liquid bonds per grain (Z) in relation with the deformation ($\varepsilon\%$) (from Gras (2011))

Souli et al. (2012) have investigated numerically (using discrete element simulation) and experimentally the influence of capillary cohesion on the peak force, in axial compression tests performed on glass beads. They have found that the peak force increases as increasing the water content within the soil in the range $w=(0-10\%)$, as shown in Fig 2.31-top numerically and experimentally. Moreover, the peak force increases as increasing the surface tension (σ) as shown in Fig 2.31-bottom. Furthermore, for the same surface tension (σ), the peak force increases as increasing the inter-particles distance (k), as shown numerically in Fig 2.31-top, due to the increase in the number of liquid bridges (i.e., the number of liquid bridges at $k=0.2$ is higher than at $k=0$).

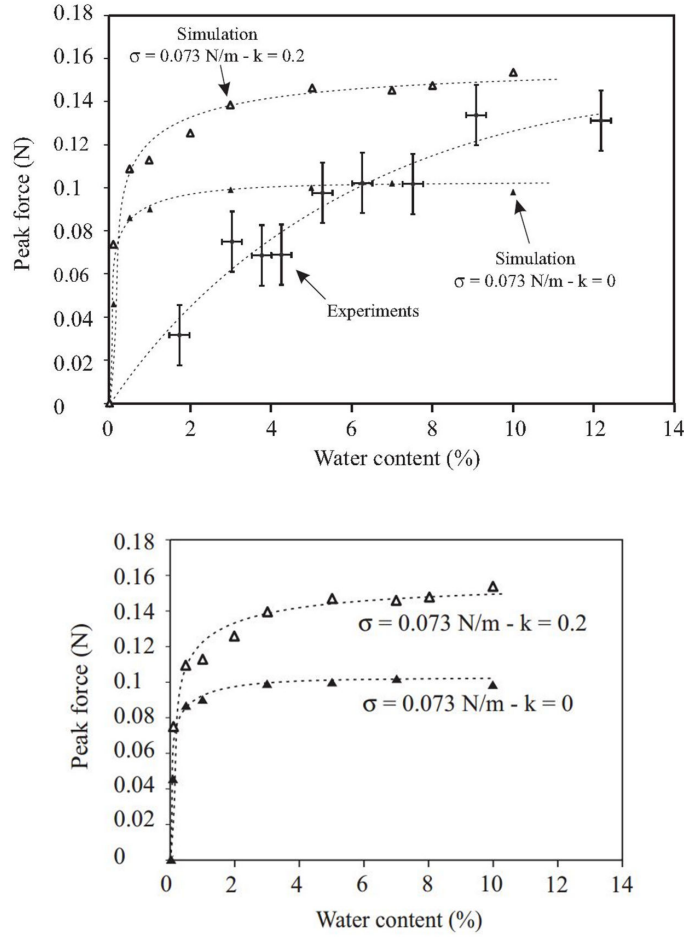


Figure 2.31: Evolution of the peak force with water content for two different values of inter-particle distances (k) (top), and for two different values of the surface tension (σ) (bottom). In Fig 2.31-top the experimental results for the evolution of the peak force with water content are shown (from Souli et al. (2012))

Micro-Directional Models (MDM) and Discrete Element Method (DEM) simulation have been developed by Scholtés et al. (2009) to study shear strength of unsaturated granular materials. The results obtained are presented in Fig 2.32. The figure shows the deviatoric stress (q) and volumetric strain (ϵ_v) versus axial strain curves obtained from triaxial tests at different degrees of saturation under a constant confining pressure (10kPa) using DEM and MDM.

As can be seen in Fig 2.32, for both MDM and DEM models, the shear strength is greater for unsaturated materials compared to dry materials, and depends on the degree of saturation. The more the specimen is wetted in the range of degree of saturation $S_r=0-10\%$, the greater the deviatoric strength is, as a result of the increase in menisci volumes and capillary forces.

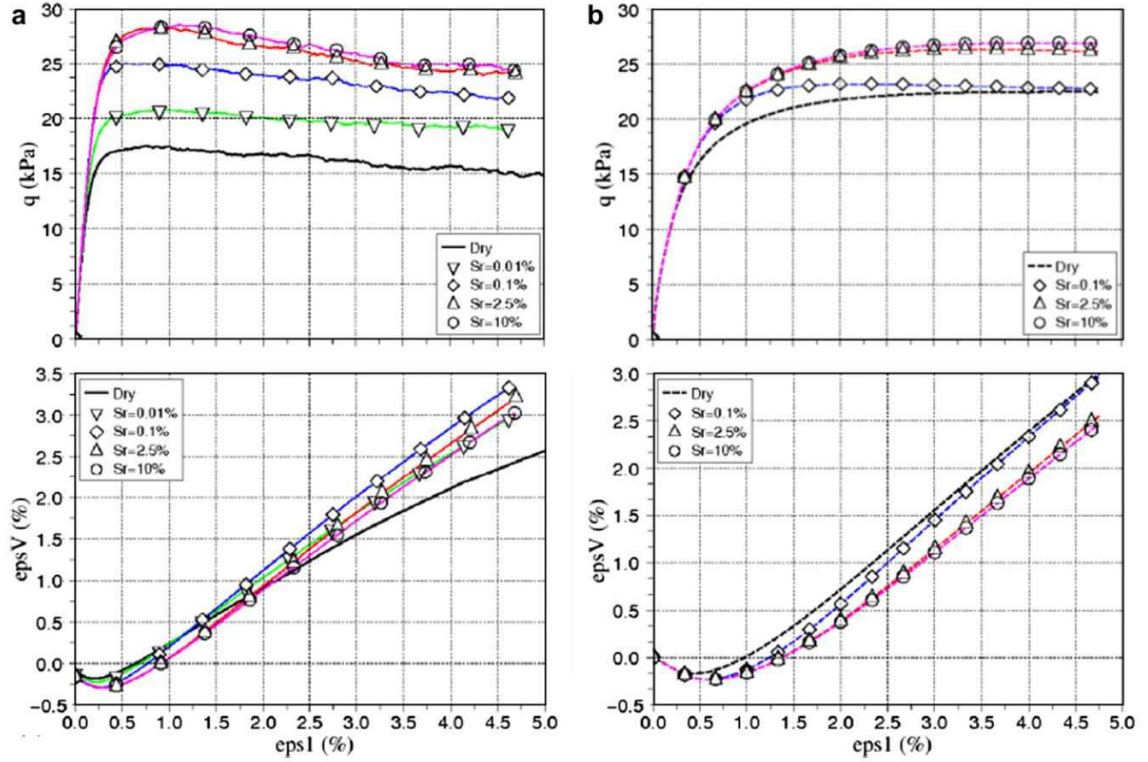


Figure 2.32: Deviatoric stress (q) and volumetric strain (epsV) versus axial strain curves obtained from triaxial tests at different degrees of saturation under a constant confining pressure (10kPa): DEM (a) and MDM (b) results (from Scholtés et al. (2009))

In conclusion, the microscopic-discrete analyses offer more information and better understanding for the evolution of cohesion with suction or water content. Several microscopic-discrete characteristics influence capillary cohesion contribution to shear strength of the soil such as the number of liquid bonds and their volume, inter-particle distance (i.e., pores size), shape and size of the particles, and pores shape (shown in hysteresis phenomenon when drying and wetting the soil, see Fig 2.21). These microscopic-discrete properties are used in this work to explain the macroscopic evolution of cohesion with suction (or water content), see chapter 4, section 4.4.4.

However, all the presented investigations of cohesion at the local scale, are considering only capillary cohesion in the regimes where capillary action is present (low water content ranges according to the microscopic-discrete studies). On the other hand, the macroscopic analyses are considering cohesion only in the high water content ranges. The definition of capillary regime is related to water retention domains presented earlier in section 2.2.7. As has been shown in this section, there is no clear and unique definition of water retention domains and the boundaries between them, whether based on the dominant acting force or fluid phase continuity.

In addition, only few analyses consider the evolution of cohesion with suction (or water content) at the microscopic-discrete scales due to the difficulty of accessing local information as the number of water bridges and clusters.

Moreover, the microscopic-discrete numerical observations are applied on glass beads which may appear macroscopically smooth. However, the microscopic grain surface is

never perfect. Usually, liquid bridges are considered in perfect sphere-sphere or sphere-plane geometries, e.g., see Hueckel et al. (2013). For most applications, this gives a good estimate of the capillary bridge force which hardly depends on the liquid volume at zero separation. However, if the liquid content is small enough, such that the dimensions of the liquid bridges become comparable to the roughness length scale, the liquid bridge force may considerably depend on the liquid volume.

In this work, x-ray CT and other developed experimental techniques (detailed in chapter 3) are used to obtain several microscopic-discrete information related to the evolution of the number of fluid bonds, their volumes and contact with loading (suction and mechanical loading) within an unsaturated soil specimen. This microscopic information is used to i) define water retention domains and the boundaries between them, ii) follow the evolutions of fluid phase with loading, iii) theoretically interpreted capillary cohesion regimes and its contribution to the hydro mechanical behaviour of the studied soil (i.e., cohesion measurement is not performed in this doctoral work).

2.3.3 Volume change and liquid distribution

Volume changes in unsaturated soils as compaction, consolidation and collapsing are expressed in terms of deformations or relative movement of the phases of the soil (i.e., relative volumes of the various phases). Different studies have showed that significant changes in the soil pore space were produced by the isotropic compression of the specimens as evident by the changes in void ratio, bulk density, and degree of saturation. These results are associated with the initial void ratio and drained-undrained condition of the test.

In an unsaturated specimen, the total volume change during compression is equal to the sum of the air and water components of volume change, assuming that the soil skeleton is incompressible. Thus, volume change is governed by the changes in water content within the soil during drained test and the change in water distribution during undrained test. Several experiments have shown that water exchanges related to the control of suction (drained test) are mainly controlled by the volume changes: shear contraction imposes water drainage, whereas shear dilatancy imposes water extraction (see Bishop et al. (1957), Zhou et al. (2012) and Wheeler et al. (2003)).

During the constant water content shearing tests (undrained test), several studies have reported a tendency for reduced volume changes and reduced suction (see Zakaria et al., 1994; Wulfsohn et al., 1998). This is largely attributed to the fact that net stresses caused a great reduction of the pore spaces (i.e. compaction) during the preceding isotropic compression stage. An explanation in terms of soil structure is that more closely packed particles result in reduced inter-connections between pore spaces as well as reduced porosity. Under these conditions, pore air and water may become trapped and less air will be expelled. Close particle packing also gives specimens more resistance to external stress, particularly for frictional soils. An implication of pore air becoming trapped in the specimen is that it may be difficult to measure volume changes during the shearing stage under high net confining pressures.

The effect of soil suction on volume change of an unsaturated soil was studied by Estabragh et al. (2012) by performing series of drained triaxial tests on unsaturated loose decomposed granitic soil. It was found that the volume of the soil specimen decreased as the mean net stress increased. This behaviour can be attributed to the influence of suction on the stiffness of the soil specimen at low confining pressure. At high confinement

pressure, suction influence is negligible.

Houston et al. (2008) have also presented the effect of soil suction on volume change. They have performed triaxial tests on unsaturated silty sand soil. Volume change measurements of these tests are presented in Fig 2.33, for net normal stress values of 20, 75, and 250kPa. The general volume change response of the soil is first compression, followed by dilation as axial strains are increased during shearing. It was observed that, for a given net normal stress, the degree of dilation increases with increasing suction. This is likely due to the higher suction resulting in more tightly bound aggregates of soil particles which behave more or less as sand-like particles. The aggregates do not shear easily but rather tend to ride up over each other (dilate) as shear stresses are increased. The tendency to dilate is most pronounced at lower net normal stress values and higher suction, but at higher net normal stress and lower values of suction, the volume change behaviour during shearing is dominated by compression except for the highest values of suction. Similar results were found by Padilla et al. (2006).

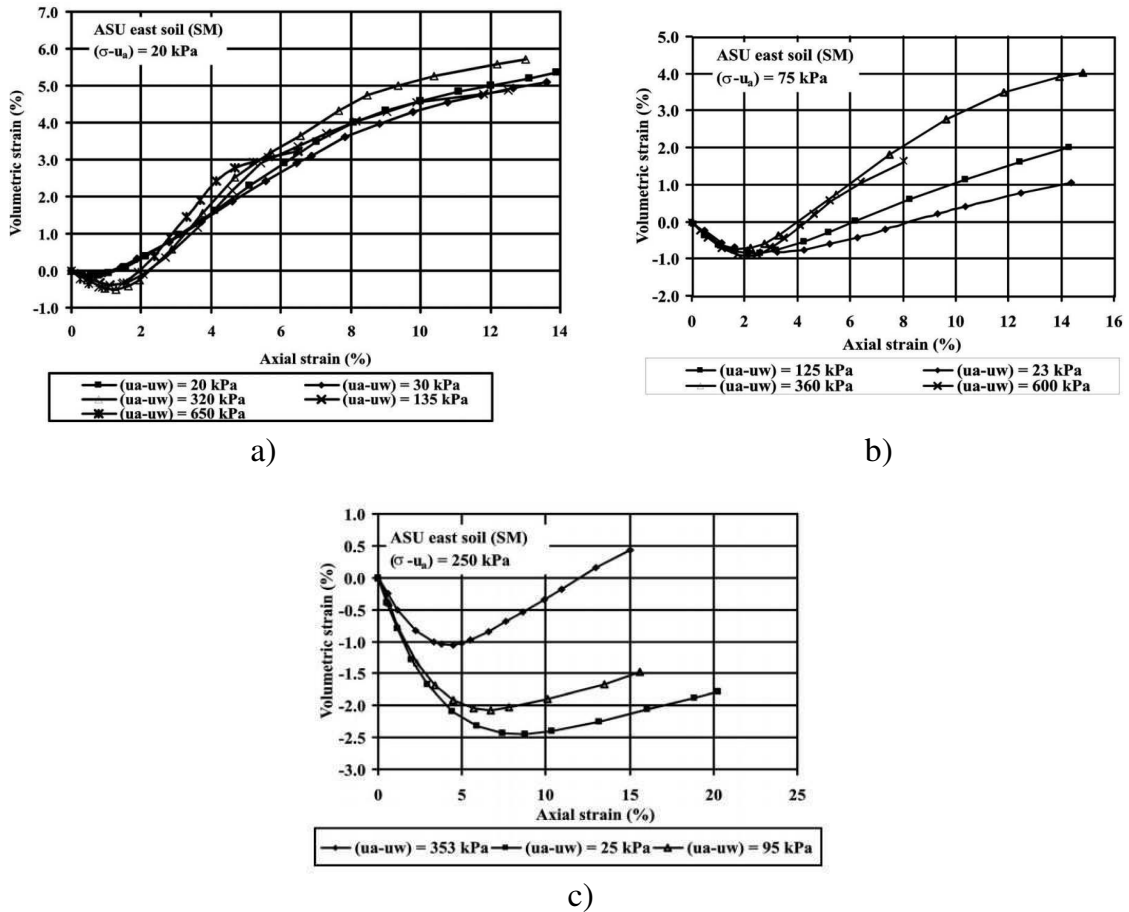


Figure 2.33: Volume change measurements for silty sand soil at net normal stress a) 20kPa b) 75kPa and c) 250kPa (from Houston et al (2008))

Volume change depends strongly in the initial void ratio of the soil (see Poulos 1971). While shearing a sand specimen in triaxial test, shows a hardening behaviour depending on the being loose, medium or dense. Loose sand undergoes compaction and medium

dense and dense sand will show an initial compaction followed by dilation and increase in volume. In undrained triaxial test, due to the generation of excess pore water pressure, (very) loose sands will undergo static liquefaction. Dense sand on the other hand can endure high levels of shear stress due to the generation of negative excess pore water pressure.

The influence of the initial void ratio on volume change can be seen in Fig 2.34, which illustrates the deformation observed on 3 specimens of dry Hostun sand: dense, medium and loose, under triaxial tests performed by Desrues (2004). The slenderness ratio for the three specimens was equal to 2 and they were subjected to same cell pressure 400kPa. As can be seen from the figure, the pattern of volumetric deformation is different for the three specimens of different void ratio.



Figure 2.34: Three specimens of Hostun sand loaded to failure at $\sigma_3=400\text{kPa}$ in drained condition. From left to right: dense, medium dense, loose (from Desrues (2004))

For unsaturated specimen, void ratio influences the distribution of water and air volumes within the specimen that is under triaxial loading. Void ratio evolves during a triaxial test. As a result, the distributions of fluid phase changes.

In fully saturated granular materials liquid is drained into dilating shear bands as porosity increases and air is not allowed to enter the dilating shear band areas. However, liquid distribution in unsaturated granular media, where a percolating air phase exists, is unclear.

The mechanical properties of soil structures strongly depend on the particular liquid distribution (see Fredlund et al. (1993) and Mitchell et al. (1976)). Thus, it is expected that liquid migration within granular media such as soils should influence its stability.

Mani (2014) has investigated liquid migration experimentally and numerically in a sheared unsaturated granular soil (spherical beads). Numerically, he presented a novel grain scale model for the investigation of liquid migration in plane shear tests, in the pendular domain, i.e., at low water content regime. In this model, volume changes are allowed due to liquid bridge rupture and formation, and due to liquid exchange between different bridges. This model is coupled to the dynamics of the particles which are modelled by contact dynamics, a special type among the discrete element methods. Gravity influence is neglected in the model.

Using this model, Mani (2014) has observed that the liquid spreads towards the top and bottom of the specimen (walls), directed away from shear band, see Fig 2.35. Although

the porosity increases in the sheared zone, the liquid content decreases. This behaviour was found to be due to two reasons. Firstly, in plane shear flows, particles undergo a diffusive motion driven by the local shear rate and therefore, also liquid which is carried by the menisci will diffuse in space (see Zik et al. (1991)). Secondly, there is a transport of liquid associated to liquid bridge rupture. The liquid is redistributed to all neighbouring liquid bridges after bridge rupture which means that locally, after a bridge rupture event, there is a liquid flux away from the rupture point. The rupture event causes a macroscopic liquid redistribution from regions of larger liquid contents towards lower liquid contents in a diffusive manner. This behaviour of the unsaturated soil in the pendular regime, where only capillary bridges exist, is the opposite of what is found in fully saturated granular materials presented earlier.

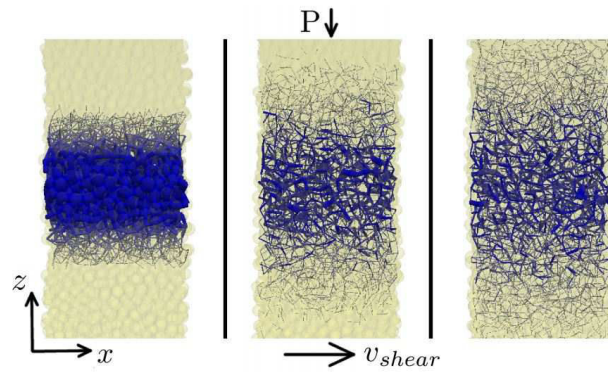


Figure 2.35: Snapshots of plane shear between two walls at the beginning (left), at an intermediate time (middle) and at the end of the simulation (right). Only the central part of the sample is shown and the (y) direction points into the plane. The capillary bridges are indicated by dark blue lines connecting the center of two spheres whose width is proportional to the bridge volume. It is seen that the liquid is spreading towards the top and the bottom wall (from Mani (2014))

Mani (2014) has investigated the influence of liquid content on the latter behaviour. He has found analytically that a certain dependency is indeed expected: since the rupture distance of a capillary bridge scales is $D \approx V^{1/3}$, where V is the volume of the bridge, thus the strain needed to rupture a capillary bridge increases with increasing bridge volume. Experimentally, Mani (2014) has validated the numerical results by observing fluid reduction patterns in shear bands using a split bottom shear cell. For the specimen preparation technique, he used glass beads mixed with 1% silicone oil (which corresponds to pendular domain). In Fig 2.36 shows that the shear band appears much brighter than the non-sheared region near the edges of the cell indicating that there is indeed a reduction in liquid content in the shear band. The experimental results are consistent with the numerical results found by Mani (2014).

To the authors knowledge, other than Mani (2014), liquid migration during shearing has not been analyzed in the past. However, this doctoral work presents water distribution while shearing qualitatively (macroscopically) using x-ray CT and quantitatively (microscopically) using several developed image processing techniques that allows following water distribution variation at each step of loading (suction and mechanical loading).

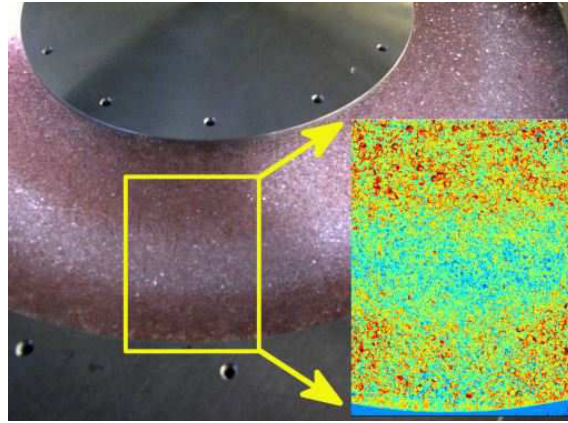


Figure 2.36: The wet granulate (silicone oil colored red), after the shearing. The shear band appears brighter indicating that there is a silicon oil reduction along the shear zone (from Mani (2014))

2.4 Summary and anticipated contribution

This chapter has reviewed some of the fundamentals concepts and the current knowledge of retention and hydro-mechanical behaviours of unsaturated soils, in the framework of this doctoral research. The definition of soil suction, water retention curve, influence of grain size and shape on water retention behaviour, water retention surface, hysteresis phenomenon and water retention domains have been described. A review on different studies on water retention behaviour has been given. Several analyses focusing on the constitutive equations of the hydro-mechanical behaviour of unsaturated soils have been presented. Shear strength, capillary cohesion, and volume change and water distribution in unsaturated soils have been discussed.

The review presented in this chapter showed that the microscopic retention and hydro-mechanical behaviour of unsaturated soils is rarely considered in the past work. Fluid volume distribution is described in the reviewed studies qualitatively, without quantitative analyses that could offer more information, related to water retention domains, hysteresis phenomenon, fluid evolution and distribution with loading (suction and the mechanical loading) and cohesion. The analyses of stress-strain response of unsaturated soils have been often accompanied macroscopically with no description of fluid distribution within the soils. Moreover, the mechanical response and the water retention properties are tested separately and the coupling link is usually missing. The contribution of capillary cohesion to shear strength is often investigated as the contribution of soil suction. Few analyses have considered cohesion evolution at the local scale, with microscopic-discrete characteristics as grain and pore size and shape distribution, inter-particle distance and number and volume of water bridges.

The present doctoral research looks to propose new techniques and methods for the microscopic-discrete analyses of retention and hydro-mechanical behaviours of unsaturated soils. These new techniques and methods allow performing microscopic-discrete measurements during water retention and triaxial tests. These measurements include porosity, degree of saturation, number of fluid clusters, their volumes and contacts, fluid phase continuity and deformation.

This work offers also further investigation on some axes of the coupled behaviour at the

microscopic-discrete scale. For example, the latter local measurements allows obtaining water retention curve, water retention surface, proposing a definition for water retention domains, better understanding of hysteresis phenomenon, characterizing capillary cohesion contribution to the hydro-mechanical behaviour of unsaturated soils, proposing capillary cohesion regimes and analyzing water distribution while loading at the grain scale.

Chapter 3

Experimental and data processing tools

3.1 General overview

The multi-scale analyses of retention and hydro-mechanical behaviours of unsaturated granular soils have required the development of advanced tools and methods by the author to take into account the microscopic-discrete scales observations. This chapter introduces in details the experimental tools used in this work to analyze 3D x-ray images obtained from water retention test and triaxial test.

The chapter starts with an introduction to x-ray tomography in section 3.2, knowing that x-ray tomography technique results are the main inputs for this work. This section describes also the used x-ray setup available in 3SR laboratory in Grenoble and its parameters. It follows on to the way in which a 3D image is reconstructed from the acquired data.

Section 3.3 details the trinarization technique that has been developed in a joint project between 3SR laboratory in Grenoble-France and Universit Libre de Bruxelles (ULB) in Belgium. In this project, the collaborative work between the author and Mir Amid HASHEMI AFRAPOLI (a PhD student in ULB) has an ambitious goal: to obtain a procedure that helps to separate the phases: solid, liquid and gas present in 3D x-ray reconstructed images of an unsaturated soil. This procedure is covered step by step in this section.

In order to perform 3D measurements of porosity and degree of saturation at the grain scale, a Representative Elementary Volume (REV) must be defined. A developed analysis that helps to define REV size is presented in section 3.4. Later, this section presents the technique to obtain 3D fields of porosity and degree of saturation.

The process of identifying (labelling) each grain, water and air cluster is described in section 3.5. The process of labelling allows following the evolution of each phase with loading (suction or mechanical loading). This evolution is detailed in section 3.5.1 and 3.5.2.

Section 3.6 introduces Digital Image Correlation (DIC) as a tool to perform kinematic analysis carried out between different configurations (i.e., between different images). It describes DIC implementation in this work using continuum DIC Tomowarp, created by Stephen Hall and discussed in Hall et al. (2010), among others.

3.2 X-ray tomography

In order to perform microscopic-discrete investigation of soils behaviour, researchers have used different advanced experimental methods. Each of these methods has its own requirements and testing condition. For example, Mercury Intrusion Porosimetry (MIP), Scanning Electron Microscopy (SEM), Focused Ion Beam (FIB) and Broad Ion Beam (BIB) are destructive methods and their application is limited to small specimens and provides high resolution up to 510nm (see Romero et al., 2009; Bogner et al., 2007; Simms et al., 2004; Mac et al., 2012). On the other hand, x-ray Computed Tomography (CT), could provide morphological information of relatively small specimen in non-destructive way and with enough high resolution (maximally $5\mu\text{m}$).

X-ray computed tomography (CT) is an established and rapidly evolving technology that provides non-destructive three-dimensional visualization, and characterization, of the internal structure of objects to be investigated. It creates images that map the variation of x-ray attenuation (attenuation coefficient) within objects, which relates closely to density. Moreover it allows the reconstruction of a three-dimensional volume of the specimen by assembling two dimensional radiographic images taken at different angles.

X-ray CT was developed as a medical imaging technique in the early 1970s (see Hounsfield 1972). The possibility of its use in engineering was soon recognized, resulting in large numbers of publications from the early 1980s onwards. Some of x-ray applications includes studies in the fields of soil science (e.g., Ringhi et al., 1996; Pierret et al., 2001; Pansu et al., 2007), petroleum geology (e.g., Tovar, 1997; Satik et al., 1998; Diabira et al., 2001), geotechnics (e.g., Blaheta et al., 2011; Ogundalu et al., 2014) and sedimentology (e.g., Ashi, 1997; Tanaka et al., 2011).

In a geomechanical context, x-ray can be used to characterize local deformations within a soil specimen in a mechanical testing device (see Desrues et al., 1996; Bornert, 2010; Hall et al., 2010; Alshibli et al., 2010). For example, Andó et al. (2012) have performed tri-axial tests and used x-ray imagery to understand the development of shear bands at the micro-structural scale. The technique allows producing full three-dimensional numerical images with details such as the shape of sand particles (see Andó et al., 2012), their spatial distribution and arrangement, as well as the pore size distribution and bulk density (see Desrues et al., 1996; Perret et al., 1999; Gantzer et al., 2002; Koliji, 2008; Tippkttter et al., 2009; Bornert et al., 2010; Doan et al., 2012).

For numerical simulations, tomographic images can be directly translated into models for mechanical analysis, as performed using level-set segmentation in porous media for Finite Element Method (FEM) numerical simulations (see Legrain et al., 2010). Vlahinic et al. (2014) have used x-ray images to extract quantitative descriptors of grain-scale processes, such as the morphological description of particles, kinematics, and the spatial interactions, through Discrete Element Method (DEM) modelling.

For unsaturated soils geo-mechanics, x-ray micro tomography can be used to calculate distributions of local void ratio in a porous media (e.g., Al-Raoush, 2006). In addition, x-ray allows pore scale measurements such as fluid distribution; interfacial area and flow process (see Culligan et al., 2004; Wildenschild et al., 2004; Culligan et al., 2006; Myers et al., 2011). Khaddour et al. (2013) have presented local measurement of porosity and degree of saturation at the grain scale, through the study of water retention behaviour of unsaturated sand using x-ray CT. These results of local measurements will be detailed in

the present doctoral work. Kim et al. (2012) have used the microstructure information from x-ray tomography data to determine pore size distribution and coordination number for granular assembly.

The main advantage of x-ray CT, in the context of the present study, is its ability to track the water within the soil. X-ray CT has been used to image fluid flow, the hydraulic conductivity and to investigate liquid phase evolution during drying process of unsaturated soils (see Wildenschild et al., 2005; Christensen et al., 2006; Guber et al., 2010; Gruber et al., 2012; Narter et al. 2012; Wang et al., 2012; Khaddour et al., 2013; Manahiloh 2013). It has been also used for some experiments in order to evaluate the influence of initial moisture content and type of infiltrating fluid on the formation of preferential flow paths (see Rimmer et al., 1998; Bauters et al., 2000). Bayer et al. (2004), Bock et al. (2011) and Kim et al. (2015) have used x-ray tomography in order to study water retention behaviour and water flow in different soils.

The coupled hydro-mechanical behaviour of unsaturated soils can be analyzed using x-ray tomography. Zhang et al. (2012) and Higo et al. (2013) have used processed tomography images to observe how the deformation becomes localized and calculate shear band thickness, identify water and air clusters and grain particles, provide local measurements of porosity and degree of saturation.

A thorough description of x-ray CT technique including the physical background, potential error sources and example applications, some of its advantages and limitations can be found in (Ketcham et al., 2001; Wildenschild et al., 2002; Scarfe et al., 2008; Taina et al., 2008; Cnudde et al., 2013).

3.2.1 X-ray scanner in 3SR laboratory

The experiments in this study are performed using x-ray setup of 3SR Laboratory at Grenoble University to visualize partially saturated granular porous media. Because water, sand and air have different x-ray attenuation coefficients, a significant contrast for the three phases is observed in an x-ray transmission image. A quantitative analysis provides detailed information on the arrangement and distribution of grains, air, and water, can be built.

The x-ray scanner is housed inside a lead-lined cabin, where the x-ray source, detector and turntable stage can be found, see Fig 3.1.

The imaging process can be summarized as follows: the cell is placed on a turntable stage whose rotation can be accurately controlled. The x-ray source generates a continuous x-ray beam; the beam passes through the object and casts an x-ray shadow onto the detector. The radiation that hits the detector is converted into an electronic charge that is subsequently passed to a computer to create a radiograph (i.e., digital image). A series of images is acquired while rotating the object step by step through 360° at a predefined angular increment. These projections contain information about the position, chemical composition and density of the absorbing features within the specimen. The data obtained is used for the numerical reconstruction of the final 3D image.

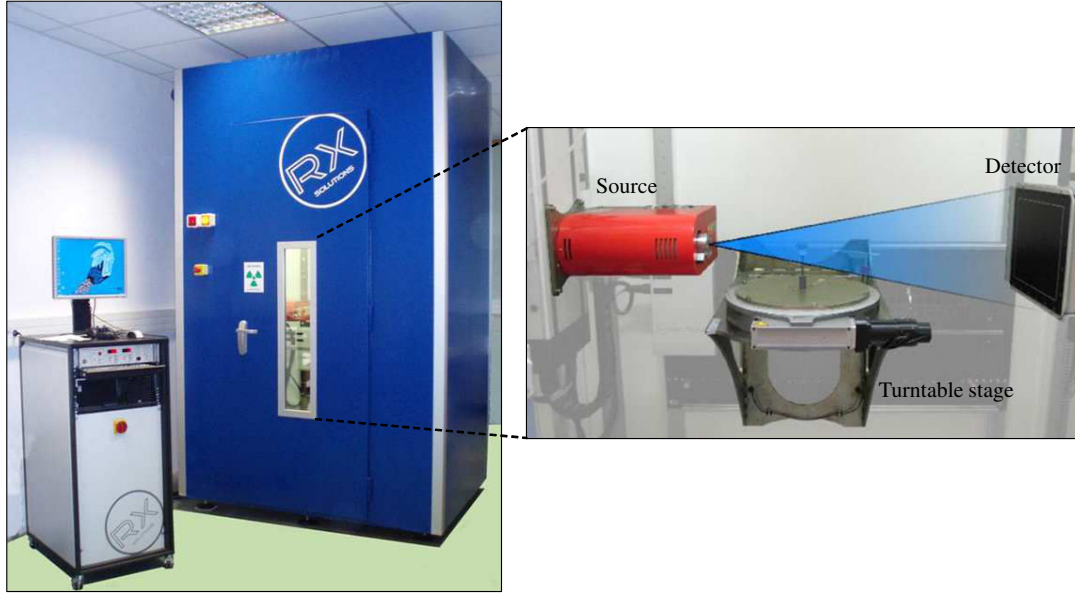


Figure 3.1: X-ray scanner in 3SR Laboratory

3.2.2 X-ray parameters

The micro-CT characterization of the specimen implies choosing a set of different parameters. The selection of the proper parameters for the acquisition is an important issue that was clarified in this study. In good tomography practice, the energy and the intensity of x-ray source, the need or not of filters and the number of radiographies have to be analyzed in order to optimize the acquisition time and obtain good quality of the resulting images (see Hsieh et al., 2009; Als-Nielsen et al., 2011). In this doctoral work, these parameters were defined separately for the two tests performed in this work, i.e., water retention and triaxial tests, separately. Table 3.1 shows a summary of what are thought to be the best parameters for x-ray acquisition, when using x-ray setup in 3SR Laboratory and working with unsaturated sand, in order to achieve a good contrast between the three phases that have to be clearly seen. Two important parameters are rotation speed of the plate and the waiting time before the acquisition of each image. Indeed, since the tests in this work are conducted on unsaturated soils, water clusters exist within the porous space of the specimen, and due to inertia they can be moved with respect to the grains if the turntable acceleration is excessive. Such an effect was observed during the set-up validation, resulting in a blurring of the water phase clusters. A proper choice of rotation speed solved the problem.

Table 3.1: Recommended parameters for x-ray CT of unsaturated geomaterials

Tomography Acquisitions	Parameter	Recommended Value	
		Water retention test	Unsaturated triaxial test
	Source Tension	100 kV	100 kV
	Current Intensity	50 μ A	100 μ A
	Number Of Images	1200	1024
	Average Between Images	5 or 6	8
	Wait Before Each Image	0,5 to 0,7 seconds	0,5 to 0,7 seconds
	Rotation Speed	Very slow (3 degree/min)	Very slow (3 degree/min)
	Acquisition Time	Around 2 hours	Around 2 hours
	Resolution (voxel size)	7,5 μ m	13 μ m

3.2.3 X-ray reconstruction

The main purpose of the process of reconstruction is to allow having 3D images of the scanned object from a series of x-ray projections (2D digital images). In this work, the reconstruction software DigiCT version 2.4.2 from Digisens is used. DigiCT uses a reconstruction algorithm based on the FDK Algorithm, after Feldkamp, Davis and Kress (for more details, see Feldkamp, 1984).

The reconstruction process results are 3D images. From these images, the distribution of the number of voxels (pixels in 2D) as a function of their intensity level (gray value) can be plotted. This distribution is called the histogram. Histograms can have different shapes according to the features present in the images that they represent. For unsaturated soils x-ray images, there are three main phases, the solid phase formed by voxels representing the grains, the liquid phase and the gas phase, which are respectively associated with voxels representing water and air. In these images, obtained by absorption contrast, the void voxels have lower intensity values than the solid voxels and thus air and water voxels look darker than the grains voxels. Therefore the typical histogram for these images, takes the form of a multi-modal distribution in which the voxels intensities are clustered around three separated values. In Fig 3.2, 8-bit reconstructed image of unsaturated sand is presented, with the histogram. The peak located at lower intensity values is associated with the air voxels which is represented on gray level images in black color, while the peak located at the higher intensity is associated with the grains which appear in gray level images in a lighter gray color, to distinguish from darker gray for water. The 3D reconstructed images are the input for all the steps of image processing and analysis and it will be used to make microscopic-discrete measurements to analyze retention and hydro-mechanical behaviours of the studied material.

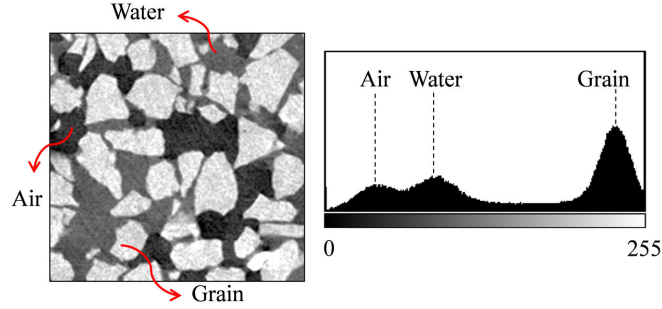


Figure 3.2: Phase contrast in x-ray 8-bit reconstructed image (left) and the corresponding histogram (right)

3.3 Trinarization

The main objective of image trinarization (or segmentation) is partitioning the image into objects of interest. It consists of labelling each voxel according to its intensity value relative to a reference parameter known as the intensity threshold.

Different methods exist for finding the threshold value, such as edge detection (see Marr et al., 1980; Canny, 1986), anisotropic diffusion (see Perona et al., 1990), split-and-merge (see Faruquzzaman et al., 2008) watershed (see Beucher et al., 1992), stochastic watershed (see Meyer, 2012), level-set (see Malladi et al., 1993; Sethian, 1999), region-growing (see Adams et al., 1994 and Pham et al., 2000) and statistical region merging (see Nock et al., 2004). These approaches were developed for classical photography to distinguish non-uniform and irregularly shaped objects. They are therefore well-adapted and efficient when few objects have to be identified.

For granular materials, the number of objects can be very high. Therefore traditional segmentation techniques might require unaffordable computational time in order to be able to identify the individual particles and the individual voids in the image.

Image segmentation into different phases is usually made through a simple histogram threshold, taken as the minimum gray value in the valley between two peaks of the histogram (for bi-modal histogram of two phases). Fig 3.3 shows the results obtained for thresholding grain-air image by choosing (T_{\min}). The results of this process are satisfactory, and the two phases are separated.

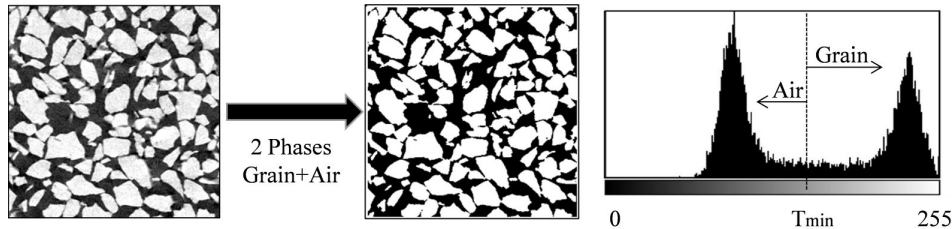


Figure 3.3: Simple threshold of an image with two distinct gray values (using Image J®)

However, the number of voxels located in the gap between two peaks can be associated with the Partial Volume Effect (PVE) caused by voxels whose intensity is an average of the attenuation of the two main materials in the soil specimens (grains and air) due to

the finite resolution of the images, (see section 3.2.2).

Due to PVE, and the presence of noise, a simple threshold of the gray value is not sufficient to properly separate the different phases, as shown in Fig 3.4. Consequently, a proper thresholding must consider not only the gray intensity of the voxels but also their relative positions.

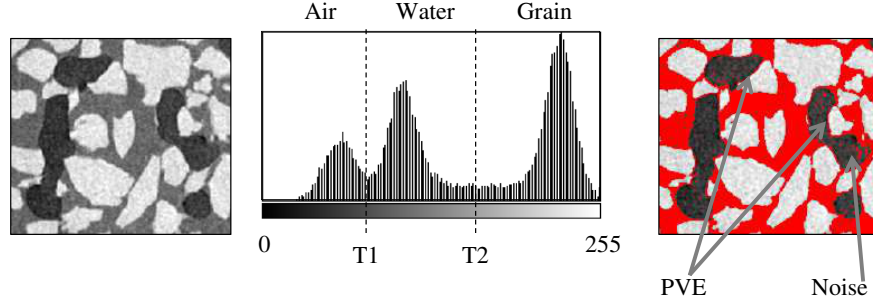


Figure 3.4: Simple threshold of an image with three distinct gray values (using Image J[®]). The segmented image shows the presence of PVE and noise

Based on the above-mentioned considerations, a region growing type segmentation was developed. The full procedure followed for the image segmentation of unsaturated soils will be detailed in the following. This procedure is applied on 3D x-ray 8-bit (0-255 gray level range) reconstructed images, and it is divided into four steps: (1) partial thresholding, (2) PVE filtering, (3) simultaneous phase growing which constitutes the main step and finally (4) interface filling (see Hashemi et al, 2013).

Fig 3.5 shows the resulted images for the four sequential steps of the segmentation procedure, applied for unsaturated sand. In these images, the color red represents the grains; the color green represents water; the color blue represents air and the color black for undefined regions.

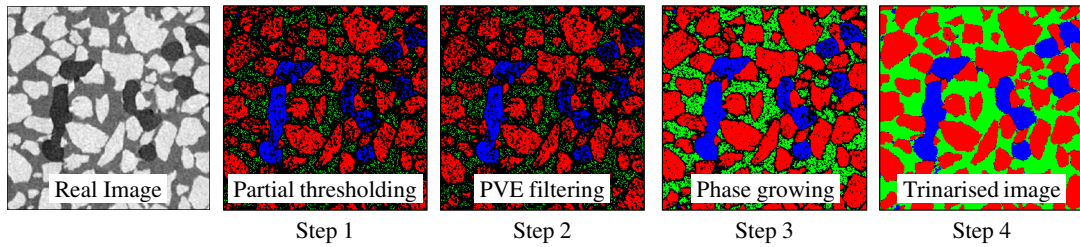


Figure 3.5: Evolution of phase segmentation process in the developed trinarization technique. The color red represents the grains; the color green represents water; the color blue represents air and the color black for undefined regions

3.3.1 Partial thresholding

The first step of this procedure is to define the regions where each phase is present. This can be done by thresholding the gray values where the histograms are not overlapping (the histogram is considered as Gaussian curves). This partial threshold is crucial for the efficiency of the method; therefore the percentage of selected voxels must be a good compromise. Selecting too few voxels would not allow having a good predictor of the phase

organization, while selecting too many could incorporate voxels from another phase. A good compromise can be considered by selecting the partial thresholds as the peaks of the histogram of the image. Fig 3.6 shows a sketch of the histogram of unsaturated sand and illustrates how to select the partial thresholds.

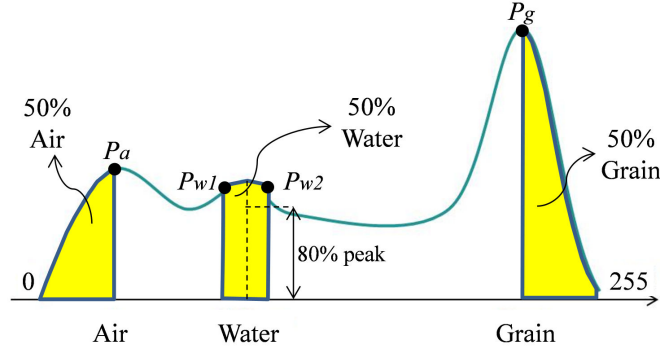


Figure 3.6: Procedure to choose the partial thresholds for each phase as the peaks of the histogram. The sand threshold (P_g), the air threshold (P_a) and the water thresholds (right- P_{w2}) and (left- P_{w1})

The thresholds are initially selected as follows: the sand threshold (P_g) isolates the 50% upper part of the sand Gaussian curve, and the air threshold (P_a) isolates the 50% lower part of the air Gaussian curve. For the water, since this is the intermediate phase, the thresholds are defined to select 25% dark (left- P_{w1}) and 25% bright (right- P_{w2}) pixels starting from the corresponding peak. This is achieved by locating where the Gaussian curve of this phase decreases to 80% of its peak.

Consequently, these four partial thresholds ($P_a < P_{w1} < P_{w2} < P_g$) will determine 50% of each phase. Fig 3.7 shows the resulted image of this step, where grains are represented in the color red; water is represented in color green; air is represented in color blue and the color black for undefined voxels, which are to be defined in the following steps.

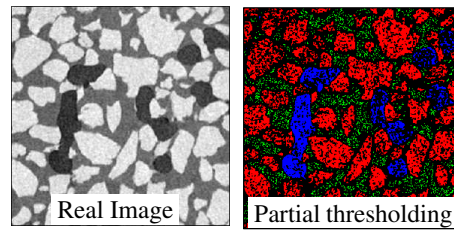


Figure 3.7: Results of partial thresholding step. Grains are represented in the color red; water is represented in color green; air is represented in color blue and the color black for undefined voxels

At this point, a needed correction should be considered for PVE. As the partial threshold for water phase is applied, not only water voxels are chosen but also PVE ones (one voxel shared between grain and air phases and considered later as water when thresholding). Fig 3.8 shows PVE presence in the partially thresholded images, represented as a sequence of water voxels around the grains. This limitation of the first step is to be corrected in the next step.

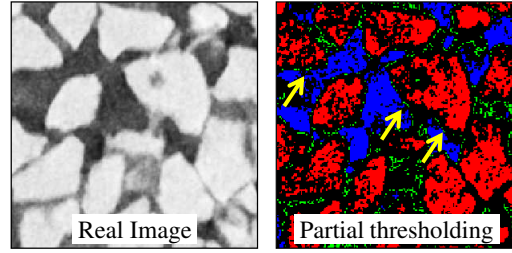


Figure 3.8: Resulted partial volume effect from partial thresholding step. PVE is represented as a sequence of water voxels around the grains. Grains are represented in the color red; water is represented in color green; air is represented in color blue and the color black for undefined voxels

3.3.2 Partial Volume Effect filtering

PVE takes place when grain and air phases are taken into account into one voxel, see Fig 3.9. This voxel is then representative of both phases showing an intermediate gray value corresponding to a balanced average of the gray levels of the two distinct phases. Therefore, the gray value of PVE depends on the percentage of each phase in the voxel. Thresholding the image by selecting the middle phase, will also select voxels located at the interface between the two others due to PVE. As the surroundings of a voxel from PVE contain voxels from both air and grain phases, thus they have high variance in their gray value, while the surroundings of a water voxel are mostly water voxels having low variance in their gray values. Basing on that, a set of STandard Deviation (STD) calculations inside a spherical selection around each voxel of the voxels considered as water in the former step is build. The optimal radius of the spheres is 2 voxels.

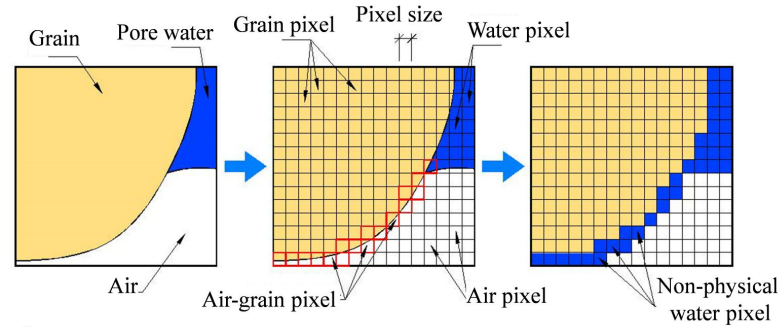


Figure 3.9: Partial volume effect definition as a voxel shared between grain and air phases, and considered when segmenting as a water voxel

As the STD of voxels representing PVE is high, it will cause on the histogram, a small increase in the STD values. In order to exclude PVE voxels, a threshold filtering (V) of the STD was used. The threshold is taken at the inflexion point on the histogram, see Fig 3.10. The result of the STD threshold is shown in Fig 3.11.

Partial volume effect filtering in this procedure shows a good efficiency by filtering most of the voxels located at the interface between voids and sand particles. After PVE filtering, all the excluded voxels were re-set to color black in order to be handled in the following steps.

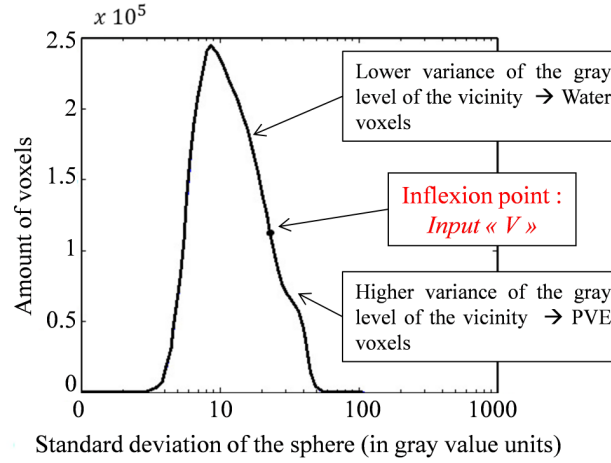


Figure 3.10: Standard deviation histogram and its threshold. PVE threshold filtering (V) defined as the inflexion point on the histogram

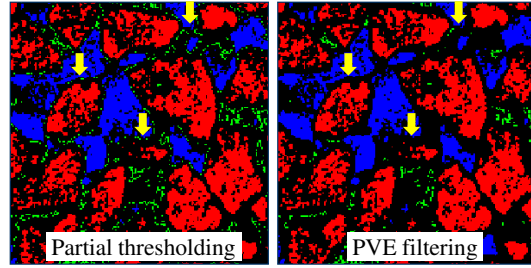


Figure 3.11: The result of partial volume effect filtering step. Grains are represented in the color red; water is represented in color green; air is represented in color blue and the color black for undefined voxels

3.3.3 Simultaneous phase growing

In order to fill the other half of each phase, (interfaces are not considered), new thresholds defined as tolerance thresholds are therefore chosen (T_a , T_{w1} , T_{w2} and T_g). These tolerance thresholds will allow the phases to grow in 3D, simultaneously, only in the directions where no other phase is present. This step will define the undefined voxels (black color) without considering the interfaces, which will be handled in the fourth step. The tolerance thresholds are chosen equal to the partial thresholds; i.e., $T_a = P_{w1}$, $T_g = P_{w2}$, $T_{w1} = P_a$ and $T_{w2} = P_g$. The gray value and the location of each voxel are examined before determining to which phase it belongs. Fig 3.12 summarizes the process of voxels examination. The questions into the boxes are asked to a voxel neighboring a cluster of voxels already identified as belonging to a given phase; hence this voxel is candidate to be attributed to this phase in the growing process.

The resulted images from simultaneous phase growing step are presented in Fig 3.13. In this figure the three phases has grown (shown as the difference between left and right images) and the black voxels, shown in the left image, have been defined to which phase they belong, in the right image.

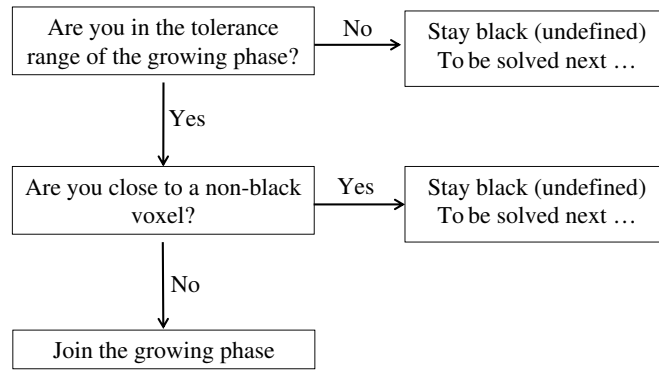


Figure 3.12: Voxel examination in simultaneous phase growing step. The questions into the boxes are asked to a voxel neighboring a cluster of voxels already identified as belonging to a given phase; hence this voxel is candidate to be attributed to this phase in the growing process

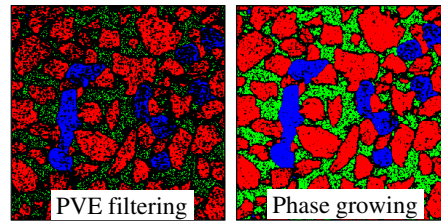


Figure 3.13: The result of simultaneous phase growing step. Grains are represented in the color red; water is represented in color green; air is represented in color blue and the color black for undefined voxels

3.3.4 Interface filling

At the end of the phase growing step, some voxels remain at the interfaces. The final step of the procedure is to determine the phases to which, these voxels of the interfaces are belonging. For each voxel at the interface, another sphere selects the surrounding voxels with a radius of 2 voxels, is taken. The most present phase inside the sphere will determine the phase segmentation. If the majority of the voxels inside the sphere belong to the phase (x), then the examined voxel is set to belong to this phase (x). Fig 3.14 shows the whole procedure of phase segmentation, including the interface filling.

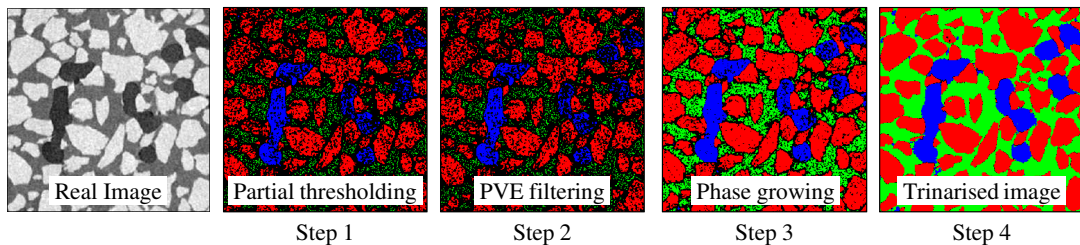


Figure 3.14: Evolution of phase segmentation process, including Interface filling step results. Grains are represented in the color red; water is represented in color green; air is represented in color blue and the color black for undefined voxels

In conclusion, trinarization technique is used to separate the phases: grains, water and air proceeding from the reconstructed x-ray images. Each phase in the trinarized volume

has one single gray value. All the grains have the same gray value 255, water has 128 and air phase has 0. The trinarization of one volume (e.g., one scan of 1500^3 voxels) lasts around 8 hours (using Matlab[®] on a high performance computer). Through the first hour, an interactive procedure allows the user to choose the values of the variables needed ($P_g, P_{w1}, P_{w2}, P_a, V, T_g, T_{w1}, T_{w2}$ and T_a), then the code will run automatically. Those variables are of the same values for one specimen, different steps of loading (i.e., suction or mechanical loading). The results of the code are TIFF images that can be manipulated using any images editor. In this work Image J[®] (Fiji) software is used for images editing.

At the end, the three phases: grains, water and air, can be separated and extracted to perform several calculations, using the number of voxels (3D calculations) representing each phase. In this work, these calculations include macro and micro porosity and degree of saturation, for both retention and triaxial tests. Later in chapter 4 and chapter 5, a validation of this technique is presented.

3.4 Representative Elementary Volume

A Representative Elementary Volume (REV) is the minimum volume over which a calculation can be performed to extract relevant macroscopic measurements from micro-structural information gathered over complex heterogeneous media like granular soils. The REV can be defined as the minimum volume of a soil specimen from which a given parameter becomes independent of the size of the specimen.

There are two main approaches commonly used to determine the REV of a given specimen in order to predict and analyze the effective macro scale parameters. The first approach determines a REV for a parameter of concern (e.g. porosity), regardless the macroscopic value of this parameter. Therefore, the size of REV in this approach is defined as the volume (of a size X) over which the measured values of the parameter of concern are coinciding; indicating that at this size of the volume, the parameter of concern is independent of the size of the volume (X). This approach is common in soil science and hydrology literature (see Clausnitzer et al., 1999; VandenBygaart et al., 1999; Brown et al., 2000).

The second approach determines a REV based on macro scale parameters (e.g., porosity) without prior determination of micro scale parameters of the specimen (e.g., local void ratio, coordination number ···etc). In this approach, REV is defined for a parameter of concern (e.g., porosity), then it is used for the micro measurements of other parameters of concern (e.g., local void ratio). This approach is commonly used in engineering mechanics literature (see Culligan et al., 2004; Al-Raoush et al., 2010; Costanza-Robinson et al., 2011; Andó et al., 2013; Bruchon et al., 2013).

The determination of REV size is by no means a trivial task as it is a function of the nature of the material being considered, and the micro scale parameter being looked for. In this work, the objective is to obtain 3D local measurement of porosity (n) and degree of saturation (S_r). Porosity and degree of saturation measurements are of a fundamental importance in unsaturated soils mechanics. They allow characterizing the state of the soil, in terms of density, granular assembly (for porosity), water distribution, hydraulic domains and evolution under suction or a mechanical loading (for degree of saturation). Porosity represents the ratio of the pore volume to the total volume of the specimen and degree of saturation represents the ratio of the pore water volume to the total pore volume:

$$\text{Porosity} \quad n = \frac{V_v}{V_t} \quad \text{Degree Of Saturation} \quad Sr = \frac{V_w}{V_v} \quad (3.1)$$

In order to achieve the former local measurements, the solid and void phases in the trinarized 3D images need to be integrated over some sub-volumes. The sub-volumes need to be sufficiently small in order to make a usefully local measurement of porosity (i.e., a sub-volume occupying most of the specimen is not describing a local measurement). The sub-volumes also need to be sufficiently large in order not to be too sensitive to the underlying material. Moreover, the sub-volume size must be chosen large enough so that when it is used to measure a granular material, considered as having a homogeneous density, it provides a relatively stable measurement. Once this sub-volume is chosen, then it is called a Representative Elementary Volume (REV).

The problem is that porosity and degree of saturation described typically as homogeneous are not really very homogeneous at the grain scale. Furthermore, a single REV may not necessarily be possible to define for a heterogeneous granular material, such as one that has undergone shear localization.

In the following the procedure to define REV size in this work is presented. This procedure considers the heterogeneous distribution of porosity and degree of saturation, for a specimen undergoing suction and a mechanical loading.

3.4.1 REV mapping

In order to define the appropriate size of REV, a mapping code was specifically written in Python, by Edward Andó, in 3SR laboratory. The code uses the trinarized 3D images where a set of nodes used for the analysis is defined.

For each node, the program grows a cube approximately centered on the node. The cube grows step by step by shifting the corners progressively away from the node, checking that the corners do not move outside the 3D image. As the cube grows, the porosity is calculated by summing the number of void voxels in the cube and then dividing this by the known volume of the cube. At the same time, the degree of saturation is calculated by summing the number of water voxels in the cube and dividing this by the void voxels. This generates, for each node, an array of cube dimensions and their corresponding porosity and degree of saturation. These readings necessarily start from a volume of 1 voxel, which has either 0% porosity (i.e., solid voxel), or 100% porosity (i.e., void voxel). Same for degree of saturation, the 1 voxel, has either 0% degree of saturation (i.e., solid or air voxel), or 100% degree of saturation (i.e., water voxel). As the sub-volume increases in size, the calculated value changes. For nodes where the increasing sub-volume does not go out of the domain of the specimen, the microscopic reading is expected to tend towards the macroscopic one. This is illustrated, for adequately chosen nodes, i.e. not too close to the boundaries of the specimen, in Fig 3.15.

In this figure, the length of the side of the cube increases from one pixel (px), to 200px. This is shown, for illustration purpose, for unsaturated sand specimen, with 50% degree of saturation, where the size of the voxel is $7.5 \times 7.5 \times 7.5$ voxels (see Table 3.1). Many aspects can be pointed out from this figure. Most importantly, for all the nodes, a value of porosity around 42% to 47% can be declared, where REV size starts to stabilize definitely. Eight nodes are present in this graph, which corresponds to node separation 140px (as an example) at the three axes. The position of these nodes within the specimen can be

estimated. Nodes (1, 2, 3) are located in a void voxel, since they start from ($n=100\%$) and decrease gradually as the size of the cube is increasing to consider a bigger volume than the one before, where grains start to be involved. Node (4, 5, 6, 7) are located in a grain voxel with ($n=0\%$) at the beginning, and as the cube size is increasing, the porosity measurement indicates that the cube is still in a grain.

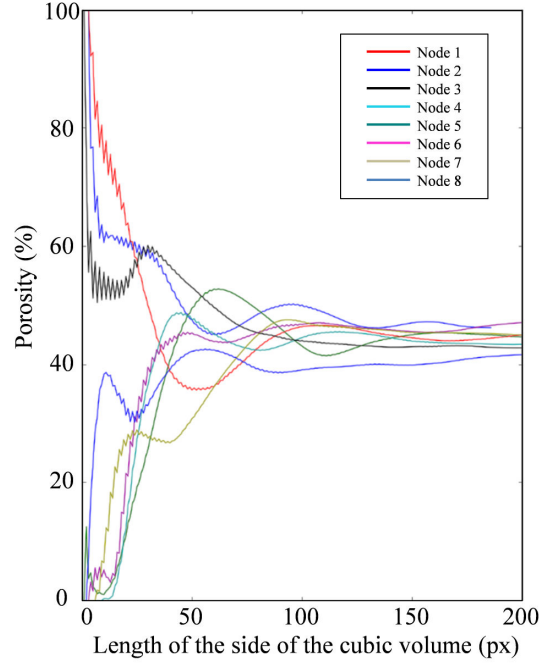


Figure 3.15: Evolution of the measurement of porosity as the side of the cubic sub-volume increases. This is shown for unsaturated sand specimen, with 50% degree of saturation

This process continues until the cube reaches a bigger volume where voids start to be involved, and at which porosity is no more null. Only node (8) is located near the border of the grain and the cube rapidly includes pore voxels in the estimation.

3.4.2 REV analysis

In order to make measurements of porosity and degree of saturation at a given point within the specimen, a size of REV needs to be selected. This can be done once for all nodes, by selecting an acceptable level of convergence using a graph like Fig 3.15. It is clear that a value of $10 \times 10 \times 10$ voxels is too small, and that $200 \times 200 \times 200$ voxels would be excessive. However, the choice of a value between these two extremes is not easy. Therefore, a set of statistical tools was developed by the author using Matlab[®], to analyze the size of sub-volume in the convergence domain.

For each ten one-pixel growing steps (ten measures of porosity and degree of saturation), a comparison based on a stability criterion is set. The stability criterion is defined so that: if the variation between ten points is equal or smaller than a tolerance value (ϵ_n for the porosity and ϵ_{Sr} for the degree of saturation), then the sub-volume size is assumed to be correct and the porosity-degree of saturation is assigned to the first of the ten points. If the variation is larger than the tolerance value of the stability criterion, a

new one-pixel-shift is performed (new point), added to the ten points and compared again. The developed program does this until the stability condition is satisfied or a predefined maximum value of REV size is reached (e.g., the value 200px in Fig 3.15).

This process is repeated for several tolerance values for the porosity and degree of saturation. Then the normal distribution of the sub-volume size determined in every node over the specimen is defined for different tolerance values of the criterion. The Standard Deviation (STD) and the peak of the normal distribution are calculated. Fig 3.16 shows the evolution of STD and peak value with respect to the criterion value for unsaturated sand specimen with a degree of saturation of 50%.

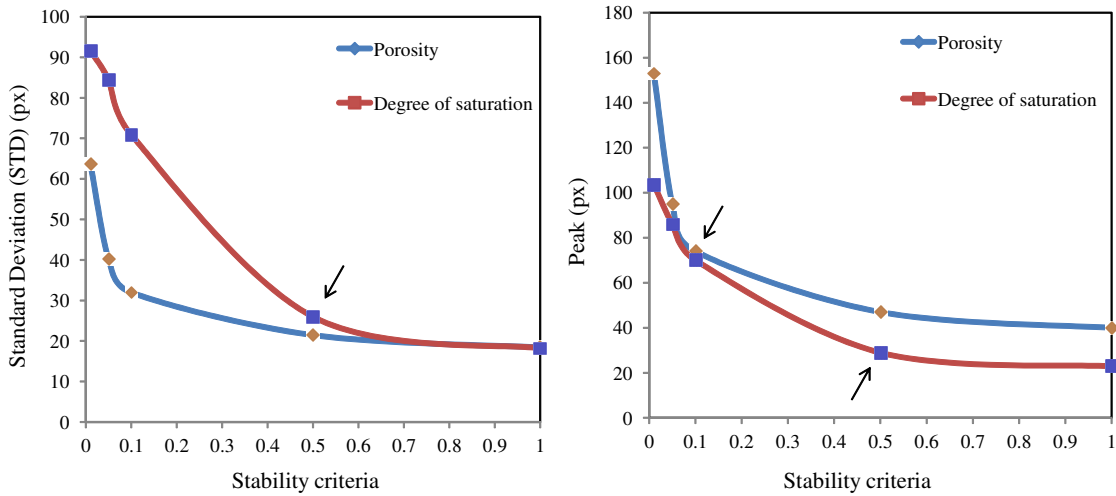


Figure 3.16: The relation between stability criteria versus the Standard deviation (left) and the peak value (right) of the corresponding sub-volume size. This is shown for unsaturated sand specimen, with 50% degree of saturation

As shown in Fig 3.16, the peak and the STD of the normal distribution of the sub-volume size decreases as increasing the stability criteria. Consequently, considering a sub-volume with a size equal to e.g., $(\text{peak} + 2 \times \text{STD})$, this size decreases when increasing the tolerance value: larger the tolerance, smaller the first sub-volume size fitting this tolerance. The slope of the latter curves changes at two points: $\Delta n = 0.1$, for the relation between the tolerance value for porosity versus STD and the peak, and $\Delta S_r = 0.5$, for the relation between the tolerance value for degree of saturation versus the STD and the peak. Beyond these two points, the peak and STD are independent of the tolerance value, thus the two tolerance values: $\Delta n = 0.1$ and $\Delta S_r = 0.5$ were chosen and fixed for this work. In Fig 3.17, the normal distribution of the sub-volume size for these values is presented considering all the nodes, for an unsaturated sand specimen, with 50% degree of saturation.

The normal distribution shows a peak value for the sub-volume size = 70px and a $\text{STD} = \sigma = 32\text{px}$ for the case of porosity (left), and a peak value for the sub-volume size = 30px and $\text{STD} = \sigma = 26\text{px}$ for the case of degree of saturation (right). In the example shown above in Fig 3.17, the sub-volume size equal to $(\text{peak} + 2 \times \text{STD})$ is 98% of the maximum size of the determined sub-volume. In other words, this value almost consider all the determined sizes of the sub-volume and thus almost all the stabilized measurements of the porosity and degree of saturation. This value is called in this work $\text{REV}_{\text{optimal}} = \text{peak} + 2 \times \text{STD}$ and it is considered as a reasonable index for the process of defining the size of REV.

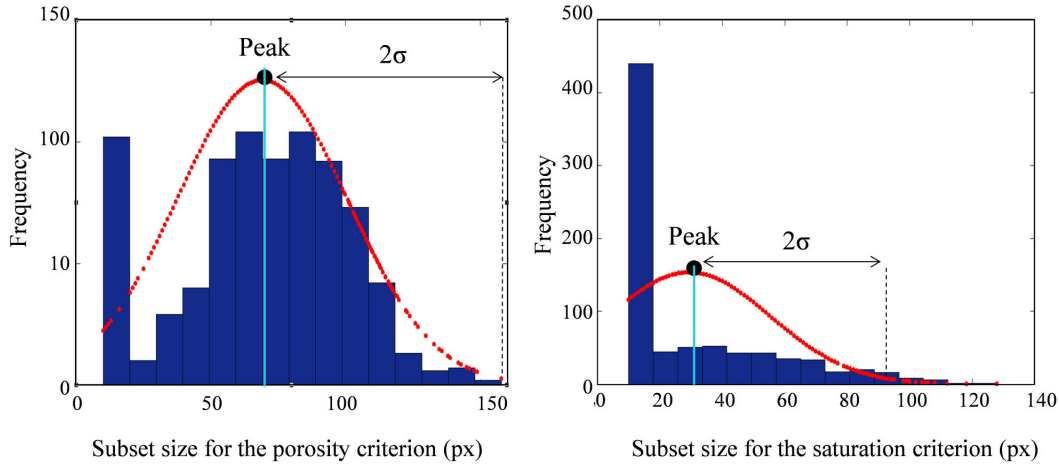


Figure 3.17: Normal distribution of sub-volume size for porosity criterion $\Delta n=0.1$ (left) and for degree of saturation criterion $\Delta S_r=0.5$ (right). This is shown for unsaturated Hostun sand specimen, with around 50% degree of saturation

REV_{optimal} is defined for porosity and degree of saturation respectively. For Fig 3.17, $REV_{\text{optimal}} = \text{peak} + 2 \times \text{STD} = 70 + (2 \times 30) = 134\text{px}$ for porosity, while for degree of saturation, $REV_{\text{optimal}} = 30 + (2 \times 26) = 82\text{px}$. A size for $REV = 134\text{px}$ takes into consideration both REV_{optimal} of porosity and degree of saturation. This size can be generalized as a minimum size of REV for the latter studied case.

This approach gave a relatively small REV size that is comparable to D_{50} of the grains ($REV \text{ size} = 134\text{px} \approx 3 \times D_{50}$ for Hostun sand). Moreover, it considers the distribution of porosity and degree of saturation by choosing the stabilized size of the sub-volume for almost all the nodes and for a defined tolerance.

The behaviour of the material studied in this work, was analyzed using two types of experiments: water retention tests and triaxial tests. The size of the specimen, the resolution of the images and the initial porosity are different for the two experiments and thus there are two sizes of REV chosen in this work. The results of REV analysis are presented in chapter 4 and 5 for water retention test and triaxial test, respectively.

3.4.3 Porosity and degree of saturation mapping

Running the developed mapping code, for the chosen REV size on the volume of interest, gives a value of porosity and degree of saturation in percentage for every point in the defined grid. Node spacing can be set smaller than REV size and thus measurement overlapping is allowed, or it can be set equal to REV size so that measurement overlapping is not allowed. The size of the mesh holds the same trade off presented for REV size (i.e., coarse mesh does not describe the local measurement while a fine mesh carries misleading information).

In this work, it is pointed to measurement overlapping (or without overlapping) when it is allowed.

The results of mapping the porosity and degree of saturation is a volume (3D images) formed by a number of voxels, where each voxel is associated to one node. These results

can be manipulated and treated as a volume map of porosity and degree of saturation.

Results of porosity and degree of saturation are shown in chapter 4 and 5 for water retention test and triaxial test, respectively. Fig 3.18 shows an example of a 2D section in a 3D porosity map, for unsaturated Hostun sand, with the grid applied to the mapped volume. In this case, measurement overlapping is not allowed.

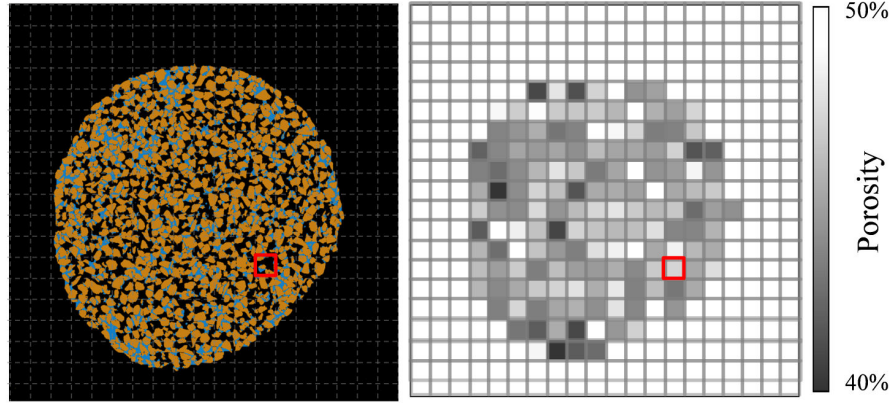


Figure 3.18: The trinarized image of unsaturated sand (left) and porosity map in 2D with the applied grid (right). Measurement overlapping is not allowed

3.5 Microscopic-discrete analyses

3.5.1 The evolution of the number of fluid clusters with loading

Using the 3D trinarized images, the number of fluid (i.e., water and air) clusters within the soil specimens is investigated. The evolution of this number is explored through the two experiments campaigns presented in this work: water retention test and triaxial test.

Water phase can be found within the soil as clusters (patches, bonds or bridges) formed between two or more grains, and water films. With the maximum resolution obtained in this work ($7.5\mu\text{m}$ for retention test and $13\mu\text{m}$ for triaxial test), only water clusters are characterized while water films cannot be imaged. The resolution to capture water films coating quartz sand (as Hostun sand studied in this work) need to be better than $0.4\mu\text{m}$ (see Crist et al., 2004; Zevi et al., 2005).

In water retention test, suction is increasing or decreasing depending on the path (drying or wetting, respectively). When suction changes, the degree of saturation (or water content) of the soil and the distribution of water volume within the soil change. This distribution is linked directly to the pores shape and size. Knowing that soil specimen structure in water retention test is the same (one specimen for the whole test in one cycle of drying and wetting) then the number of fluid clusters and their distribution within the soil will mainly vary with water content and thus with suction. On the other hand, for unsaturated triaxial test, there are two factors influencing the number of fluid clusters and their distribution: suction and the mechanical loading. The volumetric deformation induced through triaxial test will change the structure of the soil and thus it will change pores geometry. The change in pore geometry induces a change in the number of fluid

clusters and their distribution.

In this work, the evolution of fluid clusters with loading is used as an experimental tool that helps to understand the retention and hydro-mechanical behaviours of unsaturated soils and offers more information at the microscopic-discrete scales. Results of this tool are presented in chapter 4 and 5. These results are used to define water retention domains and cohesion regimes and for the investigation of the evolution of the number of fluid clusters, their volumes, fluid phase continuity and contacts with loading. Moreover, the microscopic-discrete results are used to analyze hysteresis phenomenon and soil cohesion.

The trinarized images obtained using the technique presented in section 3.3 were subsequently analyzed using a highly optimized commercial code Visilog[®] (see Bernard et al., 2011). This code offers several tools to analyze 3D trinarized x-ray images, obtained in this work. These tools will be presented in details in the following.

Using Visilog[®], the trinarized volume was separated into three volumes of the three phases: grains, water and air. Each phase volume was processed differently. In this section the processing of water phase is explained while grain phase processing is described in the following section (see section 3.4.2). Air phase is processed same way as water phase.

Water phase processing

Water phase is separated from the whole 3D volume using Visilog by setting the threshold to a gray value equal to 128 (the gray value attributed to water phase after trinarization is 128). In order to remove the noise inside the images, represented by water volumes of one voxel, morphological processes of erode and dilate by one voxel are applied. Later, water clusters are labelled. Labelling process can be summarized as giving each individual water cluster an Identification (Id). This Id is represented in the images by colors (i.e., each color represent a specific water cluster). Though, it is important to note that, for the same step of loading (suction or mechanical loading), different water clusters of different Ids might have the same color. In addition, there is no link between the color of the water cluster and the loading step, i.e. the color of water cluster changes from one step of loading to another. If a random water cluster had the same color for different steps of loading, then this would be a result of the program (Visilog[®]) that the author cannot control (i.e., water cluster is followed from one loading step to another by its Id not by its color).

The process of labelling is very useful to be able to refer to any water cluster directly by its Id number. These images where each water cluster has a specific Id and color can be considered as a mask applied to the reconstructed images (i.e., the gray scale information are always kept). At this point, more information about water clusters is needed as the number of clusters, the center of mass, 3D volume, 3D area ...etc. This information is obtained using another tool of Visilog[®] which is analysis individual. The measurements of clusters properties are saved in a DAT file type associated primarily with Data which can be read by a text editor. Fig 3.19 details water phase processing steps in 2D for simplicity, although the real process is 3D. Same processing is applied for air phase and it is presented in Fig 3.20.

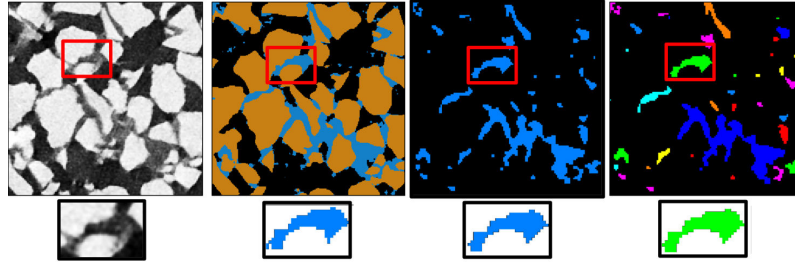


Figure 3.19: Water phase processing steps: Reconstructed, trinarized, Erode-Dilate and labelling steps, respectively from left to right

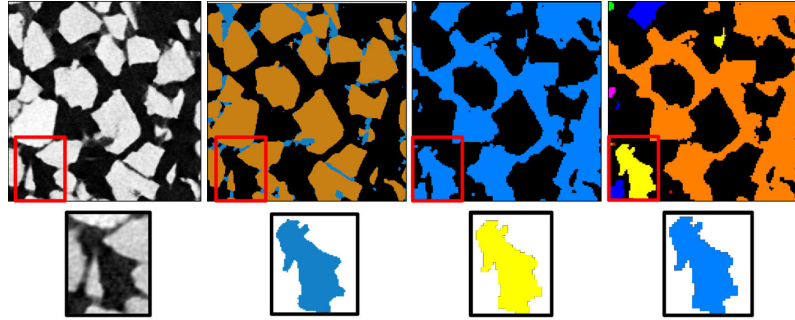


Figure 3.20: Air phase processing steps: Reconstructed, trinarized, Erode-Dilate and labelling steps, respectively from left to right

At the end of this process, the number of fluid clusters within the specimen is obtained for each increment of loading (i.e., suction increment or mechanical loading increment). In Fig 3.21 an example of the relation between the number of water clusters and suction, for water retention test is presented. This example correspond to drying path (i.e., the specimen was primarily saturated and then dried by different suction increments).

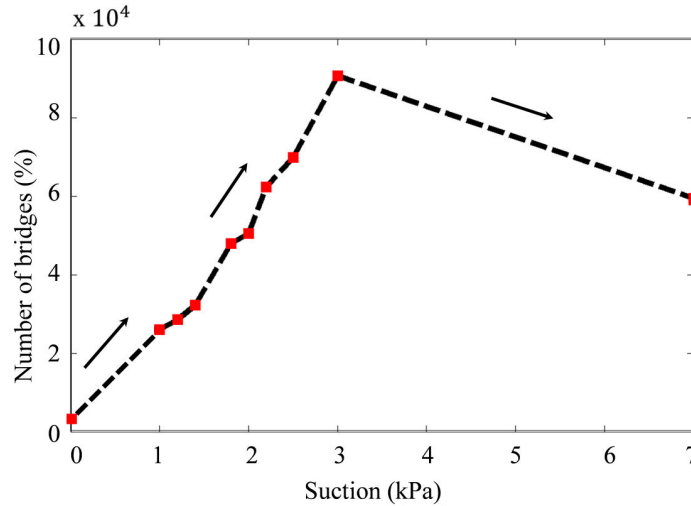


Figure 3.21: Evolution of the number of water clusters with suction. This is shown for water retention test, drying path

The test starts with a completely saturated specimen where water phase is present as

one whole big cluster. When suction is applied ($s=1\text{kPa}$) the big water cluster divides into smaller clusters and thus the number of clusters increases. As the suction is being increased, the number of clusters continues to increase and it reaches a maximum value at ($s=3\text{kPa}$). Later the number of the clusters decreases at $s=7\text{kPa}$ as the specimen gets almost dried.

More results about the evolution of the number of fluid clusters with loading, the interpretation and the use of these results are presented in chapter 4 and 5, for water retention test and triaxial test, respectively. The information obtained by Visilog[®], are also used to plot fluid cluster size distribution. This plot is similar in concept to the particle size distribution. It represents the relation between cluster dimension and the cumulative volume of the clusters.

The representative dimension of the cluster in this plot is the equivalent diameter (EqD) of a sphere having the same volume as the cluster. Two examples of water clusters size distribution are shown in Fig 3.22. Those plots are shown for water retention behaviour test where suction is 2.2kPa (curve in color black) and 3kPa (curve in color red).

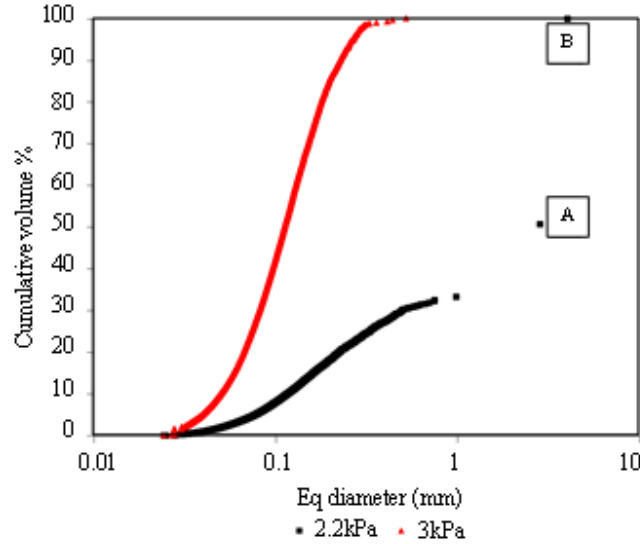


Figure 3.22: Water clusters size distribution for water retention test, for $s=2.2\text{kPa}$ and $s=3\text{kPa}$

The gradation of water cluster size is not the point of focus in this figure rather than the continuity of water phase. For example, for $s=2.2\text{kPa}$, 30% of water volume is in the form of small water clusters, 20% is in the form of one medium cluster (point A) and 50% is in the form of one big cluster (point B). In other words, water phase at $s=2.2\text{kPa}$ is partially continuous as two big clusters (point A and B) form 70% of water volume. For $s=3\text{kPa}$, all water volume is in the form of small water clusters (i.e., water phase is discontinuous).

One possible approach to evaluate the relation between suction and water continuity is by considering water cluster of the maximum volume (e.g., cluster B in Fig 3.22). The water cluster of the maximum volume (V_{wmax}) is extracted for each value of suction, and normalized by the total volume of water (V_{wt}) within the specimen. Fig 3.23 shows the relation between suction and the normalized volume of the biggest water cluster (V_{wmax}/V_{wt}).

Water volume within the specimen, from $s=0\text{kPa}$ to $s=2\text{kPa}$, is forming one big cluster (i.e., $V_{w\max} = V_{wt}$). For $s>2\text{kPa}$ the number of clusters increases while the volume of the biggest water cluster decreases. At $s=3\text{kPa}$, $V_{w\max} = V_{wt} \approx 0$.

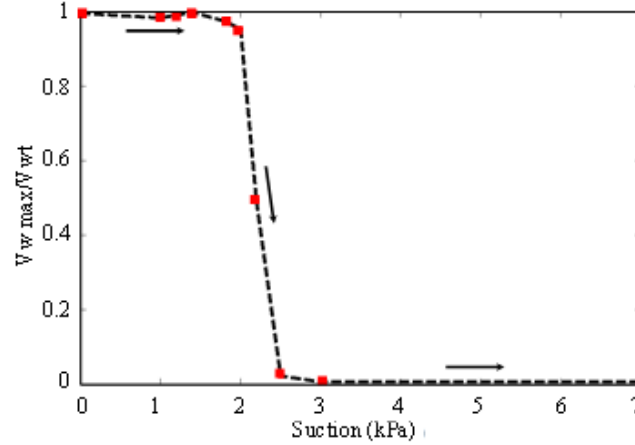


Figure 3.23: The relation between suction and the normalized volume of the biggest water cluster. This is shown for water retention test, drying path

Similar analyses are performed for air phase and they are presented in chapter 4 and 5, for water retention test and triaxial test, respectively.

3.5.2 The evolution of the number of fluid-fluid and solid-fluid interfaces with loading

Different experimental and numerical analyses have been performed to measure the suction-saturation relationship (i.e., WRC) for unsaturated soils. However, its estimation often leaves the investigator confused because the functions are hysteretic, i.e., different curves are obtained for drainage and wetting conditions. Traditionally, the hysteresis phenomenon present in WRC has been attributed to two causes: contact angle hysteresis and pore geometry, as explained in chapter 2, section 2.2.6.

Many researchers agree that hysteresis is related to the configuration and distribution of interfaces. Their theory states that the suction or capillary pressure is a unique, non-hysteretic function of the curvature of the interfaces between the phases (see Hassanizadeh et al., 1993; Scholtés et al., 2009). If capillary pressure (suction) is considered as a function of two independent variables: saturation and InterFacial Area (IFA), hysteresis would be minimized. Thus, hysteresis might be interpreted as the projection of the suction-degree of saturation-IFA surface onto the suction- degree of saturation plane.

Moreover, multiphase flow analyses base the movement of water and air in the soils on capillary pressure (suction) and IFA (e.g., Morrow et al., 1970; Wildenschild et al., 2004; Schroth et al., 2008; Porter et al., 2010).

On the other hand the overall mechanical behaviour of granular materials is intimately related to the local mechanisms taking place at the microscopic-discrete scales. In addition to dry contact interactions, the presence of water can modify local deformation, attrition, and sliding between particles. Thus the grains, water and air interact depending on the

thermodynamic equilibrium (see Culligan et al., 2004; Scholtés et al., 2009; Likos et al., 2014).

Phases interfaces have been investigated traditionally using numerical techniques (see Reeves et al., 1996; Celia et al., 1998; Helland et al., 2007; Grant et al., 2007; Joekar-Niasar et al., 2008), yet, physical experimental support has been lacking.

In this work, using x-ray micro imaging, further insight into fluid-fluid and solid-fluid interfaces (contacts) is provided. The effective specific interfacial area between water and air phases is calculated and plotted in relation with suction. Moreover, the evolution of the number of the interfaces between the phases (contacts) with the suction and the mechanical loading is analyzed.

3.5.2.1 Effective specific interfacial area

Effective specific interfacial area (water-air interfacial area) is calculated using the trinarized 3D images and Dalla et al. (2002) definition of the interfacial area taken from Grant et al. (2007). Dalla et al. (2002) calculated the effective specific interfacial area (a_{wn}) as:

$$a_{wn} = 0.5x(a_w + a_n - a_s) \quad (3.2)$$

where a_w is water 3D area, a_n is air 3D area, and a_s is grain 3D area.

Fig 3.24 shows in details the definition of effective specific interfacial area (wetting (WP)-non wetting (NWP) interfacial area) according to Dalla et al. (2002).

Visilog[®] is used to measure the 3D area of each grain, water and air cluster. 3D area of each phase is summed and the effective specific interfacial area is calculated. The relation between the degree of saturation versus the effective specific interfacial area is presented in chapter 4 for water retention test.

Water phases processing using Visilog[®], to calculate the effective specific interfacial area, is described in details in section 3.5.1. Grains phase processing using Visilog[®] is presented in the following.

Solid phase processing

Solid phase is separated from the whole 3D volume using Visilog[®] by setting the threshold to a gray value equal to 255 (the gray value attributed to grain phase after trinarization is 255). In order to remove the noise inside the images, represented by air voxels within the grains, morphological processes of dilate and erode by one voxel are applied. In general, the sand studied in this work (Hostun sand) does not have internal micro pores and thus the presence of air voxels within the grains is due to the noise coming from the insufficient resolution and the quality of the x-ray images.

Later, grains are labelled and thus each grain has an Identification (Id) and a color. More information about each grain (i.e., the number of grains, the center of mass, 3D volume, 3D area ···etc) are obtained using the tool analysis individual. Fig 3.25 details solid phase processing steps in 2D for simplicity, although the real process is 3D.

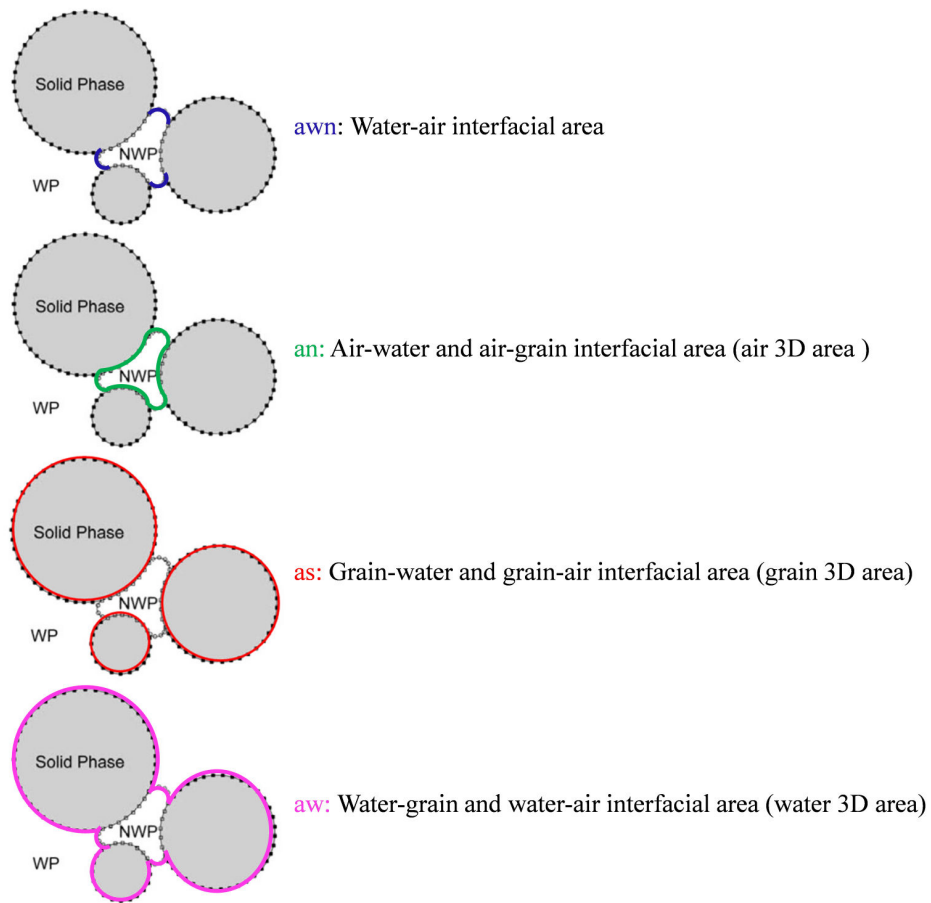


Figure 3.24: Effective specific interfacial area calculation according to Dalla et al. (2007).

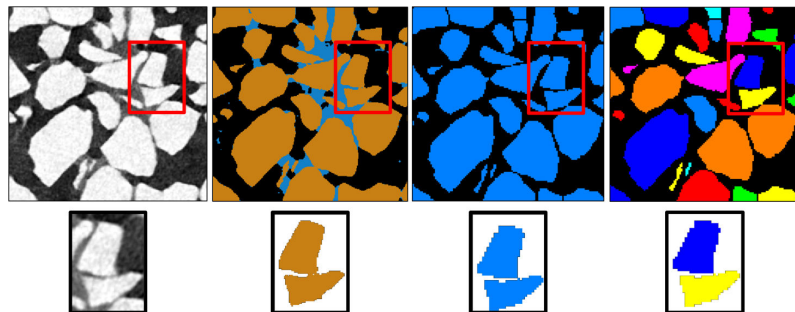


Figure 3.25: Solid phase processing steps: Reconstructed, trinarized, Dilate-Erode and labelling steps, respectively from left to right

3.5.2.2 The number of solid-fluid and fluid-fluid interfaces (contacts)

The interfaces between the different phases are described in this work as contacts. To define the number of grain-water, grain-air and water-air contacts, a python code developed by Edward Andó in 3SR laboratory, is used. The code uses the 3D labelled images (volumes) resulted from Visilog[®], where each grain, water and air cluster has a specific Id number, and establishes a contacts list for each phase.

Neighbors of each voxel in the labelled volumes are investigated within a cube ($3 \times 3 \times 3$ voxels) centered at the analyzed voxel. If a grain voxel is considered, for example, the code searches for the voxels of water or air phase within the cube in the surrounding of this grain voxel and list their labels. Same procedure is followed for water and air voxels. At the end, the results are saved in three tables written in a TSV file type associated primarily with Tab Separated Values which can be read by a text editor or excel. The first table lists grain-water contacts; i.e., for each grain Id, defines the Id of water clusters surrounding this specific grain, and thus the number of grain-water contacts (or number of water clusters per grain). The second table lists grain-air contacts; i.e., for each grain Id, defines the Id of air clusters surrounding this specific grain. The third table lists water-air contacts; i.e., for each water cluster Id, defines the Id of air clusters surrounding this specific water cluster. Consequently the relation between the number of contacts and the loading (suction or mechanical loading) can be plotted.

The relation between the number of contacts versus the loading is shown in chapter 4 and 5, for water retention test and triaxial test, respectively.

3.6 Digital Image Correlation

The measurement of displacements and displacement gradients (i.e., strains) has always been an important topic in the evaluation of material properties, such as material strengths and experimental stress analysis. Strain is defined as a dimensionless quantity describing the relative movement of material points without considering rigid-body transformation.

Digital image correlation (DIC) has been used as a tool for comparing and analyzing digital images of deforming materials, coming from different tests such as triaxial tests (e.g., Viggiani et al., 2008; Andó et al., 2011; Charalampidou et al., 2011; Hall et al., 2012; Higo et al., 2013). It provides also displacement field measurements and subsequent strain field calculations.

Continuum DIC Tomowarp, version 2.2 created by Stephen Hall (see Hall et al. (2010)) is implemented in this work. The principle of continuum DIC is to define the similarity between two images or parts of images by calculating the normalized cross correlation. It calculates the displacement, rotation and strain in 3D of material points (node) from one image to the next, on a regularly spaced grid with sub-pixel accuracy (sub-pixel refinements). DIC code follows in 3D small sub-volumes of the images between configurations to give, for each sub-volume, a 3D displacement vector mapping its displacement between the two configurations. The sub-volumes are centered on a regular grid independent of the positions of the grains. The underlying discrete granular structure present in these images is ignored, which is why this technique is called continuum.

Continuum-DIC measurements are performed on the gray scale reconstructed images. A grid of nodes is applied on the two volumes (3D x-ray images): the reference image

and the deformed image. The same nodes (in the same places) are defined in both the reference and deformed image with respect to the coordinate system. For each node a cubic sub-volume is extracted from the deformed image and a cubic sub-volume of identical dimensions and at the same position is extracted from the reference image. These sub-volumes are centered on the node around which they are extracted. The sub-volume from the deformed image is known as the correlation window. The size of the correlation window is typically an input to Tomowarp and it should be big enough to capture the different features of an image. In this work, it is chosen to be roughly the size of one grain of the studied sand. For each node, the search range is swept, to calculate the Normalized Correlation Coefficient (NCC) between the reference and the deformed images. The normalized cross-correlation between two 3D images is typically defined as follows:

$$\text{NCC}(u, v, w) = \frac{\sum_{x,y,z} I_1(x, y, z) I_2(x + u, y + v, z + w)}{\sqrt{\sum_{x,y,z} I_1(x, y, z)^2 \sum_{x,y,z} I_2(x + u, y + v, z + w)^2}} \quad (3.3)$$

where I_1, I_2 denote the local gray level in the 3D reference and deformed images, respectively. x, y, z are the coordinates in the 3D volume of the images. u, v, w are the integer displacement values along the x, y and z axis of the points of image I_2 with respect to the corresponding points in image I_1 .

The interpolation of the correlation coefficient is performed for each node. If NCC is high enough (close to one), the chosen size of the correlation window is considered correct. The primary result of the DIC process is a displacement field, from which a strain tensor field can be derived based on the spatial gradients of the displacement field (deformation gradient tensor). The scalar components coming from these measurements (e.g., the displacement ($\Delta x, \Delta y, \Delta z$), the maximum correlation coefficient \dots etc) can be saved as a 3D matrix. The 3D matrices can be turned into 3D images, and so all the image analysis tools can be used to visualize and measure the results of continuum image correlation.

DIC is used in this work to calculate the deformation field in a triaxial test of unsaturated sand. It is also used to check grains displacement in water retention test of unsaturated sand where only suction is applied. In these two tests (i.e., triaxial and retention), node spacing is $20 \times 20 \times 20$ voxels, while the size of the correlation window is $12 \times 12 \times 12$ voxels for the triaxial test, and $22 \times 22 \times 22$ voxels for the retention test. As the size of one voxel, for the retention and triaxial tests, is $7.5 \mu\text{m}$ and $13 \mu\text{m}$, respectively, thus the size of the search window is around $0.5 \times D_{50}$ of Hostun sand ($D_{50} = 0.338 \text{mm} = 338 \mu\text{m}$) for both tests.

In this work, the calculated strains are the volumetric strain (ε_{Vol}) and the deviatoric strain (maximum shear ε_s), shown in following equations:

$$\varepsilon_{\text{Vol}} = \varepsilon_1 + \varepsilon_2 + \varepsilon_3 \quad (3.4)$$

$$\varepsilon_s = \sqrt{\frac{2}{3}[(\varepsilon_1 - \varepsilon_2)^2 + (\varepsilon_2 - \varepsilon_3)^2 + (\varepsilon_3 - \varepsilon_1)^2]} \quad (3.5)$$

Where ε_i ($i=1, 2, 3$) indicates the major, intermediate and minor principal strains.

For the rotation tensor, it is an antisymmetric tensor. The result of rotation measurements is a non-directional rotation (i.e. a scalar) that represents the intensity of rotation

of the material within the sub-volume at each node (i.e., the norm of rotation in the three directions x , y and z).

It is important to note, that the displacement, strain and rotation fields presented in this work are calculated for the solid skeleton rather than for water and air clusters present in the sub-volume. This is due to that fluid clusters within the sub-volume are changing their shapes and/or volumes rather than being subjected to displacements. This change in shape and/or volume is hard to correlate between the x-ray reconstructed images (i.e. NCC value will be very low). Moreover, in the triaxial test, fluid phase is not given the time to reach equilibrium after loading (i.e., scans were performed immediately after loading), knowing that loading process takes around 30 min maximally and scanning process takes around 2 hours. This means that fluid phase is not equilibrated while scanning and a change in the shape and/or volume of fluid cluster might happen and be captured in the images. If this change in shape and/or volume of fluid cluster is considerable, this will show in the images as a blurry. However this was not the case and these changes were small enough, that they did not influence the value of NNC.

3.7 Conclusion

This chapter has presented the setup in 3SR laboratory used to acquire the x-ray images, as well as the conditions and settings in which the scans have been made in this work. The procedure for reconstructing the obtained x-ray radiographies was presented. The 3D reconstructed images are the main input in this work, and will be used to perform microscopic-discrete measurements for the investigation of retention and hydro-mechanical behaviours of the studied material.

The procedure to separate the three phases using the developed trinarization technique was detailed in this chapter. An analysis allowing defining the size of REV, using a developed mapping code and statistical tools, was presented. As the size of REV is defined, local measurements of porosity and degree of saturation can be performed using the developed mapping code.

The procedure to distinguish the individual grains, water and air clusters was detailed. As a result, the number of fluid clusters and contacts between the phases can be obtained at each step of loading and plotted in relation with suction. Furthermore, the effective specific interfacial area can be calculated at each step of loading and plotted in relation with the degree of saturation.

This chapter has also introduced digital image correlation as a procedure for making displacement, strain and rotation measurements between two images of deforming granular media. The latter experimental and image processing tools are used to analyze water retention behaviour in chapter 4, and hydro-mechanical behaviour in chapter 5, of unsaturated granular material.

Chapter 4

Water Retention Behaviour

4.1 General overview

In order to obtain water retention curve of the tested material, two laboratory tests have been performed. The laboratory tests concern the two main paths of water retention curve: drying and wetting paths. The experimental campaign of the two tests is described in this chapter. Section 4.2 details the experimental program including, the material tested, the cell, suction application technique, specimen preparation method and the experimental procedure.

In order to analyze water retention behaviour of the tested material microscopically, the experimental and data processing tools, detailed in chapter 3, have been used. The results obtained from using these tools are presented in section 4.3 including DIC, trinarization technique, REV analysis, macroscopic and microscopic measurements of porosity and degree of saturation and microscopic-discrete analyses results. The interpretation of these results is presented in section 4.4. Water retention surface and the relation between suction, porosity and degree of saturation are investigated. A definition of water retention domains and the boundaries between them is given. Hysteresis phenomenon is described at the macroscopic and microscopic scale. Soil cohesion is analyzed and its regimes are established.

4.2 Experimental program

4.2.1 The material tested

The experimental program of water retention behaviour test is conducted on Hostun sand (HN31). Hostun sand is used as a reference material in different laboratories (see Sadek et al., 2007; Andrade et al., 2008; Sunyer Amat 2008, Desrues et al., 2015). Its chemical components principally consist of silica ($\text{SiO}_2 > 98\%$). The grain shape is angular as shown in the Scanning Electron Microscope image (SEM) of a few grains of Hostun sand, taken from Flavigny et al. (1990), in Fig 4.1-a. A particle size distribution analysis for Hostun sand is shown in Fig 4.1-b.

According to the USCS classification, Hostun sand is poorly graded sand. The main properties of Hostun sand are: the density of the soil particles $\rho_s = 2.65 \text{ g/cm}^3$, the coefficient of uniformity $C_u = 1.7$, the maximum and minimum void ratio $e_{\max} = 1.041$ and

$e_{\min}=0.648$, the maximum and minimum specific weight $\gamma_{\max}=1.324\text{g/cm}^3$ and $\gamma_{\min}=1.599\text{g/cm}^3$, and the medium grain size $D_{50}=0.338\text{mm}$ (see Desrues et al., 1996).

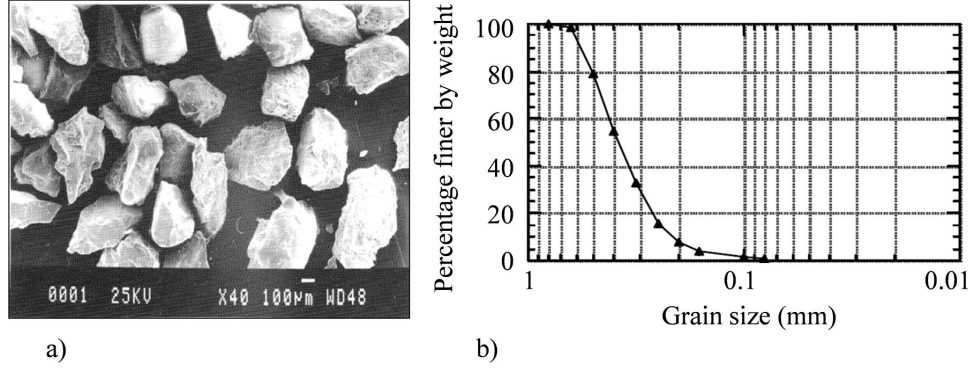


Figure 4.1: a) SEM image of Hostun sand from Flavigny et al. (1990) b) Grain size distribution of Hostun sand from Sunyer Amat (2008)

4.2.2 The cell

The study of water retention behaviour required the design of water retention cell. A previous cell was already available and used by a former master student Ismael Riedel, see Fig 4.2-right. The test performed by Ismael Riedel is Water Retention Test WRT_0 , drying path D_0 . The primary dataset obtained in this test (i.e., x-ray reconstructed images) are used in this work. All image processing steps, analyses and interpretations of D_0 data set are performed by the author.

Another Water Retention Test WRT_1 , drying D_1 and wetting W_1 paths, are performed by the author using a new cell designed specifically for this test; see Fig 4.2-left.

The two cells are designed to allow x-ray scanning while performing water retention test. The need for high resolution images imposed a relative small size of the specimen: a cylinder of 1 cm diameter and 1 cm height, see Fig 4.2-7, resulting in small cells when compared to the usual arrangements of typical soil experiments. The size of the specimen is representative to study water retention behaviour and to make microscopic-discrete measurements. The material selected to build the cells is PMMA (PolyMethylMethAcrylate), which minimizes the attenuation of x-ray beam to optimize the scanning process. Fig 4.2 shows the two cells apparatus and their components.

The cell, as can be seen in Fig 4.2, has two parts: the top (2) and the bottom (3+4+5+6+7). These parts, once screwed to each other, form an air and watertight cell. The sand specimen (7) is located above a porous stone (3) of a high permeability and of an air entry value of 500kPa, such that water continuity from the bottom and air continuity from the top are guaranteed. The design of WRT_0 cell includes the presence of upper porous stone at the top of the specimen for a technical design reason (i.e., in order not to have a free space at the top of the specimen, between the top and the bottom parts of the cell). This upper porous stone is excluded in the design of WRT_1 cell.

The removable upper part can be taken out to have access to the sand specimen. The bottom porous stone is in contact with a water filled reservoir (6) so it remains always saturated. Two tubes are connected to this reservoir (4 and 5), one for the entry of water

and the other for the exit. These tubes are used to flush the system (i.e., force the exit of any air bubbles and ensure the saturation) and, more importantly, for the application of suction.

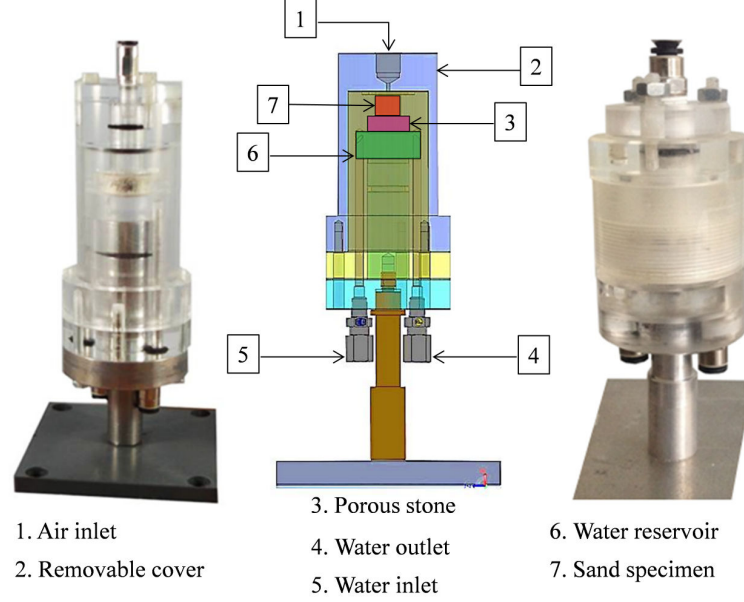


Figure 4.2: Water retention cells for WRT_0 and WRT_1 and their components

4.2.3 Suction application technique

The method used for applying the suction, for the two water retention tests WRT_0 and WRT_1 , is the tensiometry. This method allows the application of a stable pore water pressure u_w , with an accuracy of 0.01kPa. The largest applied suction in this work for the two tests is 7kPa.

Fig 4.3 shows schematically the full arrangement and illustrates how the suction is applied for WRT_0 (taken from Riedel (2011)).

A water tank (3) that can move vertically over a scaled rule is connected to water reservoir (1) at the bottom of the cell (5). The top surface of water in this tank is initially set to the zero value of the scaled rule, which coincides with the middle level of the sand specimen (6), i.e., $H=0$. In this condition the suction is equal to zero (s_0) in the middle height of the specimen and ($\gamma_w h/2=12\text{kPa}$) at the top and the bottom of the specimen. Moving the tank down, i.e., $H<0$, creates a water level difference and since there is a continuity with the liquid phase in the specimen, the porous stones (7) and the reservoir (1), suction as a negative water pressure is applied.

The full arrangement of WRT_1 , and suction application technique in this test are shown in Fig 4.4.

For WRT_1 , a pressure controller (3) that allows applying a maximum water pressure $\pm 100\text{kPa}$, with a precision 10Pa, is connected to water reservoir (1) at the bottom part of the cell (5) at the water inlet, see Fig 4.2-(5). Water outlet at the bottom of the cell, Fig 4.2-(4), is closed using a valve.

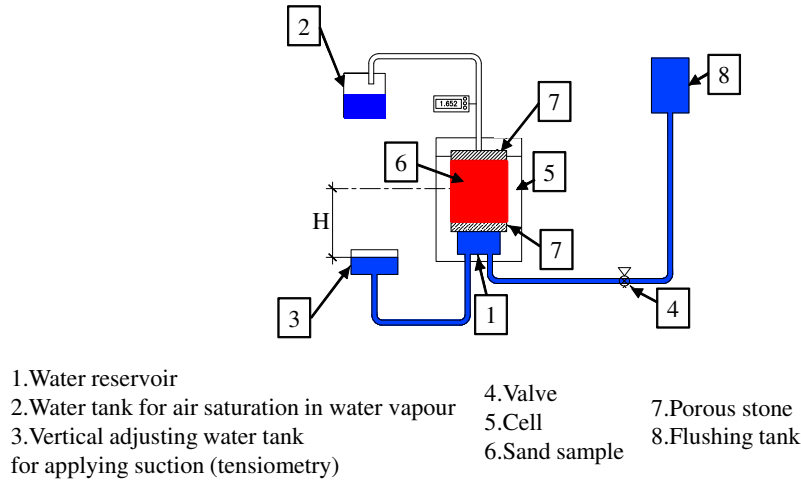


Figure 4.3: Sketch of the arrangement used to apply the suction for WRT_0 (taken from Riedel (2011))

The cell is filled with water to its top, including where the specimen (6) should be placed later, and water pressure is measured using the pressure controller. This measured value (s_0) is set to be the zero suction at the top of the specimen, and it changes as the altitude between the cell and the controller changes. In order to apply suction (s), the applied value using the pressure controller is: $P = s_0 - s$. For example, for $s_0 = 12 \text{ kPa}$ measured by the pressure controller, and in order to apply $s = 7 \text{ kPa}$, the value set and applied by the pressure controller is $P = 12 - 7 = 5 \text{ kPa}$.

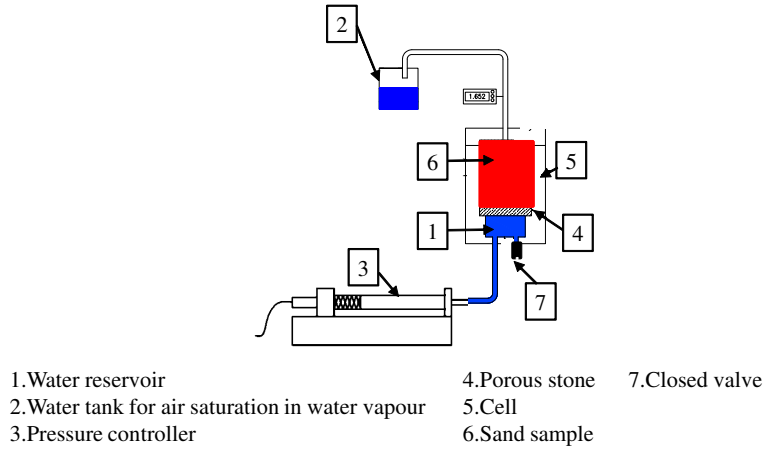


Figure 4.4: Sketch of the arrangement used to apply suction for WRT_1

Due to the height of the specimen ($h = 1 \text{ cm} = 0.1 \text{ kPa}$), there is a suction difference between the top and the bottom of the specimen, equal to 0.1 kPa , for the two tests WRT_0 and WRT_1 . For WRT_1 , for example, the suction is applied on the top of the specimen, and it is higher than the suction applied on the bottom of the specimen, by 0.1 kPa .

4.2.4 Specimen preparation technique

The preparation of the specimen is a key step that has to be done with care as it influences the homogeneity of the sand skeleton. Water retention test begins with a completely saturated state of the specimen, and thus all the pores in the specimen have to be completely filled with water in the initial state. The technique used for specimen preparation in WRT_0 and WRT_1 , is water pluviation (see Konrad et al., 2003; Juneja et al., 2010). The specimen is prepared by having the cell completely submerged under water, after that the sand is simply dropped little by little from a certain height under water, using a small spoon. Using this method, one can expect to have a completely saturated specimen at the beginning of the test. All the water used in this work is demineralized water that has been de-aired for 24 hours using a magnetic stirring heater and a vacuum system.

4.2.5 Experimental procedure

To help defining the values of suction that can be applied in water retention test, an experimentally obtained Water Retention Curve (WRC) of Hostun sand, presented in Fig 4.5, is considered as a reference curve; taken from Lins (2010). The black continuous line is a fitting curve of the experimental points. The experimental points are obtained using macroscopic measurements of degree of saturation, for a drainage process, and a void ratio of 0.9.

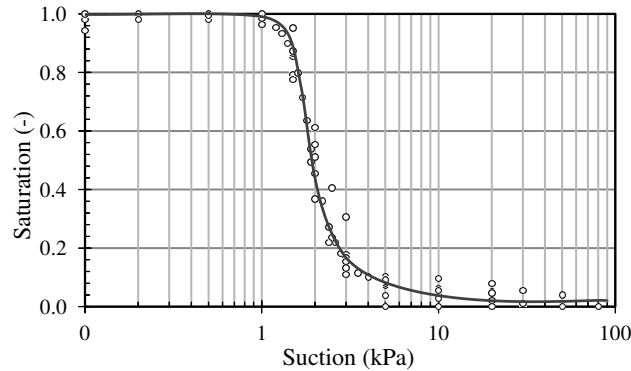


Figure 4.5: The reference experimental WRC of Hostun sand, taken from Lins (2010)

In the reference WRC, Lins (2010) defined an approximate air-entry value $s_{air}=1.4\text{kPa}$. After reaching the air-entry value, the degree of saturation decreases with increasing the suction. In order to analyze the microphysics behind water retention behaviour of Hostun sand, different points of interest are selected in the reference WRC (a given pair of values: an imposed suction (s) and the corresponding global degree of saturation (S_r)). Fig 4.6 shows the selected points for WRT_0 drying path D_0 (in blue color), where x-ray CT scans were performed. For WRT_1 , drying path D_1 , same points to WRT_0 with an additional two points, shown in red color in Fig 4.6, were selected where x-ray CT scans are performed by the author. The points for wetting path W_1 are chosen similar to those for drying path D_1 (i.e., at the same values of suction).

The values of suction are chosen in a way to cover the whole range of interest (namely from the first important change in the curve around air entry value to the other important change before reaching the residual state), and to have images in all the different water

retention domains (full saturation, funicular domain, pendular domain and residual saturation). Table 4.1 shows the program of the x-ray scans performed in this work for both WRT_0 and WRT_1 , the suction applied (s) and the corresponding expected global degree of saturation values (Sr_{exp}) taken from the reference WRC (Ref WRC). For W_1 , it is not possible to list (Sr_{exp}) in Table 4.1 as there is no reference WRC followed for the wetting path in this work.

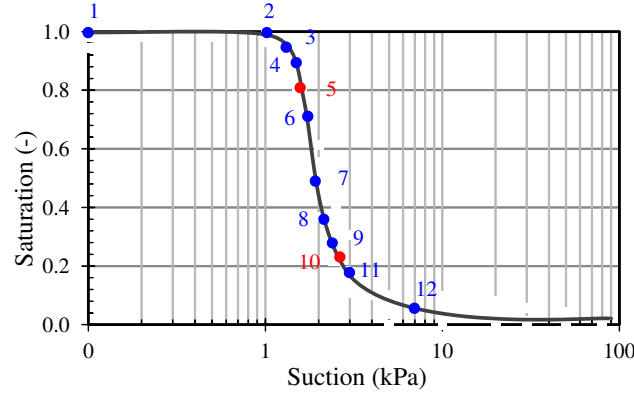


Figure 4.6: The selected points in the reference WRC, where x-ray CT scans are performed, shown in blue color for WRT_0 and blue and red colors for WRT_1

Table 4.1: Values of the applied suction and the corresponding global expected degree of saturation for WRT_0 and WRT_1

WRT_1 D_0	Point	1	2	3	4	5	6	7	8	9	10	11	12
	s (kPa)	0	1	1.2	1.4	-	1.8	2	2.2	2.5	-	3	7
WRT_2 D_1	Point	1	2	3	4	5	6	7	8	9	10	11	12
	s (kPa)	0	1	1.2	1.4	1.6	1.8	2	2.2	2.5	2.8	3	7
Ref WRC	Exp-Sr(%)	100	99	97	94	80	71	50	39	28	21	16	5
WRT_2 W_1	Point	1	2	3	4	5	6	7	8	9	10	11	12
	s (kPa)	7	3	2.8	2.5	2.2	2	1.8	1.6	1.4	1.2	1	0

The protocol for WRT_0 and WRT_1 is simple although time consuming; its summarized in the following.

The first step is to saturate the porous stone, at the bottom of the specimen to ensure water continuity between water reservoir, the porous stone and the specimen. To do that, water reservoir in the cell is filled with water, the bottom water outlet is closed using a valve, and a pressure of 100kPa is imposed for 2 hours using the pressure controller to force the water to go through the porous stone. At this step no specimen is deposited. After those 2 hours water drops are seen on the other side of the porous stone, i.e., the porous stone is saturated. Later the cell is taken to prepare the specimen. Then, the cell is placed inside the x-ray cabinet and been connected to the system of suction. The first scan, corresponding to a fully saturated specimen with zero suction applied (s_0), is performed. The scan lasts for around two hours. After that, the first suction value (s) is applied by set-

ting the controller to the value ($P=s_0-s$) as explained in section 4.2.3. For WRT_0 , suction (s) is applied by moving water tank down the scaled rule for a value $H=s\text{kPa}\approx s\times 10\text{cmH}_2\text{O}$.

When the suction is applied, some water has to move out from the specimen to water tank, Fig 4.3-(3), or to the pressure controller, Fig 4.4-(3). Therefore, before scanning, and in order to reach a stabilized condition with no flow of water (equilibrium), the cell is left for 3 days to reach a steady state. The time to reach the equilibrium state is taken from Lins (2010). Later equilibrium time was verified by performing several scans on the specimen, with time interval equal to one day between two scans, for the same value of suction, in order to verify the variation in water distribution and volume. It was found that 3 days after suction application, the changes in water distribution and volume are negligible. After reaching the equilibrium state, the specimen is scanned. Later, a new value of suction (increasing s , decreasing P) is applied; the specimen is left to reach the equilibrium and then scanned again. These steps of suction application, reaching the equilibrium state and scanning have been repeated until reaching the final point in the drying paths (i.e., $s=7\text{kPa}$). After the last scan ($s=7\text{kPa}$), pressure is applied inversely on the same specimen, following the wetting path (i.e., increasing P , decreasing s). Same to drying path procedure, before scanning, the specimen is left for 3 days to reach the steady state.

At the end of the wetting test, the cell is carefully opened; the whole volume of sand is recovered, dried in an oven for 24 hours (to eliminate any possibly remaining humidity) and then weighed. The weight of the solid phase in the specimen is needed to calculate the macroscopic porosity, using the traditional technique (i.e., weighing the specimen), and compare it to the microscopic value calculated later in section 4.3. For WRT_0 , there is no wetting path, and so the specimen is recovered after $s=7\text{kPa}$.

4.3 Water retention results

In this section, the results of using the experimental and data processing tools detailed in chapter 3 are presented for water retention tests.

4.3.1 Digital Image Correlation results

Digital image correlation is performed for WRT_1 (D_1 and W_1) in order to check the presence of deformation coming from suction application. The first state of the specimen in the drying path D_1 ($s=0\text{kPa}$, called state 1) and the last state of the same specimen in the wetting path W_1 ($s=0\text{kPa}$, called state 2) are compared. Tomowarp is run for the reconstructed x-ray images of the two compared states. The 3D image correlation is primarily performed for a coarse mesh in order to determine the adequate range for the search window. At the end of this step, the search window corresponding to the highest Normalized Correlation Coefficient (NCC) is selected and fixed. Tomowarp is run again for a fine mesh and the selected search window.

The results of the performed DIC are presented in Fig 4.7. In this figure, central vertical slices, of the same azimuth are presented for the calculated displacement on X, Y and Z.

As shown in Fig 4.7, the maximum displacement calculated on X, Y and Z are: $\Delta X=\Delta Y=0.1\text{mm}=0.333\times D_{50}$, and $\Delta Z=0.2\text{mm}=0.666\times D_{50}$. Thus, the maximum strains calculated for the specimen ($1\times 1\text{cm}^2$) are $\varepsilon_x=\varepsilon_y=1\%$ and $\varepsilon_z=2\%$.

As stated before, the displacements of the grains are thought to be due to moving the cell from the x-ray cabinet to a fixed position, after applying the suction, in order to reach equilibrium. However, the calculated displacements are small compared to D_{50} of Hostun sand. Therefore, their influences on the following measurements performed in this work (e.g., porosity, degree of saturation and contacts measurements) are thought to be negligible and can be ignored.

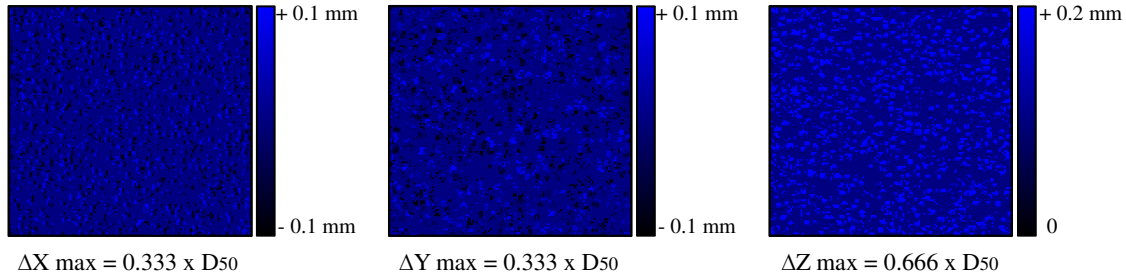


Figure 4.7: Digital image correlation results for WRT_1 (D_1 and W_1). The two correlated states are the first state of the specimen in the drying path D_1 ($s=0\text{kPa}$) and the last state of the same specimen in the wetting path W_1 ($s=0\text{kPa}$)

4.3.2 Trinarization results

Trinarization technique detailed in chapter 3, section 3.3 is used to segment the three phases (grain, water and air) in the reconstructed 3D volume of 1500^3 voxels ($1.25 \times 1.25 \times 1.25 \text{cm}^3$) for all the points (values of suction) in the three paths D_0 , D_1 and W_1 . The segmentation of the phases allowed extracting more information from the reconstructed x-ray images. This qualitative and quantitative information is related to the macro-micro porosity and degree of saturation of the sand specimen, fluid phase distribution, continuity, contacts and evolution with suction.

Trinarization code is run for the partial, tolerance and variance thresholds shown in Table 4.2. The values of these thresholds are more or less the same (± 5 gray value) for the different points in the three paths.

Table 4.2: Trinarization technique thresholds

Threshold	P_g	P_{w1}	P_{w2}	P_a	V	T_g	T_{w1}	T_{w2}	T_a
Gray value	135 ± 5	60 ± 5	70 ± 5	40 ± 5	2200	115 ± 5	30 ± 5	100 ± 5	85 ± 5

At the end, trinarization results are obtained for the three paths D_1 , W_1 and D_0 . The three colors in the trinarized images represent the three phases, i.e., brown for grains, blue for water and black for air. Each phase in the trinarized volumes has a specific gray value (255 for grains, 128 for water and 0 for air).

The validation of the trinarization technique is checked in this work. The total number of voxels considered as the solid phase (grains) in the trinarized volumes, for the same specimen in D_1 and W_1 , and for different points (i.e., values of suction) is checked. It is found that these values are comparable with a maximum difference $\pm 5\%$ of the total number of voxels representing grain phase. Therefore, the trinarization technique is

adopted in this work, with a provided precision $\pm 5\%$. Other different analyses to evaluate the efficiency of the trinarization technique are presented in Hashemi et al (2014) as the analysis of the sphericity performed on glass beads, and the comparison with different image segmentation techniques.

In the trinarized volumes of the drying and wetting paths, D_1 and W_1 , the porous stone at the bottom of the specimen and a very loose layer at the top of the specimen, of around $3 \times D_{50}$ thicknesses, are removed, see Fig 4.8. The presence of the top loose layer is certainly due to the small movement of the grains when moving the cell between two scans, to place it at a fixed place inside the x-ray cabin. Changing the place of the cell between the scans was necessary to allow using x-ray setup by other users while waiting to reach equilibrium state which takes 3 days. The layer is cut to avoid its influence on the measurements of porosity and degree of saturation. The presence of this layer causes higher porosity (loose structure) and lower degree of saturation. Thus, it is not representative to consider this layer when analyzing water retention behaviour, under hydrostatic conditions. In addition, the strains in this layer due to grain movements are not considered as they are unavoidable returns that do not present the real behaviour of the specimen. Fig 4.8 shows central vertical slices in the reconstructed and trinarized volumes, before and after removing the porous stone at the bottom of the specimen and the loose layer at the top of the specimen, shown for WRT_1 specimen.

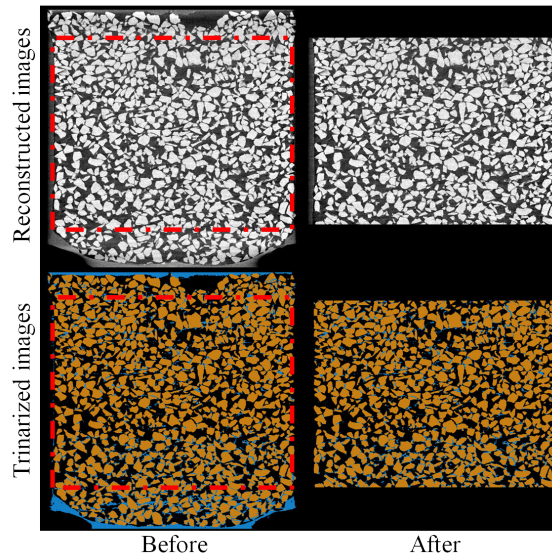


Figure 4.8: Central vertical slices in the reconstructed and trinarized volumes, before and after removing the porous stone at the bottom of the specimen and the loose layer at the top of the specimen, shown for WRT_1

Similarly, in the trinarized volume of the drying path D_0 , the upper and bottom porous stones are removed. Fig 4.9 shows central vertical slices in the reconstructed and trinarized volumes, before and after removing the porous stones at the top and the bottom of the specimen, shown for WRT_0 .

The porous stones and the top loose layer are cut from the trinarized volumes by removing all the slices passing through them. The porous stones for the two tests WRT_0 and WRT_1 do not have perfect horizontal surfaces at the top and the bottom. Thus removing the slices passing through them might remove some grains also. The number of grains in

the specimen of WRT_0 and WRT_1 is around 17×10^3 grains, obtained using Visilog[®] (see section 4.3.5.3). The number of the lost grains due to cutting the two porous stones for WRT_0 , and the porous stone and the upper loose layer for WRT_1 , is 400 to 500 grains, i.e., 2 to 2.5% of the total numbers of the grains within the specimen. This number influences the measurement of porosity and degree of saturation, when calculated from the trinarized volumes. However, as the removed grains are located near the porous stones at the top and the bottom of the specimen, their influence on the latter measurements may be considered as a boundary condition effect (i.e., including the removed top and bottom parts of the specimen would not be representative when performing porosity and degree of saturation measurements of the specimen).

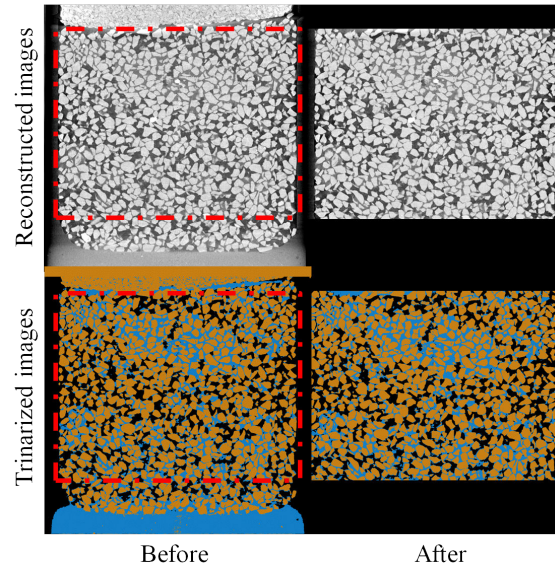


Figure 4.9: Central vertical slices in the reconstructed and trinarized volumes, before and after removing the porous stones at the top and the bottom of the specimen, shown for WRT_0

Fig 4.10, Fig 4.12 and Fig 4.14 show central horizontal (XY) slices in the trinarized volumes for all the values of suction in the three paths D_1 , W_1 and D_0 respectively. Fig 4.11, Fig 4.13 and Fig 4.15 show central vertical (XZ) slices of the same azimuth, in the trinarized volumes, after removing the porous stone and the upper loose layer for WRT_1 , and the two porous stones for WRT_0 , for all the values of suction in three paths D_1 , W_1 and D_0 respectively.

More detailed results of trinarization technique can be found in Appendix A. These results allow performing a comparison between the reconstructed and the trinarized images in the horizontal and vertical planes, and thus evaluating the efficiency of using the trinarization technique. In Appendix A, Fig (A-1), Fig (A-3) and Fig (A-5) show central horizontal slices in the reconstructed and trinarized volumes, for all the values of suction in the three paths D_1 , W_1 and D_0 , respectively. Fig (A-2), Fig (A-4) and Fig (A-6) show central vertical slices of the same azimuth in the reconstructed and trinarized volumes, for the three paths D_1 , W_1 and D_0 , respectively.

Using trinarization results (i.e., the 3D trinarized volumes), water phase distribution is analyzed qualitatively. Water phase distribution is influenced by the size and the shape of the pores, which are related to the size and the shape of the grains. The spatial distribu-

tion of the pores is a result of the chosen specimen preparation technique. However, only the qualitative analysis of pores size and shape are performed in this work, i.e., the quantitative analysis are not performed. Therefore, no strong conclusions are made regarding the influence of the distribution of pore size and shape on the distribution of water phase.

As the trinarization results are 3D volumes, they allowed the investigation of the evaluation of water and air continuity and distribution (homogeneous or heterogeneous) during drying and wetting processes. Thus a description of water retention domains can be given. However, this description is performed qualitatively in this section, while the quantitative analyses are presented in section 4.4.2.

In the following, a summary of the steps of each path of the three paths D_1 , W_1 and D_0 is given with details about fluid phase continuity and distribution, using the former XY and XZ 2D slices taken from the 3D trinarized volumes.

For the drying path D_1 , the specimen is initially saturated, and then the suction is increased gradually to allow the water to flow from the specimen to the pressure controller. Consequently, water volume within the specimen decreases as increasing the suction.

At $s=0\text{kPa}$, the specimen is completely saturated. For $s=1, 1.2$ and 1.4kPa , small air bubbles can be seen at the boundaries of the specimen. This might be due to the weak connection between the interfaces of the two different materials: Hostun sand and the cell material (i.e., the walls of the cell and the specimen). However, the vertical slices for $s=0, 1, 1.2$ and 1.4kPa show that the water fills all the voids within the specimen (excluding the boundaries) and water phase is in a continuous state (qualitative description from the images as pointed before). This state of water phase coincides with the definition of the saturated domain where water phase is continuous, and no presence of air within the soil. When increasing the suction, from $s=1.4\text{kPa}$ to $s=1.6\text{kPa}$, air enters through a net of connected empty voids at the top of the specimen. This allows to establish that the air entry value (s_{air}) is between $s=1.4\text{kPa}$ and $s=1.6\text{kPa}$. Increasing the suction beyond the air entry value to $s=1.8\text{kPa}$, air continues to empty the bigger connected voids first before the smaller ones. Within this range of suction (i.e., $s=1.6$ and 1.8kPa), that can be defined as the funicular domain, air phase is found to be discontinuous and water phases is continuous. In addition, the horizontal and the vertical slices for this range of suction show that the distribution of water within the specimen is heterogeneous. At $s=1.8\text{kPa}$, the part of the specimen shown in the left side of the horizontal and vertical slices desaturates first compared to the right side where water phase takes the form of patches (note that the specimen is cylindrical, i.e., 3D volume, with no left or right side, but the 2D slices help to point to a specific part of the specimen). This is due to the presence of bigger pores in the part of the specimen shown in the left side of the slices compared to the right side. For $s=2\text{kPa}$, water and air phases are found to be continuous. At this value of suction, the central vertical slice shows that bigger patches are formed at the top of the specimen than at the bottom (heterogeneous distribution of water). The reason behind that might be due to the presence of big connected pores at the bottom of the specimen, while at the top where narrow small pores exist, water is retained through capillarity. For the range of suction $s=2.2, 2.5$ and 2.8kPa , water phase is found to be discontinuous. Water phase is distributed in this range, in the form of small clusters while air phase is distributed in the form of patches. This low saturation region ($s=2.2, 2.5$ and 2.8kPa) that can be defined as the pendular domain, represents a transition zone between the funicular state ($s=1.6$ and 1.8kPa) and the residual state ($s=3$ and 7kPa). At $s=3$ and 7kPa , water is

drained out of the specimen, leaving traces that, could be hardly seen due to the available resolution of the images ($7.5 \mu\text{m}$). Water phase in the residual domain can be seen only on and/or near the surface of the grains.

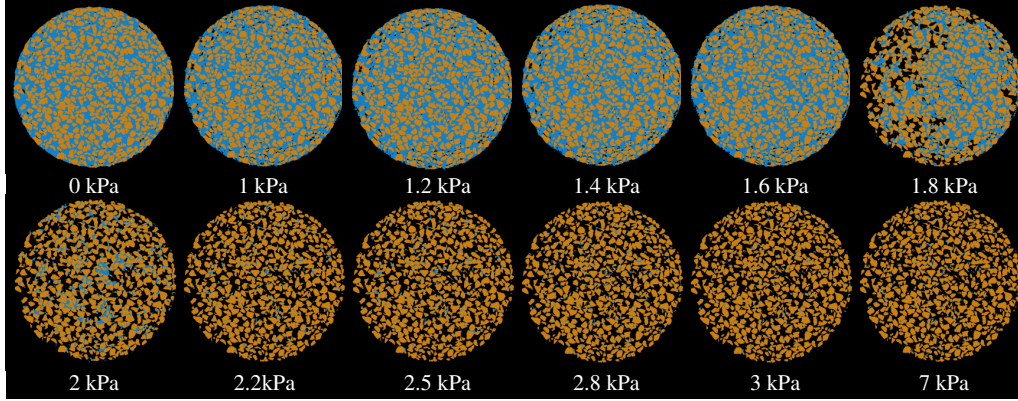


Figure 4.10: Central horizontal slices in the trinarized volumes, for all the values of suction in the drying path D_1

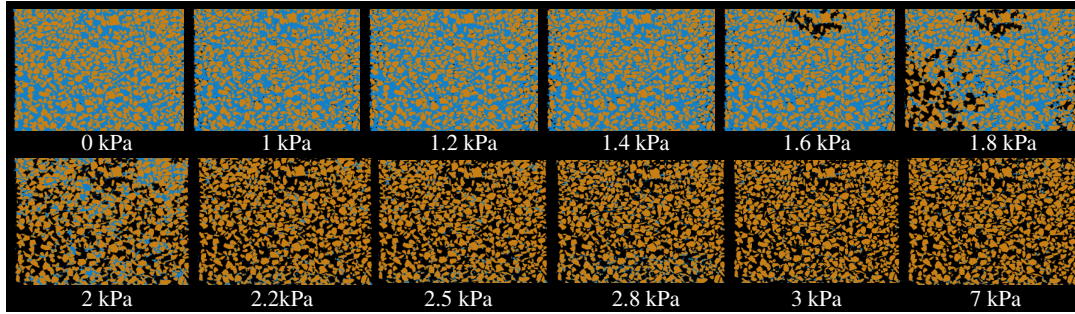


Figure 4.11: Central vertical slices of the same azimuth in the trinarized volumes, after removing the porous stone and the upper loose layer, for all the values of suction in the drying path D_1

For the wetting path W_1 , the specimen is initially in the residual state and then the suction is decreased gradually to allow the water to flow from the pressure controller to the specimen. Consequently, water volume within the specimen increases as decreasing the suction. The range of suction $s=3$ and 2.8kPa , is defined as the residual state. Decreasing the suction from $s=2.8\text{kPa}$ to $s=1.8\text{kPa}$, water clusters size increase. This range of suction can be defined as the pendular domain. At $s=1.6\text{kPa}$, water and air phases are continuous. The vertical slice shows that water content at the top of the specimen is higher compared to water content at the bottom. This is related to pore morphology described for D_1 at $s=2\text{kPa}$: drying the specimen begins by drying the big pores while wetting the specimen begins by wetting the small pores. At $s=1.4\text{kPa}$, water clusters connect and their volumes increase. For the range of suction $s=0, 1$ and 1.2kPa , there is no remarkable changes in the water volume and distribution within the specimen. Water phase within the specimen is in a continuous state while air phase is in the form of trapped clusters. The complete saturation state of the specimen at $s=0\text{kPa}$ cannot be reached due to hysteresis phenomenon (i.e., trapped air clusters). Thus, this high saturation state cannot be defined as a complete saturation domain, though suction is equal to zero. For this range

of suction $s=1.4, 1.2, 1$ and 0 kPa water phase is in a continuous state while air phase is in a discontinuous state and this corresponds to the definition of the funicular domain.

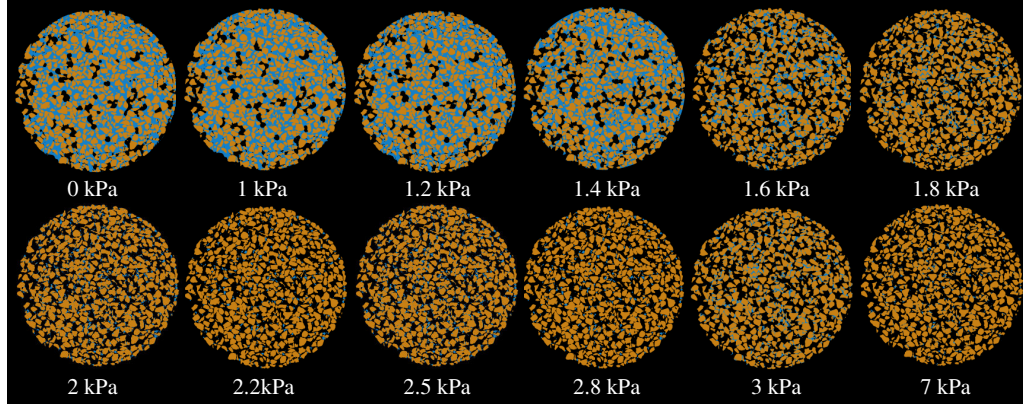


Figure 4.12: Central horizontal slices in the trinarized volumes, for all the values of suction in the wetting path W_1

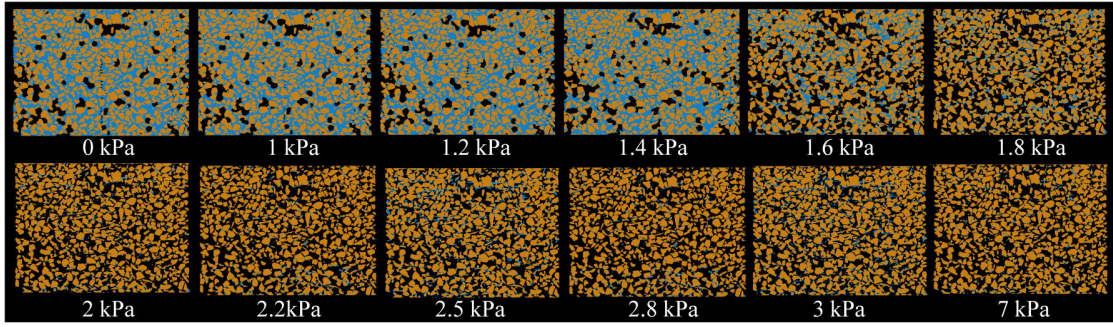


Figure 4.13: Central vertical slices of the same azimuth, in the trinarized volumes, after removing the porous stone and the upper loose layer, for all the values of suction in the wetting path W_1

For the drying path D_0 , at $s=0$ kPa, the specimen is completely saturated. When suction is applied at $s=1$ kPa, small air bubbles can be seen at the boundaries of the specimen. In this range of suction ($s=0$ and 1 kPa), water phase is in a continuous state. This state is defined as the saturated domain. When increasing the suction, from $s=1$ kPa to $s=1.2$ kPa, a net of connected empty voids is formed in the middle part of the specimen. This allows to conclude that s_{air} can be between $s=1$ kPa and $s=1.2$ kPa. Increasing the suction beyond the air entry value (i.e., $s=1.4$ and 1.8 kPa), the air continues to empty the bigger connected pores first before the smaller pores. Within this range of suction (i.e., $s=1.2, 1.4$ and 1.8 kPa), that can be defined as the funicular domain, air phase is discontinuous and water phases is continuous. The horizontal and vertical slices for this range of suction show that the distribution of water within the specimen is heterogeneous. At $s=1.2$ kPa, the part of the specimen shown in the right side of the horizontal and vertical slices desaturates first compared to the left side where water phase takes the form of patches. At $s=1.4$ and 1.8 kPa, the central vertical slices show that water phase is distributed in the form of three layers over the height of the specimen. The upper and lower layers retain larger water content comparing to the middle one. Water volume (patches) in these upper and lower layers seems to be connected, while for the middle layer, small randomly

distributed water clusters are present. The reasons causing water to flow out from the middle part of the specimen could be due to the presence of big connected pores, while for the upper and lower parts of the specimen, where narrow small pores exist, water may be retained through capillarity. At $s=2\text{kPa}$ water and air phases are found to be continuous. For the range of suction $s=2.2$ and 2.5kPa , water phase is discontinuous. Water phase is distributed in the form of small clusters while air phase is distributed in the form of patches. This low saturation region is defined as the pendular domain. At $s=3$ and 7kPa water phase is in the residual domain governed by surface tension.

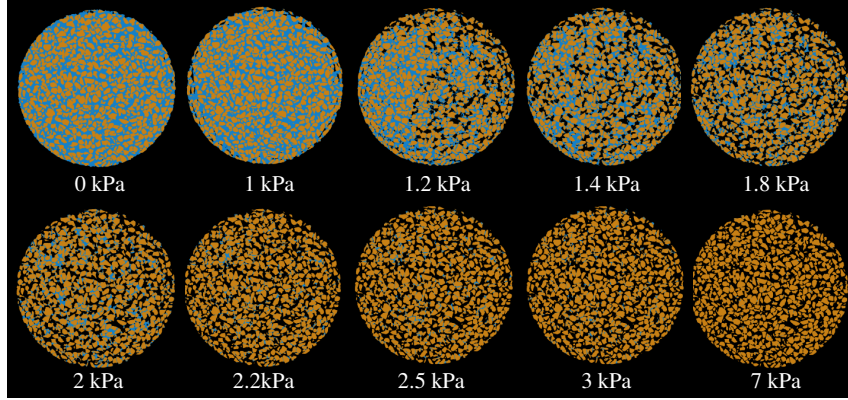


Figure 4.14: Central horizontal slices in the trinarized volumes, for all the values of suction in the drying path D_0

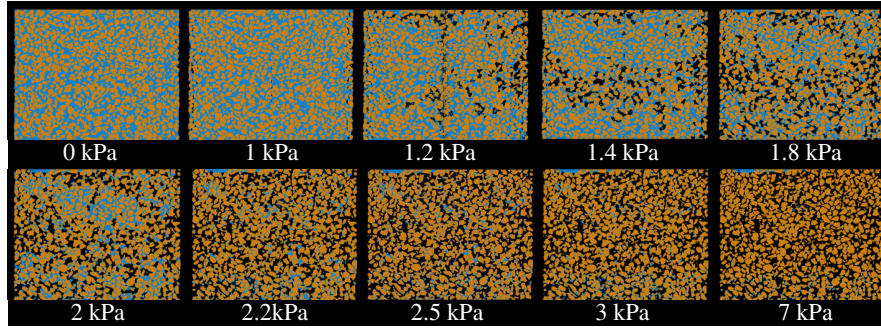


Figure 4.15: Central vertical slices of the same azimuth, in the trinarized volumes, after removing the upper and the bottom porous stones, for all the values of suction in the drying path D_0

As shown in the latter analysis, there are some points of concern before/after which the continuity of water and air phases changes, qualitatively. These points are highlighted, for the three paths, in order to be considered in a subsequent analysis in section 4.4.2.

The extracted points before/after which the continuity of water and air phases changes are:

For the drying path D_1 :

- $s=0\text{kPa}$, at which the test D_1 starts with a completely saturated specimen of a continuous water phase.

- $s=1.6\text{kPa}$, defined as air entry value, at which air enters the specimen. For $0 \leq s \leq 1.6\text{kPa}$, water phase is continuous.
- $s=2\text{kPa}$, at which both air and water phases are continuous, and before which (i.e., $1.6 \leq s < 2\text{kPa}$) water phase is continuous and air phase is discontinuous.
- $s=3\text{kPa}$, before which (i.e., $2 < s < 3\text{kPa}$) water phase is discontinuous and air phase is continuous.
- $s=7\text{kPa}$, at which the test D_1 ends after reaching the residual state. For $3 \leq s \leq 7\text{kPa}$, water phase is in the residual state and air phase is continuous.

For the Wetting path W_1 :

- $s=3\text{kPa}$, at which the test W_1 starts with a specimen of a residual water content.
- $s=2.8\text{kPa}$, that can be defined as water entry value (similar concept to air entry value), after which (i.e., $2.8 \leq s \leq 3\text{kPa}$) water phase is in the residual state and air phase is continuous.
- $s=1.6\text{kPa}$, at which both air and water phases are continuous, and after which (i.e., $1.6 < s < 2.8\text{kPa}$) water phase is discontinuous and air phase is continuous.
- $s=0\text{kPa}$, where the test ends and after which (i.e., $0 \leq s < 1.6\text{kPa}$) water phase is continuous and air phase is discontinuous.

For the drying path D_0 :

- $s=0\text{kPa}$, at which the test D_0 starts with a completely saturated specimen of a continuous water phase and no presence of air phase.
- $s=1.2\text{kPa}$, defined as air entry value, at which air enters the specimen. For $0 \leq s \leq 1.2\text{kPa}$ water phase is continuous.
- $s=2\text{kPa}$, at which both air and water phases are continuous, and before which (i.e., $1.2 \leq s < 2\text{kPa}$) water phase is continuous and air phase is discontinuous.
- $s=3\text{kPa}$, before which (i.e., $2 < s < 3\text{kPa}$) water phase is discontinuous and air phase is continuous.
- $s=7\text{kPa}$, before which (i.e., $3 \leq s \leq 7\text{kPa}$) water phase is in the residual domain and air phase is continuous.

A comparison between the two drying paths D_0 and D_1 , shows that though the Hostun sand specimen is prepared using the same technique (water pluviation technique), the retention behaviour differentiates. Air enters D_0 at air entry value ($s=1.2\text{kPa}$) smaller than the one for D_1 ($s=1.6\text{kPa}$), due to the different distribution of pore size and shape.

The distribution of pore size and shape has also influenced the distribution of fluid phase within the specimen (for example, see water distribution in the horizontal/vertical slices at the same value of suction for the two paths D_0 and D_1). More details about the variation in retention behaviour for the two specimens is given and discussed through the following sections.

For the same specimen (i.e., WRT_1), thus same pore and size distribution, the specimen retention behaviour differentiates also, depending on the path (for example, see water distribution in the horizontal/vertical slices at the same value of suction for the two paths W_1 and D_1). This variation in retention behaviour between drying and wetting paths will be discussed later with more details in the following section, and notably in section 4.4.2, where hysteresis phenomenon is investigated.

It is important to point that all the following analyses in this work (i.e. macro and micro measurements of n and S_r , obtained WRC and all the microscopic-discrete analyses) are directly performed on the trinarized volumes and, thus the results of this analyses depend significantly on the quality of the trinarization results.

4.3.3 Macroscopic porosity and degree of saturation results

In this section, porosity and degree of saturation are measured macroscopically, using the traditional technique (i.e., weighing the specimen) and the trinarized volumes. Trinarization technique is evaluated by comparing the measurement obtained using the trinarized 3D images with the results of the traditional technique. Porosity measurements for the two paths D_0 and D_1 are used to analyze the macroscopic influence of porosity on water retention behaviour of the two specimens, which have two different pore size distributions. In addition, the variation of the macroscopic porosity and degree of saturation between the different specimens, D_0 and D_1 and the different paths, D_1 and W_1 is investigated in this section.

4.3.3.1 Macroscopic porosity results

In this work, porosity is calculated macroscopically using two methods: 1) the traditional technique and 2) using the trinarized volumes.

By definition, porosity can be calculated by dividing the volume of pores over the total considered volume of the specimen, $n = V_v/V_t$. The traditional technique to calculate the macroscopic porosity is by weighing the dry soil of known volume and grain density. The weight of the dry Hostun sand within the specimen (m_s) is known since it is measured after the last scan, for WRT_0 and WRT_1 . The volume of grains is obtained through the density of the solid grains ($V_s = m_s/\rho_s$). Having the volume of the specimen in the cell $V_t \approx 0.785\text{cm}^3$ (cylinder of 1 cm diameter and 1 cm height), the global porosity can be calculated as $n = V_v/V_t = (V_t - V_s)/V_t$. Table 4.3 shows the macroscopic porosity calculated for WRT_0 and WRT_1 .

The precision of the calculated macroscopic porosity using the traditional technique depends on the precision of the balance used to weigh the dry specimen (which is $\pm 0.01\text{g}$), the loss of grains during the process of extracting the specimen from the cell to weigh it, and the precision in calculating the volume of the cell (the height and the diameter of the specimen). The final porosity could be given as $n = 44 \pm 1\%$ for D_0 and as $n = 46 \pm 1\%$ for D_1 and W_1 .

Table 4.3: Macroscopic porosity for WRT₀ and WRT₁ calculated using the traditional technique

Path	m _s (gr)	V _t (cm ³)	ρ _s (gr/cm ³)	V _s (cm ³)	n (%)
D ₀	1.16	0.785	2.65	0.44	44
D ₁ and W ₁	1.13	0.785	2.65	0.426	46

Another technique to calculate the macroscopic porosity is by using the trinarized volumes of the three paths D₀, D₁ and W₁. The histogram of the trinarized volumes in the three paths D₀, D₁ and W₁ gives the number of voxels that represent air (N_a), water (N_w) and grains (N_g). The total volume of the specimen can be calculated as $V_t = N_a + N_w + N_g$. The volume of the pores is equal to $N_w + N_a$ and thus porosity can be calculated as $n = V_v/V_t = (N_w + N_a)/(N_w + N_a + N_g)$.

Using this technique, macroscopic porosity can be calculated for all the points in the three paths D₀, D₁ and W₁ as shown in Table 4.4.

Table 4.4: Macroscopic porosity for D₀, D₁ and W₁ calculated using the trinarized volumes

Suction (kPa)	0	1	1.2	1.4	1.6	1.8	2	2.2	2.5	2.8	3	7
n (%) for D ₀	43.5	42.9	45.3	45.8	-	45.8	43.3	43.5	43.6	-	43.4	43.5
n (%) for D ₁	46.4	42.2	43.7	45.4	46.0	47.7	45.8	45.0	43.7	44.4	44.7	45.1
n (%) for W ₁	44.3	43.0	43.8	44.0	44.6	42.4	43.2	44.2	44.4	44.5	45.6	45.1

For D₀, the calculated macroscopic porosity using the trinarized images is in the range $n=(42.9-45.8\%)$ with an average value $n=44\%$. For D₁, the calculated macroscopic porosity using the trinarized images is in the range $n=42.2-47.7\%$ with an average value $n=45\%$. While for W₁, the calculated macroscopic porosity using the trinarized images is in the range $n=42.4-45.6\%$ with an average value $n=44.1\%$. This variation in the calculated values is due to the precision provided by the trinarization technique ($\pm 5\%$ of the total volume of the phase) that has been shown before.

Trinarization technique depends directly on the quality of the images acquired for each scan and the reconstruction process. For low quality x-ray radiographies and reconstruction process, noise and partial volume effect are the main factors that influence the precision of trinarization technique. This explains the extreme values of porosity obtained for the three paths, especially in the transition zone (funicular and pendular domains), where the three phases are present.

Comparing the calculated macroscopic porosity using the trinarized volumes to the ones calculated by the traditional technique (i.e., $n \approx 44\%$ for D₀ and $n \approx 46\%$ for D₁ and W₁), the trinarization technique can be evaluated as a well-adapted technique, with a precision $\pm 4\%$ for the porosity.

As shown from the latter results, higher macroscopic porosity is obtained for D₁ than for D₀. The influence of porosity (or void ratio), as presented in the literature review, appears as a larger capability to retain water for the soil of the lower porosity. For soil specimens, at the same suction, the specimen of the lower porosity retains larger water content than the specimen of the higher porosity. This influence is to be investigated in

the following section, when degree of saturation measurement is performed.

4.3.3.2 Macroscopic degree of saturation results

By definition, degree of saturation can be calculated by dividing the volume of water within the soil over the volume of the pores, $S_r = V_{wt}/V_v$. Unfortunately, the degree of saturation in this work cannot be calculated using the traditional technique because there are no available measurements for water volume exchange (ΔV_w) between the points (suction values) in the three paths D_0 , D_1 and W_1 .

Basically, water volume within the specimen can be measured using the pressure volume controller which is used to apply the suction in this work. However, due to the small size of the specimen (0.785cm^3) and thus the small volume of water within the void volume ($V_{wt} \approx 0.35\text{cm}^3$), it was hard to obtain water volume exchange (ΔV_w) accurately. The measurement of water volume exchange (ΔV_w) using the pressure volume controller was influenced by the ambient temperature and by the heating of the pressure controller water tank due to running it for a long time. If the size of the specimen is big enough, the former influences will be negligible. Moreover water volume exchange (ΔV_w) for big specimens can be measured using the rule (height of water column within the tensiometry tank, (see Fig 4.3), or by the weight of the specimen before and after applying the suction. These suggestions to measure water volume exchange (ΔV_w) are not possible in this work. Using the rule for a small specimen gives a precision of 1 mm which is insufficient for this work. Increasing the size of the specimen will decrease the resolution obtained by x-ray tomography and thus microscopic-discrete analyses cannot be performed and thus less information relative to the fluid distribution microscopic-discrete analyses can be obtained. In addition, destroying the specimen to weight water content implies to rebuild a new specimen for each point, and it is hard to maintain the same porosity for these new specimens. Moreover, using different specimens will not allow following the changes in the water distribution within the specimen.

However, macroscopic degree of saturation can be calculated using the histograms of the trinarized volumes of the three paths D_0 , D_1 and W_1 . The volume of the water V_{wt} is equal to (N_w) and the volume of the voids V_v is equal to ($N_a + N_w$). Thus the degree of saturation can be calculated as $S_r = V_{wt}/V_v$.

The macroscopic degree of saturation calculated using the trinarized volumes can be compared to $S_{r_{exp}}$ extracted from the reference WRC; see Table 4.1, for the drying paths D_0 and D_1 . For W_1 , it is not possible to perform this comparison since no reference WRC is followed for the wetting path in this work. Table 4.5 shows the macroscopic degree of saturation for the three paths D_0 , D_1 and W_1 using the trinarized volumes.

As can be shown in Table 4.5, the specimen D_0 retains larger water content (larger degree of saturation) than the specimen D_1 , for the range of suction $s=2, 2.2, 2.5, 3$ and 7kPa (i.e., in the pendular and residual domains defined qualitatively). This is consistent with the lower macroscopic porosity found for D_0 , compared to D_1 (see Table 4.4).

However, this is not true for the other values of suction $s=0$ and 1.8kPa , see Table 4.4, which are in the saturated and funicular domains defined qualitatively, respectively. In this range the macroscopic porosity measured for D_0 is lower than the one measured for D_1 , thus D_0 should retain higher water content especially in the funicular domain (considering that the specimen was not 100% saturated for D_0 at the beginning of the test)

Table 4.5: Macroscopic degree of saturation for D_0 , D_1 and W_1 calculated using the trinarized volumes

Suction (kPa)	0	1	1.2	1.4	1.6	1.8	2	2.2	2.5	2.8	3	7
Sr (%) for D_0	98.2	95	80.5	74.5	-	57.6	44.2	22.3	16.7	-	14.7	6.6
Sr (%) for D_1	100	100	100	100	95.6	74.2	29.8	19.4	9.5	6.3	4.2	4.1
Sr (%) for W_1	82.0	81.3	80.9	72.7	28.0	19.3	15.0	11.2	8.1	5.4	4.4	4.2

which is not the case. The reason behind that might be due to the different pore size and shape distribution for the two specimens, especially the big pores which are active in these two domains. During drying process, in the saturated and funicular domains, big pores are desaturated first, while in the pendular and residual domains, the influenced pores are the small pores.

This suggests that the macroscopic porosity explained the retention behaviour of the two specimens in the pendular and the residual domains, therefore, one might conclude that the macroscopic porosity is describing the influence of the small pores only, or the small pores are occupying larger portion of void volume than the big pores, and thus porosity is describing the dominant pores.

For the different paths D_1 and W_1 , Table 4.5 shows that the specimen, at the same suction, retains larger water content in the drying than in the wetting path, although the specimen is the same for drying and wetting paths (i.e. same distribution of pore size and shape, and same macroscopic porosity obtained by the traditional technique). This behaviour of the specimen (which can be explained by hysteresis phenomenon) can be only justified by local mechanisms such as ink-bottle effect. A thorough analysis of hysteresis phenomenon at the macroscopic and microscopic-discrete scale is given in section 4.4.2, for more details.

Using the calculated macroscopic degree of saturation, for all the values of suction in the three paths D_0 , D_1 and W_1 , water retention curves can be drawn. Fig 4.16 shows water retention curves for the three paths D_0 , D_1 and W_1 drawn using the degree of saturation calculated from the trinarized volume. The figure also shows the reference water retention curve (Ref WRC). As shown in Fig 4.16, the maximum difference from the reference curve, in the degree of saturation is $\Delta Sr=14\%$ for D_0 and $\Delta Sr=9\%$ for D_1 . These differences can be explained macroscopically by the influence of the different porosities of the specimens D_0 , D_1 and Ref. The specimen of the Ref WRC is of a void ratio $e=0.9$ (i.e., $n=47\%$), while the macroscopic porosity for the D_0 and D_1 is 46% and 44% respectively. However, WRCs of the three specimens are intersecting and not having a simple shift to higher or lower values of suction caused by larger or smaller porosity. This response of the three Hostun sand specimens can be explained, microscopically, by the influence of the different pore and shape size distribution.

Another reason behind the differences found in Fig 4.16 might be due to that the Ref WRC is obtained for a bigger specimen ($h \times d=20\text{cm} \times 70\text{cm}$). However, the Ref WRC is used in this work only to define the range of suction to be applied.

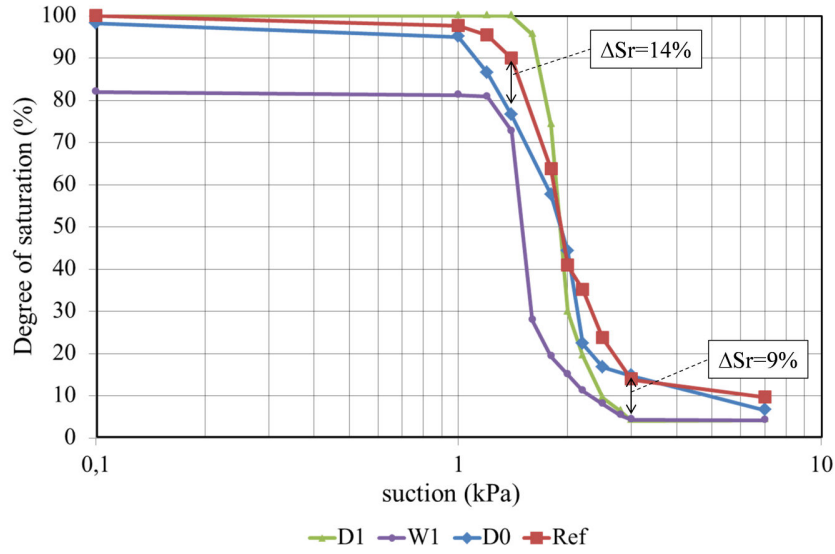


Figure 4.16: Water retention curve (WRC) for the three paths D_0 , D_1 , W_1 , and Ref WRC

4.3.4 Microscopic porosity and degree of saturation results

Porosity and degree of saturation are measured microscopically, in this work, in order to characterize water retention behaviour of Hostun sand at the local scale. For this goal, the microscopic variation of porosity and degree of saturation between the different specimens, D_0 and D_1 (i.e. different porosities) and the different paths, D_1 and W_1 (i.e. hysteresis phenomenon) are investigated and compared with the macroscopic results obtained earlier in section 4.3.3. Moreover, the microscopic measurements of porosity and degree of saturation are used later for the investigation of the relation between suction, porosity and degree of saturation.

The local measurements of porosity and degree of saturation are performed for all the values of suction in the three paths D_0 , D_1 and W_1 . Primarily, REV size over which the local porosity and degree of saturation are measured, is defined following REV analysis detailed in chapter 3, section 3.4. It was found that a size of REV (length of one side of the REV) equal or bigger than 140px is optimal for the measurements of porosity and degree of saturation, in the three paths D_0 , D_1 and W_1 . This REV is obtained for stability criteria $\Delta n = 0.1$ for porosity and $\Delta S_r = 0.5$. The $REV = 140px$ is fixed for all the following measurements of the porosity and degree of saturation. Fig 4.17 shows a window of a size equal to the size of $REV = 140px$ in 2D, compared to Hostun sand grain size. The chosen $REV = 140px$ is comparable to $D_{50} = 0.338mm$ of Hostun sand so that $REV = 140px \approx 3 \times D_{50}$. This is consistent with considering such a window as a proper REV for the measurements of the local porosity and degree of saturation.

In order to avoid the influence of the surrounding and the boundaries of the specimen on the local measurements of the porosity and degree of saturation, a volume of interest $900 \times 900 \times 1000$ voxels (i.e., $0.342cm^3$) is cut from the trinarized volumes of the size $1500 \times 1500 \times 1500$ voxels, see Fig 4.24-middle.

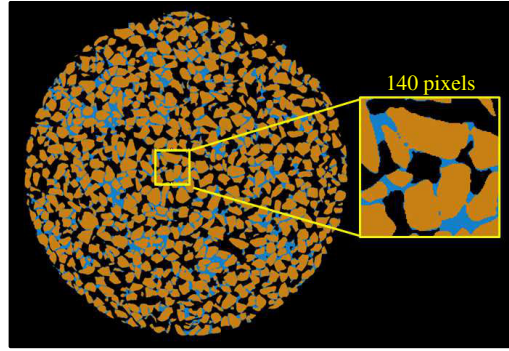


Figure 4.17: The chosen size of $REV=140px$ (length of one side of the REV) compared to the grain size of Hostun sand, for the three paths D_0 , D_1 and W_1

Later, the code of mapping the porosity and the degree of saturation detailed in chapter 3, section 3.4, is run for the chosen REV. Overlapping measurements are not allowed in the measurements of local porosity and degree of saturation performed in this section, i.e., the space between the nodes in the mapping grid is equal to the size of REV. The resulted maps of the local porosity and degree of saturation are presented by $6 \times 6 \times 7$ nodes.

4.3.4.1 Microscopic porosity results

In this section, the results of the local measurements of porosity are presented for the three paths D_0 , D_1 and W_1 . Fig 4.18, Fig 4.20 and Fig 4.22 show central horizontal (XY) slices in the porosity map, for all the values of suction, in the three paths D_1 , W_1 and D_0 respectively. Fig 4.19, Fig 4.21 and Fig 4.23 show central vertical (XZ) slices in the porosity map, of the same azimuth, for all the values of suction, in the three paths D_1 , W_1 and D_0 respectively. In these figures, n_{max} and n_{min} represent the maximum and the minimum porosity respectively (written below suction value). The maximum and the minimum porosity are obtained from the histogram of the porosity map. From this histogram, the mean and most frequent value (the mode), among other values, can be also defined (see Fig 4.26).

From the figures, it could be seen that the macroscopic porosity of the specimen in the three paths ($n=46\%$ for D_1 and W_1 , and $n=44\%$ for D_0) calculated by the traditional technique are within the range of porosity obtained from the porosity map ($n=38-52\%$ for D_1 , $n=39-52\%$ for W_1 and $n=38-49\%$ for D_0). Similarly, the average macroscopic porosity of the specimen in the three paths ($n=45\%$ for D_1 , $n=44.1\%$ for W_1 , and $n=44\%$ for D_0) calculated from the trinarized images are within the range of porosity obtained from the porosity map. This indicates that the trinarization technique and the developed mapping code are valid tools for the microscopic measurements of porosity, as their results are consistent with the macroscopic results.

It should be pointed that, having a range of the measured microscopic porosity, at each value of suction, and for each of the two specimens D_0 and D_1 (same as W_1), show that porosity distribution within the specimen is not homogenous (a result of specimen preparation technique). This can be shown also, for one specimen, from the color contrast of the horizontal and vertical slices, at a constant value of suction.

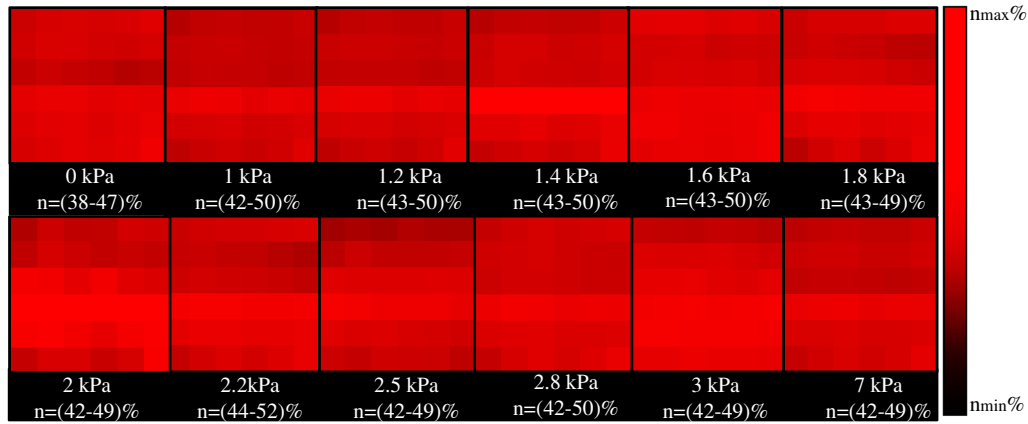


Figure 4.18: Central horizontal slices in the porosity map, for all the values of suction, in the drying path D_1 . In this figure, n_{\max} and n_{\min} represent the maximum and the minimum porosity respectively (written below the suction value)

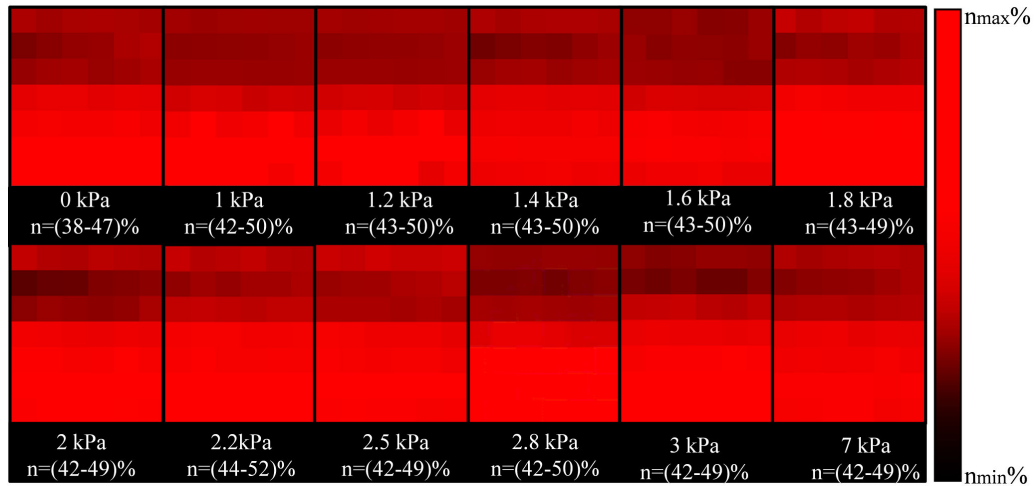


Figure 4.19: Central vertical slices in the porosity map, of the same azimuth, for all the values of suction, in the drying path D_1 . In this figure, n_{\max} and n_{\min} represent the maximum and the minimum porosity respectively (written below the suction value)

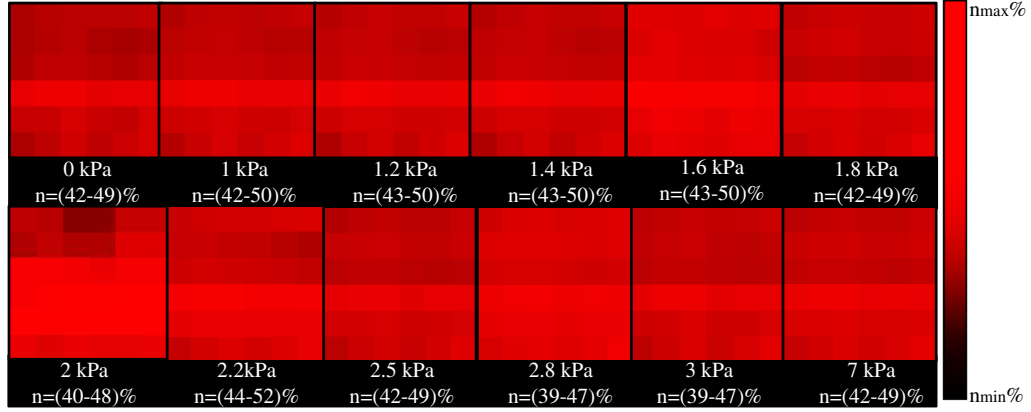


Figure 4.20: Central horizontal slices in the porosity map, for all the values of suction, in the drying path W_1 . In this figure, n_{\max} and n_{\min} represent the maximum and the minimum porosity respectively (written below suction value)

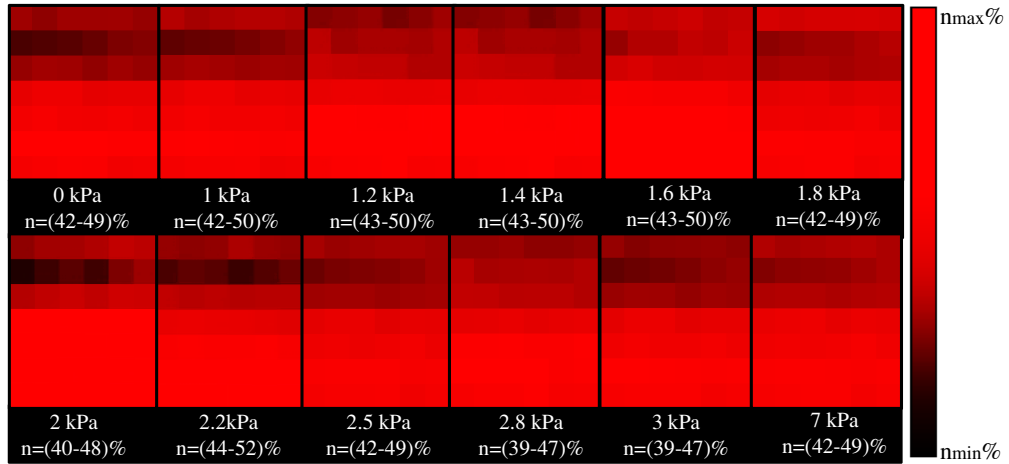


Figure 4.21: Central vertical slices of the same azimuth in the porosity map, for all the values of suction in the drying path W_1 . In this figure, n_{\max} and n_{\min} represent the maximum and the minimum porosity respectively (written below suction value)

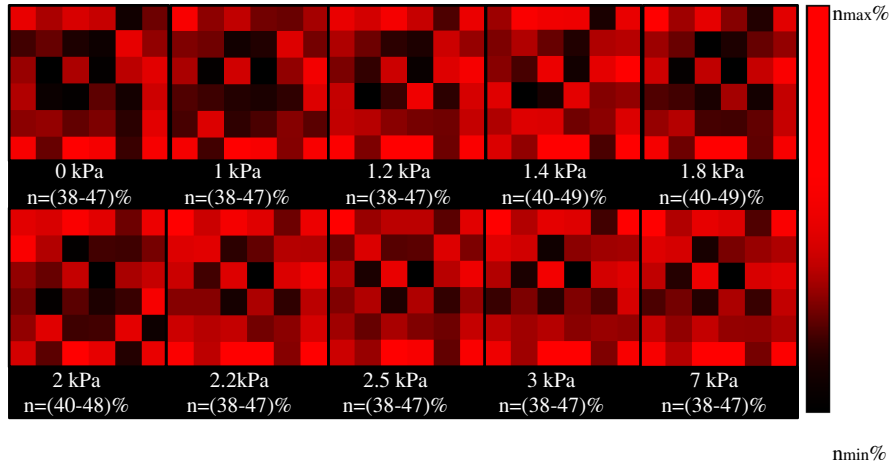


Figure 4.22: Central horizontal slices in the porosity map, for all the values of suction, in the drying path D_0

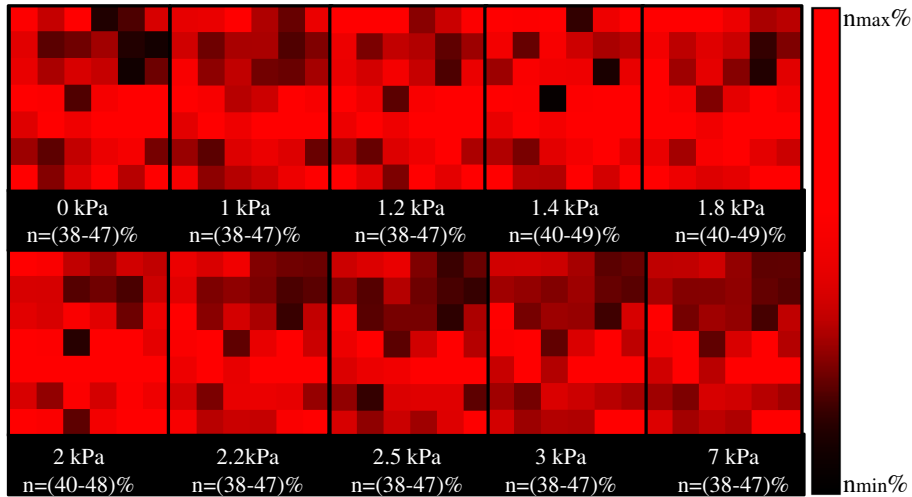


Figure 4.23: Central vertical slices of the same azimuth in the porosity map, for all the values of suction, in the drying path D_0 . In this figure, n_{\max} and n_{\min} represent the maximum and the minimum porosity respectively (written below suction value)

Porosity maps show that larger range of microscopic porosity is obtained for D_1 than for D_0 , at all the values of suction (i.e., higher microscopic porosity for D_1 than for D_0 for all the values of suction). On the other hand, smaller differences in the range of the microscopically measured porosity are found for D_1 and W_1 (i.e. same microscopic porosity for D_1 and W_1). This is expected as the two paths D_1 and W_1 are performed on the same specimen, and any differences in porosity measurement are attributed, as pointed before, to trinarization technique precision.

The vertical slices in the porosity map of D_1 , presented in Fig 4.19 shows that the porosity at the bottom of the specimen is higher than the porosity at the top. This can be seen clearly in Fig 4.24 shown for $s=2\text{kPa}$. In this figure, the mapped volume is marked by a red rectangle in the trinarized image, Fig 4.24-middle. The yellow dashed rectangle in the trinarized image marks the bottom part of the specimen where the porosity is higher than at the top. In addition, Fig 4.24 shows porosity vertical profile for the vertical slice in the mapped volume. This vertical profile shows the values of porosity for one column of voxels, shown as a yellow dashed line in the vertical slice in the porosity map.

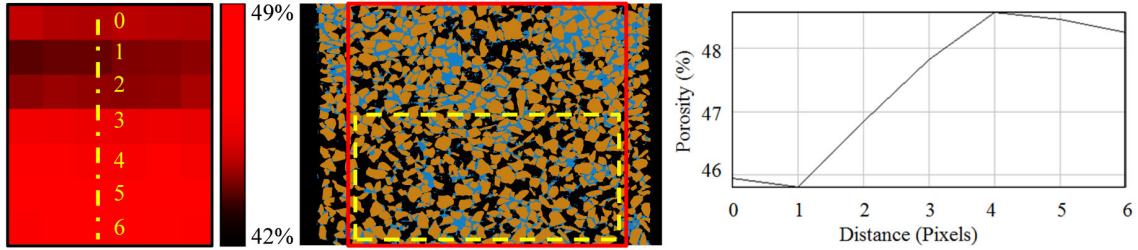


Figure 4.24: A central vertical slice in the porosity map (left), a central vertical slice in the trinarized volume (middle) and a porosity vertical profile (right) shown for $s=2\text{kPa}$, in the drying path D_1 . The mapped volume is marked by a red rectangle in the trinarized image. The yellow dashed rectangle shows the high porosity region

Porosity vertical profile shows that the porosity at the top of the specimen is $n=46\%$ at node N^0 , then the porosity increases in the middle part of the specimen to reach its maximum value $n=48.6\%$ at node N^5 at the bottom of the specimen. Similar to D_1 , the vertical slices in the porosity map of W_1 presented in Fig 4.21 shows that the porosity at the bottom of the specimen is higher than at the top, which is expected as the two tests D_1 and W_1 are performed on the same specimen.

For D_0 , the vertical slices in the porosity map presented in Fig 4.23 shows that the porosity at the middle part of the specimen is higher than the porosity in the upper and bottom parts of the specimen. This can be seen clearly in Fig 4.25 shown for $s=2\text{kPa}$. In this figure, the yellow dashed rectangle in the trinarized image marks the middle part of the specimen where the porosity is higher than the upper and bottom parts of the specimen.

Porosity vertical profile in Fig 4.25-right drawn for the yellow dashed line in Fig 4.25-left shows that the porosity at the top of the specimen is $n=43.9\%$ at node N^0 , then the porosity increases in the middle part of the specimen to reach a maximum value $n=46.3\%$ at node N^4 then the porosity decreases to $n=44.6\%$ at node N^6 at the bottom of the specimen.

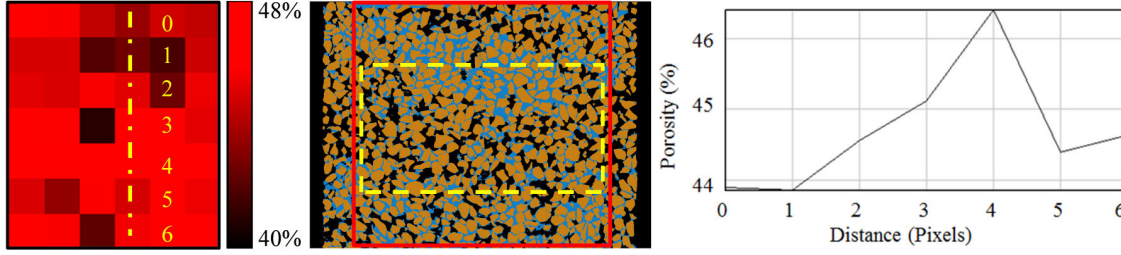


Figure 4.25: A central vertical slice in the porosity map (left), a central vertical slice in the trinarized volume (middle) and a porosity vertical profile (right) shown for $s=2\text{kPa}$, in the drying path D_0 . The mapped volume is marked by a red rectangle in the trinarized image. The yellow dashed rectangle shows the high porosity region

In the porosity histogram presented in Fig 4.26 drawn for the whole mapped volume at $s=2\text{kPa}$, for the drying path D_1 , the mean and the mode (most frequent) values of porosity are shown (marked by red rectangle).

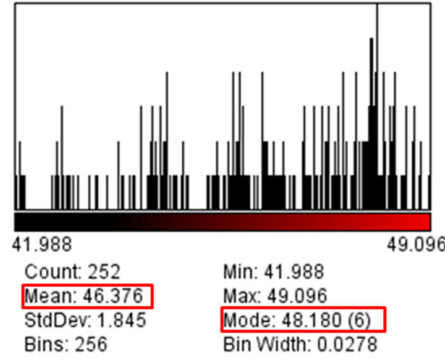


Figure 4.26: Local porosity histogram shown for $s=2\text{kPa}$ in the drying path D_1 . The mean and the most frequent (mode) porosity are marked by a red rectangle

Using porosity histogram of all the values of suction in the three paths, the mean values are extracted and averaged for each path. The average value of the mean porosity for all the values of suction in the drying and wetting paths D_1 is $n=46.8\%$. For wetting path, the average value of the mean porosity for all the values of suction in the wetting path W_1 is $n=46.2\%$. While for the drying path D_0 , the average value of the mean porosity for all the values of suction in the drying path D_0 is $n=42.7\%$.

Comparing the average mean microscopic value of porosity for the three paths D_1 , W_1 and D_0 to the macroscopic one obtained using the traditional technique ($n=46\%$ for D_1 and W_1 , and $n=44\%$ for D_0) a difference of 0.8% , 0.2% and 1.3% is found, respectively. As explained before, these differences are due to the precision provided by the trinarization technique (porosity mapping is performed on the trinarized volumes while the macroscopic one are obtained using the traditional technique).

From the other hand, the differences between the average mean microscopic value of D_1 , W_1 and D_0 and the macroscopic one obtained using the trinarized volumes, might be due to that the microscopic measurements of the porosity are performed for a volume of interest of a size $900 \times 900 \times 1000$ voxels (see Fig 4.25 where only the volume marked by a red rectangle in the trinarized volume is considered for porosity mapping), while

the macroscopic measurements (using the trinarized volumes) are performed for a volume $1300 \times 1300 \times 1200$ voxels, i.e., after removing the boundaries and the surrounding of the specimen (see Fig 4.8) where only the volume marked by a dashed red rectangle in the trinarized volume is considered for porosity macroscopic measurement).

More detailed results of porosity mapping can be found in Appendix B. These results allow performing a qualitative comparison between the mapped and the trinarized slices in the horizontal and vertical planes, and thus visualizing the variation and spatial distribution of porosity measurements over the whole specimen and obtaining quantitative description from the histogram. In Appendix B, Fig (B-1), Fig (B-3) and Fig (B-5) show central horizontal slices in the porosity map and trinarized volumes, and porosity histogram, for all the values of suction in the three paths D_1 , W_1 and D_0 respectively. Fig (B-2), Fig (B-4) and Fig (B-6) show central vertical slices of the same azimuth in the porosity map and trinarized volumes, and porosity vertical profiles, for all the values of suction in the three paths D_1 , W_1 and D_0 respectively. For a reason of better illustration, the vertical profile of the local porosity in appendix B is not performed for the same column of voxels, for the different points. Therefore, for a better presentation of the results, the chosen column of voxels is shown only for the first point in the three paths D_0 , D_1 and W_1 .

4.3.4.2 Microscopic degree of saturation results

In this section, the results of local measurements of degree of saturation are presented for the three paths D_0 , D_1 and W_1 . Fig 4.27, Fig 4.29 and Fig 4.31 show central horizontal (XY) slices in the degree of saturation map, for all the values of suction, in the three paths D_1 , W_1 and D_0 , respectively. Fig 4.28, Fig 4.30 and Fig 4.32 show central vertical (XZ) slices in the degree of saturation map, of the same azimuth, for all the values of suction, in the three paths D_1 , W_1 and D_0 , respectively. In these figure, ($S_{r_{max}}$) and ($S_{r_{min}}$) represent the maximum and the minimum degree of saturation, respectively (written below suction value). Similar to porosity mapping results, the maximum and the minimum degree of saturation are obtained from the histogram of degree of saturation plotted for the whole mapped volume.

It should be noted again, that the contrast of the color in the degree of saturation map depends on the range of degree of saturation. As the degree of saturation range is not the same for the different volumes, therefore, the color contrast is not the same.

Using the degree of saturation histogram of all the values of suction in the three paths, the mean values ($S_{r_{mean}}$) of microscopic degree of saturation are extracted for all the values of suction in each path. These values are shown in Table 4.6 to be compared to the macroscopic degree of saturation calculated from the trinarized images (see Table 4.5).

Similar to porosity, the differences between the macroscopic degree of saturation calculated from the trinarized images and the mean microscopic ones might be due to that the microscopic measurements of the porosity are performed for a smaller volume of interest of the specimen (see Fig 4.25, than the volume considered for macroscopic measurements (see Fig 4.8).

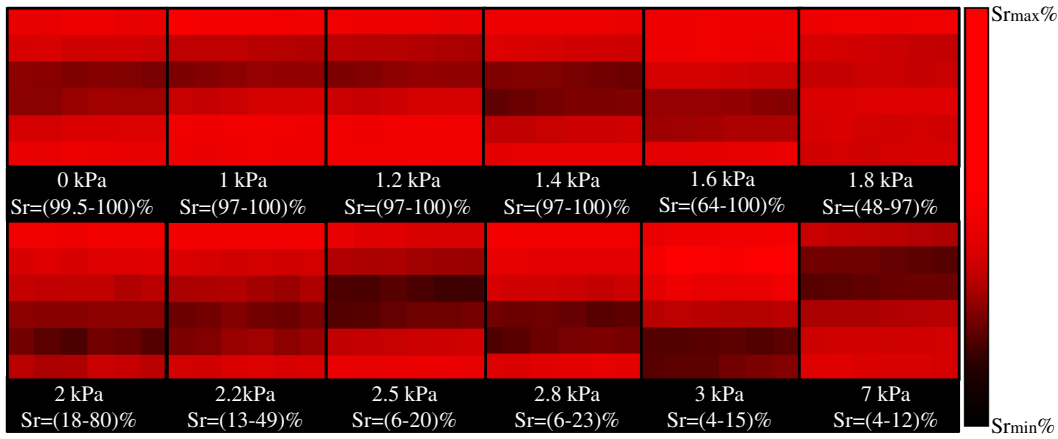


Figure 4.27: Central horizontal slices in the degree of saturation map, for all the values of suction, in the drying path D_1 . In this figure, Sr_{max} and Sr_{min} represent the maximum and the minimum degree of saturation respectively (written below suction value)

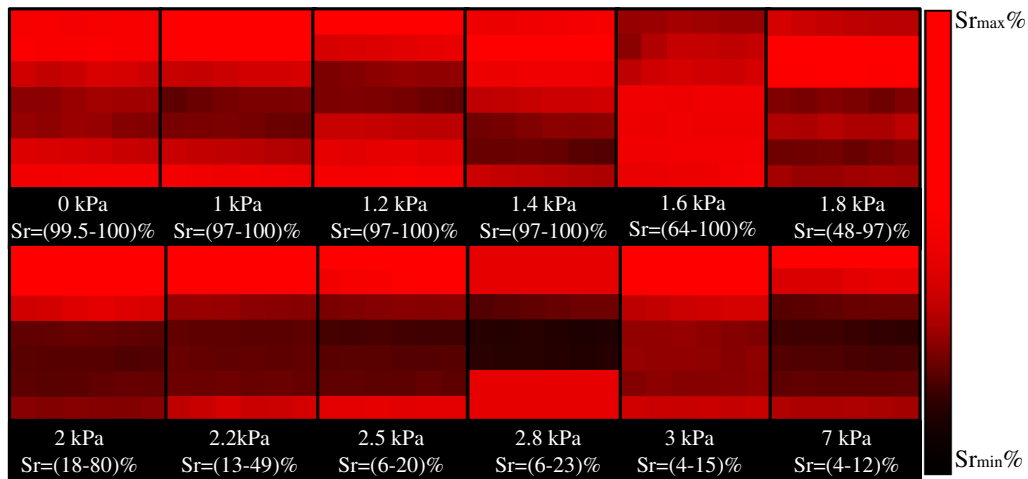


Figure 4.28: Central vertical slices of the same azimuth in the degree of saturation map, for all the values of suction, in the drying path D_1 . In this figure, Sr_{max} and Sr_{min} represent the maximum and the minimum degree of saturation respectively (written below suction value)

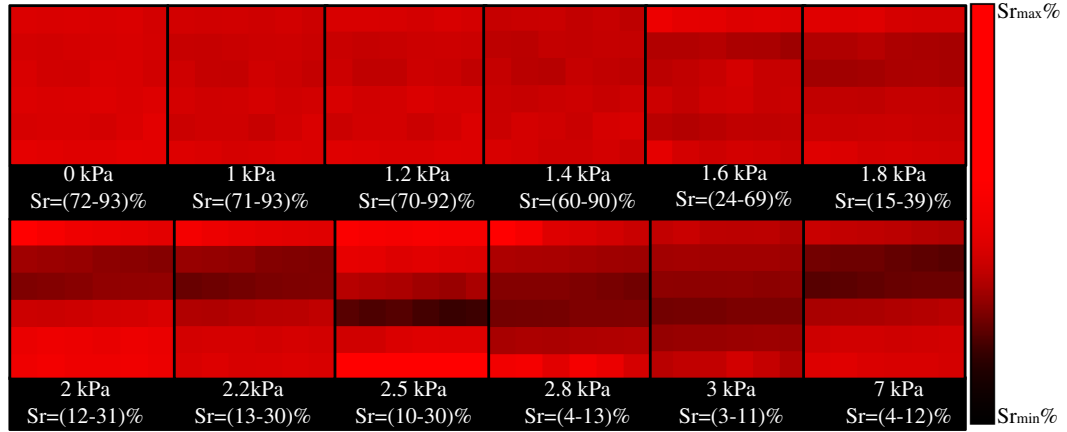


Figure 4.29: Central horizontal slices in the degree of saturation map, for all the values of suction, in the drying path W_1 . In this figure, Sr_{max} and Sr_{min} represent the maximum and the minimum degree of saturation respectively (written below suction value)

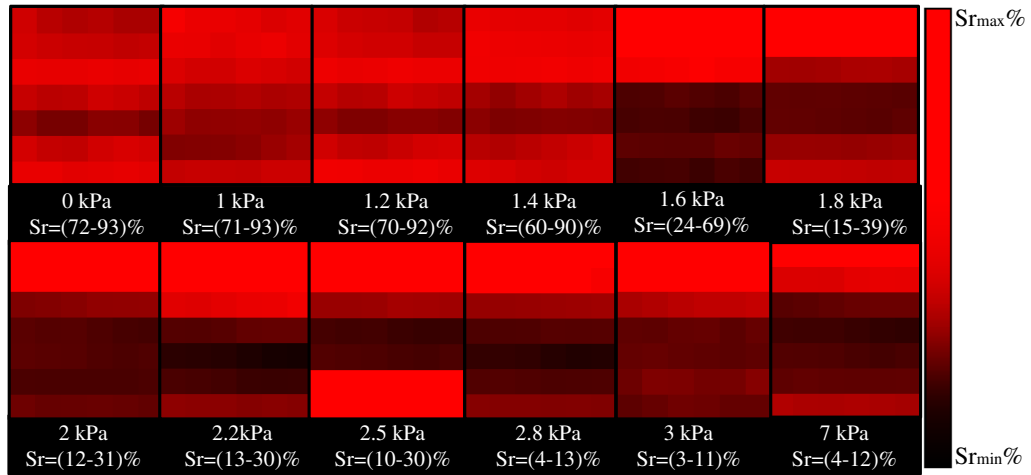


Figure 4.30: Central vertical slices in the degree of saturation map, for all the values of suction, in the drying path W_1 . In this figure, Sr_{max} and Sr_{min} represent the maximum and the minimum degree of saturation respectively (written below suction value)

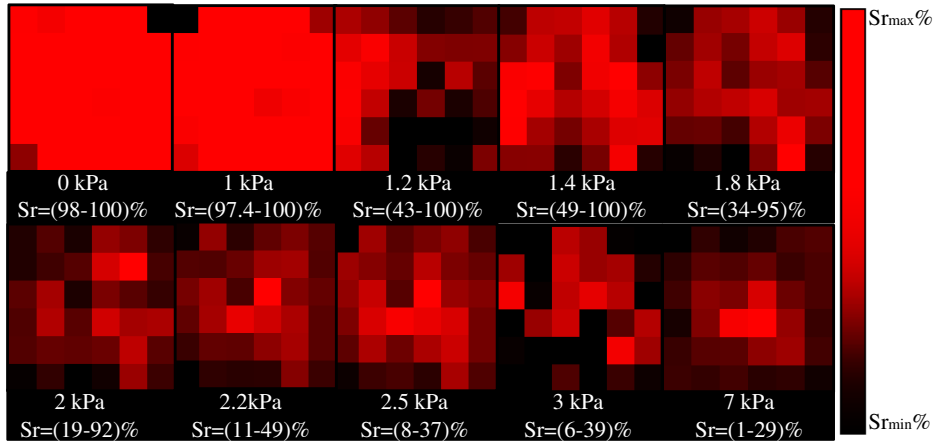


Figure 4.31: Central horizontal slices in the degree of saturation map, for all the values of suction, in the drying path D_0 . In this figure, Sr_{max} and Sr_{min} represent the maximum and the minimum degree of saturation respectively (written below suction value)

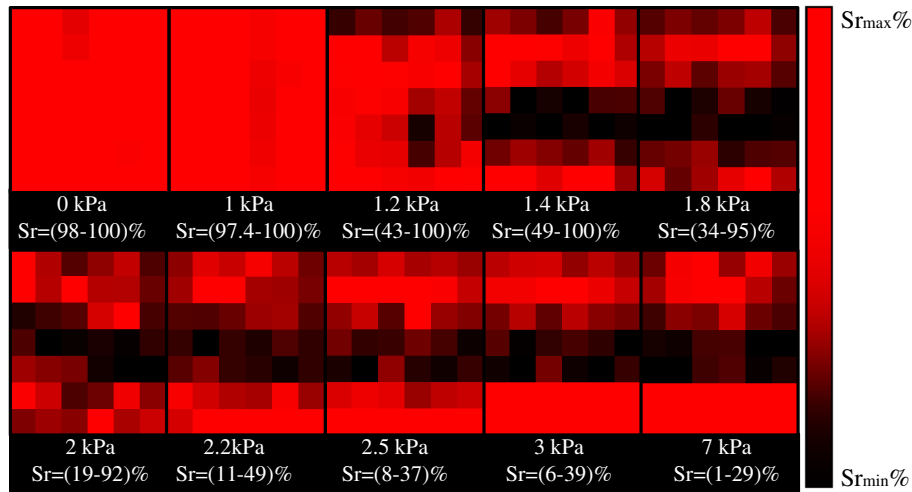


Figure 4.32: Central horizontal slices in the degree of saturation map, for all the values of suction, in the drying path D_0 . In this figure, Sr_{max} and Sr_{min} represent the maximum and the minimum degree of saturation respectively (written below suction value)

Table 4.6: Mean microscopic degree of saturation extracted from the degree of saturation histogram for the three paths D_1 , W_1 and D_0

Suction (kPa)	0	1	1.2	1.4	1.6	1.8	2	2.2	2.5	2.8	3	7
Sr-mean (%) D_0	100	100	87.9	82.5	-	65	51.2	25.3	19.1	-	16	6.7
Sr-mean (%) D_1	100	98.7	99	98.9	95.3	74.7	35.3	21.4	11.1	13.6	7.5	7.7
Sr-mean (%) W_1	81.9	82.2	81.6	60.4	37.5	23.1	20.6	20.8	17.5	8	5.5	7.7

The maps of the degree of saturation, for the drying paths D_0 and D_1 , shows that all the REV's are filled with water ($S_r \approx 100\%$) at the beginning of the tests, which implies a homogenous distribution of water phase within the specimen at the beginning of the test. Then, when suction is applied, the range of the measurements of the degree of saturation within the REV's increases, i.e., heterogeneous distribution of water phase within the specimen. At the end of the tests, the range of the measurements of the degree of saturation within the REV's decreases (i.e., the heterogeneous distribution of water phase within the specimen decreases). Similarly for the wetting path, at the beginning of the test, a narrow range of the measurements of the degree of saturation within the REV's is present. When decreasing the suction (wetting the specimen), the range of the measurements of the degree of saturation within the REV's increases, which implies increasing the heterogeneity of the specimen.

The degree of saturation maps show that, larger range of microscopic degree of saturation is obtained for the specimen D_0 than for the specimen D_1 at all the values of suction. This is consistent with the lower macroscopic porosity obtained for D_0 than for D_1 . Thus, the microscopic measurement describes better the retention behaviour of the two specimens than the macroscopic one.

Moreover, the larger range of microscopic degree of saturation obtained for D_0 than for D_1 is consistent with the larger range of microscopic porosity obtained for D_0 compared to D_1 , i.e., large range of porosity corresponds to large range of degree of saturation (as a description of the range and not the relation trend between porosity and degree of saturation).

Comparing these results to the macroscopic results found in section 4.3.3, macroscopic porosity described retention behaviour of the two specimens only at the pendular and the residual domain, knowing that mapping has been performed on the same trinarized images, but for smaller volume of interest in the case of macroscopic measurements compared to the volume of interest considered for the macroscopic measurements.

One might suggest that the macroscopically measured porosity did not describe the retention behaviour of the two specimens in the saturated and funicular domain due to the size of the volume of interest (i.e., boundary effects). If this is true then the macroscopic porosity should fail describing retention behaviour for all the values of suction due to this influence, and not only fail to describe retention behaviour in the saturated and the funicular domain. Moreover, if the microscopically measured degree of saturation is averaged, as in Table 4.6, the microscopic measurement fails to describe retention behaviour of the two specimens D_0 and D_1 , just as the macroscopic results (i.e., porosity describes retention behaviour only in the pendular and the funicular domain). This shows that the size of the volume of interest is not the reason behind not being able to describe retention behaviour but averaging the measured porosity and degree of saturation and ignoring the

influence of the microscopic pore size and shape distribution.

For the different paths D_1 and W_1 , degree of saturation map and Table 4.6 shows that the specimen, at the same suction, retains larger water content in the drying than in the wetting path, similar to the macroscopic behaviour.

For better understanding of retention behaviour at the microscopic scale, the relation between the microscopic porosity and degree of saturation is investigated qualitatively, in the following, using the mapped volumes of porosity (presented in section 4.3.4.1) and the mapped volumes of the degree of saturation (presented earlier in this section).

The vertical slices in the degree of saturation map of D_1 , presented in Fig 4.28 shows that the degree of saturation at the top of the specimen is higher than the degree of saturation at the bottom. This can be seen clearly in Fig 4.33 shown for $s=2\text{kPa}$. In this figure, the mapped volume is marked by a red rectangle in the trinarized image Fig 4.33-middle. The yellow dashed rectangle in the trinarized image marks the bottom of the specimen where the degree of saturation is higher than at the top. In addition, Fig 4.33 shows degree of saturation vertical profile for the vertical slice in the mapped volume. This vertical profile shows the values of degree of saturation for one column of voxels, shown as a yellow dashed line in the vertical slice in the degree of saturation map.

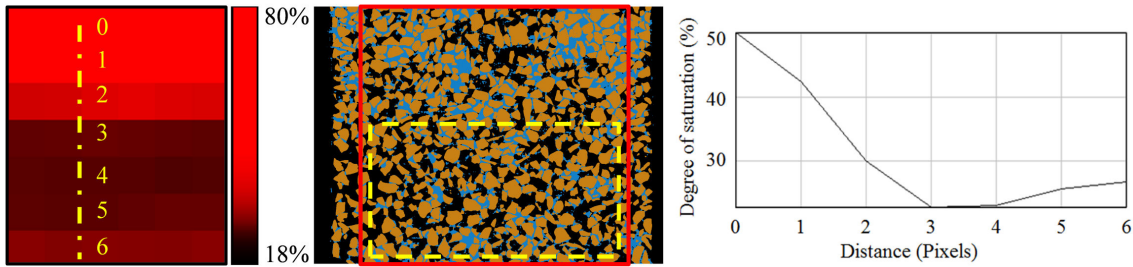


Figure 4.33: A central vertical slice in the degree of saturation map (left), a central vertical slice in the trinarized volume (middle) and a degree of saturation vertical profile (right) shown for $s=2\text{kPa}$, in the drying path D_1 . The mapped volume is marked by a red rectangle in the trinarized image. The yellow dashed rectangle shows the high degree of saturation region

The degree of saturation vertical profile in Fig 4.33-right drawn for the yellow dashed line in Fig 4.33-left shows that the degree of saturation at the top of the specimen is $S_r=50\%$ at node N^0 , then the degree of saturation decreases in the middle part of the specimen to reach $S_r=26\%$ at node N^6 at the bottom of the specimen. Similar to D_1 , the vertical slices in the degree of saturation map of W_1 presented in Fig 4.30 shows that the porosity at the bottom of the specimen is higher than at the top (same specimen).

The relation between the microscopic porosity and degree of saturation can be investigated qualitatively, from Fig 4.33. The trinarized image in Fig 4.33-middle shows that water content is lower at the bottom of the specimen than at the top. This is consistent with the higher porosity at the bottom of the specimen, found from the porosity mapping (see Fig 4.24). This implies that increasing the porosity induces a decrease in the degree of saturation.

For the drying path D_0 , the vertical slices in the degree of saturation map presented in Fig 4.32 shows that the degree of saturation at the upper and lower parts of the specimen is higher than at the middle part. This can be seen clearly in Fig 4.34 shown for $s=2\text{kPa}$.

In this figure, the yellow dashed rectangle in the trinarized image marks the bottom of the specimen where the degree of saturation is higher than at the top.

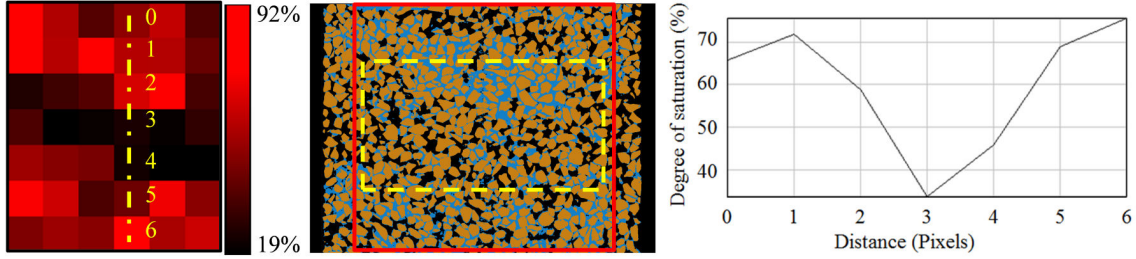


Figure 4.34: A central vertical slice in the degree of saturation map (left), a central vertical slice in the trinarized volume (middle) and a degree of saturation vertical profile (right) shown for $s=2\text{kPa}$, in the drying path D_0 . The mapped volume is marked by a red rectangle in the trinarized image. The yellow dashed rectangle shows the high degree of saturation region

The degree of saturation vertical profile in Fig 4.34-right drawn for the yellow dashed line in Fig 4.34-left shows that the degree of saturation at the top of the specimen is $S_r=67\%$ at node N^0 , then the degree of saturation decreases in the middle part of the specimen to reach a minimum value $S_r=35\%$ at node N^3 then the degree of saturation increases to $S_r=74\%$ at node N^6 at the bottom of the specimen.

The trinarized image in Fig 4.34-middle shows that water content is lower in the middle part of the specimen than in the upper and bottom parts. This is consistent with the higher porosity in the middle part found from the porosity mapping. This trend of the relation between porosity and degree of saturation is similar to that found for D_1 specimen (same to W_1). Later in section 4.4.1, the relation between microscopic porosity and degree of saturation is analyzed quantitatively, including the influence of suction on this relation.

More detailed results of degree of saturation mapping can be found in Appendix B. These results allow performing a qualitative comparison between the mapped and the trinarized slices in the horizontal and vertical planes, and thus visualizing the variation and spatial distribution of degree of saturation measurements over the whole specimen and obtaining quantitative description from the histogram. In Appendix B, Fig (B-7), Fig (B-9) and Fig (B-11) show central horizontal slices in the degree of saturation map and trinarized volumes, and degree of saturation histogram, for all the values of suction in the three paths D_1 , W_1 and D_0 , respectively. Fig (B-8), Fig (B-10) and Fig (B-12) show central vertical slices of the same azimuth in the degree of saturation map and trinarized volumes, and degree of saturation vertical profiles, for all the values of suction in the three paths D_1 , W_1 and D_0 , respectively. Similar to porosity results, for a reason of better illustration, the vertical profile of the local degree of saturation in appendix B is not performed for the same column of voxels, for the different points. Therefore, for a better presentation of the results, the chosen column of voxels is shown only for the first point in the three paths D_0 , D_1 and W_1 .

4.3.5 Microscopic-discrete analyses results

Due to the nature of the phases present in the unsaturated specimen (as grains, fluid clusters and their contacts), the three phases within the specimen are analyzed at the microscopic-discrete scales. This helps identifying and following the individual grains and

fluid clusters in 3D, and offers better understanding of the interaction between the phases and their contacts. As a result, a thorough investigation of retention behaviour can be build based on these microscopic-discrete analyses.

Using the labelled volumes for all the values of suction in the three paths D_0 , D_1 and W_1 , the evolution of the number of fluid clusters with suction is investigated. In addition, the evolution of the effective specific interfacial area with the degree of saturation is investigated. Furthermore, the evolution of the contacts between the phases with suction is analyzed for the three paths D_0 , D_1 and W_1 .

It is important to note that, in this chapter, the loading represent suction change which indicates the direction of the hydraulic loading (drying and wetting).

4.3.5.1 The evolution of the number of fluid clusters with suction

When the suction is applied, water content and the distribution of water phase within the specimen change. In this work, the evolution of water phase with suction is investigated, with respect to the number of water clusters, distribution, volume and continuity state. The increase or decrease in water content, due to suction application, is accompanied by a decrease or increase in air volume within the specimen, therefore, the evolution of air phase is investigated also. This investigation is performed to define water retention domains locally based on quantitative information describing the continuity of the fluid phase and the local changes in its distribution (number of clusters and volume of the biggest cluster). Moreover, the analyses performed in this chapter are used for the investigation of hysteresis phenomenon and soil cohesion.

Using the trinarized volumes and the commercial code Visilog[®], the three phases within the specimen are separated and analyzed. After a series of morphological processes, detailed in chapter 3, section 3.5.1, water and air clusters are labelled and a list of geometrical information (center of mass, 3D volume, 3D area ...etc) of fluid clusters is obtained. In this work, three geometrical characteristics are used. Those characteristics are: the number of fluid clusters for each point (value of suction), the volume of fluid cluster in 3D and the equivalent diameter. Later, the relation between the number of fluid clusters versus suction is plotted for all the points in the three paths D_0 , D_1 and W_1 . Then fluid cluster size distribution is obtained and fluid cluster of the maximum volume (V_{\max}) is extracted. The relation between the normalized V_{\max} and the suction is plotted. The two plots: the number of fluid clusters versus suction and the normalized V_{\max} versus suction are analyzed.

Fig 4.35, Fig 4.37 and Fig 4.39 show central vertical slices of the same azimuth in the labelled volume of water, for all the values of suction in the three paths D_1 , W_1 and D_0 . Fig 4.36, Fig 4.38 and Fig 4.40 show central vertical slices of the same azimuth in the labelled volume of air, for all the values of suction in the three paths D_1 , W_1 and D_0 . As pointed in chapter 3, the different colors in the labelled volumes represent different fluid clusters. Yet, it is important to note that, for the same value of suction, different fluid clusters of different Ids (Identifications) might have the same color. In addition, there is no link between the color of the fluid cluster and the suction, i.e. the color of fluid cluster changes from one value of suction to another. If a random fluid cluster had the same color for different values of suction, then this would be a result of the program (Visilog[®]) that the author cannot control (i.e., fluid cluster is followed from one suction value to another by its Id not by its color).

In the following, the results of labelling process are analyzed for each value of suction in the three paths D_1 , W_1 and D_0 .

In the labelled volume of fluid clusters, for D_1 and D_0 , small air clusters in the saturated range are ignored (the specimen is saturated with one big water cluster and no presence of air).

As shown in Fig 4.35, for D_1 , water phase is represented by one big cluster of the color blue (i.e., water phase is in a continuous state) for each value in the range of suction $s=0$, 1, 1.2 and 1.4kPa. Air enters the specimen at $s=1.6$ kPa and this is shown in Fig 4.36. The small air clusters shown for $s=0$, 1, 1.2 and 1.4kPa are ignored (not considered in the following analyses) because they are the result of the weak contact between the specimen and the walls of the cell and thus they do not represent the behaviour of the specimen. At $s=2$ kPa several air and water clusters are present in the specimen (i.e., both water and air phase are in a continuous state). For the range of suction $s=2.2$, 2.5 and 2.8kPa, air phase is represented by one big cluster (i.e., air phase is in a continuous state) while water phase is present in a form of several small clusters (i.e., water phase is in a discontinuous state).

For W_1 , Fig 4.37 and Fig 4.38, show that air phase is represented by one big cluster (i.e., air phase is in a continuous state) and several water clusters are present (i.e., water phase is in a discontinuous state) for the range of suction $s=7$, 3, 2.8, 2.5, 2.2 and 2kPa. At $s=1.6$ kPa, both water and air phases are present within the specimen in the form of one big cluster (both phases are continuous). For $s=0$, 1, 1.2 and 1.4kPa, several air clusters are found (i.e., air phase is discontinuous) and water phase is in the form of one big cluster (water phase is continuous).

Fig 4.39 and Fig 4.40, show that for D_0 , water phase is in the form of one big cluster (i.e., in a continuous state) in the range of suction $s=0$, 1, 1.2, 1.4 and 1.8kPa. Air enters the specimen at $s=1.2$ kPa. At $s=2$ kPa both air and water phases are in the form of one big cluster (in continuous state). For the range of suction $s=2.2$, 2.5, 2.8, 3 and 7kPa, one big air cluster is found (air phase is continuous) and water phase is in the form of several clusters (in a discontinuous state).

More detailed results of labelling process can be found in Appendix C. These results helps comparing the trinarized and labelled slices, visualizing the spatial distribution of water and air phases with respect to the grain phase and quantifying the size each fluid clusters. In Appendix C, Fig (C-1), Fig (C-2) and Fig (C-3) show central vertical slices in the water labelled volumes, trinarized volumes and air labelled volume, for all the values of suction in the three paths D_1 , W_1 and D_0 respectively.

From the fluid labelled volume shown in the former figures, the number of fluid clusters is obtained. Later, the relation between the number of fluid clusters versus suction is plotted. Fig 4.41, Fig 4.42 and Fig 4.43 shows the evolution of the number of water and air clusters with suction, for the three paths D_1 , W_1 and D_0 , respectively. For the purpose of a better interpretation of the results, these figures are read in the direction of increasing or decreasing the suction (inversely), depending on the path (drying or wetting) and the fluid phase (water or air) following the arrows presented in these figures.

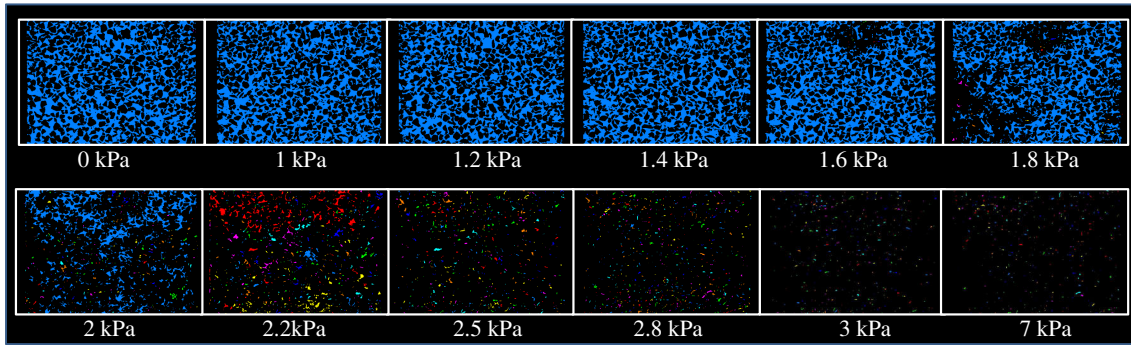


Figure 4.35: Central vertical slices of the same azimuth in the labelled volume of water, for all the values of suction in the drying path D_1

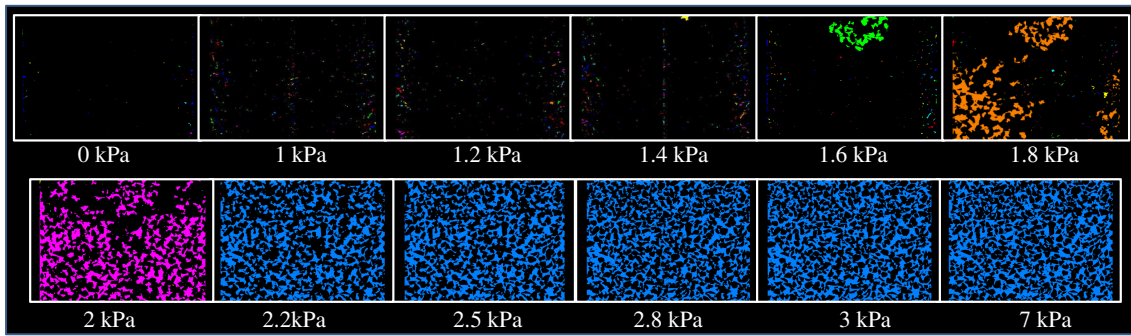


Figure 4.36: Central vertical slices of the same azimuth in the labelled volume of air, for all the values of suction in the drying path D_1

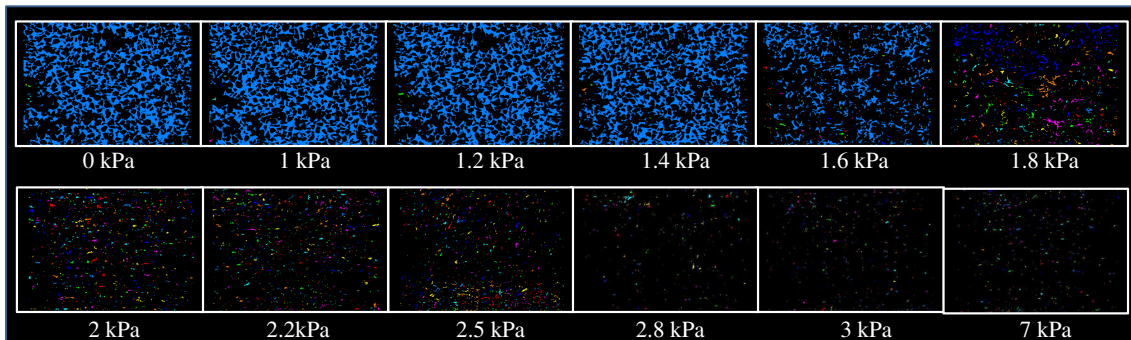


Figure 4.37: Central vertical slices of the same azimuth in the labelled water volume, for all the values of suction in the wetting path W_1

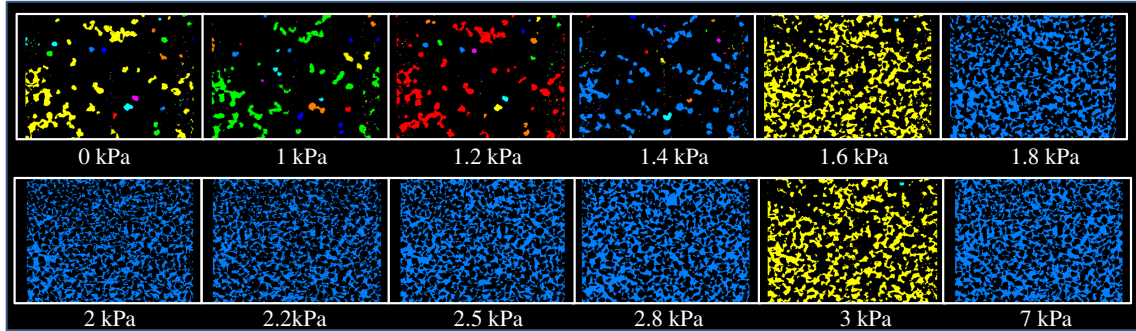


Figure 4.38: Central vertical slices of the same azimuth in the labelled air volume, for all the values of suction in the wetting path W_1

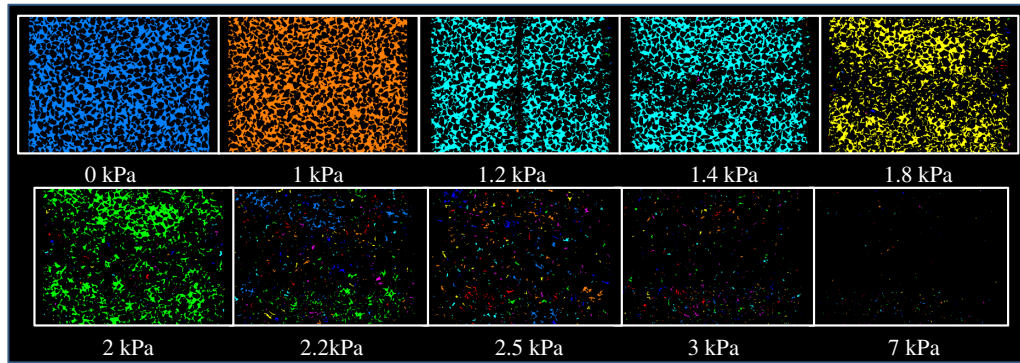


Figure 4.39: Central vertical slices in the water labelled volume, of the same azimuth for all the values of suction in the drying path D_0

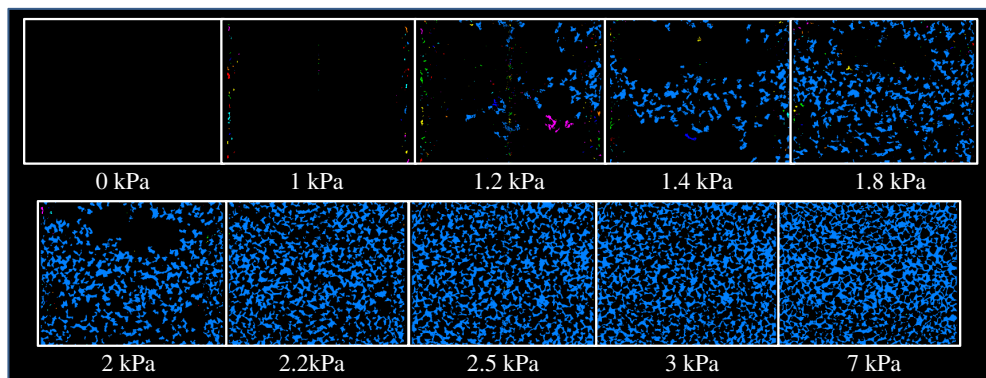


Figure 4.40: Central vertical slices in the air labelled volume, of the same azimuth for all the values of suction in the drying path D_0

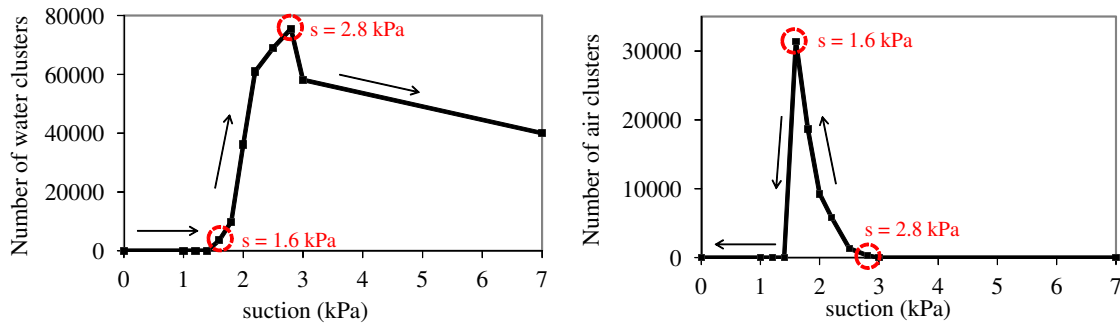


Figure 4.41: The evolution of the number of water clusters (left) and air clusters (right) with suction, for the drying path D_1

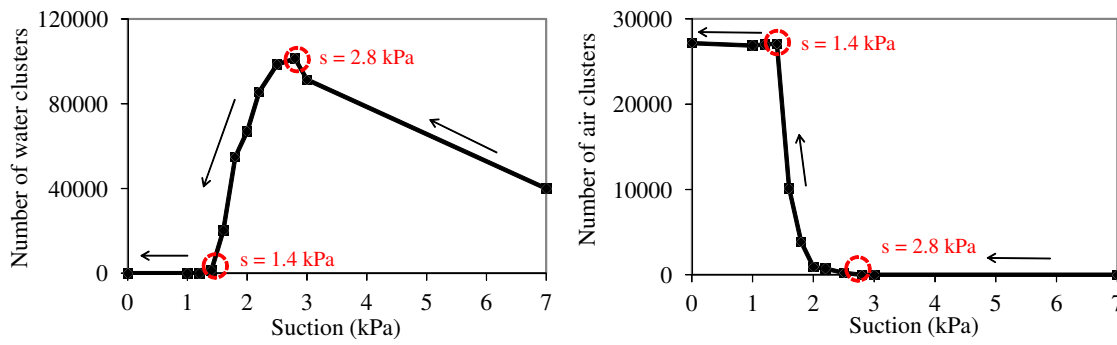


Figure 4.42: The evolution of the number of water clusters (left) and air clusters (right) versus suction, for the wetting path W_1

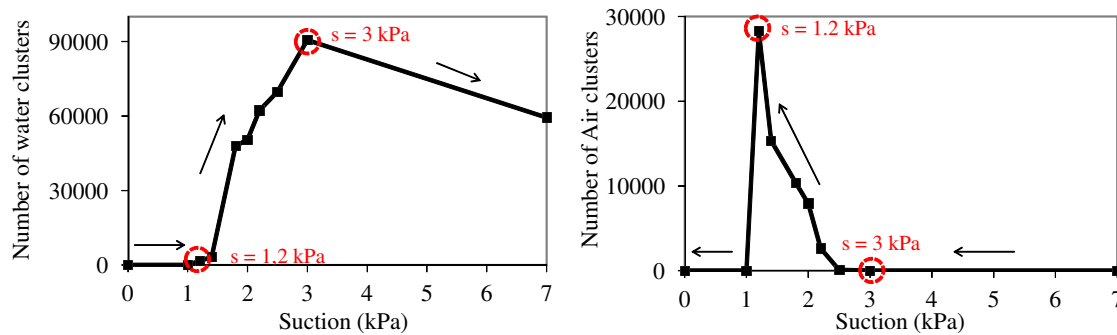


Figure 4.43: The evolution of the number of water clusters (left) and air clusters (right) versus suction, for the drying path D_0

For the evolution of the number of water clusters versus suction, in the two paths D_1 and D_0 , the figures show that the specimen is saturated at the beginning of the tests, with one big water cluster. Later, the number of the clusters increases (i.e., the one big cluster divides into smaller clusters) to reach a maximum value then decreases to reach the number of water clusters in the residual water state. For W_1 , the test begins with a number of clusters equal to the number of water clusters at the residual state. Later, the number of the clusters increases to reach a maximum value then decreases (clusters are getting connected) to reach one big water cluster at the end of the test.

It should be pointed that the number of water clusters at the residual water state, presented in Fig 4.41, Fig 4.42 and Fig 4.43 might includes noise measurements as the size of water clusters in this state is close to the resolution provided in this work.

For air clusters, the figures are read inversely for D_1 and D_0 (following the arrows). The specimen has one big air cluster at the end of the tests. Later the number of air clusters increases (i.e., the one big cluster divides into smaller clusters) then decreases to reach a minimum value with zero air clusters at the beginning of the test. For W_1 , the test begins with one big air cluster. Later the number of air clusters increases to reach a stabilized value equal to the number of trapped air clusters at the end of the test.

The latter characterization of the evolution of the number of water and air clusters in drying path, is actually describing the stage of division and later reduction in water content, and the invasion and later continuity of air phase. For wetting path, this characterization describes the continuity of water phase and the correspondent division of air phase.

In Fig 4.41, Fig 4.42 and Fig 4.43, the values of suction at which a maximum number of water and air clusters, and the values of suction at which the one big cluster of fluid is divided into smaller clusters are highlighted with a red dashed circle.

After obtaining the evolution of the number of fluid cluster with suction, water and air clusters size distribution are plotted. Fig 4.44, Fig 4.46 and Fig 4.48 shows water clusters size distribution for all the values of suction in the three paths D_1 , W_1 and D_0 respectively. Fig 4.45, Fig 4.47 and Fig 4.49 shows air clusters size distribution for all the values of suction in the three paths D_1 , W_1 and D_0 respectively. Note that in these figures, the curves can be superposed at some values of suction.

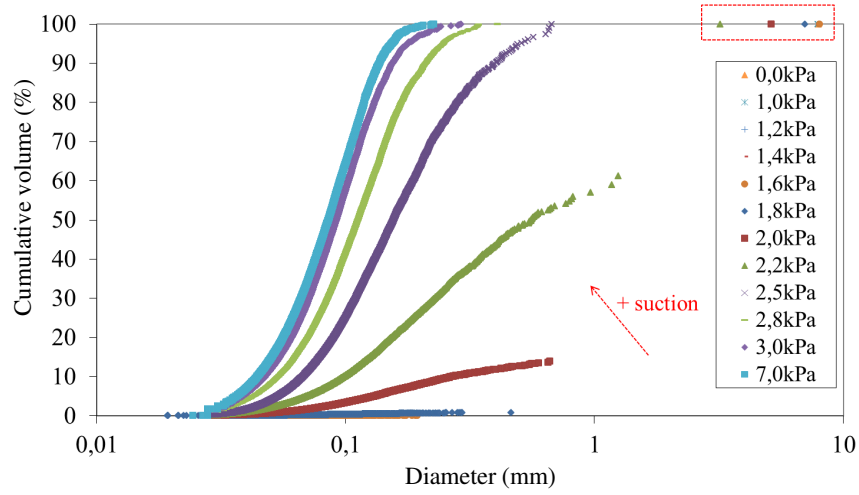


Figure 4.44: Water clusters size distribution for all the values of suction in the drying path D_1

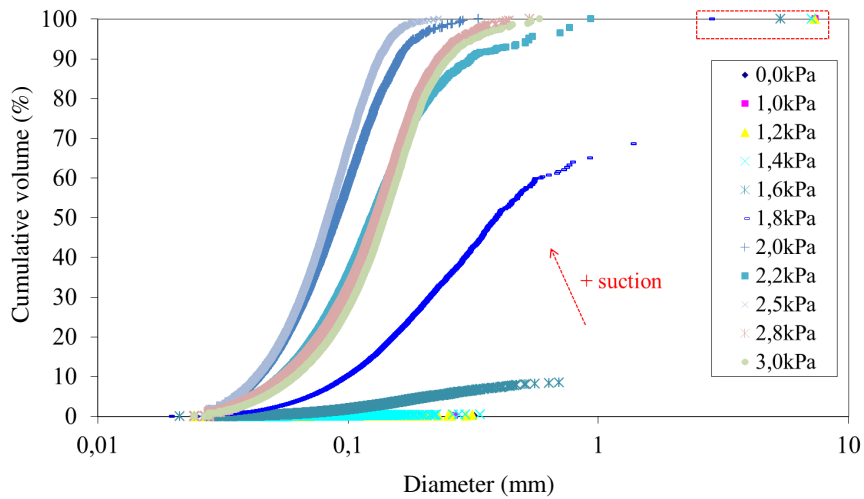


Figure 4.45: Water clusters size distribution for all the values of suction in the wetting path W_1

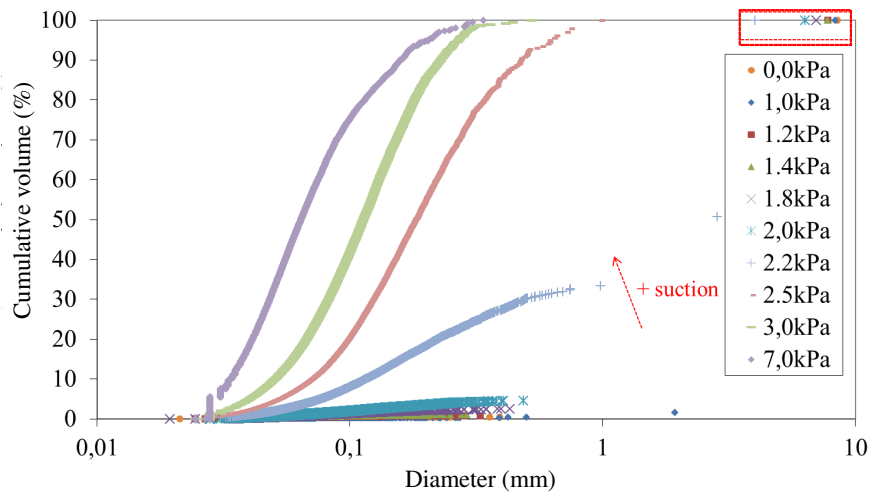


Figure 4.46: Water clusters size distribution for all the values of suction in the drying path D_0

Water clusters size distribution for the three paths D_1 , W_1 and D_0 show that when the suction is increased, the range of the EqD (Equivalent Diameter) of water clusters decreases, due to the decrease of water content. Moreover, for relatively high values of suction, water clusters are well graded, i.e. a continuous curve formed by small clusters (small EqD). For relatively low values of suction, water clusters size distribution is presented as a curve that begins with small clusters that form less than 5 - 10% of the cumulative volume of water within the specimen, and ends with a very big cluster (shown in the figures within a red dashed rectangle) that forms more than 90 - 95% of the cumulative volume of water within the specimen. For the values of suction in-between the two latter cases, water clusters distribution curve takes the form of the two cases combined, i.e. a continuous range of sizes of water clusters at the beginning and a big cluster at the end.

For air clusters size distribution, when the suction is increased, the range of the EqD of air cluster increases due to the increase of air volume within the specimen. For relatively low values of suction, air clusters are well graded, i.e. a continuous curve formed by small clusters of a continuous range of small sizes. For relatively high values of suction, air clusters size distribution is presented as a curve that begins with very small clusters that form less than 5 - 10% of the cumulative volume of air within the specimen, and ends with a very big cluster (shown in the figures within a red dashed rectangle) that forms more than 90 - 95% of the cumulative volume of air within the specimen. For the values of suction in-between the two latter cases, air clusters distribution curve takes the form of the two cases combined, i.e. a continuous range of sizes of water clusters at the beginning and a big cluster at the end. For W_1 , at relatively low values of suction, air clusters distribution curve takes the form of a continuous range of sizes of air clusters at the beginning and a big cluster at the end.

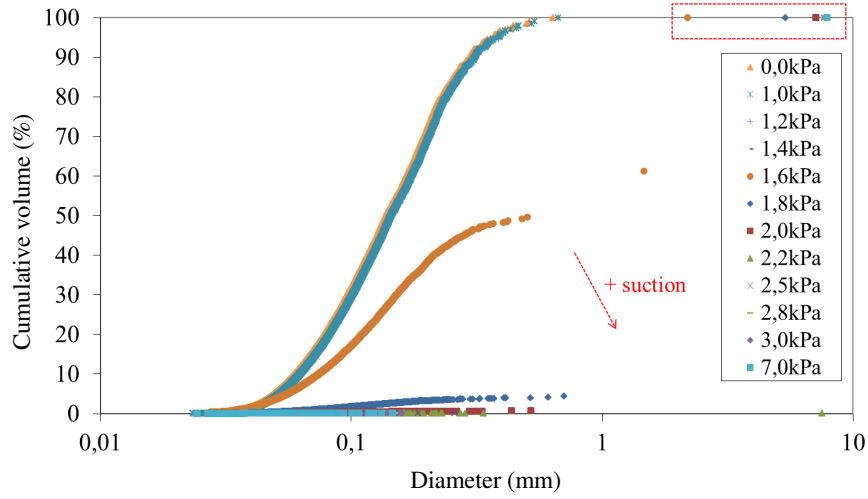


Figure 4.47: Air clusters size distribution for all the values of suction in the drying path D_1

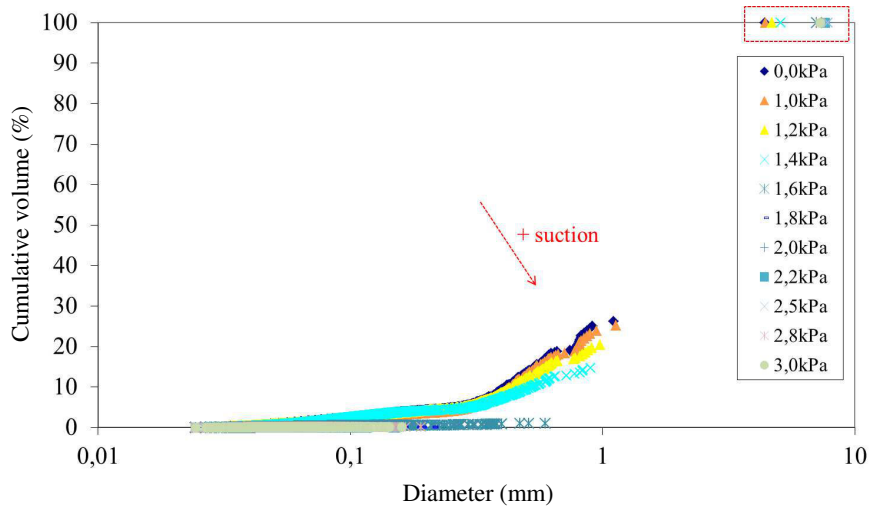


Figure 4.48: Air clusters size distribution for all the values of suction in the wetting path W_1

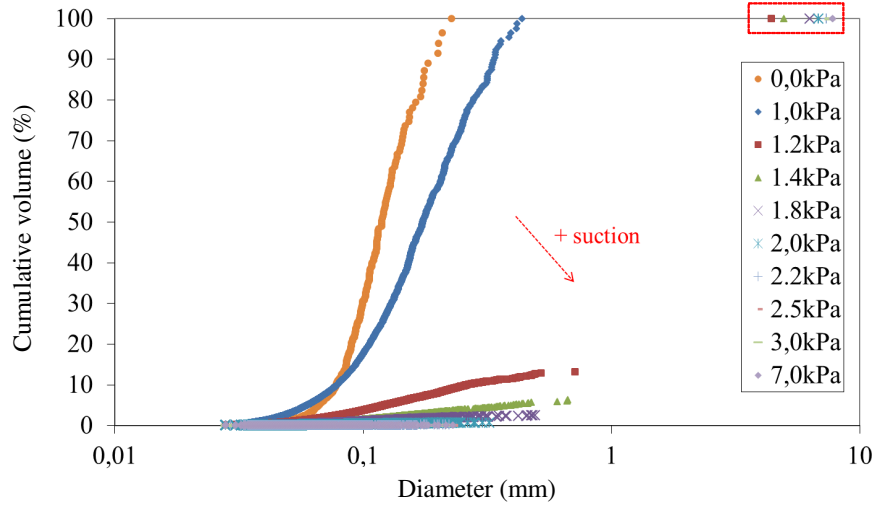


Figure 4.49: Air clusters size distribution for all the values of suction in the drying path D_0

From the fluid clusters size distribution curves, fluid clusters of the biggest size are extracted. In order to evaluate fluid phase continuity during retention tests, the relation between the normalized volumes of the biggest fluid clusters versus suction is plotted.

One might question the reason behind choosing the volume of the biggest fluid cluster and not the mean volume of all the clusters. As it has been presented before in different sections of this chapter, water distribution within the specimen is not homogeneous. Water volume (V_{wt}) within the specimen is found in the form of several small clusters of a total volume less than 5 - 10% of V_{wt} , and a big cluster that forms more than 90 - 95% of V_{wt} . Therefore, it is more representative to choose V_{max} , than V_{mean} where the influence of the small clusters (since they are in a bigger number) is considerable. Moreover the cluster of a volume equal to V_{mean} might not exist within the specimen, and thus the following analyses will be of a theoretical basis.

Fig 4.50, Fig 4.51 and Fig 4.52 show the relation between the normalized water (V_{wmax}) and air (V_{amax}) clusters versus the suction. The volume of the biggest water cluster (V_{wmax}) is normalized by the total volume of water within the specimen (V_{wt}) for each value of suction. Similarly, the volume of the biggest air cluster (V_{amax}) is normalized by the total volume of air within the specimen (V_{at}) for each value of suction.

As shown in Fig 4.50 and Fig 4.52, for D_1 and D_0 , at relatively low values of suction, the volume of the biggest water cluster is equal to the volume of water within the specimen, i.e., $V_{wmax} = V_{wt}$. Later, the volume of the biggest water cluster decreases $V_{wmax} < V_{wt}$. At relatively high values of suction, the figures show that $V_{wmax} \ll V_{wt}$. For W_1 , at relatively high values of suction, the figures show that $V_{wmax} \ll V_{wt}$. Later, the volume of the biggest water cluster increases to reach $V_{wmax} = V_{wt}$ at relatively low values of suction. For air phase (figures read inversely) in the three paths D_1 , W_1 and D_0 , the volume of the biggest air cluster, at relatively high values of suction is equal to the volume of air within the specimen, i.e., $V_{amax} = V_{at}$. Later, the volume of the biggest air cluster decreases $V_{amax} < V_{at}$. At relatively low values of suction, the figures show that $V_{amax} \ll V_{at}$. For W_1 , at relatively low values of suction, the figures show that $V_{amax} < V_{at}$.

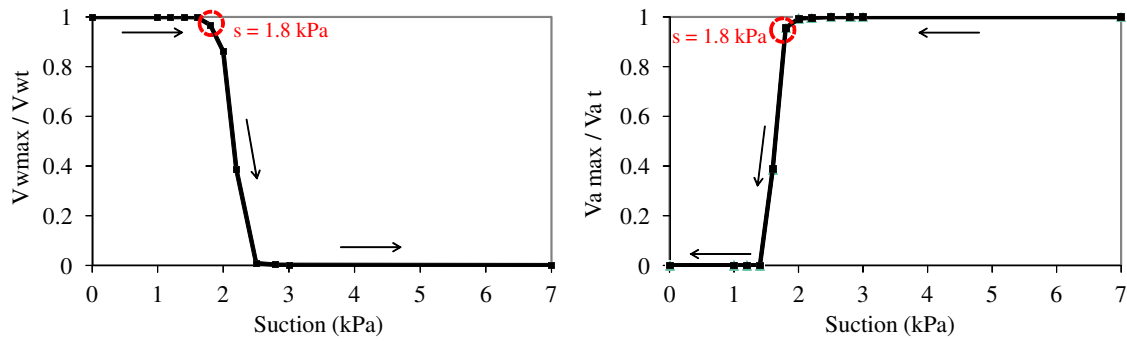


Figure 4.50: The relation between the normalized V_{max} for water clusters (left) and air clusters (right) versus the suction, for the drying path D_1

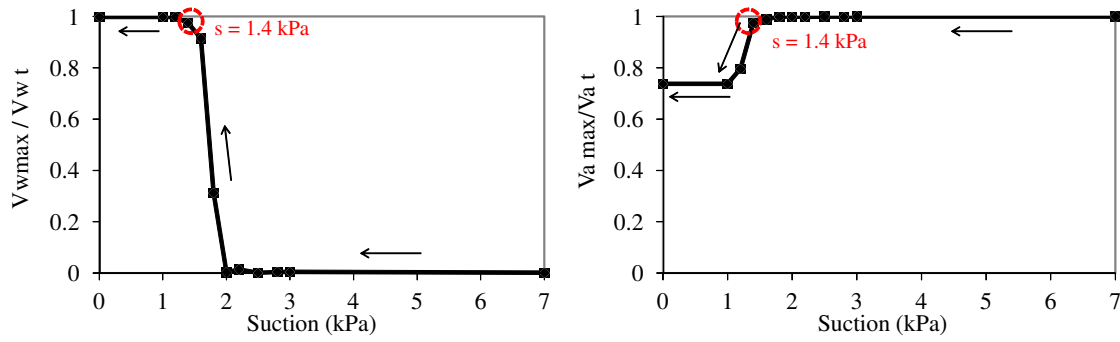


Figure 4.51: The relation between the normalized V_{max} of water clusters (left) and air clusters (right) versus the suction, for the wetting path W_1

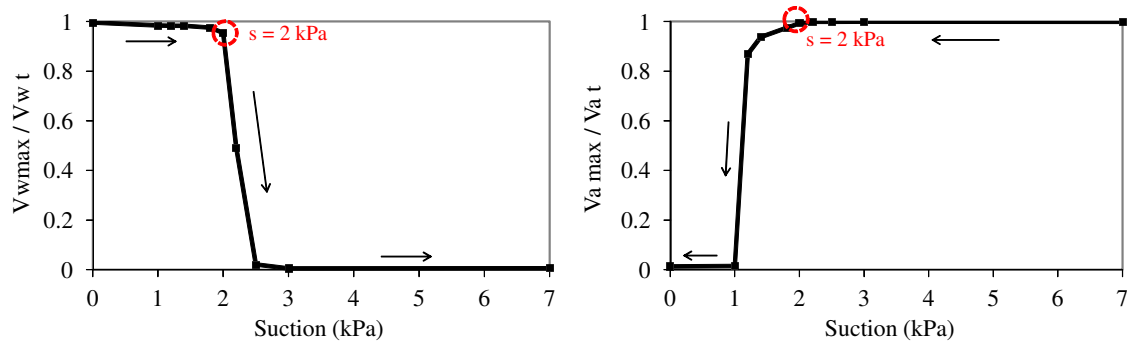


Figure 4.52: The relation between the normalized V_{max} of water clusters (left) and air clusters (right) versus the suction, for the drying path D_0

Similar to the evolution of the number of fluid clusters, the latter characterization of the evolution of the normalized V_{\max} of water and air clusters in drying path, is actually describing the division of water phase, and the correspondent continuity of air phase. For wetting path, this characterization describes the continuity of water phase and the correspondent division of air phase.

In the latter figures, some points are highlighted. These points represent the values of suction at which water/air phase changes the form from one big cluster having the same volume of water/air within the specimen $V_{\max}=V_t$ into several clusters of a volume smaller than the volume of water/air within the specimen $V_{\max}<V_t$.

In the following, all the points highlighted in this section for the evolution of the number and the normalized V_{\max} of fluid clusters water are recalled. These points are to be considered later in section 4.4.2.

For the drying path D_1 :

- $s=1.6\text{kPa}$, at which the maximum number of air clusters is found.
- $s=1.8\text{kPa}$, at which water/air phase changes the form from one big cluster having the same volume of water/air within the specimen $V_{\max}=V_t$ into several clusters of a volume smaller than the volume of water/air within the specimen.
- $s=2.8\text{kPa}$, at which the maximum number of water clusters is found.

For the wetting path W_1 :

- $s=2.8\text{kPa}$, at which the maximum number of water clusters is found.
- $s=1.4\text{kPa}$, at which water/air phase changes the form from one big cluster having the same volume of water/air within the specimen $V_{\max}=V_t$, into several clusters of a volume smaller than the volume of water/air within the specimen.
- $s\geq 1.4\text{kPa}$, at which a maximum constant number of air clusters is reached.

For the drying path D_0 :

- $s=1.2\text{kPa}$, at which the maximum number of air clusters is found.
- $s=2\text{kPa}$, at which water/air phase changes the form from one big cluster having the same volume of water/air within the specimen $V_{\max}=V_t$, into several clusters of a volume smaller than the volume of water/air within the specimen.
- $s=3\text{kPa}$, at which the maximum number of water clusters is found.

Recalling the qualitative analyses performed for the trinarized volumes, it is noted that the maximum number of air clusters for the two drying paths D_0 and D_1 is found at air entry value, while the maximum number of water clusters for the wetting path W_1 is found at water entry value.

The latter analyses shows that the maximum number of fluid clusters and repartition (continuity) of fluid clusters are found at different values of suction for the two specimens of the same material (i.e. D_0 and D_1). The reason behind that is thought to be due to that the two specimens D_0 and D_1 have different pore size and shape distributions. However, the maximum number of fluid clusters and repartition (continuity) of fluid clusters are also found at different values of suction for the same specimen, of the same pore size and shape distribution but different paths (i.e., D_1 and W_1). This indicates that not only pore size and shape distribution influence the number of fluid clusters and their distribution but also the loading direction (drying and wetting).

4.3.5.2 The evolution of the effective specific interfacial area with the degree of saturation

As has been presented in chapter 3, section 3.5.2, many researchers agree that water retention curve hysteresis is related to the configuration and distribution of the interfaces between the phases. If suction, in water retention constitutive law is considered as a function of two independent variables: the degree of saturation and the interfacial area, hysteresis would be minimized. Thus, hysteresis might be interpreted as the projection of the suction-degree of saturation saturation-interfacial area surface onto the suction-degree of saturation plane. This hypothesis has been investigated numerically, yet, physical experimental support has been lacking.

In this work, it was possible to evaluate and investigate this hypothesis experimentally for different paths (D_1 and W_1) and different specimens (D_0 and D_1) at the grain scale.

The effective specific interfacial area is calculated using the trinarized 3D images and the definition of Grant et al. (2007) presented in section 3.5.2.1. The 3D area of each phase, obtained using Visilog[®], is summed and the effective specific interfacial area is calculated following the mathematical relation: $a_{wn} = 0.5 \times (a_w + a_n - a_s)$. Then, the effective specific interfacial area a_{wn} is normalized by the volume of voids within the specimen.

The relation between the normalized effective specific interfacial area a_{wn} and the macroscopic degree of saturation calculated using the trinarized images, is presented in Fig 4.53, for D_1 , W_1 and D_0 .

As shown in Fig 4.53, the normalized effective specific interfacial area tends to increase when increasing the degree of saturation to reach a maximum value then decreases. For the drying paths D_1 and D_0 , when the specimen is saturated ($s=0\text{kPa}$, $S_r=1$), $a_{wn}=0$ as there are no air within the specimen. Later, air enters the specimen and a_{wn} increases to reach a maximum value at $S_r=19\%$ ($s=2.2\text{kPa}$) for D_1 and $S_r=58\%$ ($s=1.8\text{kPa}$) for D_0 , then decreases as the water volume decreases. Similarly for the wetting path W_1 , a_{wn} increases as the degree of saturation decreases, then at $S_r=28\%$ ($s=1.6\text{kPa}$), a_{wn} decreases.

The former results shows that the effective specific interfacial area a_{wn} differentiate for different specimens of different pore size and shape distribution (D_0 and D_1) and higher a_{wn} is obtained for drying path D_1 than for wetting path W_1 (i.e., same specimen of the same pore size and shape distribution but different loading paths).

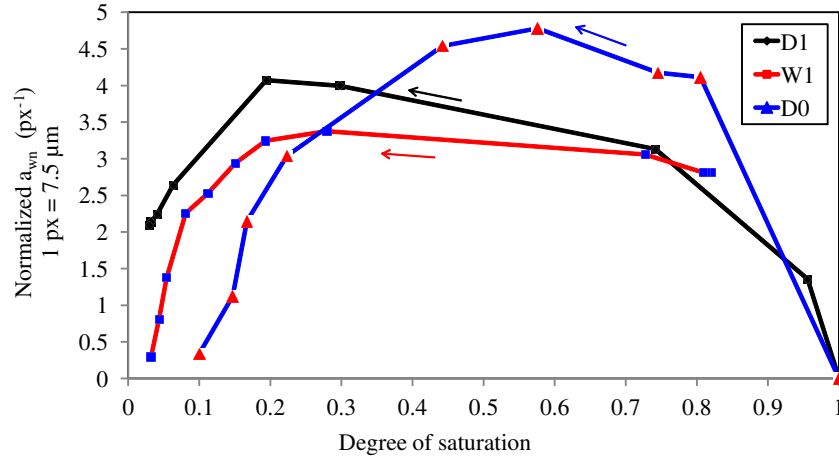


Figure 4.53: The relation between the normalized effective specific interfacial area a_{wn} (calculated following the definition of Grant et al. (2007)) versus the degree of saturation, shown for D_1 , W_1 and D_0

As shown in the figure above, the normalized effective specific interfacial area tends to increase when increasing the degree of saturation to reach a maximum value then decreases. For the drying paths D_1 and D_0 , when the specimen is saturated ($s=0\text{kPa}$, $S_r=1$), $a_{wn}=0$ as there are no air within the specimen. Later, air enters the specimen and a_{wn} increases to reach a maximum value at $S_r=19\%$ ($s=2.2\text{kPa}$) for D_1 and $S_r=58\%$ ($s=1.8\text{kPa}$) for D_0 , then decreases as the water volume decreases. Similarly for the wetting path W_1 , a_{wn} increases as the degree of saturation decreases, then at $S_r=28\%$ ($s=1.6\text{kPa}$), a_{wn} decreases.

The former results shows that the effective specific interfacial area a_{wn} differentiate for different specimens of different pore size and shape distribution (D_0 and D_1) and higher a_{wn} is obtained for drying path D_1 than for wetting path W_1 (i.e., same specimen of the same pore size and shape distribution but different loading paths).

This indicates again that the effective specific interfacial area is influenced by the pore size and shape distribution and by the loading direction.

The results obtained in Fig 4.53 are compared to the experimental (see Wildenschild et al., 2004; Joekar-Niasar et al., 2008) and numerical (see Likos, 2014; Grant et al., 2007) results found in the literature review. Wildenschild et al. (2004) investigated a_{wn} for glass beads using computed x-ray tomography. The results obtained experimentally by Wildenschild et al. (2004) are consistent with the results presented in Fig 4.53, i.e., a_{wn} increases as decreasing the degree of saturation to reach a maximum value at a specific degree of saturation then decreases. In addition, higher a_{wn} is obtained for drying path than for wetting path. Likos (2014) presented simulated a_{wn} quantified by the suction, the degree of saturation, and the contact angle. The results of the simulation coincide with the results presented in Fig 4.53.

4.3.5.3 The evolution of the number of solid-fluid and fluid-fluid interfaces with suction

In this section, the number of contacts between the phases is investigated in order to analyze the distribution, interaction and the repartition between them. In addition, this investigation offers quantitative description about the continuity of fluid phase (by analyz-

ing the repartition of water and air), which is used later for the definition of the boundaries between water retention domains. Moreover, the analyses performed in this chapter are used for the investigation of hysteresis phenomenon and soil cohesion.

Using the labelled volumes and the developed code described in chapter 3, section 3.5.2.2, the contacts between the three phases are obtained. For each of the three paths D_0 , D_1 and W_1 , the relation between the number of grain-fluid and fluid-fluid contacts versus suction is plotted and analyzed.

The labelled volumes of water and air phases are presented before in section 4.3.5.1. For grain phase, the influence of the suction on the solid structure is negligible (see section 4.3.1), thus the labelled grains volume is the same for all the values of suction applied on the same specimen. Fig 4.54 shows vertical slices in the labelled grain volume for D_1 , W_1 and D_0 . In this figure, the vertical slices are not of the same azimuth. The slices are shown after cutting the two porous stones, for D_0 , and after cutting the bottom porous stone and the upper loose layer, for D_1 and W_1 . The different colors in Fig 4.54 represent different grains though some grains of different Ids might have the same color.

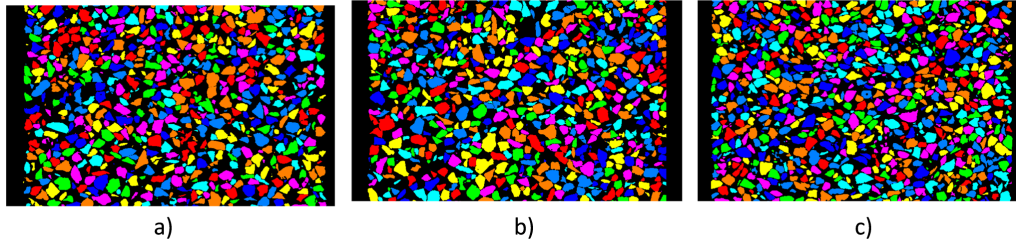


Figure 4.54: A vertical slice in the labelled grain volume for a) D_1 b) W_1 and c) D_0

The grain size distribution presented in Fig 4.55 for all the values of suction in the drying path D_1 shows that grain size distribution curves are superposed as the specimen in the drying path D_1 is the same for all the values of suction. Similar results are found for the two paths W_1 and D_0 . Grain size distribution for W_1 and D_0 are presented in Appendix C, Fig (C-4) and Fig (C-5), respectively.

In addition, the number of grains, presented in Fig 4.56, is more or less the same (with a precision ± 400 grains) for all the points (values of suction) in the drying path D_1 . These results presented in Fig 4.55 and Fig 4.56 confirm the efficiency of the trinarization technique and the morphological process followed to label the grains using Visilog[®]. Similar results are found for the two paths W_1 and D_0 . The number of grains within the specimen for W_1 and D_0 are presented in Appendix C, Fig (C-6) and Fig (C-7), respectively.

In the following, the evolution of contacts with suction is presented for the three paths D_1 , W_1 and D_0 . The results are presented for grain-water, grain-air and water-air contacts. The maximum number of contacts between each two phases is used to evaluate the evolution of contacts with suction (i.e., suction). This will make it easier to verify and evaluate the results as the maximum number of contacts in the saturated and residual domains are known for water and air phase, respectively. In the saturated domain water volume is on contact with all the grains, while in the residual domain air volume is on contact with all the grains. However, the mean number of contacts between the phases can be used.

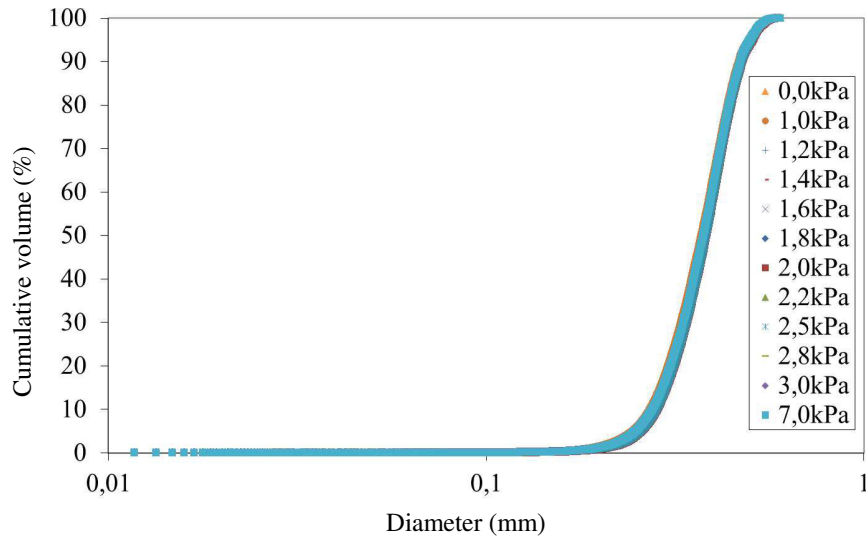


Figure 4.55: Grain size distribution for all the values of suction in the drying path D₁

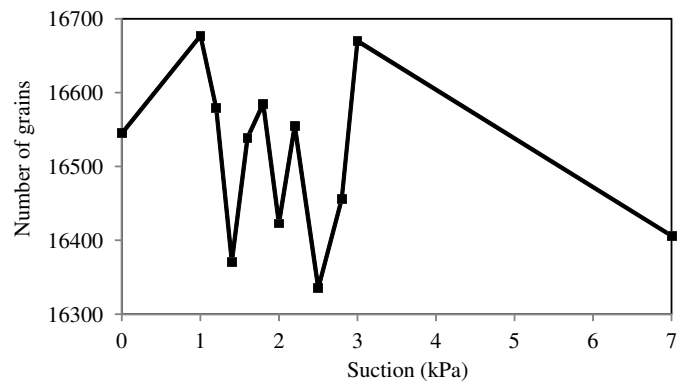


Figure 4.56: The number of grains within the specimen shown for all the values of suction in the drying path D₁

For grain-water contacts, Fig 4.57, Fig 4.58 and Fig 4.59 show the relation between the Maximum number of Grains that are in contact with one water cluster (Max Gw) versus the suction and the relation between the Maximum number of Water clusters that are in contact with one grain (Max Wg) versus the suction, for the three paths D₁, W₁ and D₀ respectively.

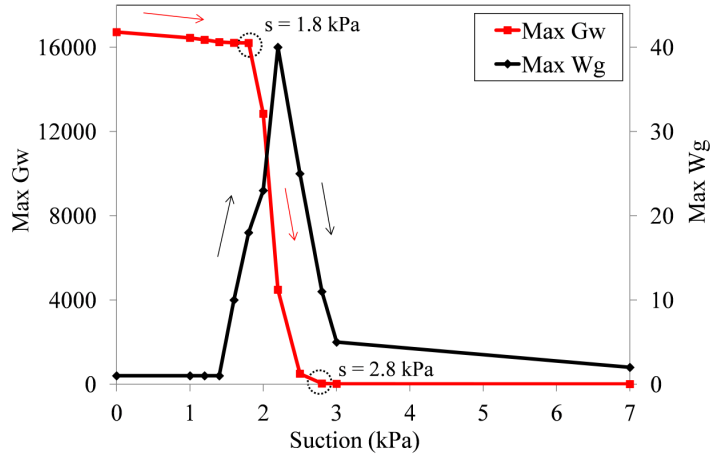


Figure 4.57: The relation between the maximum number of grains in contact with one water cluster (Max Gw) versus the suction and the relation between the maximum number of water clusters in contact with one grain (Max Wg) versus the suction, for D_1

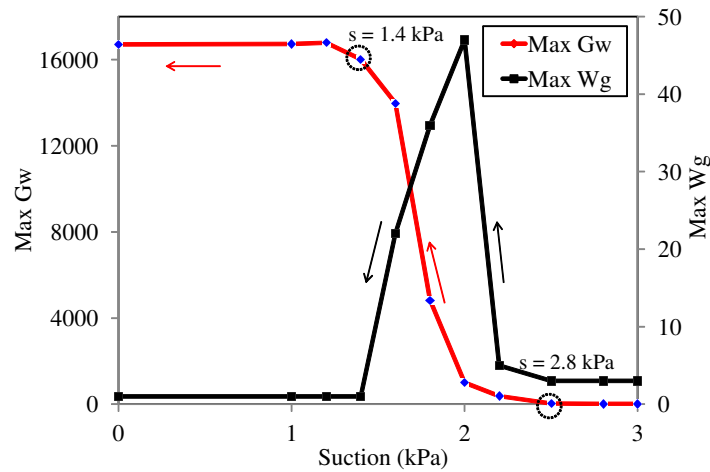


Figure 4.58: The relation between the maximum number of grains in contact with one water cluster (Max Gw) versus the suction and the relation between the maximum number of water clusters in contact with one grain (Max Wg) versus the suction, for W_1

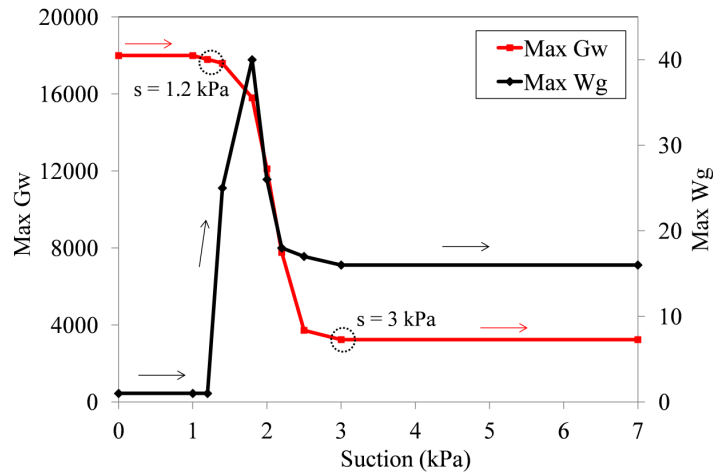


Figure 4.59: The relation between the maximum number of grains in contact with one water cluster (Max Gw) versus the suction and the relation between the maximum number of water clusters in contact with one grain (Max Wg) versus the suction, for D_0

As shown in the figures, For D_1 and D_0 , Max Gw is of maximum constant value at relatively low values of suction. When increasing the suction, Max Gw decreases to reach a minimum constant value at relatively high values of suction. Water phase is in the form of one big cluster that is in contact with all the grains within the specimen at relatively low values of suction (number of grains for D_1 and $W_1=16500\pm 400$ grains and number of grains for $D_0=18500\pm 400$ grains). Later, Max Gw decreases as increasing the suction, due to the division of the one big water cluster into several smaller clusters that are in contact with smaller number of grains. At relatively high values of suction, Max Gw reaches a minimum stable value.

For W_1 , Max Gw is of minimum constant value at relatively high values of suction. When decreasing the suction, Max Gw increases to reach a maximum constant value at relatively low values of suction, equal to the total numbers of grains (16500 ± 400 grains).

In the latter figures, the values of suction at which water cluster has a maximum and a minimum number of contacts with grain phase (Max Gw) are highlighted with a black dashed circle.

On other hand, for D_1 and D_0 , Max Wg increases as increasing the suction to reach a maximum value then decreases. At relatively low values of suction, $Max\ Wg=1$ (one water clusters in contact with all the grains within the specimen). Later, Max Wg increases to reach a maximum value. This increase is due to the division of the one big water cluster into several clusters. Later Max Wg decreases as increasing the suction (decreasing water content and thus decreasing the number of water clusters).

For W_1 , Max Wg increases as decreasing the suction to reach a maximum value then decreases. At relatively high values of suction, Max Wg represents a few clusters in the residual domain that are in contact with one grain, then Max Wg increases to reach a maximum value then decreases to reach $Max\ Wg=1$ (one water clusters in contact with all the grains within the specimen).

For grain-air contacts, the relation between the Maximum number of Grains that are in contact with one air cluster (Max Ga) versus the suction and the relation between the Maximum number of Air clusters that are in contact with one grain (Max Ag) versus the suction are presented in Fig 4.60, Fig 4.61 and Fig 4.62 for the three paths D_1 , W_1 and D_0 respectively.

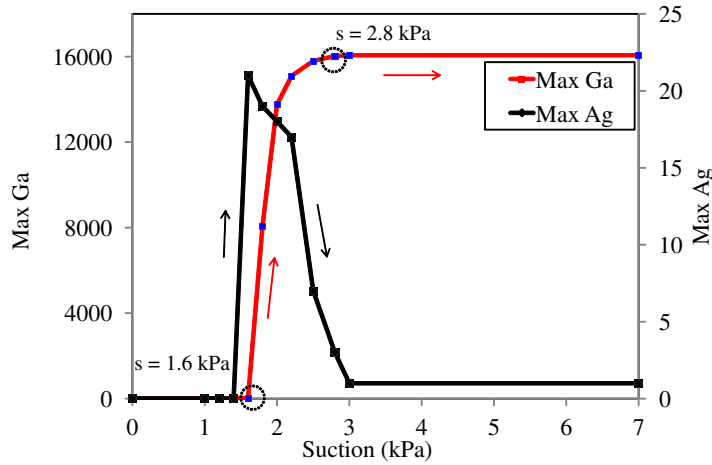


Figure 4.60: The relation between the maximum number of grains in contact with one air cluster (Max Ga) versus the suction and the relation between the maximum number of air clusters in contact with one grain (Max Ag) versus the suction, for D_1

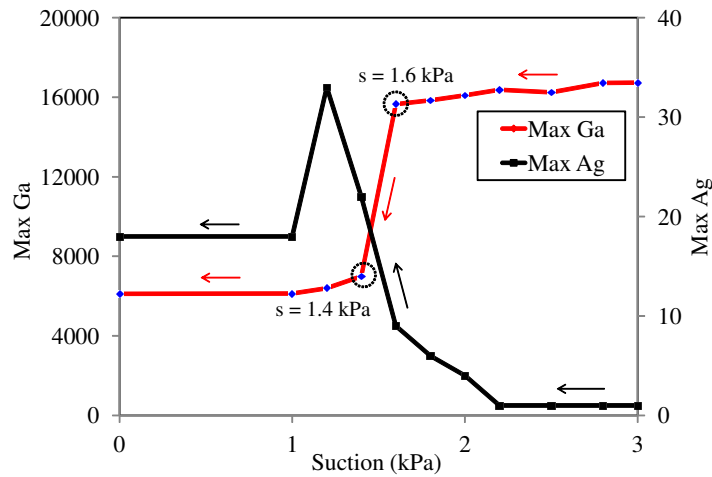


Figure 4.61: The relation between the maximum number of grains in contact with one air cluster (Max Ga) versus the suction and the relation between the maximum number of air clusters in contact with one grain (Max Ag) versus the suction, for W_1

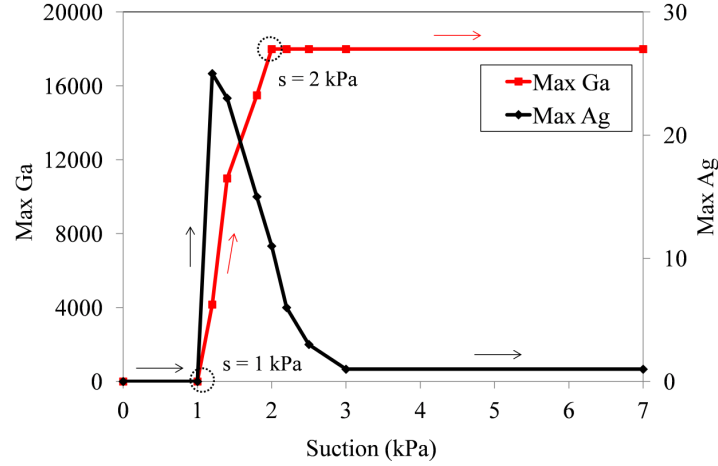


Figure 4.62: The relation between the maximum number of grains in contact with one air cluster (Max Ga) versus the suction and the relation between the maximum number of air clusters in contact with one grain (Max Ag) versus the suction, for D_0

As shown in the figures, for D_1 and D_0 , Max Ga is of minimum constant value at relatively low values of suction, for the three paths. When increasing the suction, Max Ga increases to reach a maximum constant value at relatively high values of suction. Max Ga=0, at relatively low values of suction (the specimen is saturated and no presence of air). Later, Max Ga increases to reach the number of grains within the specimen for D_1 and D_0 (one air cluster in contact with all the grains within the specimen).

For W_1 , Max Ga is of maximum constant value at relatively high values of suction. When decreasing the suction, Max Ga decreases to reach a minimum constant value at relatively low values of suction. Max Ga=1, at relatively high values of suction (one air cluster in contact with all the grains within the specimen), then Max Ga decreases. At relatively low values of suction, Max Ga \neq 0 due to the presence of trapped air clusters. In the latter figures, the values of suction at which air cluster has a maximum and a minimum number of contacts with grain phase are highlighted with a black dashed circle.

From another side, for D_1 and D_0 , Max Ag increases as increasing the suction to reach a maximum value then decreases. At relatively low values of suction, Max Ag=0 as the specimen is saturated and there is no presence of air clusters.

For W_1 , Max Ag increases as decreasing the suction to reach a maximum value then decreases. Max Ga \neq 0, at relatively low values of suction (trapped air clusters). Later, air enters the specimen and Max Ag increases to reach a maximum value then decreases to reach Max Ag=1 where only one big air cluster is found within the specimen.

For water-air contacts, the relation between the Maximum number of Water clusters that are in contact with one air cluster (Max Wa) versus the suction and the relation between the Maximum number of Air clusters that are in contact with one water cluster (Max Aw) versus the suction are presented in Fig 4.63, Fig 4.64 and Fig 4.65 for the three paths D_1 , W_1 and D_0 respectively.

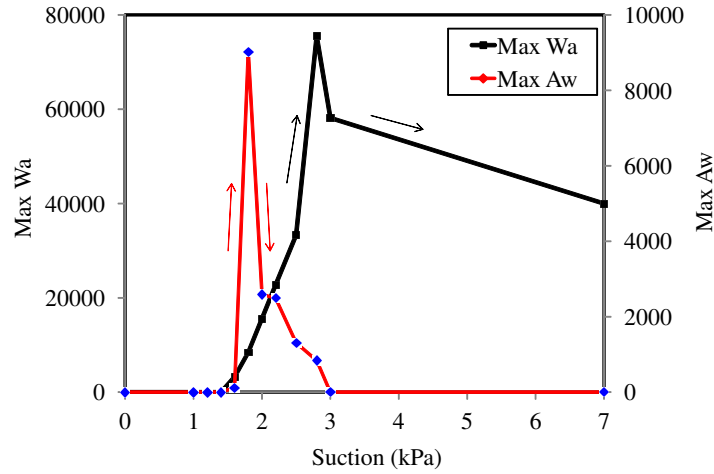


Figure 4.63: The relation between the maximum number of water clusters in contact with one air cluster (Max Wa) versus the suction and the relation between the maximum number of air clusters in contact with one water cluster (Max Aw) versus the suction, for D_1

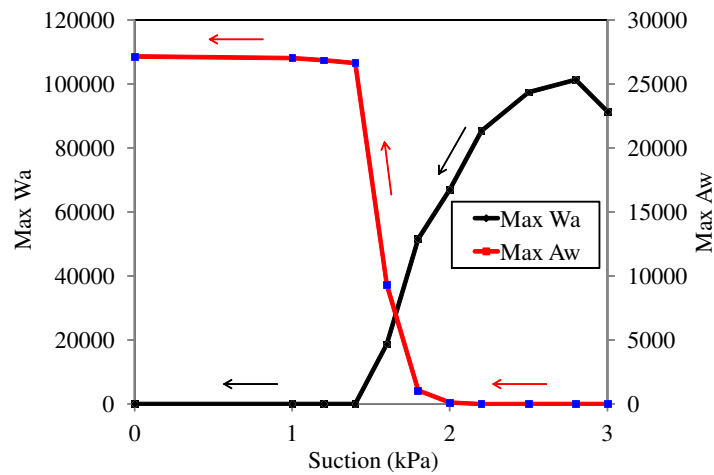


Figure 4.64: The relation between the maximum number of water clusters in contact with one air cluster (Max Wa) versus the suction and the relation between the maximum number of air clusters in contact with one water cluster (Max Aw) versus the suction, for W_1

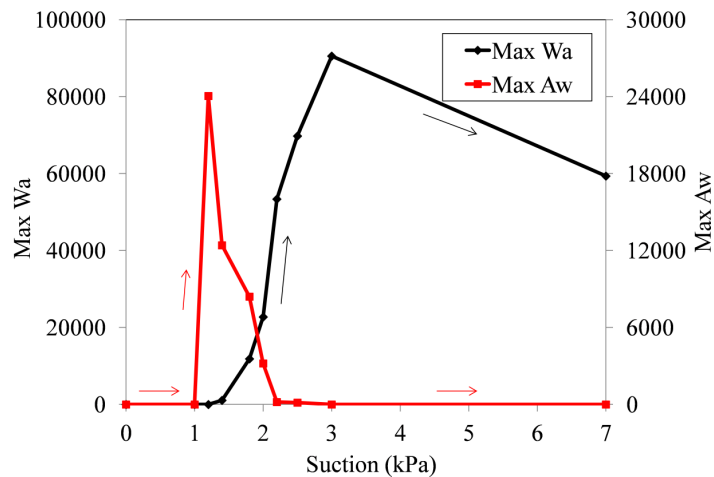


Figure 4.65: The relation between the maximum number of water clusters in contact with one air cluster (Max Wa) versus the suction and the relation between the maximum number of air clusters in contact with one water cluster (Max Aw) versus the suction, for D_0

The figures show that, for D_1 and D_0 , Max Wa increases as increasing the suction to reach a maximum value then decreases. At relatively low values of suction, $\text{Max Wa}=0$ (the specimen is saturated and no presence of air). Later, Max Wa increases to reach a maximum value then decreases to reach the number of water clusters in the residual domain.

For W_1 , Max Wa increases as decreasing the suction to reach a maximum value then decreases. At relatively high values of suction, Max Wa is equal to the number of water clusters in the residual domain. Later Max Wa decreases to reach a minimum value $\text{Max Wa}=1$ (one big water cluster in contact with all the clusters of trapped air).

On other hand, for D_1 and D_0 , Max Aw increases as increasing the suction to reach a maximum value then decreases. At relatively low values of suction, $\text{Max Aw}=0$ (no air within the specimen). Later, Max Aw increases then decreases to reach $\text{Max Aw}=1$ (one big air cluster).

For W_1 , Max Aw is of minimum constant value at relatively high values of suction. When decreasing the suction, Max Aw increases to reach a maximum constant value at relatively low values of suction. At relatively high values of suction, $\text{Max Aw}=1$ (one big air cluster). Later, Max Aw increases to reach the number of trapped air clusters within the specimen.

As has been shown in the latter discussion, the number of grains per one fluid cluster (i.e., Max Gw and Max Ga) highlights the interaction between solid (grain) and fluid (water and air), i.e., the interaction between grain and pore shapes and sizes. Similarly, the number of fluid clusters per one grain (i.e., Max Wg and Max Ag) highlights the interaction between solid and fluid. Moreover, the number of water clusters per one grain (i.e., Max Wg) can be used to evaluate capillary cohesion, as presented before in chapter 2, section 2.3.2.

The number of water clusters per one air cluster and the number of air clusters per one water cluster (i.e., Max Wa and Max Aw), from the other hand, describe the connectivity of the pores filled with different fluids (air and water). Therefore, they can be used for investigation of hysteresis phenomenon (just like ink-bottle effect that shows the influence

of the connectivity of the pores and the effective specific interfacial area which describes air-water interfacial area).

The results presented in section 4.3.5.2 showed that a maximum value of the effective specific interfacial area a_{wn} is obtained at $s=2.2\text{kPa}$ ($S_r=19\%$) for D_1 , at $s=1.8\text{kPa}$ ($S_r=58\%$) for D_0 and at $s=1.6\text{kPa}$ ($S_r=28\%$) for W_1 . These results were compared to Max Wa and Max Aw plots presented in Fig 4.63, Fig 4.64 and Fig 4.65, for the three paths D_1 , W_1 and D_0 , respectively. It has been found that the values of suction at which a maximum value of a_{wn} is obtained, represents actually the points (values of suction) close to the intersection between Max Wa and Max Aw curves rather than the peaks (maximum values) of Max Wa and Max Aw curves. Fig 4.66, Fig 4.67 and Fig 4.68 show a zoom window around the intersection point between Max Wa and Max Aw curves for the three paths D_1 , W_1 and D_0 , respectively.

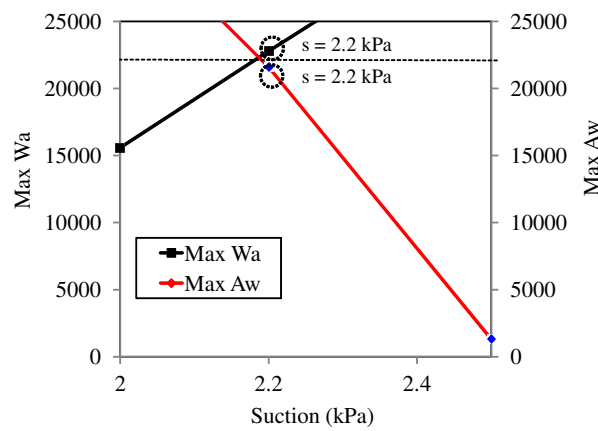


Figure 4.66: A zoom window around the intersection point between Max Wa and Max Aw curves for D_1

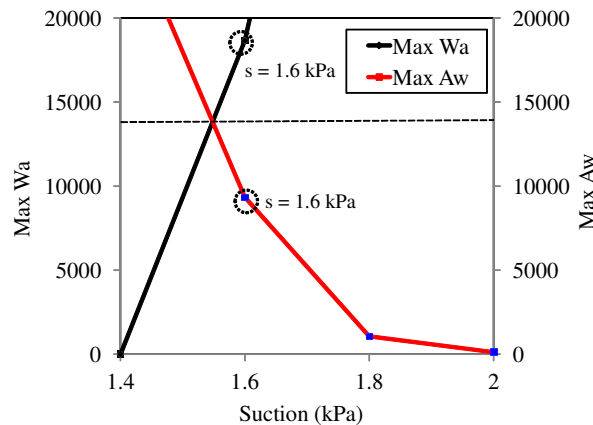


Figure 4.67: A zoom window around the intersection point between Max Wa and Max Aw curves for W_1

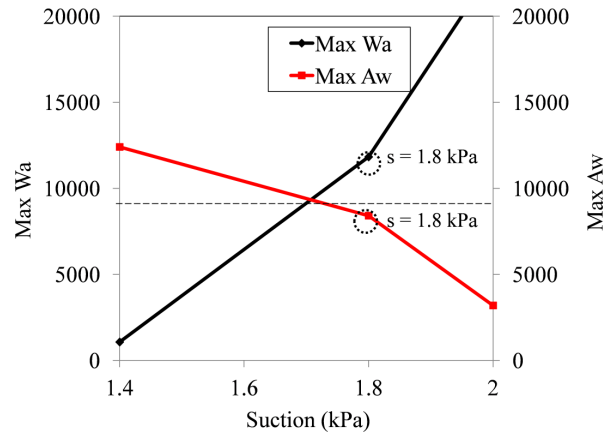


Figure 4.68: A zoom window around the intersection point between Max Wa and Max Aw curves for D_0

From the zoom figures, it is shown that the intersection point between Max Wa and Max Aw curves corresponds to the value of suction at which $\text{Max Wa} = \text{Max Aw}$. This means that the maximum value of the effective specific interfacial area a_{wn} is obtained at a value of suction that achieves $\text{Max Wa} = \text{Max Aw}$.

In the following, the points (or ranges) of the maximum and minimum number of grains in contact with air/water clusters (Max Ga and Max Gw) are extracted and listed to be considered for the analysis in section 4.4.2.

For the drying path D_1 :

- $s \geq 1.6 \text{ kPa}$, where air cluster has a minimum constant number of contacts with grain phase.
- $s \geq 1.8 \text{ kPa}$, where water cluster has a maximum constant number of contacts with grain phase. The small decrease in the maximum number of grains that are in contact with one air clusters before $s = 1.8 \text{ kPa}$, shown in Fig 4.57, is caused by air invasion to the specimen from the edges, due to the weak contact between the material of the cell (i.e., PMMA) and the grains when preparing the specimen. However, the loss of water-grain contacts due to air invasion and considered negligible.
- $s \geq 2.8 \text{ kPa}$, where water cluster has a minimum constant number of contacts with grain phase and air cluster has a maximum constant number of contacts with grain phase.

For the wetting path W_1 :

- $s \geq 1.4 \text{ kPa}$, where water cluster has a maximum constant number of contacts with grain phase and air cluster has a minimum constant number of contacts with grain phase.

- $s \geq 1.6 \text{ kPa}$, where air cluster has a maximum constant number of contacts with grain phase.
- $s \geq 2.8 \text{ kPa}$, where water cluster has a minimum constant number of contacts with grain phase.

For the drying path D_0 :

- $s \geq 1 \text{ kPa}$, where air cluster has a minimum constant number of contacts with grain phase.
- $s \geq 1.2 \text{ kPa}$, where water cluster has a maximum constant number of contacts with grain phase.
- $s \geq 2 \text{ kPa}$, where air cluster has a maximum constant number of contacts with grain phase.
- $s \geq 3 \text{ kPa}$, where water cluster has a minimum constant number of contacts with grain phase.

From the former analyses, it could be noted that the maximum/minimum number of contacts between the solid and fluid phases is obtained at different values of suction for the specimens D_0 and D_1 of the different pore size and shape distribution, and for the same specimen (i.e., same pore size and shape distribution) but in the different loading directions, i.e., D_1 and W_1 . This implies that the contacts between the phases are influenced by the pore size and shape distribution and loading direction.

4.4 Interpretation of water retention results

4.4.1 The relation between state variables $f(s, n, Sr)$

As has pointed before in chapter 2, section 2.2.5, Water Retention Surface (WRS), which represents the relation between the state variables: suction (s), porosity (n) and degree of saturation (Sr), is obtained, traditionally, using macroscopic measurements of suction, porosity and degree of saturation for different specimens. In this work, WRS is obtained using the microscopic measurements of porosity and degree of saturation performed for the different points in the three paths.

3D plot of the relation between the state variables in the drying path D_1 is presented in Fig 4.69. In this figure, the discrepancy of the experimental points is due to the use of the ranges of the microscopic porosity and degree of saturation. These ranges describe, somehow, pores size and shape distribution and its influences on the retention behaviour of the tested material, contrary to the macroscopic measurements.

3D plot of the relation between the state variables, in the wetting path W_1 and the drying path D_0 are presented in Appendix D, Fig (D-2) and Fig (D-3), respectively. In this section, the results of the relation between state variables presented for D_1 and W_1 are obtained using overlapping microscopic measurements (50% REV overlapping), while

for D_0 , the results are obtained for microscopic measurements with no REV overlapping.

In order to analyze the relation between the state variables, Fig 4.69 is investigated in 2D by considering the following planes:

- (X, Y): The relation between suction (X) and porosity (Y).
- (X, Z): The relation between suction (X) and degree of saturation (Z).
- (Y, Z): The relation between porosity (Y) and degree of saturation (Z).

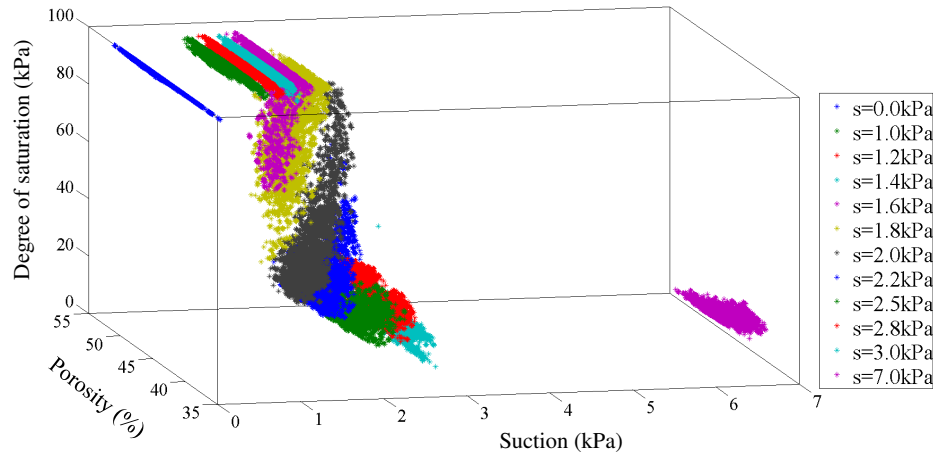


Figure 4.69: 3D relation between suction, porosity and degree of saturation for the drying path D_1

This helps comparing water retention surface obtained microscopically to the results presented in the literature review for water retention surface obtained macroscopically (see chapter 2, section 2.2.5). In the following, the results are presented for each pair of the three state variables: $n=f(s)$, $S_r=f(s)$ and $S_r=f(n)$.

4.4.1.1 The relation between suction and porosity $n=f(s)$

The relation between suction and porosity is investigated for constant ranges of degree of saturation. The microscopic measurements of the degree of saturation of all the points in D_1 , are considered and distributed into ten groups (ranges) of a length 10% degree of saturation, i.e., the first group includes all the microscopic measurement of degree of saturation in the range (0–10%), the second group includes all the microscopic measurements of degree of saturation in the range (10–20%) ...etc.

The relation $n=f(s)$ is plotted for all the ranges of degree of saturation within the specimen, in the drying path D_1 . Fig 4.70 shows the relation between suction and porosity, for two constant ranges of degree of saturation in the drying path D_1 : S_r (10–20%) and S_r (80–90%). The tendency (slope) of the microscopic measurements of the two groups is presented in Fig 4.70 by the two continuous lines.

As shown in the figure, the microscopic degree of saturation (measured within the REV) in the range S_r (10–20%) is found only for the range of suction $s \geq 2$ kPa, while the microscopic degree of saturation in the range S_r (80–90%) is found only for the range of suction $1.4 \leq s \leq 2$ kPa.

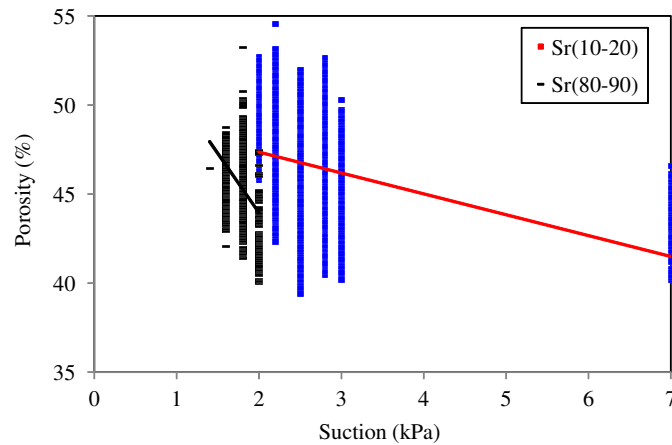


Figure 4.70: The experimental relation between suction and porosity for two constant ranges of degree of saturation in the drying path D_1 : S_r (10–20%) and S_r (80–90%). The tendency (slope) of the relation between the suction and the microscopic porosity is presented by the two continuous lines

The microscopic porosity for the two presented ranges of degree of saturation has a tendency to decrease when increasing the suction. Trying to understand this behaviour at pores scale, big pores desaturate at lower suction than small pores, i.e., as the size of the pore decrease, higher suction is needed to desaturate it.

In Fig 4.70, for the same suction, there is a discrepancy in the measurement of the microscopic porosity, e.g., for $s=1.6\text{kPa}$, porosity is ranging from $n=42\%$ to $n=48\%$. As pointed before, this discrepancy is due to that the microscopic porosity describes, relatively, the pore size and shape distribution.

Fig 4.71 shows the tendency (slope) of the relation between microscopic porosity and suction, for two ranges of degree of saturation in the path D_1 : $S_r=(0-10\%)$ and $S_r=(90-100\%)$.

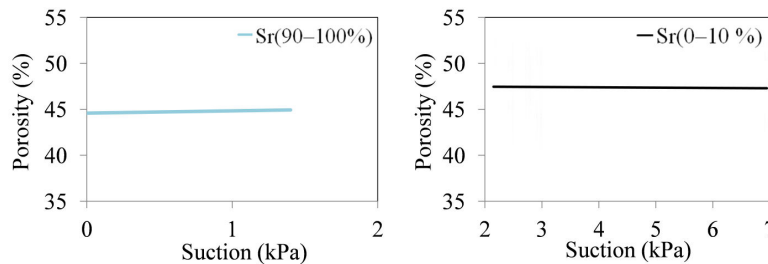


Figure 4.71: The tendency (slope) of the relation between microscopic porosity and suction, for $S_r=(0-10\%)$ (right) and $S_r=(90-100\%)$ (left) in the drying path D_1

As shown in Fig 4.71, the latter tendency of the relation between the suction and the microscopic porosity is not valid for all ranges of degree of saturation. For the saturated and residual domains, the porosity is constant regardless the suction.

Comparing the microscopic relation between suction and porosity to the macroscopic one, presented in chapter 2 (i.e., literature review), it is found that the results are consistent. In both results, porosity (or void ratio) tends to decrease as increasing the suction, see Fig 2.10 in chapter 2. This is also reasonable compared to the macroscopic behaviour of different soils (i.e., sand, silt and clay), where increasing the porosity of the soil induces

a shifting WRC for lower values of suction.

The analysis presented before is performed for all the ranges of degree of saturation in all the three paths D_1 , W_1 and D_0 . The results of this analysis can be found in Appendix D, Fig (D-4) and Fig (D-5) for D_1 , Fig (D-6) and Fig (D-7) for W_1 and Fig (D-8) and Fig (D-9) for D_0 . In Fig (D-4), Fig (D-6) and Fig (D-8), the experimental relation between suction and the microscopic porosity is presented for the three paths D_1 , W_1 and D_0 respectively, considering all the ranges of the microscopic degree of saturation. While in Fig (D-5), Fig (D-7) and Fig (D-9), the tendency of the relation between suction and the microscopic porosity is presented, for the three paths D_1 , W_1 and D_0 , respectively, considering all the ranges of the microscopic degree of saturation.

From the results presented in Appendix D, it is found that the relation between suction and microscopic porosity has the same trend, for the funicular and pendular domains, as the one presented in Fig 4.70, for the three paths D_1 , W_1 and D_0 . In the saturated and residual domains, the relation between suction and microscopic porosity has the same trend as the one presented in Fig 4.71, for the three paths D_1 , W_1 and D_0 .

4.4.1.2 The relation between suction and degree of saturation $S_r=f(s)$

The relation between suction and degree of saturation is investigated for constant ranges of porosity. This relation represents water retention curve for Hostun sand specimen of a homogeneous distribution for the porosity. The microscopic measurements of the porosity for all the points in D_1 , are considered and distributed into ranges of a length 1–2% porosity, i.e., the first group for includes all the microscopic measurement of porosity in the rang (37–39%), the first group for D_0 path includes all the microscopic measurement of porosity in the rang (37–38%) ...etc.

The relation $S_r=f(s)$ is plotted for all the ranges of porosities within the specimen, in the drying path D_1 . Fig 4.72 shows the relation between suction and the degree of saturation, for three constant ranges of porosity in the drying path D_1 : n (41–43%), n (43–45%) and n (45–47%). The experimental points shows clearly the variation in degree of saturation for each value of suction (i.e., the discrepancy of the measurements); e.g., for $s=1.8\text{kPa}$ and $n=45\text{--}47\%$, the degree of saturation varies from 30% to 100%. The microscopic measurements in Fig 4.72 are fitted and represented in Fig 4.73.

Fig 4.73 shows that, when increasing the porosity (from n (41–43%) to n (45–47%)), a shift for a smaller values of suction is obtained. This microscopic response of the soil is consistent again with the macroscopic results presented in chapter 2 (see Fig 2.6 and Fig 2.8 in chapter 2).

In Fig 4.73, three points for the three curves are extracted to allow comparing the three presented curves. The three extracted points are characteristic values, usually used to identify WRC, presented in Fig 4.73 within a dashed black circle. Those points represent: air entry value (s_{air}), the value of suction at which the curve reach a constant degree of saturation before the residual state (s_1), and the residual degree of saturation (S_{r0}). The relation between average porosity of the ranges (42, 44, and 46%) and the three variables (s_{air} , s_1 and S_{r0}) is presented in Fig 4.74.

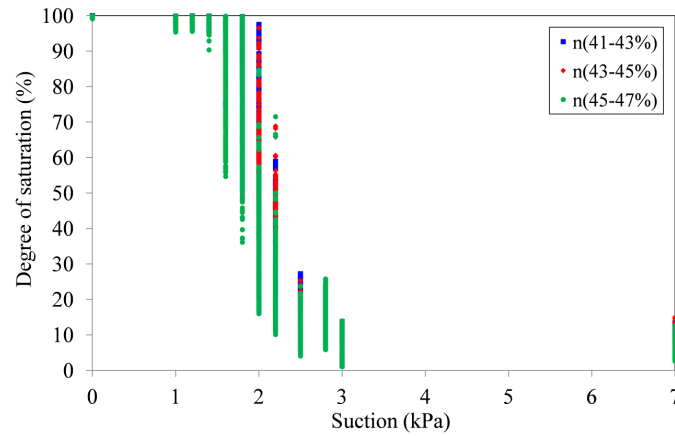


Figure 4.72: The experimental relation between suction and degree of saturation for three constant ranges of porosity in the drying path D_1 : n (41–43%), n (43–45%) and n (45–47%)

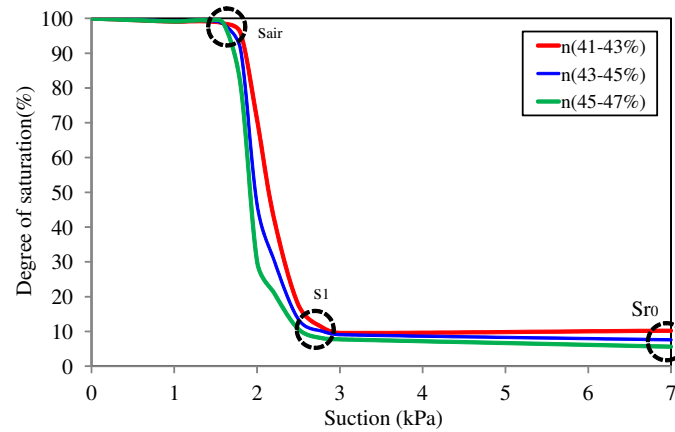


Figure 4.73: Fitting curve for the experimental points in the relation between suction and degree of saturation for three constant ranges of porosity in the drying path D_1 : n (41–43%), n (43–45%) and n (45–47%). The black dashed circles highlight air entry values s_{air} , the value of suction s_1 at which the curve reach a constant degree of saturation before the residual state, and the residual degree of saturation Sr_0

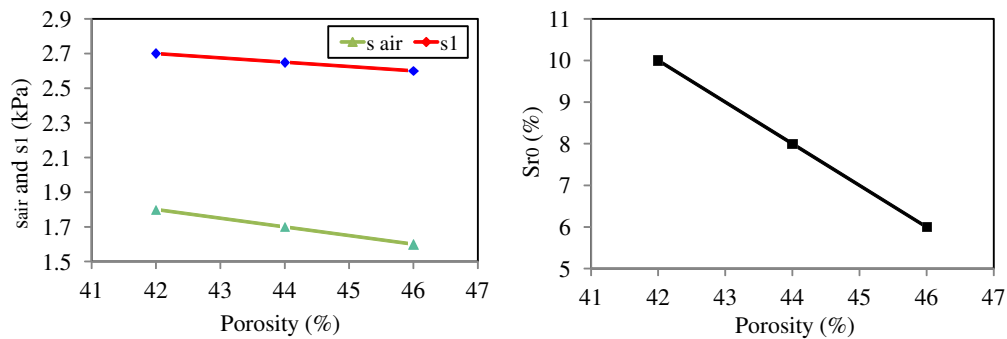


Figure 4.74: The relation between average porosity of the three ranges and the three variables, s_{air} and s_1 (left) and Sr_0 (right)

As shown in Fig 4.74-left, the value of s_{air} and s_1 decreases as increasing the porosity. Similarly, Fig 4.74-right shows that the values of Sr_0 decrease as increasing the porosity. An increment of porosity of 4% induce a decrease in s_{air} by 0.2kPa (12% of the average s_{air} , which is equal to 1.7kPa), a decrease in s_1 by 0.1kPa (4% of the average s_1 , which is equal to 2.65kPa) and a decrease in Sr_0 by 6%. In other words, at high porosity, lower suction (s_{air} and s_1) is needed to desaturate the specimen. Moreover, for the same material (Hostun sand), using local ranges of porosity, one can obtain different s_{air} , s_1 , and Sr_0 . Thus WRC is not unique for one material, and a tool describing the porosity at the local scale like pore size and shape distribution is needed to distinguish a specific WRC for a specific material of a specific pore size and shape distribution.

The analysis presented before is performed for all the ranges porosity in all the three paths. The results of this analysis can be found in Appendix D, Fig (D-10), Fig (D-11) and Fig (D-12) for D_1 , Fig (D-13), Fig (D-14) and Fig (D-15) for W_1 and Fig (D-16), Fig (D-17) and Fig (D-18) for D_0 . In Fig (D-10), Fig (D-13) and Fig (D-16), the experimental relation between suction and the microscopic degree of saturation is presented for the three paths D_1 , W_1 and D_0 , respectively, considering all the ranges of the microscopic porosity. In Fig (D-11), Fig (D-14) and Fig (D-17), the fitting curves of the experimental points in the relation between suction and degree of saturation for all the ranges of the microscopic porosity in the three paths D_1 , W_1 and D_0 respectively. Fig (D-12), Fig (D-15) and Fig (D-18), show the relation between average porosity of all the ranges of porosity and the three variables, s_{air} and s_1 (left) and Sr_0 (right) for all the three paths D_1 , W_1 and D_0 , respectively.

From the results presented in Appendix D, it is found that the relation between suction and microscopic degree of saturation has the same trend as the one presented in Fig 4.72, for the three paths D_1 , W_1 and D_0 , and all the ranges of the microscopic porosity. Moreover, the relation between average porosity and the three variables s_{air} , s_1 and Sr_0 has the same tendency as the one presented in Fig 4.74, for the three paths D_1 , W_1 and D_0 .

4.4.1.3 The relation between porosity and degree of saturation $Sr=f(n)$

The relation between the porosity and the degree of saturation is investigated for all the values of suction in the three paths D_1 , W_1 and D_0 . Fig 4.75 shows the relation between the microscopic porosity and degree of saturation, for two values of suction in the drying path D_1 : $s=2\text{kPa}$ and $s=2.5\text{kPa}$.

As shown in Fig 4.75, the degree of saturation decreases as increasing the porosity. Furthermore, when increasing the suction, a shift for a lower degree of saturation is observed. Similar results are obtained macroscopically (see Fig 2.9 in chapter 2), where increasing void ratio induces an increase in the water content and thus a decrease in the degree of saturation. For the same porosity, a range of degree of saturation can be obtained from the microscopic measurement due to the discrepancy of the measurements. Nevertheless, increasing the suction would not always imply an important change in the relation between porosity and the degree of saturation as shown in Fig 4.76. In this figure, increasing the suction in the saturated and the residual domains does not induce a remarkable change on the relation between porosity and degree of saturation.

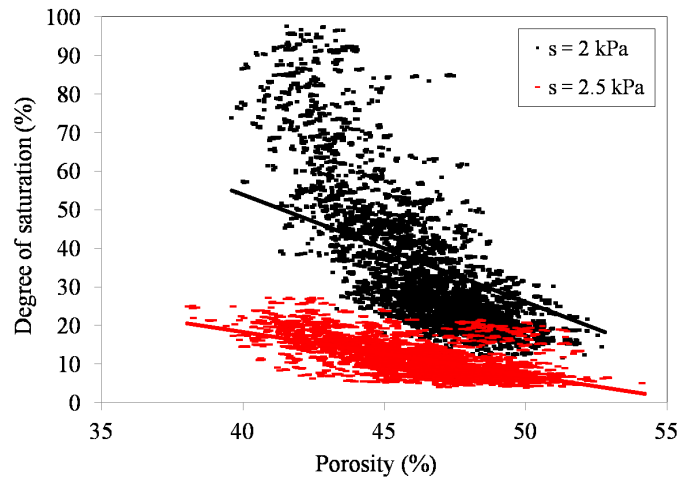


Figure 4.75: The relation between microscopic porosity and degree of saturation for the two values of suction: $s=2\text{kPa}$ and $s=2.5\text{kPa}$ in the drying path D_1 . The tendency (slope) of the relation between microscopic porosity and degree of saturation is presented by the two continuous lines

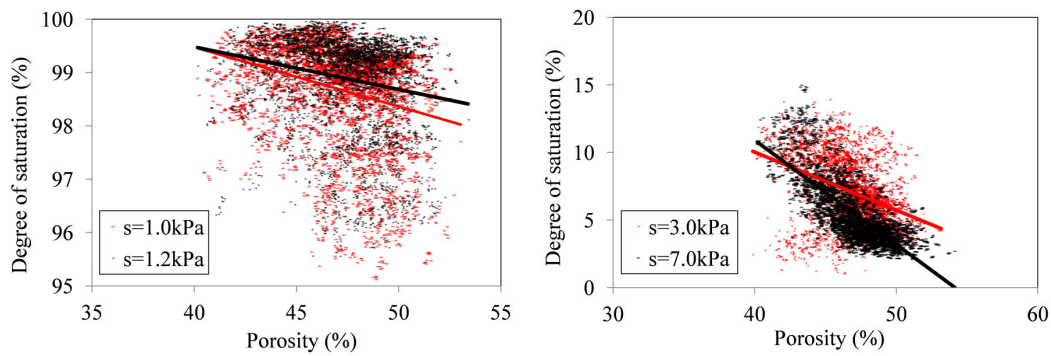


Figure 4.76: The relation between microscopic porosity and degree of saturation for the two values of suction: $s=2\text{kPa}$ and $s=2.5\text{kPa}$ in the drying path D_1

More results about the relation between microscopic porosity and degree of saturation for all the values of suction in the three paths D_1 , W_1 and D_0 , is presented in Appendix D, Fig (D-19) and Fig (D-20) for D_1 , Fig (D-21) and Fig (D-22) for W_1 and Fig (D-23) and Fig (D-24) for D_0 . In Fig (D-19), Fig (D-21) and Fig (D-23), the experimental relation between the microscopic porosity and degree of saturation for all the values of suction in the three paths D_1 , W_1 and D_0 , is presented. Fig (D-20), Fig (D-22) and Fig (D-24), show the tendency of the relation between the microscopic porosity and degree of saturation for all the values of suction in the three paths D_1 , W_1 and D_0 , is presented.

From the results presented in Appendix D, it is found that the relation between the microscopic porosity and degree of saturation, in the funicular and pendular domains has the same trend as in Fig 4.75, for all the three paths D_1 , W_1 and D_0 . In the saturated and residual domains, the relation between the microscopic porosity and degree of saturation has the same trend as in Fig 4.76, for all the three paths D_1 , W_1 and D_0 .

In conclusion, using the experimental local measurement of porosity and degree of saturation, it was possible to plot the relation between the three state variable suction, porosity and degree of saturation in 3D. However, a unique relation between suction,

porosity and degree of saturation was hard to retrieve due to the discrepancy of the microscopic porosity and degree of saturation measurements. This discrepancy shows the difficulty behind building a model at the micro scale (grain scale) that could describe the relation between these variable in 3D (i.e., water retention surface model).

4.4.2 Water retention domains

The definition of water retention domains in this work is theoretically built basing on water and air phases continuity. The concept of having continuous water and air phases is always retained; otherwise there will be no possibility to apply the suction. The continuity of water phase, especially in the pendular and the residual domain, is kept through water films of a thickness equal or less than $0.4\mu\text{m}$ for Hostun sand (silica sand). But these films, as pointed before, cannot be captured in the images obtained in this work with the available resolution ($7.5\mu\text{m}$). Thus for the analysis of water retention domains, water continuity through water films is ignored.

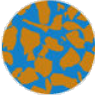
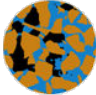
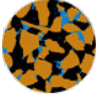

At the end of the trinarization results section (see section 4.3.2), points of concern before/after which the continuity of water and air phases changes are extracted and listed for each of the three paths D_0 , D_1 and W_1 . These points were defined qualitatively from analyzing the 3D trinarized volumes. From the microscopic-discrete analyses results, points where fluid phase changes the form from one big cluster to several clusters, maximum and minimum number of fluid clusters and maximum and minimum number of fluid clusters per grain are highlighted. These points were defined quantitatively.

The latter points allowed proposing a definition of the boundaries between water retention domains. At these boundaries, the distribution of water and air phases changes. In the following, the boundaries of water retention domains are presented for the three paths.

Drying path D_1

Table 4.7 shows water retention domains for D_1 .

Table 4.7: Water retention domains for D_1

Suction (kPa)	0	1	1.2	1.4	1.6	1.8	2	2.2	2.5	2.8	3	7
Water retention domain	Saturated				Funicular			Pendular			Residual	
Continuous phase	Water				Water			Air			Air	
												


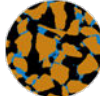
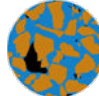
- $s=0\text{kPa}$, at which the test D_1 starts with a completely saturated specimen of a continuous water phase.
- $s=1.6\text{kPa}$, which is defined as air entry value, where air enters the specimen. Moreover at $s=1.6\text{kPa}$, a maximum number of air clusters is found. Furthermore, in the range $s \geq 1.6\text{kPa}$, air cluster has a minimum constant number of contacts with grain phase. For $0 \leq s \leq 1.6\text{kPa}$, water phase is continuous.

- $s=1.8\text{kPa}$, at which water/air phase changes the form from one big cluster having the same volume of water/air within the specimen $V_{\max}=V_t$, into several clusters of a volume smaller than the volume of water within the specimen. Moreover, for the range $s \geq 1.8\text{kPa}$, water cluster has a maximum constant number of contacts with grain phase.
- $s=2\text{kPa}$, before which (in the range $1.6 \leq s < 2\text{kPa}$) water phase is continuous and air phase is discontinuous.
- $s=2.8\text{kPa}$, at which a maximum number of water clusters is found. Moreover, in the range $s \geq 2.8\text{kPa}$, water cluster has a minimum number of contacts with grain phase. Furthermore, in the range $s \geq 2.8\text{kPa}$, air cluster has a maximum constant number of contacts with grain phase.
- $s=3\text{kPa}$, before which (in the range $2 < s < 3\text{kPa}$) water phase is discontinuous and air phase is continuous.
- $s=7\text{kPa}$, at which the test D_1 ends after reaching the residual state. For $3 \leq s \leq 7\text{kPa}$, water phase is in the residual state and air phase is continuous.

Wetting path W_1

Table 4.8 shows water retention domains for W_1 .

Table 4.8: Water retention domains for W_1

Suction (kPa)	3	2.8	2.5	2.2	2	1.8	1.6	1.4	1.2	1	0
Water retention domain	Residual		Pendular					Funicular			
	Air		Air					Water			
Continuous phase											

- $s=3\text{kPa}$, at which the test W_1 starts with a specimen of a residual water content.
- $s=2.8\text{kPa}$, after which (in the range $2.8 \leq s \leq 3\text{kPa}$) water phase is in the residual state and air phase is continuous. Moreover, at $s=2.8\text{kPa}$, a maximum number of water clusters is found. Furthermore, in the range $s \geq 2.8\text{kPa}$, water cluster has a minimum constant number of contacts with grain phase.
- $s=1.6\text{kPa}$, after which (in the range $1.6 < s \leq 2.8\text{kPa}$) water phase is discontinuous and air phase is continuous. Moreover, in the range $s \geq 1.6\text{kPa}$, air cluster has a maximum number of contacts with grain phase.
- $s=1.4\text{kPa}$, at which water/air phase changes the form from one big cluster having the same volume of water/air within the specimen $V_{\max}=V_t$, into several clusters of a volume smaller than the volume of water within the specimen. Moreover, in the

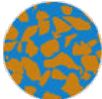
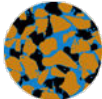
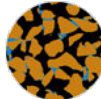

range $s \geq 1.4 \text{ kPa}$, a maximum constant number of air clusters is found. Furthermore, in the range $s \leq 1.4 \text{ kPa}$, water cluster has a maximum number of contacts with grain phase and air clusters has a minimum constant number of contacts with grain phase.

- $s=0 \text{ kPa}$, at which the test W_1 ends and after which (in the range $0 \leq s < 1.6 \text{ kPa}$) water phase is continuous and air phase is discontinuous.

Drying path D_0

Table 4.9 shows water retention domains for D_0 .

Table 4.9: Water retention domains for D_0

Suction (kPa)	0	1	1.2	1.4	1.8	2	2.2	2.5	3	7
Water retention domain	Saturated		Funicular				Pendular			Residual
	Water		Water				Air			Air
Continuous phase										

- $s=0 \text{ kPa}$, at which the test D_0 starts with a completely saturated specimen of a continuous water phase and no presence of air phase.
- $s \leq 1 \text{ kPa}$, where air cluster has a minimum number of contacts with grain phase.
- $s=1.2 \text{ kPa}$, which is defined as air entry value, where air enters the specimen. For $0 \leq s \leq 1.2 \text{ kPa}$ water phase is continuous. Moreover, at $s=1.2 \text{ kPa}$, a maximum number of air clusters is found. Furthermore, in the range $s \leq 1.2 \text{ kPa}$, water cluster has a maximum number of contacts with grain phase.
- $s=2 \text{ kPa}$, before which (in the range $1.2 \leq s < 2 \text{ kPa}$) water phase is continuous and air phase is discontinuous. Moreover, at $s=2 \text{ kPa}$, water/air phase changes the form from one big cluster having the same volume of water/air within the specimen $V_{\max}=V_t$, into several clusters of a volume smaller than the volume of water within the specimen. Furthermore, in the range $s \geq 2 \text{ kPa}$, air cluster has a maximum number of contacts with grain phase.
- $s=3 \text{ kPa}$, before which (in the range $2 < s < 3 \text{ kPa}$) water phase is discontinuous and air phase is continuous. Moreover, at $s=3 \text{ kPa}$, a maximum number of water clusters is found. Furthermore, in the range $s \geq 3 \text{ kPa}$, water cluster has a minimum number of contacts with grain phase.
- $s=7 \text{ kPa}$, at which the test D_0 ends and before which (in the range $3 \leq s \leq 7 \text{ kPa}$) water phase is in the residual domain and air phase is continuous.

The boundaries of water retention domains for the two specimens D_1 and D_0 are not similar as the criteria used to define those boundaries (i.e., maximum/minimum number of fluid clusters and contacts with grains, air entry value and change in the continuity) are influenced by the distribution of pore size and shape within these two specimens. Since the desaturation of the specimen influences the big pores first, air entry value obtained for D_1 and D_0 ($s=1.6\text{kPa}$ for D_1 higher than $s=1.2\text{kPa}$ for D_0) indicates that the big pores in D_1 specimen are smaller in size compared to the big pores in D_0 . Therefore, the saturated domain is of a bigger range of suction for D_1 than for D_0 . From the other hand, at the end of specimen desaturation, only small pores are influenced. The residual domain (i.e., the end of specimen desaturation) is reached for D_0 at a higher suction ($s=7\text{kPa}$) than for D_1 ($s=3\text{kPa}$), which indicates that the small pores in the D_0 specimen are of a smaller size than for D_1 specimen. In other words, pore size distribution of D_0 can be describes as better graded than in D_1 (i.e., larger size for the big pores and smaller for the small pores than in the specimen D_1). However, this is just a qualitative description of pore size in the two specimens and in order to be validated, the distribution of the pores, in size and shape, must be obtained quantitatively.

The pores that are influenced at the beginning of the wetting process are the small pores. A comparison between D_1 and W_1 , shows that it was possible to wet the specimen (i.e., reach the pendular domain) at smaller suction ($s=2.5\text{kPa}$) than the boundary proposed in D_1 path ($s=2.8\text{kPa}$). Similarly, in order to reach the funicular domain, small suction is needed to be applied in the W_1 ($s=1.6\text{kPa}$) than in D_1 ($s=2\text{kPa}$). However, the pressure increment needed to reach the funicular domain (similarly for the pendular domain), starting from the residual domain, in W_1 ($\Delta p=7-1.6=5.4\text{kPa}$), is higher than the pressure increment proposed in D_1 ($\Delta p=7-2=5\text{kPa}$). This extra pressure (or energy) was needed for the transition from smaller pores to bigger pores in the wetting process, which shows the influence of pores connectivity and shape on the retention capability.

Though the two paths D_1 and W_1 are conducted on the same specimen of the same pore size and shape distribution and pore connectivity, the boundaries between water retention domains are different. As explained before, this is due the influence of loading direction.

4.4.3 Hysteresis phenomenon

During the drying path D_1 , the saturated Hostun sand specimen was being desaturated, by increasing the suction, which decreased the water content. In the wetting path W_1 , followed on the same specimen of the drying path D_1 , the Hostun sand specimen of the residual water content was being saturated by decreasing the suction, which increased the water content. During the wetting process water volume increased within the specimen to reach relatively high water content where most of the pores of the soil were filled with water. However, the specimen did not get completely saturated (i.e., $S_r=100\%$), due to the formation of the trapped air. This behaviour of the soil (i.e., of not getting completely saturated when wetting), is described as hysteresis phenomenon.

In this section, an investigation of this phenomenon is presented using two kinds of analyses:

- Macro-micro analysis of hysteresis phenomenon, using the result of trinarization (macro) and microscopic measurements of porosity and degree of saturation, at

constant suction and constant degree of saturation.

- Microscopic-discrete analysis of hysteresis phenomenon using the microscopic-discrete analyses results are presented in section 4.3.5.

4.4.3.1 Macroscopic-microscopic analysis of hysteresis phenomenon

In order to achieve a better understanding of hysteresis phenomenon, it was analyzed at a constant value of suction and a constant value degree of saturation. The constant value of suction was chosen so that it shows the maximum difference in the degree of saturation between the two paths D_1 and W_1 . From Fig 4.16, it is shown that a maximum difference in the degree of saturation between D_1 and W_1 is found at $s=1.6\text{kPa}$ ($\Delta S_r \approx 19\%$). The constant degree of saturation was harder to define as this work is performed for limited pre-defined values of suction. Using Table 4.5, which shows the macroscopic degree of saturation calculated using the trinarized volumes, two values of suction at which the degree of saturation is comparable, can be extracted. At $s=2\text{kPa}$ in the drying path D_1 , the macroscopic degree of saturation is $S_r=29.8\%$ and at $s=1.6\text{kPa}$ in the wetting path W_1 , the microscopic degree of saturation is $S_r=28\%$. The degree of saturation at these two values of suction can be considered as a constant degree of saturation ($S_r \approx 30\%$), and is chosen to analyze hysteresis phenomenon.

Constant suction ($s=1.6\text{kPa}$)

Fig 4.77 shows central horizontal and vertical slices in the trinarized volumes of $s=1.6\text{kPa}$ in the drying path D_1 and $s=1.6\text{kPa}$ in the wetting path W_1 .

The figure shows that at the same suction ($s=1.6\text{kPa}$), water content for the drying path is higher than for the wetting path. Water phase for the drying path is continuous and air phase is discontinuous (i.e., funicular domain) while for the wetting path, water phase and air phase are continuous (i.e., funicular/pendular domain).

A qualitatively analysis, based on pore size and connectivity, for the changes in water content and its continuity between the two paths can be given from the trinarized images. As shown from the figure, in the vertical slice taken for the drying path, it was possible to desaturate only the big pores which are connected (surrounded) by relatively medium to big pores. The big pores surrounded by relatively small pores were not desaturated. On the other hand, when wetting the specimen, the big pores surrounded by relatively medium to big pores were not filled first with water (see the top of the specimen in vertical slice taken for wetting path). To the contrary, the first pores to be filled with water were the small pores or the big pores surrounded by medium to small pores. This description of the influence of pore size and connectivity coincides with the definition of ink-bottle hysteresis, presented in chapter 2, section 2.2.6.

The latter observation of the difference in water content between drying and wetting paths is captured quantitatively in the macroscopic and microscopic measurements of the degree of saturation. The macroscopic degree of saturation calculated for $s=1.6\text{kPa}$ in the drying path is $S_r=97.6\%$, while for $s=1.6\text{kPa}$ in the wetting path is $S_r=26\%$. For the microscopic measurements, Fig 4.78 shows central vertical slices in the porosity map, trinarized volumes and degree of saturation map for $s=1.6\text{kPa}$ in the drying path D_1 and $s=1.6\text{kPa}$ in the wetting path W_1 .

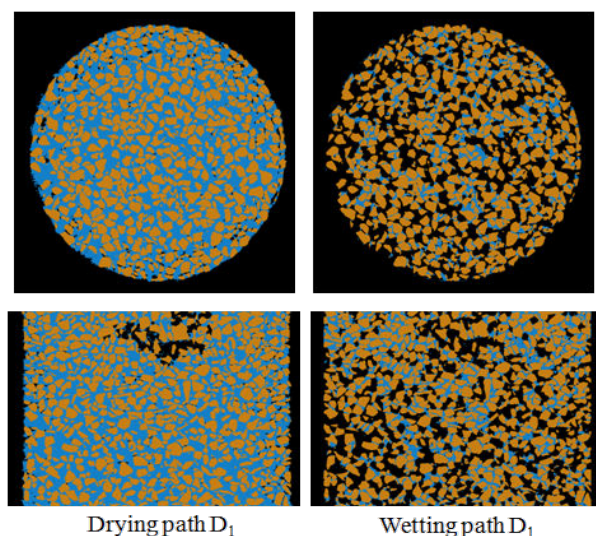


Figure 4.77: Central horizontal (up) and vertical (bottom) slices in the trinarized volumes of $s=1.6\text{kPa}$ in the drying path D_1 (left) and $s=1.6\text{kPa}$ in the wetting path W_1 (right)

The microscopic degree of saturation is ranging from $S_r=64\text{--}100\%$ for the drying path and from $S_r=24\text{--}69\%$ for the wetting path.

From Fig 4.78 it could be seen that the region of the higher degree of saturation coincides with the region of lower porosity, for the drying and wetting paths. This is more clear for $s=1.6\text{kPa}$ in wetting path, where higher degree of saturation at the top of the specimen (shown as lighter red color in the degree of saturation map) coincides with lower porosity (shown as darker red color in the porosity map).

Another way to investigate hysteresis phenomenon using the microscopic measurement is by plotting the frequency map. In this map the scattered points (pair of microscopic porosity and degree of saturation) are plotted as color points in a color map based on their frequency. The peaks in the color map are produced from the microscopic values that are the most frequent. Fig 4.79 shows the frequency map for the constant suction $s=1.6\text{kPa}$ in the drying and wetting paths. The microscopic measurements of porosity and degree of saturation in Fig 4.79 are obtained for $\text{REV}=140\text{px}$ with an overlapping equal to 50% REV, i.e., node spacing is equal to $0.5 \times \text{REV}$ size $= 0.5 \times 140 = 70\text{px}$. The overlapping is allowed in this measurement in order to increase the number of points so that a smooth distribution can be plotted using Matlab[®] frequency tools.

In Fig 4.79 the color bar represents frequency measurements. It is shown that for $s=1.6\text{kPa}$ in the drying path, the most frequent porosity is between $n=47\text{--}49\%$ and the most frequent degree of saturation is between $S_r=97\text{--}98\%$. The frequency of these ranges of porosity and degree of saturation is around 500 times over 2016 measurements (around 24% of the total measurements). The whole range for porosity is $n=42\text{--}51\%$ and for degree of saturation is $S_r=95\text{--}100\%$. For $s=1.6\text{kPa}$ in the wetting path, the most frequent porosity is between $n=48\text{--}50\%$ and the most frequent degree of saturation is between $S_r=24\text{--}27\%$. The frequency of these ranges of porosity and degree of saturation is around 180 times over 2016 measurements (around 9% of the total measurements). The whole range for porosity is $n=43\text{--}52\%$ and for degree of saturation is $S_r=15\text{--}70\%$.

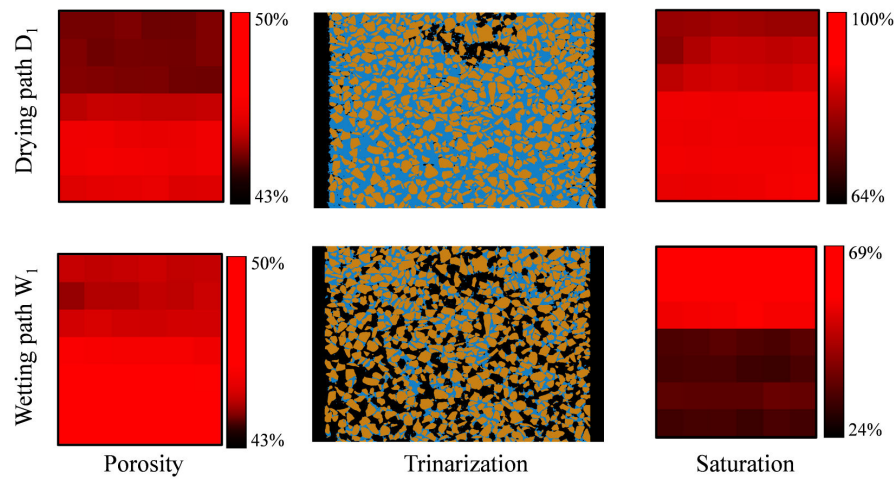


Figure 4.78: Central vertical slices in the: porosity map (left), trinarized volumes (middle) and degree of saturation map (right) for $s=1.6\text{kPa}$ in the drying path D_1 (up) and $s=1.6\text{kPa}$ in the wetting path W_1 (down)

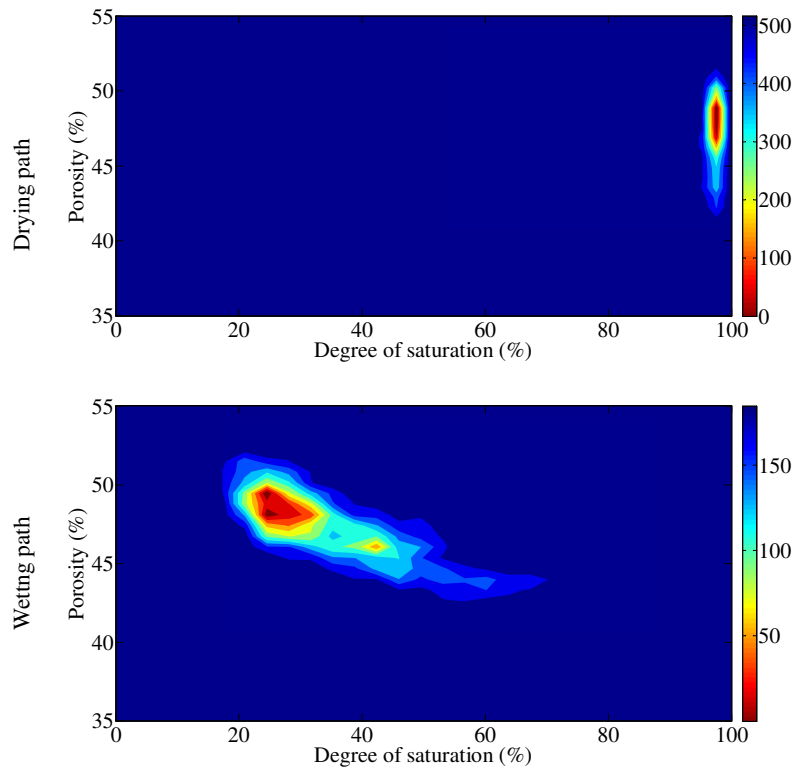


Figure 4.79: Frequency map for $s=1.6\text{kPa}$ in the drying path D_1 (up) and $s=1.6\text{kPa}$ in the wetting path W_1 (bottom)

Frequency map presented in Fig 4.79 can be used to characterize qualitatively the homogeneity/heterogeneity of water distribution within the specimen during drying and wetting process, at the same value of suction. As can be seen from the figure, during drying process, in the funicular domain (see Table 4.7 for $s=1.6\text{kPa}$) a narrow range (whole range) of degree of saturation is obtained, which indicates a homogeneous distribution of the water within the specimen. On the other hand, the whole range of the degree of saturation during wetting process, in the funicular/pendular domain (see Table 4.8 for $s=1.6\text{kPa}$) is wider compared to the one for drying, which indicate a decrease in the homogeneity of water distribution (or a heterogeneous water distribution). The range of porosity is the same for drying and wetting, which is expected as suction application influence on the soil skeleton (grain and volume of voids) is negligible.

More results about frequency map can be found in Appendix D, Fig (D-25), Fig (D-26) and Fig (D-27) for the three paths D_1 , W_1 and D_0 respectively. All frequency map results for the three paths D_1 , W_1 and D_0 are obtained for microscopic measurements with 50% REV overlapping. The results presented in Appendix D, for all the paths D_1 , W_1 and D_0 shows that the distribution of water within the specimen is more homogeneous for the saturated and residual domains compared to pendular and funicular domains. Porosity distribution is the same during the same path. Moreover, the distribution of water during drying is found to be more homogeneous compared to wetting process, in the range of suction $s=0-1.6\text{kPa}$ (i.e., saturated domain) and $s=2.8-7\text{kPa}$ (i.e., residual domain). In between these two ranges of suction, the distribution of water is heterogeneous during wetting than drying process.

Constant degree of saturation

Fig 4.80 shows central horizontal and vertical slices in the trinarized volumes for $S_r \approx 30\%$ which correspond to $s=2\text{kPa}$ in the drying path D_1 and $s=1.6\text{kPa}$ in the wetting path W_1 .

In order to obtain $S_r \approx 30\%$, smaller suction is needed to be applied in the case of wetting ($s=1.6\text{kPa}$) than in the case of drying ($s=2\text{kPa}$). Water phase for the drying path is continuous and air phase is discontinuous (i.e., funicular domain) while for the wetting path, water phase is discontinuous and air phase are continuous (i.e., pendular domain). As can be seen from Fig 4.80, water phase distribution with respect to pore size and connectivity seems to be independent of loading direction at constant degree of saturation, contrary to the distribution at constant suction. Water content at the top of the specimen is higher than at the bottom, for drying and wetting paths.

This can be seen clearly in Fig 4.81. In this figure, central vertical slices in the porosity map, trinarized volumes and degree of saturation map are presented for $s=2\text{kPa}$ in the drying path D_1 and for $s=1.6\text{kPa}$ in the wetting path W_1 . The figure shows higher degree of saturation (shown as lighter red color in the degree of saturation map) at the top of the specimen during drying and wetting. The region of the higher degree of saturation, at the top of the specimen, coincides with a lower porosity shown in the porosity map.

In Fig 4.82, the frequency map for $s=2\text{kPa}$ in the drying and for $s=1.6\text{kPa}$ in the wetting paths are presented.

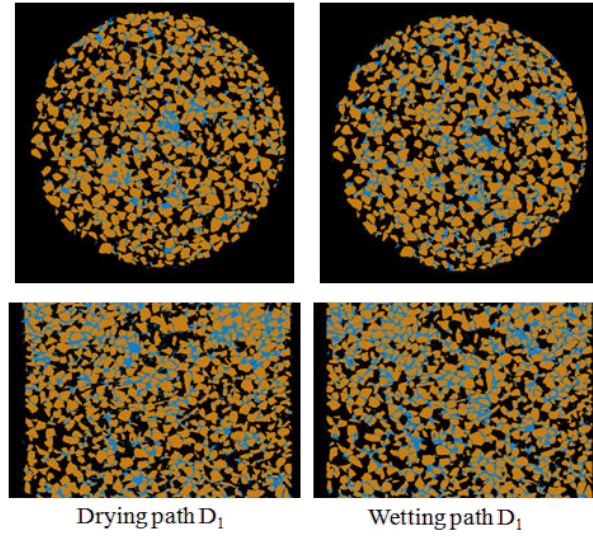


Figure 4.80: Central horizontal (up) and vertical (bottom) slices in the trinarized volumes, for $S_r \approx 30\%$ which correspond to $s=2\text{kPa}$ in the drying path D_1 (left) and $s=1.6\text{kPa}$ in the wetting path W_1 (right)

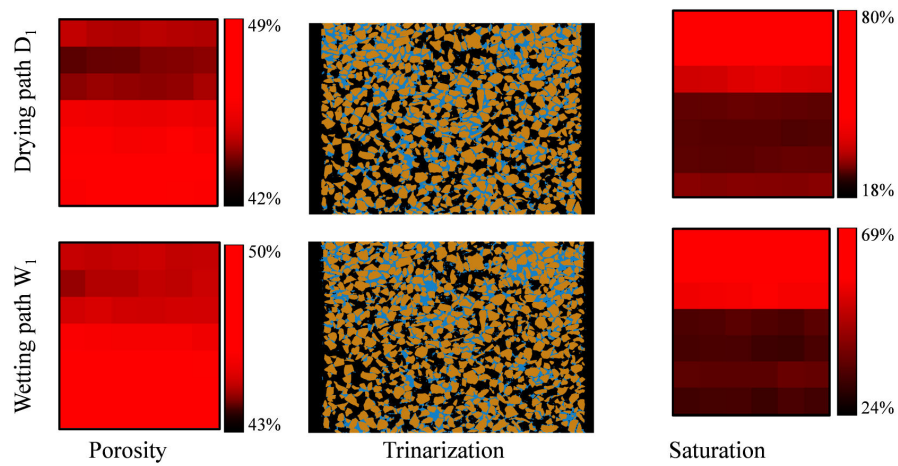


Figure 4.81: Central vertical slices in the: porosity map (up), trinarized volumes (middle) and degree of saturation map (bottom) for $s=2\text{kPa}$ in the drying path D_1 (left) and for $s=1.6\text{kPa}$ in the wetting path W_1 (right)

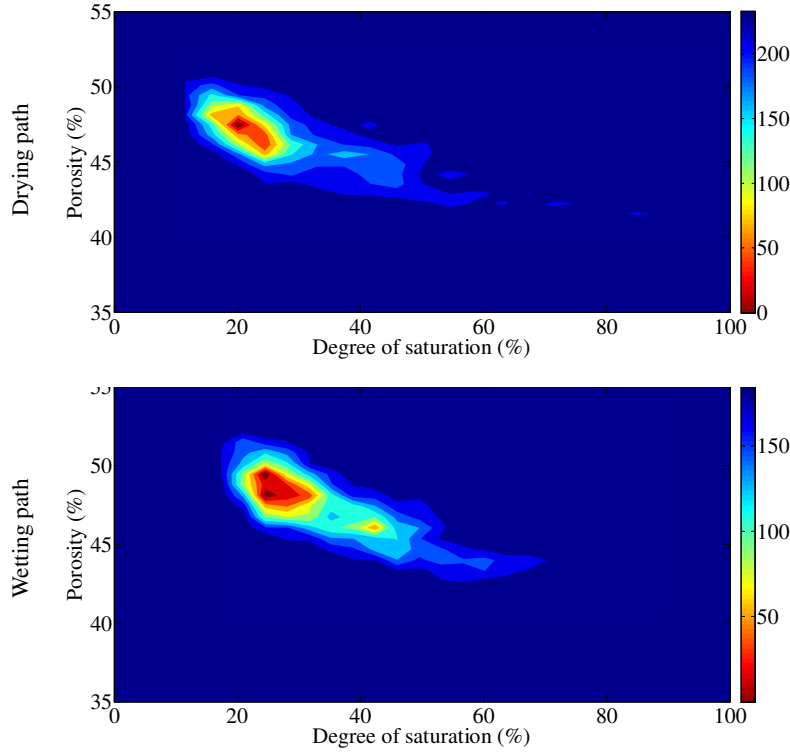


Figure 4.82: Frequency map for $s=2\text{kPa}$ in the drying path D_1 (up) and for $s=1.6\text{kPa}$ in the wetting path W_1 (bottom)

For $s=2\text{kPa}$ in the drying path, the most frequent porosity is between $n=47\text{--}48\%$ and the most frequent degree of saturation is between $S_r=19\text{--}21\%$. The frequency of these ranges of porosity and degree of saturation is around 230 times over 2016 measurements (around 11% of the total measurements). The whole range of porosity is $n=42\text{--}51\%$ and for the degree of saturation is $S_r=10\text{--}97\%$. For $s=1.6\text{kPa}$ in the wetting path, the most frequent porosity is between $n=48\text{--}50\%$ and the most frequent degree of saturation is between $S_r=24\text{--}27\%$. The frequency of these ranges of porosity and degree of saturation is around 180 times over 2016 measurements (around 9% of the total measurements). The whole range of porosity is $n=43\text{--}52\%$ and for the degree of saturation is $S_r=15\text{--}70\%$. The homogeneity/heterogeneity of water distribution within the specimen, at constant degree of saturation, seems to be independent of the loading direction.

4.4.3.2 Microscopic-discrete analysis of hysteresis phenomenon

Using the microscopic-discrete analyses results, the differences between drying and wetting processes of the specimen can be summarized as following:

For water phase, Fig 4.83 shows the evolution of the number of water clusters and the normalized V_{\max} for water clusters, with suction, for drying and wetting paths. In this figure, it is shown that the evolution of the number of water clusters with suction has the same trend for D_1 and W_1 , i.e., the number of water clusters increases as increasing the suction to reach a maximum value (shown in Table 4.10) then decreases. However, the maximum number of water clusters is bigger for W_1 compared to D_1 . For the evolution

of the normalized V_{\max} (the volume of the biggest fluid clusters), $V_{w\max}$ evolves in the same trend with suction for drying and wetting paths, i.e., the volume of the biggest water cluster decreases as increasing the suction.

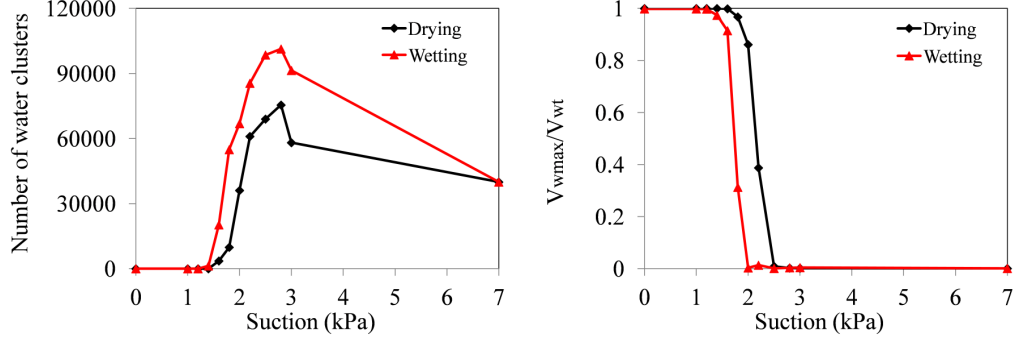


Figure 4.83: The evolution of the number of water clusters (left) and the normalized V_{\max} for water clusters (right), with suction, for drying and wetting paths

This evolution of water phase during drying and wetting processes can be interpreted at the specimen scale by division and coalescence mechanisms of water clusters and at the local scale by pores connectivity. During drying the big water cluster in the complete saturation state divides into small cluster due to air invasion. However, air cannot enter all the pores, i.e., the pores surrounded by relatively small saturated pores cannot be de-saturated. In wetting process, on the other hand, air is already present in the specimen, and water clusters present in the small pores coalesce. Yet, it is hard for the water clusters present in the small pores to coalesce as the surrounding big pores are full of air; therefore, their number is governed by filling their surroundings. These mechanisms during drying and wetting explain the bigger number of water clusters obtained during wetting then drying.

For air phase, Fig 4.84 shows the evolution of the number of air clusters and the normalized V_{\max} for air clusters, with suction, for drying and wetting paths. In this figure, it is shown that air clusters evolution with suction differentiates between the two paths D_1 and W_1 , mainly at relatively low values of suction where the number of air clusters does not decrease as wetting the specimen (i.e., trapped air clusters). At relatively high values of suction, the number of air clusters increases as decreasing the suction to reach a maximum value (see Table 4.10), then at relatively low values of suction, the number of air clusters decreases to reach zero value when drying and becomes constant when wetting (i.e., constant value equal to the maximum number of air clusters).

The maximum number of air clusters is comparable for the two paths D_1 and W_1 . For the evolution of the normalized V_{\max} , at relatively high values of suction, $V_{a\max}$ decreases as decreasing the suction to reach zero when drying, and non-zero value ($V_{a\max}/V_{at}=73\%$) when wetting (trapped air). Division process of water phase during drying, and air phase during wetting occurs almost at the same of V_{\max}/V_t (see Table 4.10).

Similar to water phase, the evolution of air phase during drying and wetting processes can be interpreted at the specimen scale by division and coalescence mechanisms of air clusters and at the local scale by pores connectivity.

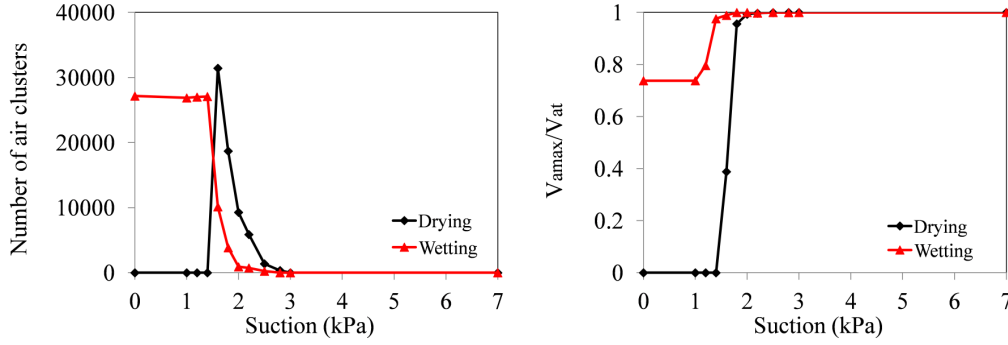


Figure 4.84: The evolution of the number of air clusters (left) and the normalized V_{\max} for air clusters (right), with suction, for drying and wetting paths

In conclusion, Wetting process does not allow the reduction of the number of air clusters and their volumes at relatively low values of suction that are lower than the inflection point in WRC ($s=1.4\text{ kPa}$), i.e., air entry value for drying process. This is due to that these air clusters are surrounded by small pores that are filled with water, therefore, they are trapped and cannot be saturated. On the other hand, air phase at suction values smaller than air entry value ($s_{\text{air}}=1.6\text{ kPa}$), for drying process, does not exist.

The evolution of the effective specific interfacial area (a_{wn}) for the two paths D_1 and W_1 , presented in Fig 4.85 shows that a_{wn} increases as decreasing the degree of saturation, to reach a maximum value (shown in Table 4.10) then decreases. However, due to the presence of air at the end of wetting process (at high saturation and low suction), the normalized $a_{\text{wn}}=2.8\text{ px}^{-1}$, while $a_{\text{wn}}=0$ at the beginning of drying process.

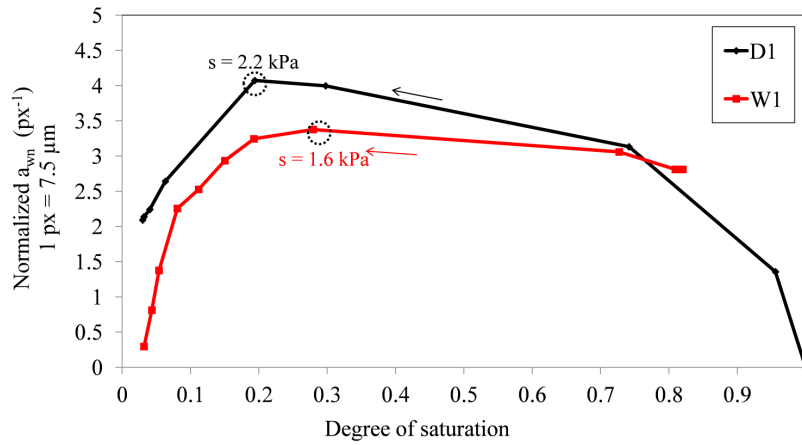


Figure 4.85: The evolution of the effective specific interfacial area (a_{wn}) with the degree of saturation, for drying and wetting paths

The evolution of Max Gw (maximum number of grains per water cluster) and Max Wg (maximum number of water clusters per grain) with suction are presented in Fig 4.86. From this figure, it is shown that these two evolutions has the same trend when drying and wetting the specimen, i.e., Max Gw decreases, and Max Wg increases to reach a maximum value then decreases as increasing the suction.

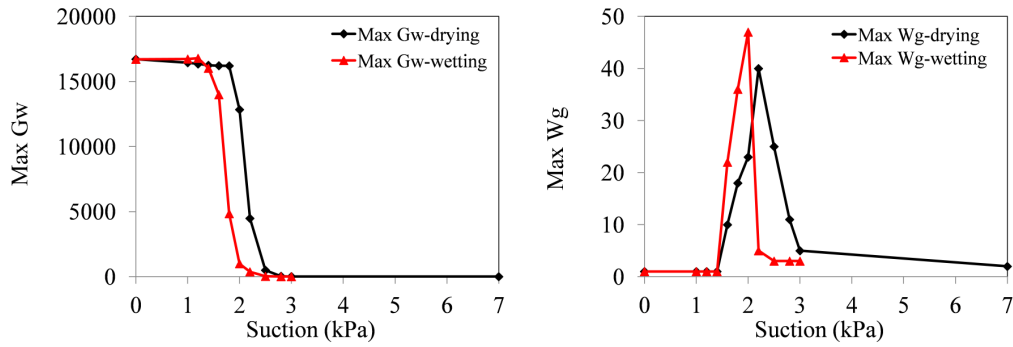


Figure 4.86: The evolution of the maximum number of grains per water cluster Max Gw (left) and the maximum number of water clusters per grain Max Wg (right), with suction, for drying and wetting paths

The evolution of Max Ga (maximum number of grains in contact with one air cluster) and Max Ag (maximum number of air clusters in contact with one grain) with suction are presented in Fig 4.87. The figure shows that Max Ga and Max Ag evolve with suction in the same way when comparing drying and wetting process, i.e., Max Ga increases and Max Ag increases to reach a maximum value then decreases as increasing the suction. However, at relatively low values of suction, due to the presence of air at the end of wetting process (i.e., at relatively low values of suction), Max Ga and Max Ag have a non-zero values (6000 and 18 contacts respectively) while at relatively low values of suction Max Ga=Max Ag=0 for drying process.

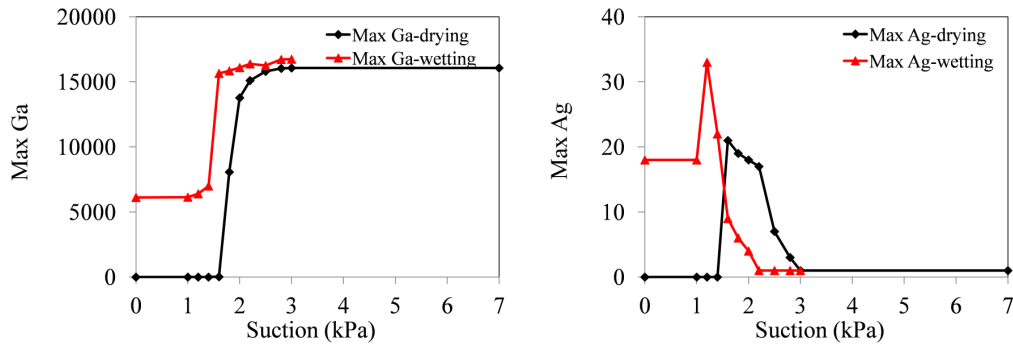


Figure 4.87: The evolution of the maximum number of grains per air cluster Max Ga (left) and the maximum number of air clusters per grain Max Ag (right), with suction, for drying and wetting

The evolution of Max Wa (maximum number of water clusters per air cluster) and Max Aw (maximum number of air clusters per water cluster with suction are presented in Fig 4.88. As shown in the figure, the evolution of Max Wa with suction has the same trend when drying and wetting the specimen, i.e., Max Wa increases as increasing the suction to reach a maximum value then decreases. On the other hand, Max Aw increases as decreasing the suction to reach a maximum value then at relatively low values of suction, Max Aw decreases to zero for drying and become constant for wetting (constant value equal to the maximum value $\approx 27 \times 10^3$).

The latter local changes offer better understanding, not only for hysteresis phenomenon but also for retention behaviour during drying and wetting process.

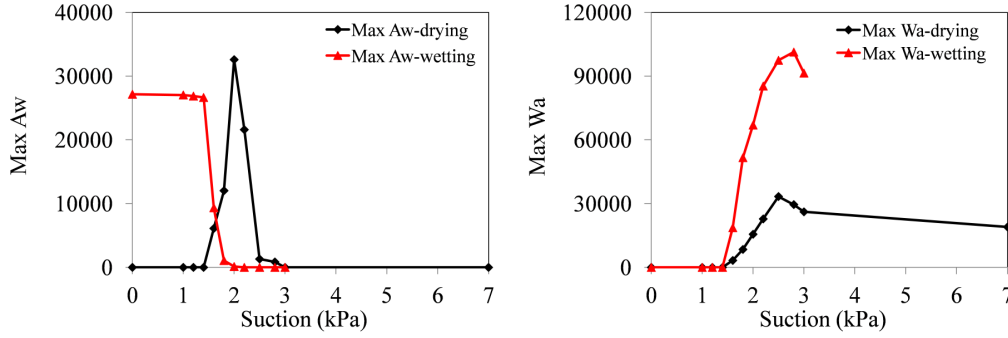


Figure 4.88: The evolution of the maximum number of air cluster per water cluster Max Aw (left) and the maximum number of water clusters per air cluster Max Wa (right), with suction, for drying and wetting

In the following, a local description of drying and wetting process is given. This description highlights the main differences between the two processes, and thus explains hysteresis phenomenon, with the available local measurements.

At the beginning of the drying test D_1 the specimen is completely saturated with one big water cluster that is in contact with all the grains within the specimen. At $s=1.6\text{kPa}$, air enters the specimen (air entry value) and a maximum number of air clusters is obtained. However, these air clusters have a minimum (Max Ga), i.e., minimum number of grains that are in contact with one air cluster in the range $s=0\text{kPa}$ to $s=1.6\text{kPa}$. This is due to that there are only few small air clusters within the specimen at this range of suction that are in contact with few grains. Increasing the suction to $s=1.8\text{kPa}$, water phase divides into smaller water clusters. From this value of suction (i.e., $s=1.8\text{kPa}$) Max Gw of water clusters decreases, i.e., water clusters loses their contacts with the grains due to division process.

At $s\approx 2.2\text{kPa}$, the number of water clusters that are in contact with one air clusters is equal to the number of air clusters that are in contact with one water cluster (i.e., $\text{Max Wa}=\text{Max Aw}$). This corresponds to having a maximum effective specific interfacial area a_{wn} .

For air clusters, which have already reached their maximum number at the air entry value, only at $s=2.8\text{kPa}$, they get their maximum (Max Ga), i.e., maximum number of grains that are in contact with one air clusters. This number (i.e., Max Ga), stays constant until the end of the test. From the other hand, at 2.8kPa suction, water phase reaches its maximum number of clusters. Yet these clusters have already lost their contacts with the grains due to division process and the decrease in their number.

From this summary of drying process, it is clear that the maximum (Max Gw or Max Ga) are not obtained at the same suction where a maximum number of water and air clusters is obtained. Division process increases the number of water clusters and decreases their contacts with the grains. On the other hand, at the beginning of the invasion process a maximum number of air clusters is obtained and as the invasion process continues, the number of grains that are in contact with air clusters increases.

When suction is applied at the beginning of the drying test, it affects the big pores. Due to the presence of the small pores connecting these big pores, and not enough suction is applied to affect them, the division process takes place. At the same time, once water is drained out the big pores, air occupies the volume of these pores. When increasing the

suction, the small pores get influenced by the suction applied and water drain out from them.

For wetting process, the specimen is in the residual state at the beginning of the test. Wetting path shared the same characteristics as drying path till $s=2.8\text{kPa}$ (i.e., maximum number of water clusters whose contacts with the grains is minimum and maximum contacts between grains and air). Decreasing the suction to $s=1.6\text{kPa}$, air clusters loses their contacts with the grains as their number is increasing due to division process which starts at $s=1.4\text{kPa}$.

Moreover, at $s=1.6\text{kPa}$ the number of water clusters that are in contact with one air cluster is equal to the number of air clusters that are in contact with one water clusters (i.e., $\text{Max } W_a = \text{Max } A_w$ and a maximum a_{wn} is reached).

Due to the division process influencing air phase, the maximum number of air clusters is reached with minimum contacts with the grains. However, water phase which occupied the volume of pores drained out of air, reach its maximum number of clusters at $s=1.4\text{kPa}$. This number stays constant until the end of the test. Yet the specimen does not reach the complete saturation state at the end of the test.

Similar to drying path, the maximum ($\text{Max } G_w$ or $\text{Max } G_a$) are not obtained at the same suction where a maximum number of water and air clusters is obtained. However, the dividing phase in this path is air phase (water phase in the drying path). The division process increases the number of air clusters and decreases their contacts with the grains. On the other hand, water phase which was already present within the specimen in the residual state was getting connected as decreasing the suction. The connection process of water phase induced a decrease in the number of water clusters but their contacts with the grains were increasing as decreasing the suction.

When suction is applied at the beginning of the wetting path, it affects the small pores. These small pores got filled with water first before the big pores.

Table 4.10 shows the characteristic measurements presented in the latter discussion for drying and wetting paths.

In conclusion, as has been presented, water retention curve hysteresis at the macroscopic scale can be described by grain-fluid and fluid-fluid interaction hysteresis at the microscopic scale. The microscopic-discrete investigation showed that the macroscopic change in water content (or degree of saturation) at the same suction when drying and wetting the specimen, corresponds to a microscopic change in the number of fluid clusters, their contacts, phase division and continuity (domains) and the interfacial area.

Table 4.10: The microscopic-discrete characteristics for drying and wetting paths

Characteristic-	Suction value in D_1 (kPa)	Characteristic value in D_1	Suction value in W_1 (kPa)	Characteristic value in W_1
Maximum number of air clusters	1.6	$\approx 31 \times 10^3$	$s \geq 1.4$	$\approx 27 \times 10^3$
Minimum (Max Ga)	$s \leq 1.6$	0	$s \leq 1.4$	≈ 6000
Division process	1.8	$Vw_{max} / Vw_t = 96\%$	1.4	$Va_{max} / Va_t = 97\%$
Maximum (Max Gw)	$s \leq 1.8$	$\approx 16 \times 10^3$	$s \leq 1.4$	$\approx 16.5 \times 10^3$
Maximum a_{en}	2.2	≈ 4	1.6	≈ 3
Maximum (Max Ga)	$s \geq 2.8$	$\approx 16 \times 10^3$	$s \geq 1.6$	$\approx 16.5 \times 10^3$
Maximum number of water clusters	2.8	$\approx 75.5 \times 10^3$	2.8	$\approx 101 \times 10^3$
Minimum (Max Gw)	$s \geq 2.8$	9	$s \geq 2.8$	10

4.4.4 Cohesion regimes

As has been presented in chapter 2, section 2.3.2, cohesion is analyzed experimentally and numerically in relation with suction (or water content) at the macroscopic scale. At the microscopic scale, cohesion is investigated experimentally and numerically in relation with several microscopic properties as the inter-particle distance, grain shape and size and the number of liquid bridges and clusters per grain.

In this doctoral work, the macroscopic-microscopic observations obtained by the other researchers are used to link cohesion to the number of water clusters per grain (i.e., Max Wg). However, soil cohesion is not measured in this work; therefore, the results are shown in term of suction rather than cohesion.

Scheel et al. (2008), reviewed in chapter 2, section 2.3.2, have found that the number of liquid bridges per grain increases as increasing water content, in low water content regimes, to reach a maximum value then decreases. Cohesion is maximal, at water content value that corresponds to the maximum number of water clusters per grain. On the other hand, at high water content regimes, cohesion increases as increasing the suction according to Leal-Vaca et al. (2012), Delage (2008-c) and Gan et al. (1988). In between the low water content and high water content regimes, Mitarai et al. (2006), suggested that cohesion may either increases or decreases with water content in this regime.

The results found in this work, for drying and wetting paths, were consistent with the results found by Scheel et al. (2008). Max Wg increases as increasing the suction to reach a maximum value then decreases (see Fig 4.57, Fig 4.58 and Fig 4.59). The maximum number of water clusters per grain (Max Wg) is obtained for the three paths D_1 , W_1 and D_0 at peak suctions ($s=2.2$, 2 and 1.8 kPa, respectively) that correspond to water content $w=10\%$, 10% and 29% , respectively, in the pendular domain for D_1 and W_1 and in the funicular domain for D_0 . Max Wg is almost the same for the two drying paths D_1 and D_0 , of the different porosities, but at different values of suction (higher suction for the higher porosity D_1 $s=2.2$ kPa, than for the lower porosity D_0 $s=1.8$ kPa).

Following Scheel et al. (2008), it would be reasonable to suggest that soil cohesion increases as increasing water content to reach its maximum value at $w=10\%$, 10% and 29% . At relatively low values of suction (i.e., high water content), the analysis performed in this work showed that the number of water clusters per grain is small (Max Wg=1) due to the continuity of water phase, therefore, it is suggested that the only factor influencing cohesion in this regime is suction (following Leal-Vaca et al. (2012), Delage (2008-c) and Gan et al. (1988)).

Based on the latter discussion, and on the concept of capillary regimes presented in chapter 2, section 2.3.2, by Mitarai et al. (2006), soil cohesion can have three regimes, at which, cohesion depends on different factors:

- Low water content regime, at which cohesion depends on the number of water clusters per grain.
- Medium water content, at which cohesion depends on water content.
- High water content regime, at which cohesion depends on suction.

These three regimes can be interpreted on a soil specimen as follows: when drying a saturated soil specimen, i.e., at high water content ranges, cohesion increases as increasing

the suction due to the increase of the number of water bridges and clusters. The big connected volume of water at saturation divides into smaller volumes (clusters and bridges) as increasing the suction. On the other hand, when wetting a dry (or at residual water content) specimen, i.e., low water content regimes, the increase of cohesion as increasing water content (or decreasing the suction) is due to the increase in the number and volume of water clusters and bridges. Proceeding from a specimen in the residual domain (or dry specimen) with few water bridges, the increase of water content induces the formation of more water bridges and clusters. As increasing water content in this regime, the volume of these bridges and clusters increases. At water content ranges in between, the latter mentioned ranges, both mechanisms are active (division and coalescence).

For Hostun sand, cohesion regimes can be established for the three paths D_1 , W_1 and D_0 as shown in Table 4.11, Table 4.12 and Table 4.13, respectively. The boundaries between these regimes are defined as following:

For the drying path D_1 :

Table 4.11: Cohesion regimes for D_1

Suction (kPa)	0	1	1.2	1.4	1.6	1.8	2	2.2	2.5	2.8	3	7
Cohesion regime	High water content				Medium water content				Low water content			
Cohesion dependency	Suction				Water content				Max Wg			

Where:

- In the range $s=0, 1, 1.2$ and 1.4 kPa, $\text{Max Wg}=1$ and the cohesion is depending on suction.
- In the range $s=1.6, 1.8, 2$ and 2.2 kPa, Max Wg increases as decreasing water content (or increasing the suction), from 1 to a maximum value at $s=2.2$ kPa. In this range cohesion is a function of water content.
- In the range, $s=2.5, 2.8, 3$ and 7 kPa, Max Wg increases as increasing water content (decreasing the suction). In this range cohesion is a function of Max Wg .

For the wetting path W_1 :

Table 4.12: Cohesion regimes for W_1

Suction (kPa)	0	1	1.2	1.4	1.6	1.8	2	2.2	2.5	2.8	3	7
Cohesion regime	High water content				Medium water content				Low water content			
Cohesion dependency	Suction				Water content				Max Wg			

Where:

- In the range $s=0, 1, 1.2$ and 1.4kPa , $\text{Max } W_g=1$ and the cohesion is depending on suction.
- In the range $s=1.6, 1.8$ and 2kPa , $\text{Max } W_g$ increases as decreasing water content (or increasing the suction), from 1 to a maximum value at $s=2\text{kPa}$. In this range cohesion is a function of water content.
- In the range, $s=2.2, 2.5, 2.8, 3$ and 7kPa , $\text{Max } W_g$ increases as increasing water content (decreasing the suction). In this range cohesion is a function of $\text{Max } W_g$.

For the drying path D_0 :

Table 4.13: Cohesion regimes for D_0

Suction (kPa)	0	1	1.2	1.4	1.8	2	2.2	2.5	3	7
Cohesion regime	High water content			Medium water content		Low water content				
Cohesion dependency	Suction			Water content		Max W_g				

Where:

- In the range $s=0, 1$ and 1.2kPa , $\text{Max } W_g=1$ and the cohesion is depending on suction.
- In the range $s=1.4$ and 1.8kPa , $\text{Max } W_g$ increases as decreasing water content (or increasing the suction), from 1 to a maximum value at $s=1.8\text{kPa}$. In this range cohesion is a function of water content.
- In the range, $s=2, 2.2, 2.5, 3$ and 7kPa , $\text{Max } W_g$ increases as increasing water content (decreasing the suction). In this range cohesion is a function of $\text{Max } W_g$.

As can be seen from Table 4.11 and Table 4.13 for D_1 and D_0 , respectively, the boundaries between cohesion regimes are not the same. The reasons behind that are the different porosities of the two specimens, at the macroscopic scale, and the different grain and pore size and shape distribution at the microscopic scale.

The comparison between Table 4.11 and Table 4.12 for D_1 and W_1 , respectively, shows that WRC hysteresis induces a variation in the boundaries between cohesion regimes for these two paths. Though there was no influence of the porosity on suction values in the high water content regime (same porosity for the same specimen), yet at the microscopic scale, in the low water content regimes, the influence of pores shape cannot be ignored. The macroscopic analyses presented in chapter 2, section 2.3.2 showed that higher cohesion is expected for wetting than for drying. However, this conclusion cannot be verified in this work as cohesion is not measured.

Similar investigation was performed recently, for unsaturated pyroclastic soil, by a PhD student Mariagiovanna Moscariello, in a joint work between 3SR laboratory and University of Salerno/Italy. The results of this investigation were consistent with the results obtained in this work.

4.5 Conclusion

This chapter presented water retention tests performed in this work for the drying and wetting paths (D_0 , D_1 and W_1). The experimental program including the analyzed material, the cells, suction application technique, specimen preparation technique and the experimental procedure was introduced.

Digital image correlation was performed for WRT_1 , in order to check the presence of deformation coming from suction application. It was found that the grains displacement is negligible compared to D_{50} of Hostun sand and can be ignored.

Trinarization results were presented and analyzed for the three paths. Using the trinarization results, points of concern, before/after which the continuity of fluid phase changes were defined. The macroscopic porosity and degree of saturation were calculated for all the points in the three paths D_0 , D_1 and W_1 , using two techniques: the trinarized volumes (number of voxels representing each phase) and traditional technique (weighing the specimen). The results of macroscopic porosities and degree of saturation calculated by the two presented techniques were comparable. Later, porosity and degree of saturation were calculated at the micro scale within an REV. REV size was defined using the statistical technique described in chapter 3, section 3.4.1. Using the mapping code, microscopic porosity and degree of saturation were obtained for all the points in the three paths. The macroscopic and microscopic porosity and degree of saturation were found comparable.

Moreover, microscopic-discrete analyses were presented in this chapter. The three phases were labelled and each grain/fluid cluster was given an Id. The evolution of the number of fluid clusters was analyzed for the different paths. Points where water/air phase changes the form from one big cluster into several clusters, maximum and minimum number of clusters were extracted. In addition, the evolution of the effective specific interfacial area with the degree of saturation was obtained. Furthermore, the evolution of the contacts between the phases was analyzed for the three paths. Points at which fluid cluster had a maximum and a minimum number of contacts with grain phase were highlighted.

At the end, water retention results were interpreted. A definition of the boundary between water retention domains was proposed using the extracted points from trinarization and microscopic-discrete analyses results.

The relation between each pair of the three state variables: suction, porosity and degree of saturation, was investigated. It was found that the microscopic porosity tends to increase as increasing the suction. However, this is not true for the ranges of suction in the saturated and residual domain. In these two ranges, porosity tends to be constant regardless the suction. The experimental relation between suction and the microscopic degree of saturation has the same trend of water retention curve. From the Fitting curves of the experimental points in the relation between suction and degree of saturation, three characteristic values were extracted: air entry value (s_{air}), the value of suction (s_1) at which the curve reach a constant degree of saturation before the residual state, and the residual degree of saturation (Sr_0). It was found that these three characteristic variables decrease as increasing the porosity. The relation between microscopic porosity and degree of saturation showed that a shift for a higher degree of saturation is obtained as increasing the suction. In addition, microscopic porosity tends to decrease as increasing the microscopic degree of saturation. Eventually, it was hard to retrieve a unique relation between the three state variables due to the discrepancy of the measurement and the need

of a tool that characterize micro scale mechanisms such as pore size and shape distribution.

Hysteresis phenomenon was investigated at the macroscopic-microscopic and microscopic-discrete scales. At the macroscopic-microscopic scales, hysteresis phenomenon was analyzed at two conditions: constant suction and constant degree of saturation. At the same value of suction, due to hysteresis, two different values of degree of saturation were found for the drying and wetting processes (higher degree of saturation for the drying than the wetting). At the same degree of saturation, due to hysteresis, two different corresponding values of suction were found (higher suction for the drying than for the wetting). Moreover, it was found that the distribution of water within the specimen is more homogeneous for drying than for wetting, in the saturated and residual domains compared to pendular and funicular domains where water distribution is heterogeneous for both processes. The microscopic-discrete investigation showed that the macroscopic observations for hysteresis phenomenon can be related to local changes in the number of fluid clusters, their contacts, phase division and continuity (domains) and the interfacial area.

Soil cohesion was analyzed in the frame of water retention test. It has been shown that cohesion can have three regimes at which cohesion is a function of suction, water content or $\text{Max } W_g$, depending on the cohesion regime. For the same soil, cohesion depends on the porosity, macroscopically, and on the grain and pore size and shape distribution, microscopically. Hysteresis phenomenon affects the boundaries between cohesion regimes due to the influence of pore shape distribution.

Chapter 5

Hydro mechanical behaviour (Triaxial tests)

5.1 General overview

This chapter introduces the hydro-mechanical behaviour of a granular material, obtained by performing several triaxial compression tests. The material and the experimental methods are detailed in section 5.2, including a description of the performed triaxial tests, the material tested, the cell, specimen preparation technique, suction application technique, the experimental procedure, loading system and procedure and the experimental program.

The experimental results describing the hydro-mechanical response of the tested material are presented in section 5.3. This section shows stress-strain and volumetric responses of the specimens tested. The results obtained using the experimental tools detailed in chapter 3 are also presented in this section, including trinarization, macroscopic and microscopic porosity and degree of saturation, microscopic-discrete analyses and digital image correlation results. Section 5.4 presents the interpretation of the experimental results, including the evolution of porosity and degree of saturation inside and outside the sheared zone and the influence of water distribution on shear strength.

5.2 Material and methods

5.2.1 Triaxial tests

Triaxial tests are performed in this work in order to investigate the evolution of fluid phase (water and air) with the mechanical loading, mainly in the shear band, and to obtain stress-strain curve of the unsaturated sand tested in this work.

Three triaxial tests conditions are planned for this work: saturated drained, unsaturated drained and unsaturated undrained.

In order to perform these tests, triaxial setup available in 3SR laboratory, at Grenoble University is used. This setup can be divided into three parts: bottom, middle and upper part.

The bottom part includes a Pressure Controller (PC_1) connected to the bottom of the specimen to allow suction application as a negative pore water pressure with respect to air pressure which is assigned equal to the atmospheric pressure. The middle part includes

the axial loading system, cell pressure system and the triaxial cell, see Fig 5.1(b, c). The upper part includes a pressure controller (PC_2) connected to the top of the specimen by a connection T. PC_2 is used for the application of back pressure in the saturated drained triaxial test. Another system connected to the top of the specimen is the vacuum system. Vacuum application to the inside of the specimen allows the specimen to stand resisting its own weight during the preparation step. Fig 5.1 shows the whole arrangement of triaxial setup inside x-ray cabinet used to perform the three triaxial tests.

The whole configurations, conditions, loading processes and analyses of the triaxial tests performed in this work are detailed in the following section.

5.2.2 The material tested

Similar to water retention behaviour tests, the experimental program of the triaxial tests is conducted on Hostun sand HN31 (see chapter 4, section 4.2.1).

5.2.3 The cell

The triaxial cell used in this work is designed to allow x-ray scanning and to fit to the mechanical loading system available in 3SR Laboratory. The cell is made of PMMA (similar to water retention tests) which is transparent to x-ray, and it is shaped to resist the cell pressure applied during the triaxial tests. Fig 5.2 shows the PMMA cell in front of x-ray source, with the specimen installed at its place inside the cell.

5.2.4 Specimen preparation technique

The specimen prepared for the triaxial tests is a cylindrical specimen of 1 cm diameter and 2 cm height (slenderness ratio 2). The technique used for specimen preparation in the triaxial tests is water pluviation, similar to water retention tests, and thus all the pores in the specimen are completely filled with demineralized water in the initial state, i.e., a completely saturated specimen at the beginning of the tests. Fig 5.3 illustrates the procedure by which the specimen is prepared in this work, for the three triaxial tests. All the details related to the procedure followed to prepare the specimen are given in section 5.2.5.

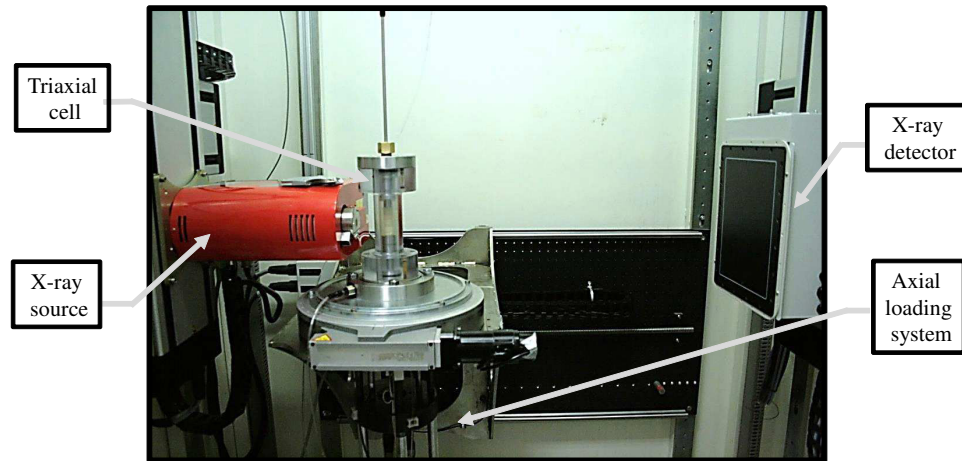


Figure 5.1: The whole arrangement of triaxial setup inside x-ray cabinet used to perform the three triaxial tests

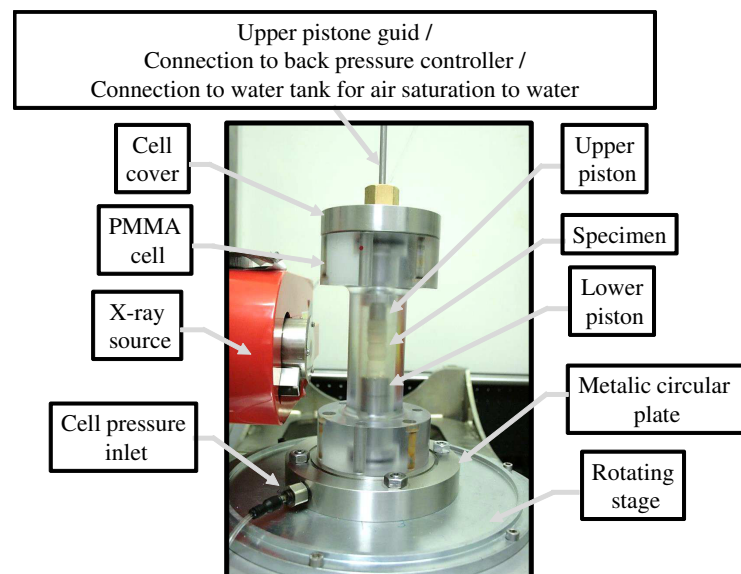


Figure 5.2: The triaxial cell in front of x-ray source

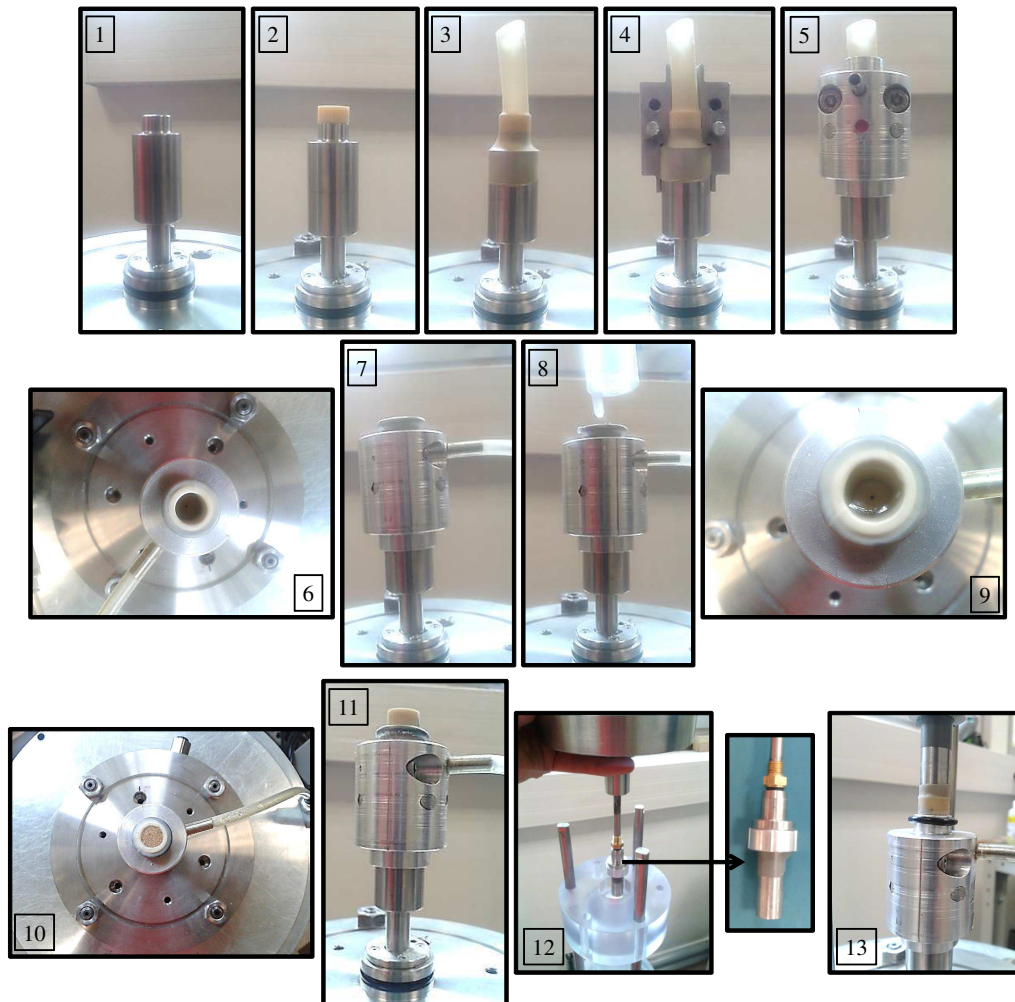


Figure 5.3: A series of photographs illustrating the procedure by which a specimen is prepared in this work. In frame 1, only the lower head (piston) of the setup is seen; then in frame 2 the porous stone is placed, followed by the latex membrane (3); frame 4 and 5 illustrate the mounting of the 2-parts mould around the bottom piston end, porous stone and membrane; frame 6 and 7 show connecting the mold to the vacuum system; then in frame 8 and 9 the inside of the membrane is filled with water; between frames 9 and 10 the material is pluviated into the membrane; frame 10 shows the specimen pluviated inside the membrane followed by installing the ceramic stone at the top (11); frame 12 shows installing the upper part of the cell (the inset shows the upper piston); finally in frame 13 the upper piston is placed at the top of the specimen

5.2.5 Suction application technique

The method used for applying the suction for the tests is the tensiometry (similar to water retention tests). The suction is applied by the pressure controller (PC_1) connected to the bottom of the specimen. PC_1 allows applying a maximum water pressure 100kPa, with a precision 10Pa.

The value of suction to be applied for the saturated drained test is $s=0$ kPa at the top of the specimen, i.e., zero suction pressure (s_0). This value of suction is maintained through the whole test, thus the specimen is completely saturated through the test. In order to measure (s_0), the space inside the membrane is filled with water to its top, Fig 5.3-9, and PC_1 is connected to the bottom end of the specimen, allowing the measurement of (s_0). Later, PC_1 is set to the value $P=s_0$ and thus $s=0$ at the top of the specimen. Suction system and triaxial setup for the saturated drained test are shown in Fig 5.4.

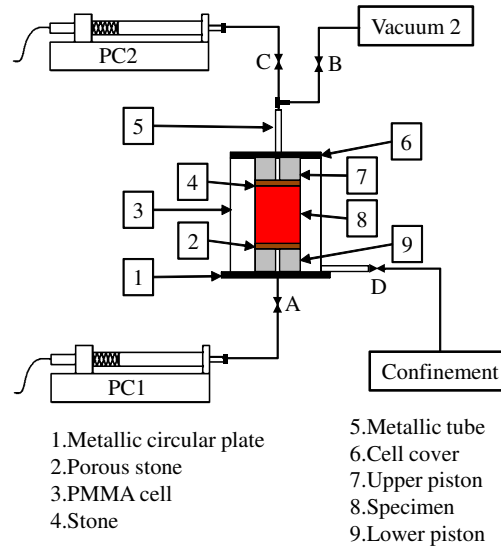


Figure 5.4: A sketch illustrates the triaxial setup and suction system for the saturated drained test

For the unsaturated drained test, the specimen at the beginning of the test is completely saturated. A first scan is performed to characterize the initial state, and then suction is applied. The value of suction applied in this test is $s=2.2$ kPa and it is maintained constant through the rest of the test. This value is chosen from WRC of Hostun sand, so that the degree of saturation can be estimated ($S_r=19.4\%$ for D_1 of a porosity $n=46\%$ and $S_r=22.3\%$ for D_0 of a porosity $n=44\%$). However, as shown in chapter 4, the degree of saturation for a constant suction changes depending on the porosity. The porosity of the triaxial test specimen cannot be imposed while preparing the specimen, thus there is no guarantee that the degree of saturation will be within the range $S_r=(19.4-22.3\%)$.

Similarly for the unsaturated undrained test, the specimen at the beginning of the test is completely saturated. After scanning the saturated specimen suction is applied. The value of suction applied in this test is the same as for the unsaturated drained tests (i.e., $s=2.2$ kPa), which will allow the comparison between the two tests in a following step.

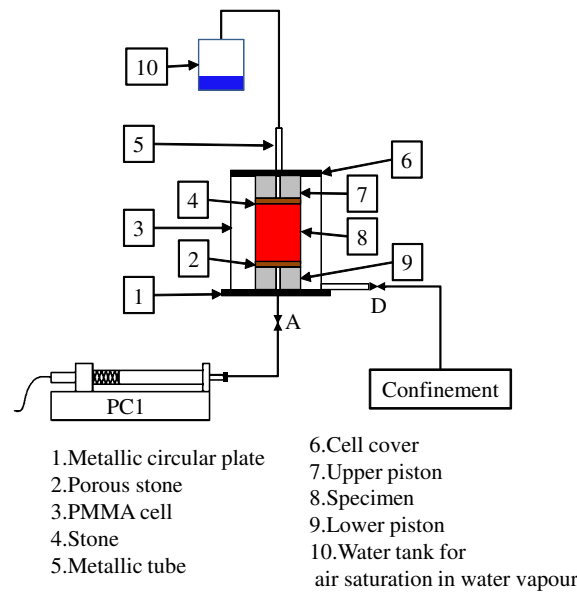


Figure 5.5: A sketch illustrates the triaxial setup and suction system for the unsaturated tests (drained and undrained)

This value allows having constant water content in this test similar to the one obtained initially for the unsaturated drained test. After applying the suction, the specimen is left for three days to reach equilibrium time then scanned. Later a valve (A), see Fig 5.5, connecting PC₁ and the specimen is closed to impose undrained test condition with no water flowing in/out the specimen. Triaxial setup and suction system for the unsaturated tests is shown in Fig 5.5.

5.2.6 Experimental procedure

The procedure to perform the three triaxial tests (including specimen preparation procedure) is detailed in the following:

At the beginning, the loading system of the triaxial setup is placed inside x-ray cabinet in order to prepare the specimen, see Fig 5.5. A lower piston shown in Fig 5.3-1 is installed inside a metallic circular plate, see Fig 5.3, above the rotating stage of the x-ray setup. The diameter of the upper part of the lower piston is 1 cm (same to the specimen). The pressure controller PC₁, which is placed outside x-ray cabinet, is connected to the lower piston by a tube and an opened valve (A), see Fig 5.4. The lower piston is a hollow steel piston, which allows the water coming from PC₁ to flow out through it. Later, a porous stone of a diameter 1 cm and of a high permeability (air entry value of 100kPa) is placed and glued at the top of the lower piston, Fig 5.3-2, and a pressure of 80kPa is imposed for 5 hours using PC₁ to force the water to go through the porous stone. After those 5 hours water drops are seen on the other side of the porous stone, i.e., the porous stone is saturated and water continuity between PC₁ and the porous stone is guaranteed.

A latex membrane of a diameter 1 cm and a thickness 0.3mm is installed on the lower piston and the porous stone, see Fig 5.3-3. Within this membrane, the specimen will be created later. The position of the membrane is regulated by hand to ensure that the membrane is both vertical, as well as well-centered with respect to the porous stone. A rubber

O-ring is put over the membrane, pressing it against the lower piston, to better guarantee the sealing which protects the inside of the specimen from invasion of the confining water (the O-ring is not shown in Fig 5.3 but was used when preparing for the real tests).

In order to maintain the shape of the specimen until cell pressure is applied, a mold is used. The mold is greased to lessen the friction between it and the membrane. Then both sides of the mold are closed around the specimen. Later, the top of the membrane is folded over the mold, allowing having an access to the inside of the membrane from the top, see Fig 5.3-(4 and 5). The membrane is stretched over the lower piston and the porous stone, by applying vacuum on the space between the mold and the outside of membrane, see Fig 5.3-(6 and 7). Vacuum of around 30kPa is applied using a vacuum pump connected to the tube going out from the mold. The application of the vacuum pushes the membrane against the mold, so that it adopts its shape, which is the desired shape of the outside of the specimen. Later the space inside the membrane is filled with water, see Fig 5.3-(8 and 9). The sand is then pluviated with a simple tapping on the edges of the mold, so that grains accelerate due to gravity and fall through the water to the space inside the membrane. The pluviation of the grains is stopped when the height of the specimen is achieved and then the external grains are removed with a flat surface (rule) to help ensure a flat and horizontal top surface, see Fig 5.3-10. A stone with a hole drilled through it, is added to the top surface of the specimen, see Fig 5.3-11. This stone will help applying vacuum (by the vacuum system) and back water pressure (by PC₂) through the hole. For unsaturated triaxial test, where no back pressure is applied, the presence of the hole ensures the continuity of high humidity air between the top of the specimen and a water tank for air saturation. A filter paper is placed between the stone and the top of the specimen to prevent sand from being sucked through the hole of the stone, when applying vacuum to the inside of the specimen.

Thereafter, three metallic holders are installed on the rotating stage of x-ray setup in order to guide the PMMA cell. The PMMA cell position is fixed above the mold by around 2 cm using a screw lock D ring around one of the three metallic holders, in order to keep having an access to the specimen for the next preparation steps. Later, an upper piston connected to a metallic tube is installed so that it passes through the top end of the PMMA cell; see Fig 5.3-12. The upper piston is made as a hollow steel piston similar to the lower piston. The metallic tube at the top of the upper piston is connected to PC₂, by a connection T and an opened valve (C), see Fig 5.4. In order to ensure the full saturation of the upper system above the specimen, a pressure of 10kPa is set by PC₂ so that water flows out from PC₂ through the metallic tube to the upper piston. Once water drops are seen going out of the upper piston, the upper piston is dragged down through the PMMA cell to be placed above the upper stone. The three metallic holders of the PMMA cell and the metallic tube connected to the upper piston allow well-centering the upper piston with respect to the upper stone. After that, the top of the membrane is folded over the upper piston, see Fig 5.3-13, allowing positioning another rubber O-ring over the membrane, to guarantee the seal protecting the inside of the specimen from invasion of the confining water. Before putting the rubber O-ring over the membrane, the valve C is closed in order to stop water flow through the upper piston to the top of the specimen.

Later, zero suction is applied by PC₁, (s_0 at the top of the specimen) to guarantee the full saturation of the whole installed system: PC₁, the porous stone and the specimen. In this condition, the whole circuit: PC₁, specimen and PC₂ is fully saturated. Then

another vacuum system (different than the vacuum connected to the mold) is connected to the metallic tube of the upper piston through a valve (B), see Fig 5.4. The vacuum applied to the inside of the specimen is increased gradually from 0kPa to 50kPa while decreasing the vacuum between the mold and the outside of the membrane. Applying a vacuum to the inside of the specimen allows the specimen to stand resisting its own weight, thus the mold can be removed. Removing the vacuum between the mold and the outside of the membrane means that the membrane will be straightened over the assembly of the porous stone, the lower and upper pistons and pressing on the granular skeleton.

At this point air leakage is inspected; if air is present in the specimen or the upper circuit above the specimen, air bubbles will be seen moving through the transparent connecting tubes due to the vacuum applied to the inside of the specimen. In this case, the source of air leakage is inspected, and if air leakage is coming from the upper circuit (tubes, connection ...etc), the vacuum is stopped and the upper circuit is re-saturated again. If air leakage is not found in the upper circuit, then it is coming from the specimen through a hole in the membrane. In this case, the specimen is abandoned and the procedure is repeated. If air bubbles are not seen through the transparent tubes, after applying the vacuum to the inside of the specimen, then the procedure is continued.

The mold is removed carefully, and the specimen is inspected for its verticality. If not found to be acceptable, the procedure is started again from the beginning, using a new membrane. Once the desired specimen is obtained, the screw lock D ring is opened and the PMMA cell is pushed down slowly so that the cell can be closed. Later, three screws are used to fix the position of the PMMA cell to the metallic circular plate, on the rotating stage as shown in Fig 5.2. On the top of the PMMA cell, a cell cover is placed and screwed to the cell by another three screws. The cell cover is metallic circular plate designed specifically so it fits to the PMMA cell. Later, the cell is filled with water, through a cell pressure inlet shown in Fig 5.2. Once the cell is filled, an adjustable screw at the top of the cell cover is closed. This adjustable screw fix the position of the upper metallic tube connected to the upper piston and thus the position of the upper piston, which is already in contact with the specimen, is fixed. After that, positive air pressure is applied gradually through the cell pressure inlet while decreasing the vacuum applied to the inside of the specimen. When the vacuum applied to the inside of the specimen is zero, the valve B is closed.

The applied positive air pressure is coming from a compressor connected through a pressure regulator, to a pressure-meter, and finally into the bottom of the cell in order to pressurise the confining water.

- In the unsaturated drained and undrained tests, the cell pressure is gradually increased from 0kPa to 200kPa, while decreasing the vacuum applied to the inside of the specimen, with no back pressure. After applying the cell pressure, the upper metallic tube is disconnected from the upper circuit and let to equilibrate with the atmospheric pressure through a water tank used here only for air saturation in water vapour.
- For the saturated drained test, the valve C connecting the upper metallic tube to PC₂ is opened in order to apply back water pressure which will ensure the complete saturation state of the specimen. The aimed values of the cell pressure and back pressure are 250kPa and 50kPa, respectively (i.e., $\sigma_3 = 250 - 50 = 200\text{kPa}$). Thus when

applying cell pressure, air pressure is increased gradually from 0kPa to 200kPa (at this point the vacuum applied to the inside of the specimen is decreased gradually to zero and no back pressure is applied). Then cell pressure and back pressure are increased gradually by 10kPa (for five steps to reach 250kPa and 50kPa respectively) so that the difference between the two is kept equal or less than 200kPa, which is the aimed value of (σ_3) .

Eventually, the specimen is prepared within x-ray cabinet, subjected to zero suction at its top, and cell pressure (isotropic compression) on the surrounding. Later, the three metallic bars guiding the PMMA cell are removed in order not to block x-ray beam when scanning. The position of the specimen is adjusted with respect to the x-ray source and the first scan for a completely saturated specimen is performed. The obtained x-ray radiographies (of a resolution $13\mu\text{m}$) are reconstructed to verify the state of full saturation of the specimen. If air is found within the specimen, the specimen is abandoned and the whole latter procedure is repeated.

Due to the small size of the specimen and the design of the triaxial cell, having a geometrically well prepared saturated specimen at the beginning of the three triaxial tests has proved to be a hard task. The main problems present when preparing the specimen problems can be summarized as:

- The presence of air within the aimed saturated specimen: in this case, the specimen is abandoned and the specimen preparation procedure is repeated.
- The verticality of the specimen: this problem was unavoidable for some performed tests, due to problems in the design of the triaxial cell related to centering the upper piston with respect to the upper stone at the top of the specimen.
- Alignment errors resulted from non-perpendicularity of the end faces of the specimen to the vertical axis of symmetry. This problem caused folding of the membrane in the space between the top of the specimen and the bottom of the upper stone. The specimen preparation procedure in this case is repeated until having the best shape of the specimen that can be obtained with less membrane folding.
- Bedding errors caused by the irregularity of the ends of the bottom porous stone. This problem was unavoidable for some performed tests and caused the presence of some big pores at the top and the bottom of the specimen.

At the end of specimen preparation procedure, the saturated specimen is scanned. For the saturated test, loading process is started immediately after scanning the saturated specimen. For the unsaturated drained test, suction is applied and the specimen is left for three days to reach equilibrium. Later, the specimen is scanned then loaded. Due to the axial shortening and the volumetric changes of the specimen in the drained test (saturated and unsaturated), resulting from loading process, water moves from/to the specimen to/from water tank of the pressure controller. As the suction is constant through the test, thus pore water pressure is constant (i.e., $\Delta u=0$ no excess pore pressure and thus the total stress is equal to the effective stress $\Delta\sigma=\Delta\sigma^{?}$). In the drained tests (saturated and unsaturated), the applied suction is recorded and verified to be constant for the whole test. Unfortunately, water volume exchange cannot be obtained in the triaxial tests, for similar reason mentioned for water retention tests, i.e., small size of the specimen, induced

small water volume that its changes cannot be measured with the pressure controller due to the influence of the ambient temperature and the temperature of the water tank of the controller running for a long time.

For the unsaturated undrained test, suction is applied and the specimen is left for three days to reach equilibrium. After reaching the equilibrium, the valve connecting the specimen to PC_1 (valve A) is closed. In this condition, water content will be constant within the specimen for the whole test ($\Delta V_w=0$) without any possibility for the water to flow in or out the specimen. Due to the axial shortening and the volumetric changes of the specimen in the undrained test, resulted from loading, excess pore pressure is built up (i.e., $\Delta u \neq 0$ and $\Delta \sigma'^u$). Pore water pressure is not measured in this test as the valve connecting PC_1 to the specimen is closed to prevent water flow in/out the specimen.

All the scans in the triaxial tests are performed for x-ray parameters shown in Table 5.1.

As will be shown later in the obtained results of the triaxial tests performed inside x-ray cabinet, a few problems related to the measurement of force and displacement (detailed in section 5.2.9) imposed the necessity of re-performing the three tests outside x-ray cabinet. In these tests (i.e., outside x-ray cabinet), it was hard to verify the presence of leakage due to the small size of the specimen, and thus the small volume of water within the specimen. Since the tests are performed outside x-ray cabinet (i.e., no x-ray acquisition), it was not possible to get x-ray images of the specimen, in order to compare it at the different steps of the test to verify leakage.

5.2.7 Loading system

When setting up for the triaxial tests, and before preparing the specimen, the loading system is installed under the rotation stage, see Fig 5.6. Then, the height of the Lower piston is checked, and if was too high (i.e., not enough space is left for the lower piston and the specimen), the loading head is lowered causing the lower piston to descend. Later, a force meter is installed onto the loading head, and a Linear Variable Differential Transformer (LVDT) is set, by hand, to the beginning of its range, locked in place and zeroed.

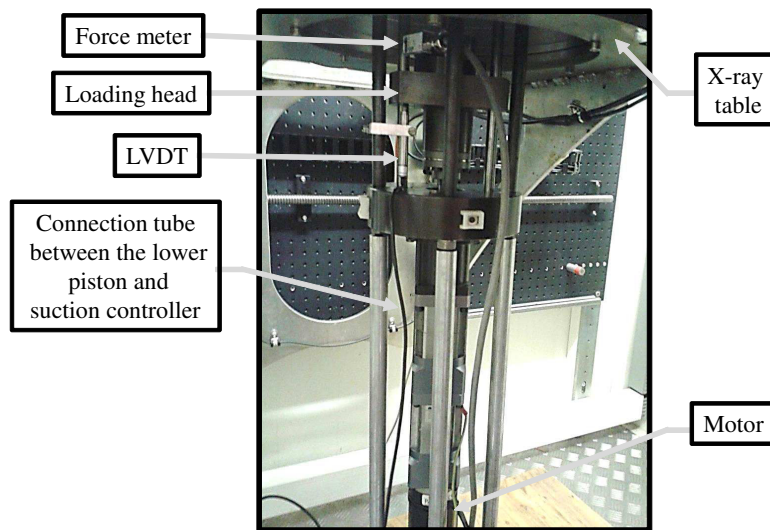


Figure 5.6: Triaxial loading system installed inside x-ray cabinet

After specimen preparing, in order to apply loading on the specimen, the lower piston is advanced by the loading system towards the upper piston. The position of the upper piston, which is already in contact with the specimen through the stone at the top of the specimen, is fixed. Thus advancing the lower piston allows applying the loading. The loading system applies and measures the axial force compressing the specimen from below, and the vertical displacement of the lower piston. The maximum axial force that can be measured by the force meter, which is in contact with the bottom of the lower piston, is 0.5kN. The measurement of the axial displacement is made by the LVDT (shown in Fig 5.1-c, which is attached to a tie bar and measures the vertical displacement of the loading head. These measurements allow plotting the relation between the axial stress and axial shortening during the triaxial test. The speed range for the loading head, shown in Fig 5.1-c, is from $0.1\mu\text{m}/\text{min}$ to $100\mu\text{m}/\text{min}$, which corresponds to a strain rate from 0.0005% to 0.5% per minute (for a specimen of a height 20mm). The speed range considered in this work for the different triaxial tests is $20\mu\text{m}/\text{min}$ (strain rate is 0.1% for a specimen of a height 20mm). The motor is driven remotely from a laptop used for data acquisition. The system of data acquisition registers the force, the cell pressure and LVDT measurements which were calibrated at the beginning of the test. The data acquisition (axial force, axial displacement and cell pressure) is started, before applying air pressure on the confining water, with recording every one second while loading and 60 seconds while scanning. Data acquisition is lowered while scanning since the duration of the test performed in this work (several days) means that recording file can become large, and no change in the measurement is expected during a scan.

5.2.8 Loading procedure

Loading steps are defined in this work from a previous triaxial tests program of dry Hostun sand performed by Edward Andó. In these tests (of a cell pressure 100 and 300kPa), a loading step of 1% is applied. In the stress-strain curves obtained for these tests, a peak is found at loading step (5–8%), followed by strain softening until a plateau of residual stress is reached at (15–20%). Therefore, loading steps, in this work, are chosen so that the previous changes in the stress-strain curve are covered. Table 5.1 shows loading steps for the triaxial tests performed in this work. Suction is applied between the two steps 00 and 01.

Table 5.1: Loading steps for the three triaxial tests performed in this work

Loading Step number	00	01	02	03	04	05	06	07	08	09	10
Axial shortening (ϵ %)	0	1.5	3	4.5	6	8	10	12	15	18	21

The time to apply one loading step is around 15 to 30 min. Once loading step is completed, the specimen is scanned; then reloaded again. The procedure of loading-scanning is repeated until reaching the last loading step 21%. After that, a valve (D), see Fig 5.4, is closed, cell pressure is decreased gradually, pressure controllers are stopped (if any is working), the cell is carefully opened; the whole volume of sand is recovered, dried in an oven for 24 hours (to eliminate any possibly remaining humidity) and then weighed. The weight of the solid phase in the specimen is used to calculate the macroscopic porosity and compare it to the microscopic value calculated in section 5.3.5. In some tests, recovering

process of the whole specimen at the end of the tests was not possible due to the loss of some grains. The small size of the specimen, the use of grease, and the irregularity of the ends of the bottom porous stone are the main factors that caused grain loss. Therefore, the macroscopic porosity measured using the traditional weighing technique for the triaxial tests is not accounted in this work.

Water content within the specimen could not be measured after removing the specimen due to the small size of the specimen, presence of water on the membrane coming from the confining water (i.e., water cell pressure), the presence of saturated filter paper at the top of the specimen, the connectivity of the components of the system: porous stone, specimen and upper piston, which will make separating the specimen from the other components without losing/gaining water content a very hard task. Moreover, the presence of water in the metallic tube above the specimen for the saturated drained test made it hard to recover the specimen without extra water flowing from the tube to the specimen when opening the cell.

5.2.9 Experimental program

Table 5.2 shows a list of the performed and reference tests presented in this work, in order to facilitate recalling them. All the listed tests were performed on Hostun sand specimens. The reference tests were performed, by Edward Andó, on dry Hostun sand specimens, which were slightly bigger in size than the prepared specimens in this work. The dry tests (of different cell pressure) are used only for comparison.

Different problems were faced in the triaxial campaign. Some of these problems were related to having water/air leakage throughout the test. The triaxial setup was examined to define the source of leakage (i.e., by checking and changing tubes and connections, changing O-rings, using grease to ensure water/air tight ...etc). The first test was performed using a thicker membrane (0.5mm than 0.3mm) because it was doubted that the source of leakage might be a significant permeability of the membrane to air, allowing air invasion. However, the membrane was verified later not to be the source of air leakage. Other problems in this campaign are related to technical problems with the data and x-ray acquisition systems. Due to the small size of the specimen and unavoidable contribution of some small vibrations of x-ray equipment in operation, the measurement obtained by data acquisition system was noisy (as will be shown in stress strain curves). The measurement obtained by data acquisition system for the tests performed on dry sand was less noisy compared to the tests performed for saturated/unsaturated sand. Dry sand skeleton seemed to be less influenced by the contribution of the unavoidable vibration of x-ray cabinet, than wet sand. To investigate this influence of vibration, the triaxial tests were re-performed outside x-ray cabinet, as pointed before, by the author with help from a master student Erika Timoschenko. The results obtained for these tests were of the least noisy measurement compared to dry, saturated and unsaturated tests performed inside x-ray cabinet.

Table 5.2: The performed and reference tests presented in this work

Test description	Test name	Specimen size (d x h) (mm)	Cell pressure (kPa)	Performed by	Note
Saturated Drained test (SD)	HN01	10 x 20	250	Author	Membrane thickness 0.5 mm 50 kPa back pressure
Unsaturated Drained test (UD)	HN02	10 x 20	200	Author	-
Unsaturated Undrained test (UU)	HN03	10 x 20	200	Author	Water leakage at loading step 4.5 %
Unsaturated Undrained test (UU)	HN04	10 x 20	200	Author + Erika Timoschenko	Water leakage at loading step 12 %
Saturated Drained test (SD)	HN05	10 x 20	250	Author + Erika Timoschenko	Problem with data acquisition system 50 kPa back pressure
Saturated Drained test (SD-out)	HN06	10 x 20	250	Author + Erika Timoschenko	Outside x-ray cabinet 50 kPa back pressure
Unsaturated Drained test (UD-out)	HN07	10 x 20	200	Author + Erika Timoschenko	Outside x-ray cabinet
Unsaturated Undrained test (UU-out)	HN08	10 x 20	200	Author	Outside x-ray cabinet
Dry test (D)	HN09	11 x 22	100	Edward Andò	-
Dry test (D)	HN010	11 x 22	100	Edward Andò	-
Dry test (D)	HN11	11 x 22	300	Edward Andò	-
Dry test (D)	HN12	11 x 22	300	Edward Andò	-

5.3 Triaxial tests results

5.3.1 Stress-Strain curve

Stress-strain curves, which represent the relation between the axial strain and the axial stress, are presented in the following for all the tests listed in Table 5.2. The axial stress is calculated by the axial force measured over the cross-section of the specimen at each loading increment. The axial force comes from the raw measurement of force with the contribution of the cell pressure being exerted on the cross section of the lower piston removed. The cross-section of the specimen at each loading increment is calculated basing on the assumption of zero volumetric change. The membrane correction has not been applied to these data. The axial strain ($\varepsilon\%$) is obtained from the shortening applied by axial compression of the specimen, with respect to its initial height.

Fig 5.7 shows stress-strain curves for saturated drained HN01 (SD), unsaturated drained HN02 (UD) and unsaturated undrained HN03 (UU) triaxial tests.

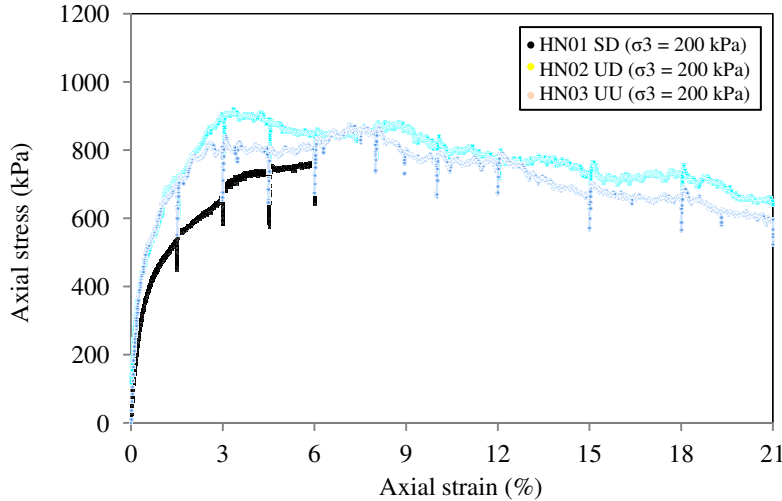


Figure 5.7: Stress-strain curves for HN01 (SD), HN02 (UD) and HN03 (UU)

As shown in Fig 5.7, the stress-strain curve of HN01 (SD) is not presented completely. Unfortunately, a part of the data was missed while performing data processing, therefore, the stress-strain curve of this test is not analysed thoroughly in this work. However, the specimen saturation state was excellent through the whole test (i.e., no leakage problems), as well as the image quality, thus DIC has been performed for this test and presented in this work.

For HN03 (UU), it was supposed that water content should be constant through the whole tests. Conversely, it was found that water content decreases slightly at the beginning of the test (at $\varepsilon=4.5\%$). However, the test has been continued and water leakage was observed, from x-ray reconstructed images, to be increasing until reaching a completely dry specimen at the end of the test. Therefore, this test was not considered in this work.

Nevertheless, the test HN02 (UD), presented none of these problems. Therefore, the analysis of HN02 (UD) test will be specially elaborated in this work. The stress-strain curve of the specimen shows a progression to a slightly descending plateau, showing peri-

odic oscillations, which are believed to be due to some perturbations in the measurement system. The plateau is considered to be reached at axial strain $\varepsilon=4.5\%$, and continue with no apparent changes until $\varepsilon=21\%$.

Fig 5.8 shows stress-strain curves for unsaturated undrained HN04 (UU) and saturated drained HN05 (SD) triaxial tests. These two tests were the main set of tests performed in the master thesis of Erika Timoschenko with help of the author.

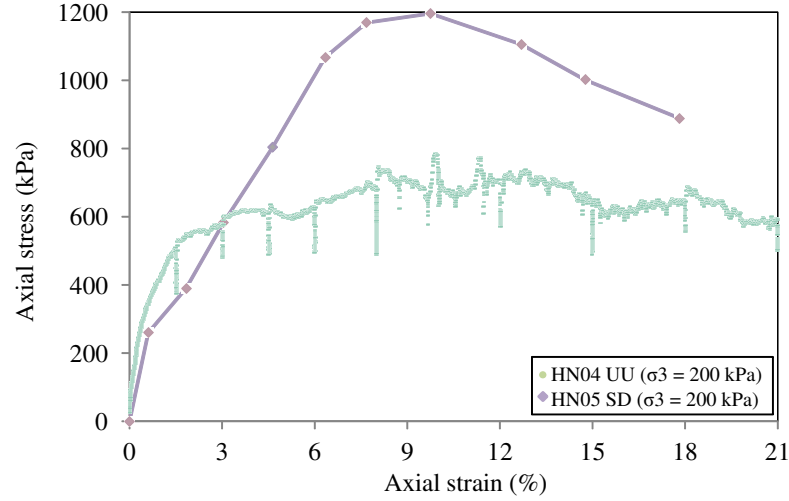


Figure 5.8: Stress-strain curves for HN04 (UU) and HN05 (SD)

In the test HN04 (UU), leakage was observed at 12% then it increased through the test to reach a completely dry specimen at the end of the test. However, DIC was performed for this test by Erika Timoschenko and will be presented in this work for comparison. For HN05 (SD), as shown in Fig 5.8, the measurement of stress-strain curve was problematic, therefore the test was not considered.

Fig 5.9 shows stress-strain curves for saturated drained HN06 (SD), unsaturated drained HN07 (UD) and unsaturated undrained HN08 (UU) triaxial tests. These tests were performed outside x-ray cabinet.

As shown in the figure, the measurements of stress-strain of the three tests were smooth compared to HN02 (UD), for example, performed inside x-ray cabinet. However, without x-ray scanning, one cannot guarantee the presence of leakage (if any).

The three tests HN06 (SD), HN07 (UD) and HN08 (UU), have relatively similar macroscopic porosity (38.3%, 38.9% and 38.9%, relatively), measured using the traditional technique (i.e., weighing the specimen at the end of the test). The three specimens behave as expected for a dense granular material: there is a peak in the specimens axial stress response, followed by strain softening until a plateau of residual stress is reached. The peak is reached for the three tests HN06 (SD), HN07 (UD) and HN08 (UU), at axial strain $\varepsilon=8\%$, $\varepsilon=10\%$ and $\varepsilon=6\%$, and at axial stress $\sigma=1098\text{kPa}$, $\sigma=975\text{kPa}$ and $\sigma=743\text{kPa}$, respectively. The residual stress for HN06 (SD), HN07 (UD) and HN08 (UU), is $\sigma=847\text{kPa}$, $\sigma=803\text{kPa}$ and $\sigma=607\text{kPa}$, respectively.

The differences in the stress-strain curves of the three specimens HN06 (SD), HN07 (UD) and HN08 (UU), are suggested to be due to that the three tests are performed at different conditions (saturated/unsaturated and drained/undrained). Water content (or

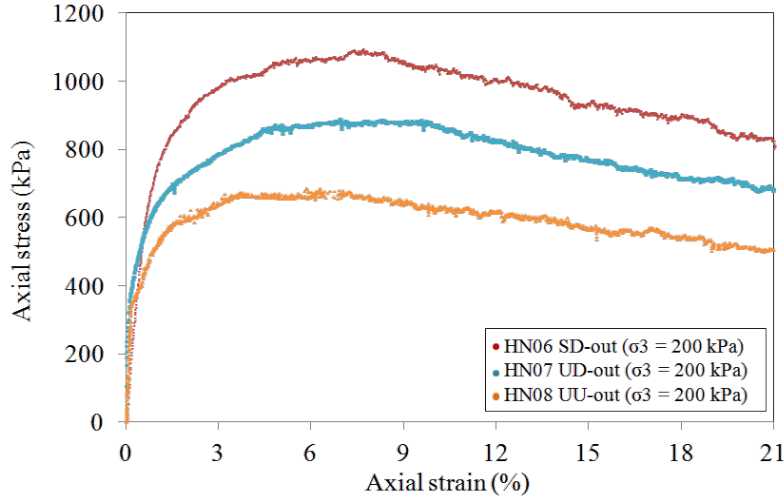


Figure 5.9: Stress-strain curves for HN06 (SD), HN07 (UD) and HN08 (UU)

suction) influence can be used to justify these differences, however, cohesion contribution cannot be considered when comparing the behaviour of the three specimens, due to the high cell pressure (200–250kPa) applied in these tests. Moreover, the macroscopic porosity which showed to be more or less the same for the three tests, may not be reliable due to grain loss (as pointed before). The macroscopic porosity influence could also be used to justify the differences in stress-strain curves for the three tests, when reliably obtained.

For all the latter reasons, , the differences in the hydro-mechanical behaviour of the three tests HN06 (SD), HN07 (UD) and HN08 (UU) cannot be well-interpreted, therefore, these tests are presented in this work, only to show the influence of the perturbation, due to x-ray data acquisition, on stress-strain curve.

Finally, stress-strain curves for all the tests, including the reference tests are presented in Fig 5.10. In Fig 5.10-bottom, the axial stress (σ_1) is normalized by the cell pressure (σ_3) in order to exclude the influence of the different values of cell pressure.

From the figure, it is shown that the saturated and unsaturated drained (HN01, HN02 and HN05) and the unsaturated undrained tests (HN03 and HN04) performed inside x-ray cabinet are comparable to the saturated and unsaturated drained (HN06 and HN07) and unsaturated undrained (HN08) tests performed outside x-ray cabinet. As stated before, the noise (multi-peaks) in the stress-strain curves performed inside x-ray is attributed to the unavoidable contribution of the vibration of x-ray equipment in operation. The saturated drained triaxial tests show different stress-strain responses, though they are performed for the same $\sigma_3=200\text{kPa}$. The reason behind that can be due to the different initial porosities or the problems in the acquisition system when measuring the axial force and displacement. The tests performed by the author (i.e., saturated and unsaturated, drained and undrained tests) for $\sigma_3=200\text{kPa}$ are of a smaller stress ratio compared to the dry tests performed for $\sigma_3=100\text{kPa}$ and $\sigma_3=300\text{kPa}$. This is due to the higher relative density of the dry tests (73–95%) compared to the relative density for the saturated and unsaturated tests (62–68%). The reduction in the axial stress for the saturated and unsaturated tests can be explained by the change in suction and water content when compared to the dry tests, however, when working with sand, cohesion contribution at high cell

pressure is negligible and cannot be analyzed.

In conclusion, the tests that will be analysed in this work are listed in the following:

- Saturated drained triaxial test HN01: only DIC analysis is performed for this test.
- Unsaturated drained triaxial test HN02: the main test in this work.
- Unsaturated undrained triaxial test HN04: only DIC analysis is performed for this test.

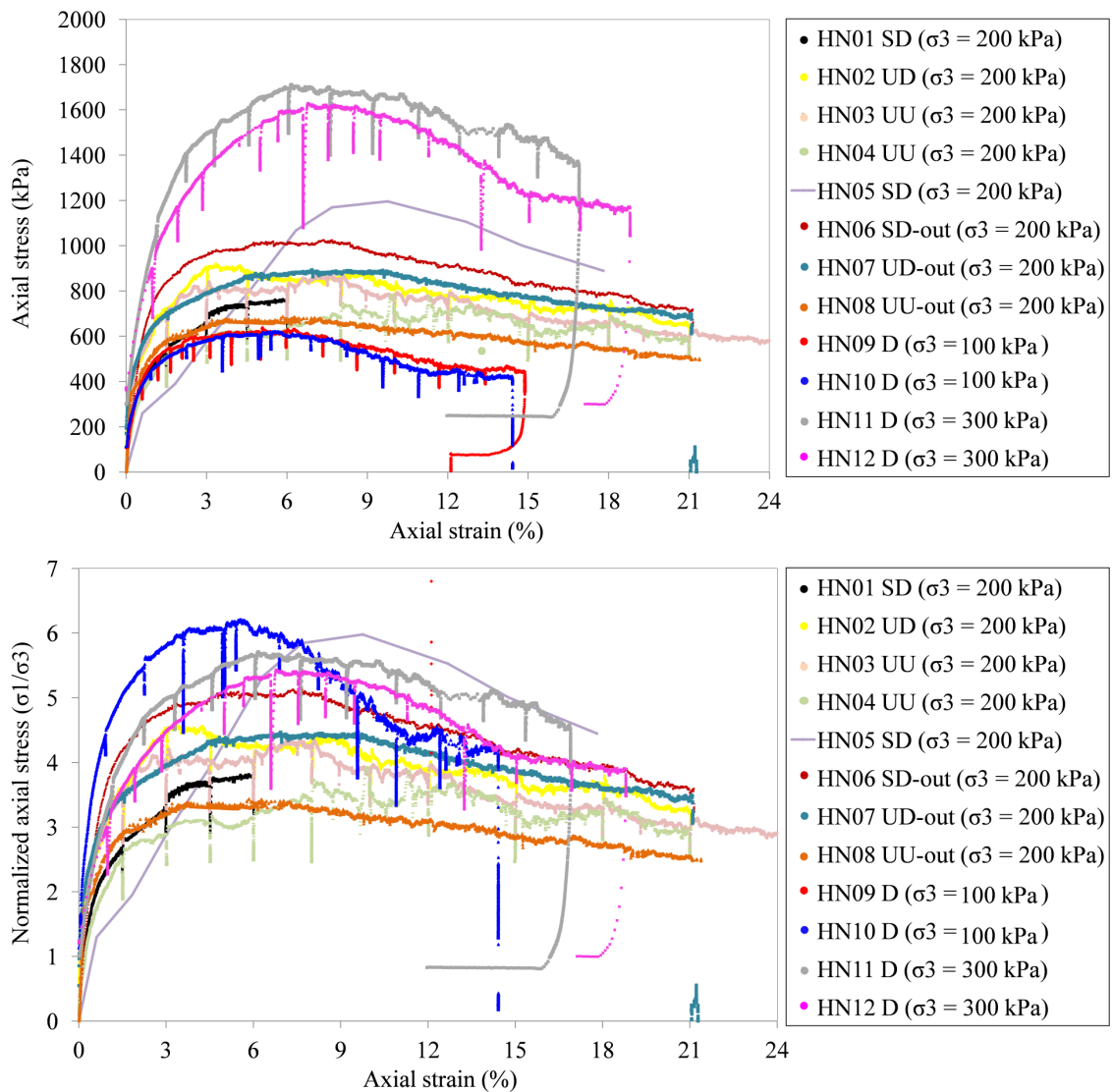


Figure 5.10: Stress-strain curves for all the performed and reference triaxial tests. In Fig 5.10-bottom, the axial stress (σ_1) is normalized by the cell pressure (σ_3) in order to exclude the influence of the different cell pressure

5.3.2 Volumetric response

Using image processing tool Fiji and the trinarized images (to be presented in section 5.3.3), the bulk volume of the specimen is obtained. The bulk volume is defined in this work as the volume of pores and solid within the membrane surrounding the specimen and between the porous stones. Trinarization technique allowed separating the membrane and the two porous stones in the images. The two porous stones are cut from the trinarized volumes by cutting all the slices that pass through them. As has been presented in chapter 4, cutting the porous stones might remove also some grains (400–500 grains). The number of grains within the triaxial specimen, obtained using Visilog[®], is 45000 grains. Similar to water retention tests, the influence of the removed grains at the top and the bottom of the triaxial specimen may be considered as a boundary condition effect (i.e., including the removed top and bottom parts of the specimen would not be representative when performing porosity measurements of the specimen).

In order to obtain the bulk volume, grain phase was separated from the trinarized images using Fiji by applying a simple threshold equal to grains value in the trinarized images (255 gray value). Then grain phase in the images was dilated in 3D 10 times (a number estimated to fill almost all of the pores in the specimens tested). Later, the fill holes process (one of the tools provided by Fiji) was applied and when the volume appeared with zero porosity, it was eroded 10 times so it would return to its initial perimeter (in order to obtain the original grain outlines, on the edge of the volume). The result of this process is 3D volumes (images), in which voxels belong either to the inside of the specimen or to the outside of the specimen. Counting the number of voxels inside the specimen (from the histogram), the bulk volume can be computed.

The bulk volume was computed at each loading step and the volumetric strain was calculated accordingly, with respect to the initial volume of the specimen and the volume of the specimen after applying the suction (i.e., at $\varepsilon=0\%$). The procedure is illustrated in 2D in Fig 5.11.

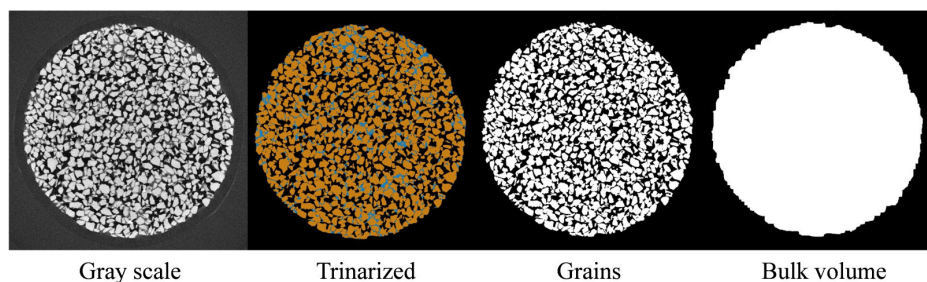


Figure 5.11: The specimen volume measurement procedure

The volumetric strain plots for the unsaturated drained test HN02 (UD) and the reference dry test HN09 (D) are shown in Fig 5.12. Fig 5.12-top shows the volumetric strain for HN02 (UD) computed with respect to the initial volume of the specimen and Fig 5.12-bottom shows the volumetric strain for HN02 (UD) computed with respect to the volume of the specimen after applying the suction (i.e., at $\varepsilon=0\%$).

The specimen HN02 (UD) can be seen to have a considerable contraction when suction is applied (shown by vertical segment on the Y axis, from 0 towards 2, in Fig 5.12-top). Later, beyond $\varepsilon=4.5\%$, the volumetric response of the specimen is dilatant.

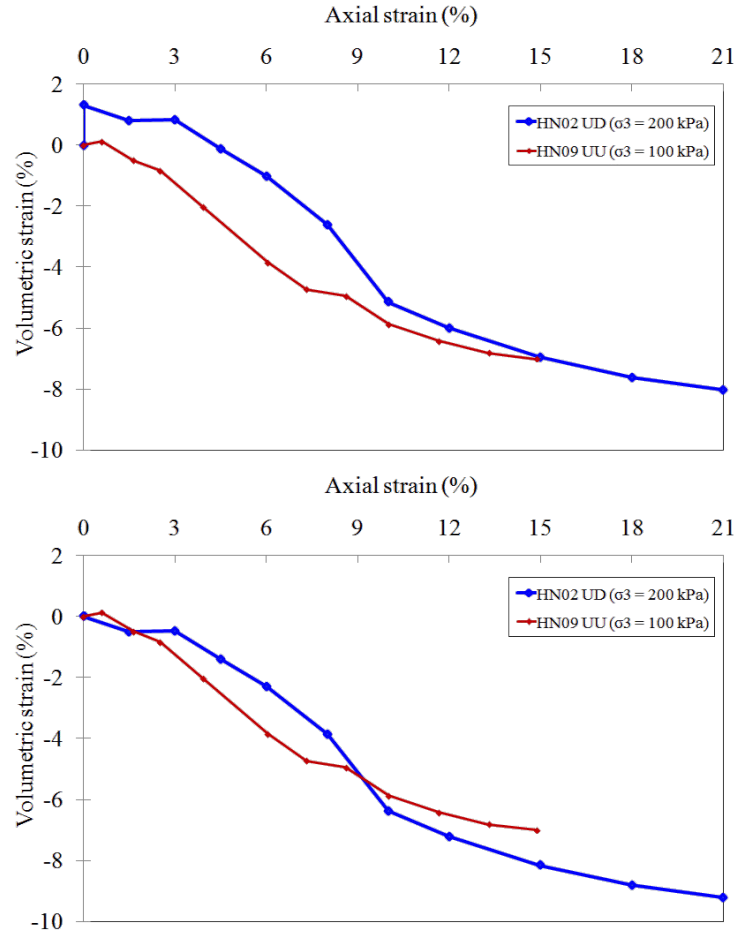


Figure 5.12: The volumetric strain for the unsaturated drained test HN02 (UD) and the reference dry test HN09 (D). In the top plot, the bulk volume for HN02 (UD) is computed with respect to the initial volume of the specimen and in the bottom plot the bulk volume for HN02 (UD) is computed with respect to the volume of the specimen after applying the suction (i.e., at $\varepsilon=0\%$)

The specimen HN09 (D) is less contracted at the beginning of the test compared to HN02 (UD). The dilatancy slope of HN09 (D) is more or less the same as for HN02 (UD), in their main dilatancy zone (from 3% to 9%), then HN02 (UD) has a short excess of dilatancy (steeper slope around 9% as shown in Fig 5.12-bottom) while HN09 (D) has a short loss of dilatancy, and finally HN09 (D) plateau shows less overall dilatancy than HN02 (UD).

5.3.3 Trinarization results

Similar to retention tests, the segmentation process of the phases is performed to extract more qualitative and quantitative information from the reconstructed x-ray images. This information is related to the macro-micro porosity and degree of saturation of the sand specimen, fluid phase distribution, continuity, contacts and evolution with the mechanical loading.

Fig 5.13 shows central vertical slices of the same azimuth (same direction in the horizontal plane), in the trinarized volumes, after removing the upper and the bottom porous stones, for all the loading steps in the triaxial test HN02 (UD).

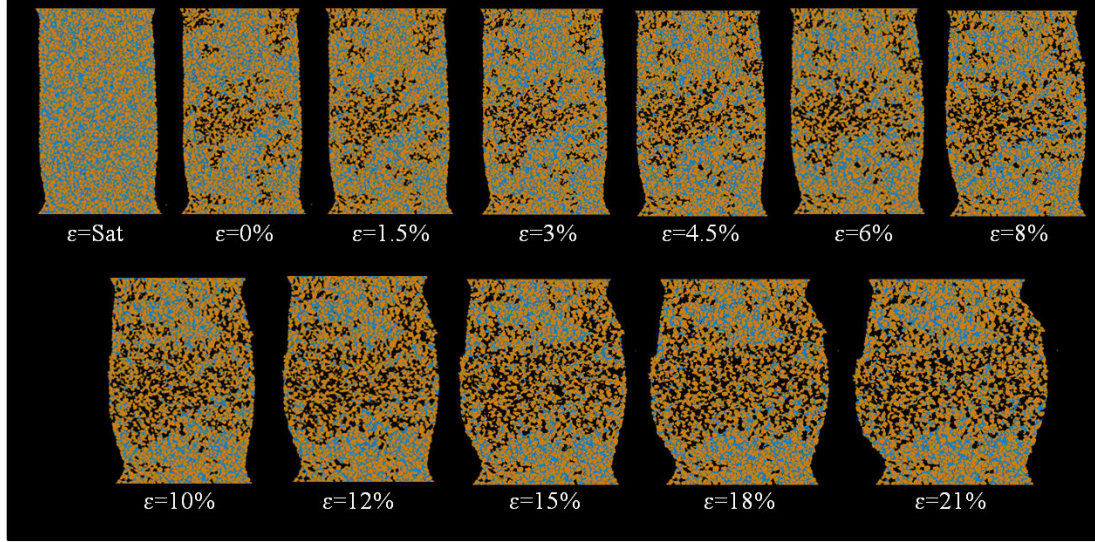


Figure 5.13: Central vertical slices of the same azimuth, in the trinarized volumes, after removing the upper and the bottom porous stones, for all the loading steps ($\varepsilon=0\%$) in the triaxial test HN02 (UD)

At the beginning of the test, the specimen is completely saturated. Then suction is applied. After reaching equilibrium, loading is started. It is clear from the trinarized images that higher porosity is found in the middle part of the specimen (see Fig 5.13 at axial strain $\varepsilon=0\%$). As the test is drained, water volume within the specimen is changing with loading. Water flow out first from the middle part of the specimen and gets concentrated in the upper and lower parts (see Fig 5.13 at axial strain $\varepsilon=21\%$).

It is important to note that water flow in triaxial tests could be local or global. The local flow of water includes the redistribution of water phase within the specimen. This flow can be present in drained and undrained triaxial tests. The global flow highlights the flow of water in/out of the specimen (present only in drained triaxial test), i.e., water content within the specimen is increasing/decreasing with loading. Moreover, in the triaxial tests performed in this work, including HN02 (UD), loading process was directly followed by scanning the specimen without allowing water phase to reach equilibrium after loading. However, the porous stone used in the triaxial tests performed in this work (located below the specimen and of air entry value 100kPa) is of high permeability, therefore, it is expected the equilibrium state of water phase is reached. Furthermore, the time needed to reach equilibrium, using a porous stone of air entry value 100kPa is not known (the time to reach equilibrium using a porous stone of air entry value 500kPa as in the retention test is 3 days). This time extends the duration of the whole triaxial test and block x-ray acquisition for other users as the triaxial test cannot be removed to the outside of x-ray cabinet. Therefore, and due to time limitation it was not possible in this triaxial campaign to verify equilibrium state of water phase.

More detailed results of trinarization technique can be found in Appendix E. These results allow performing a comparison between the reconstructed and the trinarized im-

ages in the horizontal and vertical planes, and thus evaluating the efficiency of using the trinarization technique, for the triaxial test HN02 (UD). In this appendix, Fig (E-1) shows central vertical slices in the reconstructed and trinarized volumes for all loading steps in the unsaturated drained triaxial test HN02 (UD).

5.3.4 Macroscopic porosity and degree of saturation results

Macroscopic measurements of porosity and degree of saturation are performed for the triaxial test HN02 (UD), in order to analyze the macroscopic influence of these two variables on the hydro-mechanical behaviour of the Hostun sand specimen (i.e., shear strength, volumetric response and water distribution). Using the trinarized images, macroscopic porosity and degree of saturation is calculated for each loading step. The histogram of the trinarized images gives the number of voxels that represent air (N_a), water (N_w) and grains (N_g). Porosity is calculated as $n = V_v/V_t = (N_w + N_a)/(N_w + N_a + N_g)$ and the degree of saturation is calculated as $S_r = V_{wt}/V_v = N_w/(N_w + N_a)$. Fig 5.14 shows the evolution of the macroscopic porosity and degree of saturation calculated from the trinarized volumes, with loading for the triaxial test HN02 (UD).

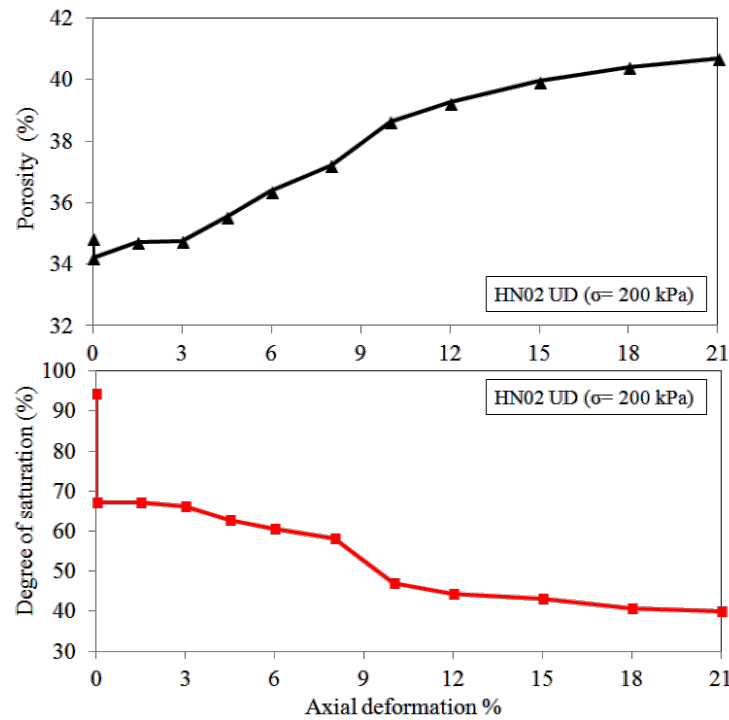


Figure 5.14: The evolution of the macroscopic porosity (up) and degree of saturation (down) with loading for the triaxial test HN02 (UD)

After suction application on the saturated specimen, the degree of saturation changes from $S_r=100\%$ to $S_r=67\%$. The porosity of the specimen at the beginning of the triaxial test is $n=34.6\%$. When loading is applied, the porosity slightly decreases then increases as the loading is increasing to reach a maximum value at the end of the test $n=40.7\%$. Simultaneously, the degree of saturation decreases as increasing the loading to reach a minimum value at the end of the test $S_r=39.9\%$.

At $\varepsilon=8\%$, the degree of saturation changes remarkably (shown by an increase in the slope in Fig 5.14) by $\Delta Sr=11\%$, while before and after $\varepsilon=8\%$, $\Delta Sr \leq 3.4\%$.

The evolution of the macroscopic porosity is consistent with the volumetric response of the specimen presented in Fig 5.12. The compaction of the specimen at the beginning of the test is accompanied by a reduction in the porosity. Similarly, the dilation of the specimen through the test is accompanied by an increase in the porosity.

5.3.5 Microscopic porosity and degree of saturation results

The local measurements of porosity and degree of saturation are performed for all loading steps in the unsaturated drained triaxial test HN02 (UD), in order to characterize the hydro-mechanical behaviour of Hostun sand at the local scale. The optimal REV size, over which the local porosity and degree of saturation are measured, is defined following the analysis presented in chapter 3, section 3.4. It is found that a size of REV (length of one side of the REV) equal or bigger than 80px ($\approx 3 \times D_{50}$) is optimal for the measurements of porosity and degree of saturation, in the triaxial tests HN02 (UD). This REV is obtained for stability criteria $\Delta n=0.1$ for porosity and $\Delta Sr=0.5$. In this work, a size of REV equal to 80px is fixed for all the following measurements of the porosity and degree of saturation. The resulted maps of the local porosity and degree of saturation are presented by $20 \times 20 \times (19-15)$ nodes, i.e., the number of measurements on Z direction is ranging between 19 to 15 measures as the height of the specimen is decreasing. Overlapping of the measurement is not allowed for local porosity measurement in this section, nor for degree of saturation; i.e., in both cases, node spacing is set to be equal to the size of REV.

Fig 5.15 show central vertical (XZ) slices in the porosity map, of the same azimuth, for all loading steps, in the unsaturated drained triaxial test HN02 (UD). In this figure, n_{\max} and n_{\min} represent the maximum and the minimum porosity respectively (written below loading step). Fig 5.16 show central vertical (XZ) slices in the degree of saturation map, of the same azimuth, for all loading steps, in the unsaturated drained triaxial test HN02 (UD).

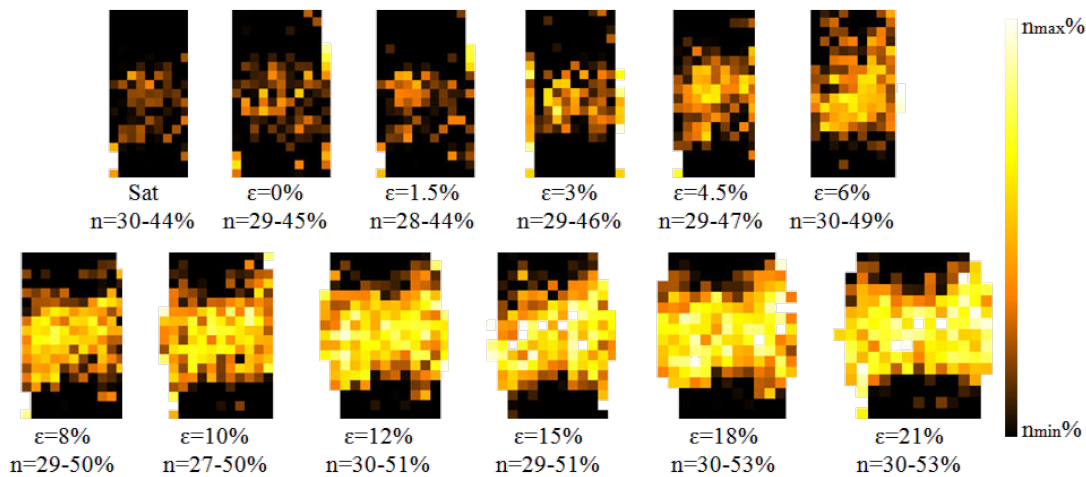


Figure 5.15: Porosity map for all the steps of loading in the unsaturated drained triaxial test HN02 (UD). In this figure, n_{\max} and n_{\min} represent the maximum and minimum microscopic porosity, respectively, shown below loading step

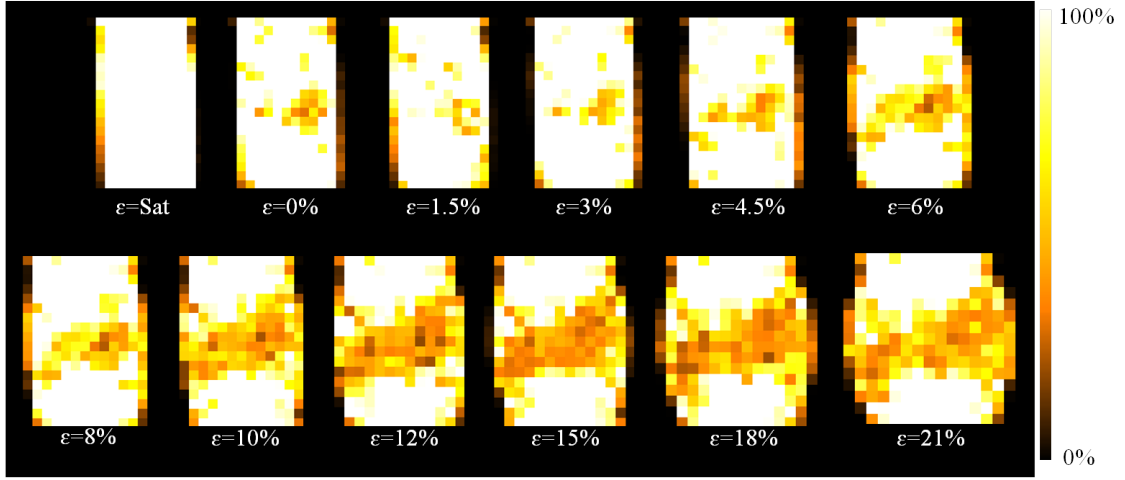


Figure 5.16: Degree of saturation map for all the steps of loading in the unsaturated drained triaxial test HN02 (UD)

The macroscopic porosity calculated using the trinarized images ($n=34\text{--}40.7\%$) is within the range of the microscopic porosity $n=(28\text{--}53\%)$, obtained from porosity map presented in Fig 5.15. Similarly, the macroscopic degree of saturation calculated using the trinarized images ($S_r=40\text{--}100\%$) is within the range of the microscopic degree of saturation $S_r=(0\text{--}100\%)$, obtained from degree of saturation map presented in Fig 5.16. The contrast of the degree of saturation maps show that water distribution within the specimen at the beginning of the test is homogeneous (almost all REV's are of $S_r=100\%$). After suction application the homogeneity of water distribution decreases as increasing the loading. The ranges of the microscopic porosity indicate a heterogeneous distribution of the porosity within the specimen.

The vertical slices in the porosity map, presented in Fig 5.15 show that the porosity at the top and bottom of the specimen is lower than the porosity in the middle part of the specimen. Conversely, the degree of saturation at the top and bottom of the specimen is higher than the degree of saturation in the middle part of the specimen. This can be seen clearly in Fig 5.17 shown for $\varepsilon=21\%$ in the triaxial test HN02 (UD). In this figure, the red dashed rectangle in the trinarized image marks the middle part of the specimen where higher porosity is consistent with lower degree of saturation. The red vertical dashed line in Fig 5.17 represents a column of 14 voxels, for which the vertical profile of porosity and degree of saturation is plotted in Fig 5.18.

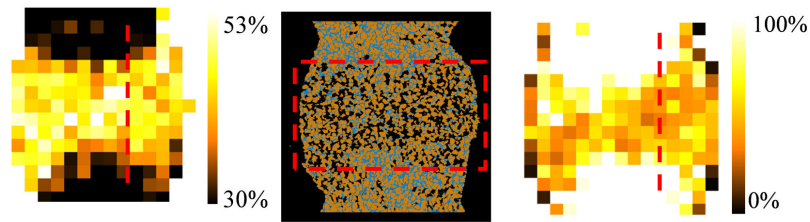


Figure 5.17: Central vertical slices in the porosity map (left), trinarized volume (middle) and degree of saturation map (right) for loading step $\varepsilon=21\%$ in triaxial test HN02 (UD)

The trend of the relation between porosity and degree of saturation during the triaxial test HN02 (UD) is similar to the one found for the retention tests, i.e., an increase in the porosity induces a decrease in the degree of saturation.

From Fig 5.15 and Fig 5.16, the evolution of the sheared zone of the specimen can be given qualitatively. As shown in the figures, the middle part of the specimen showed a higher porosity region at suction application step. As increasing the loading, this region dilated and its water content decreased. These observations indicate the presence of higher deformation (shearing) in the middle part of the specimen highlighted by the contrast difference in the porosity and degree of saturation maps.

Using porosity and degree of saturation histograms, the mean microscopic porosity and degree of saturation is defined. Table 5.3 shows the mean microscopic porosity and degree of saturation for all loading steps in the triaxial test HN02 (UD). The mean microscopic measurements show that, the porosity is increasing with loading while the degree of saturation is decreasing, which is consistent with the macroscopic measurements.

Table 5.3: Mean microscopic porosity and degree of saturation for all loading steps in the triaxial test HN02

Axial shortening(ϵ %)	0	0 ($s=2.2$ kPa)	1.5	3	4.5	6	8	10	12	15	18	21
Mean microscopic n (%)	36	35.7	35.8	36.2	38.1	39.3	39.4	40.3	42.9	42.9	47	47.4
Mean microscopic S_r (%)	94.1	67.4	66.6	67.2	63.6	60.5	57.7	44.7	40.6	39.4	36	38.1

Porosity and degree of saturation vertical profiles are shown in Fig 5.18. The two vertical profiles are drawn for the red dashed lines in the porosity and degree of saturation maps shown in Fig 5.17, which represent columns of 14 voxels in the porosity and degree of saturation maps.

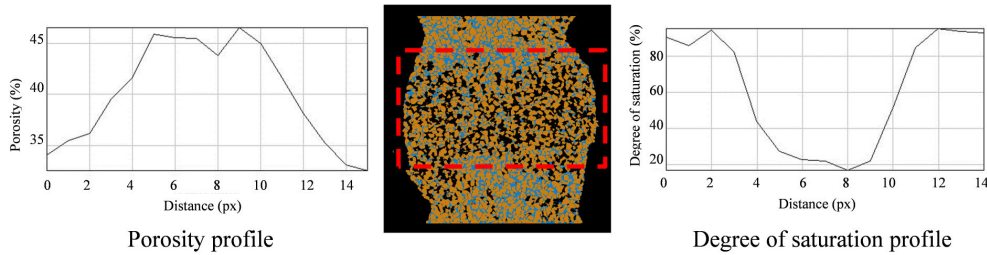


Figure 5.18: Porosity vertical profile (left), central vertical slice in the trinarized volume (middle) and degree of saturation vertical profile (right) for loading step $\epsilon=21\%$ in triaxial test HN02

As shown from Fig 5.18-left, the porosity increases gradually from $n=34.8\%$ at the top of the specimen, to reach a maximum value in the middle part of the specimen $n=45.2\%$ then decreases at the bottom of the specimen $n=34.6\%$. Simultaneously, the degree of saturation decreases from $S_r=90\%$ at the top of the specimen, to reach a minimum value in the middle part of the specimen $S_r=18\%$ then increases at the bottom of the specimen $S_r=96\%$, as shown in Fig 5.18-right.

More detailed results of porosity and degree of saturation mapping can be found in Appendix E. These results allow visualizing the variation and spatial distribution of porosity

and degree of saturation measurements over the whole specimen and obtaining quantitative description from the histogram, during the triaxial test HN02 (UD). In this appendix, Fig (E2) shows central vertical slices in the porosity map, histogram and vertical profile for all loading steps in the unsaturated drained triaxial test HN02 (UD). Fig (E-3) shows central vertical slices in the degree of saturation map, histogram and vertical profile for all loading steps in the unsaturated drained triaxial test HN02 (UD).

5.3.6 Microscopic-discrete analyses results

Microscopic-discrete analyses are performed in this chapter in order to identify and follow the individual grains and fluid clusters within the specimen in 3D, for HN02 (UD) test, and to understand the interaction between the phases and their contacts during shearing. Moreover, the microscopic-discrete results can be used to evaluate the contribution of suction or water content (i.e. cohesion) to shear strength of the tested sand. In addition, the microscopic-discrete results can help to explain the homogeneity/heterogeneity of the specimen for HN02 (UD) test, with respect to water distribution due to suction application at the beginning of the test, and loading and the correspondent deformation during the test.

5.3.6.1 The evolution of the number of fluid clusters with the mechanical loading

Using the trinarized volumes and the commercial code Visilog[®], the three phases within the specimen HN02 (UD) are labelled and analyzed. Later, the relation between the number of fluid clusters versus the axial strain is plotted. Then fluid cluster size distribution is obtained and fluid cluster of the maximum volume (V_{\max}) is extracted. The relation between the normalized V_{\max} and the axial strain is plotted.

Fig 5.19 shows central vertical slices of the same azimuth in the labelled volume of water, for all the loading steps in the triaxial test HN02 (UD). Fig 5.20 shows central vertical slices of the same azimuth in the labelled volume of air, for all the loading steps in the triaxial test HN02 (UD).

More detailed results of labelling process can be found in Appendix E. These results helps comparing the trinarized and labelled slices, visualizing the spatial distribution of water and air phases with respect to the grain phase and quantifying the size each fluid clusters, during the triaxial test HN02 (UD). In this appendix, Fig (E-4) shows central vertical slices in the water labelled volumes, trinarized volumes and air labelled volume, for all loading steps in the unsaturated drained triaxial test HN02 (UD).

The different colors in all the labelled volumes of fluid phase in HN02 (UD) represent different fluid clusters. Though, it is important to note that, for the same loading step, different fluid clusters of different Identifications (Ids) might have the same color. In addition, there is no link between the color of the fluid cluster and the loading step, i.e. the color of fluid cluster changes from one loading step to another. Fluid cluster in HN02 (UD) test is followed from one loading step to another by its Id not by its color.

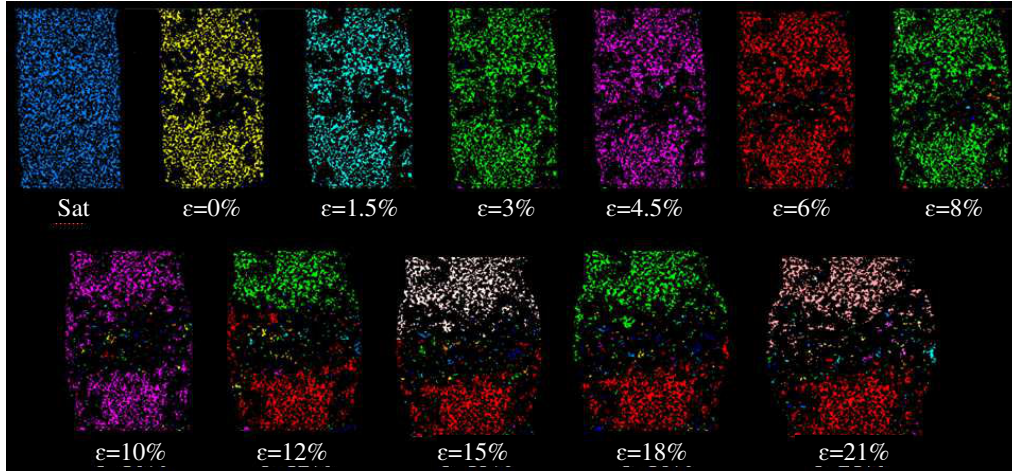


Figure 5.19: Central vertical slices in the water labelled volume, of the same azimuth for all loading steps in the triaxial test HN02 (UD)

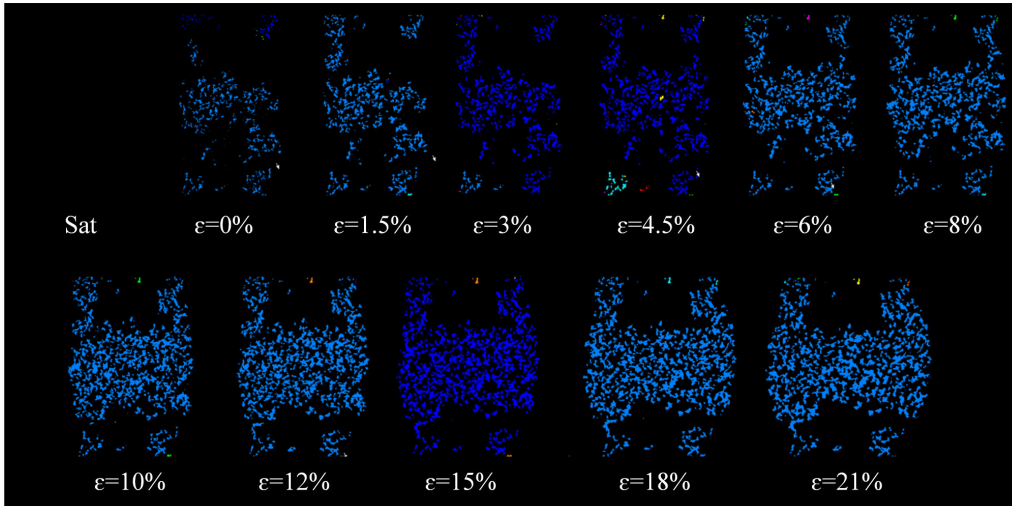


Figure 5.20: Central vertical slices in the air labelled volume, of the same azimuth for all loading steps in the triaxial test HN02 (UD)

As shown in Fig 5.19 and Fig 5.20, the specimen is completely saturated at the beginning of the test, with one big water cluster and no air clusters (i.e., water phase is continuous). As suction is applied, water volume decreases and air enters the specimen, mainly in the middle part and the boundaries. When loading is applied, water and air volumes redistribute within the specimen.

At $\epsilon=10\%$ water big cluster is divided into two big clusters, located at the top and the bottom of the specimen, and small water clusters are randomly distributed in the middle part of the specimen. On the other hand, air phase is in the form of one big cluster (i.e., air phase is continuous) and randomly distributed small clusters through the whole triaxial test.

Using the labelled volume of fluid phase the number of fluid clusters is obtained. Later, the relation between the number of fluid clusters versus the axial strain is plotted. Fig

5.21 shows the evolution of the number of water and air clusters with axial strain, for all loading steps in the triaxial test HN02 (UD). As shown in Fig 5.21, the number of water clusters increases with the mechanical loading while the number of air clusters decrease at the beginning of the tests then becomes constant. The evolution of the number of water clusters versus the axial strain shows that the specimen is saturated at the beginning of the test, with one big water cluster. Later, the number of the clusters increases (i.e., the one big cluster divides into smaller clusters) as the suction $s=2.2\text{kPa}$ is applied. Through the test, when increasing the loading step, the number of water clusters within the specimen increases to reach a maximum value at the end of the test $\varepsilon=21\%$. For air clusters, the specimen has no air clusters at the beginning of the test since the specimen is completely saturated. Later, once suction is applied, the number of air clusters increases. As the first loading step $\varepsilon=1.5\%$ is applied, the number of air clusters decreases. Increasing the loading beyond $\varepsilon=1.5\%$, no remarkable changes in the number of air clusters within the specimen are observed.

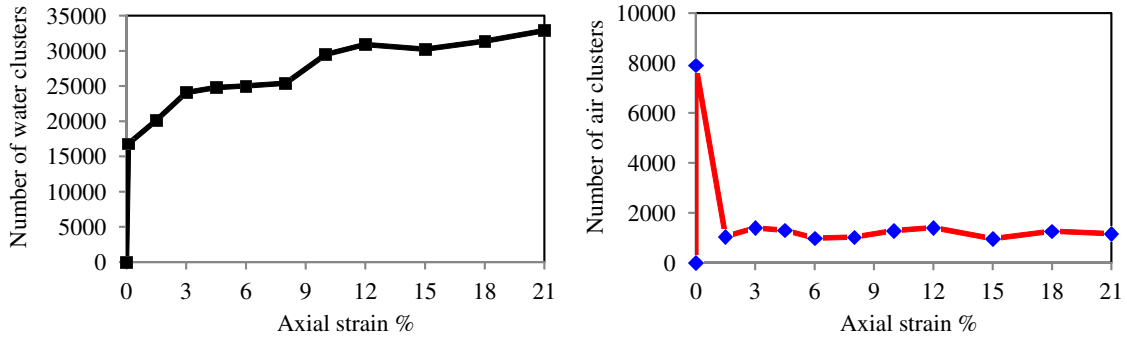


Figure 5.21: The evolution of the number of water clusters (left) and air clusters (right) with loading, for the triaxial test HN02 (UD)

In Fig 5.22 and Fig 5.23 water and air clusters size distribution are presented for the triaxial test HN02 (UD), respectively. The different curves refer to different cluster size distribution at different loading steps, defined by the global axial strain ($\varepsilon\%$). Note that in the figures showing fluid size distribution, the curves can be superposed.

Water clusters size distribution in Fig 5.22 shows that when the loading is increased, water clusters size distribution curve moves upward and the size of the biggest water cluster decreases, i.e., the volume of water in the small clusters increases. The physical process behind this representation is the following : as the loading progresses, the specimen deforms and dilates, not quite homogeneously, inducing the biggest water cluster in the specimen to divide into a larger number of clusters and thus the volume of the biggest cluster decreases and the total volume of the smaller clusters increases. When the specimen is saturated, the biggest cluster forms around 99% of the total volume of water within the specimen. For suction application step and loading steps in the range $\varepsilon=(0-8\%)$, the curves in the Fig 5.22 shows that the volume of the smaller clusters forms around 5% of the water volume, and the biggest cluster forms more than 95% of the total volume of water within the specimen. When increasing the loading in the range $\varepsilon=(10-21\%)$, several big clusters are found in the specimen and they form about 80% of the total volume of water within the specimen. Water clusters distribution curves, for all loading steps, take the form of a continuous range of sizes of water clusters at the beginning and a big cluster at

the end (shown within the red dashed rectangle). For the range $\varepsilon=(10-21\%)$, several big clusters are found in between the biggest cluster and the small clusters (shown in Fig 5.22 within a black dashed rectangle).

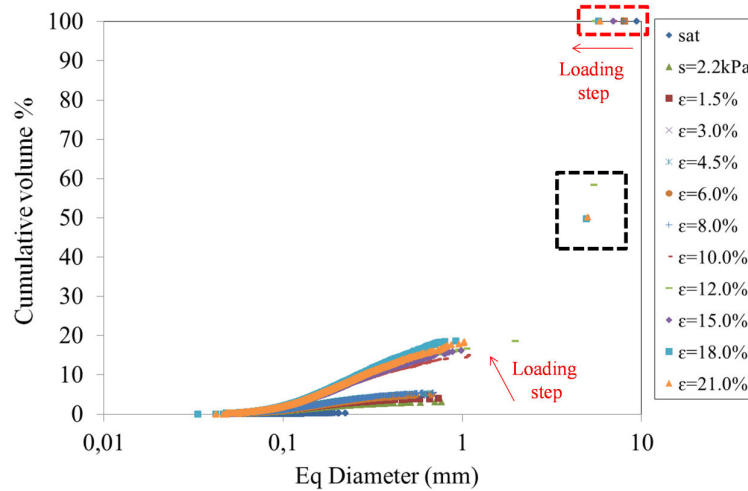


Figure 5.22: Water clusters size distribution for all loading steps in the triaxial test HN02 (UD)

For air clusters size distribution, when the specimen is saturated, air clusters do not exist within the specimen (no curve). As suction is applied, air enters the specimen. Through the test, when the loading is increased, the EqD of the biggest air cluster increases as shown within the red dashed rectangle in Fig 5.23. In this figure, air clusters size distribution is presented as a curve that begins with very small clusters that form less than 1% of the cumulative volume of air within the specimen, and ends with a very big cluster (shown in the figures within a red dashed rectangle). In between several big clusters exist within the specimen (within the black dashed rectangle in Fig 5.23) and forms with the biggest cluster more than 99% of the cumulative volume of air within the specimen.

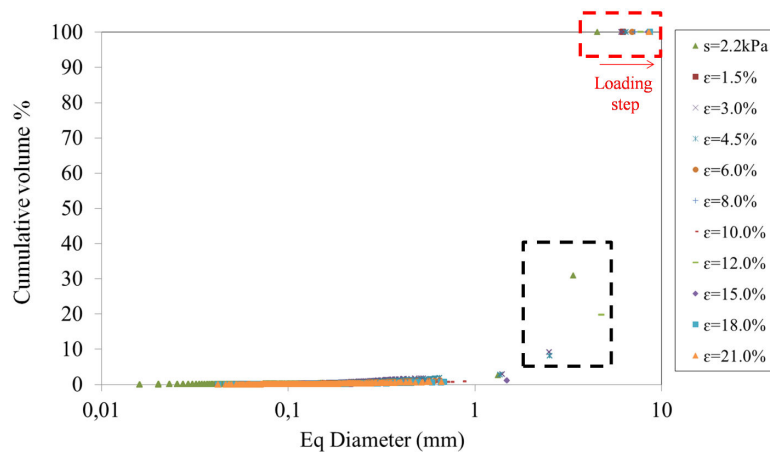


Figure 5.23: Air clusters size distribution for all loading steps in the triaxial test HN02 (UD)

From the fluid clusters size distribution curves, fluid clusters of the biggest size are extracted. The volume of the biggest water cluster (V_{wmax}) is normalized by the total

volume of water within the specimen (V_{wt}) for each loading step. Similarly, the volume of the biggest air cluster (V_{amax}) is normalized by the total volume of air within the specimen (V_{at}) for each loading step.

Similar to water retention test, V_{max} which forms around (80–99%) of water phase is considered to be more representative of water phase than V_{mean} which presents the influence of the small clusters (since they are in a bigger number).

The relation between the normalized volumes of the biggest fluid clusters (V_{max}) versus the axial strain is thereafter plotted. Fig 5.24 shows the relation between the normalized water (V_{wmax}) and air (V_{amax}) clusters versus the axial strain for HN02 (UD).

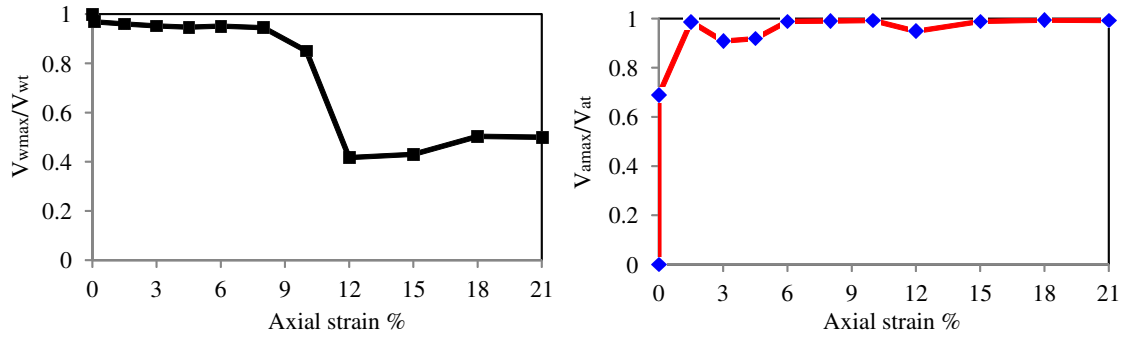


Figure 5.24: The evolution of the normalized V_{max} for water clusters (left) and air clusters (right) with loading for all loading steps in the triaxial test HN02 (UD)

At the beginning of the test, the specimen is saturated, $V_{wmax}=V_{wt}=1$. When suction is applied, V_{wmax} slightly decreases ($V_{wmax}\approx V_{wt}$). At the beginning of loading process $V_{wmax}\approx V_{wt}$, then at $\varepsilon=8\%$, the volume of the biggest water cluster decreases and $V_{wmax} < V_{wt}$. Later, for $\varepsilon\geq 12\%$, V_{wmax} is stable with no remarkable changes and $V_{wmax} < V_{wt}$.

For V_{amax} , at the beginning of the test, no presence of air and thus $V_{amax}=V_{at}=0$. When suction is applied, V_{amax} increases remarkably and $V_{amax} < V_{at}$. As the loading is applied V_{amax} increases and $V_{amax}\approx V_{at}$.

Consequently, Water phase and air phase are continuous for $\varepsilon\leq 8\%$. For $\varepsilon>8\%$, the big water cluster divides into other relatively big clusters: one at the top and the other at the bottom of the specimen. The two relatively big water clusters are of $V_{wmax}/V_{wt}\approx 40\%$. However, water phase continues to be in a continuous state for $\varepsilon>8\%$, as the two big clusters form more than 80% as shown in Fig 5.22.

5.3.6.2 The evolution of the number of solid-fluid and fluid-fluid interfaces with the mechanical loading

Fig 5.25 shows a vertical slice in the labelled grain volume for loading step $\varepsilon=21\%$ in the triaxial test HN02 (UD), and the number of grains within the specimen shown for all loading steps in the triaxial test HN02 (UD). In this figure, the different colors represent different grains though some grains of different Ids might have the same color. Through the triaxial test, grains displace and rotate and the whole solid skeleton deforms. However, with the small axial forces applied on the specimen and the relatively small cell pressure, the number of grains should not change (i.e., no grain crushing). In Fig 5.25, the number of grains changes slightly (± 400 grains) due to the applied trinarization technique and the

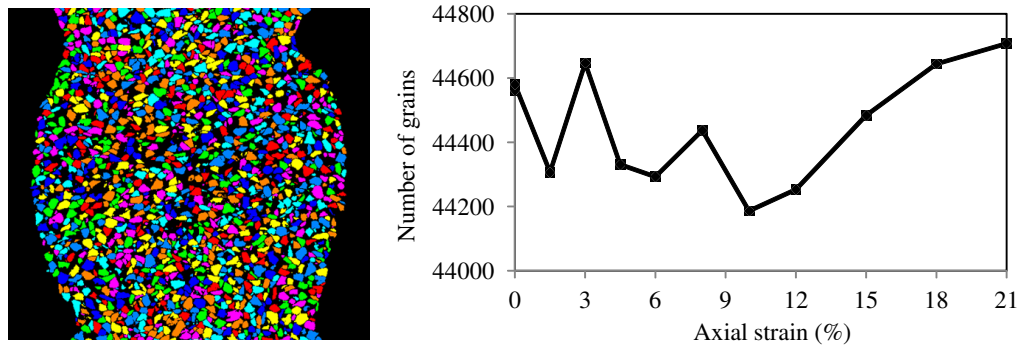


Figure 5.25: A vertical slice in the labelled grain volume for loading step $\varepsilon=21\%$ in triaxial test HN02 (UD) (left) and the number of grains within the specimen shown for all loading steps in the triaxial test HN02 (UD)

morphological processes applied before labelling (Erode/dilate/separate). Yet, there is no remarkable influence of loading on the number of the labelled grains. This is shown in Fig 5.26, where grain size distribution within the specimen is the same for all loading steps (the curves are superposed).

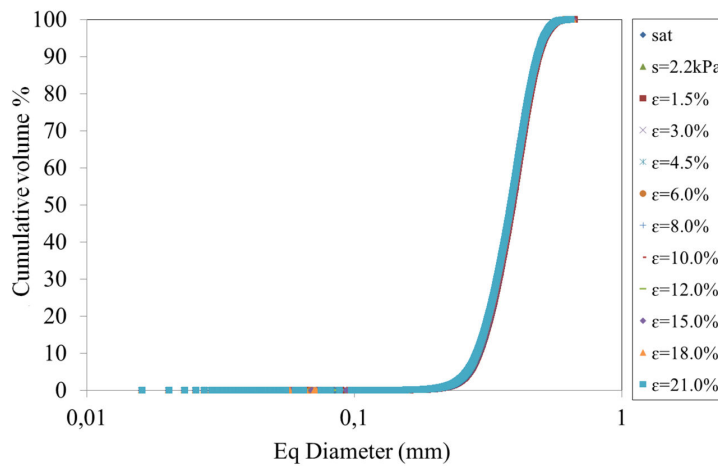


Figure 5.26: Grain size distribution for all loading steps in the triaxial test HN02 (UD)

In the following, the evolution of the contacts between the phases with the axial strain is presented for all the loading steps in the triaxial test HN02 (UD). The results are presented for grain-water, grain-air and water-air contacts.

As explained earlier in chapter 4, the maximum number of contacts between each two phases is used to evaluate the evolution of contacts with loading, in order to make it easier to verify and evaluate the results. For example, the maximum number of contacts for the saturated specimen is known for water and air phase: in the saturated case water volume is on contact with all the grains, while air phase is not present. However, the mean number of contacts between the phases can be used also.

For grain-water contacts, Fig 5.27 shows the relation between the Maximum number of Grains that are in contact with one water cluster (Max Gw) versus the axial strain and the relation between the Maximum number of Water clusters that are in contact with one

grain (Max Wg) versus the axial strain, for all the loading step in the triaxial test HN02 (UD).

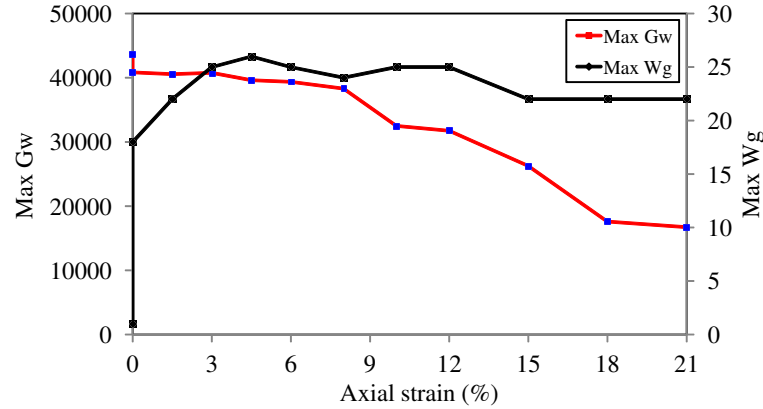


Figure 5.27: The relation between the maximum number of grains in contact with one water cluster (Max Gw) versus the axial strain and the relation between the maximum number of water clusters in contact with one grain (Max Wg) versus the axial strain for the triaxial test HN02 (UD)

As shown in Fig 5.27, at the beginning of the test, the specimen is completely saturated and water phase is in the form of one big cluster that is in contact with all the grains within the specimen (number of grains 45000 ± 400 grains). Later, Max Gw decreases as the suction is applied. At the beginning of loading application, Max Gw decreases slightly then at $\epsilon=8\%$, Max Gw decreases rapidly to reach a minimum value at the end of the test.

On other hand, at the beginning of the test, Max Wg=1 (one water clusters in contact with all the grains within the specimen). Later, Max Wg increases as the suction is applied. When loading is applied, Max Wg increases slightly then changes by ± 3 contacts with increasing the loading, until the end of the test.

The evolution of Max Gw and Ma Wg presented in Fig 5.27 is consistent with the evolution of the macroscopic degree of saturation presented in Fig 5.14. As the degree of saturation decreases with the loading due to the dilation of the specimen in the drained triaxial test, the number of water clusters increases (see Fig 5.21) and their volume decreases (see Fig 5.22, and thus the number of grains per water cluster Max Gw) decreases and the number of water clusters per grain (Max Wg) increases.

For grain-air contacts, the relation between the Maximum number of Grains that are in contact with one air cluster (Max Ga) versus the axial strain and the relation between the Maximum number of Air clusters that are in contact with one grain (Max Ag) versus the axial strain are presented in Fig 5.28, for all the loading steps in the triaxial test HN02 (UD).

As shown in the figure, at the beginning of the test the specimen is saturated with no presence of air, thus Max Ga=0. Later, Max Ga increases as the suction and the loading are applied. Similarly, Max Ag=0 at the beginning of the test then Max Ag increases as the suction is applied. When the loading is applied, Max Ag changes slightly (± 1 contact) until the end of the test.

The evolution of Max Ga is consistent with the evolution of the macroscopic porosity with loading. The increase of the porosity with loading shown in Fig 5.14, induces a

decrease in the number of air clusters (see Fig 5.21) at the beginning of the test, and an increase in their volumes (see Fig 5.22), and thus Max Ga increases.

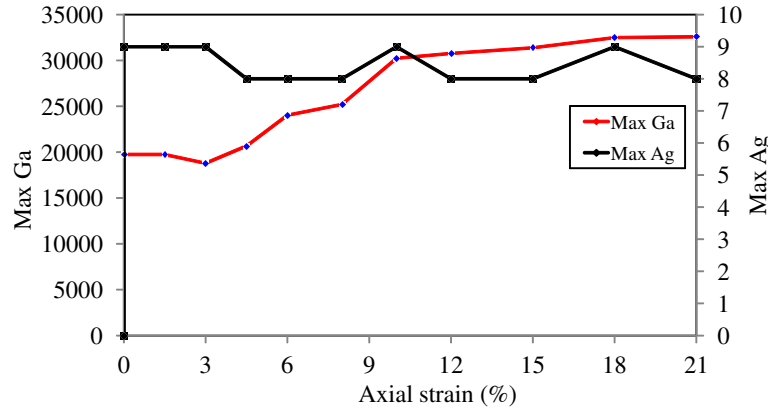


Figure 5.28: The relation between the maximum number of grains in contact with one air cluster (Max Ga) versus the axial strain and the relation between the maximum number of air clusters in contact with one grain (Max Ag) versus the axial strain, for the triaxial test HN02 (UD)

For water-air contacts, the relation between the Maximum number of Water clusters that are in contact with one air cluster (Max Wa) versus the axial strain and the relation between the Maximum number of Air clusters that are in contact with one water cluster (Max Aw) versus the axial strain are presented in Fig 5.29 for HN02 (UD).

The figure shows that, at the beginning of the test Max Wa=0 (the specimen is saturated and no presence of air). Later, Max Wa increases as suction and loading are applied to reach a maximum value at the end of the test. Similarly, at the beginning of the test, Max Aw=0 (no air within the specimen). Later, Max Aw increases as suction is applied. When the loading is applied, Max Aw changes (± 300 contacts) and it reaches a maximum value at the end of the test.

The evolution of Max Wa is consistent with the evolution of the macroscopic degree of saturation and porosity, see Fig 5.14. The increase of porosity with loading, which induce an increase in the number of air clusters (at the beginning of the test), and the decrease of degree of saturation with loading, which induces an increase in the number of water clusters (see Fig 5.21), causes an increase in Max Wa.

Similar to water retention tests, the number of grains per fluid cluster (i.e., Max Gw, Max Ga, Max Wg and Max Ag) can be used in the analysis of hydro-mechanical behaviour (triaxial test) of the specimen HN02 (UD) to highlight the interaction between solid (grain) and fluid (water and air), i.e., the interaction between grain and pore shapes and sizes. Moreover, the number of water clusters per one grain (i.e., Max Wg) can be used to investigate the contribution of water content or suction (i.e., cohesion) to shear strength, as presented before in chapter 2, section 2.3.2. The number of water clusters per one air cluster and the number of air clusters per one water cluster (i.e., Max Wa and Max Aw), from the other hand, describe the connectivity of the pores filled with different fluids (air and water).

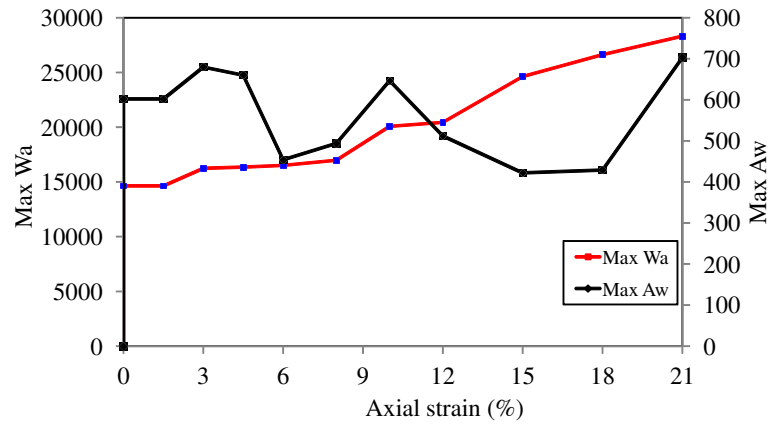


Figure 5.29: The relation between the maximum number of water clusters in contact with one air cluster (Max Wa) versus the axial strain and the relation between the maximum number of air clusters in contact with one water cluster (Max Aw) versus the axial strain, for the triaxial test HN02 (UD)

5.3.7 Digital Image Correlation results

Digital image correlation is performed on the incremental loading steps for the three triaxial tests: saturated drained test HN01 (SD), unsaturated drained test HN02 (UD) and unsaturated undrained test HN04 (UU). For each test, every two sequential states of the specimen are compared.

Similar to the process used for the water retention tests, the 3D image correlation for 3D images of the triaxial specimens under loading is primarily performed for a coarse mesh in order to determine the adequate range for the search window. At the end of this step, the search window corresponding to the highest Normalized Correlation Coefficient (NCC) is selected and fixed. Tomowarp is run again for a fine mesh and the selected search window. DIC is performed for the triaxial tests with a spacing of DIC grid 20 voxels and correlation window $12 \times 12 \times 12$ voxels.

The results of continuum DIC represent the deformation (displacement, rotation and strains) of the solid skeleton within the correlation window, measured from the reconstructed images, i.e., the specimens discrete nature is ignored, and the kinematics of the deforming material are measured at regularly spaced intervals.

In the following the results of DIC are presented for the triaxial test HN02 (UD). Fig 5.30 shows the horizontal incremental displacement in the coordinate direction X, normalized by the axial strain step, for all the loading steps in the triaxial test HN02 (UD).

As can be seen from Fig 5.30 the top and the bottom parts of the specimen are of zero incremental normalized displacement for all the steps of loading (see the color contrast at the top and the bottom of the specimen). The middle-right part of the specimen (in the shown slices) displaces to the right, and the middle-left part displaces to the left of the coordinate direction X.

The horizontal incremental displacement in the coordinate direction Y normalized by the axial strain step, for all the loading steps in the triaxial test HN02 (UD) is presented in Fig 5.31.

The middle-right part of the specimen (in the shown slices) displaces to the right, and the middle-left part displaces to the left of the coordinate direction Y. The bottom part

of the specimen displace to the right in the range $\varepsilon=10\text{--}15\%$, (see the color contrast at the bottom part of the specimen, in this range).

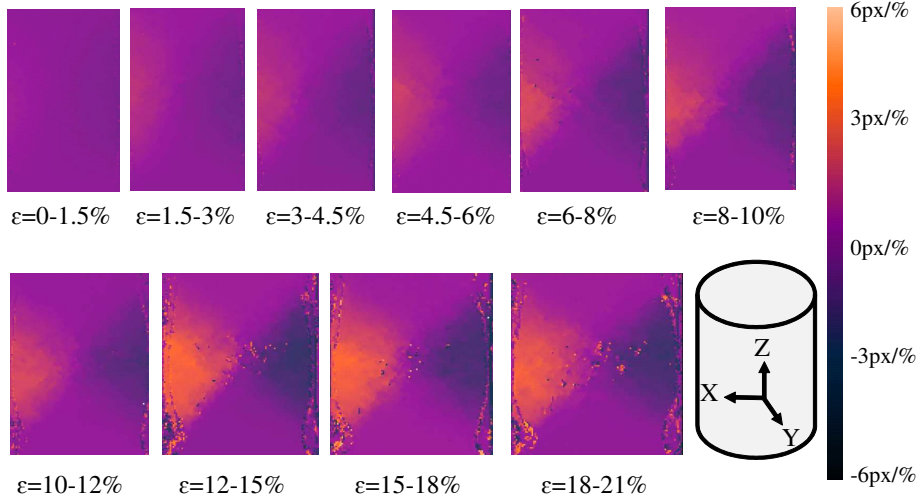


Figure 5.30: X incremental displacement field normalized by the axial strain step, for all the loading steps in the triaxial test HN02 (UD)

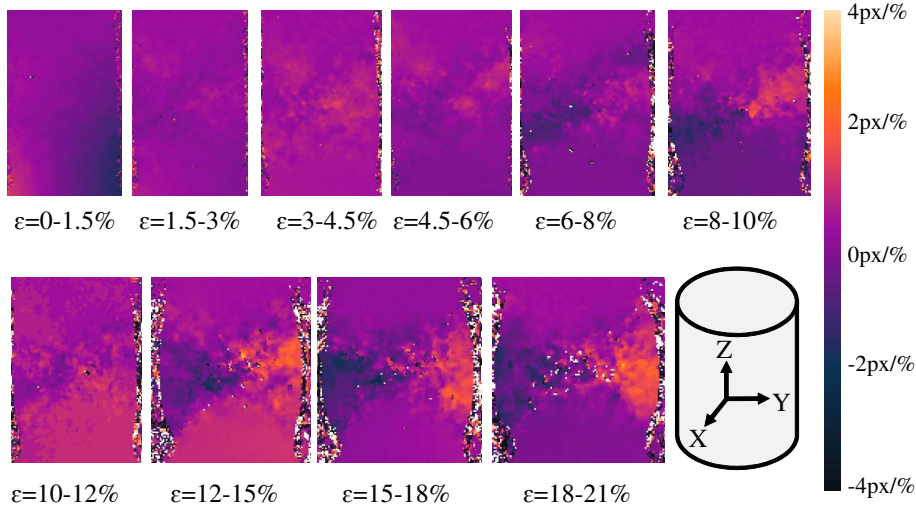


Figure 5.31: Y incremental displacement field normalized by the axial strain step, for all the loading steps in the triaxial test HN02 (UD)

As can be seen in Fig 5.30 and Fig 5.31, the deformation process in the middle part of the specimen is the same in the two coordinate directions X and Y, i.e., the middle-right part of the specimen (in the shown slices) displaces to the right, and the middle-left part displaces to the left. However, in the bottom part of the specimen, the deformation process is not symmetric, i.e., zero displacement on X, and a non-zero displacement on Y.

The vertical incremental displacement in the coordinate direction Z normalized by the axial strain step, for all the loading steps in the triaxial test HN02 (UD) is presented in Fig 5.32.

As the specimen is being loaded from the bottom to the top by the loading head, the incremental normalized displacement of the top part of the specimen is negligible.

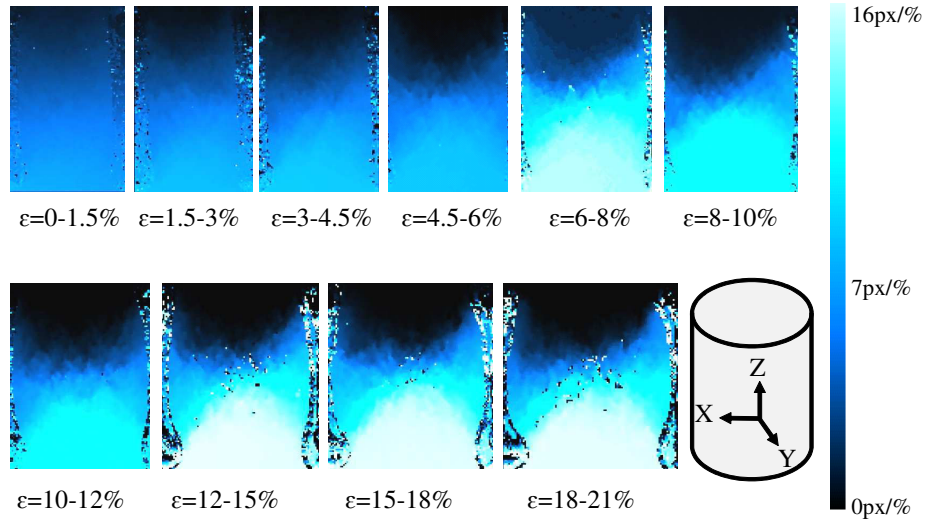


Figure 5.32: Z incremental displacement field normalized by the axial strain step, for all the loading steps in the triaxial test HN02 (UD)

The incremental normalized displacement of the bottom part of the specimen in the direction Z (to the top) increases as increasing the loading, (see the color contrast at the bottom of the specimen).

Using DIC, the rotation of the solid skeleton is obtained. Fig 5.33 shows the rotation of the solid skeleton within the correlation window, calculated as the norm of rotation in the three directions x, y and z, for all the loading steps in the triaxial test HN02 (UD).

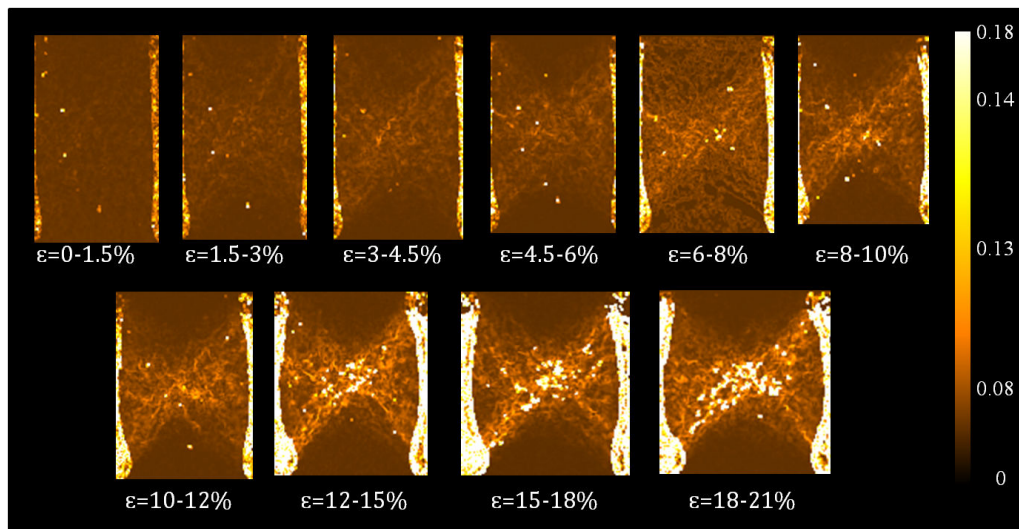


Figure 5.33: The rotation of the solid skeleton, for all the loading steps in the triaxial test HN02 (UD)

Fig 5.33 shows that, the rotation of the solid skeleton increases as increasing the loading. Moreover, the rotation of the solid skeleton at the top and the bottom of the specimen

is negligible compared to the rotation in the middle part of the specimen, (see the color contrast in the middle part of the specimen).

The volumetric strain and the deviatoric strain are presented in Fig 5.34 and Fig 5.35, respectively, for all the loading steps in the triaxial test HN02 (UD).

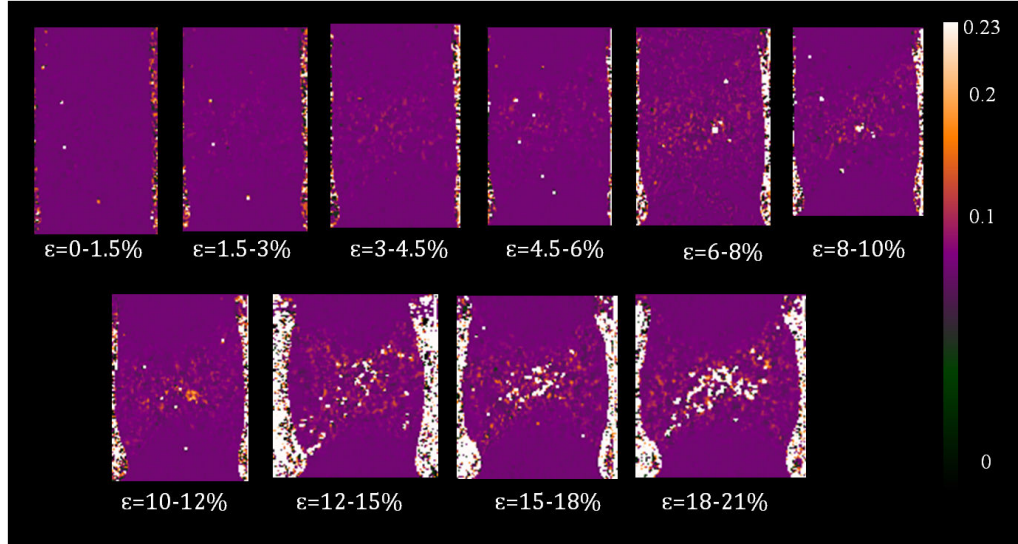


Figure 5.34: Volumetric strain field for all the loading steps in the triaxial test HN02 (UD)

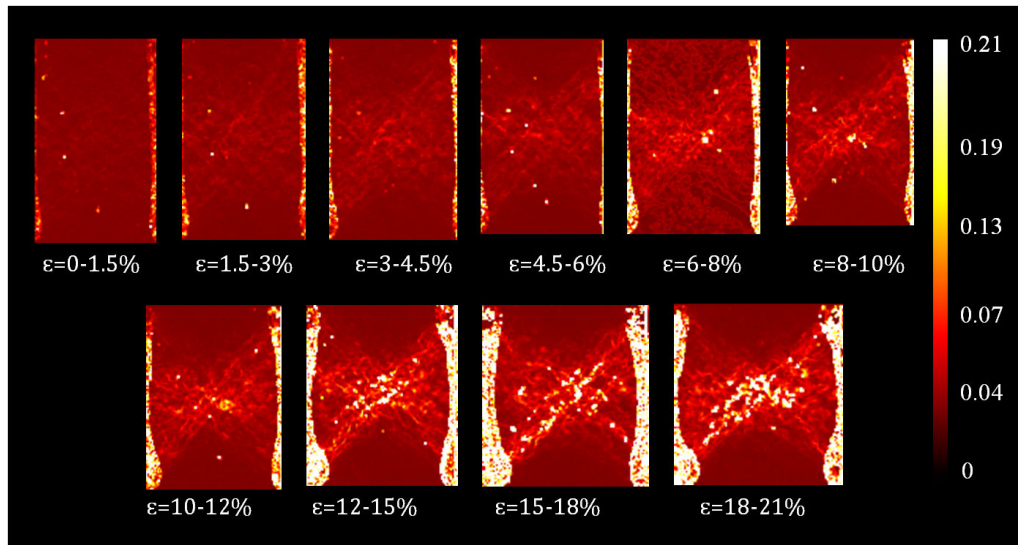


Figure 5.35: Deviatoric (maximum shear) strain field for all the loading steps in the triaxial test HN02 (UD)

As can be seen in Fig 5.34 and Fig 5.35, there is no clear concentration of strains in the earlier increments of loading, at the specimen scale. However, at the local scale, the middle part of the specimen in the earlier steps of loading shows a proliferation of tiny local intersecting shear bands of a preferable orientation 45° . At the increment of loading $\varepsilon=6-8\%$, deformation starts to be formed and localized in the middle part of the specimen, with a shearing of 13%. Later, strains increases within the middle part of the

specimen to reach a maximum value at the last increment of loading $\varepsilon=18-21\%$, with a clear localization of the deformation in the middle part of the specimen. The top and the bottom parts of the specimen present negligible strains compared to the middle part. These results are consistent with porosity mapping results presented in Fig 5.15, where a considerable dilation in the middle part of the specimen is observed at $\varepsilon=6\%$. However, the form of the sheared part of the specimen is not clearly defined by considering the specimens central vertical plane only in one azimuth orientation; therefore, an investigation of the deformation pattern is performed, as seen in different azimuth directions.

The 3D map of the deviatoric strain is analyzed and sliced vertically for each 10° increment in azimuth angle. Fig 5.36, Fig 5.37 and Fig 5.38 show central vertical slices each 10° increment, in the deviatoric strain map of three loading increments, namely $\varepsilon=3-4.5\%$, $\varepsilon=8-10\%$ $\varepsilon=18-21\%$ in the triaxial test HN02 (UD), respectively.

At loading increment $\varepsilon=3-4.5\%$, the deviatoric map shows the beginning of formation of the deformation pattern in the middle part of the specimen. The deformation pattern develops more clearly at loading increment $\varepsilon=8-10\%$, and at $\varepsilon=18-21\%$, the deformation takes the final form. However, the deformation pattern does not show the traditional narrow layer of intense shearing (shear band), or two X shaped shear band, but rather a 3D deformed volume of intense shearing. For a purpose of a better presentation, higher contrast is applied on the deviatoric map at $\varepsilon=18-21$ and it is sliced horizontally and vertically as shown in Fig 5.39. In this figure, four horizontal and vertical slices are taken in the deformed part of the specimen: at the top, centre and the bottom.

The deformed part of the specimen appears in the horizontal slices at the top and the bottom, as a lateral shear bands while in the central horizontal slice, it appears as diffused shear bands concentrated around the centre of the specimen. On the other hand, the central vertical slices show that the undeformed part at the bottom and the top of the specimen has a shape of a cone, while in the middle deformed part of the specimen, the heterogeneous strain field appears as a butterfly shape pattern in the 2D cuts. The 3D complete pattern corresponding to these 2D butterfly patterns has the form of a thick double inverted cone (or diabolo-like).

This strain pattern is triggered at loading increment $\varepsilon=6-8\%$, see Fig 5.35, and becomes well defined and more distinct as increasing the loading.

In the final increment $\varepsilon=18-21\%$ illustrated in Fig 5.39, the horizontal slices at the top, bottom and especially middle-height of the specimen show a special orientation of the deformed zone at 45° approximately, therefore two vertical perpendicular slices in this direction are presented in this figure, line 4. These horizontal and vertical slices show that the deformed zone develops eventually into a 2D plane strain mechanism in a given azimuth direction (45° degrees in the present case) with a form that is close to X shaped pair of conjugate shear bands.

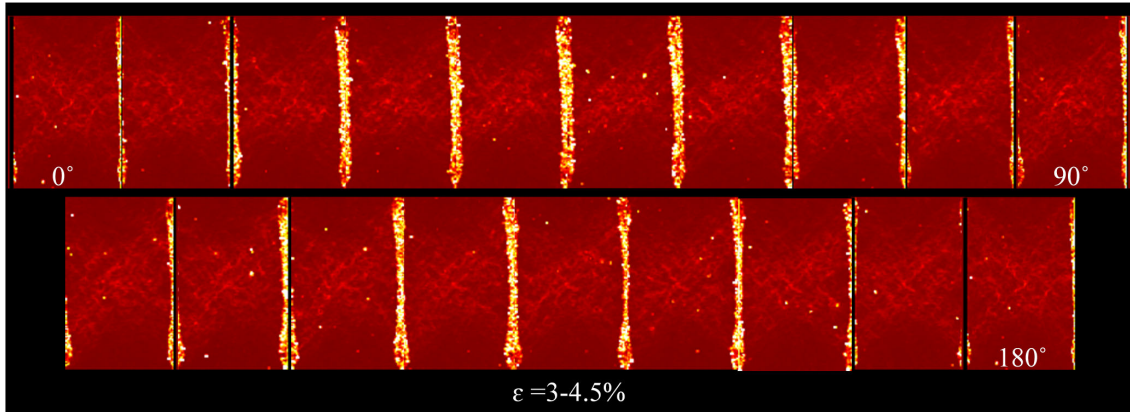


Figure 5.36: Central vertical slices each 10° increment, in the deviatoric strain map of the loading increment $\epsilon=3-4.5\%$ in the triaxial test HN02 (UD)

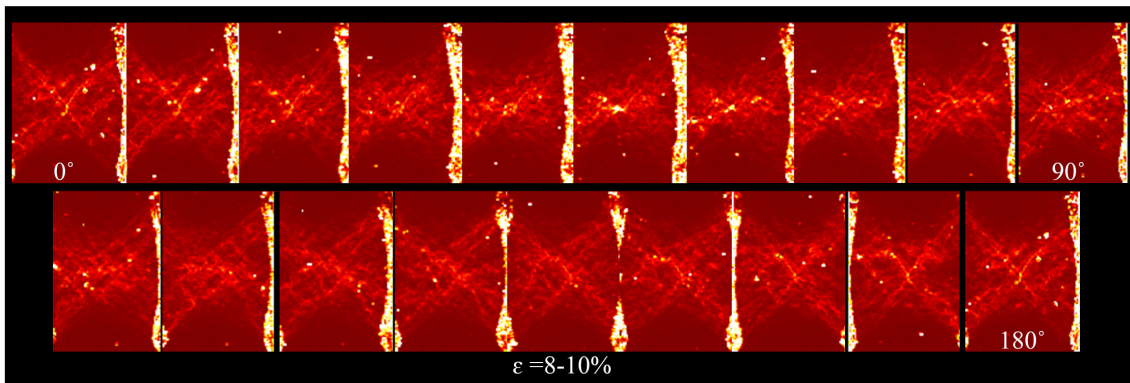


Figure 5.37: Central vertical slices each 10° increment, in the deviatoric strain map of the loading increment $\epsilon=8-10\%$ in the triaxial test HN02 (UD)

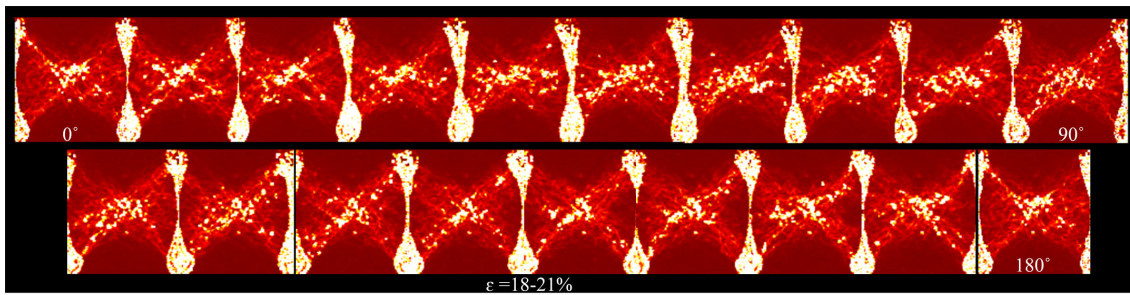


Figure 5.38: Central vertical slices each 10° increment, in the deviatoric strain map of the loading increment $\epsilon=18-21\%$ in the triaxial test HN02 (UD)

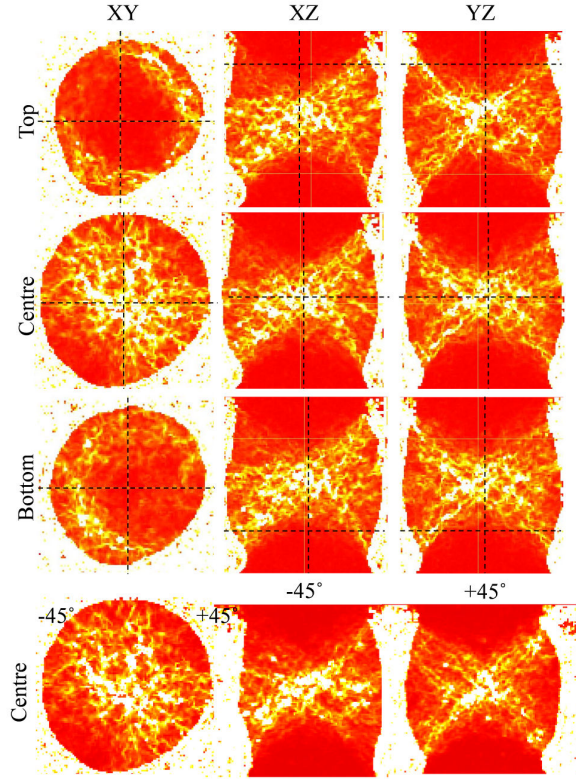


Figure 5.39: Horizontal and vertical slices in the deviatoric strain map of the loading increment $\varepsilon=18\text{--}21\%$ in the triaxial test HN02 (UD)

The deviatoric strain and the deformation pattern for the specimen HN02 (UD) is compared to those for HN01 (SD), HN04 (UU) and HN09 (D). Fig 5.40 shows vertical slices in the deviatoric strain map of the triaxial tests HN01 (SD), HN02 (UD), HN04 (UU) and HN09 (D). For the triaxial test HN04 (UU), DIC is performed for the loading increments at which water leakage is not observed (i.e., from $\varepsilon=0\%$ to $\varepsilon=12\%$).

The deviatoric strains measurements are comparable for the three tests HN01 (SD), HN02 (UD) and HN04 (UU). However, the deformation is more localized for HN04 (UU) at the specimen scale, earlier than for HN01 (SD) and HN02 (UU). The relative density at the beginning of the three tests HN01 (SD), HN02 (UD) and HN04 (UU) is $D_d=68\%$, $D_d=62\%$ and $D_d=65\%$, respectively, which indicates that a higher stress is expected for the lower porosity (i.e., HN02 (UD)). The Stress-strain curves of the three tests shows that the latter conclusion is true (i.e., a higher stress is found for HN02 (UD)).

For the comparison between HN02 (UD) to HN09 (D), it is important to point that, the main differences between the two tests are the presence of water in HN02 (UD), cell pressure, and the lower piston in HN09 (D) which allows the rotation of the specimen while rotation is not allowed for HN02 (UD). The results of DIC for the triaxial test HN09 (D) are obtained using the discrete grain-based DIC technique.

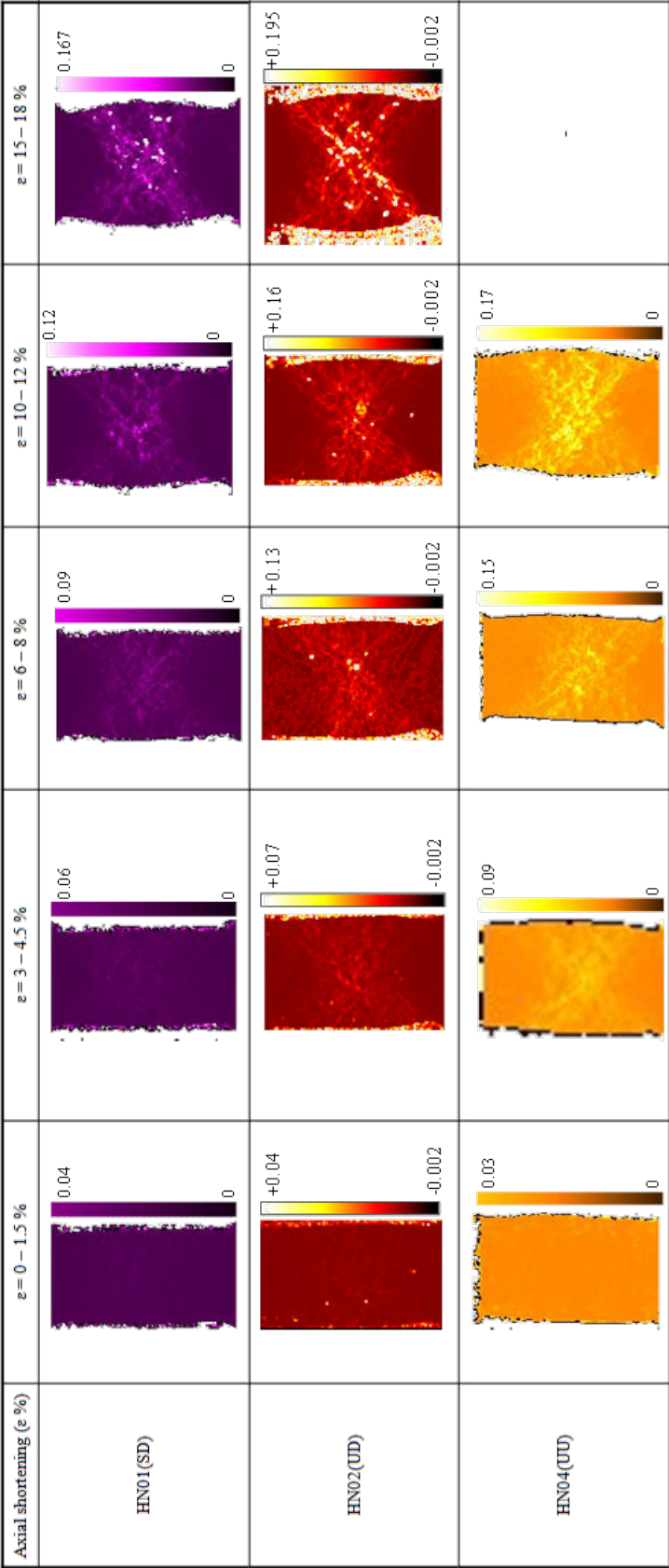
From Fig 5.40 it is found that strain measurements for HN09 (D) are higher than strains for HN02 (UD). Both specimens are dilatant through the test. However, the volumetric strains for specimen HN09 (D) are higher than those for specimen HN02 (UD), see Fig 5.12.

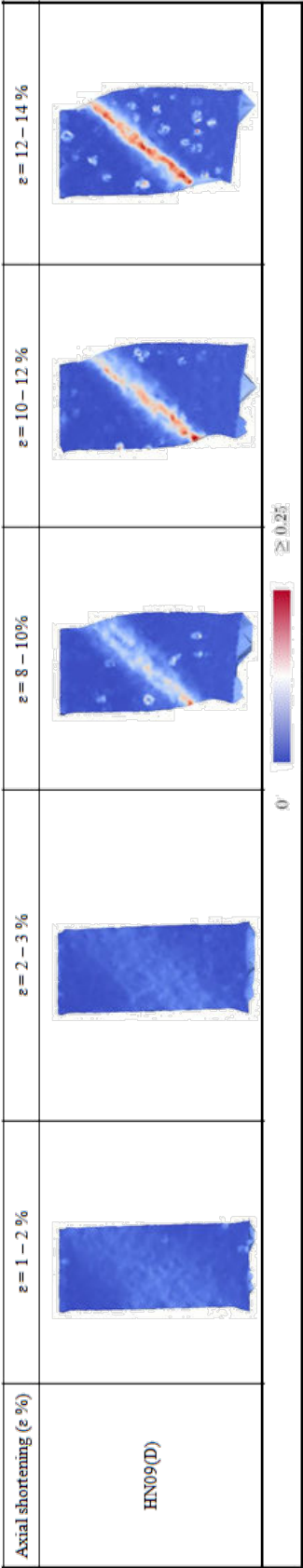
The localization of the deformations for the test HN09 (D) is more concentrated compared to the test HN02 (UD). A single shear band is triggered for the test HN09 (D) at $\varepsilon=8\%$, while for HN02 (UD) a complex shape (butterfly pattern) of the deformed zone is obtained. As stated before, the lower piston in HN09 (D) is free to rotate which allows the shear band to develop and concentrate into a narrow pattern.

As shown in Fig 5.7, stress-strain curve for HN02 (UD) does not show a clear peak, however, at $\varepsilon=6-8\%$ a wide region of relatively small diffused strains exists. This might indicate that at loading increment $\varepsilon=6-8\%$, the sheared zone is triggered or localized.

Moreover, the local changes taking place at $\varepsilon=6-8\%$, support this suggestion by showing heterogeneous behaviour of the specimen at this increment of loading. At $\varepsilon=8\%$, the degree of saturation changes remarkably by $\Delta Sr=11\%$, see Fig 5.14. In addition, beyond $\varepsilon=8\%$, the big water cluster divides into two relatively big clusters at the top and the bottom of the specimen, see Fig 5.22, and the volume of the biggest water cluster decreases so that $V_{wmax} < V_{wt}$, see Fig 5.24. Furthermore, at $\varepsilon=8\%$ Max Gw decreases rapidly to reach a minimum value at the end of the test. Thus, it is thought that at $\varepsilon=8\%$, a peak stress is reached.

Figure 5.40: Vertical slices in the deviatoric strain map of the triaxial tests HN01 (SD), HN02 (UD), HN04 (UU) and HN09 (D)





5.4 Interpretation of triaxial tests results

5.4.1 The evolution of porosity and degree of saturation inside/outside the sheared zone

The evolution of porosity and degree of saturation inside and outside the sheared zone is investigated in this work for the test HN02 (UD). In order to do that, two cubes ($200 \times 200 \times 200$ voxels) are extracted from the trinarized volume in the large deformed zone (localized zone) and outside the deformed zone. The porosity and degree of saturation are calculated using the number of voxels representing each phase.

Fig 5.41 shows the cubes extracted inside and outside the deformed zone, where porosity and degree of saturation are calculated for the triaxial test HN02 (UD). In this figure, it is shown that the position of the cubes is checked by comparing the trinarized volume to the deviatoric map.

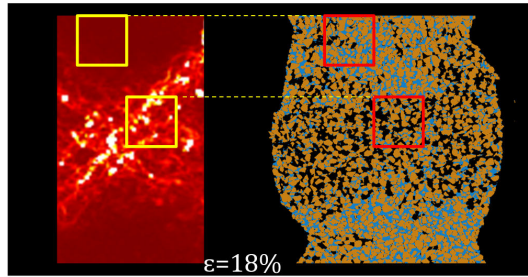


Figure 5.41: The cubes extracted inside and outside the sheared zone, where porosity and degree of saturation are calculated for the triaxial test HN02 (UD)

Fig 5.42 shows porosity measurements inside and outside the sheared zone for the triaxial test HN02 (UD).

Porosity measurements inside the sheared zone ($In_n\%$) shows that porosity increases with loading through the test, from $n=40.2\%$ to reach a plateau of $n=46.5\%$ at $\varepsilon=12\%$. On the other hand, porosity outside the sheared zone ($Out_n\%$) increases slightly with loading only in the range $n=(34.4-35.1\%)$.

Fig 5.43 shows degree of saturation measurements inside and outside the sheared zone for the triaxial test HN02 (UD). The first step of evolution corresponding to suction application is shown in the figure as a vertical line along the Y axis. Degree of saturation measurements inside the sheared zone ($In_Sr\%$) decreases gradually with loading through the test from $Sr=40\%$ to $Sr=21.2\%$. This is consistent with the increase of porosity (see Fig 5.42) inside the sheared zone. Outside the sheared zone, degree of saturation ($Out_Sr\%$) increases slightly with loading in the range $Sr=(76.5-81.8\%)$.

Similar procedure is performed for another cube $200 \times 200 \times 200$ voxels inside and outside the sheared zone, see Fig 5.44 the green box, in order to verify the former results. In addition, porosity and degree of saturation are measured for the whole sheared zone (see volume B in Fig 5.44), and compared to the measurements of porosity and degree of saturation for the whole specimen and the two cubes (see the red and green cubes in Fig 5.44).

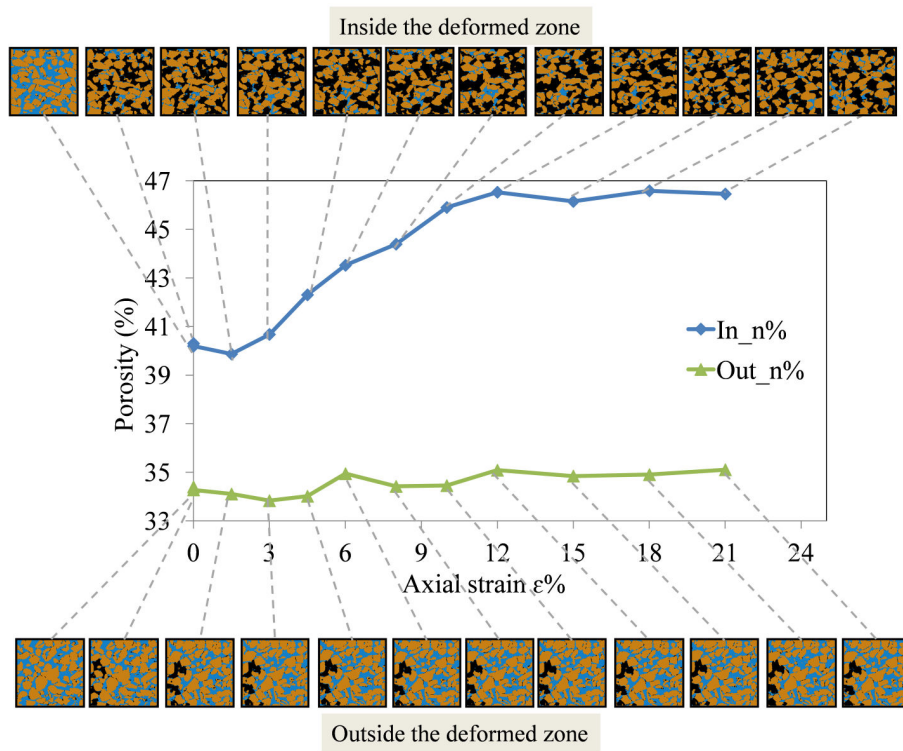


Figure 5.42: Porosity measurements inside and outside the sheared zone for the triaxial test HN02 (UD)

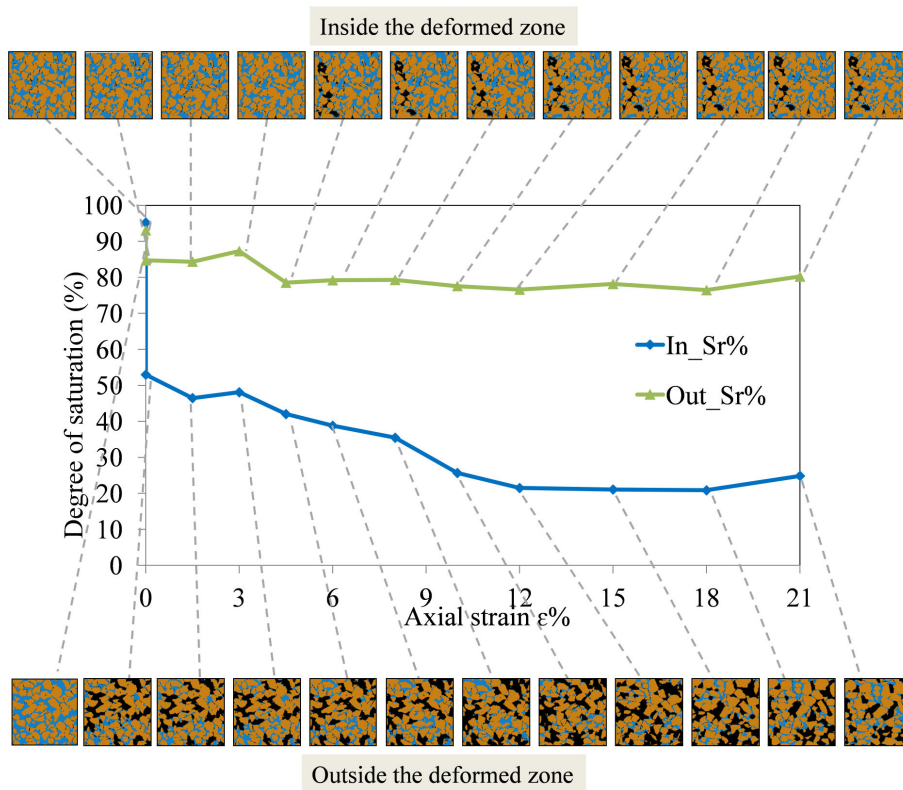


Figure 5.43: Degree of saturation measurements inside and outside the sheared zone for the triaxial test HN02 (UD)

The measurements of porosity for the cubes inside/outside the sheared zone, the whole sheared zone and the specimen are shown in Fig 5.45. The measurements of degree of saturation for the cubes inside/outside the sheared zone, the whole sheared zone and the specimen are shown in Fig 5.46.

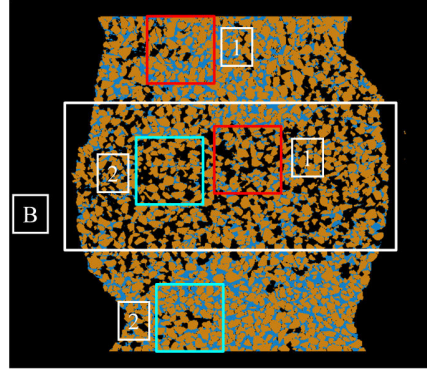


Figure 5.44: The two cubes for which porosity and degree of saturation are measured inside and outside the sheared zone. The volume B defines the zone considered as the sheared zone for the triaxial test HN02 (UD)

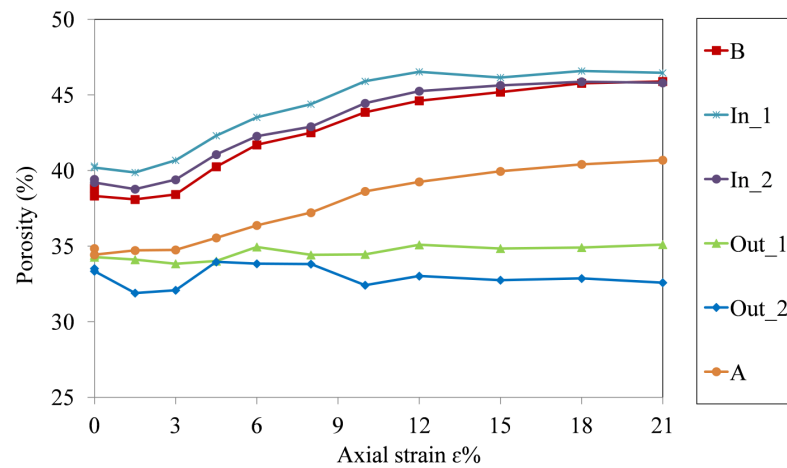


Figure 5.45: The measurements of porosity for the cubes inside/ outside the sheared zone, the whole sheared zone (B) and the specimen (A), for the triaxial test HN02 (UD)

As can be seen in Fig 5.45, porosity measurement for the whole sheared zone and for the two cubes inside the sheared zone have the same trend, i.e., an increase in the porosity with loading through the test. The measurement of porosity outside the sheared zone has the same trend, up to $\epsilon=6\%$, i.e., slight decrease in porosity which indicates compaction behaviour in the upper and lower parts of the specimen, but afterward its evolution seems to be stopped. More importantly, porosity measurements for the whole specimen have the same trend as the sheared zone, and in the proportion of the respective volumes in/out the sheared zone. All these observations are consistent with the dilatant behaviour of the sheared zone and the specimen globally.

For the degree of saturation, the measurements for the whole sheared zone and for the two cubes inside the sheared zone have the same trend, i.e., a decrease in the degree

of saturation with loading through the test, as shown in Fig 5.46. The measurements of degree of saturation outside the sheared zone show a common trend in both measured cubes, i.e., slight increase in the degree of saturation at first, then no more significant evolution. Degree of saturation measurements for the whole specimen has the same trend as the sheared zone, and in the proportion of the respective volumes in/out the sheared zone.

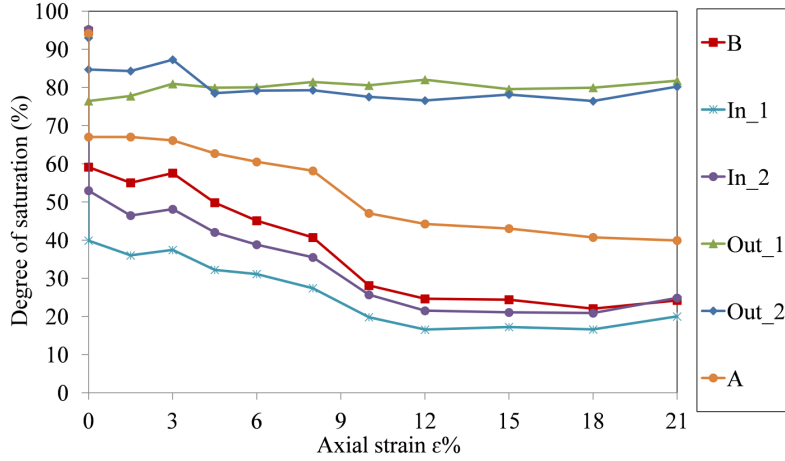


Figure 5.46: The measurements of degree of saturation for the cubes inside/ outside the sheared zone, the whole sheared zone and the specimen for the triaxial test HN02

In conclusion, the evolution of porosity and degree of saturation within the sheared zone has the same trend of the evolution of these two variables within the whole specimen.

5.4.2 Cohesion and water distribution

It has been presented in chapter 2, section 2.3.3 that liquid distribution within a granular specimen changes with the mechanical loading. Mani (2014) has shown that liquid spreads away from the sheared zone, which induces a decrease in the degree of saturation within the sheared zone while the porosity is increasing. Similar behaviour of water phase is captured for the triaxial test HN02 (UD) performed in this work, i.e., water flows away from the sheared zone to the top and the bottom part of the specimen.

According to Mani (2014)), this behaviour is due to liquid bridge rupture. The liquid is redistributed to all neighboring liquid bridges after bridge rupture which means that locally, after a bridge rupture event, there is a liquid flux away from the rupture point.

Moreover, in chapter 2, section 2.3.2, the microscopic-discrete analyses have shown that the influence of the distribution of water phase on the shear strength can be related to the contribution of cohesion to shear strength, though cohesion contribution to shear strength is negligible for sand at usual cell pressures. This is true only in cohesion regime at which cohesion is a function of the number of water clusters per grain (Max Wg), as suggested in the cohesion regimes discussion, presented in chapter 4, section 4.4.4.

In this section, cohesion regime and its contribution to shear strength are discussed for the triaxial test HN02 (UD).

It was found in chapter 4, section 4.4.4, that cohesion can have three regimes, at which cohesion is a function of suction, water content and Max Wg. These regimes were defined using the evolution of Max Wg and they differentiate from one specimen to another (of the same material), depending on the porosity macroscopically, and the grain and pore size and shape distribution, microscopically.

As the specimen in the triaxial test HN02 (UD), is different than those for the retention test, capillary regime for the triaxial test HN02 (UD) cannot be defined just by knowing the applied suction or the degree of saturation. Moreover, due the volumetric change of the specimen in the triaxial test HN02 (UD), water distribution within the specimen is heterogeneous (the middle part of the specimen is of less water content compared to the top and the bottom parts of the specimen which are saturated). Therefore, it would be reasonable to assume different capillary regimes for the different parts of the specimen in the triaxial test HN02 (UD). This suggestion is explained in the following, using Fig 5.47 which shows the evolution the number of water clusters per grain (Max Wg) and stress-strain curve for the triaxial test HN02 (UD).

At the beginning of the triaxial test HN02 (UD), the specimen is completely saturated (one big water cluster), thus capillary is a function of suction at this step of the test. When suction is applied, on the saturated specimen, Max Wg increases from 1 (one big water cluster) to several clusters, due to the decrease in the degree of saturation from 100% for the saturated specimen to $S_r=67\%$. At this step (i.e., after suction application and before the mechanical loading), water phase was also in the form of one big water cluster of a volume equal to the total volume of water within the specimen (i.e., $V_{wmax} \approx V_{wt}$), see Fig 5.24). Therefore, at this step of the test cohesion cannot be dependent on Max Wg, but rather on suction or water content.

When the mechanical loading is applied, the degree of saturation decreased as increasing the mechanical loading. Simultaneously, the number of water clusters increased (see Fig 5.21), the volume of water clusters decreased (see Fig 5.24), and Max Wg increased as increasing the mechanical loading. However, only at $\varepsilon=12\%$, the one big water clusters divided into 2 relatively big clusters at the top and the bottom of the specimen, and other randomly distributed small clusters in the middle part of the specimen (see Fig 5.24 and Fig 5.19). In other words, after the mechanical loading application, the specimen was divided into 3 parts : the top and the bottom parts which were saturated and cohesion in these two parts can be considered as a function of suction, and the middle part where cohesion can be considered as a function of either water content or Max Wg.

Considering the latter conclusion and referring to Fig 5.47, the evolution of Max Wg with the mechanical loading (after suction application beyond the segment of the curve which is a vertical line along Y axis) presents actually water clusters in the middle part. If the number of big water clusters (1 cluster before and after suction application, 1 cluster in the range $\varepsilon < 12\%$, and 2 clusters in the range $\varepsilon > 12\%$) is extracted from Fig 5.47, the rest of the clusters belongs actually to the middle part of the specimen where the sheared zone develop through the test.

In order investigate cohesion regime in the middle part of the specimen, i.e., whether it is a function of water content or Max Wg, the evolution of degree of saturation in the middle part of the specimen is verified from Fig 5.46. As can be seen from this figure, the degree of saturation in the middle part decreases from $S_r=60\%$ to $S_r=26\%$. Another related remark is that stress-strain curve evolution has the same trend as the one

for the evolution of Max Wg with loading, with several apparent peaks. For these two reasons, it is suggested that in the middle part of the specimen, cohesion is a function of Max Wg, i.e., low water content regime at which cohesion increases as increasing Max Wg.

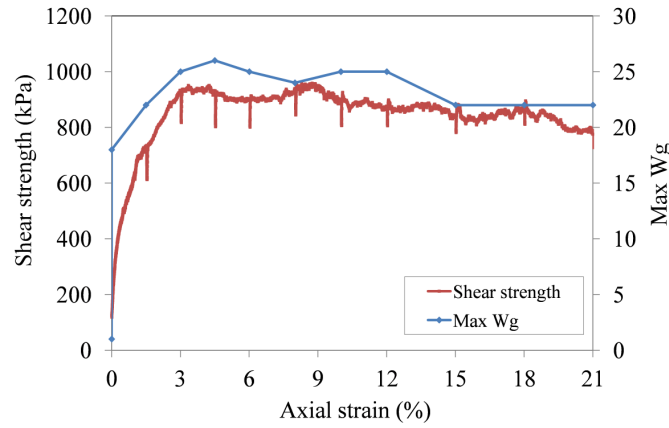


Figure 5.47: Stress strain curve and the evolution of Max Wg with loading for the triaxial test HN02 (UD)

As shown in Fig 5.47, Max Wg decrease slightly as increasing the loading due to the decrease in water content through the test. The relation between Max Wg and the degree of saturation is presented in Fig 5.48. In this figure, it is shown that the evolution of Max Wg with the degree of saturation is similar to the evolution of cohesion with the degree of saturation presented in chapter 2, section 2.3.2, by Leal-Vaca et al. (2012), see Fig 2.21-c. The number of water clusters per grain (Max Wg) increases as decreasing the degree of saturation (due to the division process) to reach a maximum value then decreases.

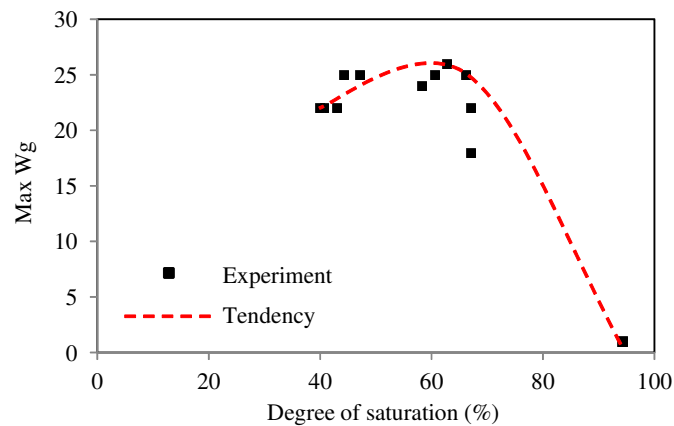


Figure 5.48: The experimental points and the tendency of the relation between Max Wg and the degree of saturation for HN02 (UD)

In conclusion, though cohesion contribution to shear strength for unsaturated sand is negligible at the relatively high cell pressure, the evolution of cohesion with loading can be related to the evolution of the number of water clusters per grain (Max Wg) with loading.

5.5 Conclusion

This chapter presented the triaxial tests performed in this work for saturated and unsaturated Hostun sand at different conditions (drained and undrained). The material tested (Hostun sand) and the experimental methods including the cell, specimen preparation technique, suction application technique, the experimental procedure, loading system and procedure and the experimental program were introduced. In the experimental program, the different tests performed in this work and the reference tests performed on dry Hostun sand were presented. In addition, some of the technical problems faced in this campaign were described.

Stress-strain curves of the triaxial tests performed in this work and the reference tests were compared and analyzed. Due to the technical problems presented earlier, some of the tests performed in this work could not be fully used for the final data analysis. The unsaturated drained triaxial test HN02 (UD) performed at cell pressure 200kPa was the main result of the triaxial program developed in this work.

The volumetric response of HN02 (UD) showed that the specimen go through a considerable contraction when suction is applied. Later the volumetric response of the specimens is dilatant.

Trinarization results, macroscopic and microscopic porosity and degree of saturation and microscopic-discrete analyses results were introduced for HN02. The microscopic-discrete analyses included the evolution of the number of fluid clusters, solid-fluid and fluid-fluid contacts with loading. The results showed that the number of water clusters within the specimen increases with the loading to reach a maximum value at the end of the test. On the other hand, the number of air clusters showed no remarkable changes when increasing the loading.

The X, Y and Z incremental normalized displacement, the rotation, the deviatoric strain and the volumetric strain for the test HN02 (UD) were acquired using continuum DIC and analyzed. It was found that the top and the bottom parts of the specimen were of zero X and Y incremental normalized displacement for almost all the steps of loading. As the specimen is being loaded from the bottom to the top, the incremental normalized displacement of the top part of the specimen was negligible in the direction Z.

The deviatoric and the volumetric strains showed that there is no clear concentration of strains in the earlier increments of loading, at the specimen scale. Later, deformation started to be formed and localized in the middle part of the specimen. The top and the bottom parts of the specimen presented negligible strains compared to the middle part.

In order to investigate the pattern of deformation, the 3D map of the deviatoric strain was analyzed. The primary observation was that the shape of the deformed zone, once localisation started to develop, was close to a butterfly pattern in the 2D slices in all horizontal directions, revealing a diabolo-like 3D localisation pattern. However, a deeper investigation had shown that in its fully-developed final stage, at a global axial strain about 20%, the deformed zone had developed a 2D plane strain mechanism in a given azimuth direction (45° degrees in the present case) with a form that is close to X shaped pair of conjugate shear bands.

Digital image correlation was also performed for the saturated drained test HN01 (SD) and unsaturated undrained test HN04 (UU), in order to compare their deviatoric strain

measurements to the one of HN02 (UD). The three tests were performed at the same cell pressure, i.e., 200kPa. The deviatoric strains measurements were comparable for the three tests. Strain measurements for a dry triaxial test HN09 (D), performed at 100kPa by Edward Andó, were compared to those of HN02 (UD). The localization of the deformations for the test HN09 (D) was more concentrated compared to the test HN02 (UD), which is attributed to the different bottom piston (i.e., free orientation in HN09 (D)). A single shear band was found for the test HN09 (D) compared to a butterfly pattern or X shape band for HN09 (UD). The local observations allowed to suggest that the sheared zone in HN02 (UD) was triggered at $\varepsilon=8\%$, which helped to indicate a peak stress at this axial strain value.

The interpretation of the triaxial test results allowed the investigation of the evolution of porosity and degree of saturation inside and outside the sheared zone for the test HN02 (UD).

The evolution of porosity and degree of saturation within the sheared zone had the same trend of the evolution of these two variables within the whole specimen.

Cohesion and water distribution were analyzed for the test HN02 (UD). The results showed that the evolution of cohesion with loading can be related to the evolution of the number of water clusters per grain (Max Wg) with loading.

Chapter 6

Summary, conclusion and outlook for future work

6.1 Summary and conclusion

This project work has investigated retention and hydro-mechanical behaviour of an unsaturated granular material, Hostun sand, at the micro-discrete scale. To achieve this goal, two series of tests were performed: water retention tests and triaxial tests. The present study has made use of the advances in x-ray computed tomography to generate 3D images of the unsaturated soil microstructure non-destructively. X-ray set up available at 3SR Laboratory in Grenoble University was used in this study.

Although already very rich, the information that is directly given by the 3D x-ray images needs to be complemented by image analysis methods to extract as much information as possible from the images. Therefore, several experimental tools and methods have been developed for the purpose of filling this lack. Trinarization technique is a region growing systematic technique that has been developed to allow the separation of the phases (i.e., grains, water and air) in the 3D images, and performing different measurements at the micro-discrete scale. This technique was used to trinarize x-ray reconstructed images obtained for the two tests. The application of this technique requires the definition of several parameters through an interactive procedure, then running the corresponding code automatically.

Using the trinarized images, porosity and degree of saturation of Hostun sand specimens were measured macroscopically and microscopically. To obtain the macroscopic measurements of the two variables, porosity and degree of saturation, the number of voxels representing each phase was counted, and used in the corresponding definition of porosity and degree of saturation. The microscopic measurements have been performed over an REV, and obtained using a developed mapping code. The size of the REV was determined using a developed analysis based on statistical tools. The obtained REV for the two tests performed in this study was comparable to D_{50} of Hostun sand, i.e. $REV=3 \times D_{50}$ ($REV=140px$ for the retention test and $80px$ for the triaxial test). The study also presented developed microscopic-discrete analyses that allow investigating the evolution of fluid phase with loading. Then, the experimental results were interpreted for the two series of tests.

To analyze water retention behaviour of Hostun sand, a pressure plate apparatus has

been developed. This apparatus allowed x-ray scanning of the variation of water phase between two steps of loading (i.e., suction) after reaching equilibrium. Suction values, to be applied using tensiometry technique, were chosen from a reference water retention curve. The specimen (cylindrical 1×1 cm) was prepared using water pluviation technique and scanned with a resolution $7.5 \mu\text{m}$. A detailed description of the whole experimental program was presented, including the material tested, the cell, suction application technique, specimen preparation technique and the experimental procedure.

Digital Image Correlation (a 3D continuum DIC code) was performed for water retention test to verify any deformations caused by suction application. It was found that, the calculated displacements were small compared to D_{50} of Hostun sand and their influences on the measurements performed in this work (e.g., porosity, degree of saturation and contacts measurements) were thought to be negligible, therefore, they were ignored.

The two paths, drying and wetting, were investigated in this study, which allowed analyzing hysteresis phenomenon. At the beginning of the water retention test, in the drying path, the specimen was completely saturated then drained gradually till reaching residual water content. Later, in the wetting path, the specimen in the residual state obtained in the drying path was wetted gradually till reaching $s=0$ kPa. The whole range of applied suction was $s=(0-7)$ kPa.

The results of the macroscopic and microscopic measurement of porosity and degree of saturation were consistent. The map of porosity and degree of saturation allowed viewing regions of higher porosity and the corresponding region of lower degree of saturation, within the specimen.

Through the developed microscopic-discrete analyses the evolution of water and air phases with suction was acquired. The number of water and air clusters at each step of suction was defined using the commercial software Visilog[®]. Moreover it was possible to analyze the continuity and discontinuity of the fluid phase during water retention test. To reach that, the biggest water and air clusters were used to represent water and air phase, respectively. The evolution of the effective interfacial specific area, defined as water-air interface surface, with the degree of saturation was comparable to the results presented in the literature review (i.e., an increase to reach a maximum value then a decrease, as increasing the degree of saturation).

The contacts between the three phases present within the specimen were investigated at each step of suction using a developed code for this purpose. The number of grain-water, grain-air and water-air contacts was obtained at each value of suction.

The experimental results were interpreted. The relation between the state variables suction, porosity and degree of saturation was investigated using the local measurement performed earlier in this work. The relation was analyzed in three planes: porosity-degree of saturation, suction-porosity, and suction-degree of saturation. It was found that the porosity increases as decreasing the degree of saturation and a shift for higher degree of saturation was obtained when decreasing the suction. This influence of suction on the relation between porosity and degree of saturation was not valid for the saturated and residual domains. Microscopic porosity showed a tendency to decrease when increasing suction. However, porosity was found to be constant for the saturated and the dry domains. The relation between suction and degree of saturation had the same tendency as water retention curve. To achieve a better analysis of suction-degree of saturation relation, three points were extracted: air entry value, the residual degree of saturation and

the value of suction at which the curve reaches a constant degree of saturation before the residual state. The relation between these three points with porosity was investigated. It was found that those three variables decrease as increasing the porosity.

Water retention domains and the boundary between them were defined. In order to do that the following points needed to be extracted. These points represented the values of suction before/after which the continuity of water and air phases changes; values of suction at which fluid phase changes the form from one big cluster to several clusters; values of suction at which a maximum and minimum number of fluid clusters is obtained, and values of suction at which a maximum and minimum number of fluid clusters per grain is obtained. These were used to define the ranges of suction corresponding to each domain. Basing on the continuity state of the water and air phases, defined from the latter points, the boundaries between the saturated, pendular, funicular and residual domain were established.

Hysteresis phenomenon was investigated at the macroscopic-microscopic and microscopic-discrete scales. At the macroscopic-microscopic scale, hysteresis phenomenon was analyzed at two conditions: constant suction and constant degree of saturation. At the same value of suction, due to hysteresis, two different values of degree of saturation were found for the drying and wetting processes (higher degree of saturation for the drying than the wetting). At the same degree of saturation, due to hysteresis, two different corresponding values of suction were found (higher suction for the drying than for the wetting). Moreover, it was found that the distribution of water within the specimen is more homogeneous for drying than for wetting, in the saturated and residual domains compared to pendular and funicular domains where water distribution is heterogeneous for both processes. The microscopic-discrete investigation showed that the macroscopic observations for hysteresis phenomenon can be related to local changes in the number of fluid clusters, their contacts, phase division and continuity (domains) and the interfacial area.

Soil cohesion was analyzed in the frame of water retention test. It was shown that cohesion can have three regimes at which cohesion is a function of suction, water content or Max Wg , depending on the cohesion regime. For the same soil, cohesion depends on the porosity, macroscopically, and on the grain and pore size and shape distribution, microscopically. Hysteresis phenomenon affects the boundaries between cohesion regimes due to the influence of pore shape distribution.

The hydro-mechanical behaviour of unsaturated soils was analyzed by means of triaxial tests, performed at three conditions: saturated drained, unsaturated drained and unsaturated undrained. A triaxial apparatus that can be placed inside the x-ray cabinet was developed in order to facilitate monitoring the changes in sand microstructure and water distribution when subjecting soil specimen to loading. The whole experimental program including the triaxial cell, specimen preparation technique, suction application technique, the experimental procedure and loading system and procedure and the experimental program was presented.

The Hostun sand specimen (cylinder of $h \times d = 2 \times 1 \text{ cm}$), prepared using water pluviation was completely saturated at the beginning of the three tests (conditions). Later for the drained test, suction was applied by tensiometry technique using pressure controller, and kept constant for the whole test. For the undrained test, suction of similar value to the one of the drained test, was applied then the valve connecting the controller to the specimen was closed, allowing to have undrained condition. The cell pressure and loading

rate were the same for the three tests (200kPa and 20 μ m/min). The specimen was loaded then scanned, repeatedly till reaching 21% axial strain for the three tests. Simultaneously, stress- strain curve was obtained by the acquisition data system (as a part of triaxial setup available in 3SR laboratory in Grenoble University).

Trinarization technique was used for all the steps of loading, which allowed performing macroscopic and microscopic measurements of porosity and degree of saturation. The trinarized images allowed the calculation of the volumetric strain through a developed technique detailed in this research.

For the unsaturated drained specimen HN02 (UD), which was the main result of the triaxial campaign performed in this work, stress-strain curve did not show a clear peak, and the volumetric response showed that the specimen had a considerable contraction when suction is applied. Later, the volumetric response of the specimens was dilatant.

Through the trinarized images and porosity and degree of saturation maps, the low porosity region was linked to the high degree of saturation.

Similar to water retention test, the evolution of fluid phase was investigated with the mechanical loading. The number of grains, water and air clusters was obtained for each step of loading. The contacts between the phases were also obtained.

The local changes taking place at $\varepsilon=6-8\%$, showed heterogeneous behaviour of HN02 (UD) specimen. Thus, it is thought that at $\varepsilon=8\%$, a peak stress is reached.

Digital image correlation was used to define deformation fields for the tested specimens, using a grid 20 voxels and correlation window 12 \times 12 \times 12 voxel. The incremental normalized (by loading step) displacement in the X and Y coordinate direction, showed that the top and the bottom parts of the HN02 (UD) specimen were almost of zero displacement for all the steps of loading. The middle-right part of HN02 (UD) specimen displaces to the right, and the middle-left part displaces to the left of the coordinate direction X and Y. As the HN02 (UD) specimen is being loaded from the bottom to the top by the loading head, the displacement of the top part of the specimen on the coordinate direction Z is negligible. Conversely, the displacement of the bottom part of the specimen in the direction Z (to the top) is increasing gradually through the test. The rotation of the solid skeleton in HN02 (UD) specimen increased as increasing the loading. Moreover, the rotation of the solid skeleton at the top and the bottom of the specimen is negligible compared to the rotation in the middle part of the specimen.

The volumetric and deviatoric strains, for the specimen HN02 (UD) showed that, the sheared zone is triggered at loading increment $\varepsilon=6-8\%$, at the specimen scale. At the local scale, the middle part of the specimen in the earlier steps of loading showed local intersecting shear bands of a preferable orientation 45°. Later, strains increased within the middle part of the specimen to reach a maximum value at the last loading increment $\varepsilon=18-21\%$, with a clear localization of the deformation in the middle part of the specimen.

In order to investigate the pattern of deformation, the 3D map of the deviatoric strain was analyzed. The primary observation was that the shape of the deformed zone, once localization started to develop, was close to a butterfly pattern in the 2D slices in all horizontal directions, revealing a diabolo-like 3D localization pattern. However, a deeper investigation had shown that in its fully-developed final stage, at a global axial strain about 20%, the deformed zone had developed a 2D plane strain mechanism in a given azimuth direction (45° degrees in the present case) with a form that is close to X shaped

pair of conjugate shear bands.

The DIC results of the unsaturated drained test HN02 (UD) were compared to the saturated drained test HN01 (SD), unsaturated undrained test HN04 (UU) and reference dry test HN09 (D). The deviatoric strains were comparable for the four tests. However, the deformations were better localized for HN04 (UU) and HN09 (D) earlier than the other two tests.

In order to investigate specimen heterogeneity with respect to water phase distribution, for the specimen HN02 (UD), porosity and degree of saturation measurements were performed inside and outside the sheared zone. Later, these measurements were compared to the measurement of porosity and degree of saturation for the whole sheared zone and for the whole specimen. The measurements inside and outside the sheared zone were performed over a cube $200 \times 200 \times 200$ voxels located inside the sheared zone, at the top of the specimen and above the sheared zone and at the bottom of the specimen and below the sheared zone.

The measurements for the cube inside/outside the sheared zone, the whole sheared zone and the specimen showed that, the porosity increase and the degree of saturation decrease as increasing the loading, and the evolution of these two variables within the sheared zone was similar to the one the whole specimen.

The high degree of saturation at the top and the bottom of the sheared zone indicated that water moved away from the sheared zone, which induced the decrease in the degree of saturation within the sheared zone while the porosity is increasing.

Cohesion and water distribution were analyzed for the test HN02 (UD). The results showed that the evolution of cohesion with loading can be related to the evolution of the number of water clusters per grain (Max Wg) with loading.

6.2 Outlook for future work

The literature review performed in this work revealed the need for an experimental study of the retention and hydro-mechanical behaviours of unsaturated soils at the grain scale. The experimental knowledge was lacking, particularly, the relation between the microscopic state variables: suction, porosity and degree of saturation; clear definition of water retention domains; the variation of water phase distribution with the mechanical loading and cohesion regimes. However, this work does not cover all the latter lacking axes, especially the one related to pores size and shape distribution measurements and cohesion measurements.

It was recognized, in this work, that major improvements are still needed to enhance the investigation of retention and hydro-mechanical behaviours of unsaturated granular soils. For example, a quantitative description of pore size and shape distribution can be used to characterize soil behaviour at the grain scale. Different numerical models, image-based techniques and impregnation techniques exist to measure pore size distribution and pore connectivity exist and can be used for a future characterization of the retention and hydro-mechanical behaviours at the grain scale. Analyzing retention and hydro-mechanical behaviour of different materials can also help highlighting the influence of different grain size and shape distributions and thus the influence of different pore size and shape distributions on these two behaviours.

An improvement of the used triaxial setup to prevent leakage and acquire better measurements of the applied axial force is required. In addition, several other conditions of the specimen must be considered, e.g., different water content in the undrained test and different suction values in the drained tests. This helps to understand the influence of suction and water content on the hydro-mechanical behaviour of the unsaturated soils and link it to cohesion contribution to shear strength.

Pore water pressure measurement for the undrained tests and water volume exchange for the drained tests should be considered in the future analyses, which offers better understanding of the volumetric response of the soil. Important contribution to the triaxial campaign can be gained by considering the influence of different initial void ratio on shear strength, cohesion, water distribution and volumetric changes. Cohesion measurements at low cell pressure present cohesion contribution to shear strength of the soil.

The results of the latter proposed considerations (experiments), including this work, could be used for the development of numerical simulations and models using Finite Elements Method (FEM), Discrete Element Method (DEM) and FEM \times DEM. Such developments would be of great interest for a wide range of engineering problems (geotechnical, agricultural, hydraulic, oil/petroleum/ground water/gas \cdots etc) and can be used for several applications such as the waste disposals and stability of oil and gas reservoirs.

Bibliography

- Alla, P. (2009). Dynamic Behavior of Unsaturated Soils (Doctoral dissertation, Faculty of the Louisiana State University and Agricultural and Mechanical College In partial fulfillment of the Requirements for the degree of Master of Science in Civil Engineering in The Department of Civil and Environmental Engineering By Prathima Alla Bachelor of Technology, Jawaharlal Nehru Technological University, India).
- Alonso, E. E., Gens, A., & Josa, A. (1990). A constitutive model for partially saturated soils. *Géotechnique*, 40(3), 405-430.
- Al-Raoush, R., & Alshibli, K. A. (2006). Distribution of local void ratio in porous media systems from 3D X-ray micro tomography images. *Physica A: Statistical Mechanics and its Applications*, 361(2), 441-456.
- Al-Raoush, R., & Papadopoulos, A. (2010). Representative elementary volume analysis of porous media using X-ray computed tomography. *Powder technology*, 200(1), 69-77.
- Alshibli, K. A., Batiste, S. N., Sture, S., & Lankton, M. (2010). Micro-characterisation of shearing in granular materials using computed tomography. *Advances in X-ray Tomography for Geomaterials*, 118, 17.
- Als-Nielsen, J., & McMorrow, D. (2011). *Elements of modern X-ray physics*. John Wiley & Sons.
- Andò, E., Hall, S., Viggiani, G., Desrues, J., & Besuelle, P. (2011). Analyzing the evolution of grains and contacts in sand under load. *Geomechanics and Geotechnics: from Micro to Macro*, 375-379.
- Andò, E., Hall, S. A., Viggiani, G., Desrues, J., & Bésuelle, P. (2012). Experimental micromechanics: grain-scale observation of sand deformation. *Géotechnique Letters*, (July-September), 107-112.
- Andò, E., Hall, S. A., Viggiani, G., Desrues, J., & Bésuelle, P. (2012). Grain-scale experimental investigation of localized deformation in sand: a discrete particle tracking approach. *Acta Geotechnica*, 7(1), 1-13.
- Andò, E. (2013), Experimental study of the evolution of the microstructure of a granular medium under mechanical loading using tomography X-ray, PhD thesis, Laboratory 3SR, Grenoble, France. (Cit. on pp. 102-105).
- Ashi, J. (1997). Computed tomography scan image analysis of sediments. *Proceeding of the Ocean Drilling Program, Scientific Results* 156:151-159.
- Adams, R., & Bischof, L. (1994). Seeded region growing. *Pattern Analysis and Machine Intelligence, IEEE Transactions on*, 16(6), 641-647.
- Andrade, J. E., & Ellison, K. C. (2008). Evaluation of a predictive constitutive model for sands. *Journal of geotechnical and geoenvironmental engineering*, 134(12), 1825-1828.
- Baltodano-Goulding, R. (2006). Tensile strength, shear strength, and effective stress for unsaturated sand (Doctoral dissertation, University of Missouri–Columbia).

- Bastian, P. (1999). Numerical computation of multiphase flow in porous media (Doctoral dissertation, habilitationsschrift).
- Bauters, T. W. J., DiCarlo, D. A., Steenhuis, T. S., & Parlange, J. Y. (2000). Soil water content dependent wetting front characteristics in sands. *Journal of hydrology*, 231, 244-254.
- Bayer, A., Vogel, H. J., & Roth, K. (2004). Direct measurement of the soil water retention curve using X-ray absorption. *Hydrology and Earth System Sciences*.
- Beddoe, R. (2009). Evaluation of the Water Retention Behaviour of Geosynthetic Clay Liners.
- Beddoe, R. A., Take, W. A., & Rowe, R. K. (2011). Water-retention behavior of geosynthetic clay liners. *Journal of Geotechnical and Geoenvironmental Engineering*, 137(11), 1028-1038.
- Bernard, L., Fave, S., Noirfalise, E., and Saragaglia, A. (2011), Visilog 7 Reference Guide, Manual, Noesis S.A. (cit. on pp. 78, 79).
- Beucher, S., & Meyer, F. (1992). The morphological approach to segmentation: the watershed transformation. *Optical engineering* NewYork-Marcel Dekker incorporated, 34, 433-433.
- Bishop, A. W., & Henkel, D. J. (1957). The measurement of soil properties in the triaxial test.
- Blaheta, R., Kohut, R., KolcunO, A., Soucek, K., & Stas, L. (2011). X-Ray Computer Tomography in Geotechnics. In *Proc. NDE for Safety conf.*, Ostrava.
- Blatz, J. A. (2000). Elastic-plastic modeling of unsaturated high plastic clay using results from a new triaxial test with controlled suction.
- Blatz, J. A., Cui, Y. J., & Oldecop, L. (2009). Vapour equilibrium and osmotic technique for suction control. In *Laboratory and Field Testing of Unsaturated Soils* (pp.49-61). Springer Netherlands.
- Boso, M. (2005). Shear strength behaviour of a reconstituted partially saturated clayey silt (Doctoral dissertation, Dissertation for the Doctoral Degree. Trento, Italy: Universit degli Studi di Trento).
- Brockman, F. J., & Selker, J. S. (2004). Integrated field, laboratory, and modeling studies to determine the effects of linked microbial and physical spatial heterogeneity on engineered vadose zone bioremediation. Pacific Northwest National Laboratory.
- Bock, J. J. (2011). A geometric study of liquid retention in open-cell metal foams (Doctoral dissertation, University of Illinois at Urbana-Champaign).
- Bogner, A., Jouneau, P. H., Thollet, G., Basset, D., & Gauthier, C. (2007). A history of scanning electron microscopy developments: towards wet-STEM imaging. *Micron*, 38(4), 390-401.
- Bornert, M. (2010). X-ray micro CT for studying strain localization in clay rocks under triaxial compression. *Advances in X-ray Tomography for Geomaterials*, 118, 35.
- Brown, G. O., Hsieh, H. T., & Lucero, D. A. (2000). Evaluation of laboratory dolomite core specimen size using representative elementary volume concepts. *Water Resources Research*, 36(5), 1199-1207.
- Bruchon, J. F., Pereira, J. M., Vandamme, M., Lenoir, N., Delage, P., & Bornert, M. (2013). Full 3D investigation and characterization of capillary collapse of a loose unsaturated sand using x-ray CT. *Granular Matter*, 15(6), 783-800.
- Canone, D., Ferraris, S., Sander, G., & Haverkamp, R. (2008). Interpretation of water retention field measurements in relation to hysteresis phenomena. *Water resources re-*

search, 44(4).

- Cavinato, M. (2011). High shear wet granulation: process understanding and scale up.
- Costanza-Robinson, Molly S., Benjamin D. Estabrook, and David F. Fouhey. "Representative elementary volume estimation for porosity, moisture saturation, and air-water interfacial areas in unsaturated porous media: Data quality implications." *Water Resources Research* 47.7 (2011): W07513.
- Cui, Y. J., Tang, A. M., Loiseau, C., & Delage, P. (2008). Determining the unsaturated hydraulic conductivity of a compacted sandbentonite mixture under constant-volume and free-swell conditions. *Physics and Chemistry of the Earth, Parts A/B/C*, 33, S462-S471.
- Culligan, K. A., Wildenschild, D., Christensen, B. S. B., Gray, W. G., & Rivers, M. L. (2006). Pore-scale characteristics of multiphase flow in porous media: a comparison of airwater and oilwater experiments. *Advances in water resources*, 29(2), 227-238.
- Canny, J. (1986). A computational approach to edge detection. *Pattern Analysis and Machine Intelligence, IEEE Transactions on*, (6), 679-698.
- Celia, M. A., Gray, W. G., Montemagno, C. D., & Reeves, P. C. (1998). On the inclusion of interfacial area in models of two-phase flow in porous media. *IAHS Publication (International Association of Hydrological Sciences)*, (250), 81-87.
- Charalampidou, E. M., Hall, S. A., Stanchits, S., Lewis, H., & Viggiani, G. (2011). Characterization of shear and compaction bands in porous sandstone deformed under triaxial compression. *Tectonophysics*, 503(1), 8-17.
- Christensen, B. S. B., Wildenschild, D., & Jensen, K. H. (2006). Using X-ray computed tomography to evaluate the initial saturation resulting from different saturation procedures.
- Clausnitzer, V., & Hopmans, J. W. (1999). Determination of phase-volume fractions from tomographic measurements in two-phase systems. *Advances in water resources*, 22(6), 577-584.
- Cnudde, V., & Boone, M. N. (2013). High-resolution X-ray computed tomography in geosciences: a review of the current technology and applications. *Earth-Science Reviews*, 123, 1-17.
- Costanza-Robinson, Molly S., Benjamin D. Estabrook, and David F. Fouhey. (2011). Representative elementary volume estimation for porosity, moisture saturation, and air-water interfacial areas in unsaturated porous media: Data quality implications. *Water Resources Research* 47.7.
- Crist, J. T., McCarthy, J. F., Zevi, Y., Baveye, P., Throop, J. A., & Steenhuis, T. S. (2004). Pore-scale visualization of colloid transport and retention in partly saturated porous media. *Vadose Zone Journal*, 3(2), 444-450.
- Culligan, K. A., Wildenschild, D., Christensen, B. S., Gray, W. G., Rivers, M. L., & Thompson, A. F. (2004). Interfacial area measurements for unsaturated flow through a porous medium. *Water Resources Research*, 40(12).
- Culligan, K. A., Wildenschild, D., Christensen, B. S. B., Gray, W. G., & Rivers, M. L. (2006). Pore-scale characteristics of multiphase flow in porous media: a comparison of airwater and oilwater experiments. *Advances in Water Resources*, 29(2), 227-238.
- Dalla, E., Hilpert, M., & Miller, C. T. (2002). Computation of the interfacial area for two-fluid porous medium systems. *Journal of contaminant hydrology*, 56(1), 25-48.
- Delage, P., & Cui, Y. J. (2008-a). An evaluation of the osmotic method of controlling suction. *Geomechanics and Geoengineering: An International Journal*, 3(1), 1-11.
- Delage, P., Romero, E., & Tarantino, A. (2008-b, June). Recent developments in the

- techniques of controlling and measuring suction in unsaturated soils. In Key note Lecture, Proc. 1st Eur. Conf. on Unsaturated Soils (pp. 33-52).
- Delage, P. (2008-c). Experimental unsaturated soil mechanics. arXiv preprint arXiv:0803.1434.
 - Desrues, J., Chambon, R., Mokni, M., & Mazerolle, F. (1996). Void ratio evolution inside shear bands in triaxial sand specimens studied by computed tomography. *Géotechnique*, 46(3), 529-546.
 - Desrues, J. (2004). Tracking strain localization in geomaterials using computerized tomography. *X-ray CT for Geomaterials*, 15-41.
 - Desrues, J., & Andò, E. (2015). Strain localization in granular media. *Comptes Rendus Physique*, 16(1), 26-36.
 - Diabira, I., Castanier, L. M., & Kovscek, A. R. (2001). Porosity and permeability evolution accompanying hot fluid injection into diatomite. *Petroleum science and technology*, 19(9-10), 1167-1185.
 - Doan, D. H., Delage, P., Nauroy, J. F., Tang, A. M., & Youssef, S. (2012). Microstructural characterization of a Canadian oil sand. *Canadian Geotechnical Journal*, 49(10), 1212-1220.
 - Dorin, S. F. C. Z., & Lucian, P. V. Soil porosity and pore size distribution.? *Scientific Bulletin of the University "Politehnica" University of Timisoara* (2011): 59-62.
 - Eko, R. M. (2004). Use of isotropic stress state framework to evaluate the effect of suction on some mechanical parameters of sainte-rosalie clay submitted to confined compression. *Agricultural Engineering International: CIGR Journal*.
 - Eral, H. B., & Oh, J. M. (2013). Contact angle hysteresis: a review of fundamentals and applications. *Colloid and polymer science*, 291(2), 247-260.
 - Estabragh, A. R., & Javadi, A. A. (2012). Effect of suction on volume change and shear behaviour of an over-consolidated unsaturated silty soil. *Geomechanics and Engineering*, 4(1), 55-65.
 - Feia, S., Ghabezloo, S., Bruchon, J. F., Sulem, J., Canou, J., & Dupla, J. F. (2014). Experimental evaluation of the pore-access size distribution of sands. *Geotech Test J*, 37(4), 1-8.
 - Feldkamp, L. A., Davis, L. C., & Kress, J. W. (1984). Practical cone-beam algorithm. *JOSA A*, 1(6), 612-619.
 - Flekky, E. G., Schmittbuhl, J., Lvholt, F., Oxaal, U., Mly, K. J., & Aagaard, P. (2002). Flow paths in wetting unsaturated flow: Experiments and simulations. *Physical Review E*, 65(3), 036312.
 - Fredlund, D. G., & Morgenstern, N. R. (1976). Constitutive relations for volume change in unsaturated soils. *Canadian Geotechnical Journal*, 13(3), 261-276.
 - Fredlund, D. G. (1979). Second Canadian Geotechnical Colloquium: Appropriate concepts and technology for unsaturated soils. *Canadian Geotechnical Journal*, 16(1), 121-139.
 - Fredlund, D. G., & Rahardjo, H. (1993). *Soil mechanics for unsaturated soils*. John Wiley & Sons.
 - Fredlund, D. G., Xing, A., Fredlund, M. D., & Barbour, S. L. (1996). The relationship of the unsaturated soil shear to the soil-water characteristic curve. *Canadian Geotechnical Journal*, 33(3), 440-448.
 - Fredlund, M. D., Fredlund, D. G., & Wilson, G. W. (1997, April). Prediction of the soil-water characteristic curve from grain-size distribution and volume-mass properties. In *Proc., 3rd Brazilian Symp. On Unsaturated Soils* (Vol. 1, pp. 13-23). Rio de Janeiro.

-
- Fredlund, D. G. (2002, March). Use of soil-water characteristic curves in the implementation of unsaturated soil mechanics. In *Proceedings of the 3rd International Conference on Unsaturated Soils*, Recife, Brazil (pp. 20-23).
 - Fredlund, D. G., Rahardjo, H., & Fredlund, M. D. (2012). *Unsaturated soil mechanics in engineering practice*. John Wiley & Sons.
 - Fredlund, D. G. (2014). The emergence of unsaturated soil mechanics. *Canadian Geotechnical Journal*, 51(12), ix-x.
 - Faruquzzaman, A. B. M., Paiker, N. R., Arafat, J., Ali, M. A., & Sorwar, G. (2008). Literature on image segmentation based on split and merge techniques. In *Proceedings of the 5th International Conference on Information Technology and Applications (ICITA 2008)* (pp. 120-125).
 - Flavigny, E., Desrues, J., & Palayer, B. (1990). Note technique-le sable dhostun RF. *Revue française de géotechnique*, (53).
 - Gallipoli, D., S. J. Wheeler, and M. Karstunen. "Modelling the variation of degree of saturation in a deformable unsaturated soil." *Géotechnique*. 53.1 (2003): 105-112.
 - Gallipoli, D., Gens, A., Sharma, R., & Vaunat, J. (2003). An elasto-plastic model for unsaturated soil incorporating the effects of suction and degree of saturation on mechanical behaviour. *Géotechnique*., 53(1), 123-136.
 - Gallipoli, D. (2012). A hysteretic soil-water retention model accounting for cyclic variations of suction and void ratio. *Geotechnique*, 62(7), 605-616.
 - Gan, J. K. M., Fredlund, D. G., & Rahardjo, H. (1988). Determination of the shear strength parameters of an unsaturated soil using the direct shear test. *Canadian Geotechnical Journal*, 25(3), 500-510.
 - Gan, Y., Maggi, F., Buscarnera, G., & Einav, I. (2013). A Particle-Water Based Model for Water Retention Hysteresis. *arXiv preprint arXiv:1307.5372*.
 - Gantzer, C. J., & Anderson, S. H. (2002). Computed tomographic measurement of macroporosity in chisel-disk and no-tillage seedbeds. *Soil and tillage research*, 64(1), 101-111.
 - Geromichalos, D., Kohonen, M. M., Scheel, M., & Herminghaus, S. (2003). The number of capillary bridges in a wet granular medium. *Phys Rev Lett* 90: 168702.
 - Grant, G. P., & Gerhard, J. I. (2007). Simulating the dissolution of a complex dense non-aqueous phase liquid source zone: 1. Model to predict interfacial area. *Water resources research*, 43(12), doi: 10.1029/2007WR006038, in press.
 - Gras, J. P. (2011). *Approche micromécanique de la capillarité dans les milieux granulaires: rétention d'eau et comportement mécanique* (Doctoral dissertation, Université Montpellier II-Sciences et Techniques du Languedoc).
 - Gras, J. P., Delenne, J. Y., Soulié, F., & El Youssoufi, M. S. (2011). DEM and experimental analysis of the water retention curve in polydisperse granular media. *Powder Technology*, 208(2), 296-300.
 - Gruber, I., Zinovik, I., Holzer, L., Flisch, A., & Poulikakos, L. D. (2012). A computational study of the effect of structural anisotropy of porous asphalt on hydraulic conductivity. *Construction and Building Materials*, 36, 66-77.
 - Guber, A. (2010). The Through Porosity of Soils as the Control of Hydraulic Conductivity. In *Proceedings of the 19th World Congress of Soil Science: Soil solutions for a changing world*, Brisbane, Australia, 1-6 August 2010. Working Group 1.2 Architecture of soil structural diversity (pp. 80-83). International Union of Soil Sciences (IUSSO).
 - Hall, S. A., Bornert, M., Desrues, J., Pannier, Y., Lenoir, N., Viggiani, G., & Bésuelle,

- P. (2010). Discrete and continuum analysis of localized deformation in sand using X-ray CT and volumetric digital image correlation. *Geotechnique*, 60(5), 315-322.
- Hall, S. A., Desrues, J., Viggiani, G., Bésuelle, P., & Andò, E. (2012). Experimental characterization of (localized) deformation phenomena in granular geomaterials from specimen down to inter-and intra-grain scales. *Procedia IUTAM*, 4, 54-65.
 - Halsey, T. C., & Levine, A. J. (1998). How sandcastles fall. *Physical Review Letters*, 80(14), 3141.
 - Hamid, T. B., & Miller, G. A. (2009). Shear strength of unsaturated soil interfaces. *Canadian Geotechnical Journal*, 46(5), 595-606.
 - Hashemi, M. A., Khaddour, G., Franois, B., Massart, T. J., & Salager, S. (2014). A tomographic imagery segmentation methodology for three-phase geomaterials based on simultaneous region growing. *Acta Geotechnica*, 9(5), 831-846.
 - Hassanizadeh, S. M., & Gray, W. G. (1993). Thermodynamic basis of capillary pressure in porous media. *Water Resources Research*, 29(10), 3389-3405.
 - Heidarian, P. (2012). Effect of Initial Water Content and Stress History on Water-Retention Behaviour of Mine Tailings (Doctoral dissertation, Carleton University Ottawa).
 - Helland, J. O., & Skjaeveland, S. M. (2007). Relationship between capillary pressure, saturation, and interfacial area from a model of mixed wet triangular tubes. *Water resources research*, 43(12).
 - Higo, Y., Oka, F., Sato, T., Matsushima, Y., & Kimoto, S. (2013). Investigation of localized deformation in partially saturated sand under triaxial compression using micro focus X-ray CT with digital image correlation. *Soils and Foundations*, 53(2), 181-198.
 - Ho, D. Y., & Fredlund, D. G. (1982, January). Increase in strength due to suction for two Hong Kong soils. In *Engineering and Construction in Tropical Soils ASCE Speciality Conf. Hawaii* (pp. 263-295).
 - Hoek, E. (1990, June). Estimating Mohr-Coulomb friction and cohesion values from the Hoek-Brown failure criterion. In *International Journal of Rock Mechanics and Mining Sciences & Geomechanics Abstracts* (Vol. 27, No. 3, pp. 227-229).
 - Hounsfield, G. N. (1976). U.S. Patent No. 3,940,625. Washington, DC: U.S. Patent and Trademark Office.
 - Houston, S. L., Perez-Garcia, N., & Houston, W. N. (2008). Shear strength and shear-induced volume change behaviour of unsaturated soils from a triaxial test program. *Journal of geotechnical and geoenvironmental engineering*, 134(11), 1619-1632.
 - Hsieh J. (2003). *Computed Tomography: Principles, Design, Artifacts, and Recent Advances*. Bellingham: SPIE Press.
 - Hueckel, T., Mielniczuk, B., & El Youssefi, M. S. (2013). Micro-scale study of rupture in desiccating granular media. In *Proceedings of Geo-Congress* (pp. 808-817).
 - Izady, A., Ghahraman, B., & Davari, K. (2010). Hysteresis: phenomenon and modeling in soil-water relationship. *Iran Agricultural Research*, 27(1.2), 47-64.
 - Joekar-Niasar, V., Hassanizadeh, S. M., & Leijnse, A. (2008). Insights into the relationships among capillary pressure, saturation, interfacial area and relative permeability using pore-network modeling. *Transport in Porous Media*, 74(2), 201-219.
 - Juneja, A., & Raghunandan, M. (2010, December). Effect of specimen preparation on strength of sands. In *Indian Geotechnical Conference, Mumbai, India* (pp. 327-330).
 - Kaddhour, G., Andò, E., Salager, S., Bésuelle, P., Viggiani, C., Hall, S., & Desrues, J. (2013). Application of X-ray Tomography to the Characterisation of Grain-Scale Mechanisms in Sand. In *Multiphysical Testing of Soils and Shales* (pp. 195-200). Springer Berlin

Heidelberg.

- Kaestner, A., et al. "Mapping the 3D water dynamics in heterogeneous sands using thermal neutrons." *Chemical Engineering Journal* 130.2 (2007): 79-85.
- Karunaratna A, A. K., Chhoden A, T., Kawamoto A, K., Komatsu A, T., Moldrup B, P., & de Jonge C, L. W. (2010). Estimating hysteretic soil-water retention curves in hydrophobic soil by a mini tensiometer-TDR coil probe. In *19th World Congress of Soil Science, Soil Solutions for Changing World*.
- Ketcham, R. A., & Carlson, W. D. (2001). Acquisition, optimization and interpretation of X-ray computed tomographic imagery: applications to the geosciences. *Computers & Geosciences*, 27(4), 381-400.
- Khaddour, G., Hashemi, A., Salager, S., Desrues, J., Massart, T. J., & Francois, B. (2013). Phase segmentation in 3D X-ray images of unsaturated granular materials. In *XVI French-Polish Colloquium of Soil and Rock Mechanics*, Montpellier, France.
- Khalili, N., Habte, M. A., & Valliappan, S. (2007). Monotonic and cyclic analysis of granular soils. In *Computational Methods in Engineering & Science* (pp. 59-70). Springer Berlin Heidelberg.
- Kim, D. H., Yang, H. J., Kim, K. Y., & Yun, T. S. (2015). Experimental Investigation of Evaporation and Drainage in Wetttable and Water-Repellent Sand.
- Kim, F. H., Penumadu, D., Gregor, J., Kardjilov, N., & Manke, I. (2012). High-Resolution Neutron and X-Ray Imaging of Granular Materials. *Journal of Geotechnical and Geoenvironmental Engineering*, 139(5), 715-723.
- Koliji, A. (2008). Mechanical behavior of unsaturated aggregated soils (Doctoral dissertation, Lausanne University EPFL, France).
- Konrad, J. M., & Dubeau, S. (2003). Cyclic strength of stratified soil specimens. In *Submarine Mass Movements and Their Consequences* (pp. 47-57). Springer Netherlands.
- Lam, L., Fredlund, D. G., & Barbour, S. L. (1987). Transient seepage model for saturated-unsaturated soil systems: a geotechnical engineering approach. *Canadian Geotechnical Journal*, 24(4), 565-580.
- Lamb, T. W., & Whitman, R. V. (1969). *Soil mechanics*. Massachusetts Institute of Technology, Cambridge, MA.
- Leal-Vaca, J. C., Gallegos-Fonseca, G., & Rojas-Gonzalez, E. (2012). The Decrease of the Strength of Unsaturated Silty Sand. *Ingeniera Investigación y Tecnológica*, 13(4), 393-402.
- Legrain, G., Cartraud, P., Perreard, I., & Mos, N. (2011). An X-FEM and level set computational approach for image-based modelling: Application to homogenization. *International Journal for Numerical Methods in Engineering*, 86(7), 915-934.
- Leong, E. C., Rahardjo, H., & Fredlund, D. G. (2001). Application of unsaturated soil mechanics in geotechnical engineering. In *Proc., 8th East Asian Pacific Conf. on Structural Engineering and Construction*.
- Likos, W. J., & Lu, N. (2002, June). Hysteresis of capillary cohesion in unsaturated soils. In *15th ASCE Engineering Mechanics Conference* (Vol. 150, pp. 2-5).
- Likos, W. J. (2014). Effective stress in unsaturated soil: Accounting for surface tension and interfacial area. *Vadose Zone Journal*, 13(5).
- Lim, P. C., Barbour, S. L., & Fredlund, D. G. (1998). The influence of degree of saturation on the coefficient of aqueous diffusion. *Canadian geotechnical journal*, 35(5), 811-827.
- Lin, B., & Cerato, A. B. (2012). Hysteretic Water Retention Behavior of Two Highly Clayey Expansive Soils. In *GeoCongress 2012@ sState of the Art and Practice in Geotechnical Engineering* (pp. 1205-1212). ASCE.

- Lins, Y. (2010). Hydro-mechanical properties of partially saturated sand. Dissertation as a requirement of the degree of Doctor Engineer. Faculty of Civil Engineering University Bochum.
- Loll, P; & Moldrup, P. (2000). Soil Characterization and Polluted Soil Assessment. Aalborg University, Denmark, p25.
- Lu, N., & Likos, W. J. (2004). Unsaturated soil mechanics. Wiley.
- Lu, N., & Likos, W. J. (2006). Suction stress characteristic curve for unsaturated soil. *Journal of Geotechnical and Geoenvironmental Engineering*, 132(2), 131-142.
- Maaaitah, O. N. (2012). Soil-Water Characteristic Curve Model-Silty Sand Soil.
- Mac, M., Desbois, G., Pardo, P., & Casanova, I. (2012). Ion beam tomography of the nano-and microstructure of cementitious materials. In *Proceedings of the 4th International Symposium on Nanotechnology in Construction (NICOM-4)*.
- Malladi, R., Sethian, J. A., & Vemuri, B. C. (1993, June). Topology-independent shape modeling scheme. In *SPIE's 1993 International Symposium on Optics, Imaging, and Instrumentation* (pp. 246-258). International Society for Optics and Photonics.
- Maqsoud, A., Bussire, B., Mbonimpa, M., & Aubertin, M. (2004, October). Hysteresis effects on the water retention curve: a comparison between laboratory results and predictive models. In *Proceedings of the 57th Canadian Geotechnical Conference and the 5th Joint CGS-IAH Conference, Québec City, Que* (pp. 24-27).
- Manahiloh, K. N. (2013). Microstructural analysis of unsaturated granular soils using X-ray computed tomography (Doctoral dissertation, Washington state university).
- Mani, R. A. (2014). Capillary interactions, shear thickening and liquid migration in wet granular media (Doctoral dissertation, Diss., Eidgenössische Technische Hochschule ETH Zurich, Nr. 21809).
- Marinho, F. A. M., Take, W. A., & Tarantino, A. (2008). Measurement of matric suction using tensiometric and axis translation techniques. *Geotechnical and Geological Engineering*, 26(6), 615-631.
- Marr, D., & Hildreth, E. (1980). Theory of edge detection. *Proceedings of the Royal Society of London. Series B. Biological Sciences*, 207(1167), 187-217.
- Main, D. (2011). An effective stress based model for the dependency of a water retention curve on void ratio.
- Matsuoka, H., Sun, D. A., Kogane, A., Fukuzawa, N., & Ichihara, W. (2002). Stress-strain behaviour of unsaturated soil in true triaxial tests. *Canadian Geotechnical Journal*, 39(3), 608-619.
- Meyer, F. (2012). The watershed concept and its use in segmentation: a brief history. *arXiv preprint arXiv:1202.0216*.
- Mitarai, N., & Nori, F. (2006). Wet granular materials. *Advances in Physics*, 55(1-2), 1-45.
- Mitchell, J. K., & Soga, K. (1976). *Fundamentals of soil behaviour* (p. 422). New York: Wiley.
- Monroy, R. (2006). The influence of load and suction changes on the volumetric behaviour of compacted London Clay (Doctoral dissertation, Imperial College London (University of London)).
- Morrow, N. R. (1970). Physics and thermodynamics of capillary action in porous media. *Industrial & Engineering Chemistry*, 62(6), 32-56.
- Murthy, V. N. S. (2002). *Geotechnical engineering: principles and practices of soil mechanics and foundation engineering*. CRC Press.

-
- Myers, G. R., Kingston, A. M., Varslot, T. K., Turner, M. L., & Sheppard, A. P. (2011). Dynamic X-ray micro-tomography for real time imaging of drainage and imbibition processes at the pore scale. In International Symposium of the Society of Core Analysts, Austin, TX, 1821 September (pp. 1-12).
 - Narter, M. (2012). Characterizing Non-Wetting Fluid in Natural Porous Media Using Synchrotron X-Ray Micro tomography.
 - Nasta, P., Romano, N., Assouline, S., Vrugt, J. A., & Hopmans, J. W. (2013). Prediction of spatially variable unsaturated hydraulic conductivity using scaled particle-size distribution functions. *Water Resources Research*, 49(7), 4219-4229.
 - Newman, G. P., & Wilson, G. W. (1997). Heat and mass transfer in unsaturated soils during freezing. *Canadian Geotechnical Journal*, 34(1), 63-70.
 - Nguyen, G. D., & Gan, Y. (2014). A multiphase constitutive modeling framework for unsaturated soil behavior. *Unsaturated Soils: Research & Applications*, 1, 335.
 - Nimmo, J. R. (1992). Semi empirical model of soil water hysteresis. *Soil Science Society of America Journal*, 56(6), 1723-1730.
 - Nimmo, J. R. (2004). Porosity and pore size distribution. *Encyclopedia of Soils in the Environment*, 3, 295-303.
 - Nishigaki, M., Sun, Y., & Kohno, I. (1994). A Study on the Elasto-plastical Constitutive Equation for Unsaturated Soil. *Memoirs of the Faculty of Engineering, Okayama University*, 28(2), 59-75.
 - Nock, R., & Nielsen, F. (2004). Statistical region merging. *Pattern Analysis and Machine Intelligence, IEEE Transactions on*, 26(11), 1452-1458.
 - Nuntasarn, R., & Wannakul, V. (2012). The Relationship between Soil Suction and the Maximum Unsaturated Undrained Shear Strengths of Compacted Khon Kaen Soil. *International journal of GEOMATE: geotechnique, construction materials and environment*, 2(1), 166-170.
 - Nuth, M., & Laloui, L. (2008). Effective stress concept in unsaturated soils: Clarification and validation of a unified framework. *International journal for numerical and analytical methods in Geomechanics*, 32(7), 771-801.
 - Nuth, M. (2009). Constitutive modelling of unsaturated soils with hydro-geo mechanical couplings (Doctoral dissertation, école polytechnique fédérale de Lausanne).
 - Ogundalu, A., & Oyekan, G. (2014). Mineralogical and Geotechnical Characterization of Maiduguri Black Cotton Soil by X-Ray Diffraction (XRD), X-Ray Photoelectron (XPS) And Scanning Electron Spectroscopy (SEM). *International Journal of Engineering and Technology*, 4(6).
 - Padilla, J. M., Houston, W. N., Lawrence, C. A., Fredlund, D. G., Houston, S. L., & Perez, N. P. (2006). An automated triaxial testing device for unsaturated soils. *Geotechnical Special Publication*, 147(2), 1775.
 - Pansu, M., & Gautheyrou, J. (2007). *Handbook of soil analysis: mineralogical, organic and inorganic methods*. Springer Science & Business Media.
 - Papagianakis, A. T., & Fredlund, D. G. (1984). A steady state model for flow in saturated-unsaturated soils. *Canadian Geotechnical Journal*, 21(3), 419-430.
 - Parkinson, J. H., & Brans, P. L. (1977). *The mechanics of soils, an introduction to critical state soil mechanics* (No. Monograph).
 - Perona, P., & Malik, J. (1990). Scale-space and edge detection using anisotropic diffusion. *Pattern Analysis and Machine Intelligence, IEEE Transactions on*, 12(7), 629-639.
 - Perret, J., Prasher, S. O., Kantzas, A., & Langford, C. (1999). Three-dimensional quan-

tification of macropore networks in undisturbed soil cores. *Soil Science Society of America Journal*, 63(6), 1530-1543.

- Pham, D. L., Xu, C., & Prince, J. L. (2000). Current methods in medical image segmentation 1. *Annual review of biomedical engineering*, 2(1), 315-337.

- Pham, H. Q. (2005). A volume-mass constitutive model for unsaturated soils.

- Pierret, A., Capowiez, Y., Belzunces, L., & Moran, C. J. (2002). 3D reconstruction and quantification of macro pores using X-ray computed tomography and image analysis. *Geoderma*, 106(3), 247-271.

- Plaisted, M. D. (2014). Characterization of soil unsaturated flow properties using steady state centrifuge methods (Doctoral dissertation).

- Porter, M. L., Wildenschild, D., Grant, G., & Gerhard, J. I. (2010). Measurement and prediction of the relationship between capillary pressure, saturation, and interfacial area in a NAPL water glass bead system. *Water Resources Research*, 46(8).

- Poulos, S. J. (1971). The stress-strain curves of soils. *Geotechnical Engineers Incorporated*.

- Reeves, P. C., & Celia, M. A. (1996). A functional relationship between capillary pressure, saturation, and interfacial area as revealed by a pore scale network model. *Water Resources Research*, 32(8), 2345-2358.

- Richefeu, V., El Youssoufi, M. S., & Radjai, F. (2006). Shear strength properties of wet granular materials. *Physical Review E*, 73(5), 051304.

- Richefeu, V., El Youssoufi, M. S., Peyroux, R., & Radjai, F. (2008). A model of capillary cohesion for numerical simulations of 3D poly-disperse granular media. *International Journal for Numerical and Analytical Methods in Geomechanics*, 32(11), 1365-1383.

- Riedel, I. (2011) Characterization and micro-scale analysis of Hostun sand water retention behavior. "Master's thesis, University of Joseph Fourier Grenoble, 2011.

- Riedel I., Andò E., Salager S., Bésuelle P., Viggiani G. (2012). Water retention behavior explored by x-ray CT analysis. *Springer Series in Unsaturated Soils: Research and Applications 2012, Part 1*, 81-88.

- Righi, D., & Elsass, F. (1996). Characterization of soil clay minerals: decomposition of X-ray diffraction diagrams and high-resolution electron microscopy. *Clays and clay minerals*, 44(6), 791-800.

- Rimmer, A., DiCarlo, D. A., Steenhuis, T. S., Bierck, B., Durnford, D., & Parlange, J. Y. (1998). Rapid fluid content measurement method for fingered flow in an oilwatersand system using synchrotron X-rays. *Journal of contaminant hydrology*, 31(3), 315-335.

- Romero, E., & Simms, P. H. (2008). Microstructure investigation in unsaturated soils: a review with special attention to contribution of mercury intrusion porosimetry and environmental scanning electron microscopy. *Geotechnical and Geological engineering*, 26(6), 705-727.

- Sadek, T., Lings, M., Dihoru, L., & Muir Wood, D. (2007). Wave transmission in Hostun sand: multiaxial experiments. *Rivista Italiana Geotecnica*, 41(2), 69-84.

- Salager, S. (2007). Etude de la rétention d'eau et de la consolidation des sols dans un cadre thermo-hydro-mécanique (Doctoral dissertation, Université Montpellier 2, sciences et techniques du Languedoc).

- Salager, S., El Youssoufi, M. S., & Saix, C. (2010). Definition and experimental determination of a soil-water retention surface. *Canadian Geotechnical Journal*, 47(6), 609-622.

- Salager, S., Khaddour, G., Charrier, P., & Desrues, J. (2014). An investigation into unsaturated states of granular media using X-ray computed tomography. *Unsaturated*

Soils: Research & Applications, pages: 703-709, CRC Press.

- Salarashayeri, A. F., & Siosemarde, M. (2012). Prediction of soil hydraulic conductivity from particle-size distribution. *World Acad. Sci. Eng. Technol*, 61(61), 454-458.
- Satik, C., & Horne, R. N. (1998). A measurement of steam-water relative permeability. In *Proceedings of 23rd Workshop on Geothermal Reservoir Engineering*, Stanford University, Stanford, California.
- Sethian, J. A. (1999). Advancing interfaces: level set and fast marching methods. ICIAM.
- Scarfe, W. C., & Farman, A. G. (2008). What is cone-beam CT and how does it work *Dental Clinics of North America*, 52(4), 707-730.
- Schanz, T., & Alabdullah, J. (2007). Testing unsaturated soil for plane strain conditions: A new double wall biaxial device. In *Experimental Unsaturated Soil Mechanics* (pp. 169-178). Springer Berlin Heidelberg.
- Scheel, M., Seemann, R., Brinkmann, M., Di Michiel, M., Sheppard, A., Breidenbach, B., & Herminghaus, S. (2008). Morphological clues to wet granular pile stability. *Nature Materials*, 7(3), 189-193.
- Scholts, L., Chareyre, B., Nicot, F., Darve, F. (2009). Discrete modelling of capillary mechanisms in multi-phase granular media. *Computer Modeling in Engineering and Sciences* (52), pages 297318.
- Scholts, L., Chareyre, B., Nicot, F., & Darve, F. (2009). Micromechanics of granular materials with capillary effects. *International journal of engineering science*, 47(1), 64-75.
- Schroth, M. H., Oostrom, M., Dobson, R., & Zeyer, J. (2008). Thermodynamic model for fluid-fluid interfacial areas in porous media for arbitrary drainage-imbibition sequences.
- Sethian, J. A. (1999). Advancing interfaces: level set and fast marching methods. ICIAM.
- Sheng, D., Smith, D. W., Sloan, S., & Gens, A. (2003). Finite element formulation and algorithms for unsaturated soils. Part II: Verification and application. *International Journal for Numerical and Analytical Methods in Geomechanics*, 27(9), 767-790.
- Sheng, D., Fredlund, D. G., & Gens, A. (2008). A new modelling approach for unsaturated soils using independent stress variables. *Canadian Geotechnical Journal*, 45(4), 511-534.
- Simms, P. H., & Yanful, E. K. (2004). A discussion of the application of mercury intrusion porosimetry for the investigation of soils, including an evaluation of its use to estimate volume change in compacted clayey soils. *Geotechnique*, 54(6), 421-426.
- Soulié, F., El Youssoufi, M. S., Cherblanc, F., & Saix, C. (2012). Capillary Cohesive Local Force: Modelling and Experiment. In *Mechanics, Models and Methods in Civil Engineering* (pp. 271-278). Springer Berlin Heidelberg.
- Sreedeeep, S., & Singh, D. N. (2005). Estimating unsaturated hydraulic conductivity of fine-grained soils using electrical resistivity measurements. *Journal of ASTM International*, 2(1), 10-1520.
- Sun, D. A., D. Sheng, L. Xiang, and S. W. Sloan (2008). Elasto plastic prediction of hydro-mechanical behavior of unsaturated soils under undrianed conditions. *Computers and Geotechnics* 35, 845852.
- Sunyer Amat, A. (2008). Elastic stiffness moduli of Hostun sand.
- Szymkiewicz, A. (2013). Mathematical Models of Flow in Porous Media. In *Modelling Water Flow in Unsaturated Porous Media* (pp. 9-47). Springer Berlin Heidelberg.
- Taina, I. A., Heck, R. J., & Elliot, T. R. (2008). Application of X-ray computed tomog-

- raphy to soil science: A literature review. *Canadian Journal of Soil Science*, 88(1), 1-19.
- Tanaka, A., Nakano, T., & Ikehara, K. (2011). X-ray computerized tomography analysis and density estimation using a sediment core from the challenger mound area in the porcupine sea bight, off western Ireland. *Earth, planets and space*, 63(2), 103-110.
 - Tang, A. M., & Cui, Y. J. (2005). Controlling suction by the vapour equilibrium technique at different temperatures and its application in determining the water retention properties of MX80 clay. *Canadian Geotechnical Journal*, 42(1), 287-296.
 - Tang, A. M., Cui, Y. J., Qian, L. X., Delage, P., & Ye, W. M. (2010). Calibration of the osmotic technique of controlling suction with respect to temperature using a miniature tensiometer. *Canadian Geotechnical Journal*, 47(3), 359-365.
 - Tarantino, A. and Hoffmann, C. (2008). Effect of grain size distribution on water retention behavior of well graded coarse material. *Unsaturated Soils. Advances in Geo-Engineering*, 291297.
 - Tarantino, A., Romero, E., Cui, Y.-J. (2009). *Laboratory and Field Testing of Unsaturated Soils*; Springer: Amsterdam, The Netherlands; p. 220.
 - Tedesco, D. (2006). *Hydro-mechanical behaviour of lime-stabilised soils* (Doctoral dissertation, PhD thesis, Università degli Studi di Cassino Facoltà di Ingegneria).
 - Terzaghi, K., Peck, R. B., & Mesri, G. (1996). *Soil mechanics in engineering practice*. John Wiley & Sons.
 - Thieu, N. T. M., Fredlund, M. D., Fredlund, D. G., & Vu, H. Q. (2001, October). Seepage modelling in a saturated/unsaturated soil system. In *Proceedings of the International Conference on Management of the Land and Water Resources*, Hanoi, Vietnam (pp. 20-22).
 - Tippkötter, R., Eickhorst, T., Taubner, H., Gredner, B., & Rademaker, G. (2009). Detection of soil water in macropores of undisturbed soil using microfocus X-ray tube computerized tomography (muCT). *Soil and Tillage Research*, 105(1), 12-20.
 - Taina, I. A., Heck, R. J., & Elliot, T. R. (2008). Application of X-ray computed tomography to soil science: A literature review. *Canadian Journal of Soil Science*, 88(1), 1-19.
 - Tanaka, A., Nakano, T., & Ikehara, K. (2011). X-ray computerized tomography analysis and density estimation using a sediment core from the challenger mound area in the porcupine sea bight, off western Ireland. *Earth, planets and space*, 63(2), 103-110.
 - Tovar, R. A. (1997). *Measurements of relative permeability for stream-water flow in porous media*, Phd thesis, Stanford University, USA.
 - Uchaipichat, A. (2010-a). Hydraulic hysteresis effect on compressibility of unsaturated soils. *Journal of Engineering and Applied Sciences*, Vol. 5 Issue 10, p92.
 - Uchaipichat, A. (2010-b). Prediction of shear strength for unsaturated soils under drying and wetting processes. *Electronic Journal of Geotechnical Engineering*, 15, 1087-1102.
 - Vanapalli, S. K., Fredlund, D. G., Pufahl, D. E., & Clifton, A. W. (1996). Model for the prediction of shear strength with respect to soil suction. *Canadian Geotechnical Journal*, 33(3), 379-392.
 - Vanapalli, S. K., Sillers, W. S., & Fredlund, M. D. (1998, October). The meaning and relevance of residual state to unsaturated soils. In *Proceedings of the 51st Canadian Geotechnical Conference*, Edmonton, Alta (pp. 4-7).
 - Vanapalli, S. K., Fredlund, D. G., & Pufahl, D. E. (1999). The influence of soil structure and stress history on the soilwater characteristics of a compacted till. *Géotechnique*, 49(2), 143-159.
 - Vanapalli, S. K., & Fredlund, D. G. (2000). Comparison of different procedures to predict

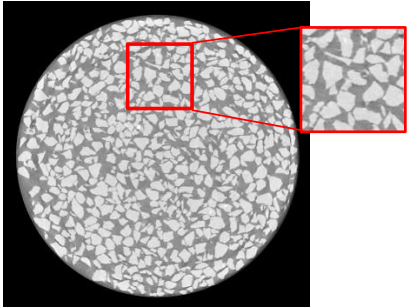
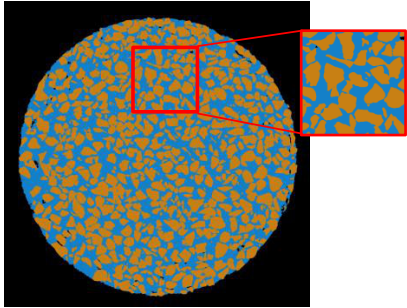
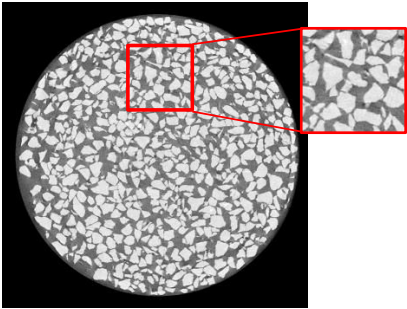
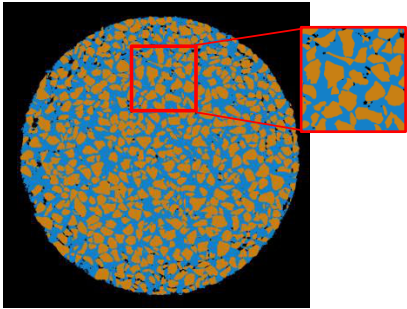
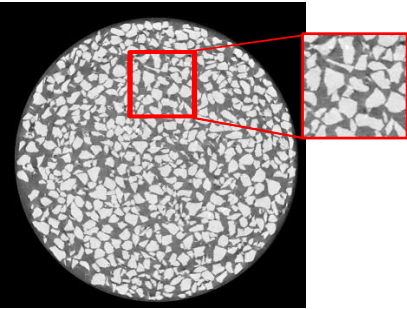
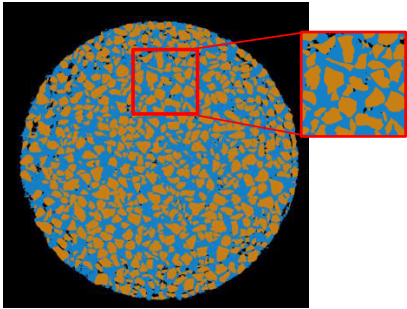
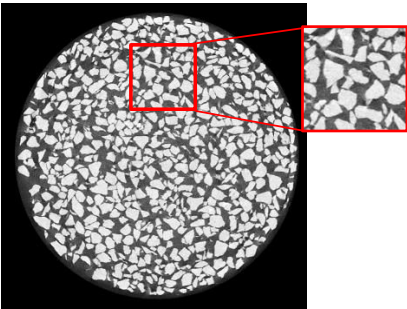
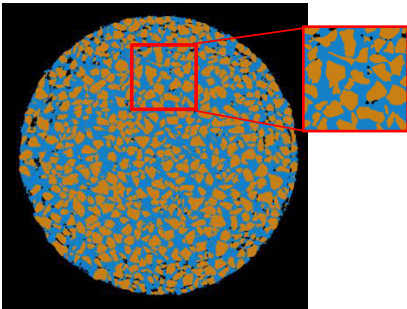
- unsaturated soil shear strength. Geotechnical Special Publication, 195-209. - Vanapalli, S. K., & Lane, J. J. (2002, April). A simple technique for determining the shear strength of fine-grained unsaturated soils using the conventional direct shear apparatus. In 2nd Canadian Specialty Conference on Computer Applications in Geotechnique, Winnipeg (pp. 245-253).
- Vanapalli, S. K., Pufahl, D. E., & Fredlund, D. G. (2002). Effect of Compaction on The Unsaturated Shear Strength of a Compacted Till. In Proceedings of 3rd Int. Conf. on Unsaturated Soils 10-13 march, Recife-Brazil (Vol. 1, pp. 271-276).
- Vanapalli, S. K., Nicotera, M. V., & Sharma, R. S. (2008). Axis translation and negative water column techniques for suction control. *Geotechnical and Geological Engineering*, 26(6), 645-660.
- Van Genuchten, M. T. (1980). A closed-form equation for predicting the hydraulic conductivity of unsaturated soil. *Soil Sci. Soc. Am. J.* 44, 892-898.
- Vanoudheusden, E., Sultan, N., & Cochonat, P. (2004). Mechanical behaviour of unsaturated marine sediments: experimental and theoretical approaches. *Marine Geology*, 213(1), 323-342.
- VandenBygaart, A. J., & Protz, R. (1999). The representative elementary area (REA) in studies of quantitative soil micromorphology. *Geoderma*, 89(3), 333-346.
- Viggiani, G. and Hall, S.A. (2008). Full-field measurements, a new tool for laboratory experimental geomechanics. Keynote Fourth Symposium on Deformation Characteristics of Geomaterials, 22-24 September 2008, Atlanta, USA (eds Burns, S.E., Mayne, P.W. & Santamarina, J.C.) Amsterdam, IOS Press, 1, 3-26.
- Vlahinic, I., Andò, E., Viggiani, G., & Andrade, J. E. (2014). Towards a more accurate characterization of granular media: extracting quantitative descriptors from tomographic images. *Granular Matter*, 16(1), 9-21.
- Wang, Q., Minh Tang, A., Cui, Y. J., Delage, P., Barnichon, J. D., & Ye, W. M. (2013). The effects of technological voids on the hydro-mechanical behavior of compacted bentonite and mixture. *Soils and foundations*, 53(2), 232-245.
- Wayllace, A., & Lu, N. (2011). A transient water release and imbibitions method for rapidly measuring wetting and drying soil water retention and hydraulic conductivity functions. *Geotechnical Testing Journal*, 35(1), 1-15.
- Wheeler, S. J. (1986). The stress-strain behaviour of soils containing gas bubbles (Doctoral dissertation, University of Oxford).
- Wheeler, S. J., R. S. Sharma, and M. S. R. Buisson (2003). Coupling of hydraulic hysteresis and stress-strain behavior in unsaturated soils. *Géotechnique* 53, 415-444.
- Wildenschild, D., Vaz, C. M. P., Rivers, M. L., Rikard, D., & Christensen, B. S. B. (2002). Using X-ray computed tomography in hydrology: systems, resolutions, and limitations. *Journal of Hydrology*, 267(3), 285-297.
- Wildenschild, D., Culligan, K. A., & Christensen, B. S. (2004, October). Application of x-ray micro tomography to environmental fluid flow problems. In *Optical Science and Technology, the SPIE 49th Annual Meeting* (pp. 432-441). International Society for Optics and Photonics.
- Wildenschild, D., Hopmans, J. W., Rivers, M. L., & Kent, A. J. R. (2005). Quantitative analysis of flow processes in a sand using synchrotron-based X-ray micro tomography. *Vadose Zone Journal*, 4(1), 112-126.
- Winfield, K. A. (2000). Factors controlling water retention of alluvial deposits western Mojave Desert.

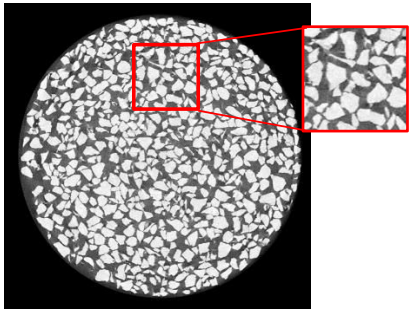
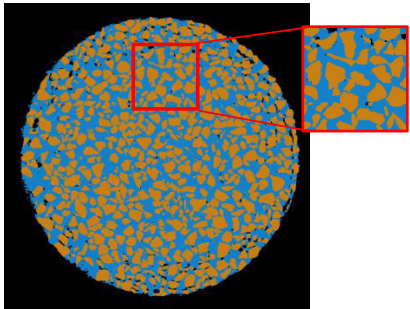
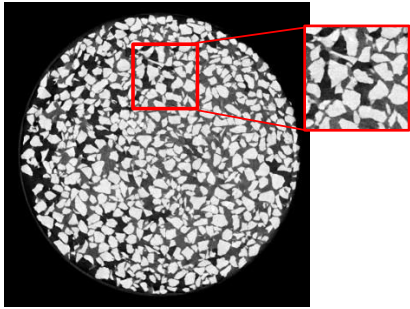
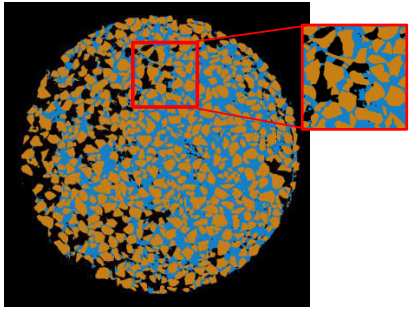
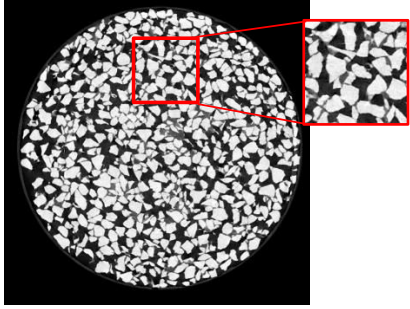
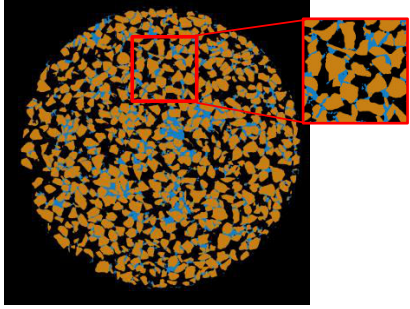
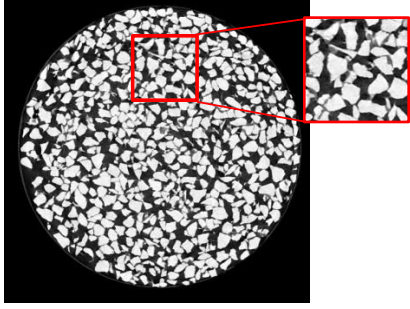
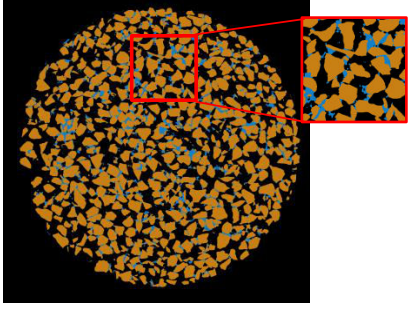
- Wulfsohn, D., Adams, B. A., & Fredlund, D. G. (1998). Triaxial testing of unsaturated agricultural soils. *Journal of agricultural engineering research*, 69(4), 317-330.
- Wang, Y., Kharaghani, A., Metzger, T., & Tsotsas, E. (2011). Visualization of liquid in drying particle aggregates by X-ray microtomography and use for pore-scale modeling. In: *Proceedings of the 3rd European Drying Conference (EuroDrying)*, 26-28 October, Balearic Island, Spain, ISBN 978-84-694-7298-9.
- Yadav, P., Chauhan, J. S., Kannoja, P., Jain, N. K., & Tomar, V. (2010). A Review: On Scale-Up Factor Determination of Rapid Mixer Granulator. *Scholar Research Library* ISSN, 0975-8071.
- Yang, C., Cui, Y. J., Pereira, J. M., & Huang, M. S. (2008). A constitutive model for unsaturated cemented soils under cyclic loading. *Computers and Geotechnics*, 35(6), 853-859.
- Yuan, Y., & Lee, T. R. (2013). Contact angle and wetting properties. In *Surface science techniques* (pp. 3-34). Springer Berlin Heidelberg.
- Zakaria, I. (1994). Yielding of unsaturated soil.
- Zevi, Y., Dathe, A., McCarthy, J. F., Richards, B. K., & Steenhuis, T. S. (2005). Distribution of colloid particles onto interfaces in partially saturated sand. *Environmental science & technology*, 39(18), 7055-7064.
- Zhang, L., & Fredlund, D. G. (2005). A General Air-phase Permeability Function for Airflow through Unsaturated Soils. In *Slopes and Retaining Structures Under Seismic and Static Conditions* (pp. 1-15). ASCE.
- Zhang, Y., Gallipoli, D., & Augarde, C. (2007, January). Parallel computing of unsaturated soils using element-by-element and domain decomposition methods. In *3rd Asian conference on unsaturated soils*, Nanjing (pp. 425-30).
- Zhang, X., Li, L., & Lytton, R. L. (2012). Fast Determination of Soil Behavior in the Capillary Zone Using Simple Laboratory Tests.
- Zhou, A. N., Sheng, D., Sloan, S. W., & Gens, A. (2012). Interpretation of unsaturated soil behaviour in the stressSaturation space, I: Volume change and water retention behaviour. *Computers and Geotechnics*, 43, 178-187.
- Zhou, A. N. (2013). A contact angle-dependent hysteresis model for soilwater retention behaviour. *Computers and Geotechnics*, 49, 36-42.
- Zik, O., & Stavans, J. (1991). Self-diffusion in granular flows. *EPL (Europhysics Letters)*, 16(3), 255.
- Zisman, W. A. (1964). Relation of the equilibrium contact angle to liquid and solid constitution.

Appendix A

Trinarization results

A.1 Drying path D_1

Suction (kPa)	a)	b)
Complete saturation $s = \text{kPa}$		
$s = 1 \text{ kPa}$		
$s = 1.2 \text{ kPa}$		
$s = 1.4 \text{ kPa}$		

$s = 1.6 \text{ kPa}$		
$s = 1.8 \text{ kPa}$		
$s = 2 \text{ kPa}$		
$s = 2.2 \text{ kPa}$		

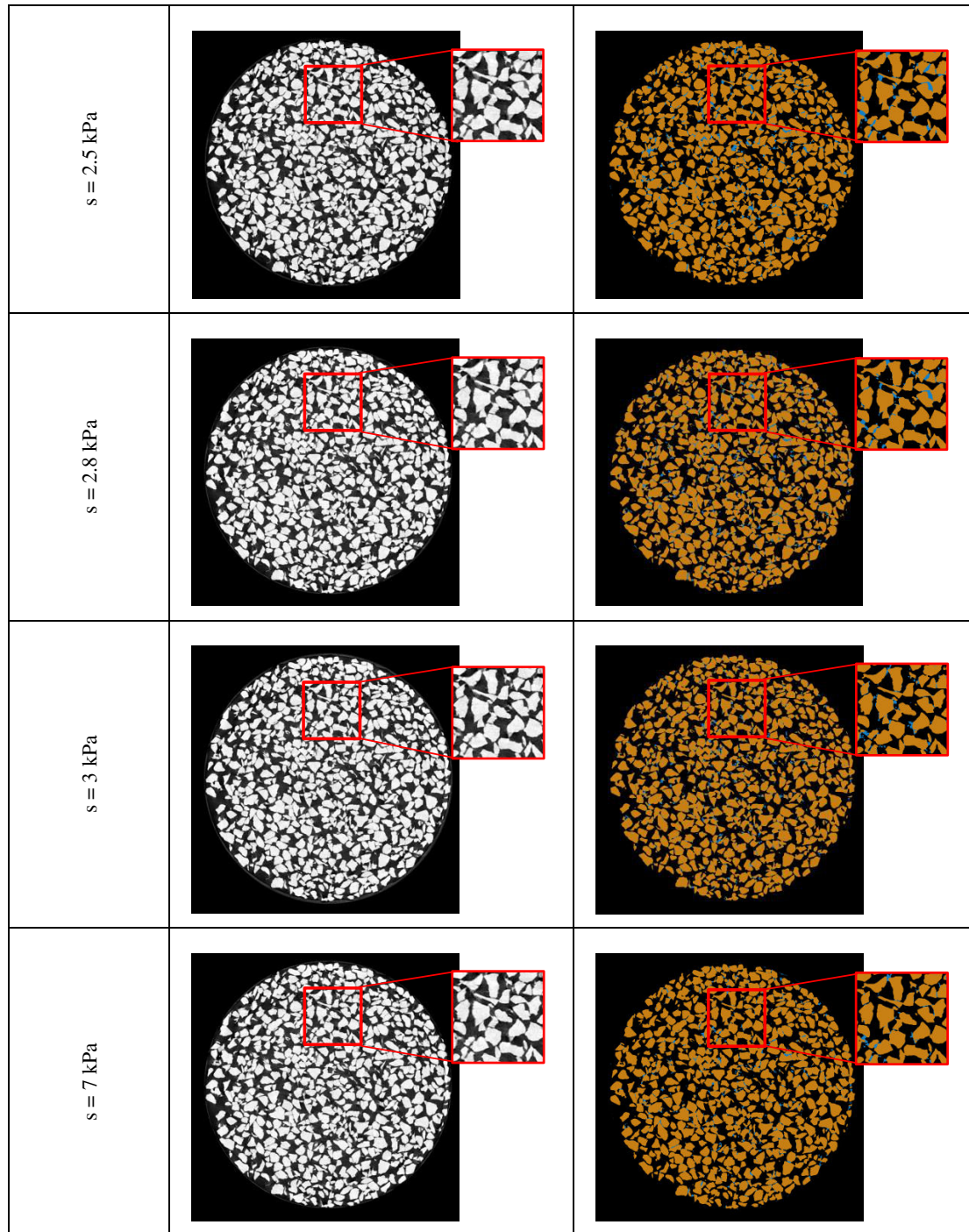
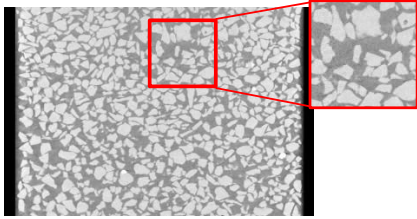
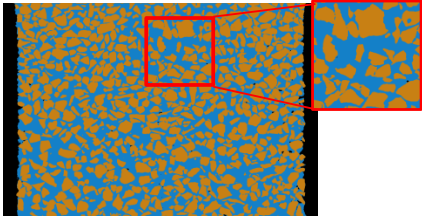
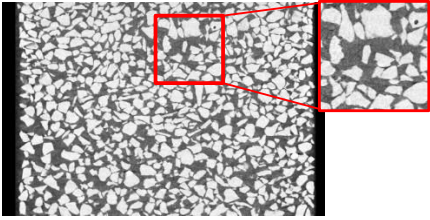
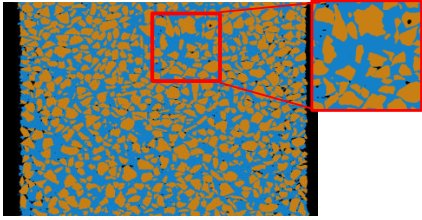
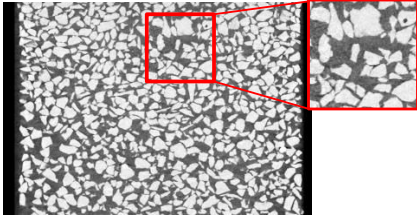
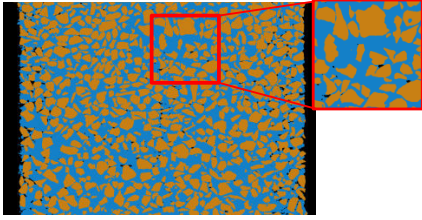
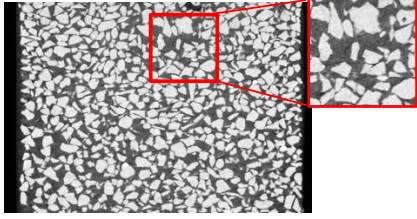
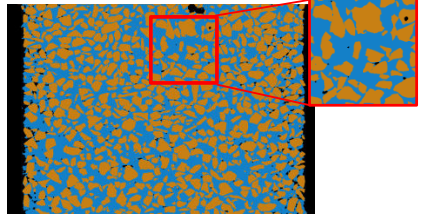
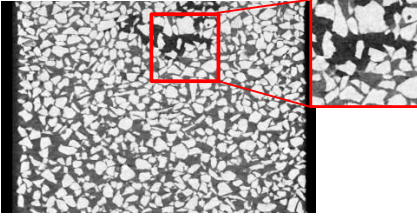
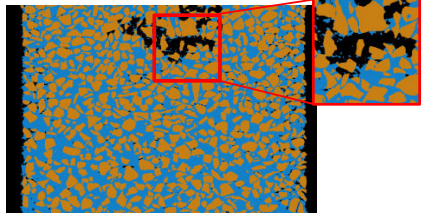
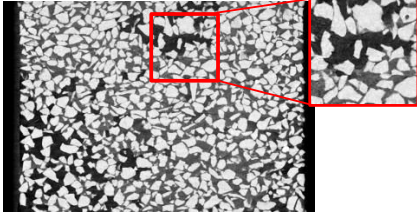
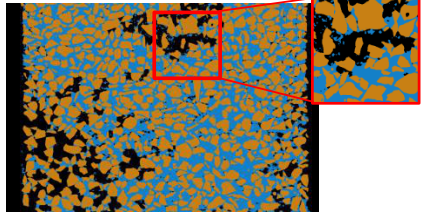


Figure A-1: Central horizontal slices in the a) reconstructed volumes b) trinarized volumes, for all the values of suction in the drying path D_1

Suction (kPa)	a)	b)
Complete saturation $s = 0$ kPa		
$s = 1$ kPa		
$s = 1.2$ kPa		
$s = 1.4$ kPa		
$s = 1.6$ kPa		
$s = 1.8$ kPa		

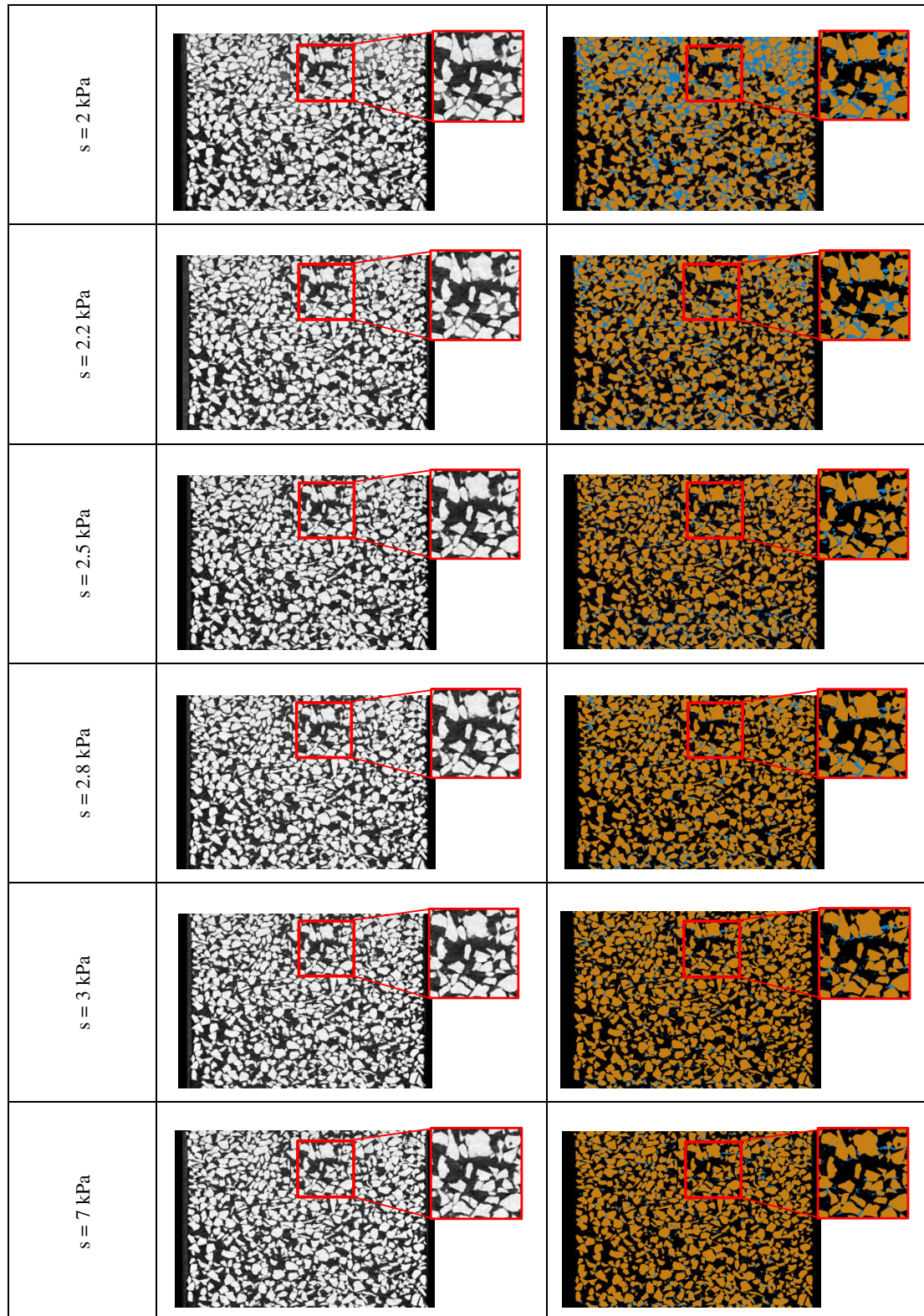
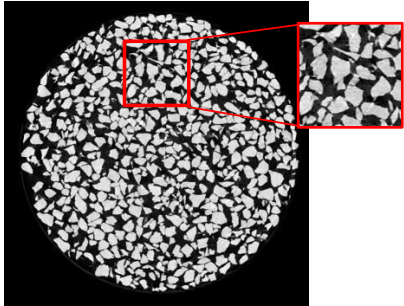
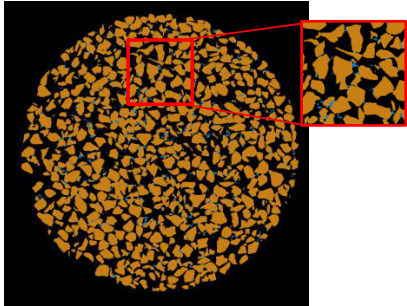
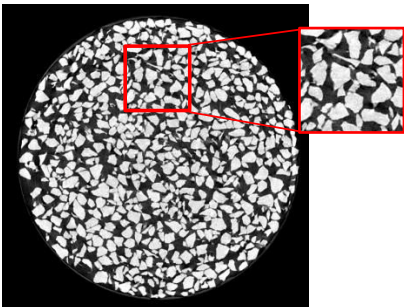
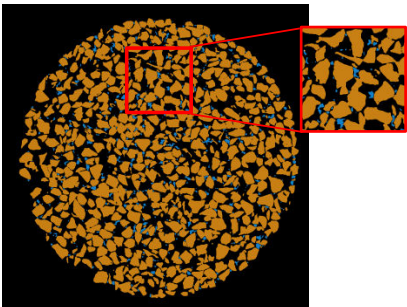
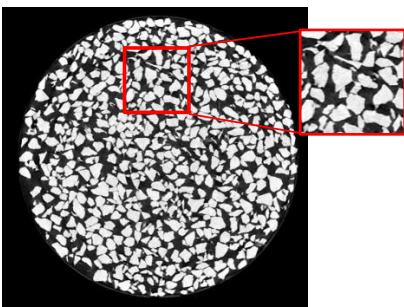
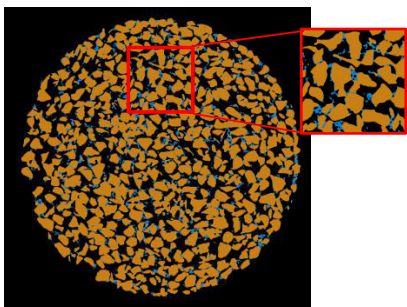
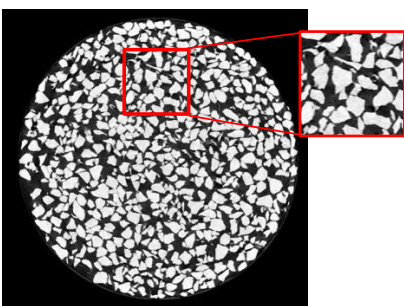
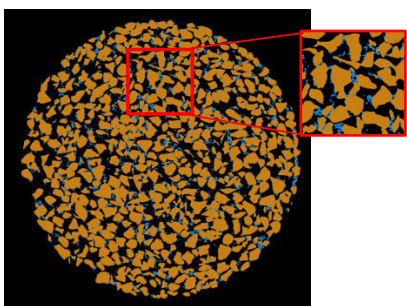
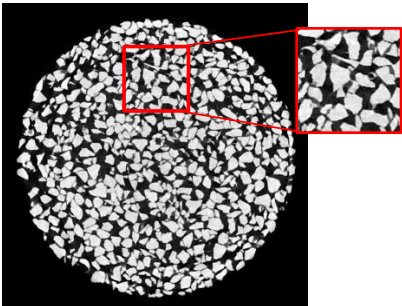
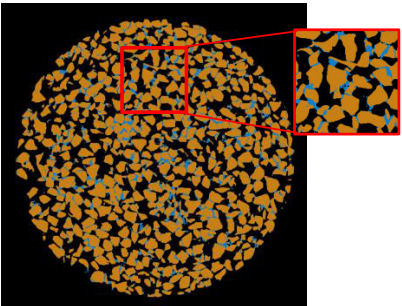
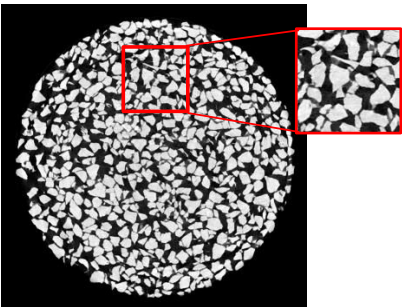
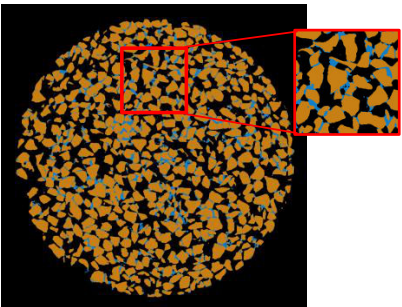
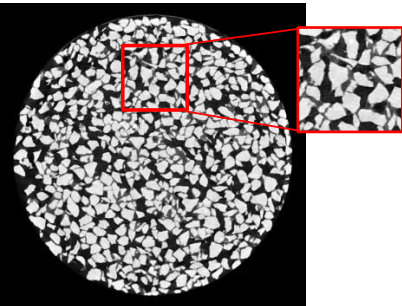
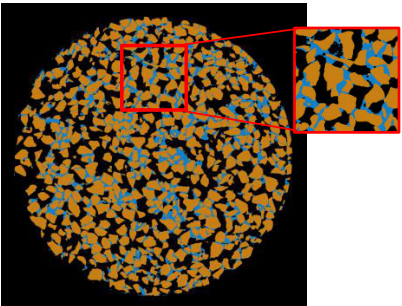
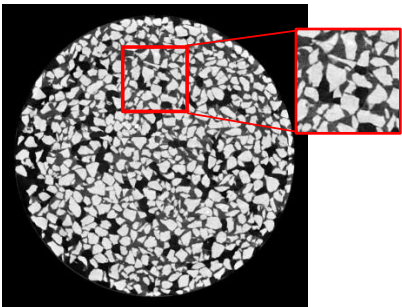
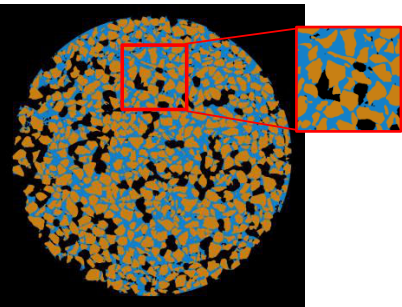


Figure A-2: Central vertical slices in the a) reconstructed volumes b) trinarized volumes, of the same azimuth, after removing the porous stone and the upper loose layer, for all the values of suction in the drying path D_1

A.2 Wetting path W_1

Suction (kPa)	a)	b)
$s = 3 \text{ kPa}$		
$s = 2.8 \text{ kPa}$		
$s = 2.5 \text{ kPa}$		
$s = 2.2 \text{ kPa}$		

$s = 2 \text{ kPa}$		
$s = 1.8 \text{ kPa}$		
$s = 1.6 \text{ kPa}$		
$s = 1.4 \text{ kPa}$		

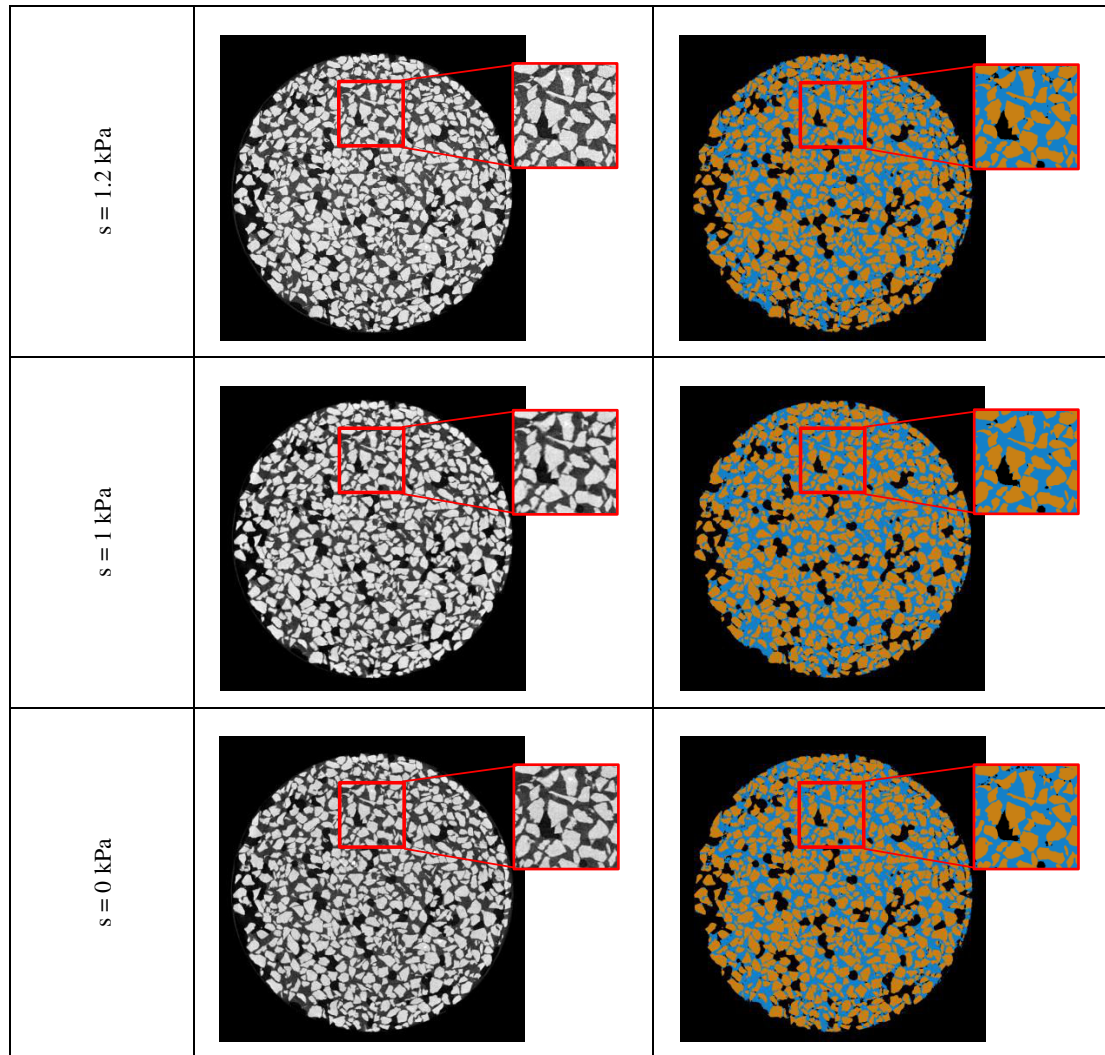
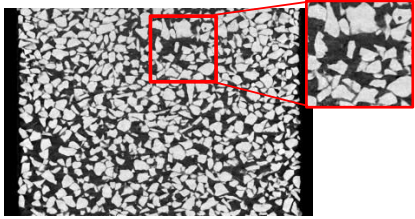
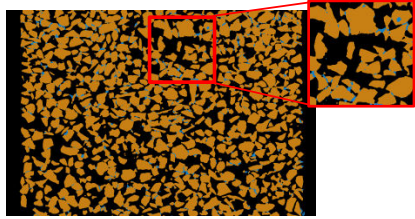
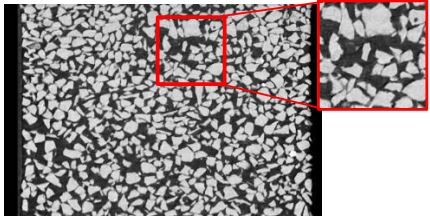
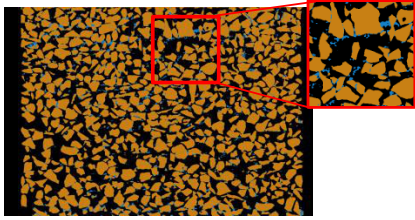
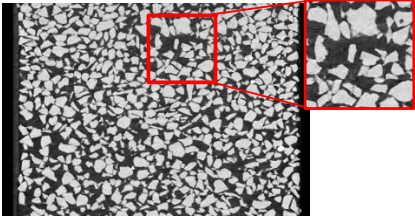
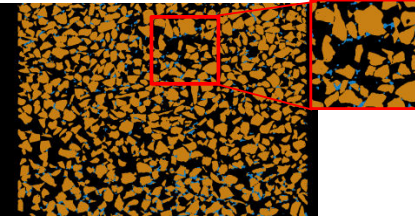
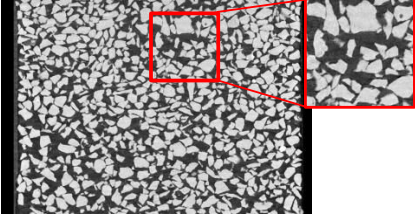
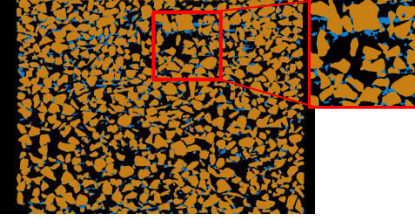
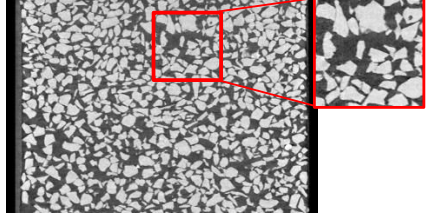
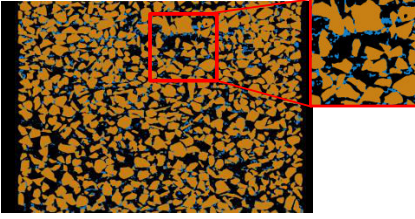
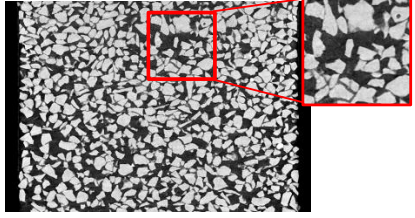
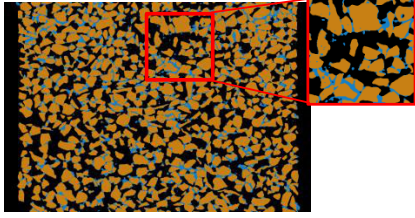


Figure A-3: Central horizontal slices in the a) reconstructed volumes b) trinarized volumes, for all the values of suction in the wetting path W_1

Suction (kPa)	a)	b)
$s = 3$ kPa		
$s = 2.8$ kPa		
$s = 2.5$ kPa		
$s = 2.2$ kPa		
$s = 2$ kPa		
$s = 1.8$ kPa		

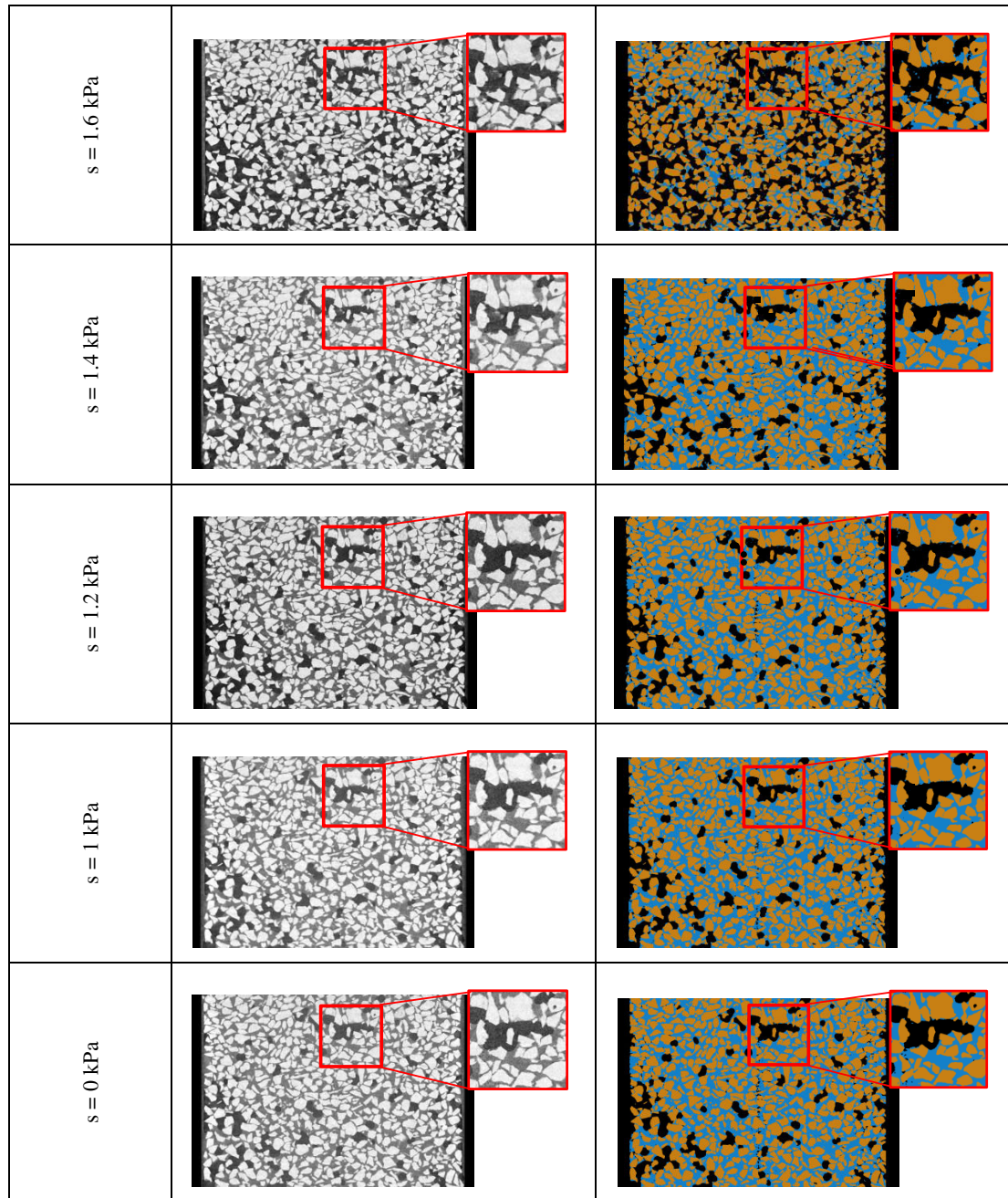
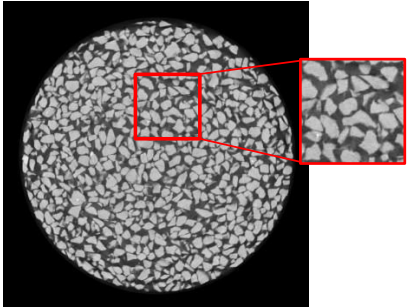
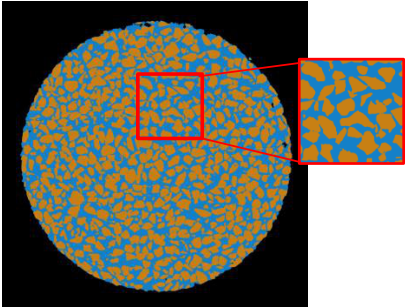
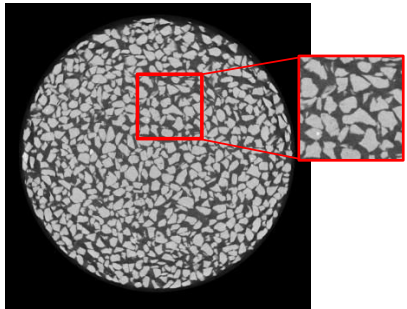
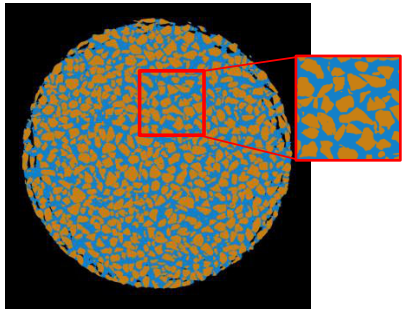
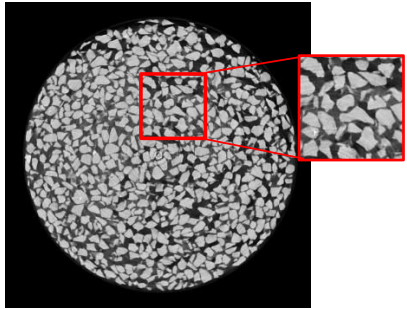
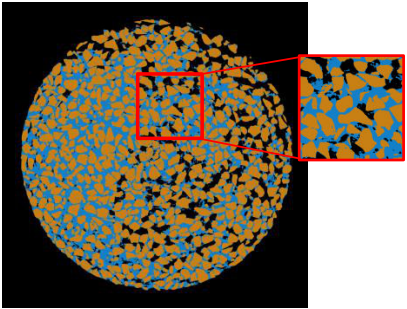
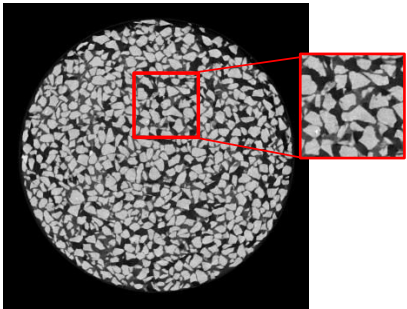
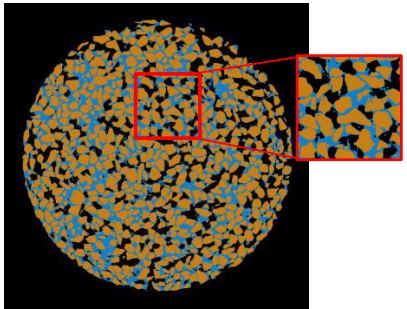
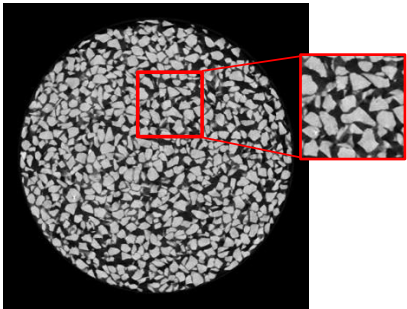
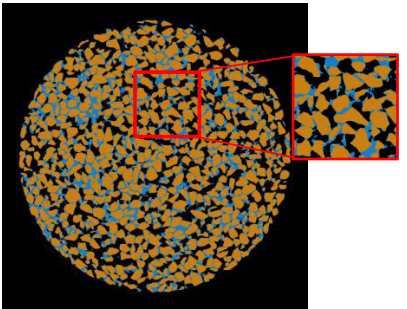
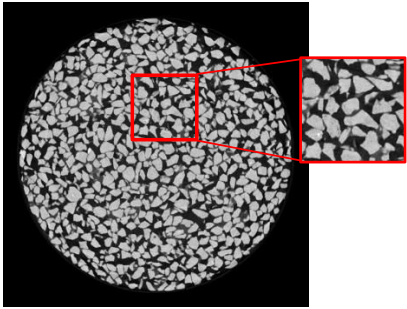
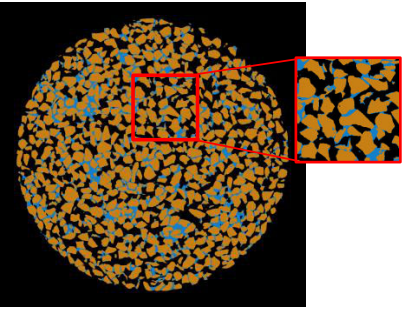
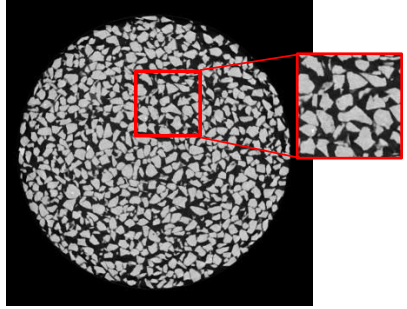
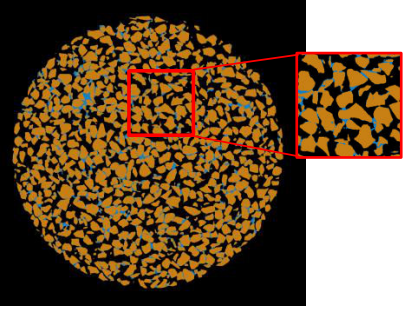
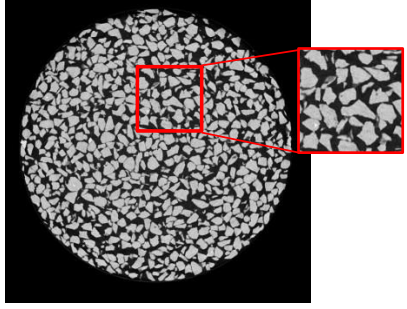
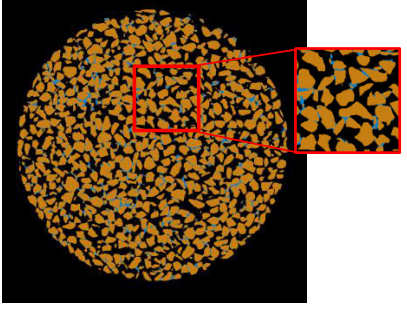


Figure A-4: Central vertical slices in the a) reconstructed volumes b) trinarized volumes, of the same azimuth, after removing the porous stone and the upper loose layer, for all the values of suction in the wetting path W_1

A.3 Drying path D_0

Suction (kPa)	a)	b)
Complete saturation $s = 0$ kPa		
$s = 1$ kPa		
$s = 1.2$ kPa		
$s = 1.4$ kPa		

$s = 1.8 \text{ kPa}$		
$s = 2 \text{ kPa}$		
$s = 2.2 \text{ kPa}$		
$s = 2.5 \text{ kPa}$		

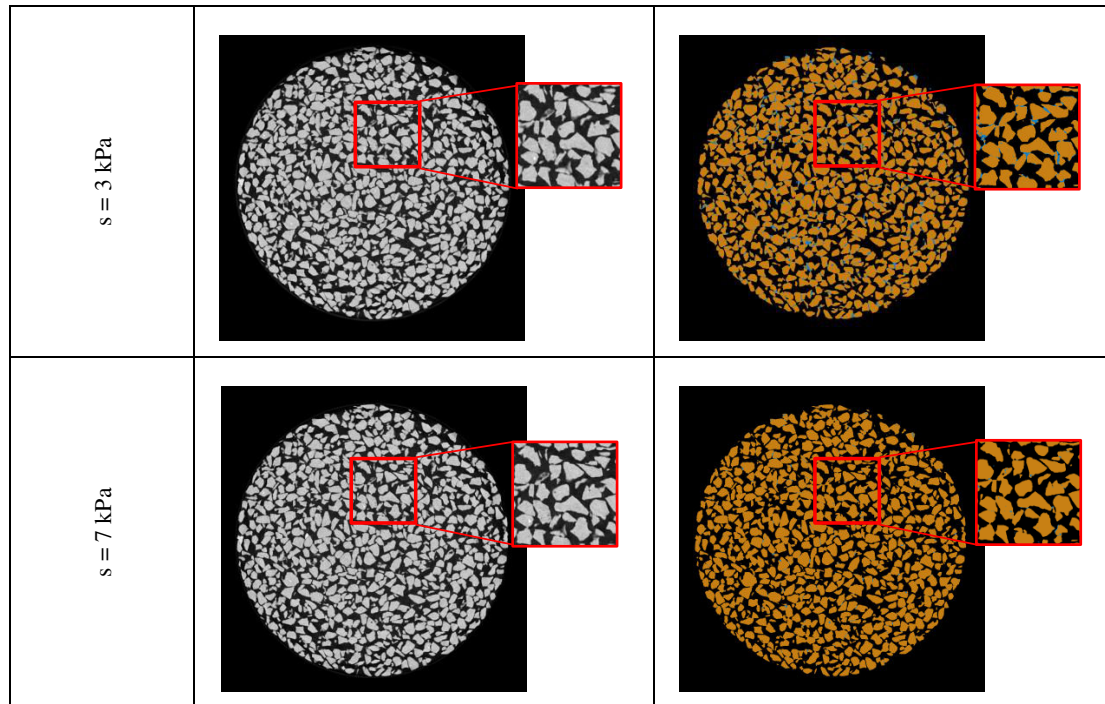
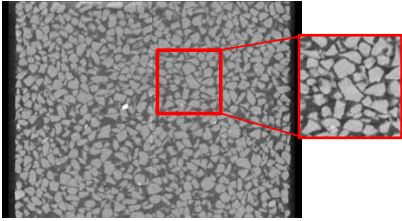
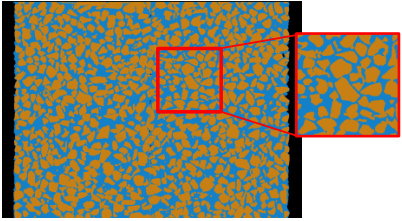
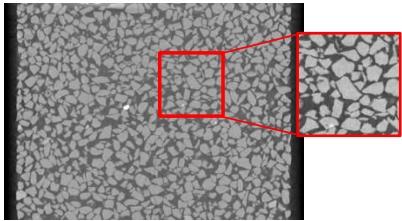
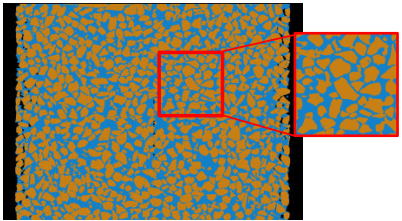
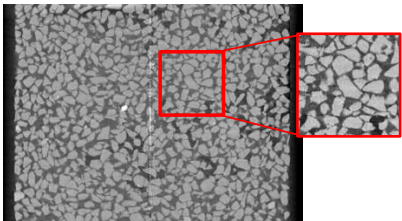
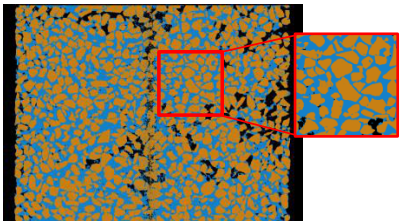
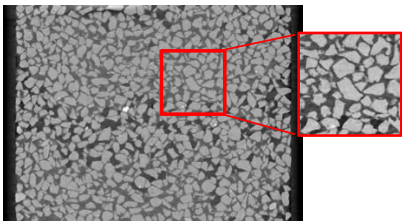
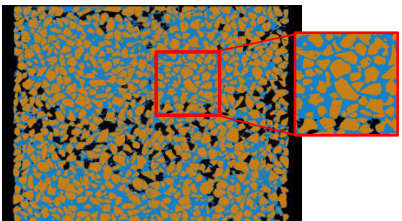
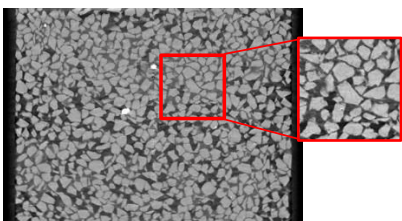
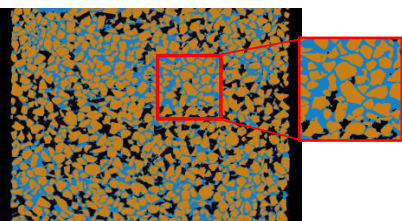
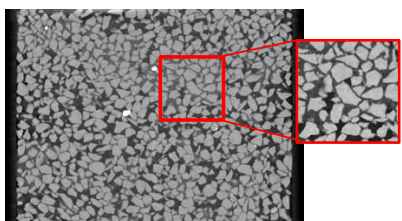
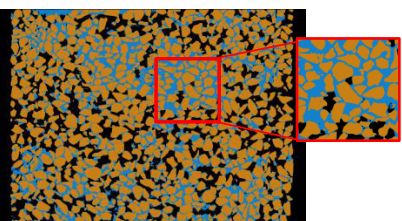


Figure A-5: Central horizontal slices in the a) reconstructed volumes b) trinarized volumes, for all the values of suction in the drying path D_0

Suction (kPa)	a)	b)
Complete saturation $s = 0$ kPa		
$s = 1$ kPa		
$s = 1.2$ kPa		
$s = 1.4$ kPa		
$s = 1.8$ kPa		
$s = 2$ kPa		

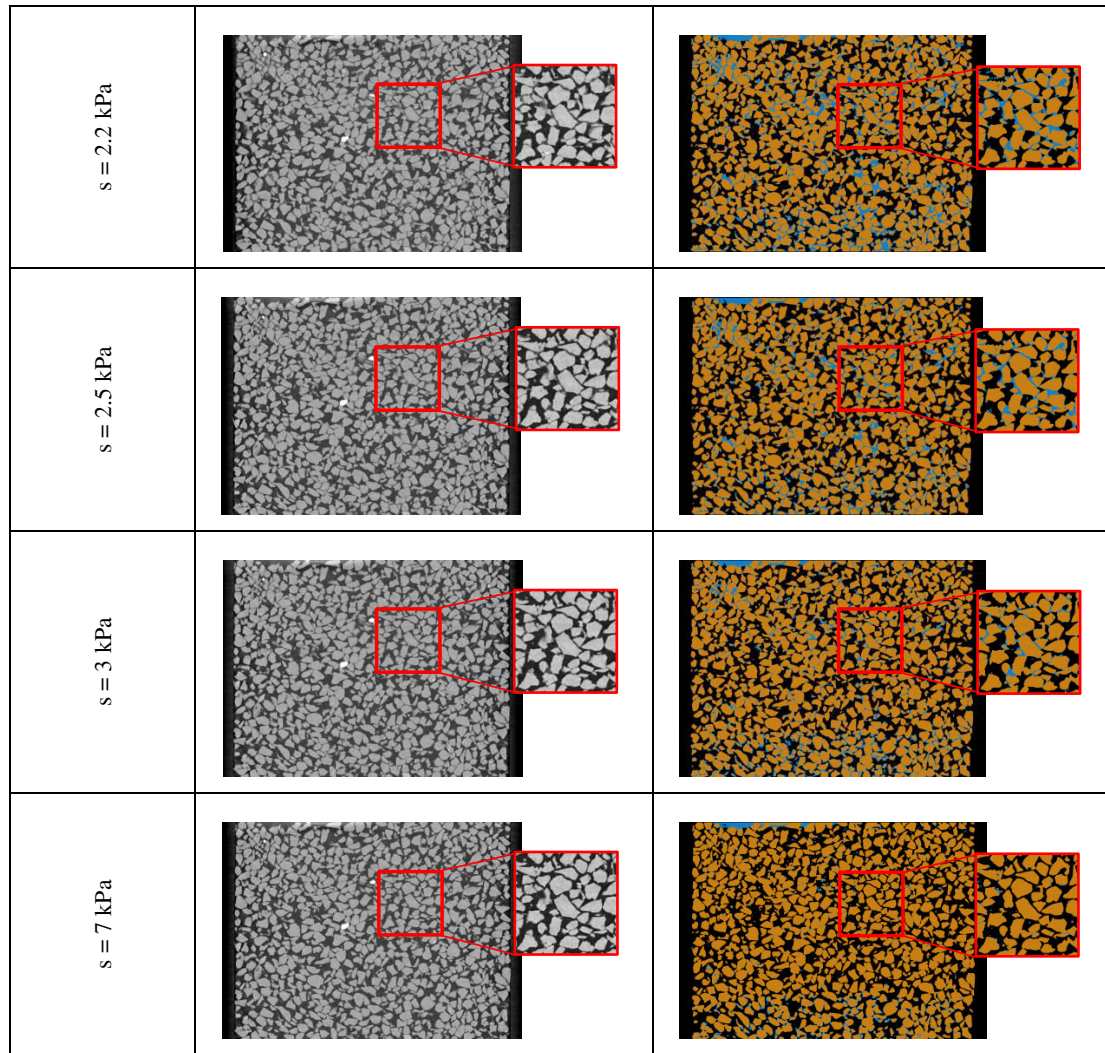



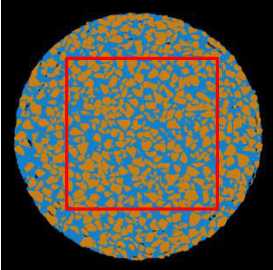
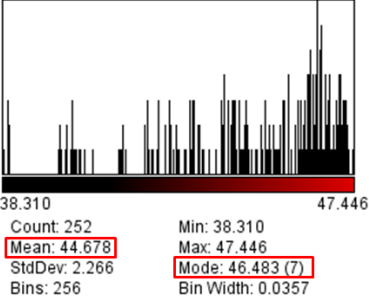
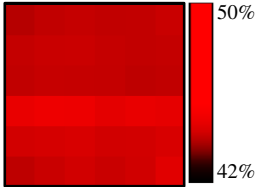
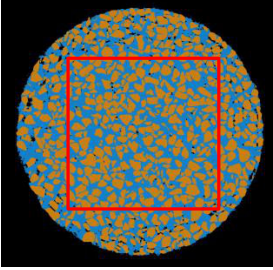
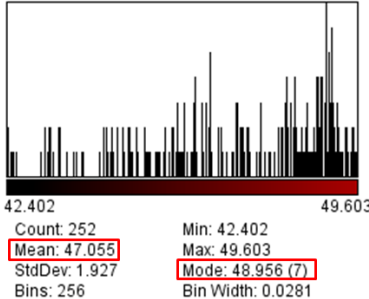
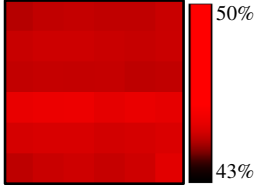
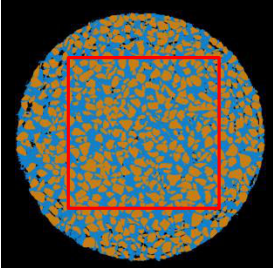
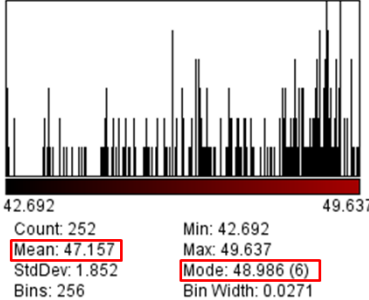
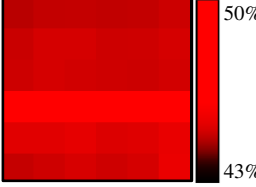
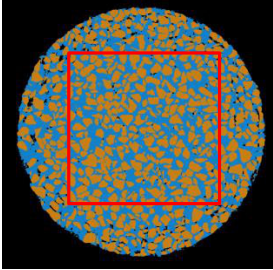
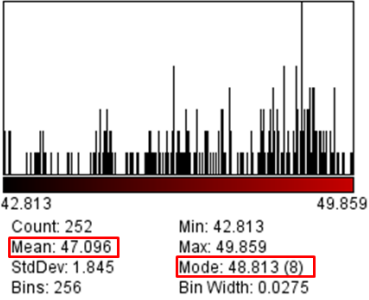
Figure A-6: Central vertical slices in the a) reconstructed volumes b) trinarized volumes, of the same azimuth, after removing the porous stones, for all the values of suction in the drying path D_0

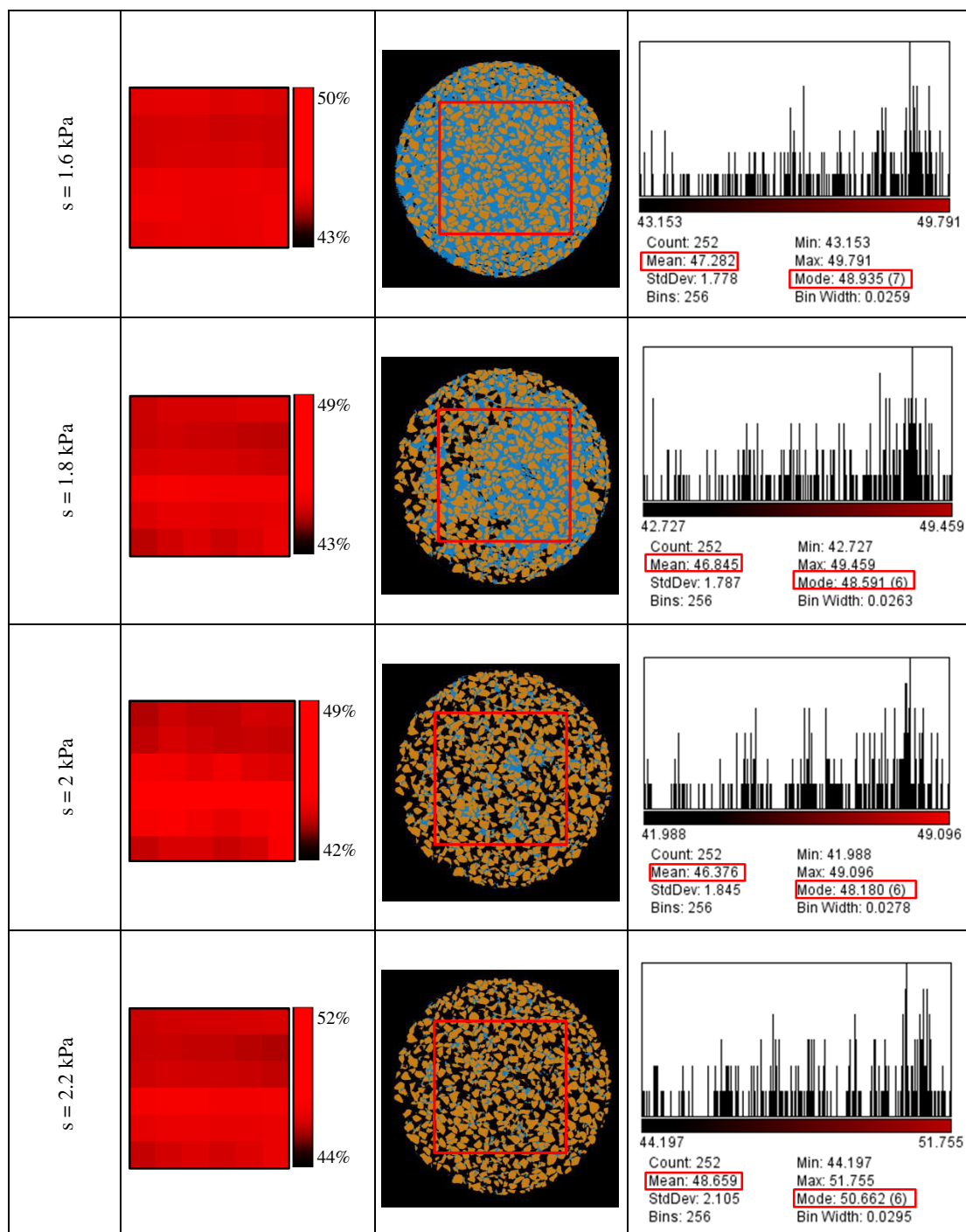
Appendix B

Porosity and degree of saturation mapping results

B.1 Porosity mapping results

B.1.1 Drying path D_1

Suction (kPa)	a)	b)	c)
Complete saturation $s = 0$ kPa			
$s = 1$ kPa			
$s = 1.2$ kPa			
$s = 1.4$ kPa			



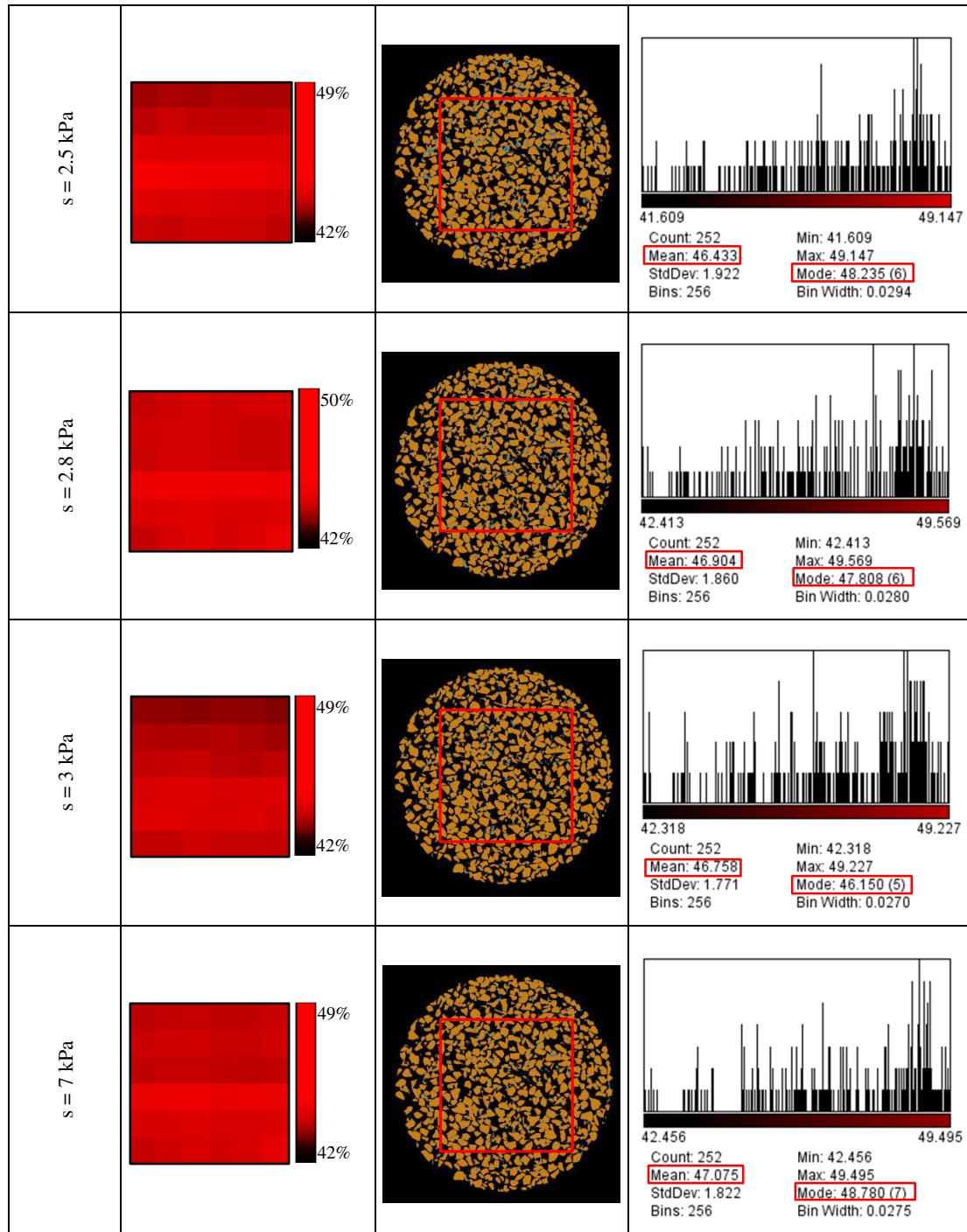
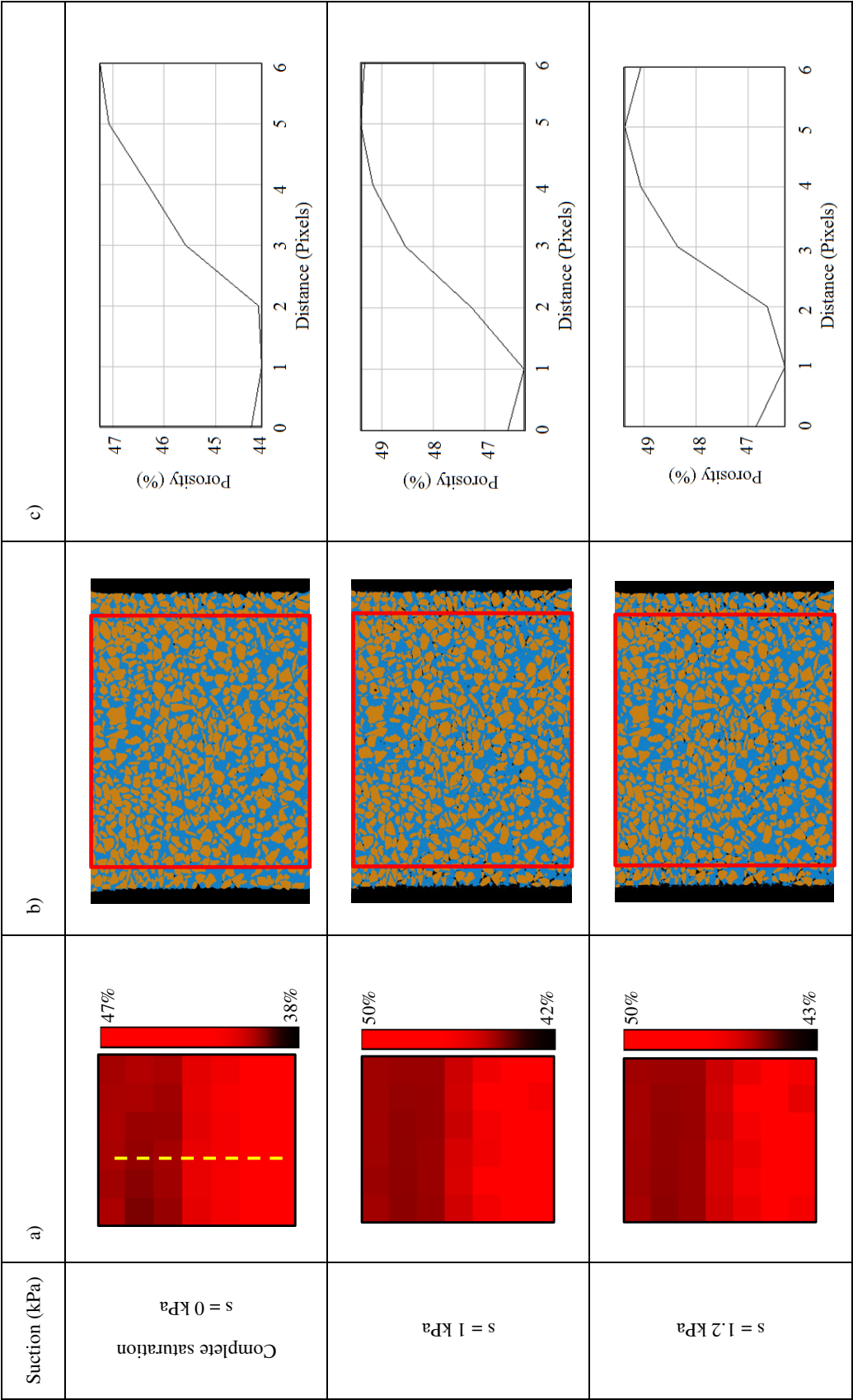
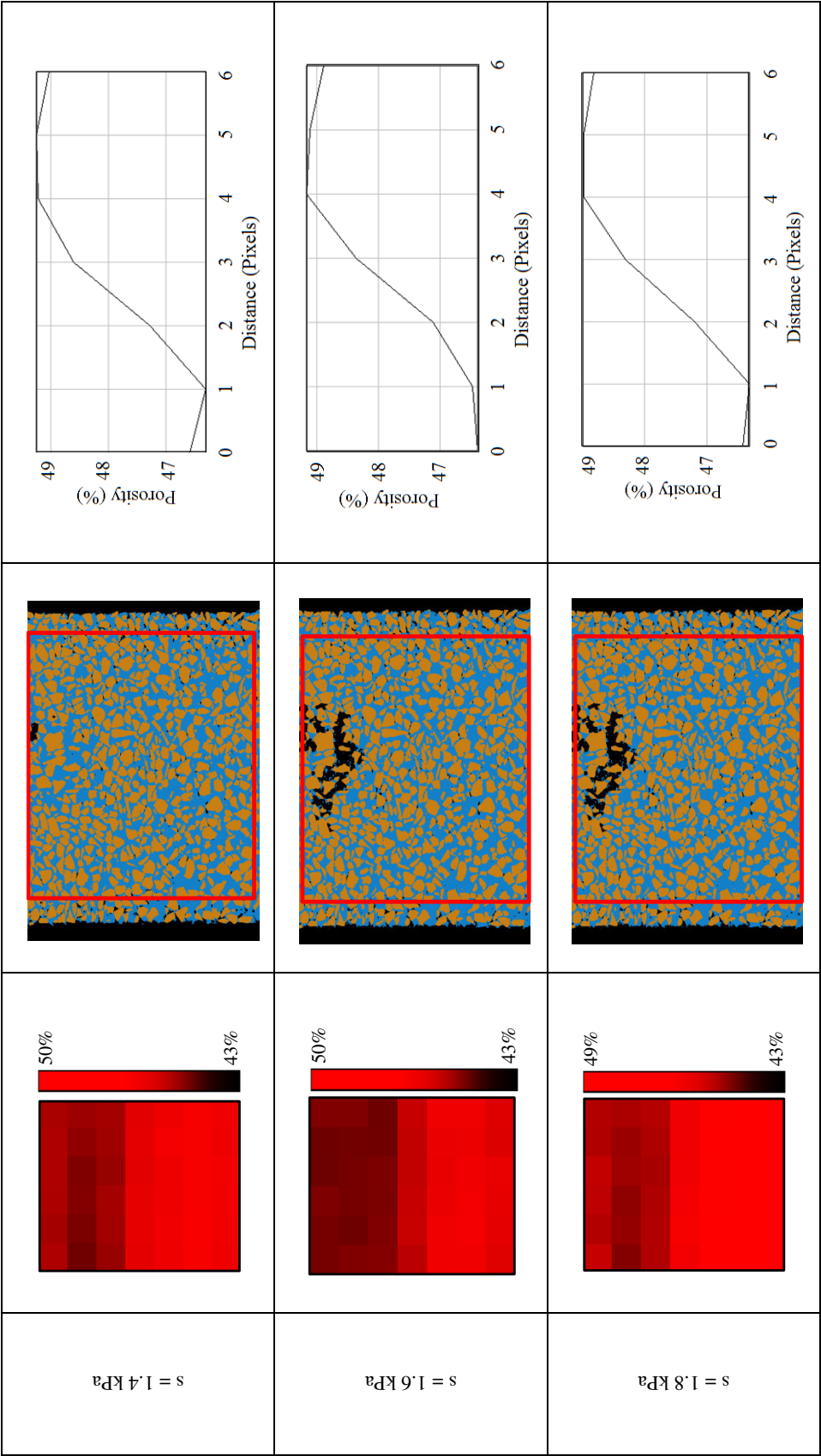
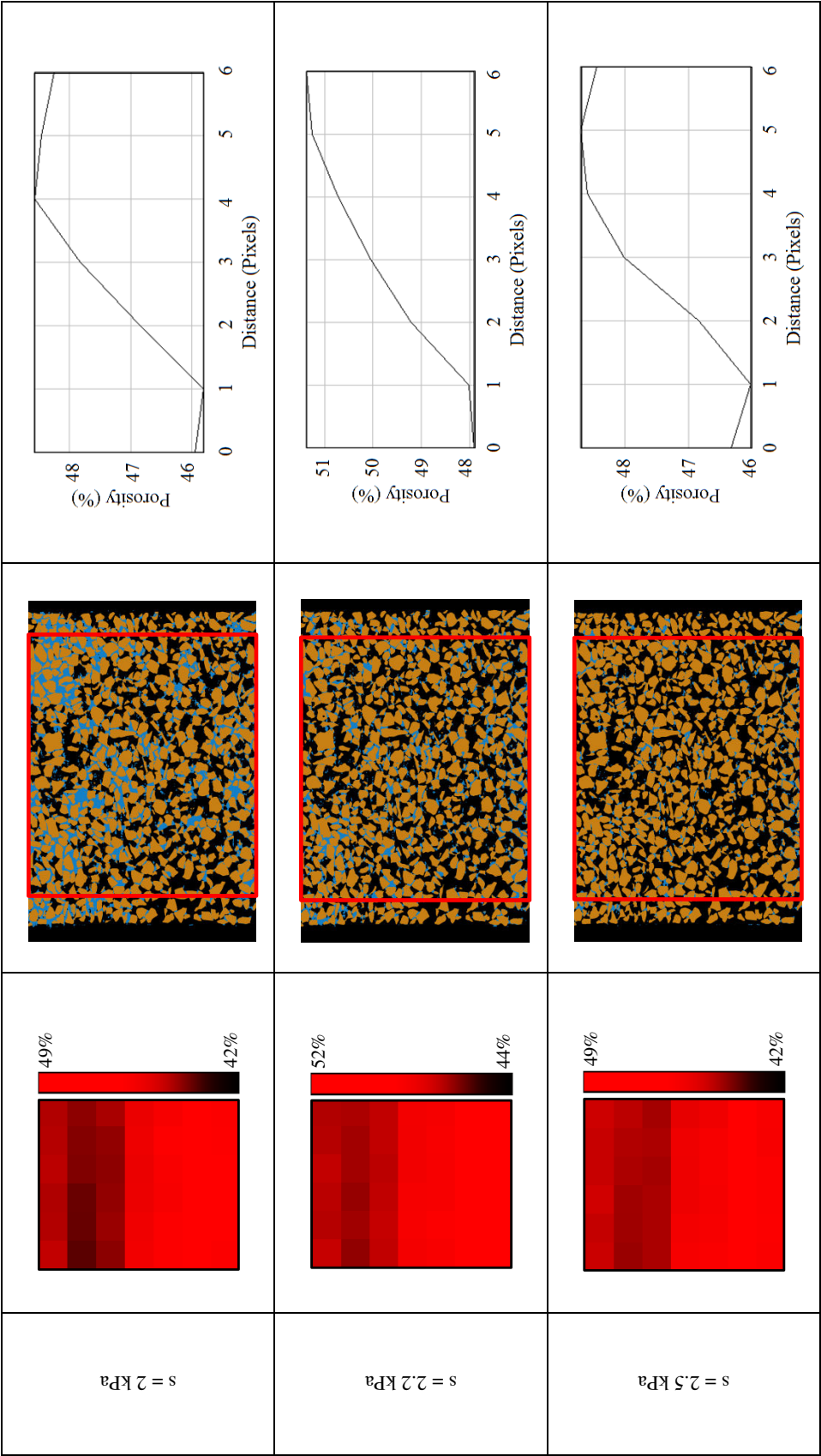


Figure B-1: a) Central horizontal slices in the porosity map b) Central horizontal slices in the trinarized volumes c) Porosity histogram, for all the values of suction in the drying path D_1







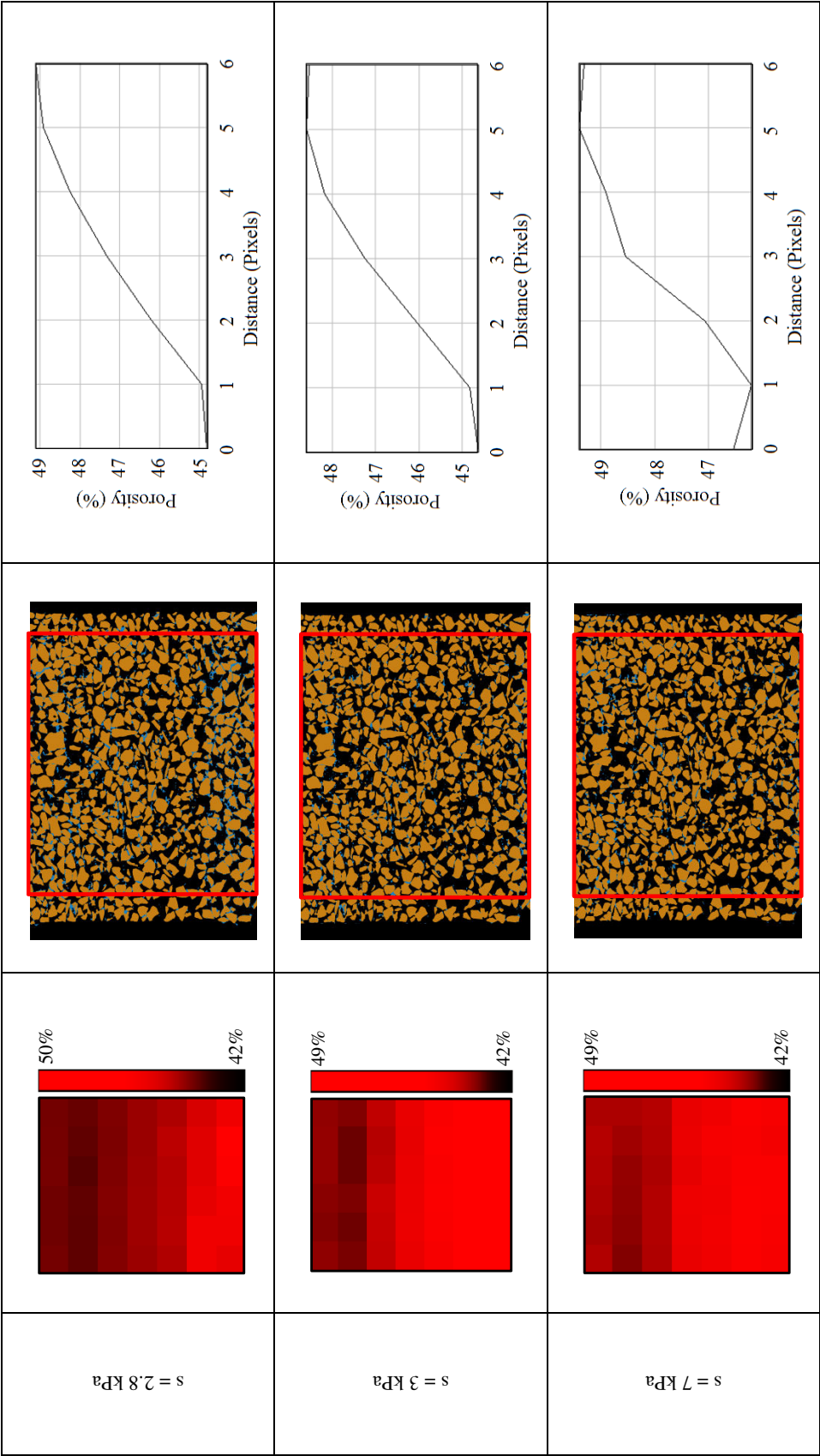
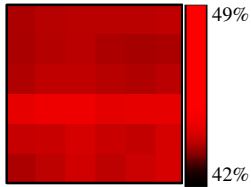
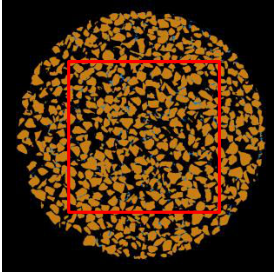
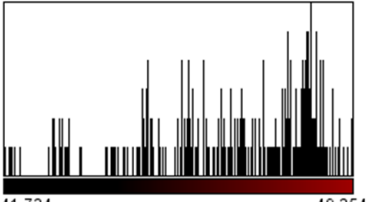
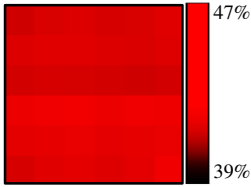
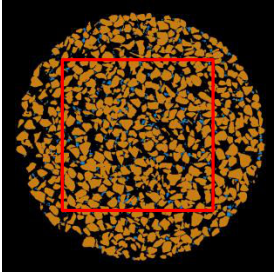
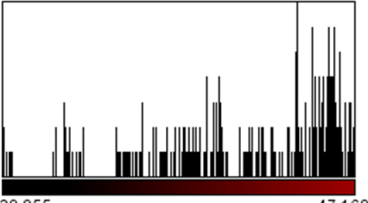
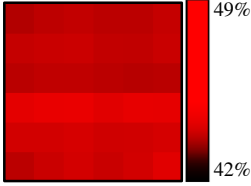
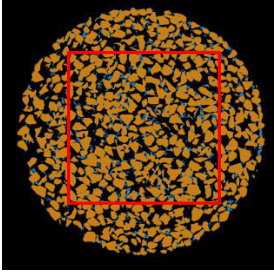
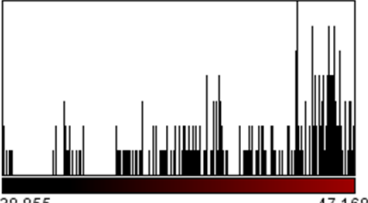
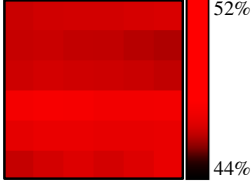
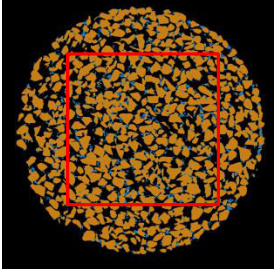
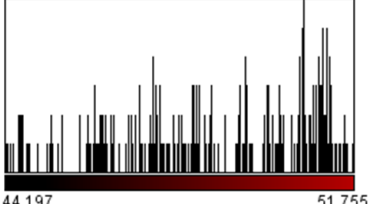
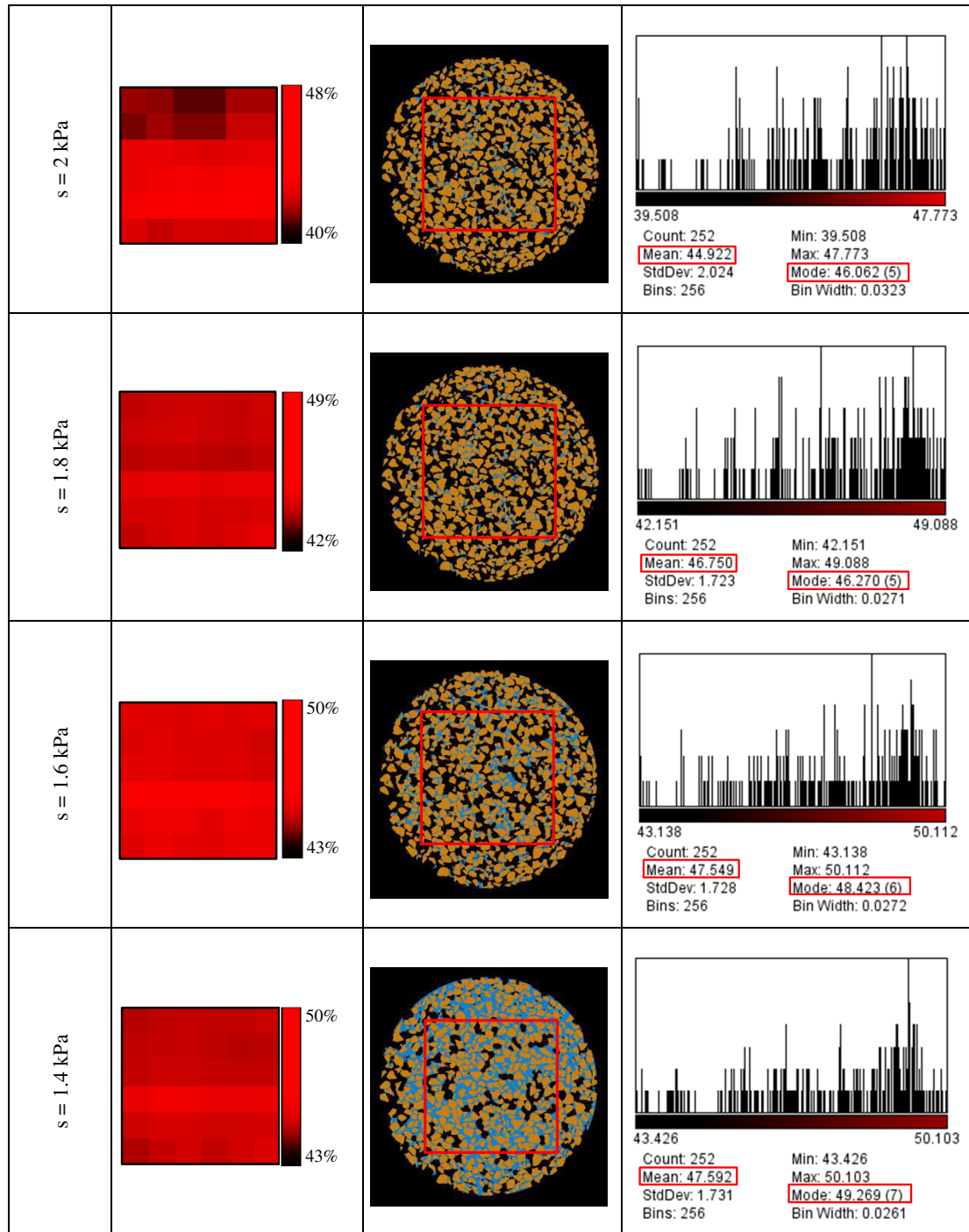


Figure B-2: a) Central vertical slices in the porosity map b) Central vertical slices in the trinarized volumes c) Porosity vertical profile, for all the values of suction in the drying path D_1 . All the vertical slices are of the same azimuth. The yellow dashed line on the central vertical slices in the porosity map for $s = 0 \text{ kPa}$ represents the column of voxels for which porosity vertical profile is drawn

B.1.2 Wetting path W_1

Suction (kPa)	a)	b)	c)
$s = 3 \text{ kPa}$			 Count: 252 Mean: 46.576 StdDev: 1.848 Bins: 256 Min: 41.734 Max: 49.254 Mode: 48.343 (6) Bin Width: 0.0294
$s = 2.8 \text{ kPa}$			 Count: 252 Mean: 44.510 StdDev: 2.159 Bins: 256 Min: 38.855 Max: 47.168 Mode: 45.804 (7) Bin Width: 0.0325
$s = 2.5 \text{ kPa}$			 Count: 252 Mean: 44.510 StdDev: 2.159 Bins: 256 Min: 38.855 Max: 47.168 Mode: 45.804 (7) Bin Width: 0.0325
$s = 2.2 \text{ kPa}$			 Count: 252 Mean: 48.659 StdDev: 2.105 Bins: 256 Min: 44.197 Max: 51.755 Mode: 50.662 (6) Bin Width: 0.0295



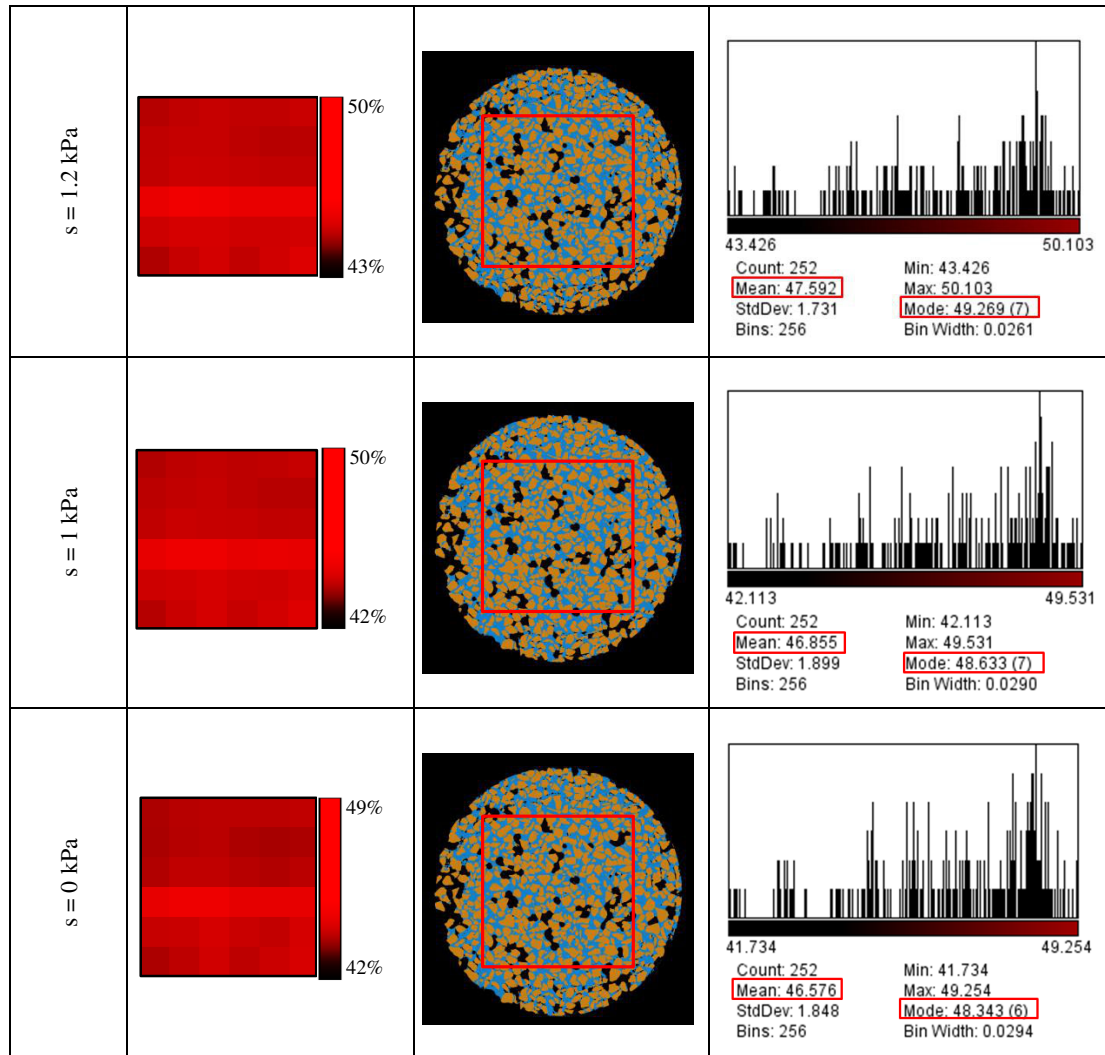
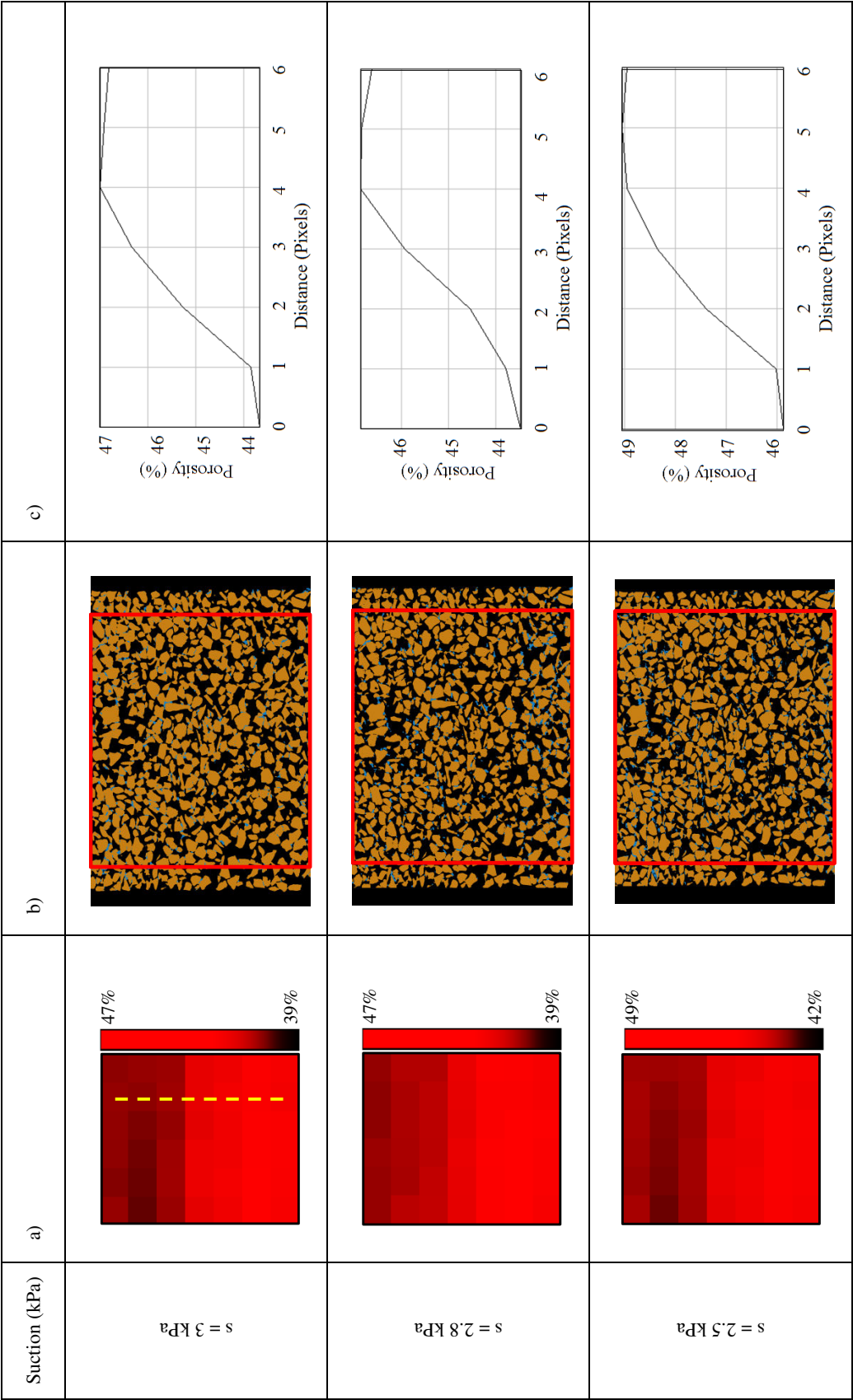
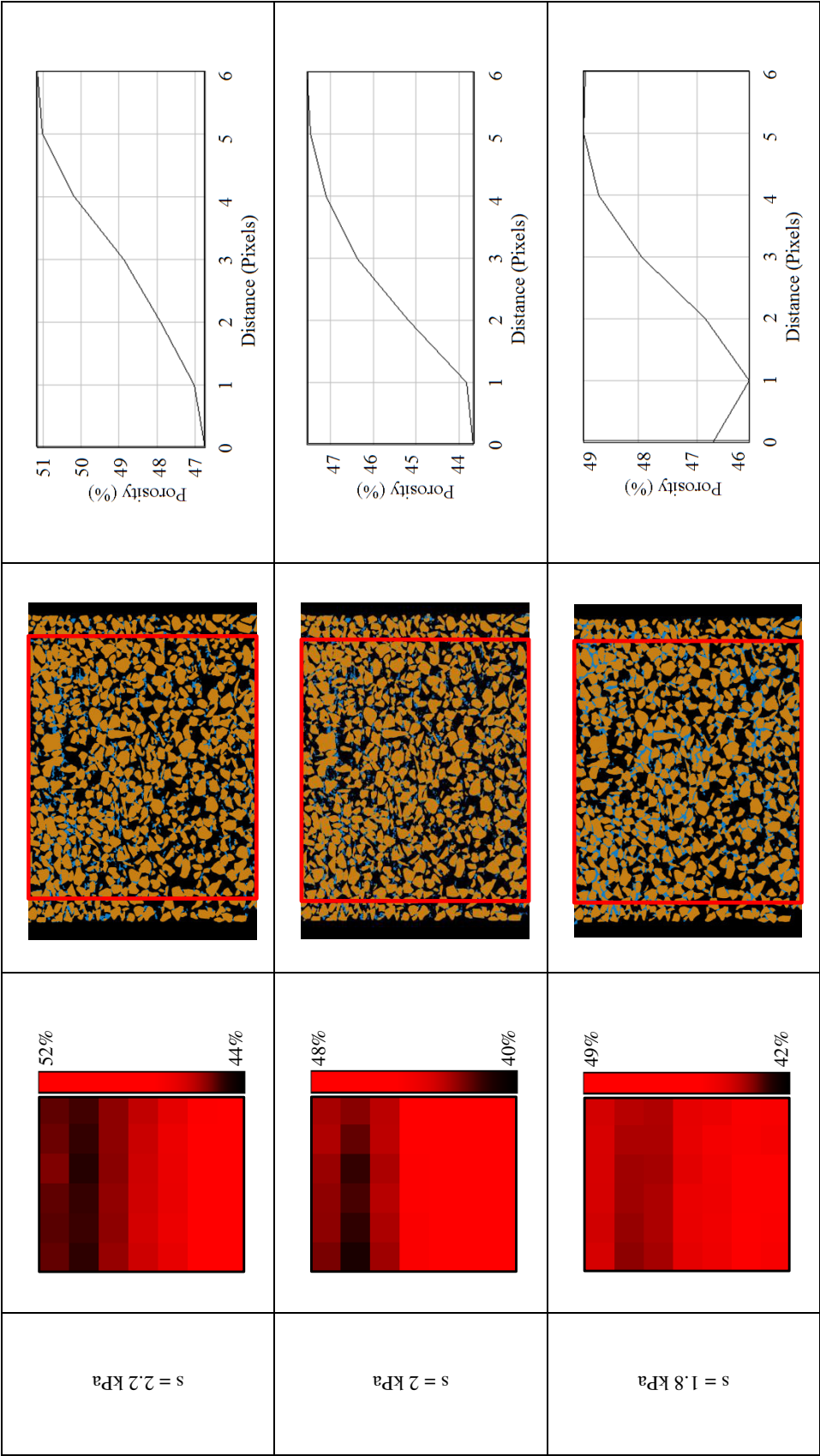
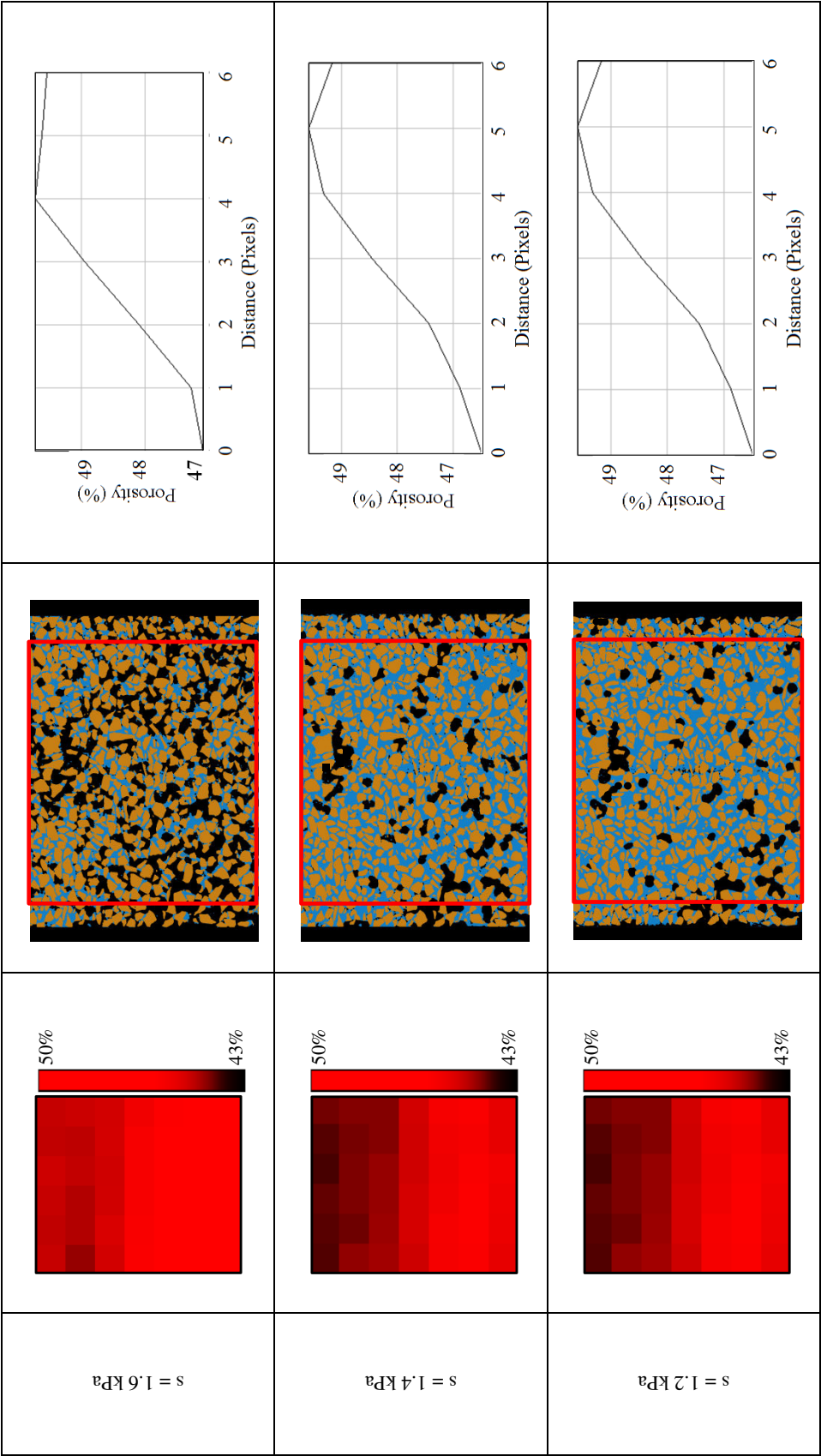


Figure B-3: a) Central horizontal slices in the porosity map b) Central horizontal slices in the trinarized volumes c) Porosity histogram, for all the values of suction in the wetting path W_1







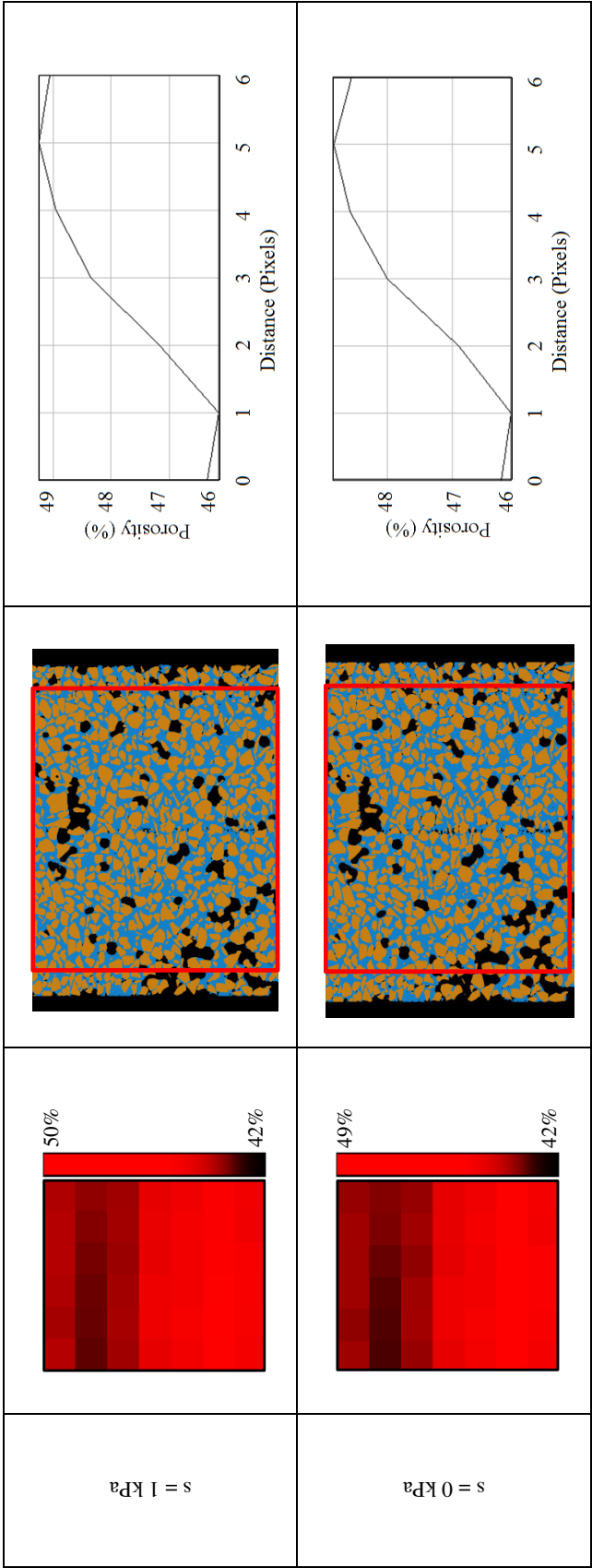
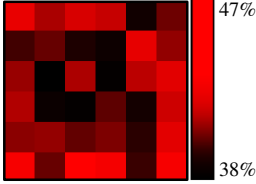
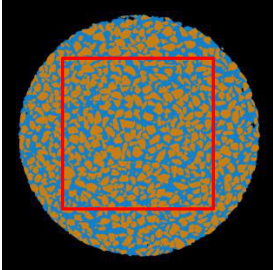
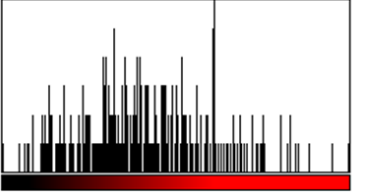
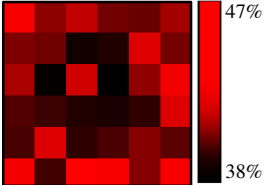
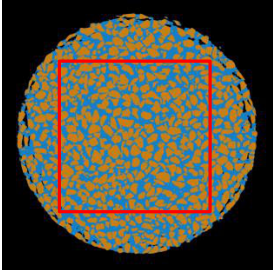
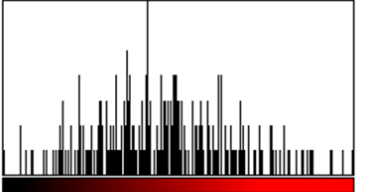
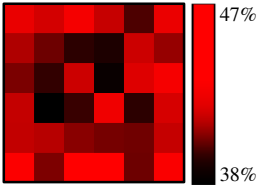
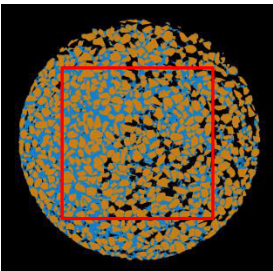
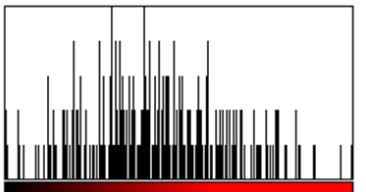
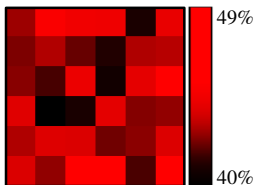
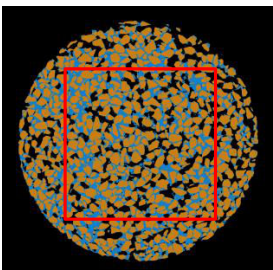
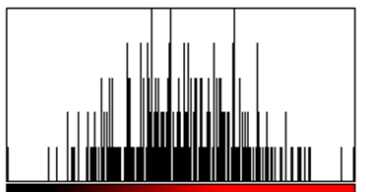
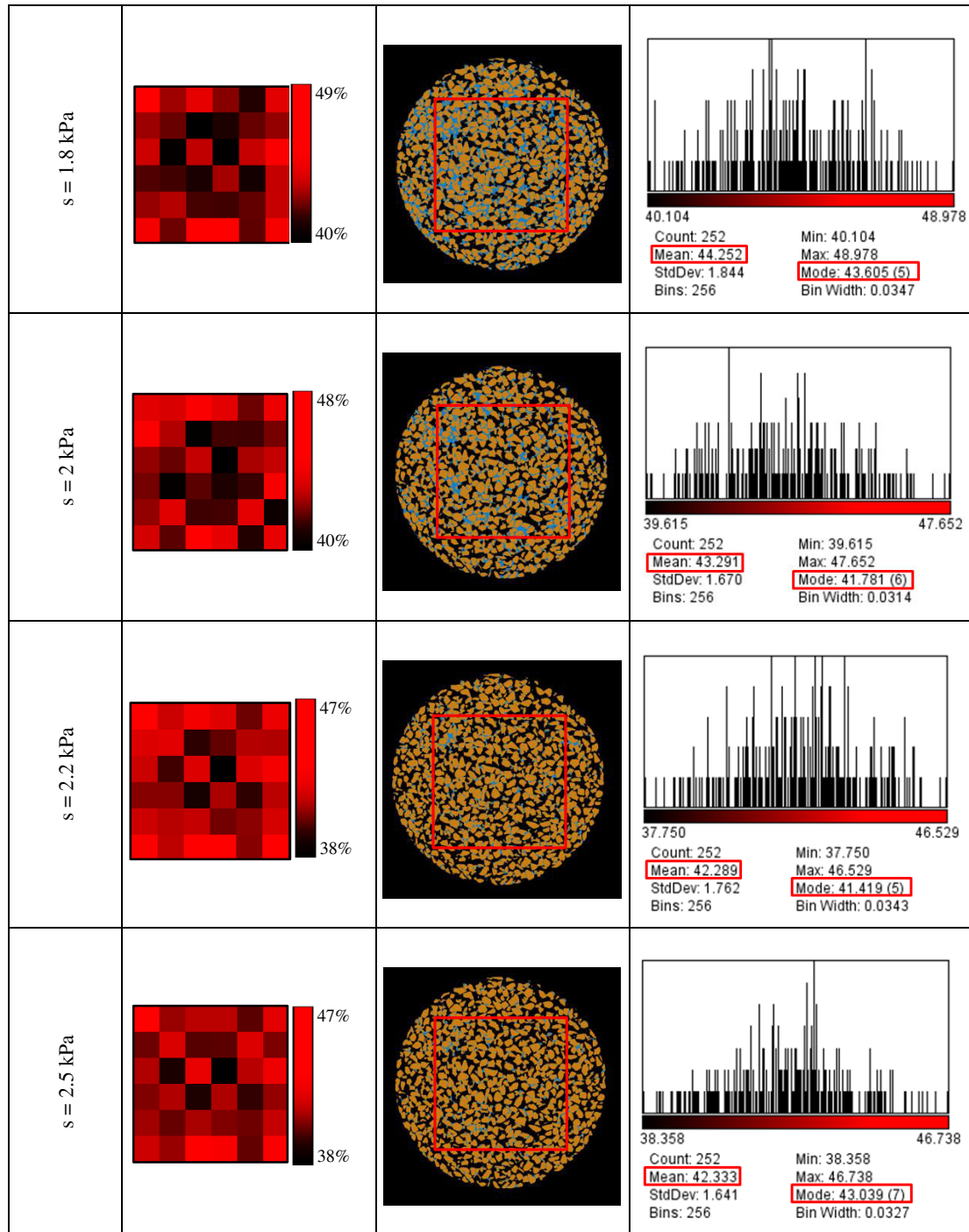


Figure B-4: a) Central vertical slices in the porosity map b) Central vertical slices in the trinarized volumes c) Porosity vertical profile, for all the values of suction in the wetting path W_1 . All the vertical slices are of the same azimuth. The yellow dashed line on the central vertical slices in the porosity map for $s = 3 \text{ kPa}$ represents the column of voxels for which porosity vertical profile is drawn

B.1.3 Drying path D_0

Suction (kPa)	a)	b)	c)
Complete saturation $s = 0$ kPa			 Count: 252 Min: 37.864 Max: 47.207 Mean: 41.741 StdDev: 1.786 Bins: 256 Bin Width: 0.0365 Mode: 43.557 (6)
$s = 1$ kPa			 Count: 252 Min: 37.772 Max: 47.041 Mean: 42.042 StdDev: 1.809 Bins: 256 Bin Width: 0.0362 Mode: 41.574 (7)
$s = 1.2$ kPa			 Count: 252 Min: 38.411 Max: 47.325 Mean: 42.312 StdDev: 1.788 Bins: 256 Bin Width: 0.0348 Mode: 41.127 (5)
$s = 1.4$ kPa			 Count: 252 Min: 40.083 Max: 49.346 Mean: 44.746 StdDev: 1.589 Bins: 256 Bin Width: 0.0362 Mode: 43.918 (5)



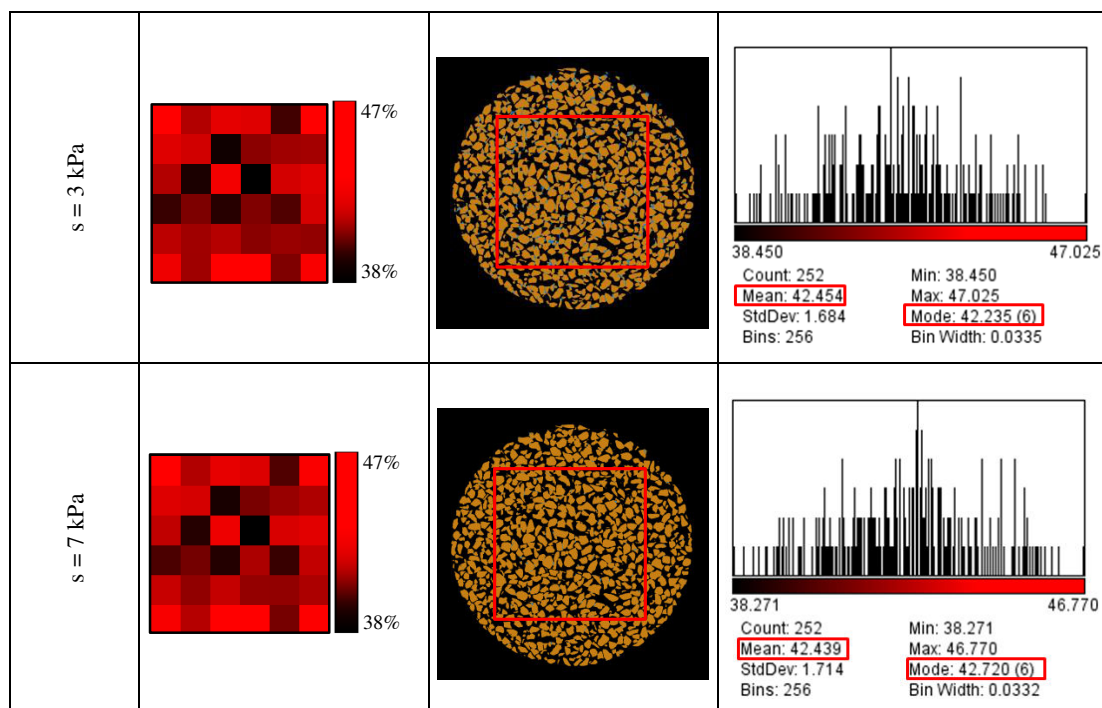
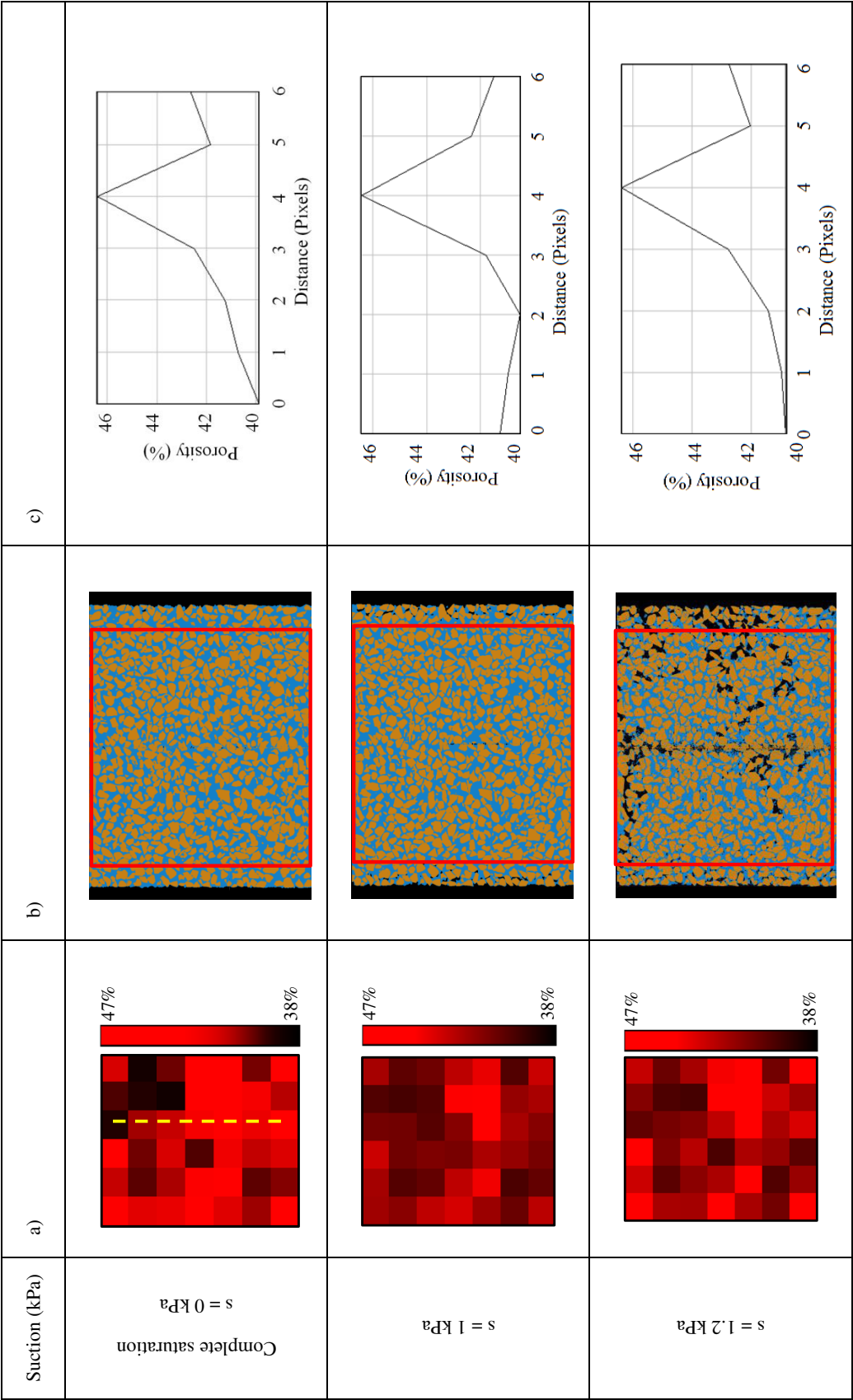
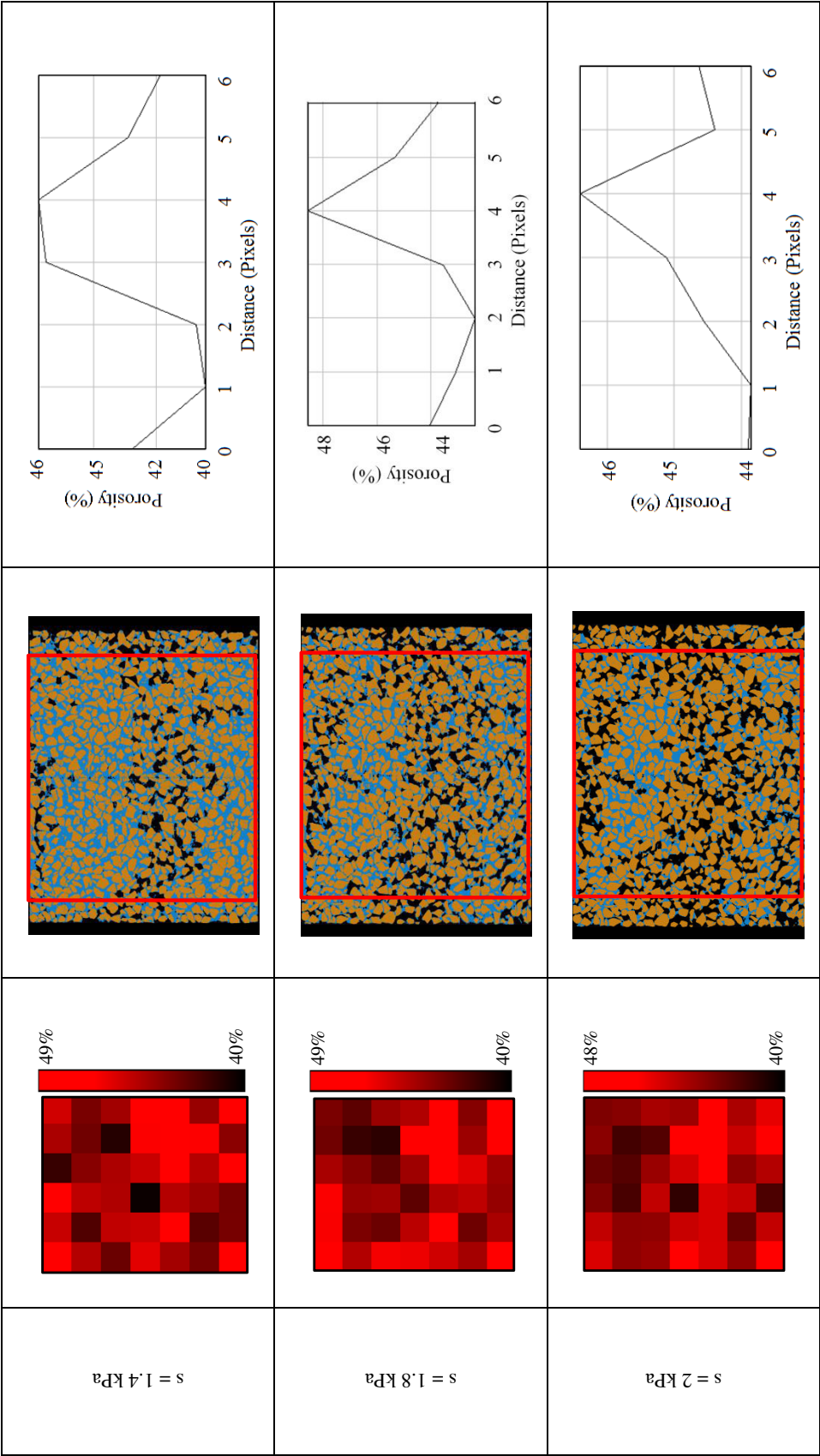
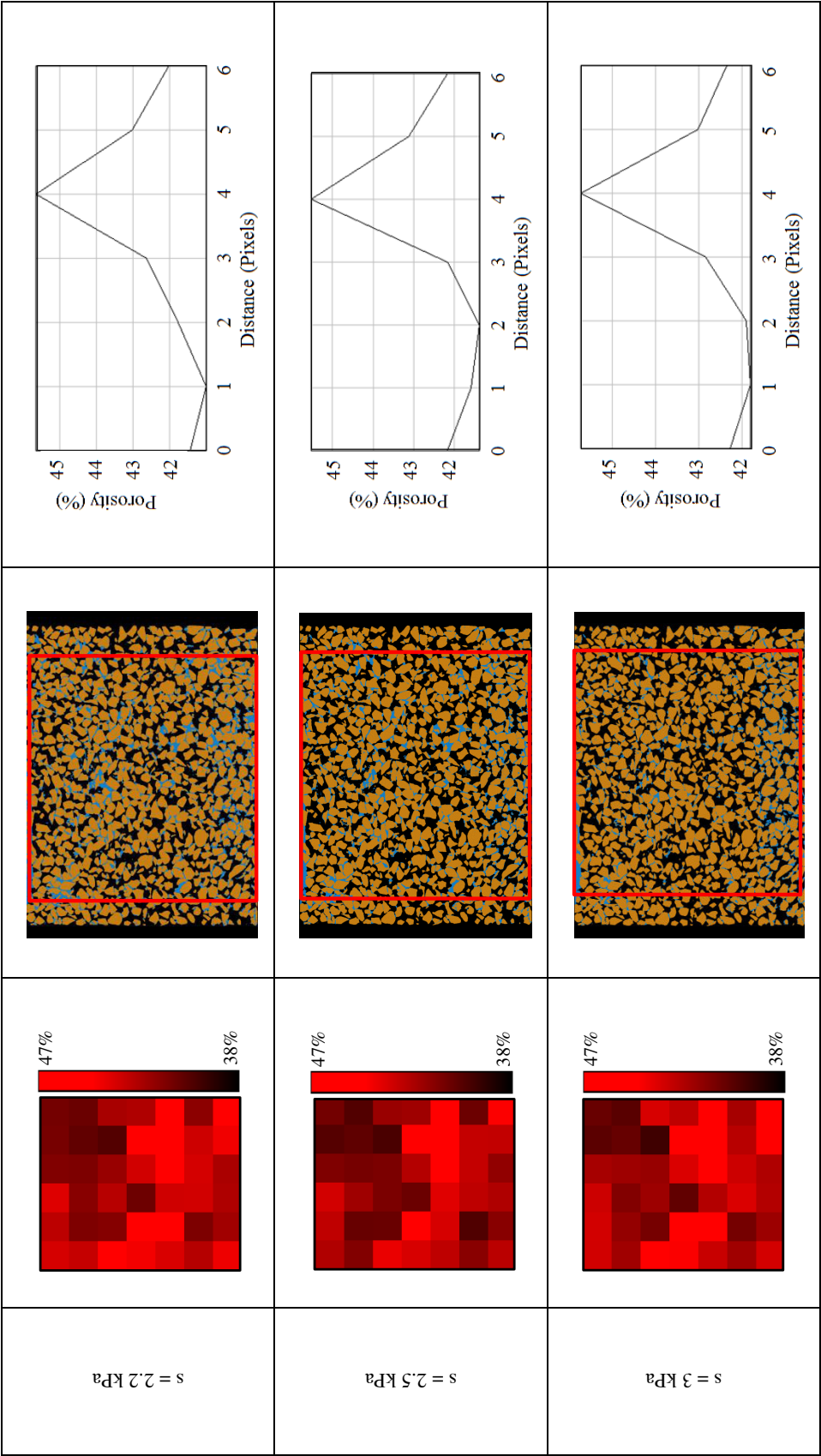


Figure B-5: a) Central horizontal slices in the porosity map b) Central horizontal slices in the trinarized volumes c) Porosity histogram, for all the values of suction in the drying path D_0







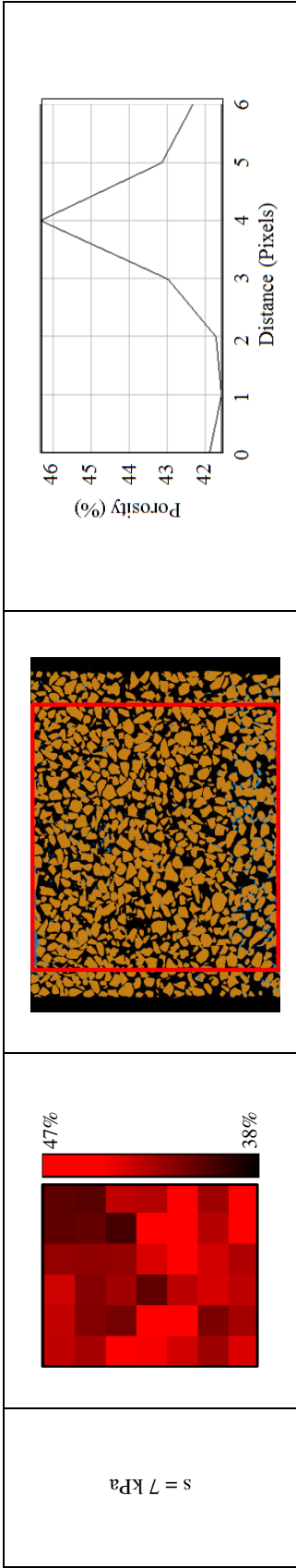
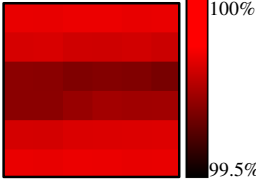
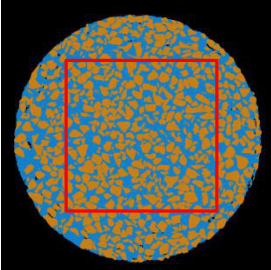
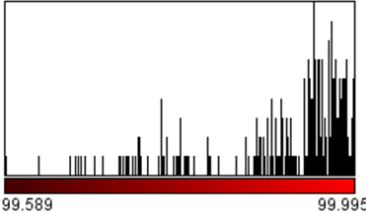
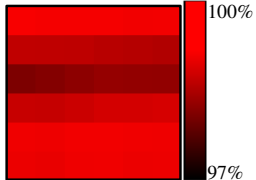
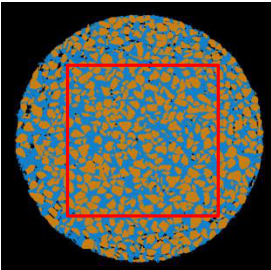
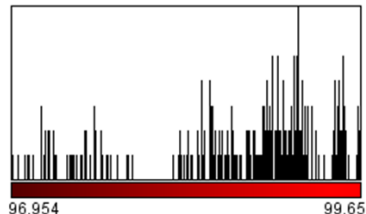
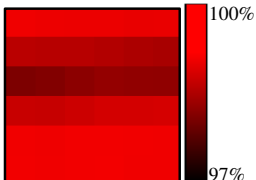
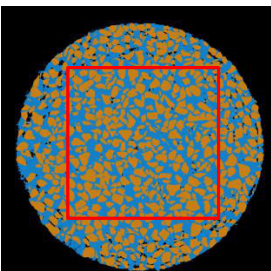
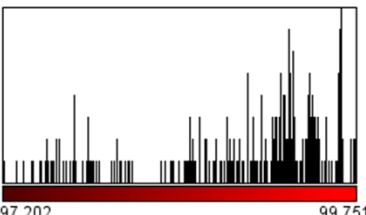
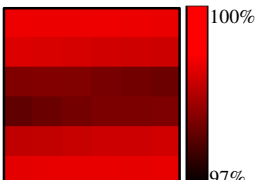
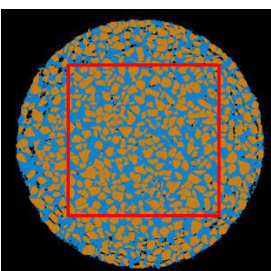
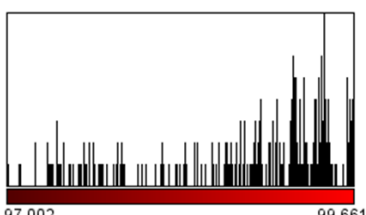
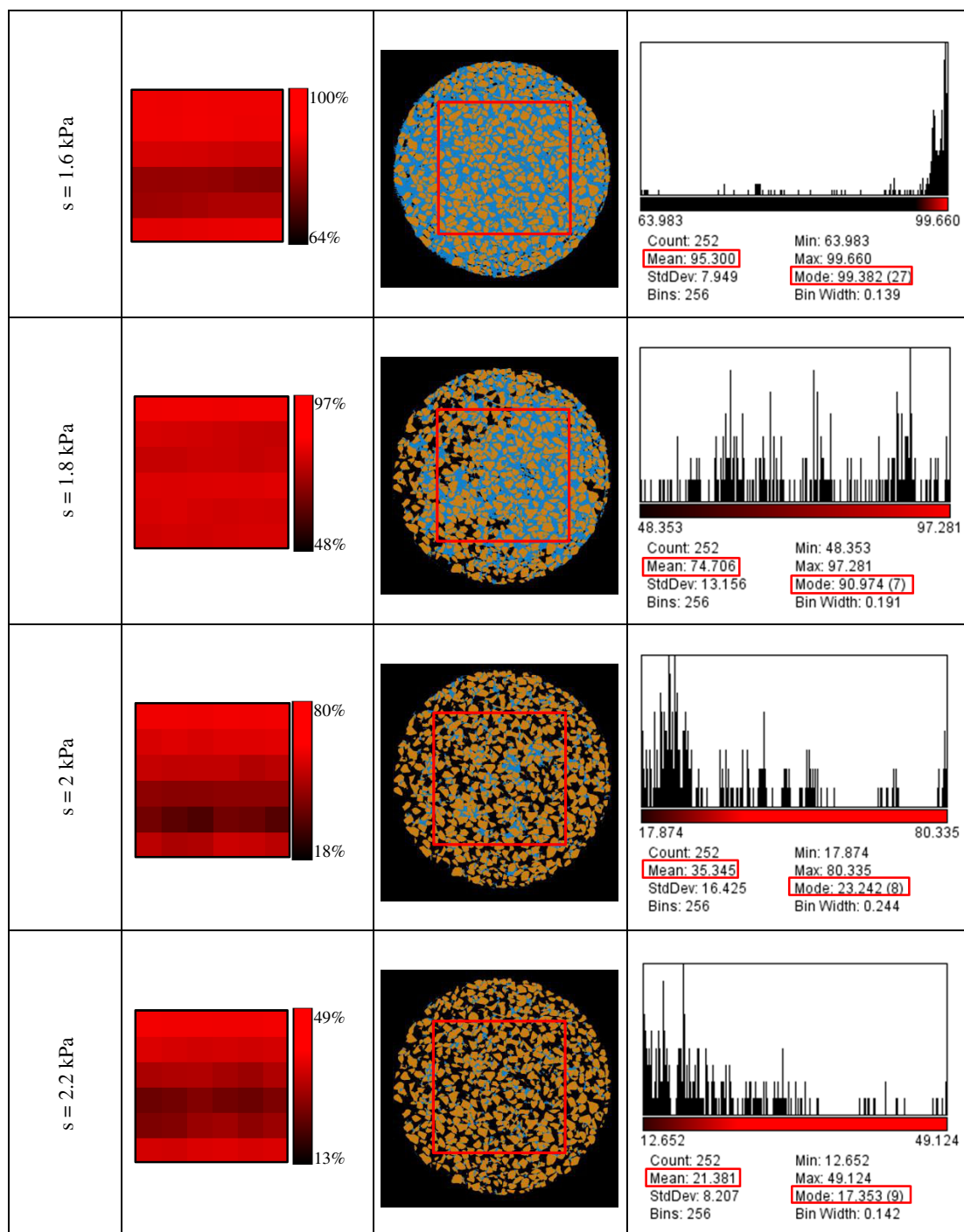


Figure B-6: a) Central vertical slices in the porosity map b) Central vertical slices in the trinarized volumes c) Porosity vertical profile, for all the values of suction in the drying path D_0 . All the vertical slices are of the same azimuth. The yellow dashed line on the central vertical slices in the porosity map for $s = 0 \text{ kPa}$ represents the column of voxels for which porosity vertical profile is drawn

B.2 Degree of saturation mapping results

B.2.1 Drying path D_1

Suction (kPa)	a)	b)	c)
Complete saturation $s = 0$ kPa			 Count: 252 Mean: 99.910 StdDev: 0.0859 Bins: 256 Min: 99.589 Max: 99.995 Mode: 99.947 (9) Bin Width: 0.00159
$s = 1$ kPa			 Count: 252 Mean: 98.690 StdDev: 0.709 Bins: 256 Min: 96.954 Max: 99.658 Mode: 99.172 (7) Bin Width: 0.0106
$s = 1.2$ kPa			 Count: 252 Mean: 98.910 StdDev: 0.663 Bins: 256 Min: 97.202 Max: 99.751 Mode: 99.642 (8) Bin Width: 0.00996
$s = 1.4$ kPa			 Count: 252 Mean: 98.805 StdDev: 0.716 Bins: 256 Min: 97.002 Max: 99.661 Mode: 99.433 (8) Bin Width: 0.0104



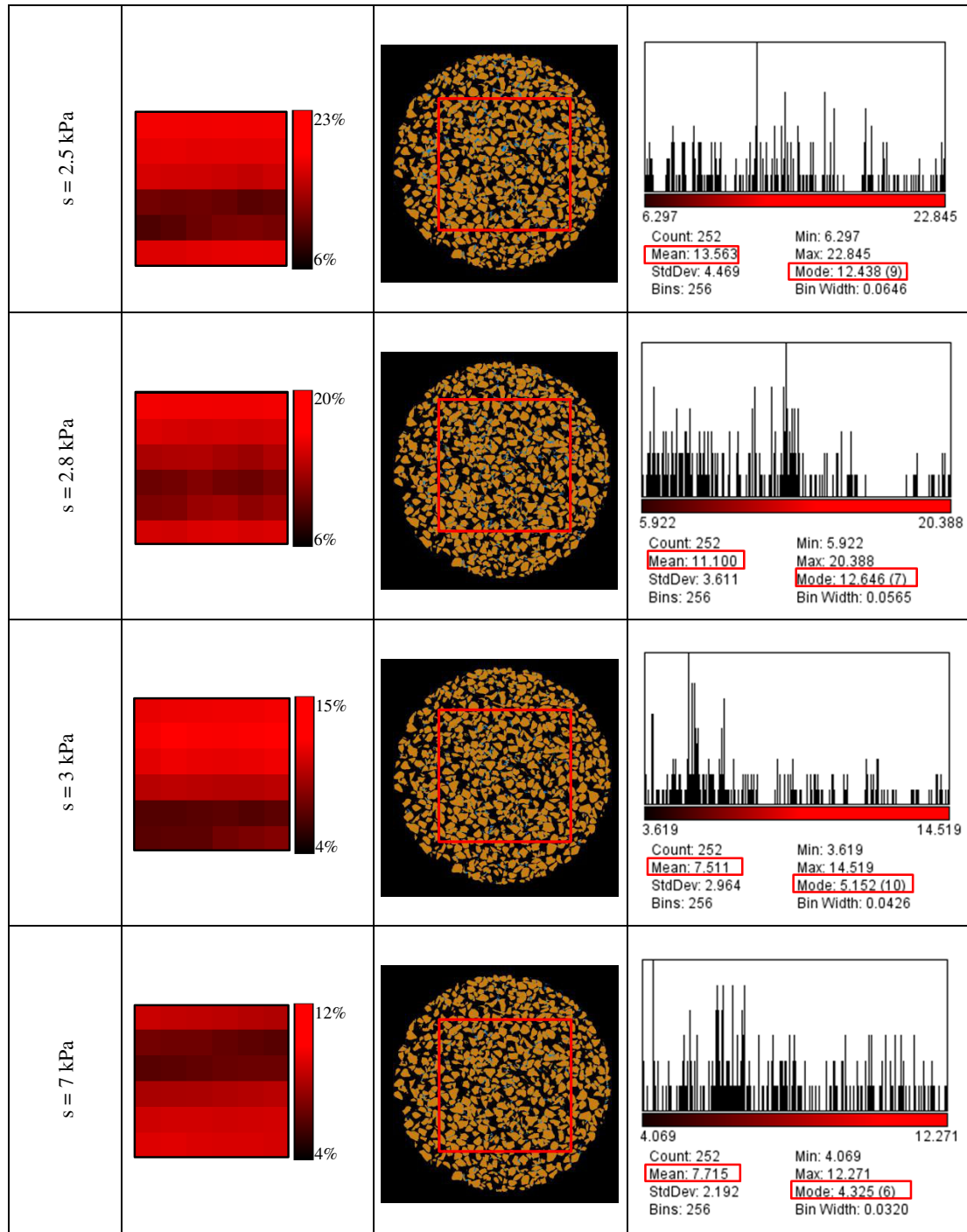
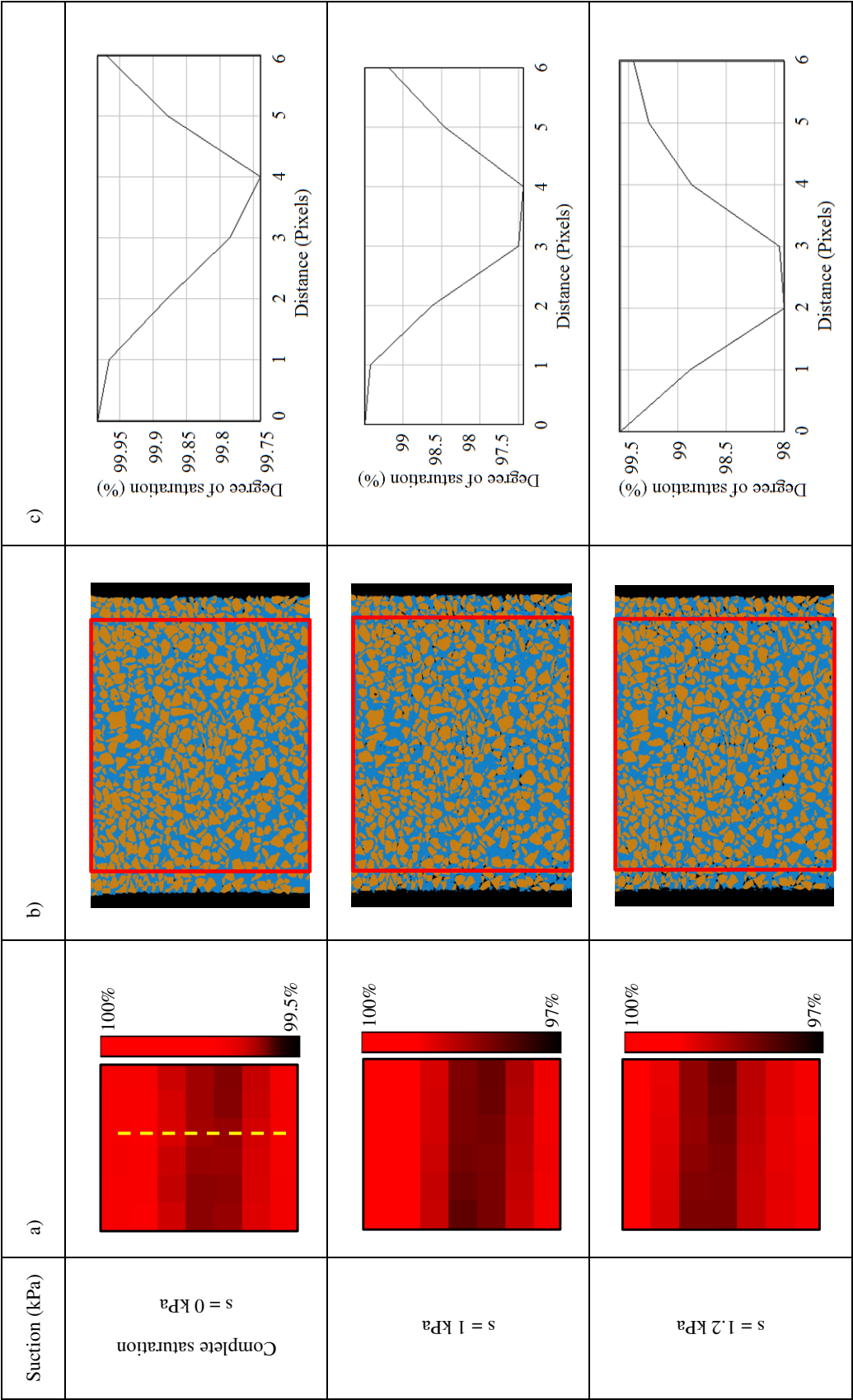
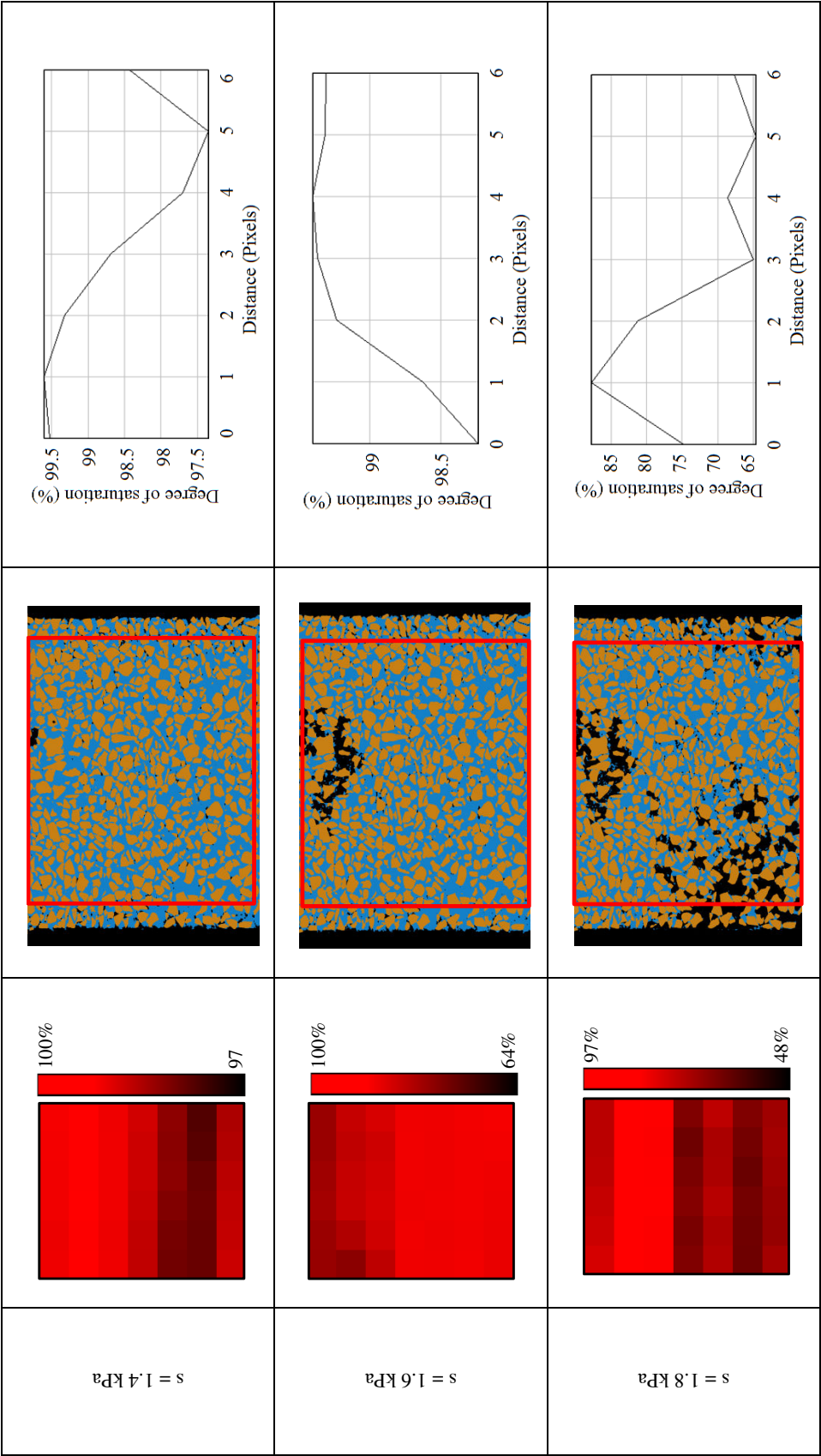
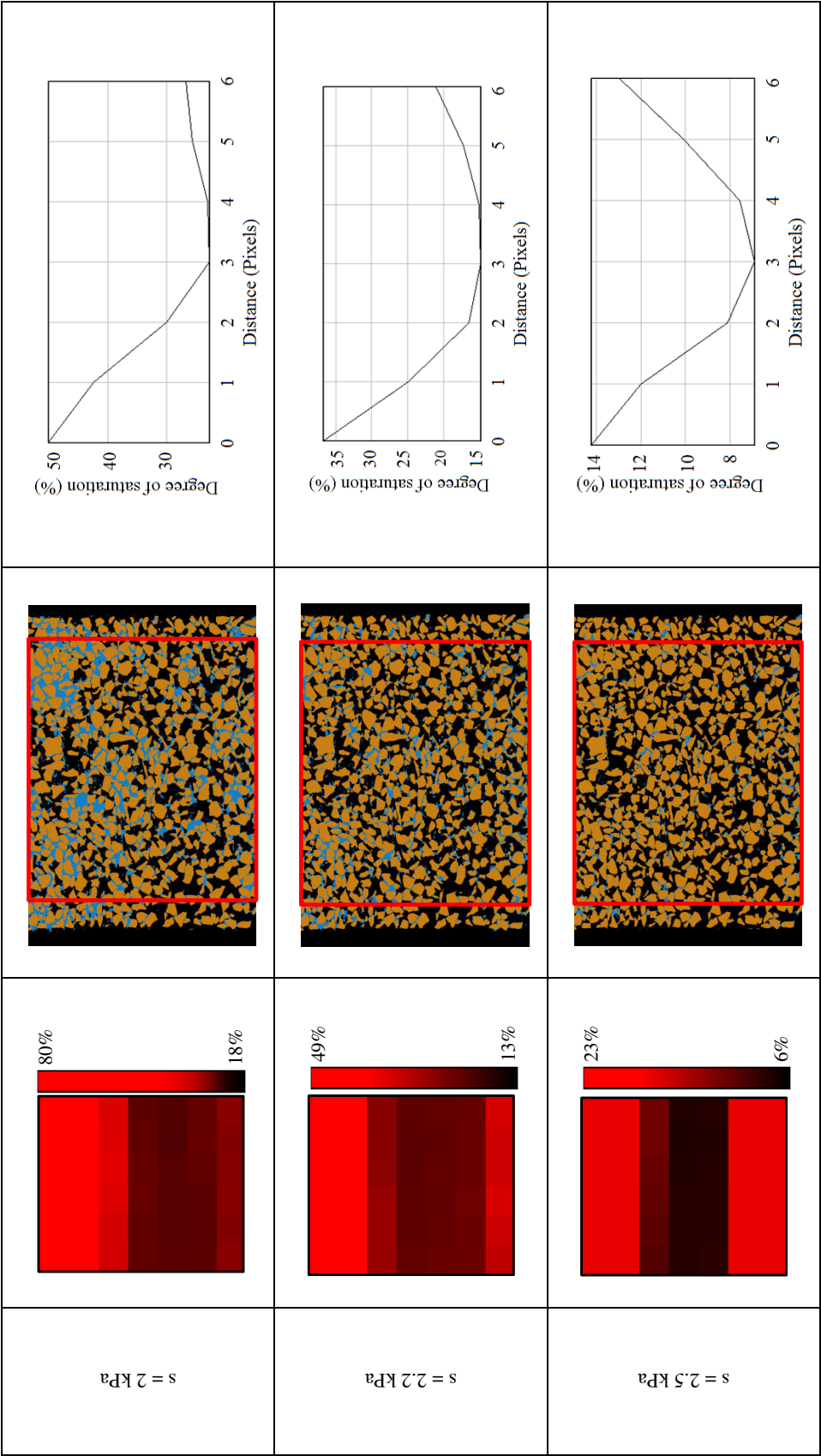


Figure B-7: a) Central horizontal slices in the degree of saturation map b) Central horizontal slices in the trinarized volumes c) Degree of saturation histogram, for all the values of suction in the drying path D_1







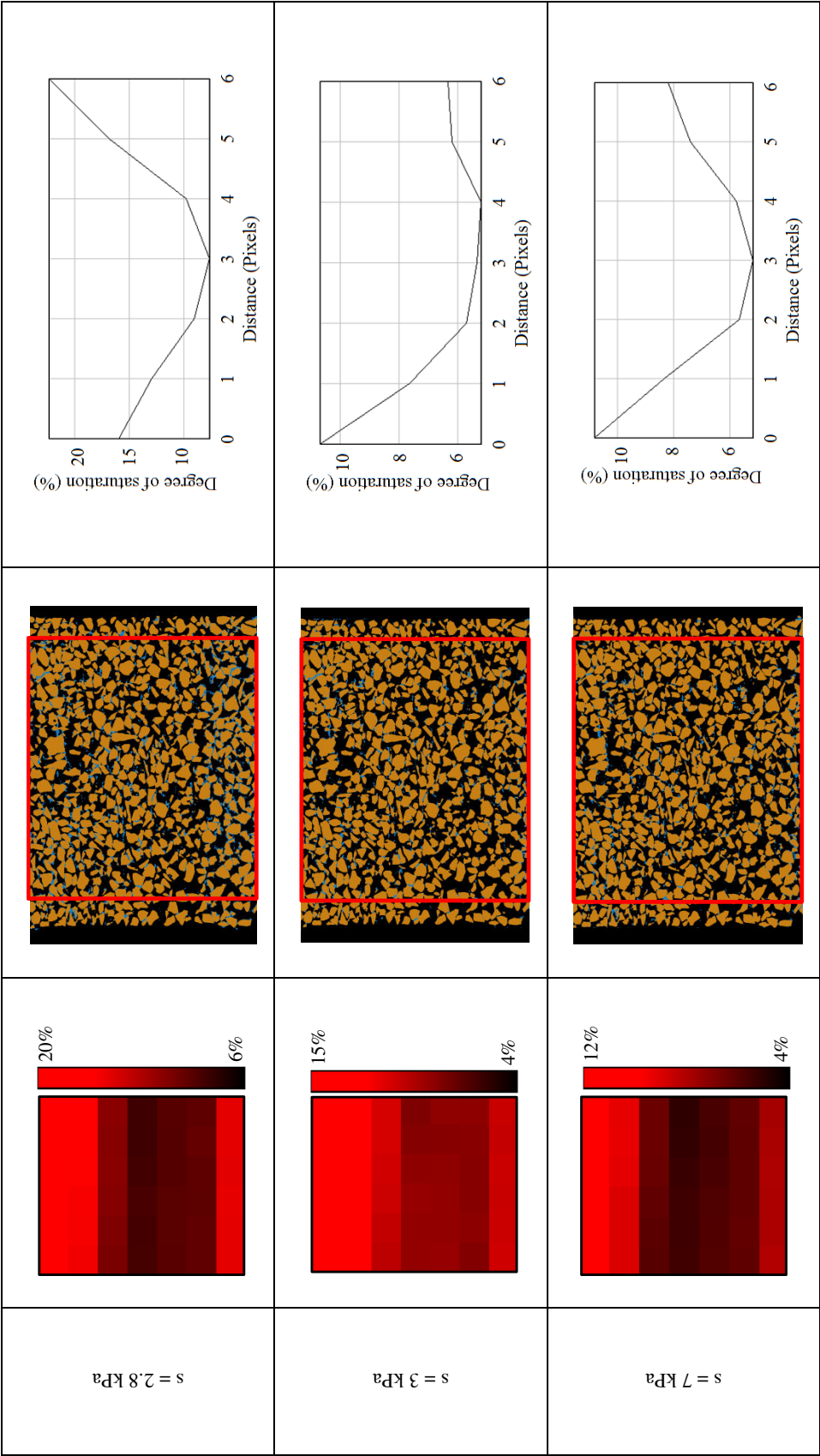
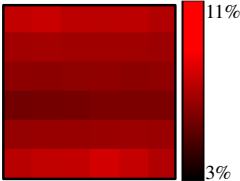
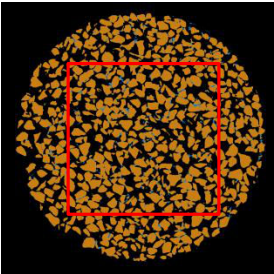
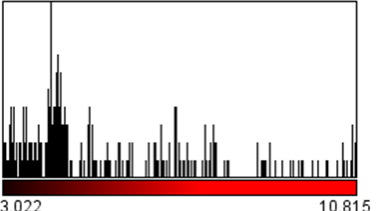

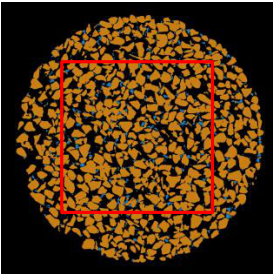
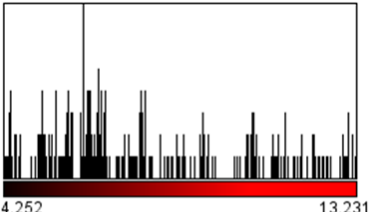
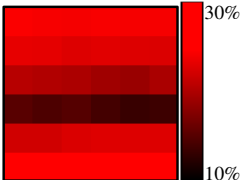
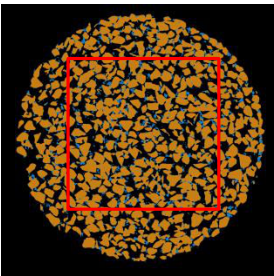
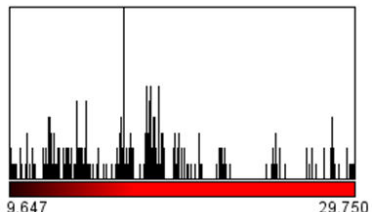

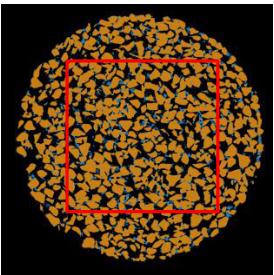
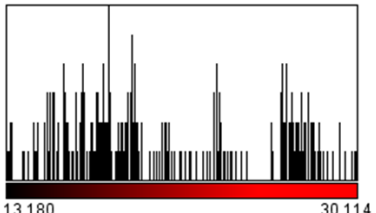
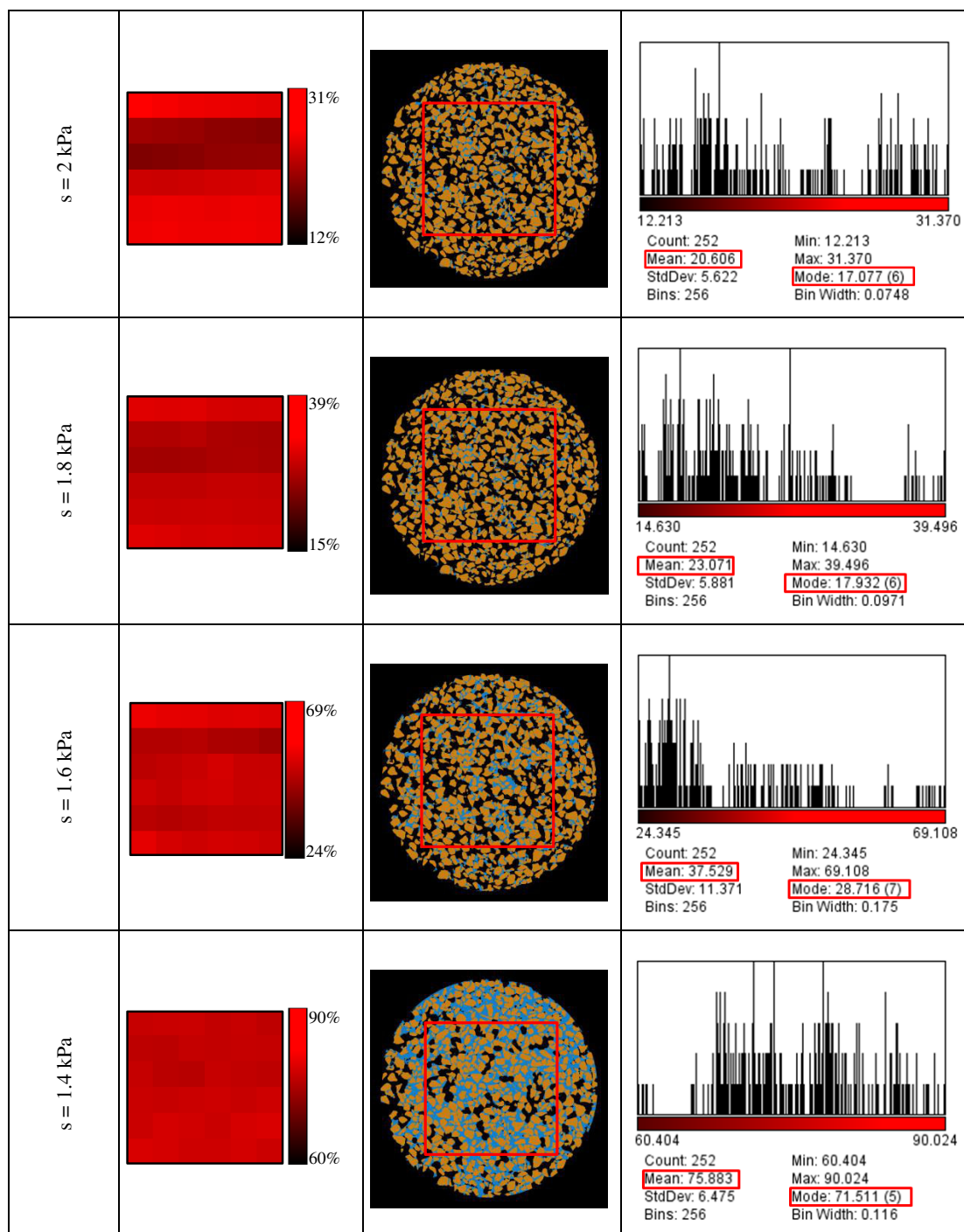


Figure B-8: a) Central vertical slices in the degree of saturation map b) Central vertical slices in the trinarized volumes c) Degree of saturation vertical profile, for all the values of suction in the drying path D_1 . All the vertical slices are of the same azimuth. The yellow dashed line on the central vertical slices in the degree of saturation map for $s = 0 \text{ kPa}$ represents the column of voxels for which degree of saturation vertical profile is drawn

B.2.2 Wetting path W_1

Suction (kPa)	a)	b)	c)
$s = 3$ kPa			 Count: 252 Mean: 5.449 StdDev: 2.082 Bins: 256 Min: 3.022 Max: 10.815 Mode: 4.057 (10) Bin Width: 0.0304
$s = 2.8$ kPa			 Count: 252 Mean: 7.951 StdDev: 2.524 Bins: 256 Min: 4.252 Max: 13.231 Mode: 6.251 (8) Bin Width: 0.0351
$s = 2.5$ kPa			 Count: 252 Mean: 17.510 StdDev: 5.045 Bins: 256 Min: 9.647 Max: 29.750 Mode: 16.243 (11) Bin Width: 0.0785
$s = 2.2$ kPa			 Count: 252 Mean: 20.779 StdDev: 4.686 Bins: 256 Min: 13.180 Max: 30.114 Mode: 18.075 (6) Bin Width: 0.0661



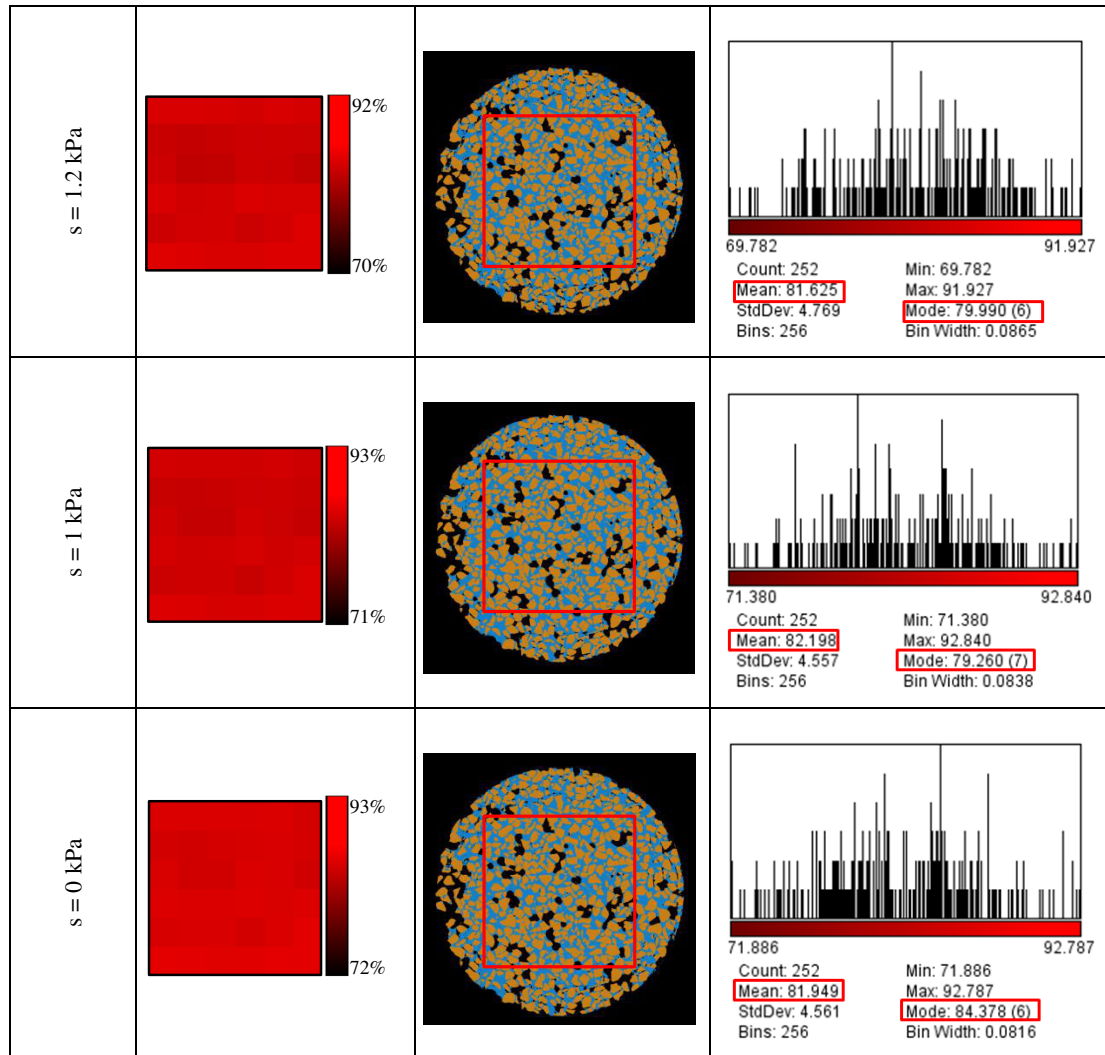
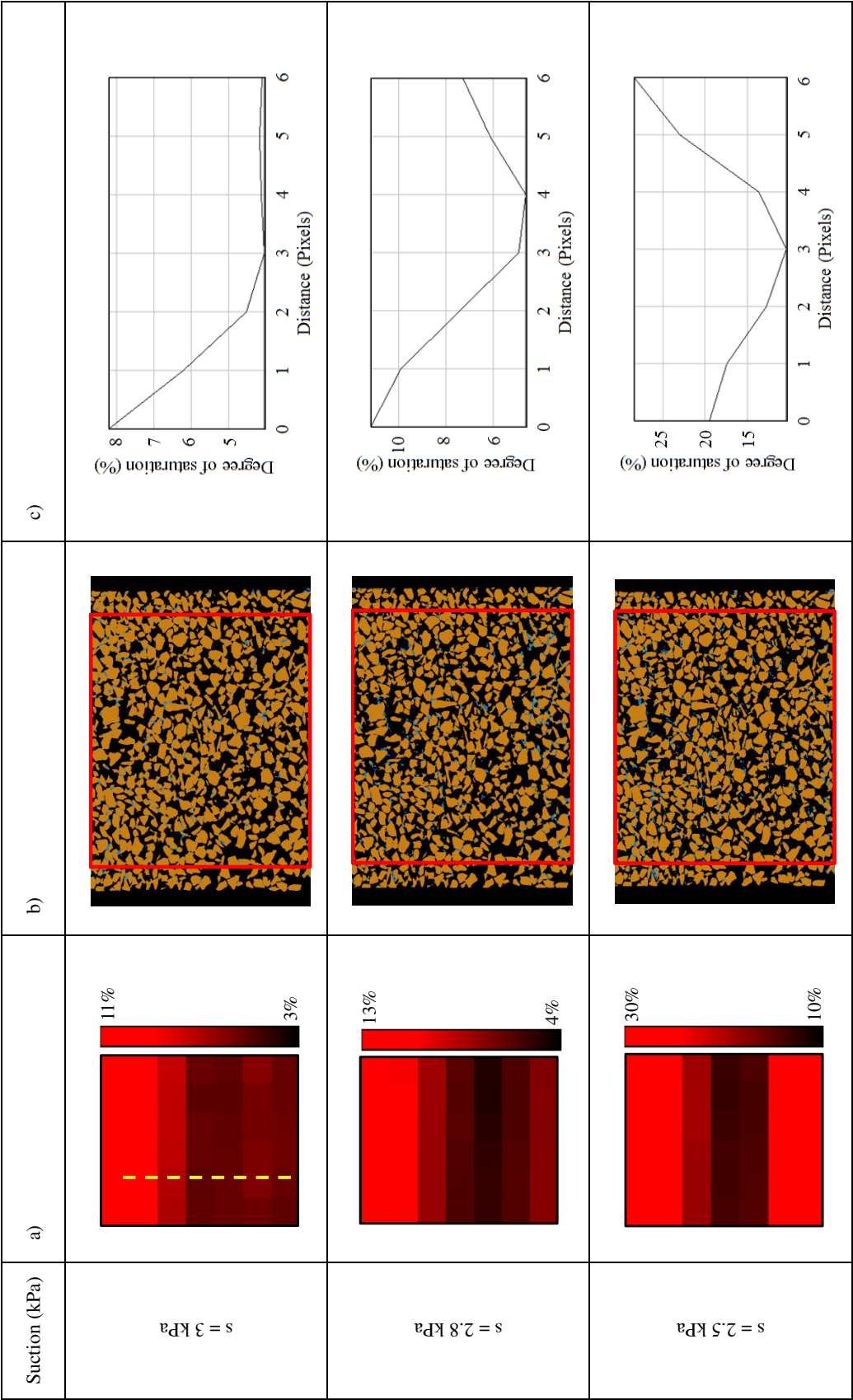
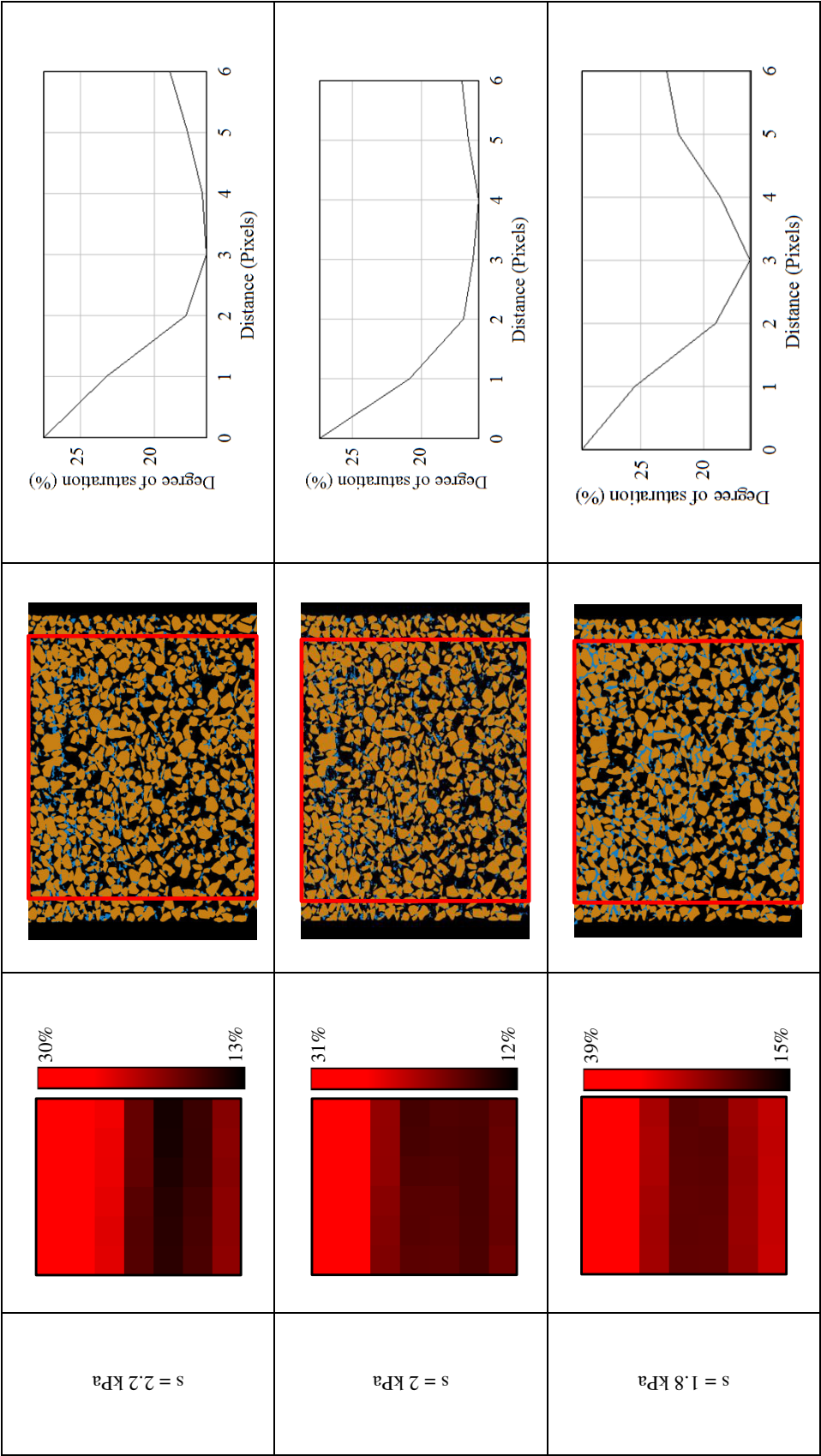
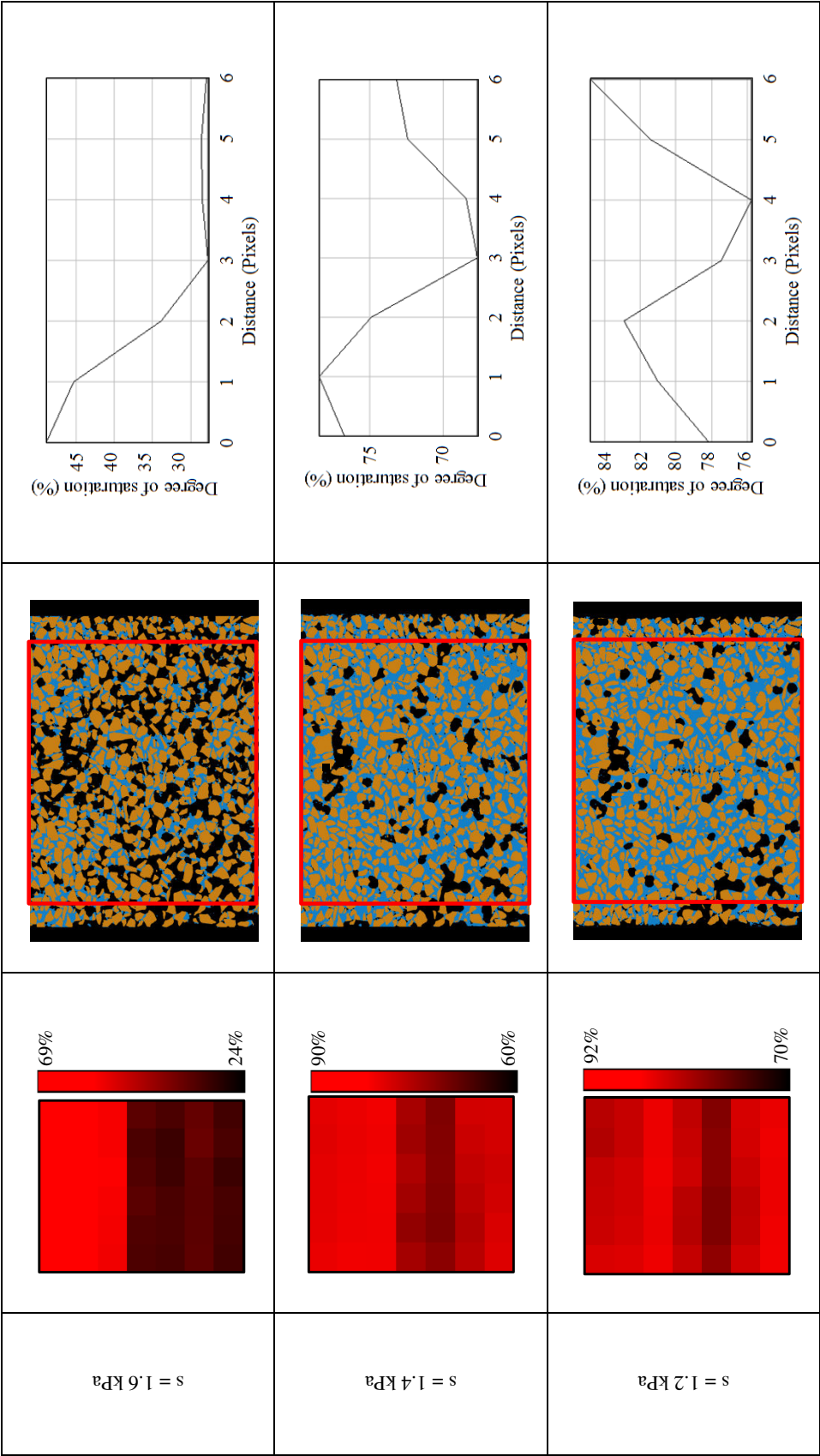


Figure B-9: a) Central horizontal slices in the degree of saturation map b) Central horizontal slices in the trinarized volumes c) Degree of saturation histogram, for all the values of suction in the wetting path W_1







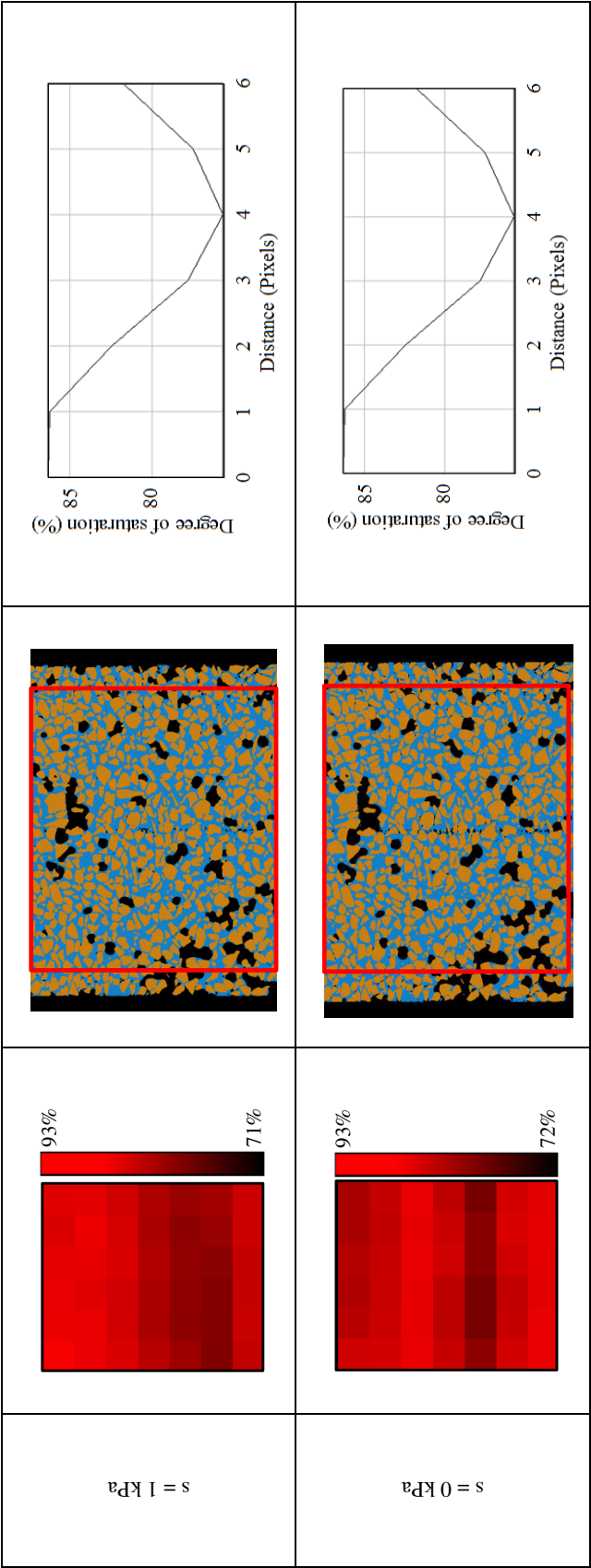
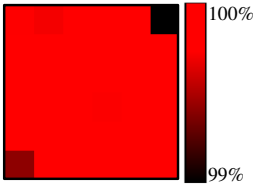
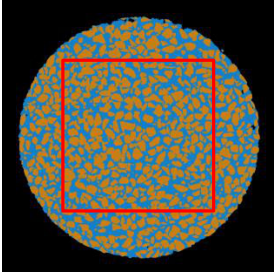
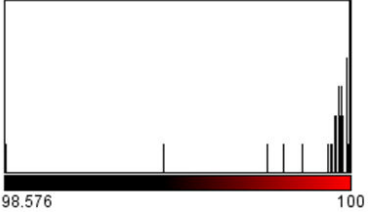
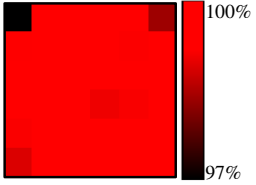
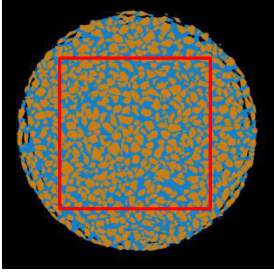
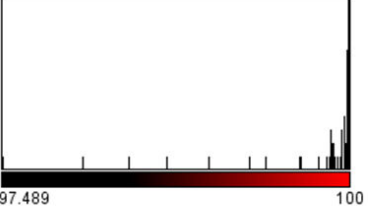
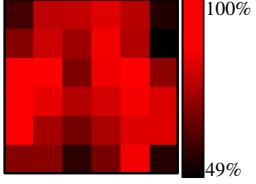
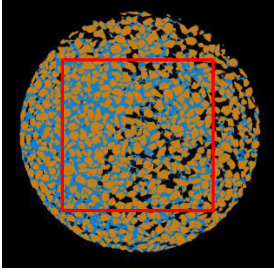
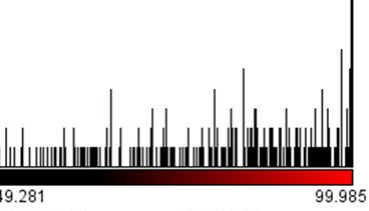
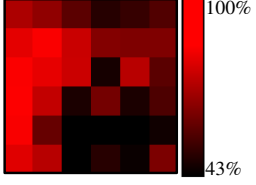
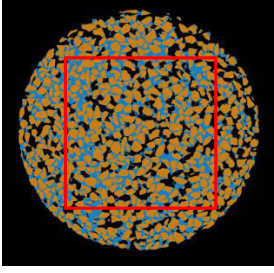
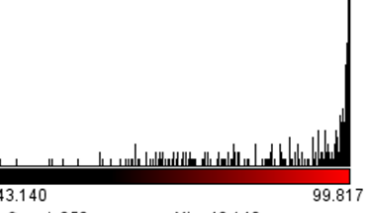
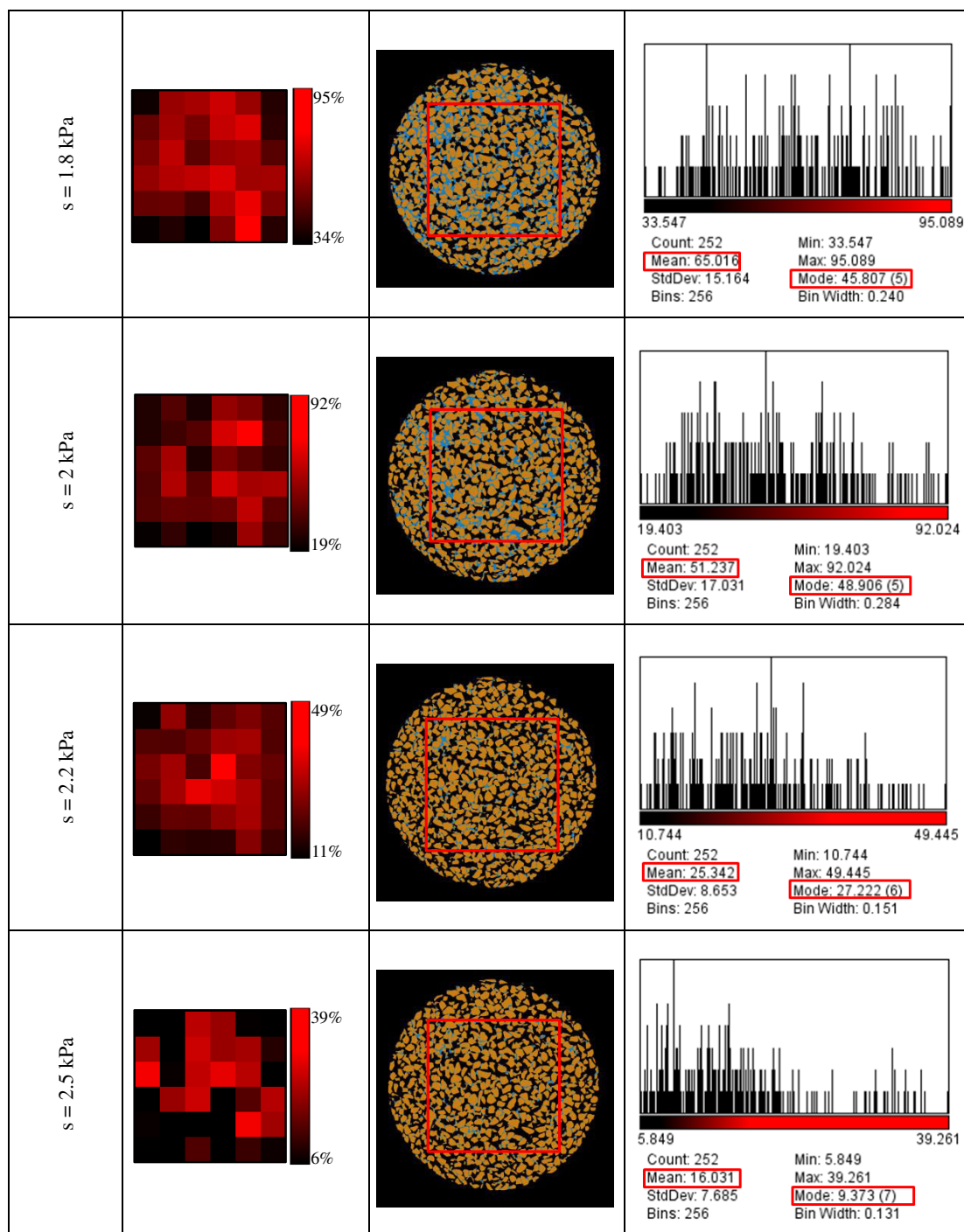


Figure B-10: a) Central vertical slices in the degree of saturation map b) Central vertical slices in the trinarized volumes c) Degree of saturation vertical profile, for all the values of suction in the wetting path W_i . All the vertical slices are of the same azimuth. The yellow dashed line on the central vertical slices in the degree of saturation map for $s = 3 \text{ kPa}$ represents the column of voxels for which degree of saturation vertical profile is drawn

B.2.3 Drying path D_0

Suction (kPa)	a)	b)	c)
Complete saturation $s = 0$ kPa			 98.576 Count: 252 Mean: 99.984 StdDev: 0.106 Bins: 256 Min: 98.576 Max: 100 Mode: 99.994 (225) Bin Width: 0.00556
$s = 1$ kPa			 97.489 Count: 252 Mean: 99.950 StdDev: 0.253 Bins: 256 Min: 97.489 Max: 100 Mode: 99.990 (212) Bin Width: 0.00981
$s = 1.2$ kPa			 49.281 Count: 252 Mean: 82.490 StdDev: 14.244 Bins: 256 Min: 49.281 Max: 99.985 Mode: 99.787 (26) Bin Width: 0.198
$s = 1.4$ kPa			 43.140 Count: 252 Mean: 87.946 StdDev: 13.082 Bins: 256 Min: 43.140 Max: 99.817 Mode: 99.596 (24) Bin Width: 0.221



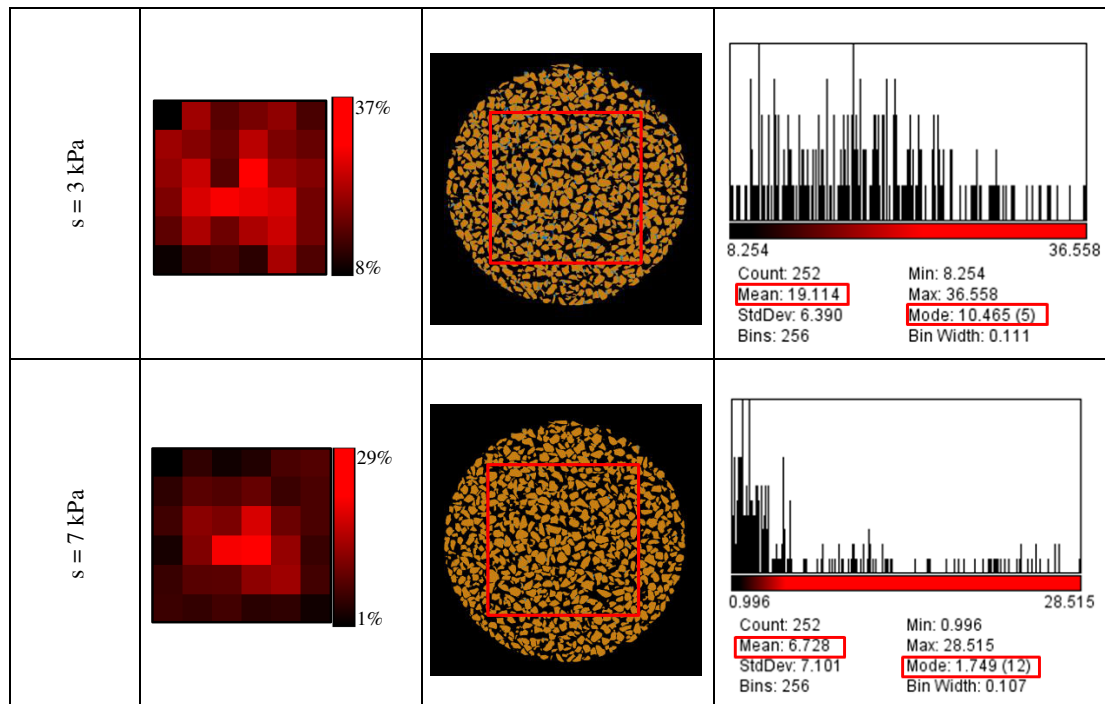
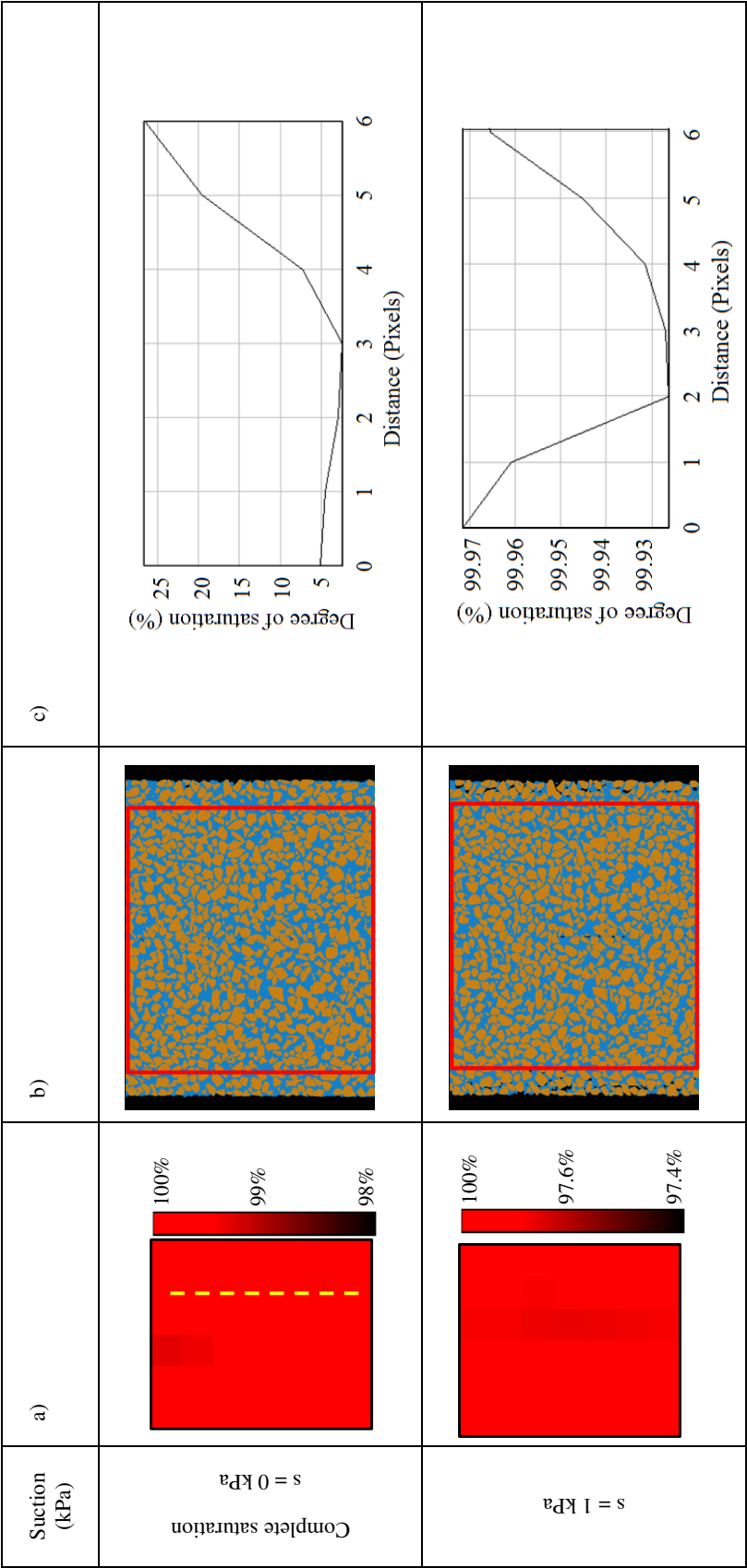
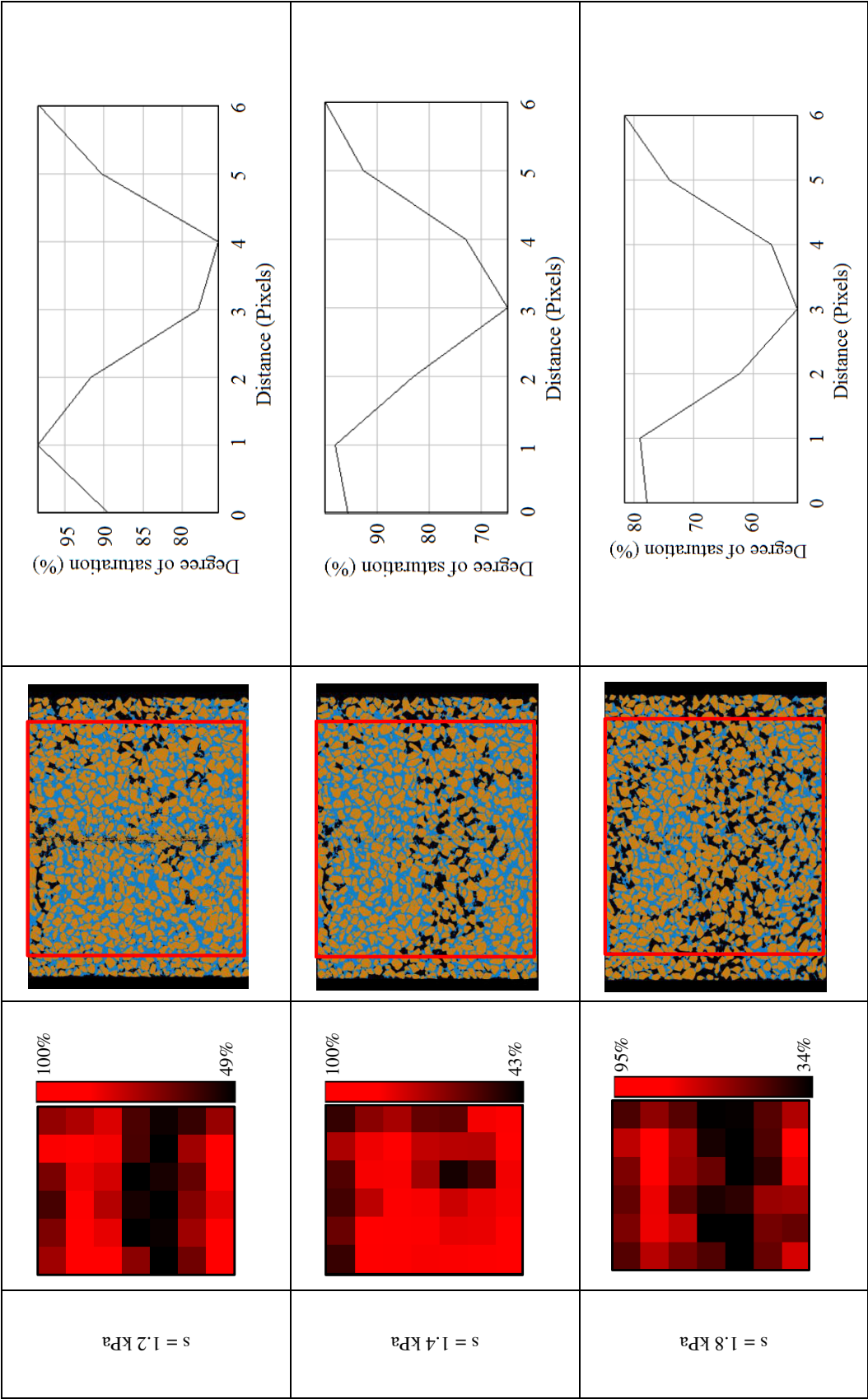
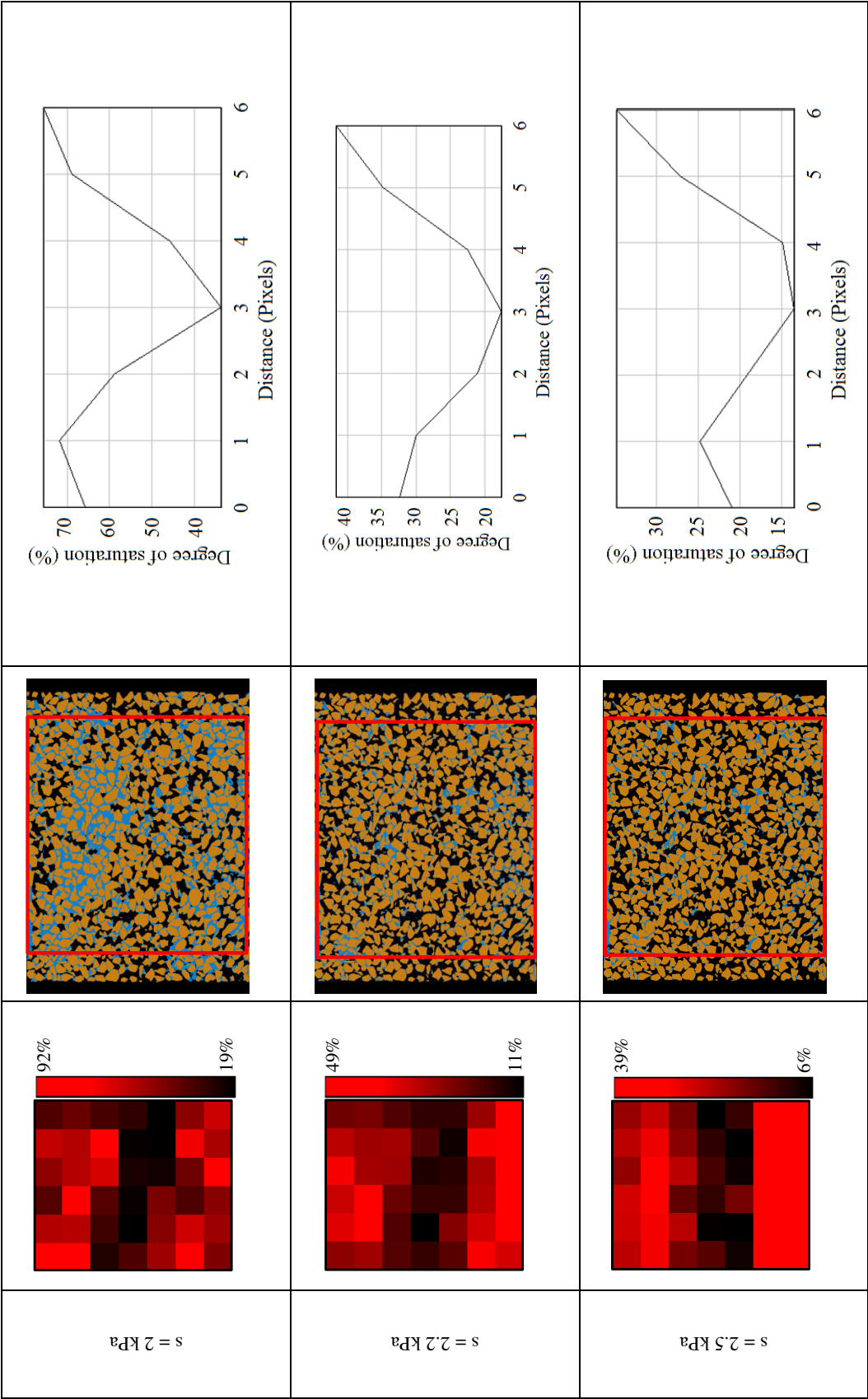


Figure B-11: a) Central horizontal slices in the degree of saturation map b) Central horizontal slices in the trinarized volumes c) Degree of saturation histogram, for all the values of suction in the drying path D_0







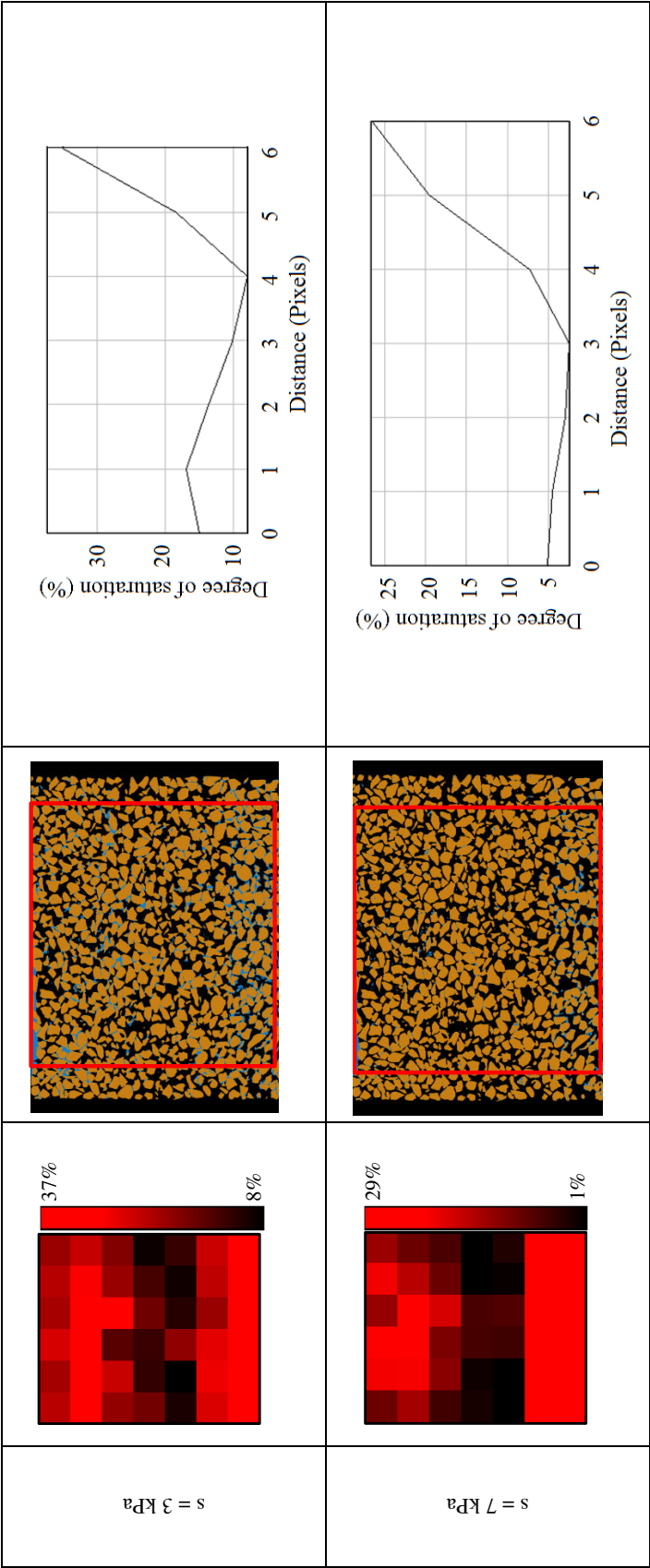


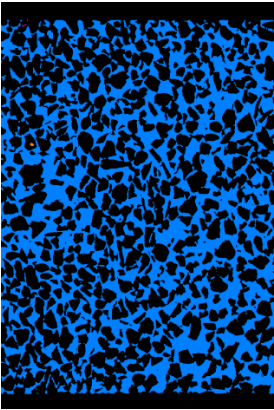
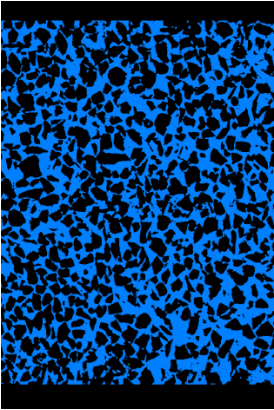
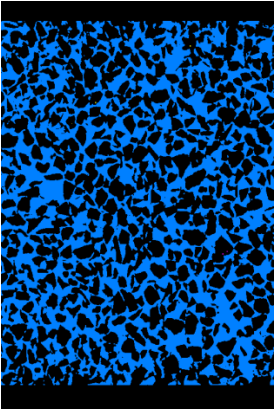
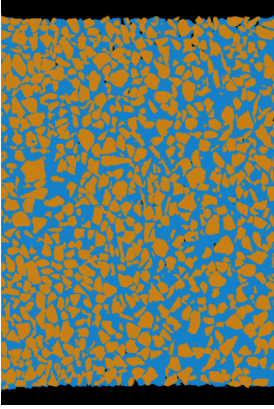
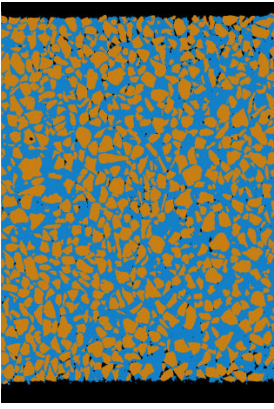
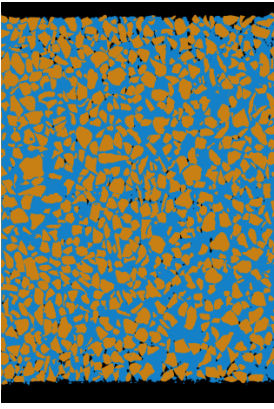
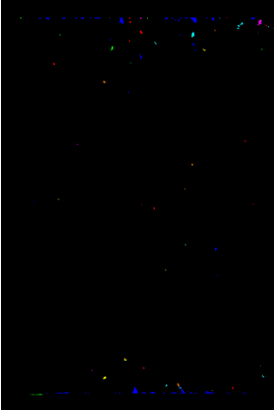
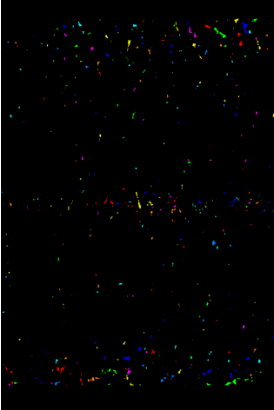
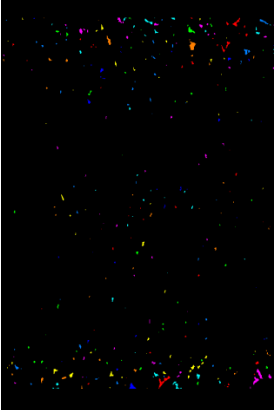
Figure B-12: a) Central vertical slices in the degree of saturation map b) Central vertical slices in the trinarized volumes c) Degree of saturation vertical profile, for all the values of suction in the drying path D_0 . All the vertical slices are of the same azimuth. The yellow dashed line on the central vertical slices in the degree of saturation map for $s = 0 \text{ kPa}$ represents the column of voxels for which degree of saturation vertical profile is drawn

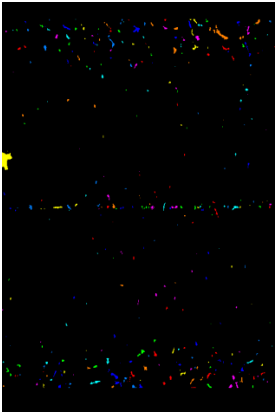
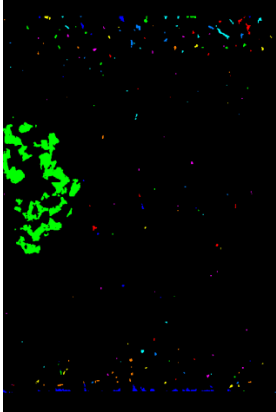
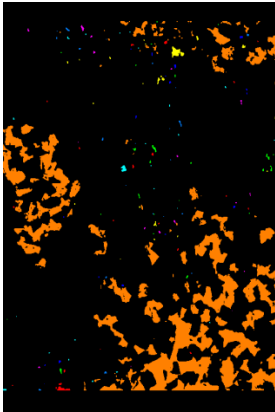
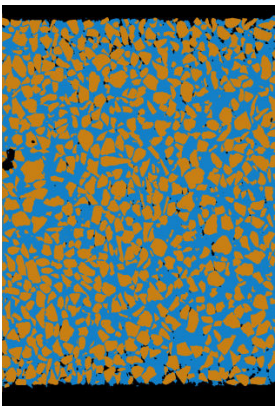
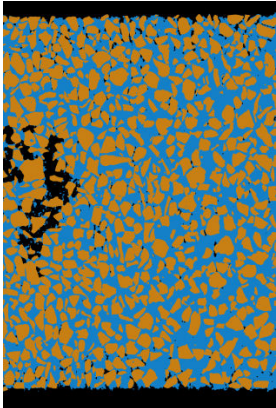
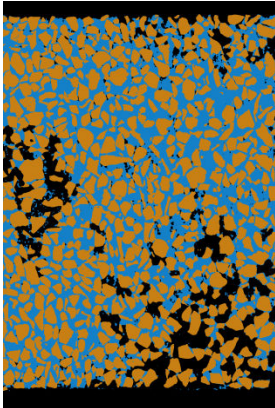
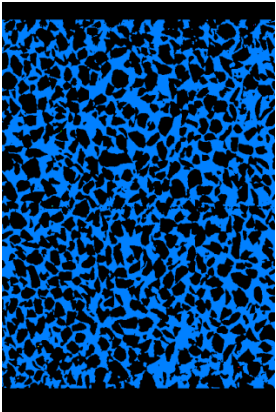
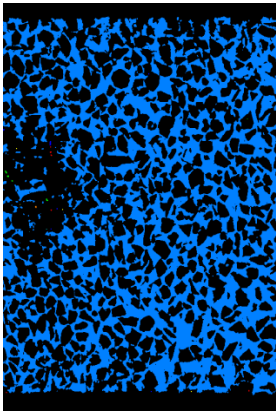
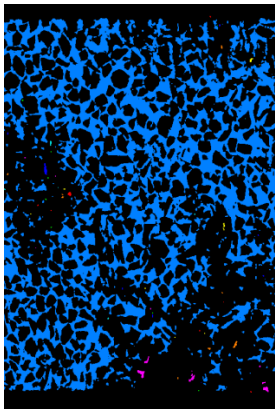
Appendix C

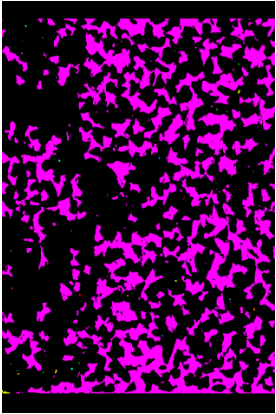
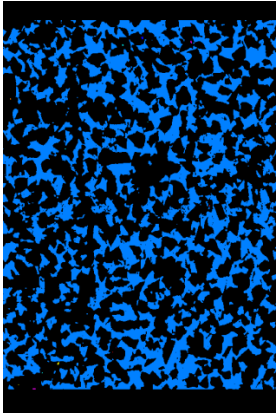
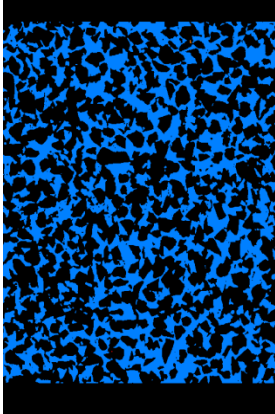
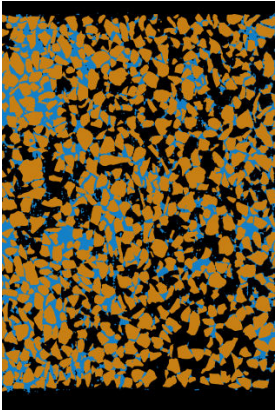
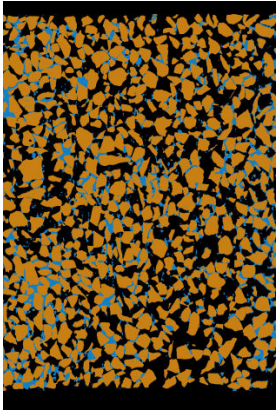
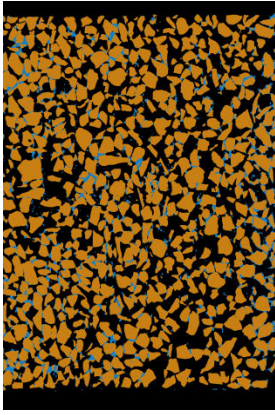
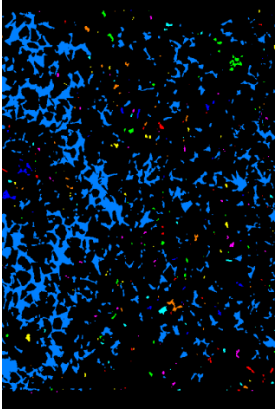
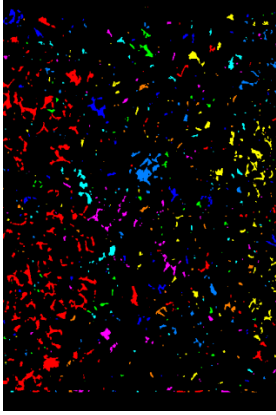
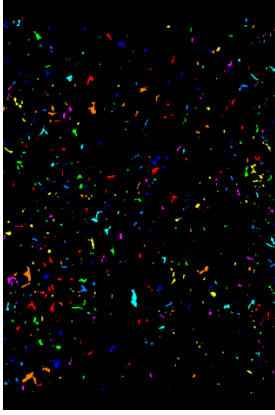
Microscopic-discrete analyses results

C.1 Results of labelling process for water and air phases

C.1.1 Drying path D_1

Suction (kPa)	Saturated $s = 0$ kPa	$s = 1$ kPa	$s = 1.2$ kPa
a)			
b)			
c)			

		
		
		
$s = 1.4 \text{ kPa}$	$s = 1.6 \text{ kPa}$	$s = 1.8 \text{ kPa}$

		
		
		
$s = 2 \text{ kPa}$	$s = 2.2 \text{ kPa}$	$s = 2.5 \text{ kPa}$

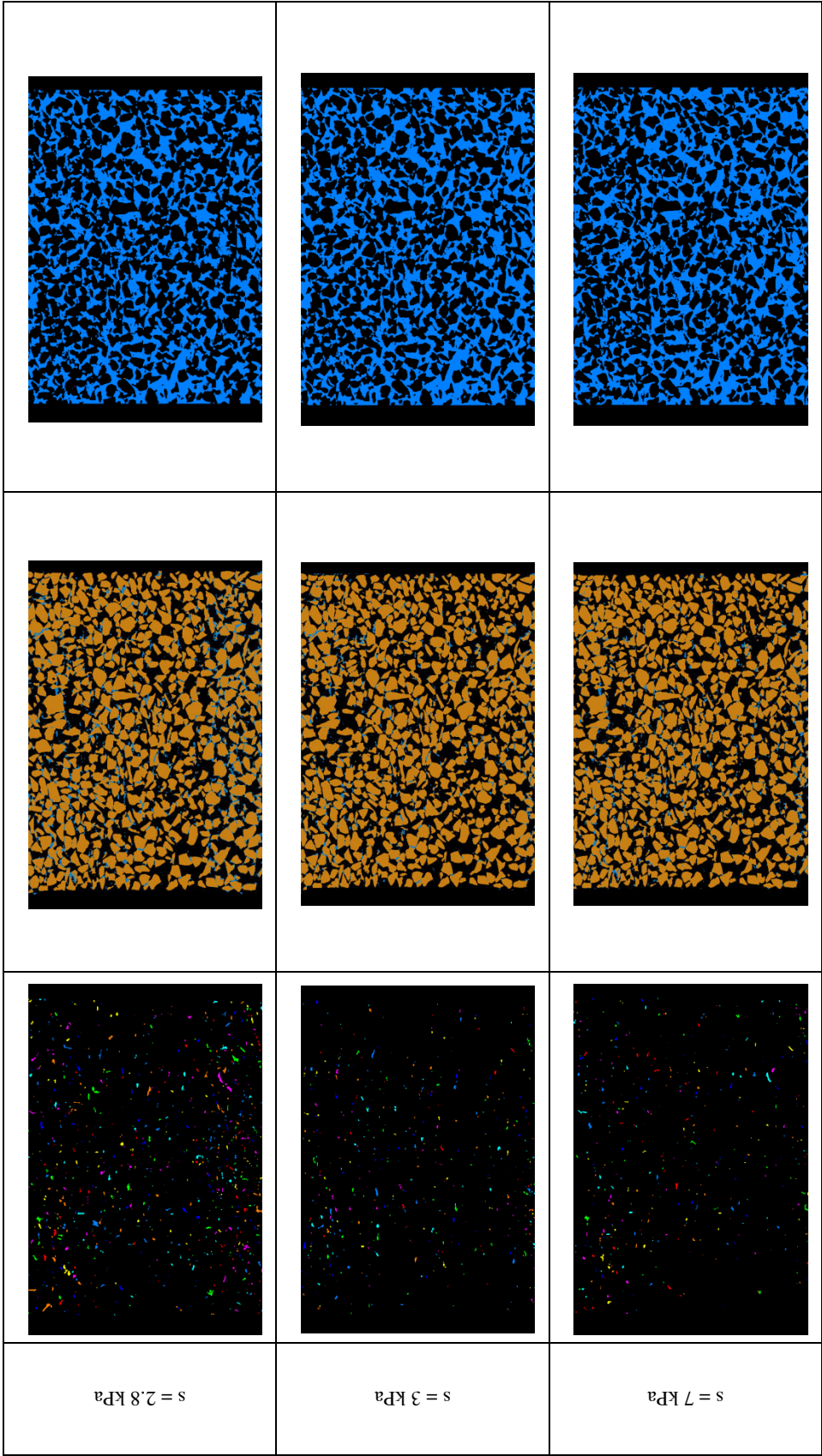
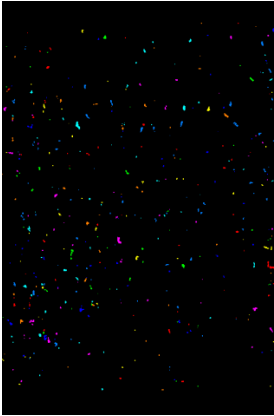
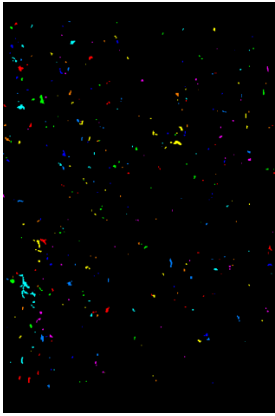
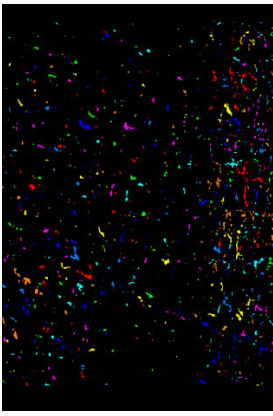
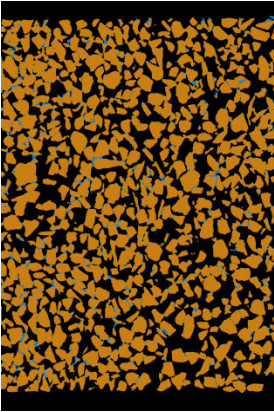
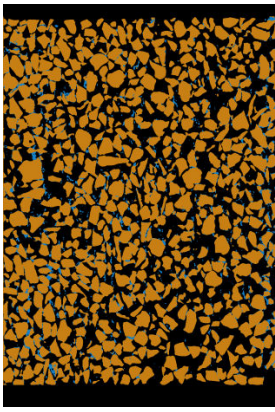
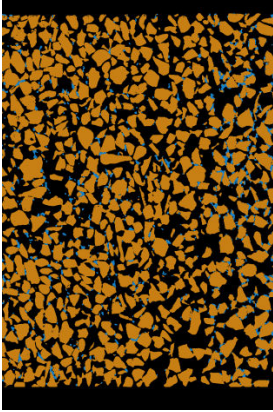
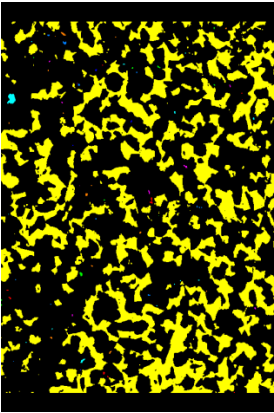
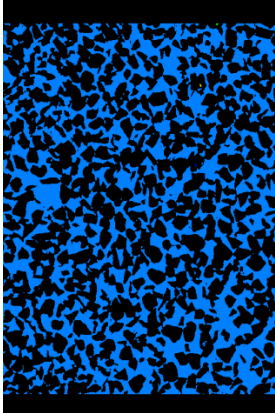
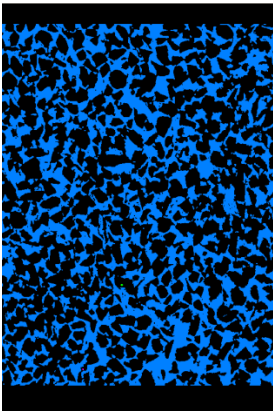
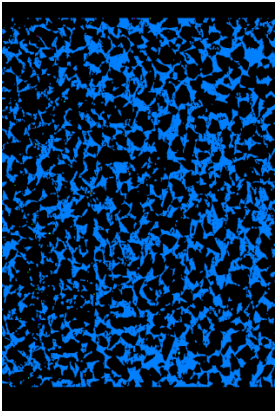
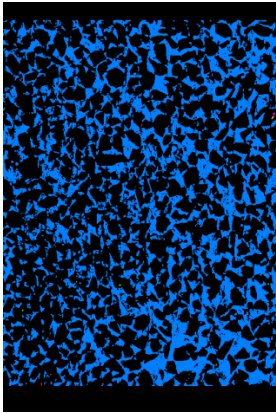
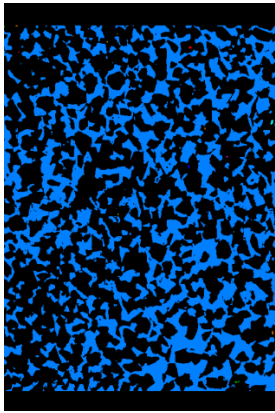
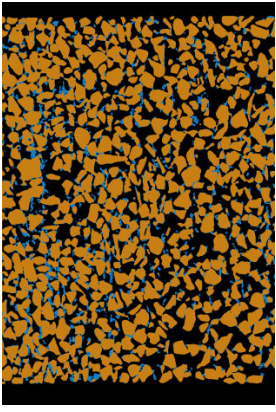
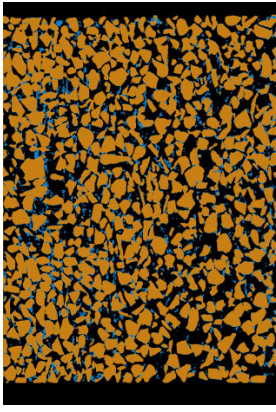
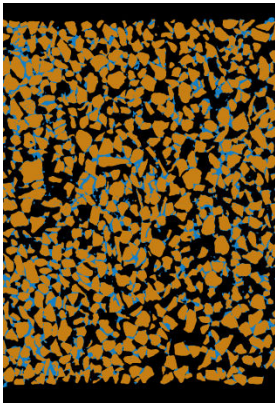
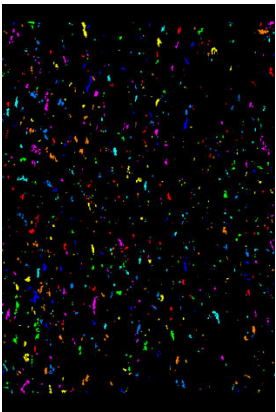
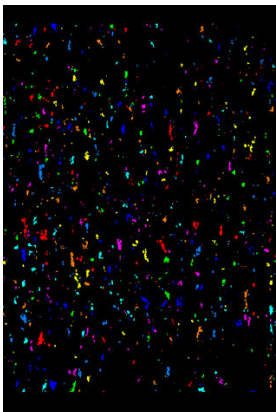
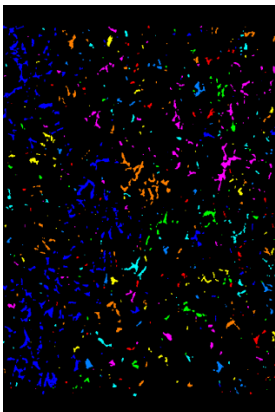
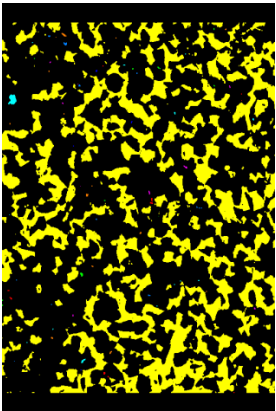
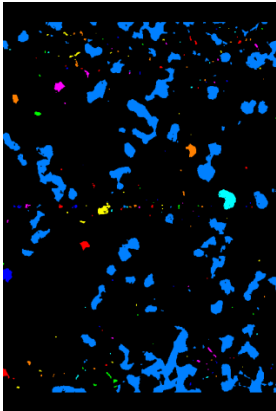
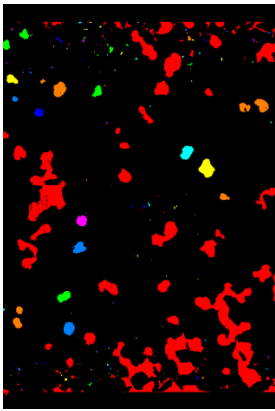
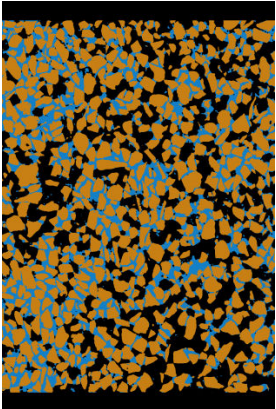
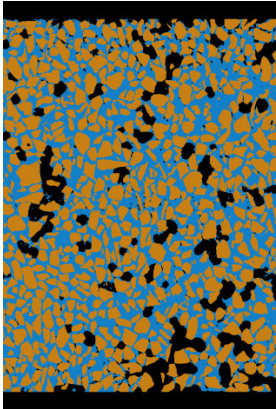
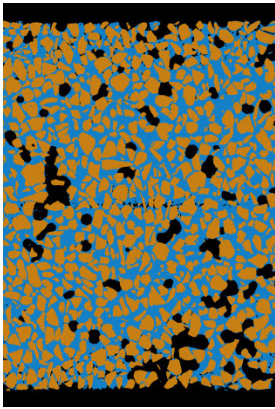
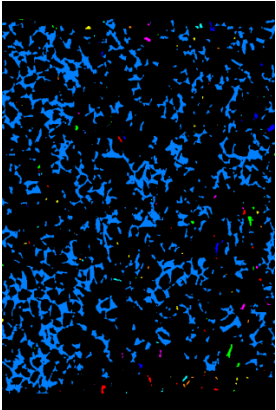
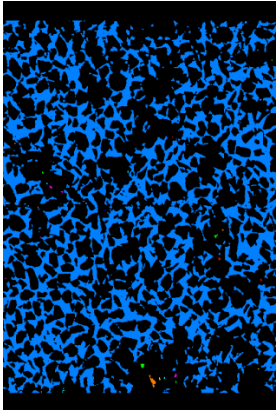
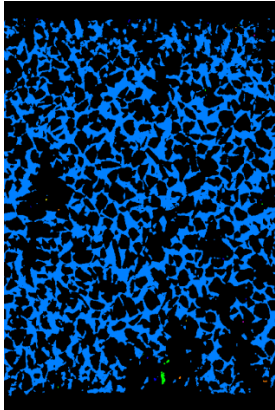


Figure C-1: Central vertical slices in the a) water labelled volumes b) trinarized volumes c) air labelled volumes, for all the values of suction in the drying path D_1

C.1.2 Wetting path W_1

Suction (kPa)	$s = 3 \text{ kPa}$	$s = 2.8 \text{ kPa}$	$s = 2.5 \text{ kPa}$
a)			
b)			
c)			

		
		
		
$s = 2.2 \text{ kPa}$	$s = 2 \text{ kPa}$	$s = 1.8 \text{ kPa}$

		
		
		
$s = 1.6 \text{ kPa}$	$s = 1.4 \text{ kPa}$	$s = 1.2 \text{ kPa}$

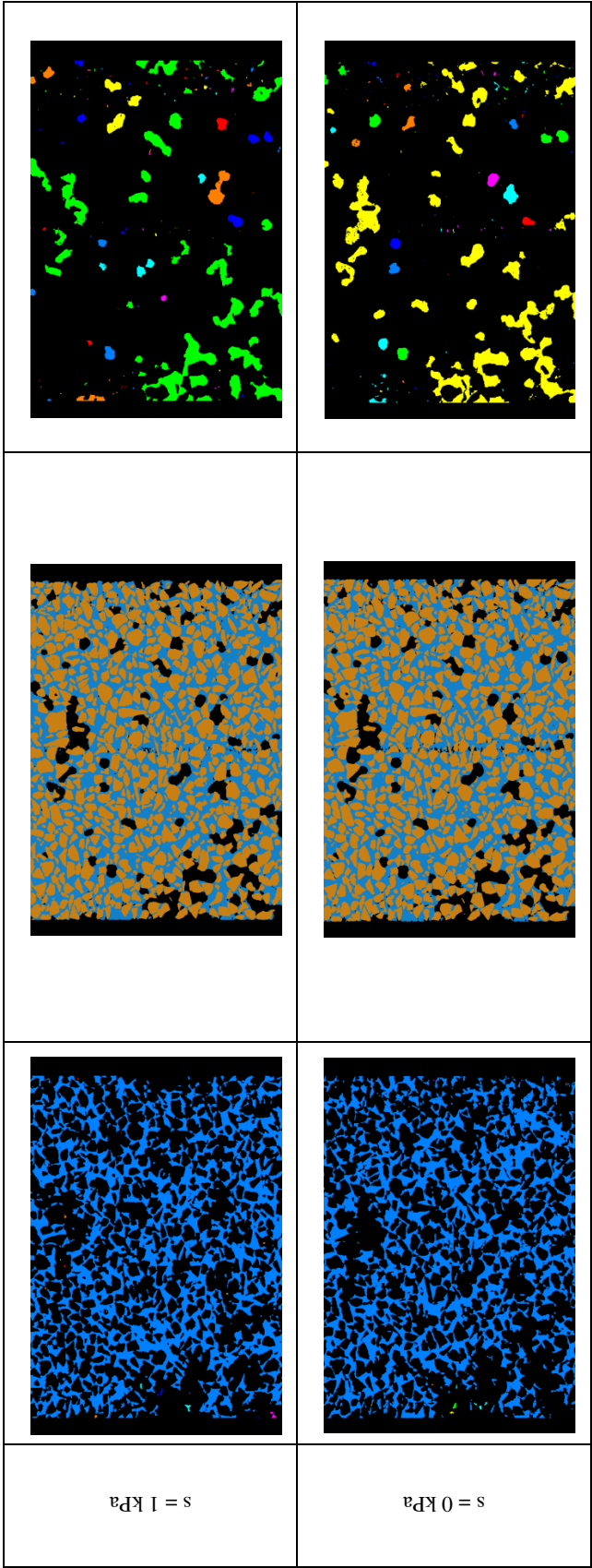
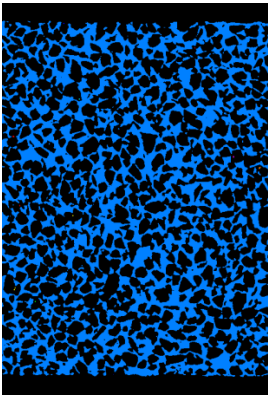
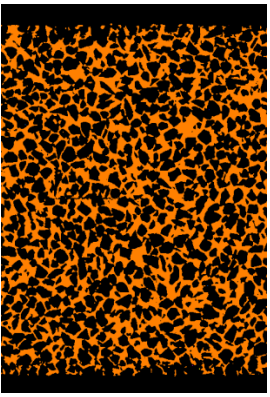
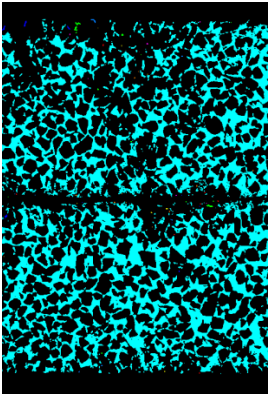
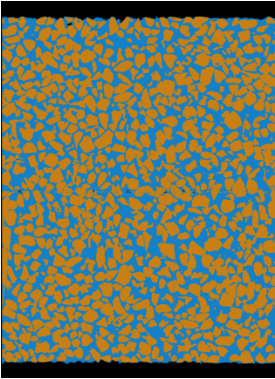
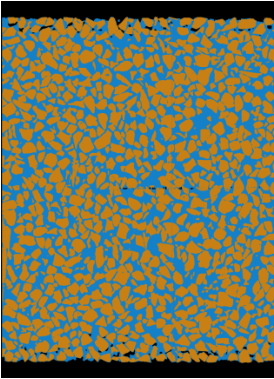
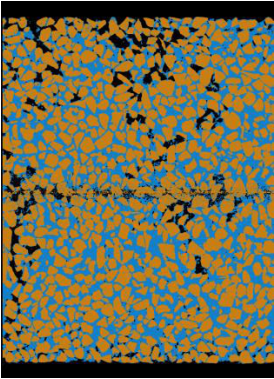
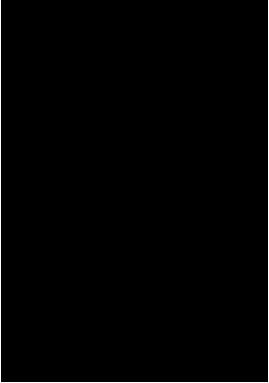

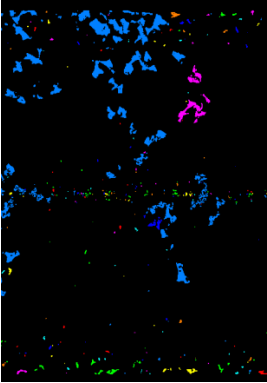

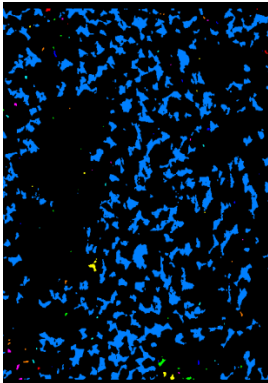
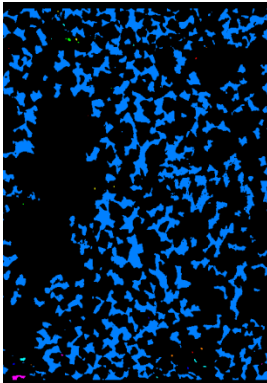
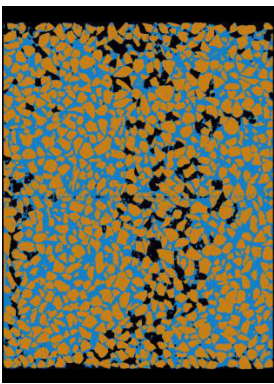
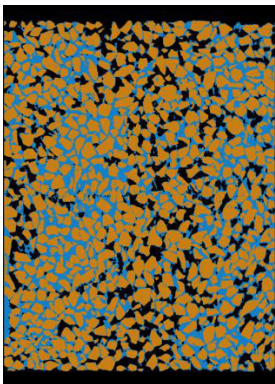
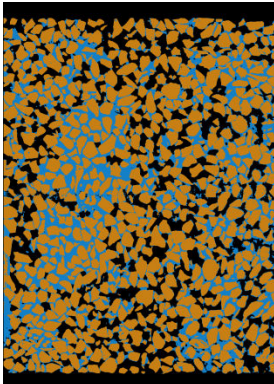
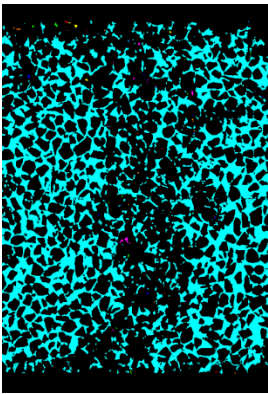
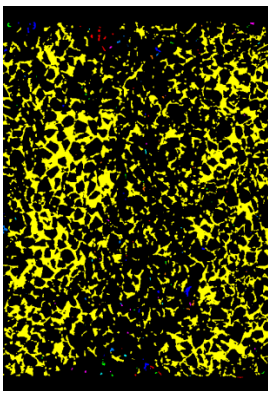
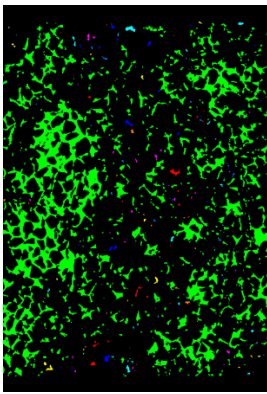
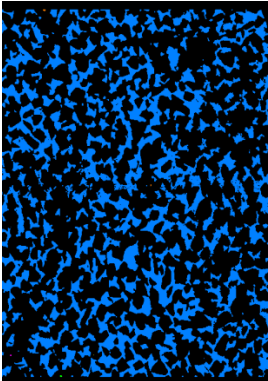
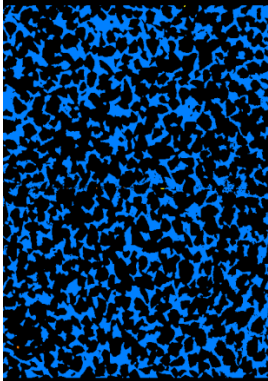
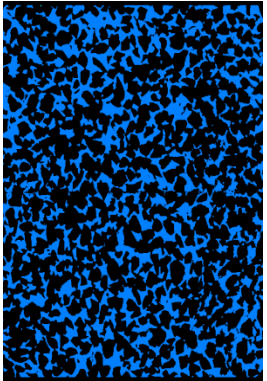
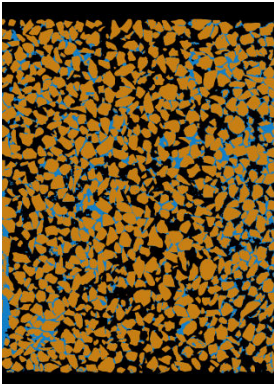
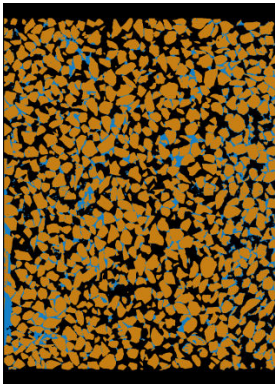
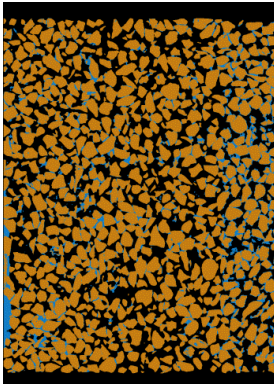
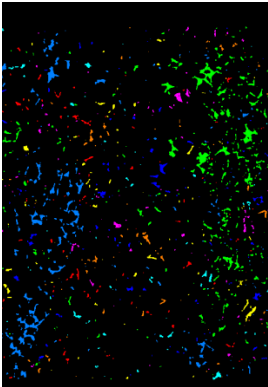
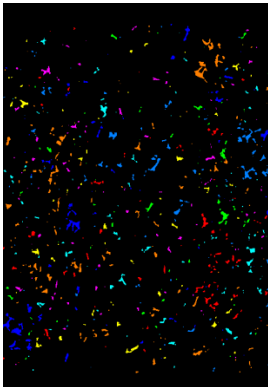
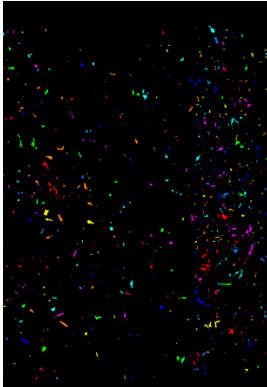


Figure C-2: Central vertical slices in the a) water labelled volumes b) trinarized volumes c) air labelled volumes, for all the values of suction in the wetting path W_1

C.1.3 Drying path D_0

Suction (kPa)	Saturated $s = 0$ kPa	$s = 1$ kPa	$s = 1.2$ kPa
a)			
b)			
c)			

		
		
		
$s = 1.4 \text{ kPa}$	$s = 1.8 \text{ kPa}$	$s = 2 \text{ kPa}$

		
		
		
$s = 2.2 \text{ kPa}$	$s = 2.5 \text{ kPa}$	$s = 3 \text{ kPa}$

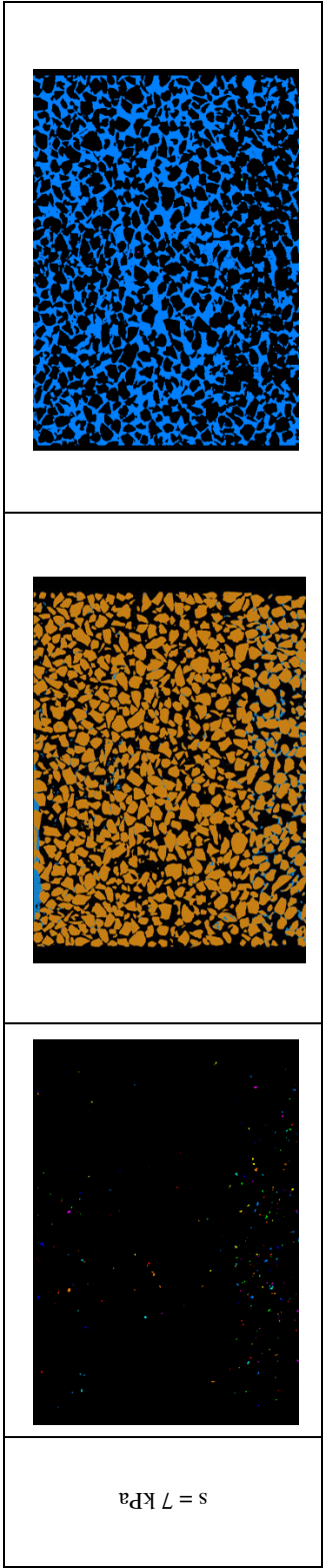


Figure C-3: Central vertical slices in the a) water labelled volumes b) trinarized volumes c) air labelled volumes, for all the values of suction in the wetting path D_0

C.1.4 Results of grain size distribution and the number of grains for W_1 and D_0

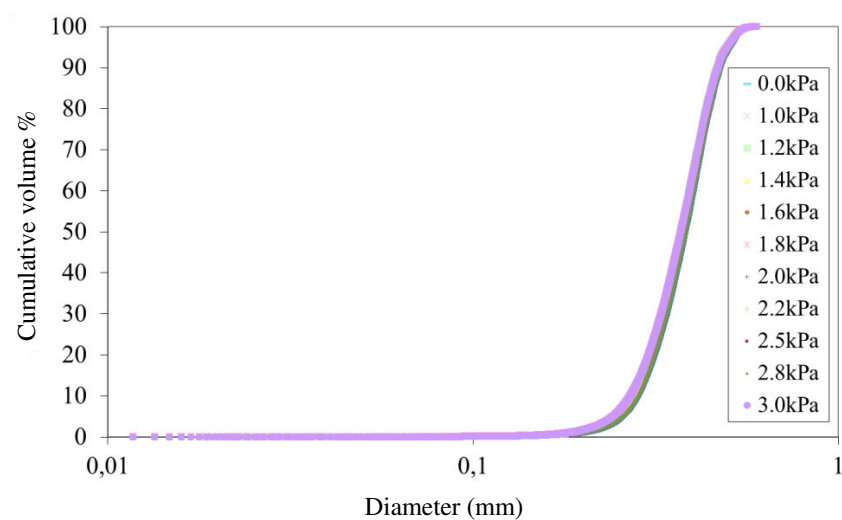


Figure C-4: Grain size distribution for all the values of suction in the wetting path W_1

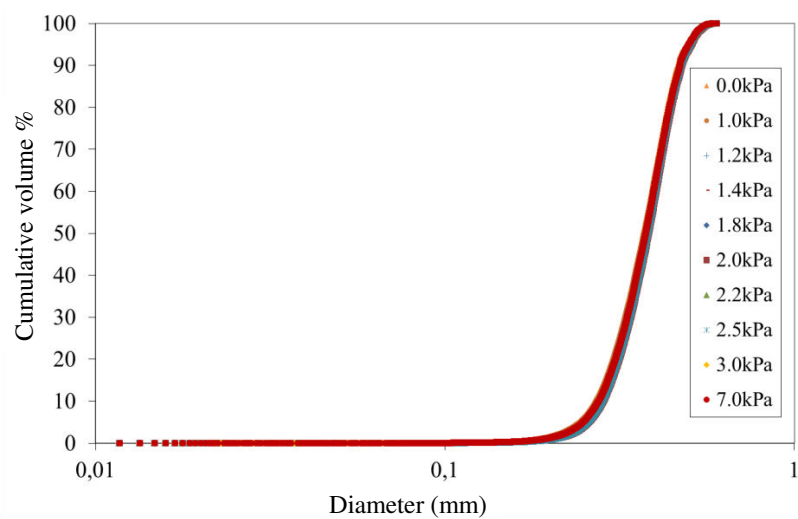


Figure C-5: Grain size distribution for all the values of suction in the drying path D_0

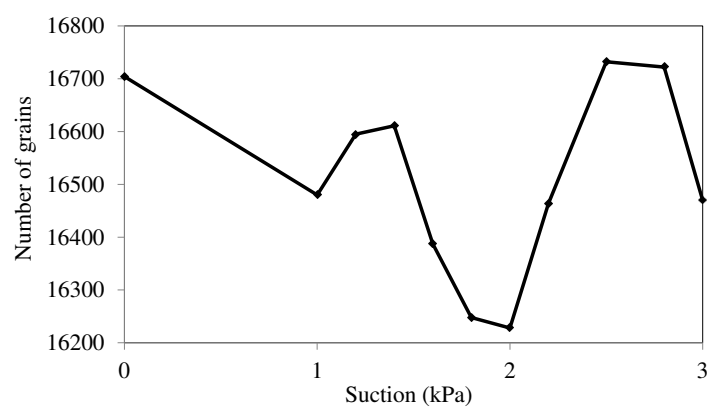


Figure C-6: The number of grains within the specimen shown for all the values of suction in the wetting path W_1

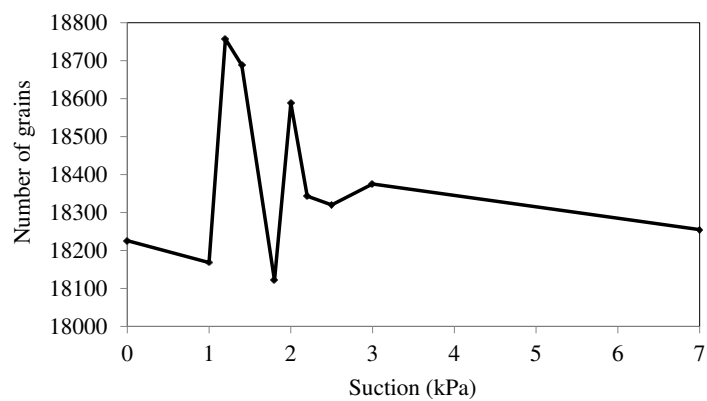


Figure C-7: The number of grains within the specimen shown for all the values of suction in the drying path D_0

Appendix D

Interpretation of the microscopic discrete analyses results

D.1 Results of the relation between state variables (s , n , S_r)

D.1.1 3D relation between state variables (s , n , Sr)

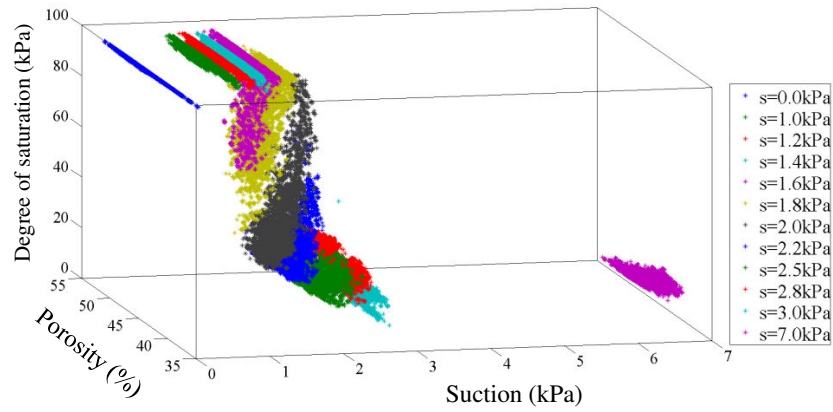


Figure D-1: 3D experimental relation between suction, porosity and degree of saturation for the drying path D_1 . The points considered in this plot are microscopic measurements with overlapping allowed

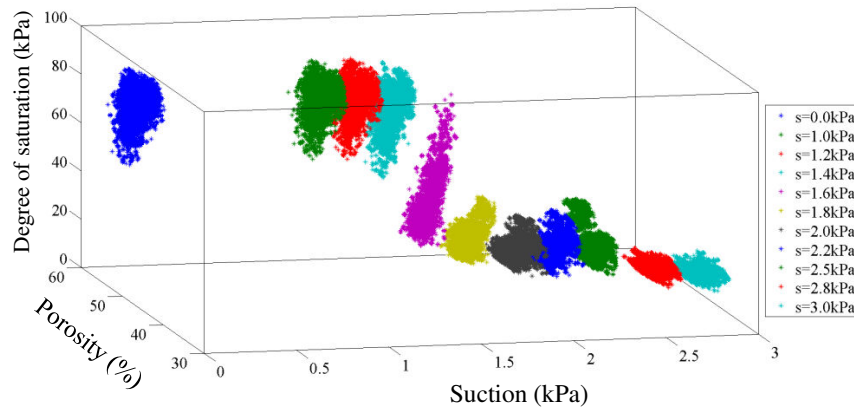


Figure D-2: 3D experimental relation between suction, porosity and degree of saturation for the drying path W_1 . The points considered in this plot are microscopic measurements with overlapping allowed

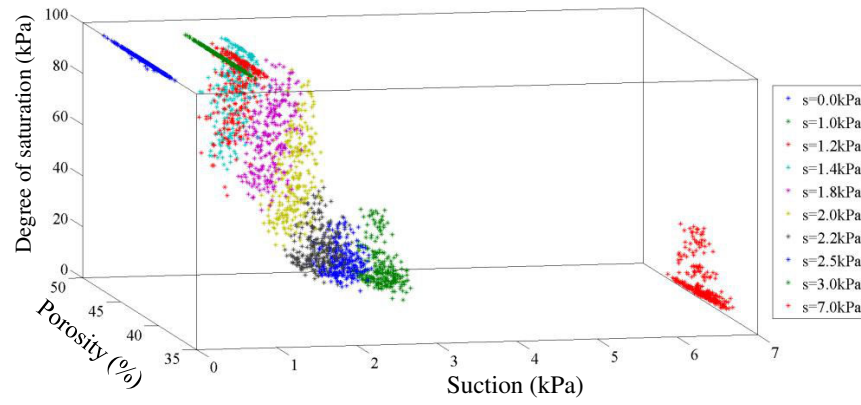


Figure D-3: 3D experimental relation between suction, porosity and degree of saturation for the drying path D_0 . The points considered in this plot are microscopic measurements with no overlapping

D.1.2 The relation between suction and porosity $n=f(s)$

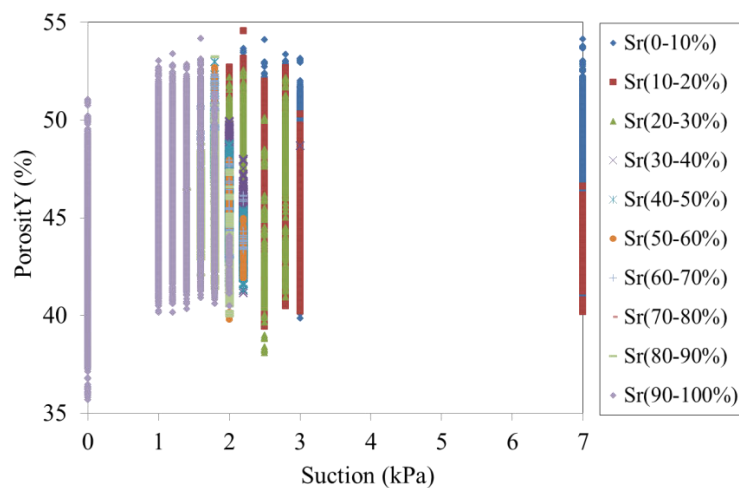


Figure D-4: The experimental relation between suction and porosity for all the ranges of degree of saturation in the drying path D_1

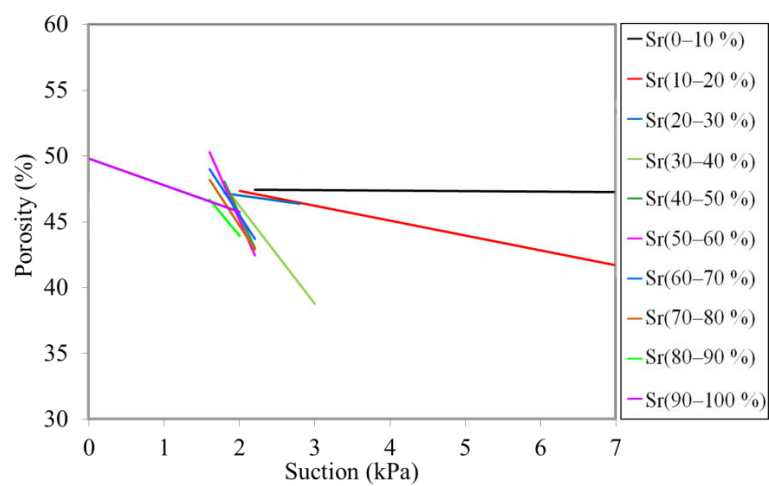


Figure D-5: The tendency of the relation between suction and porosity for all the ranges of degree of saturation in the drying path D_1

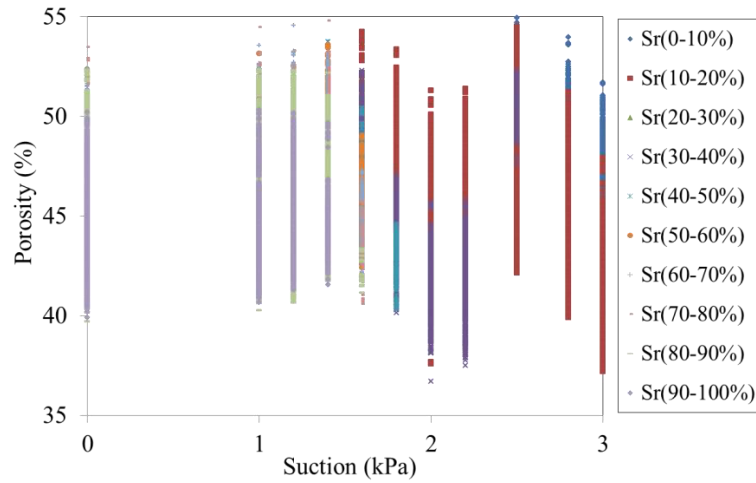


Figure D-6: The experimental relation between suction and porosity for all the ranges of degree of saturation in the wetting path W_1

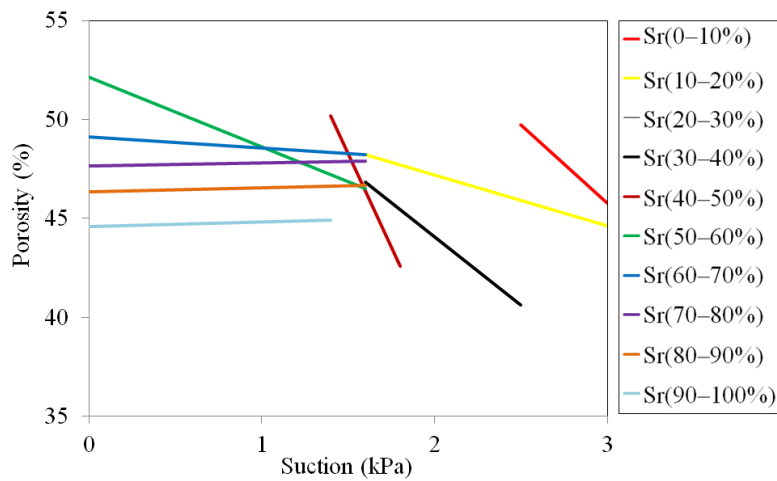


Figure D-7: The tendency of the relation between suction and porosity for all the ranges of degree of saturation in the wetting path W_1

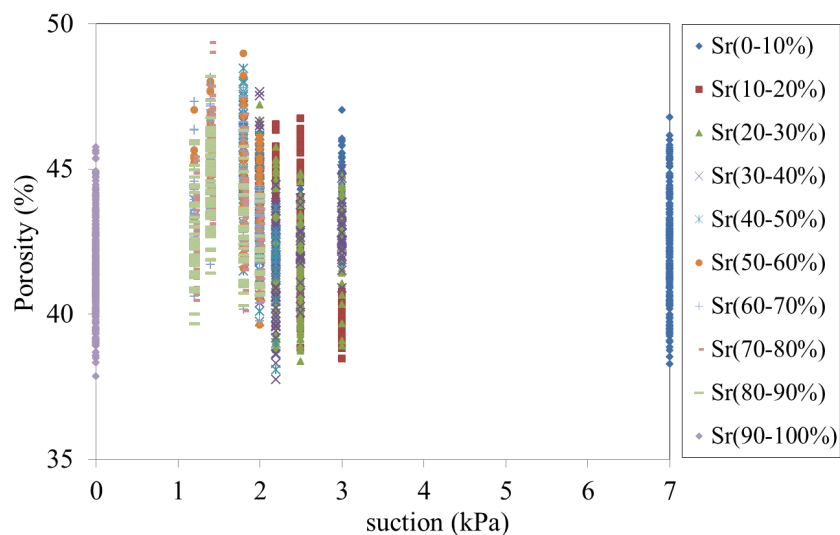


Figure D-8: The experimental relation between suction and porosity for all the ranges of degree of saturation in the drying path D_0

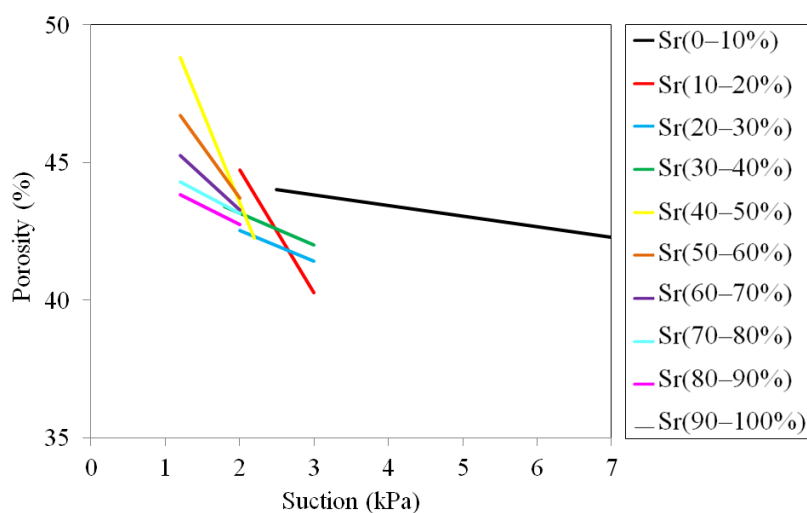


Figure D-9: The tendency of the relation between suction and porosity for all the ranges of degree of saturation in the drying path D_0

D.1.3 The relation between suction and degree of saturation $S_r=f(s)$

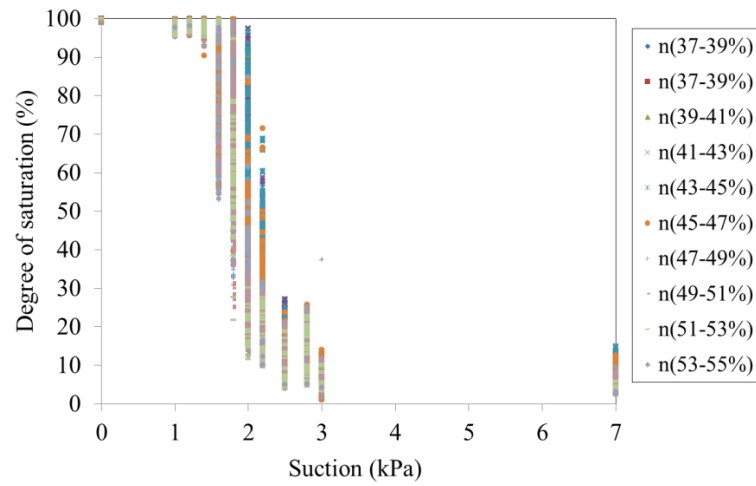


Figure D-10: The experimental relation between suction and degree of saturation for all the ranges of porosity in the drying path D_1

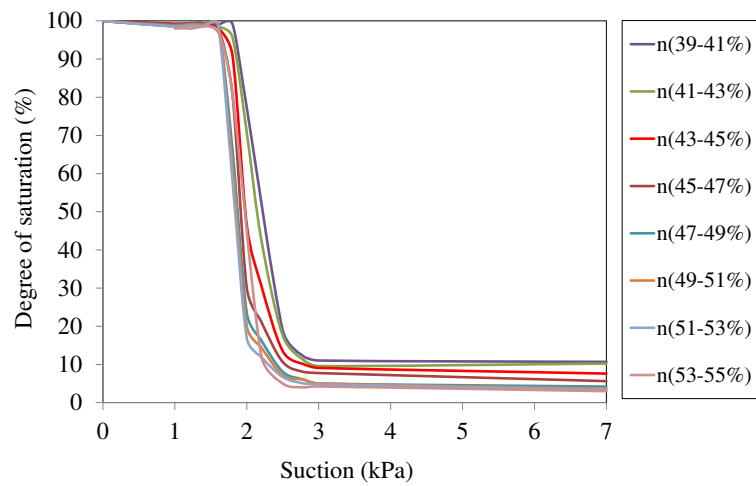


Figure D-11: Fitting curves of the experimental points in the relation between suction and degree of saturation for all the ranges of porosity in the drying path D_1

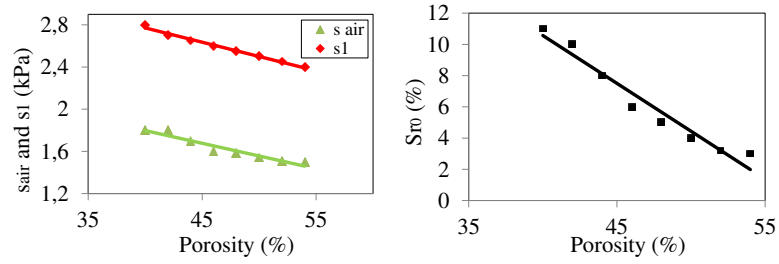


Figure D-12: The relation between average porosity of all the ranges of porosity and the three variables, s_{air} and s_l (left) and S_{r0} (right) for the drying path D_1

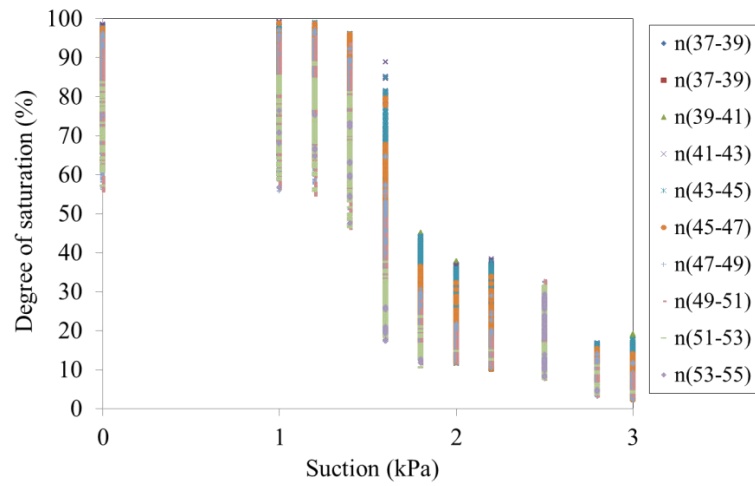


Figure D-13: The experimental relation between suction and degree of saturation for all the ranges of porosity in the drying path W_1

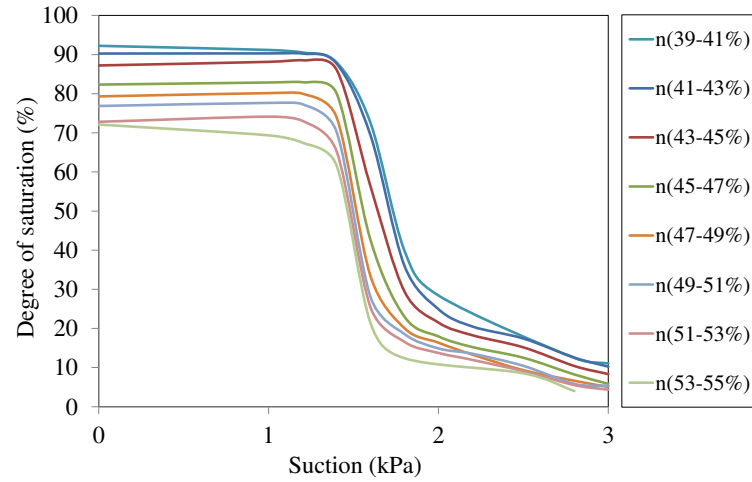


Figure D-14: Fitting curves of the experimental points in the relation between suction and degree of saturation for all the ranges of porosity in the wetting path W_1

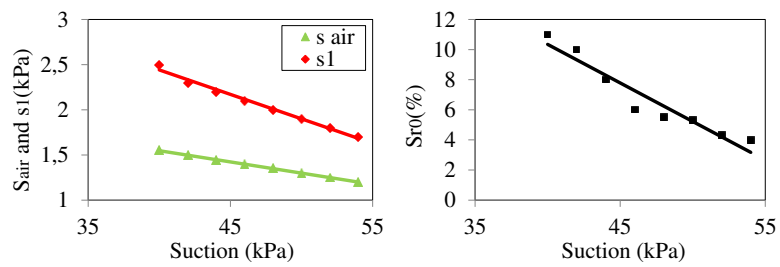


Figure D-15: The relation between average porosity of all the ranges of porosity and the three variables, s_{air} and s_1 (left) and Sr_0 (right) for the wetting path W_1

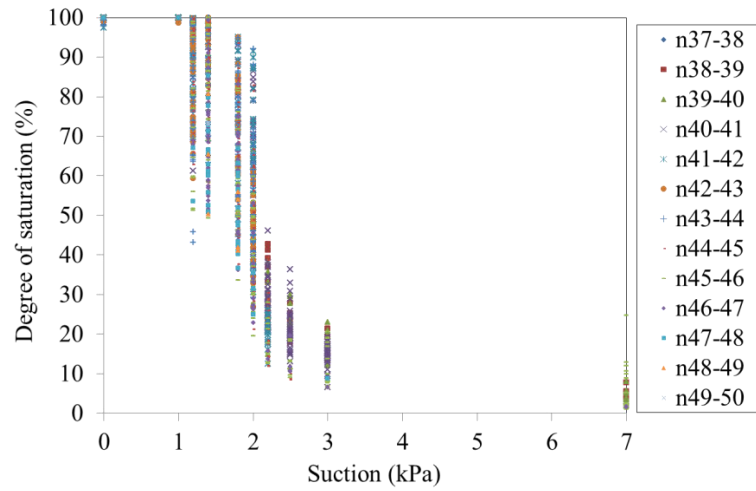


Figure D-16: The experimental relation between suction and degree of saturation for all the ranges of porosity in the drying path D_0

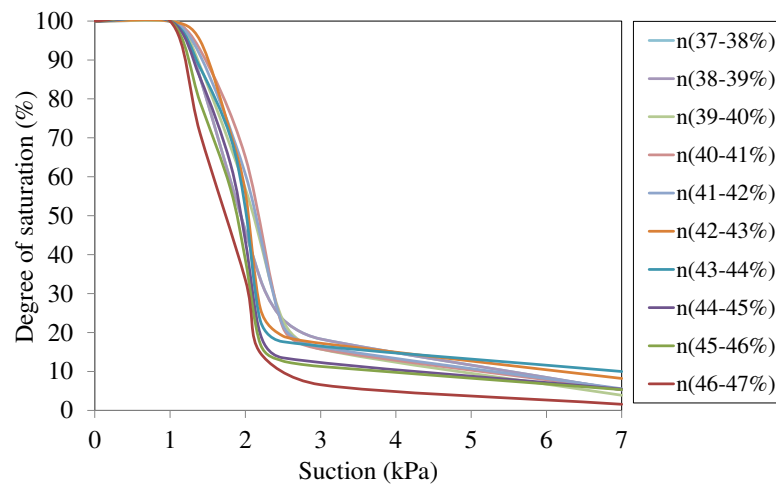


Figure D-17: Fitting curves of the experimental points in the relation between suction and degree of saturation for all the ranges of porosity in the drying path D_0

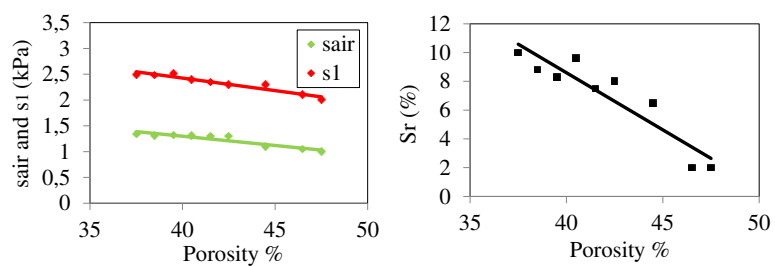


Figure D-18: The relation between average porosity of all the ranges of porosity and the three variables, s_{air} and s_1 (left) and S_r (right) for the drying path D_0

D.1.4 The relation between porosity and degree of saturation $S_r=f(n)$

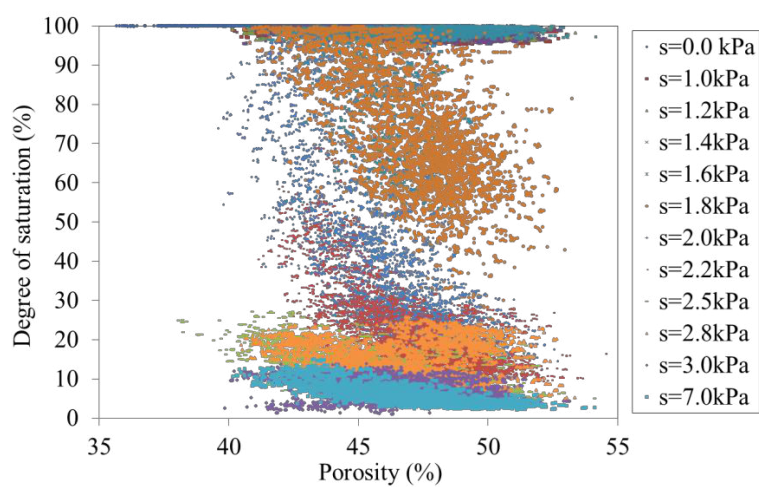


Figure D-19: The experimental relation between the porosity and the degree of saturation for all the values of suction in the drying path D_1

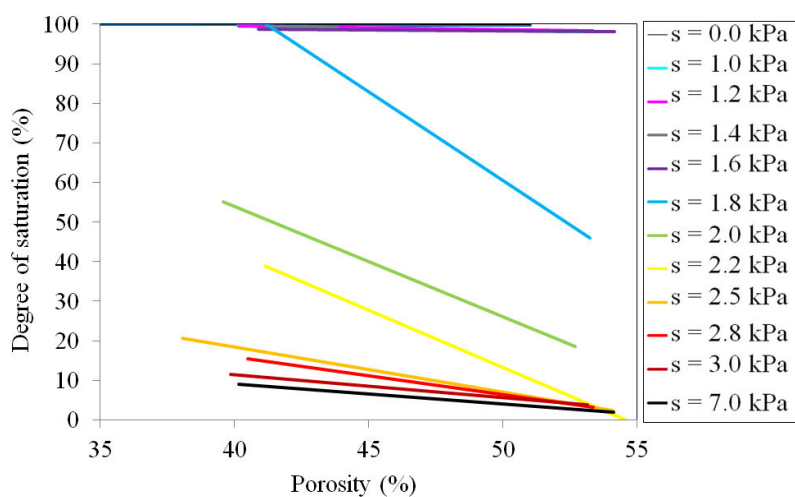


Figure D-20: The tendency of the relation between porosity and degree of saturation for all the values of suction in the drying path D_1

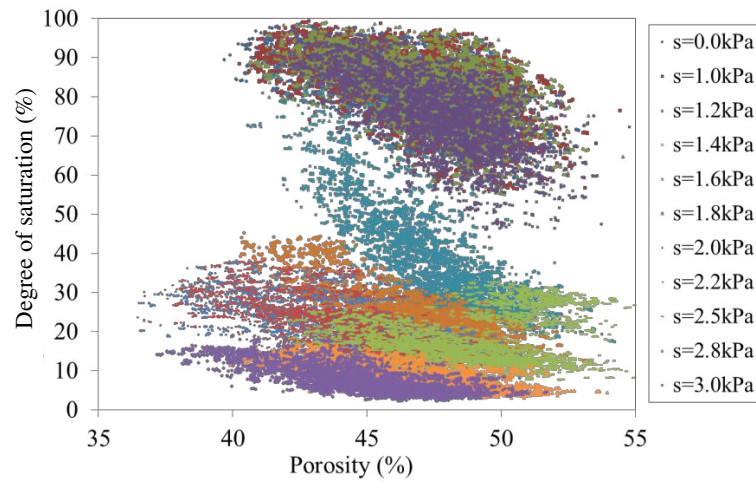


Figure D-21: The experimental relation between the porosity and the degree of saturation for all the values of suction in the wetting path W_1

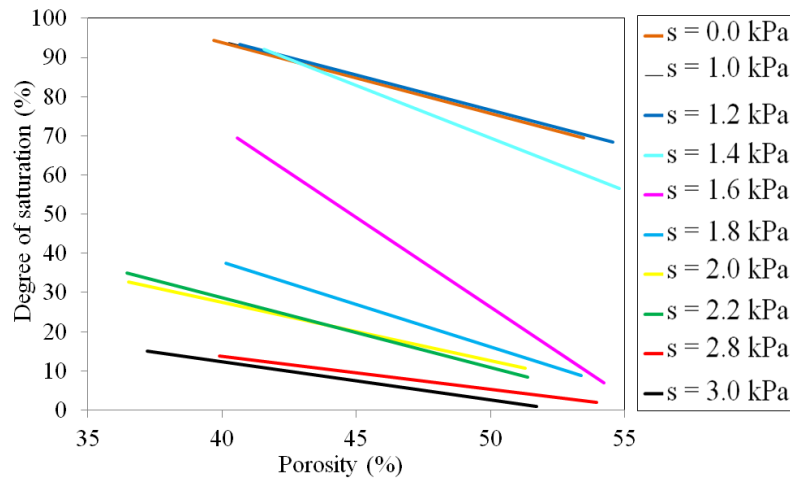


Figure D-22: The tendency of the relation between porosity and degree of saturation for all the values of suction in the wetting path W_1

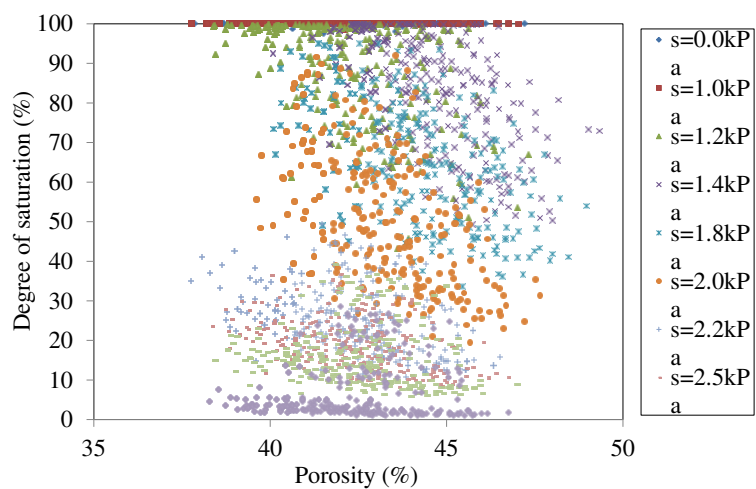


Figure D-23: The experimental relation between the porosity and the degree of saturation for all the values of suction in the drying path D_0

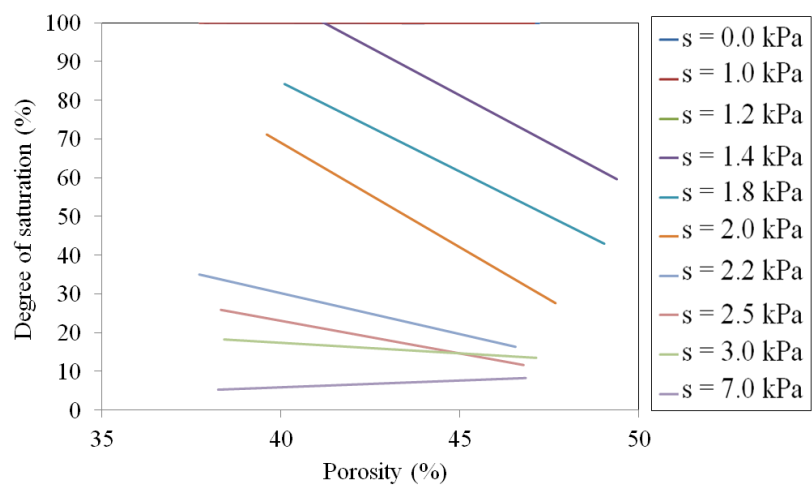
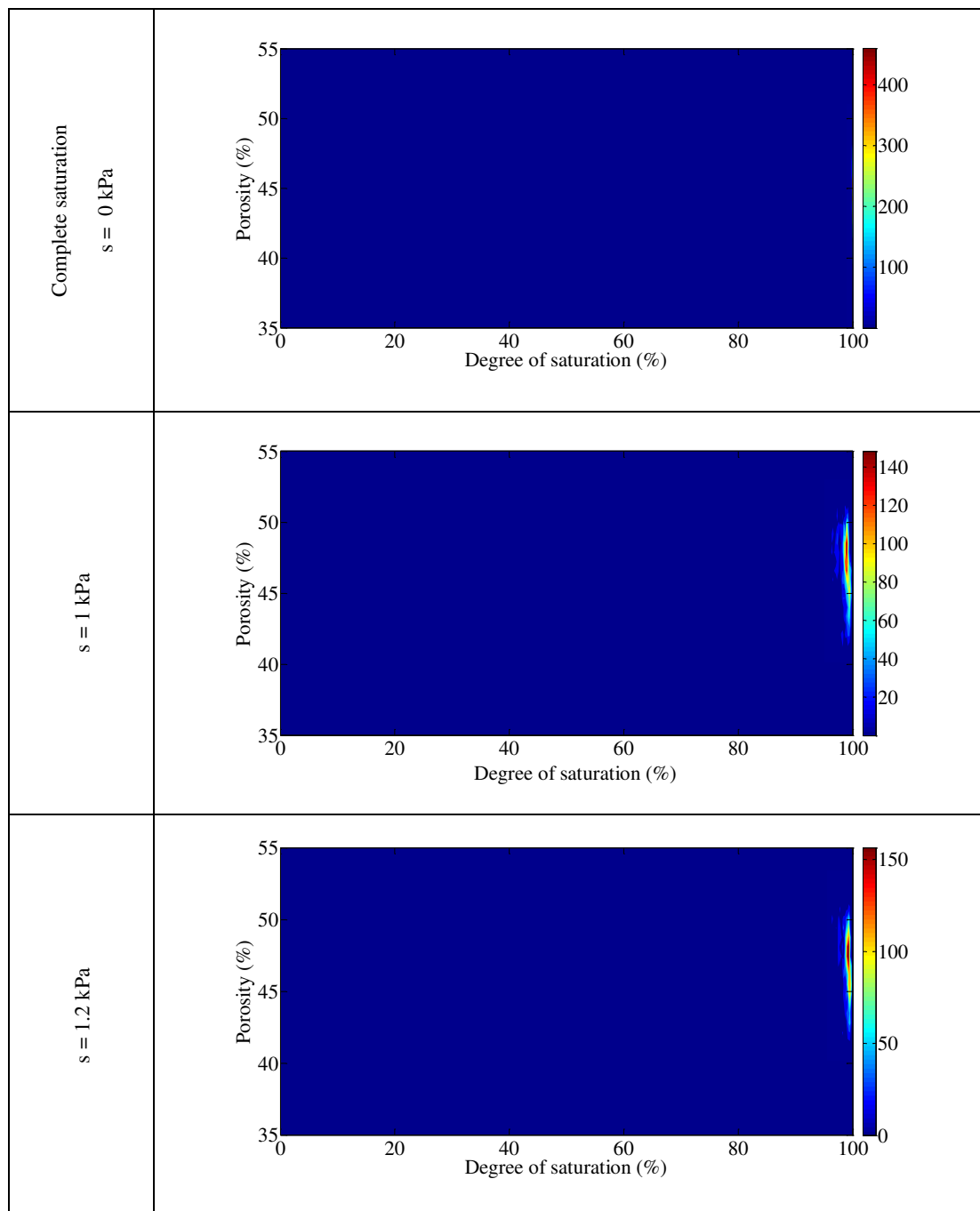
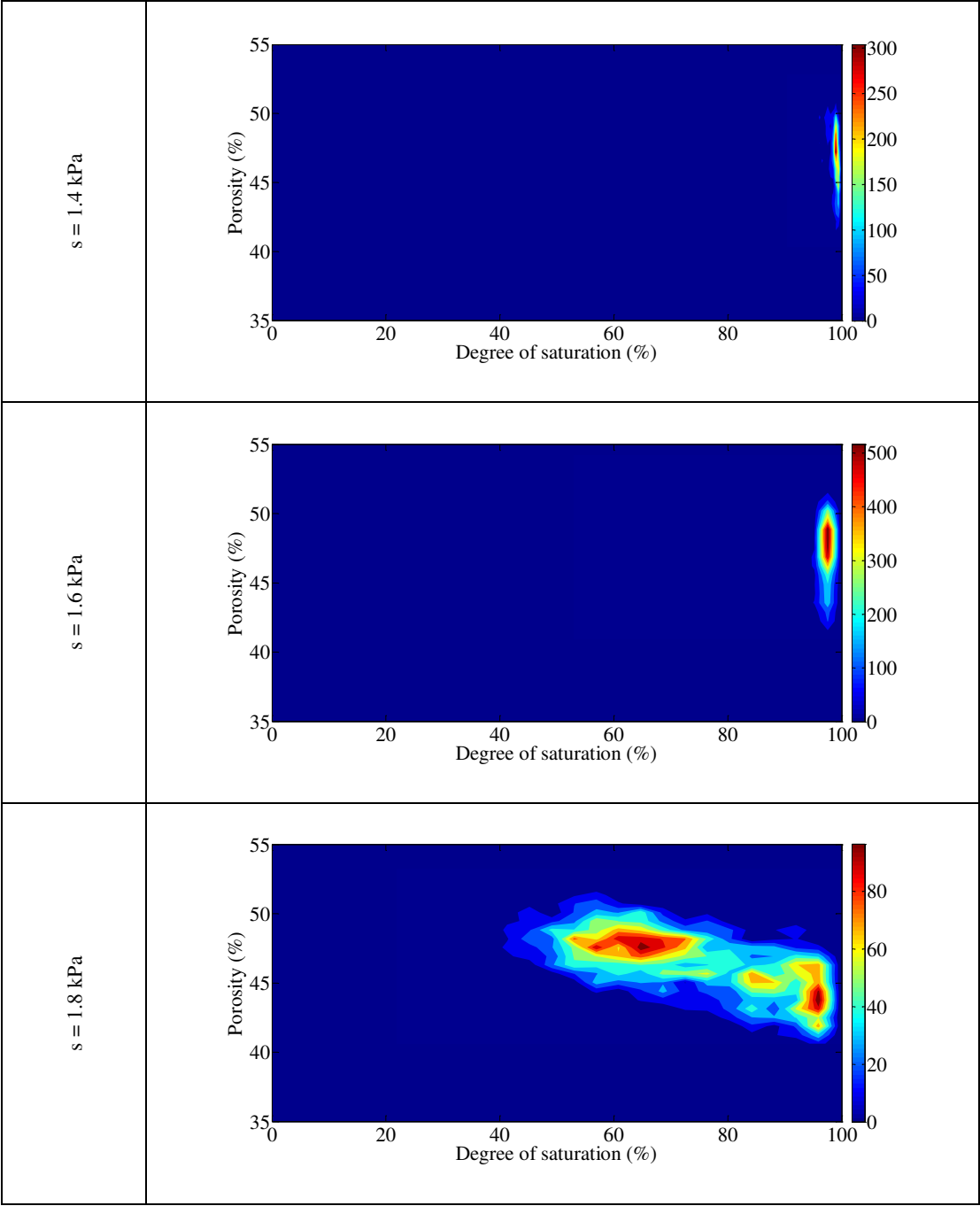


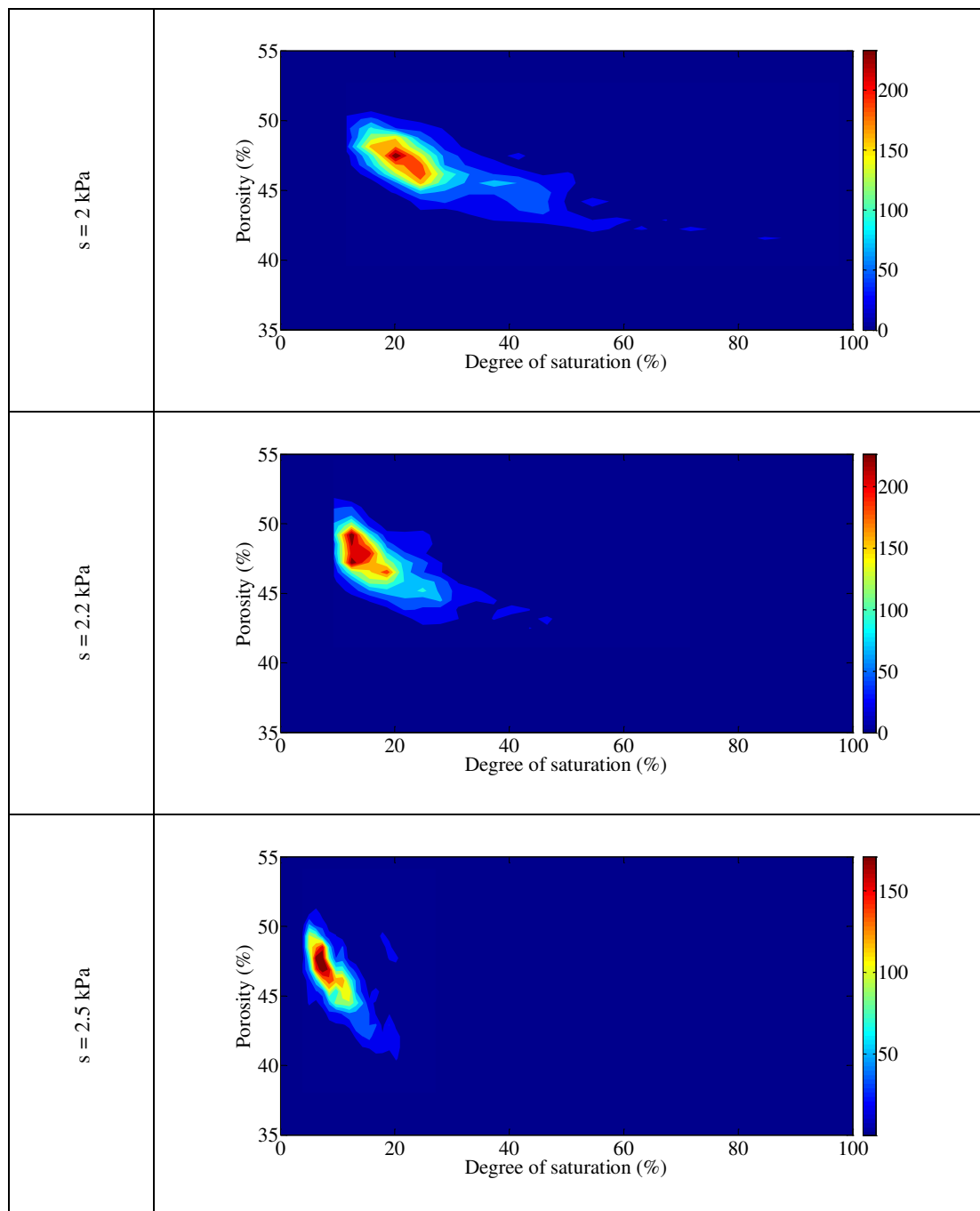
Figure D-24: The tendency of the relation between porosity and degree of saturation for all the values of suction in the drying path D_0

D.1.5 Frequency map results

D.1.5.1 Drying path D_1







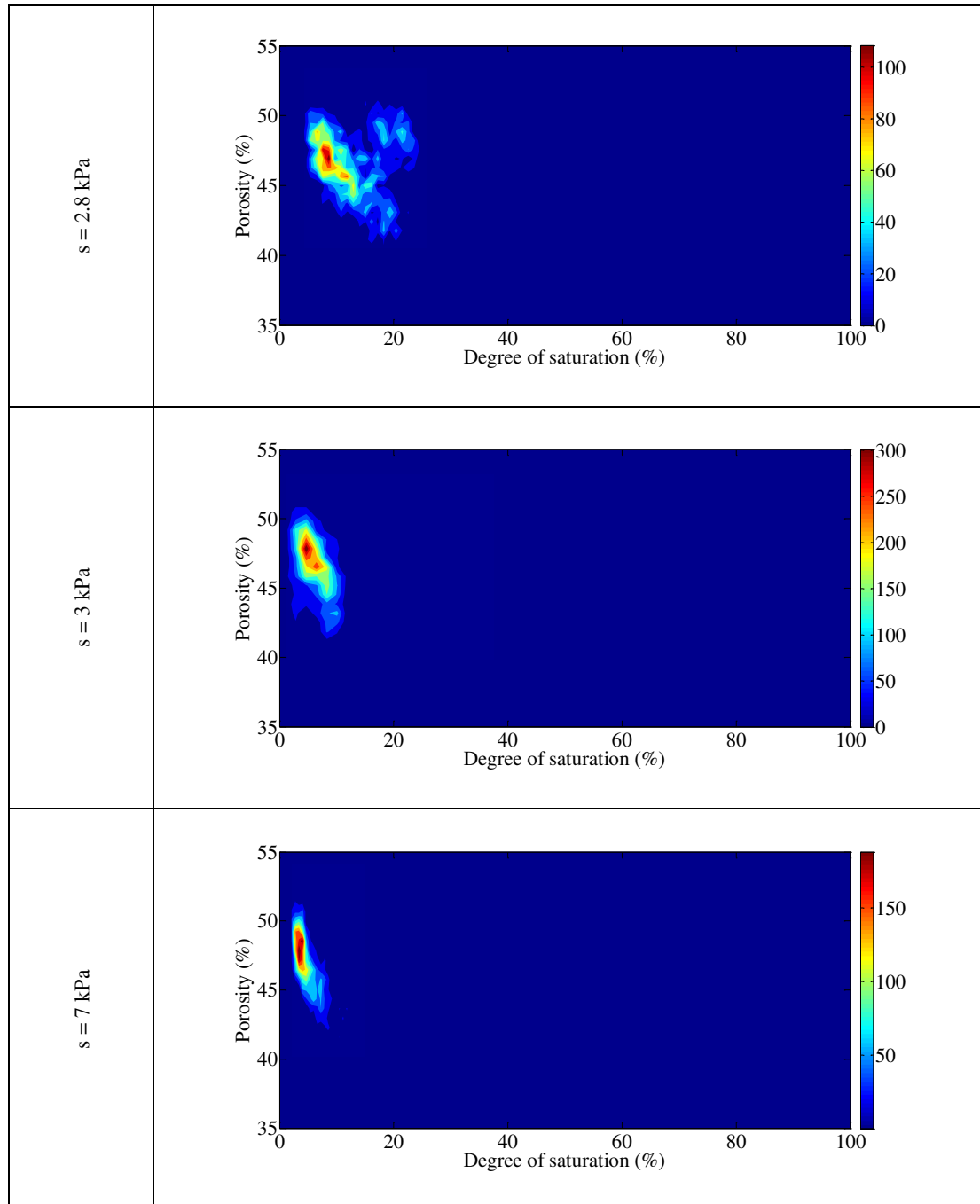
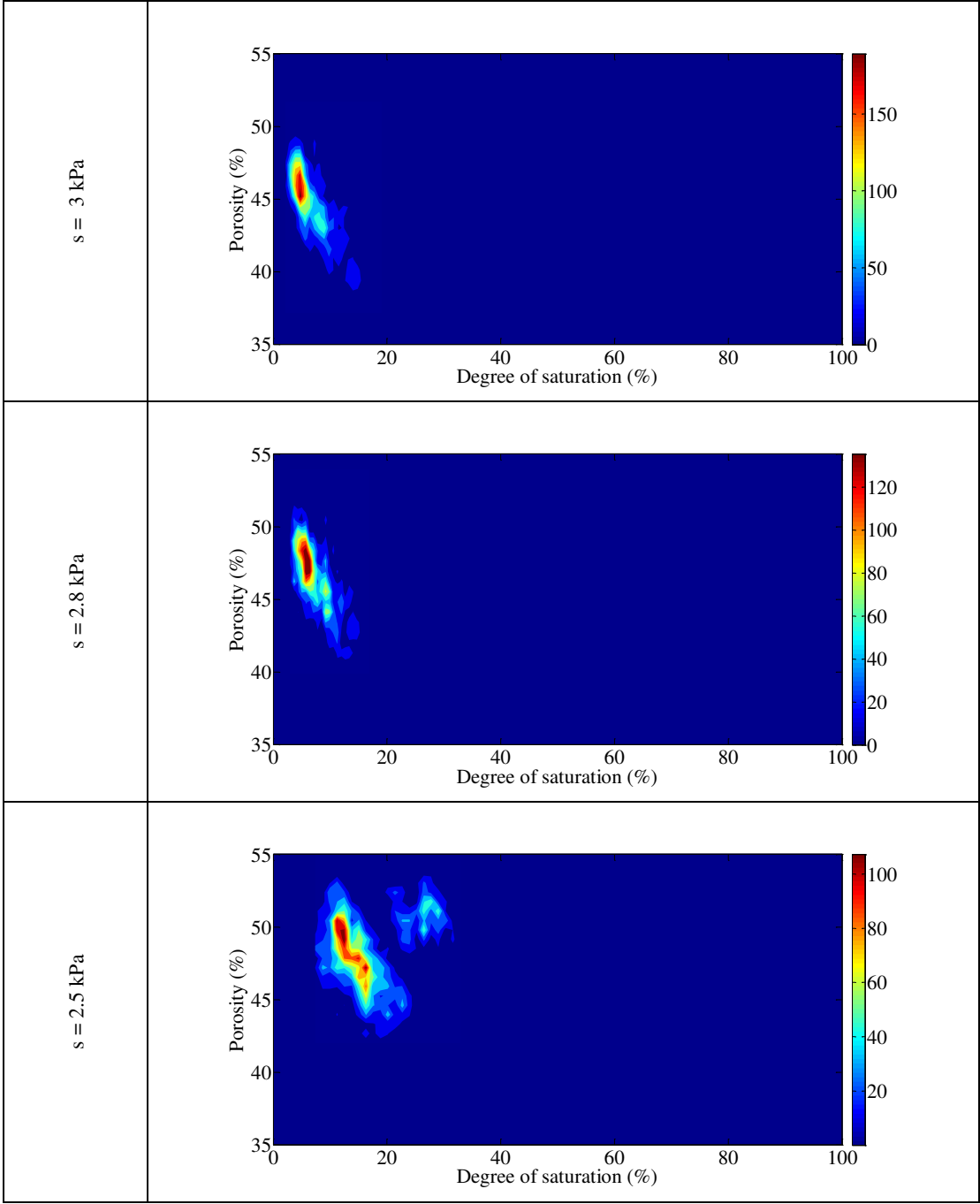
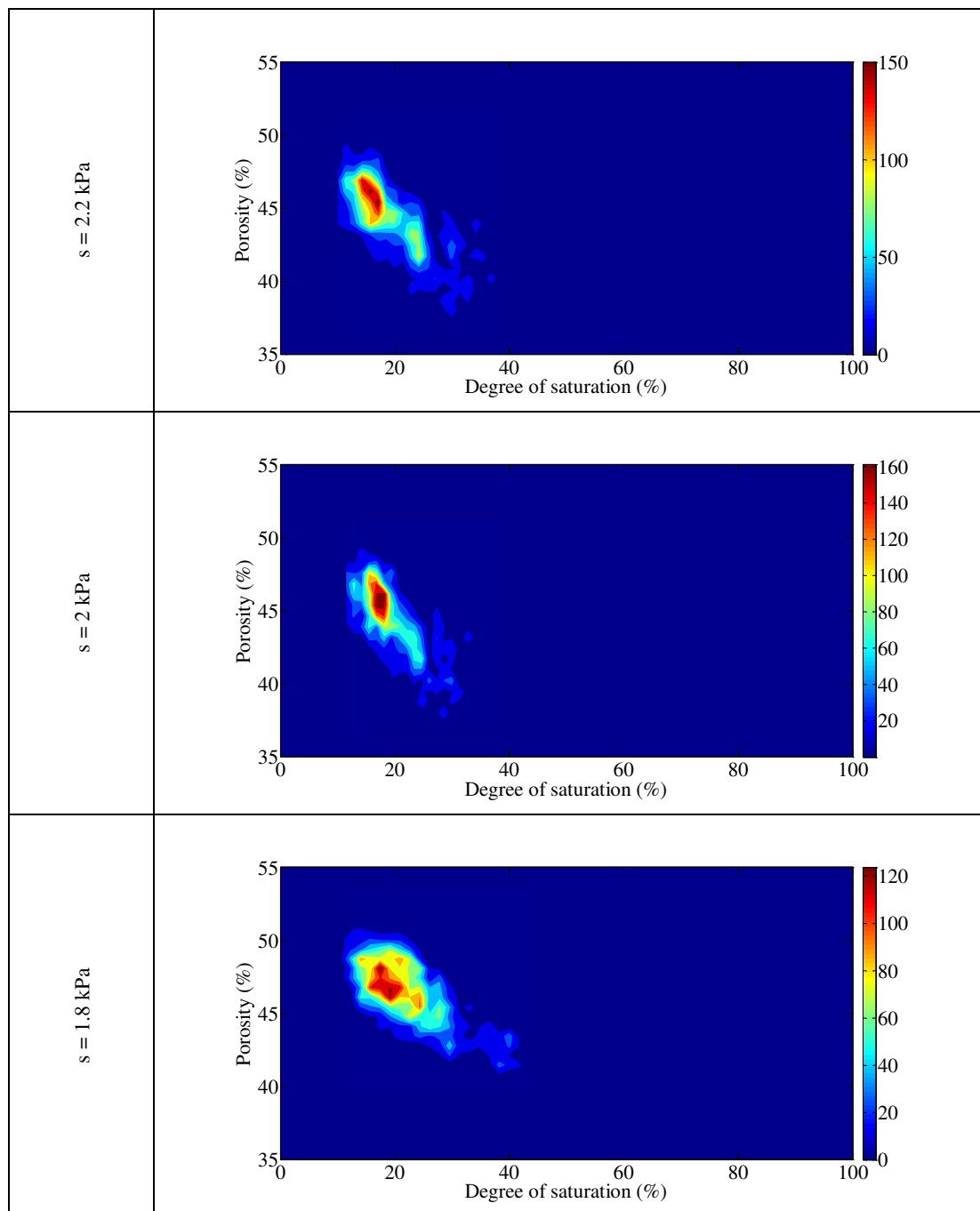
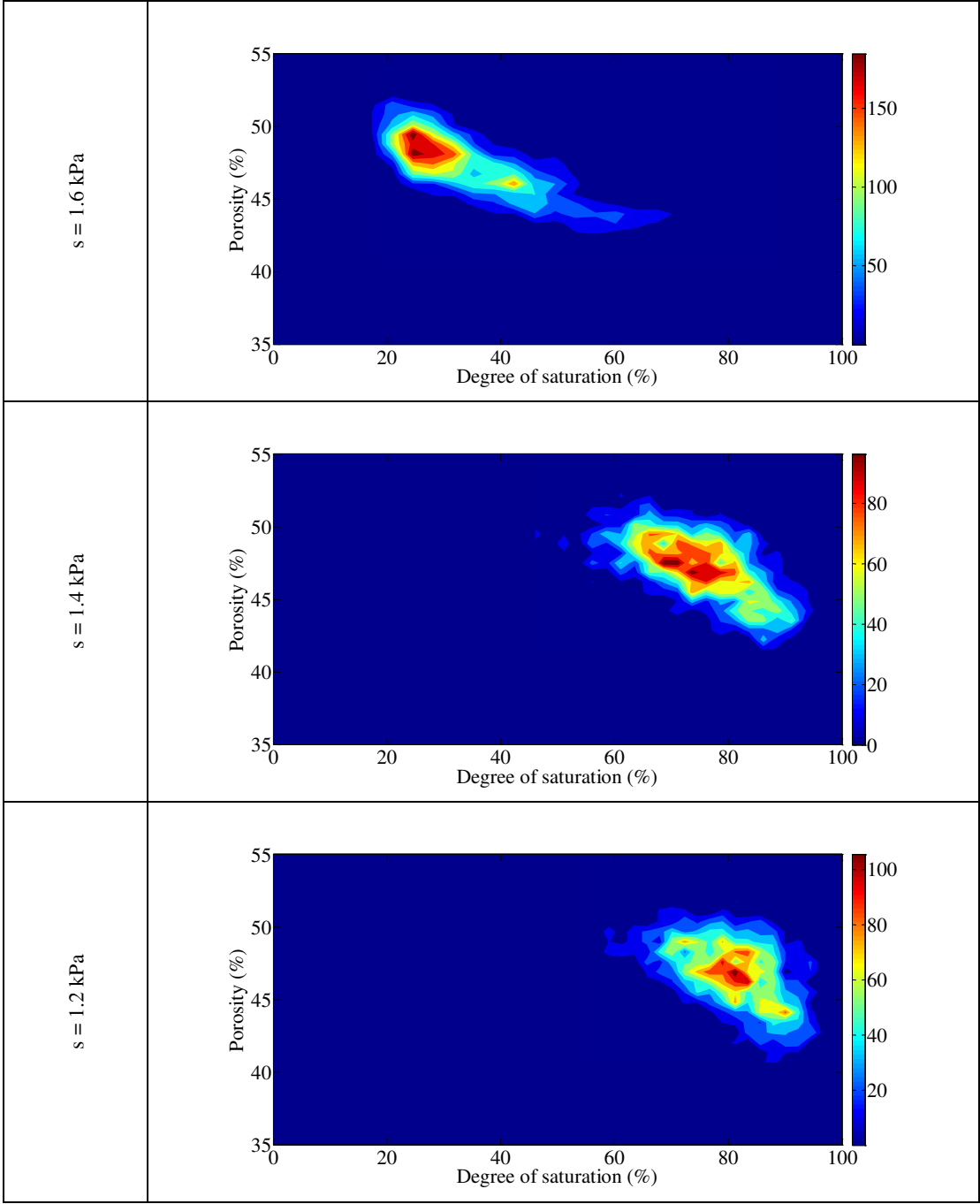


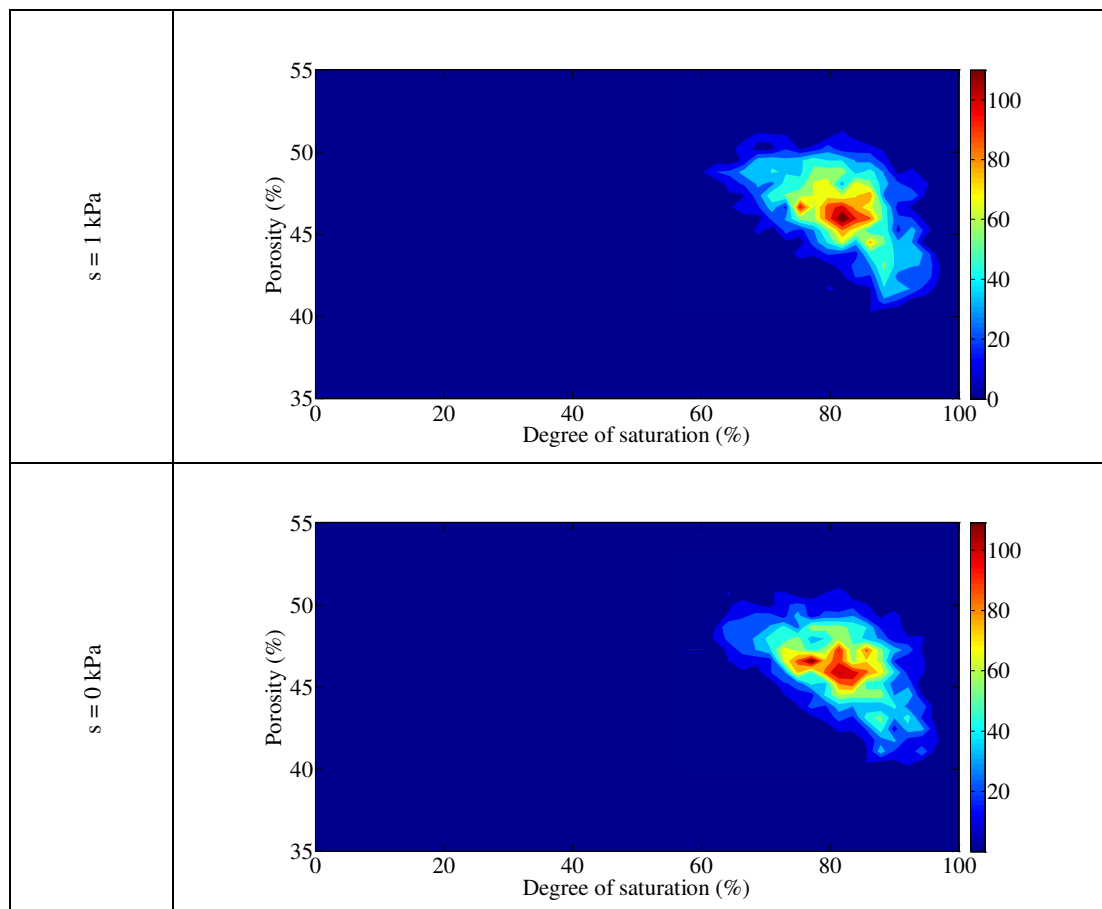
Figure D-25: Frequency map for all the points in the drying path D_1

D.1.5.2 Wetting path W_1

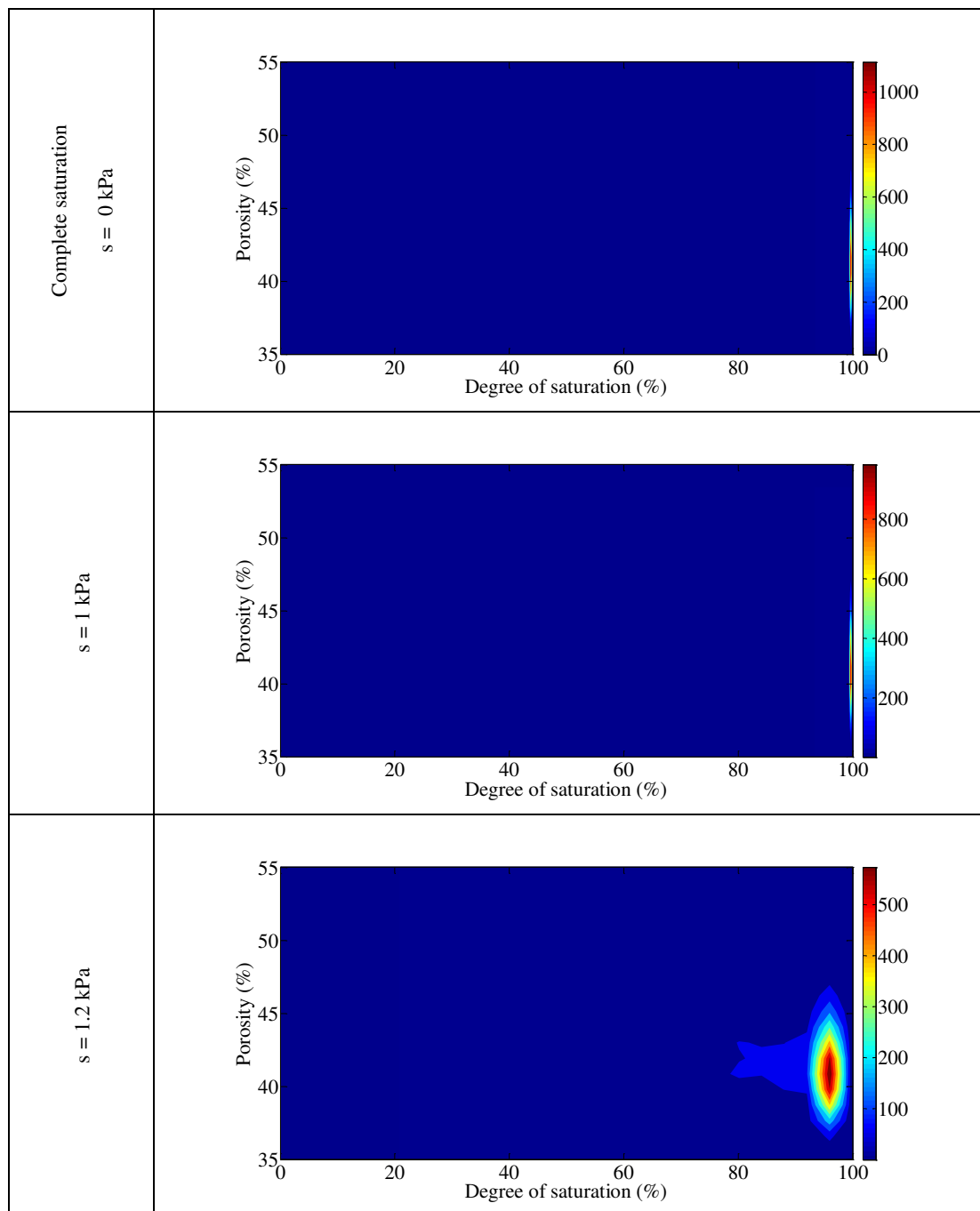


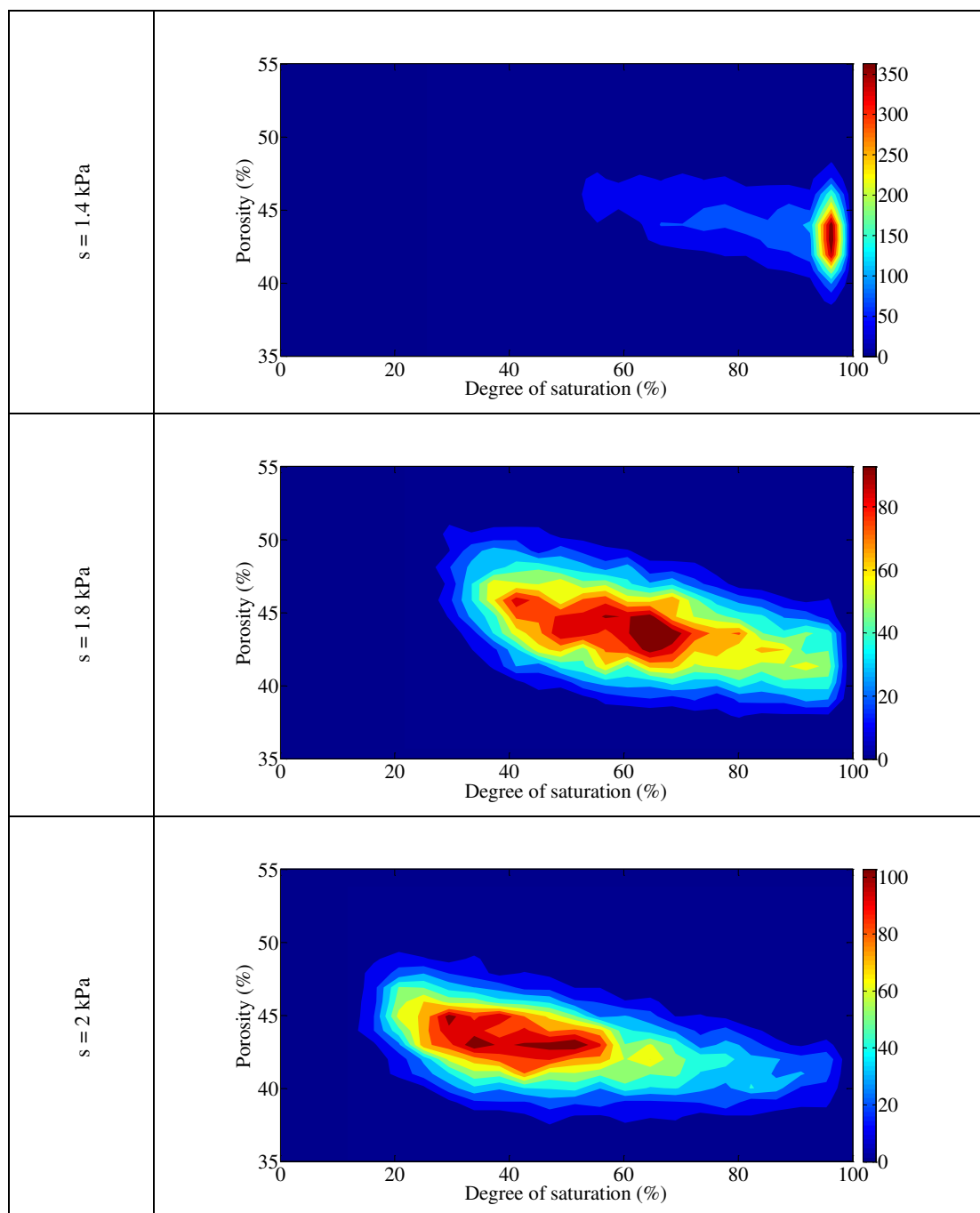


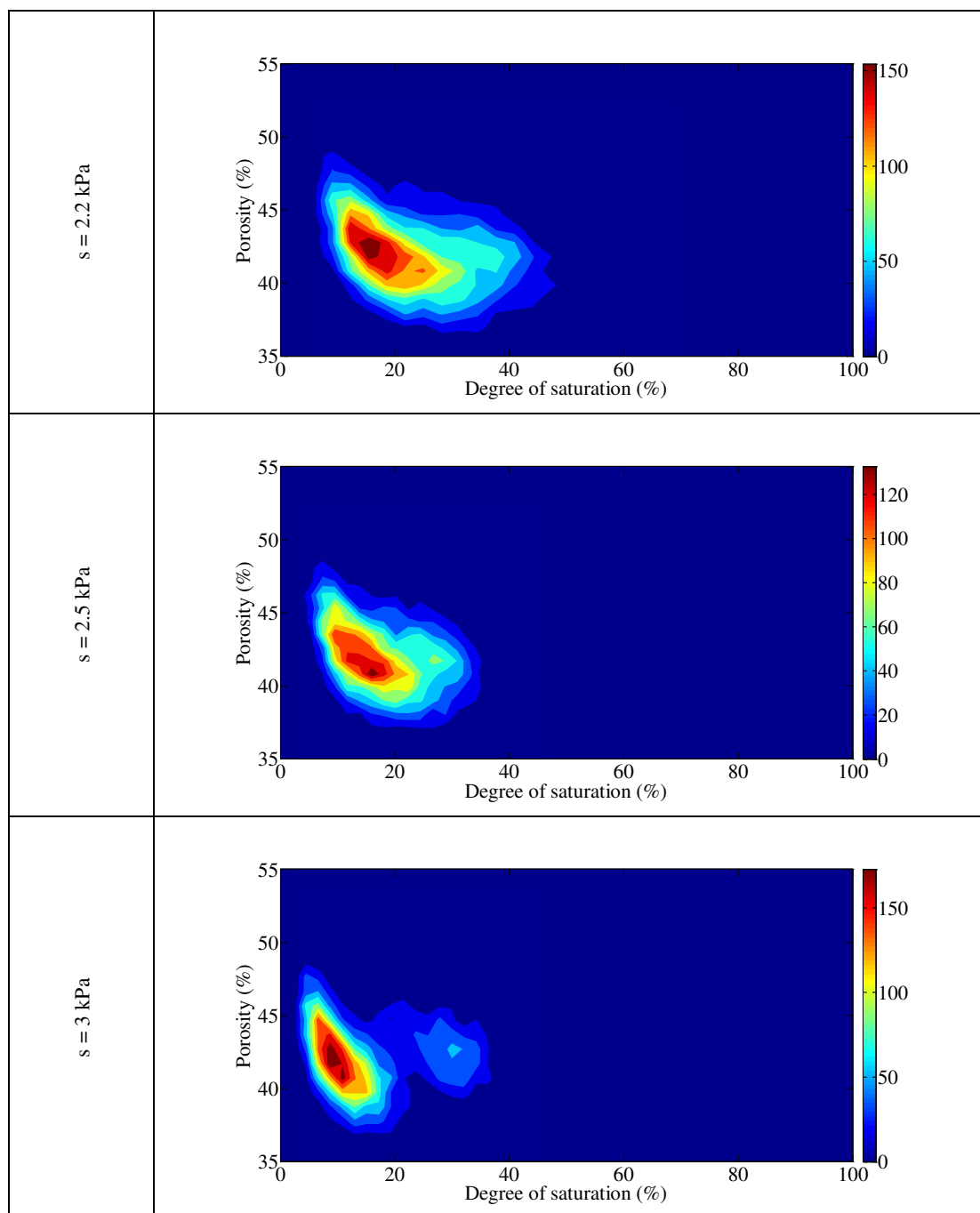


Figure D-26: Frequency map for all the points in the wetting path W_1

D.1.5.3 Drying path D_0







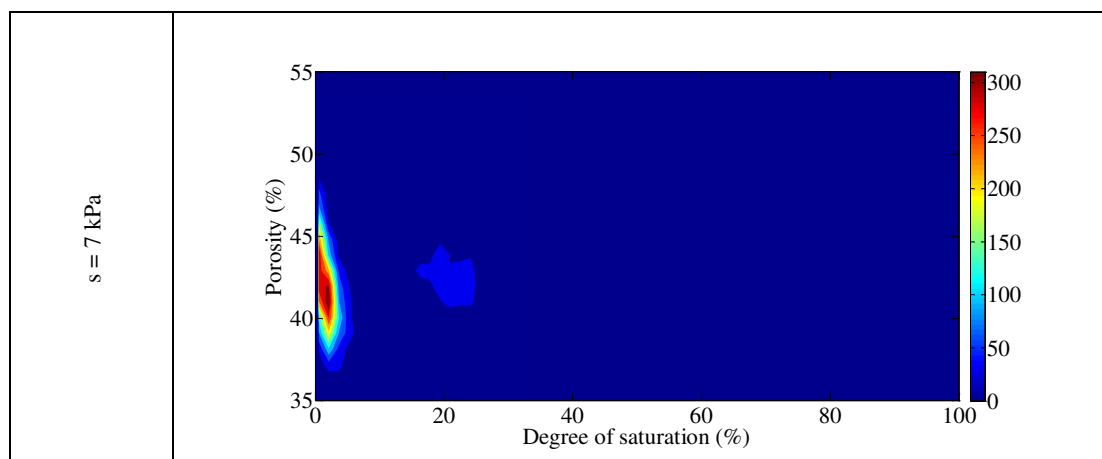


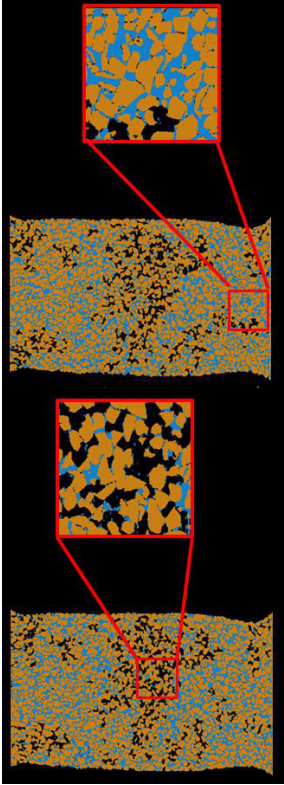
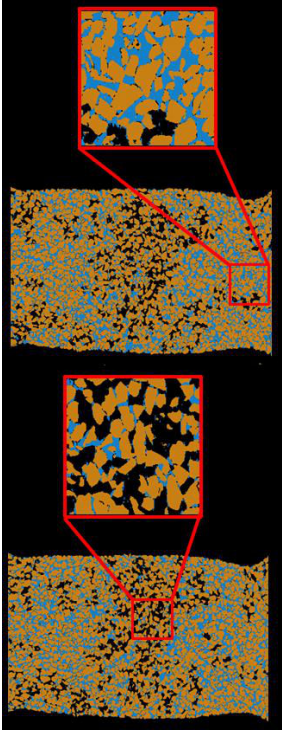
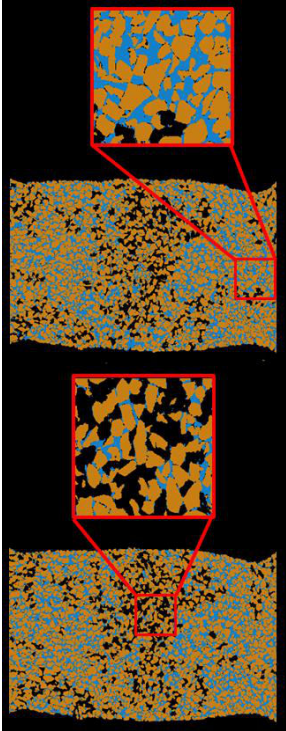
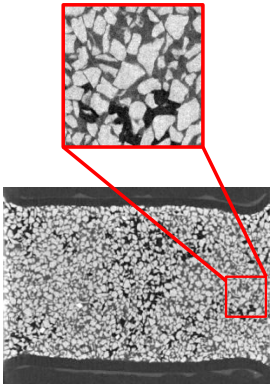
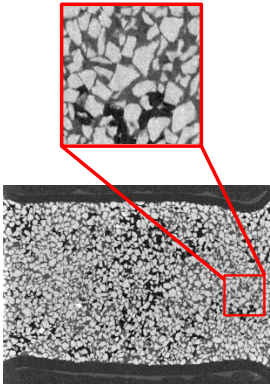
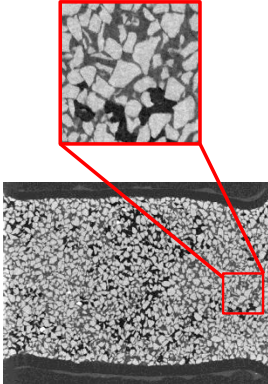
Figure D-27: Frequency map for all the points in the drying path D_0

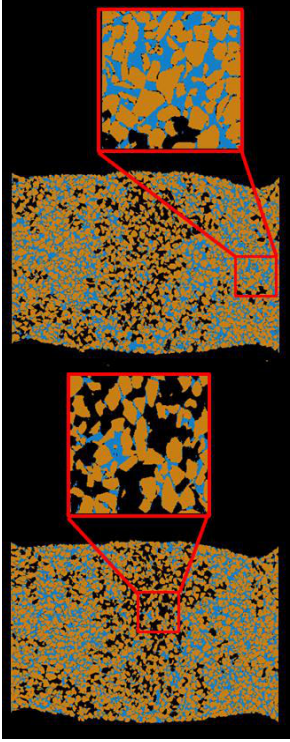
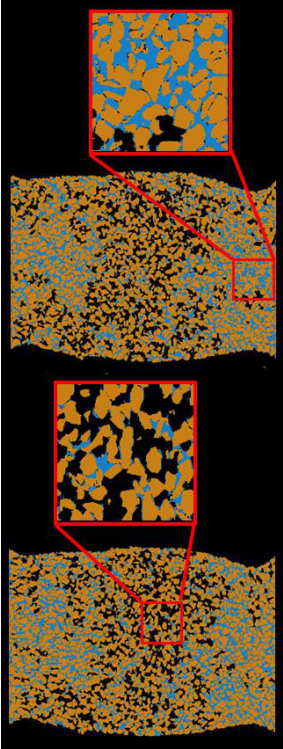
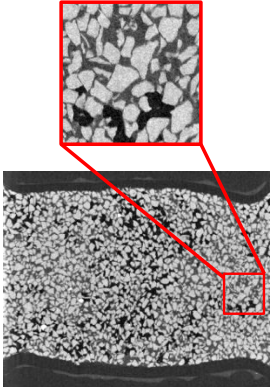
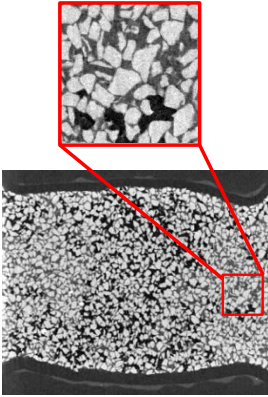
Appendix E

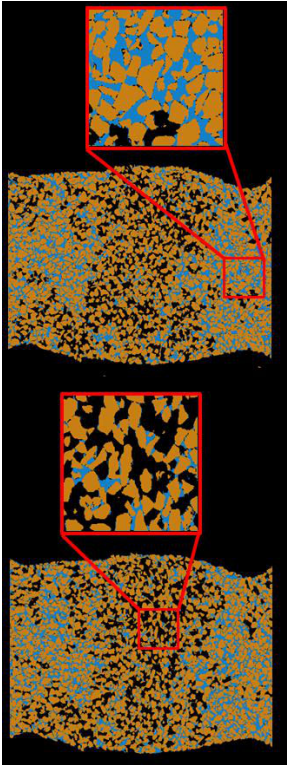
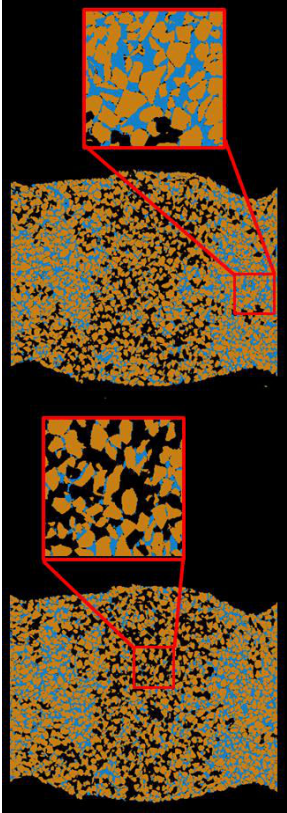
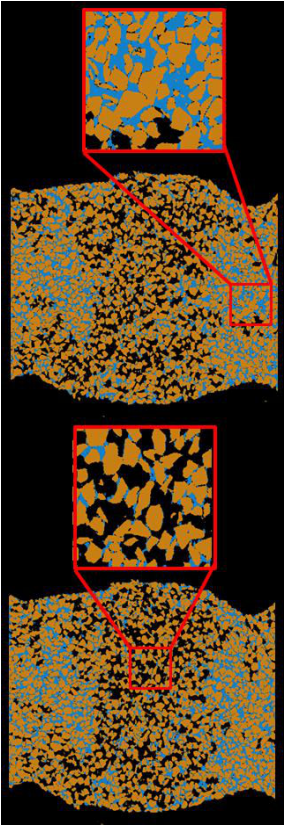
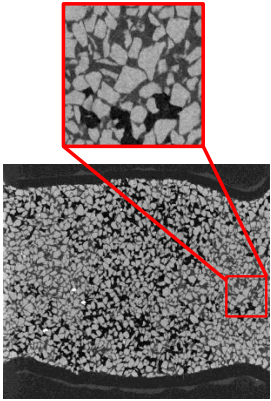
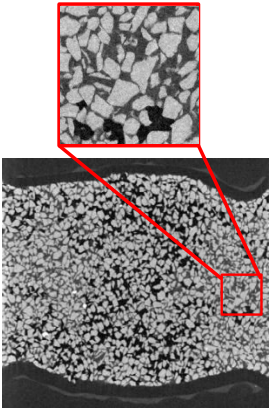
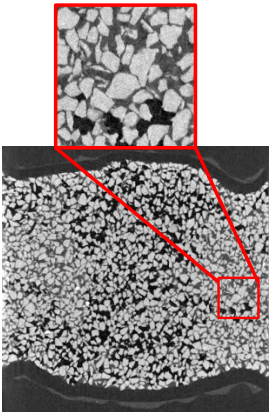
Triaxial test results

E.1 Trinarization results

Loading step ε %	<div>Complete saturation $s = 0$ kPa $\varepsilon = 0$ %</div>	<div>a)</div>	<div>b)</div>
$s = 2.2$ kPa $\varepsilon = 0$ %			
$\varepsilon = 1.5$ %			

		
		
$\varepsilon = 3 \%$	$\varepsilon = 4.5 \%$	$\varepsilon = 6 \%$

	
	
<p>% 8 = 3</p>	<p>% 01 = 3</p>

		
		
$\varepsilon = 12\%$	$\varepsilon = 15\%$	$\varepsilon = 18\%$

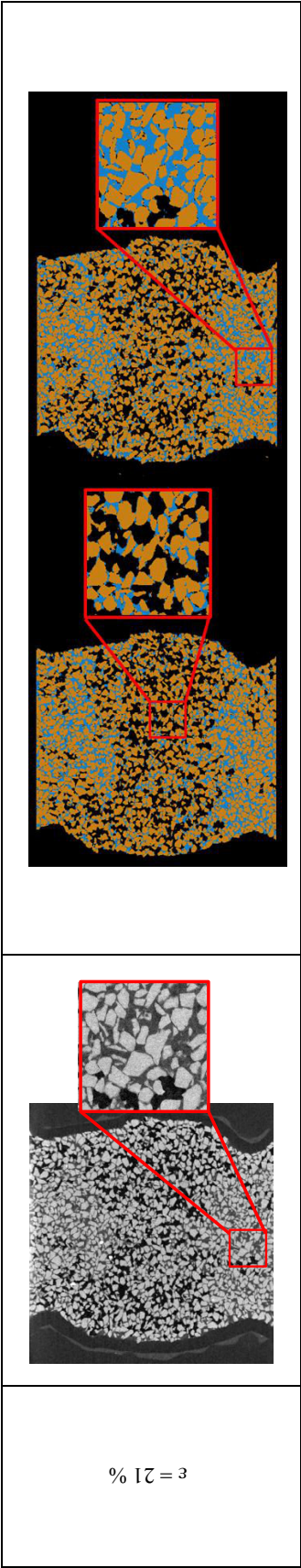
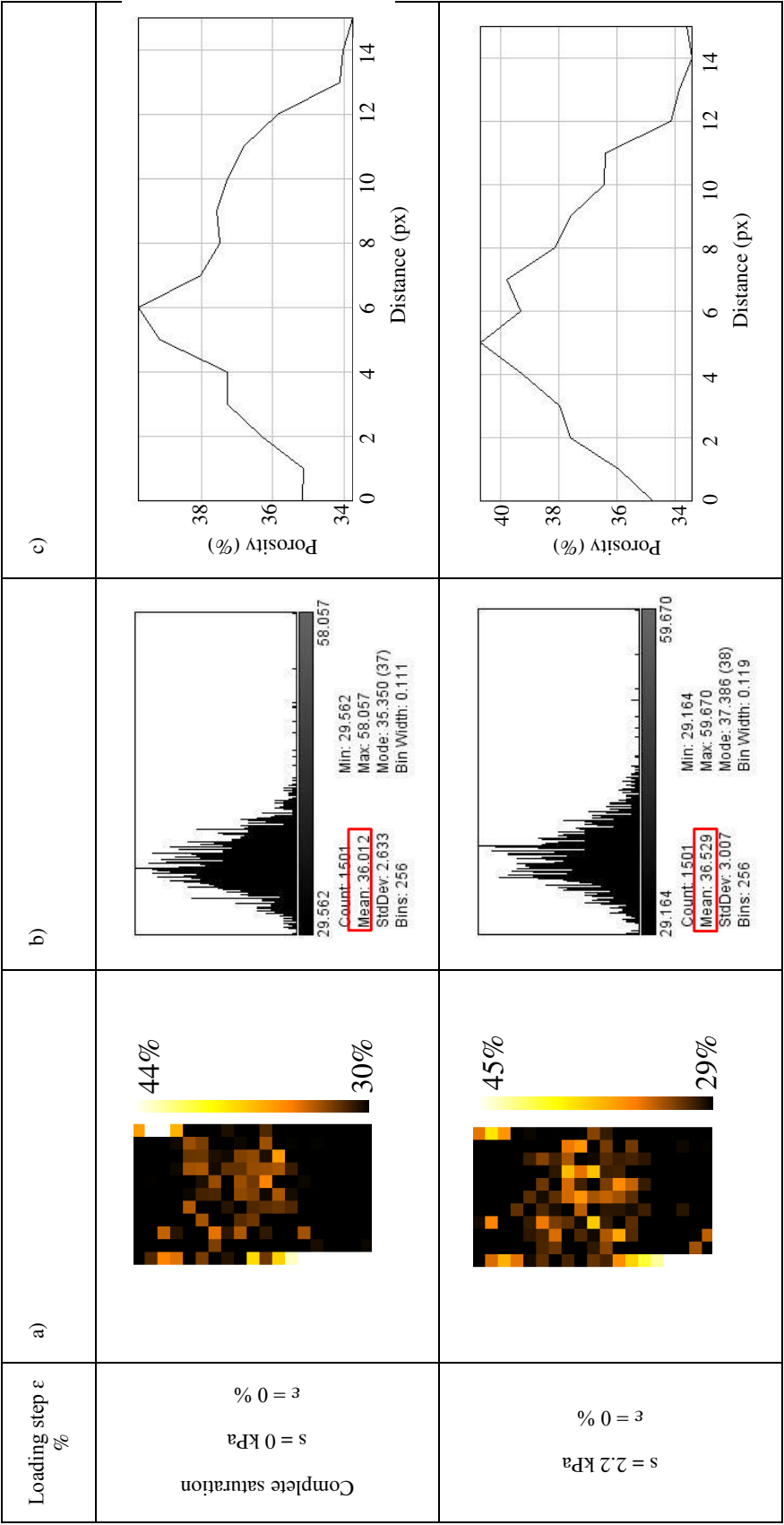
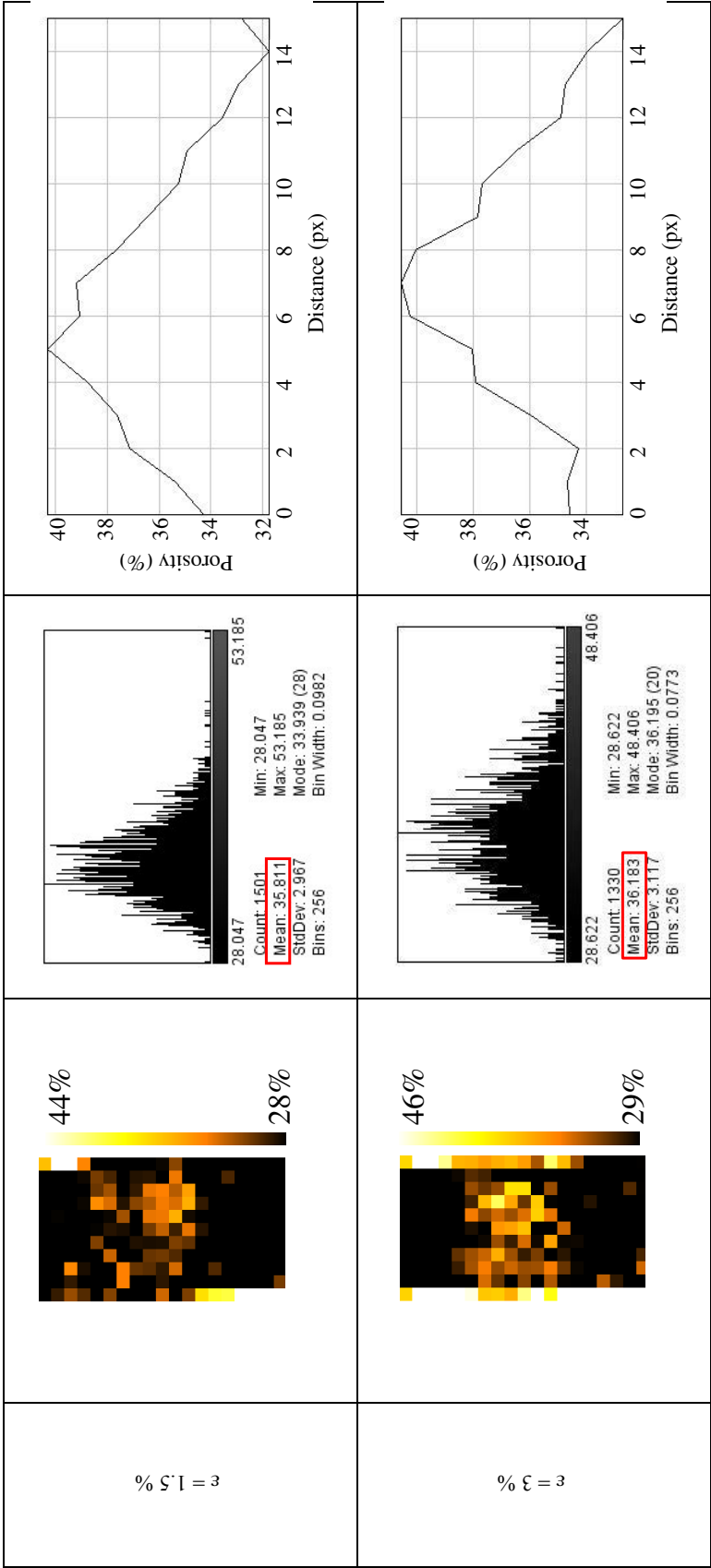
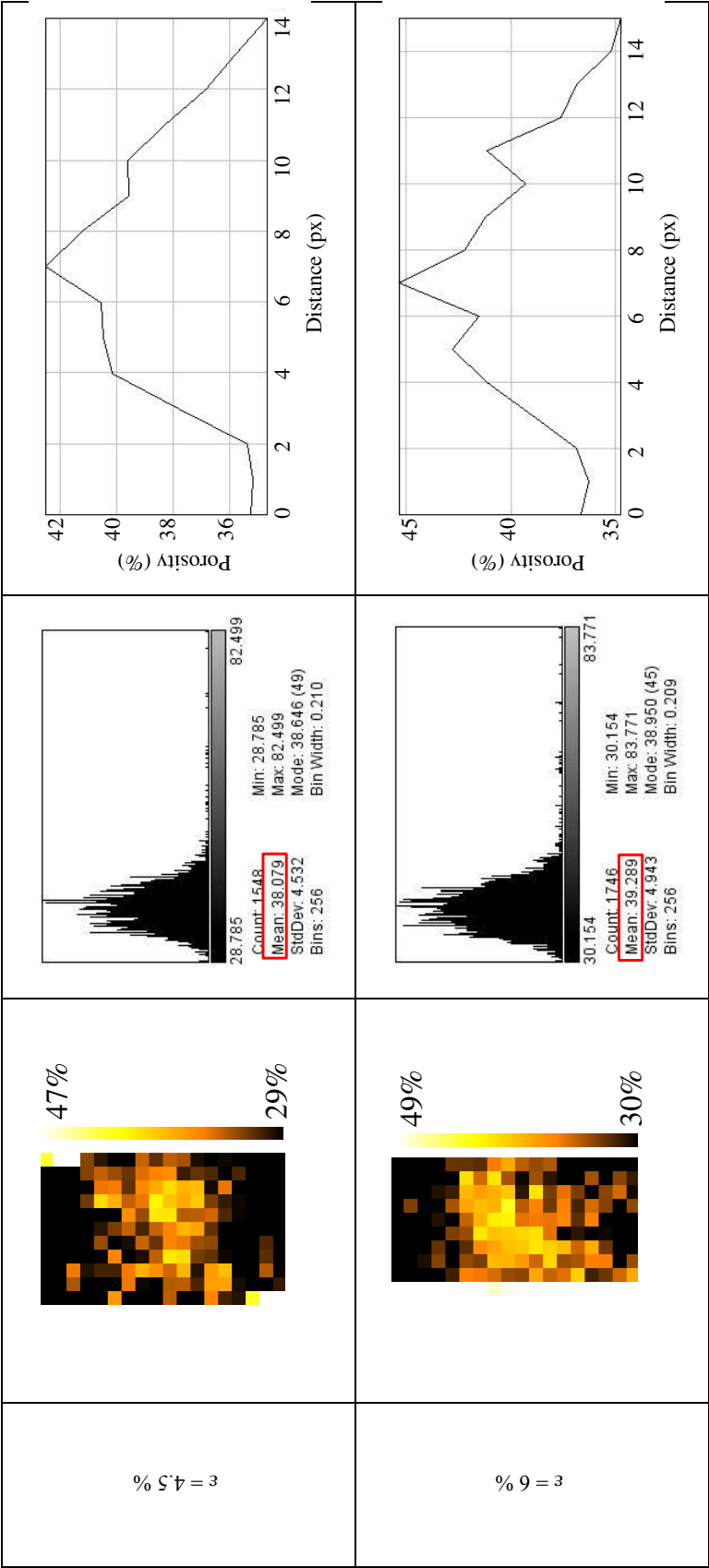


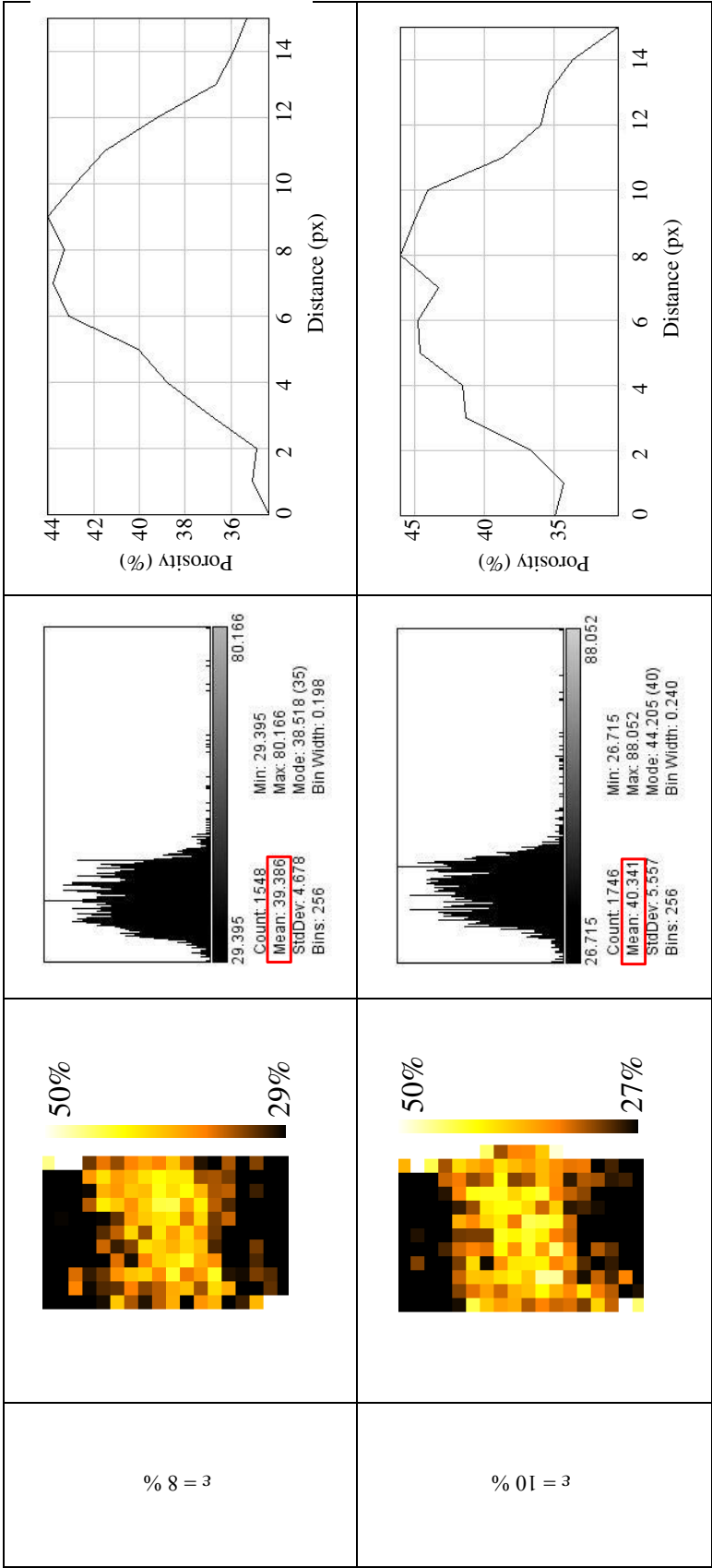
Figure E-1: Central vertical slices in the a) reconstructed volumes b) trinarized volumes for all loading steps in the unsaturated drained triaxial test HN02

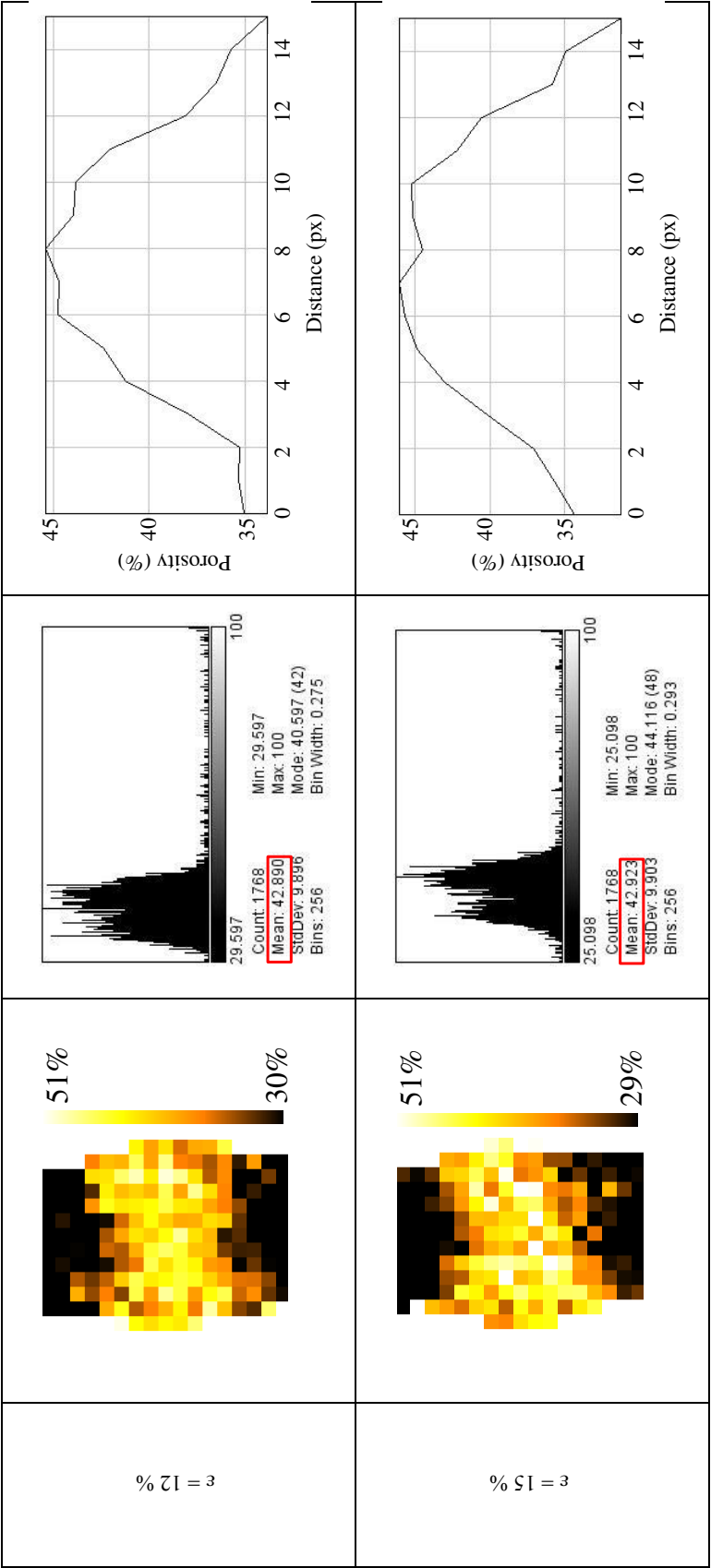
E.2 Porosity mapping results











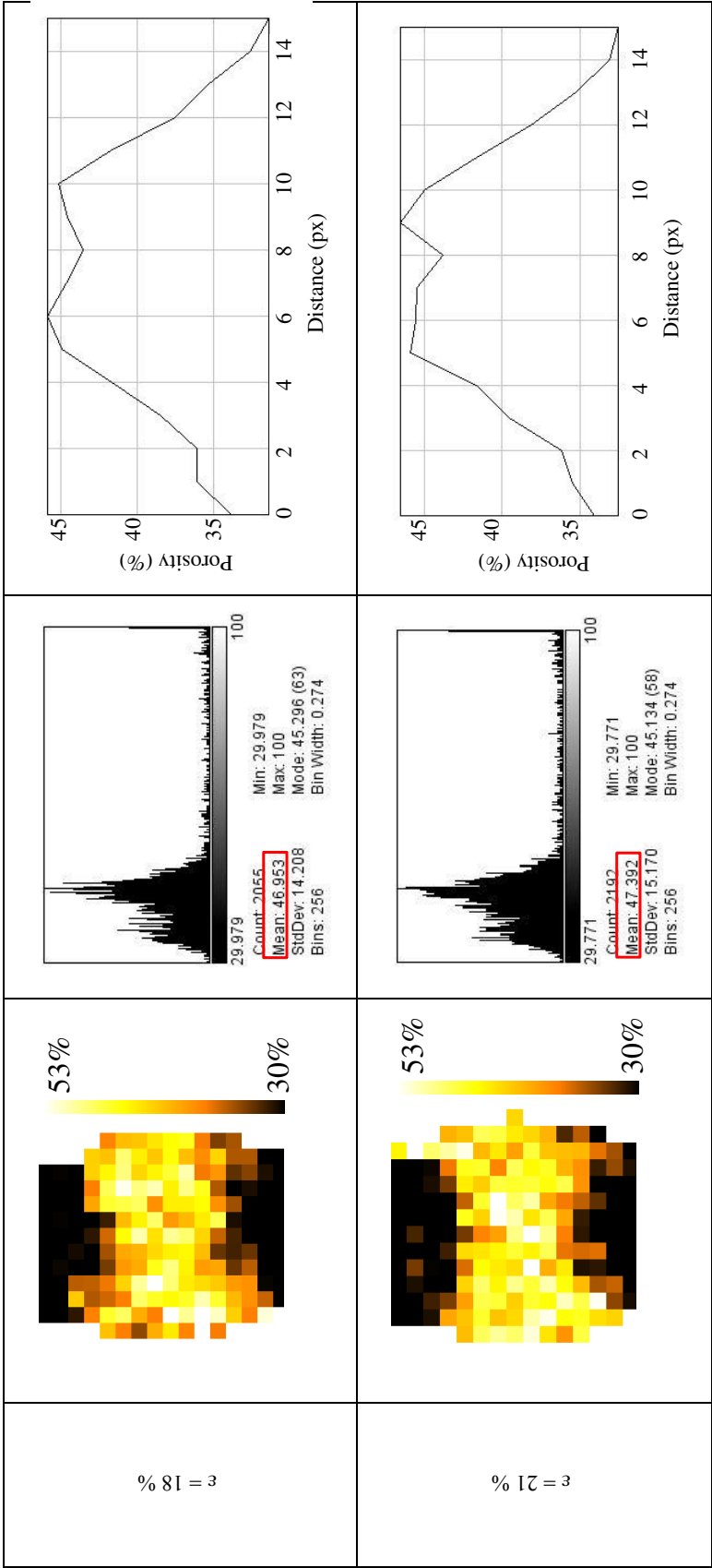

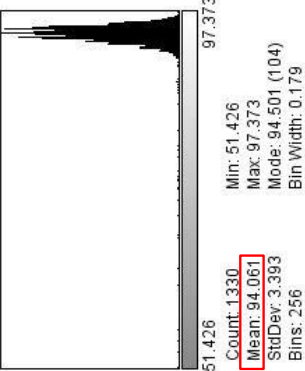
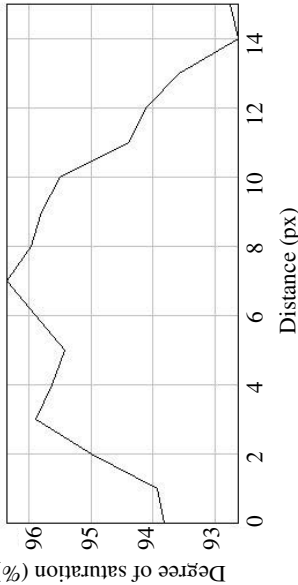
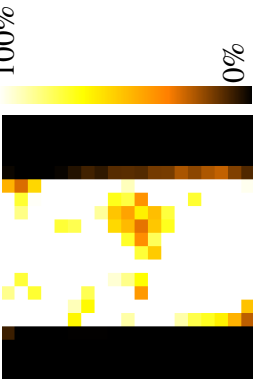
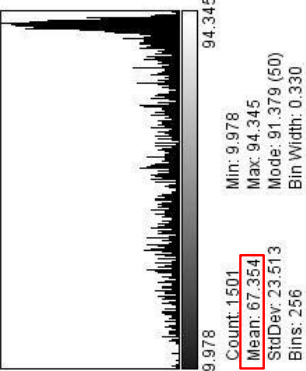
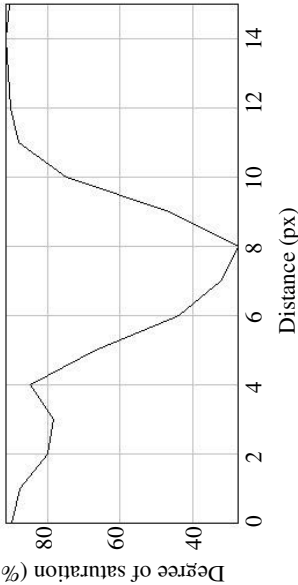
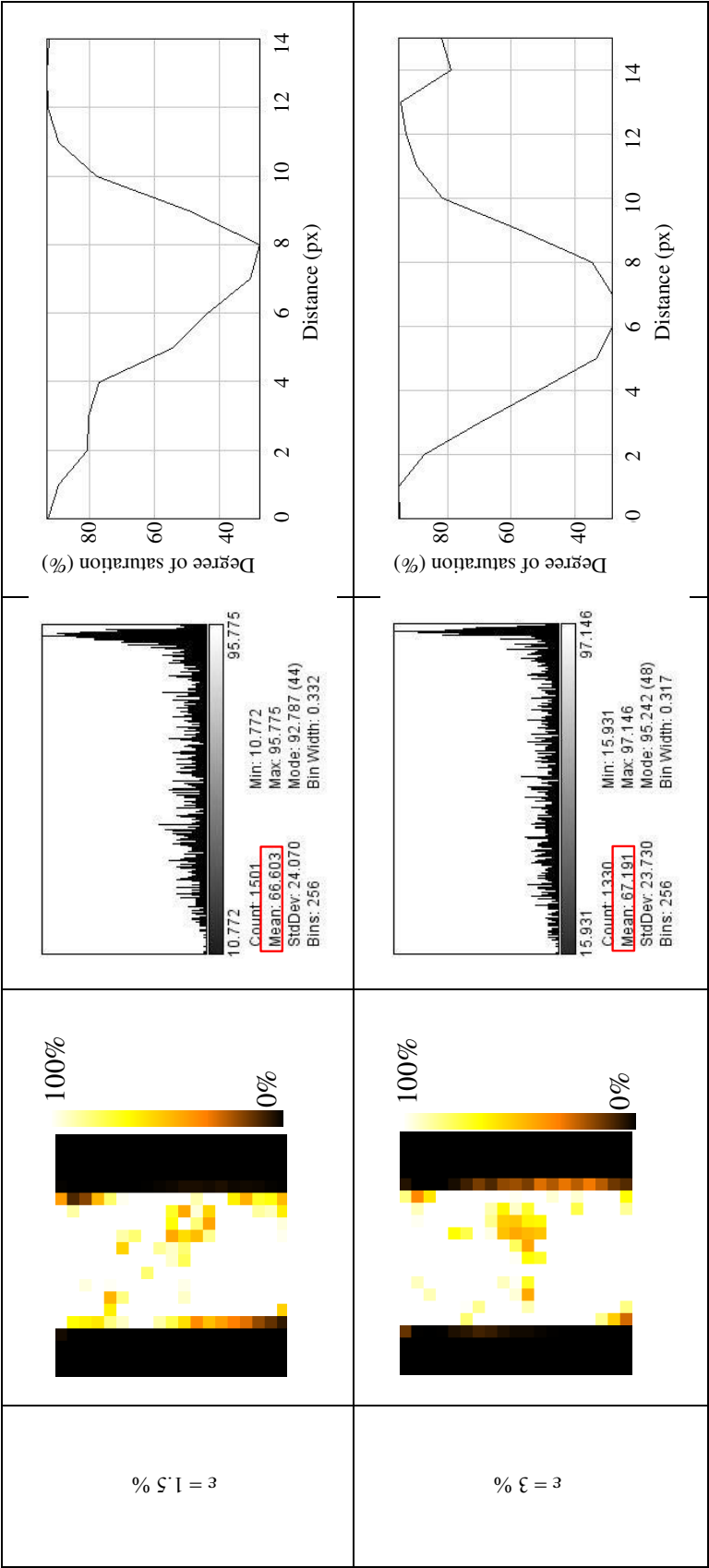
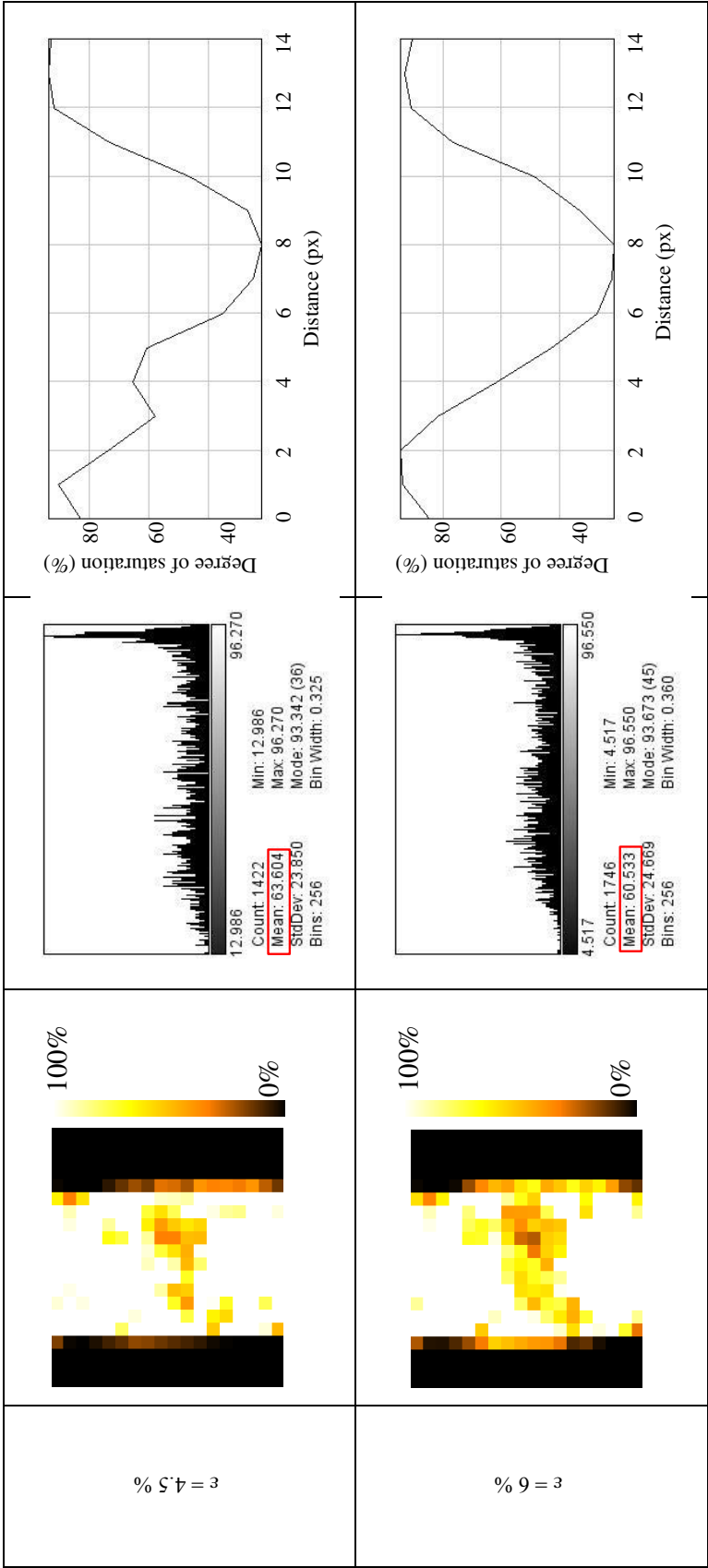


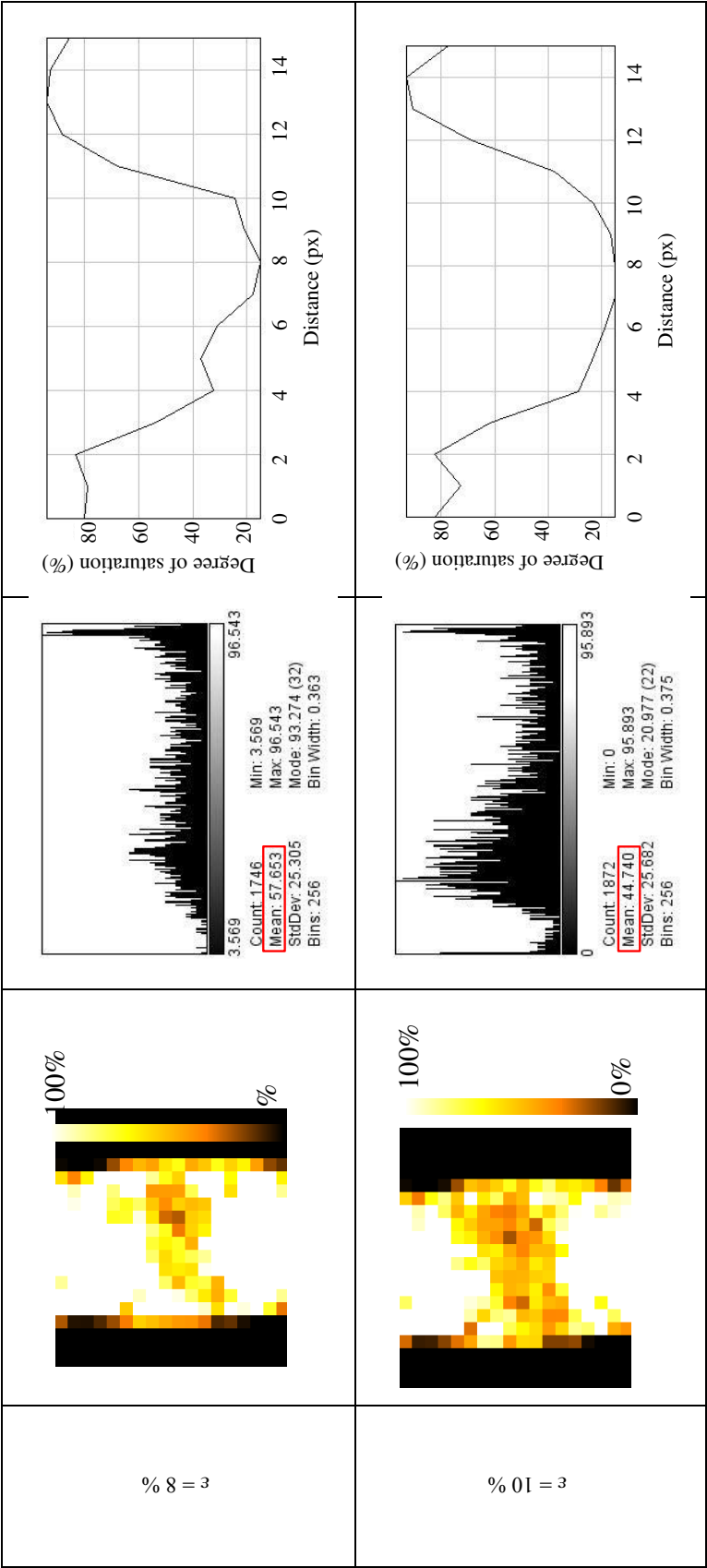
Figure E-2: a) Central vertical slices in the porosity map b) Porosity histogram, c) Porosity vertical profile, for all loading steps in the unsaturated drained triaxial test HN02

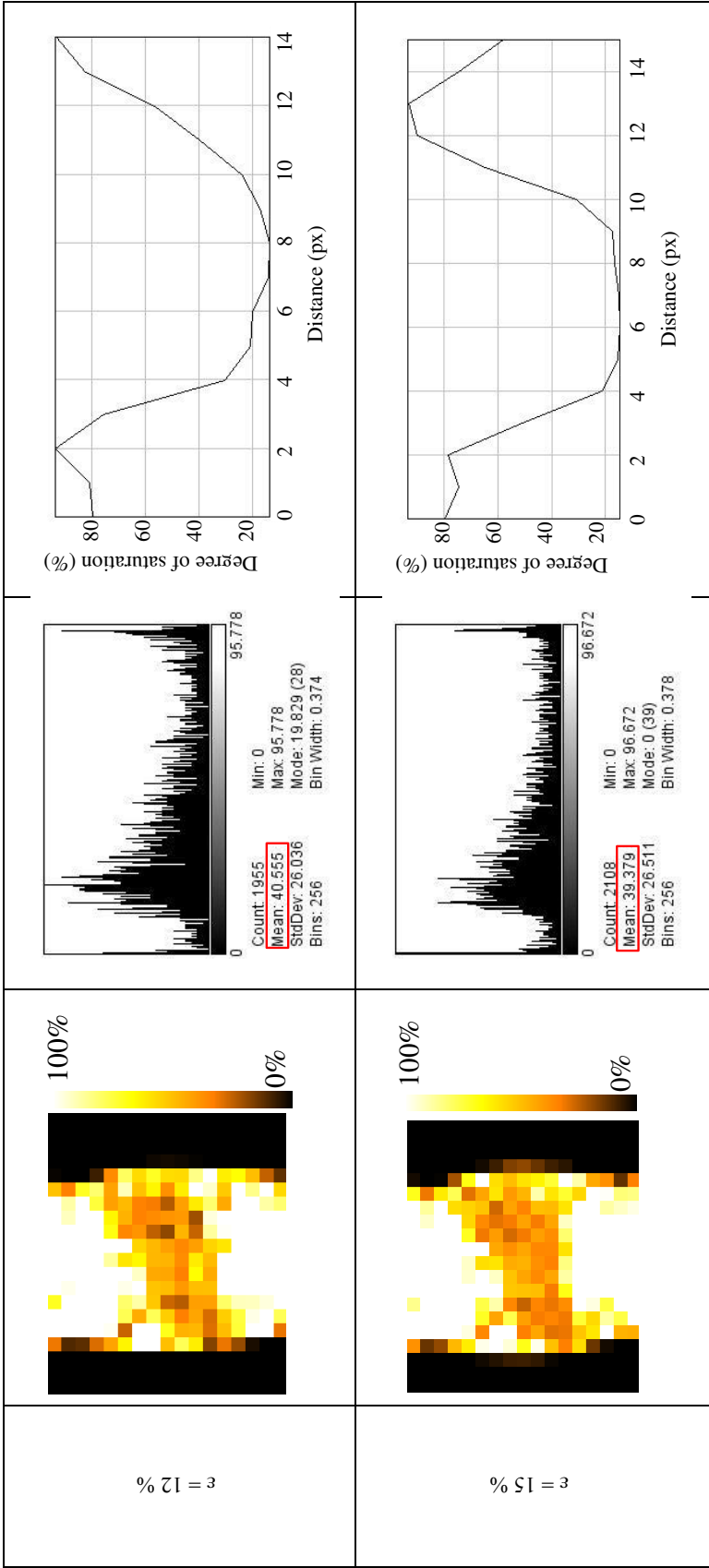
E.3 Degree of saturation mapping results

Loading step ϵ %	a)	b)	c)
Complete saturation $s = 0$ kPa $\epsilon = 0$ %			
$s = 2.2$ kPa $\epsilon = 0$ %			









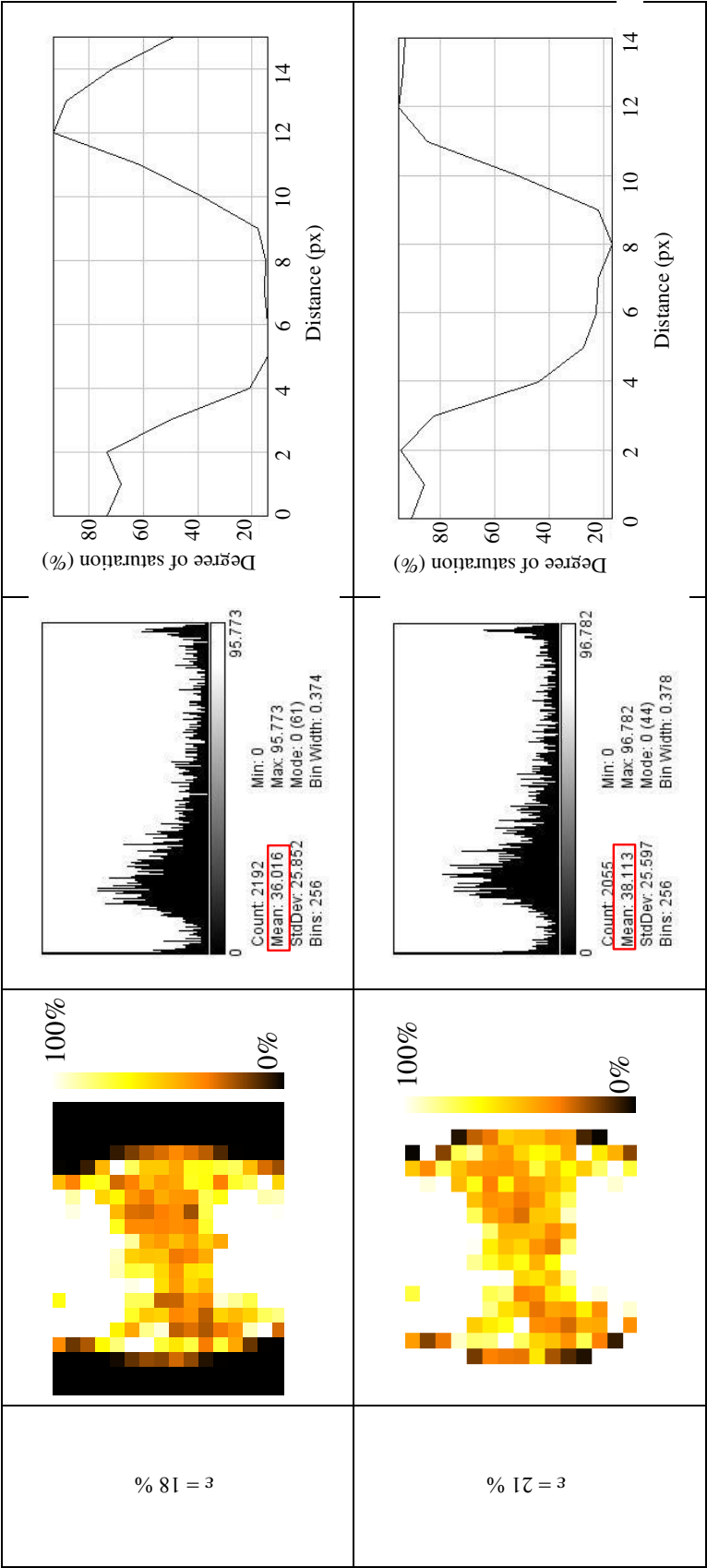
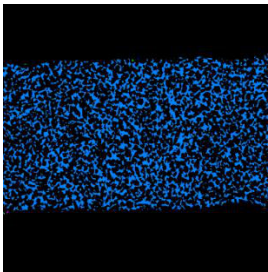
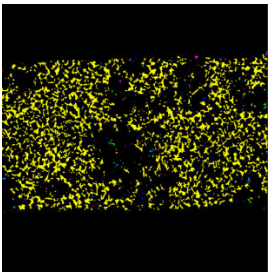
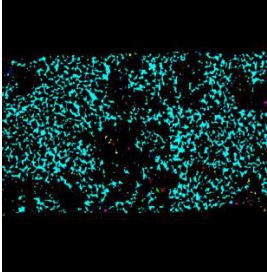
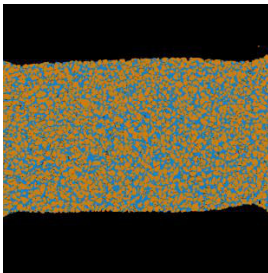
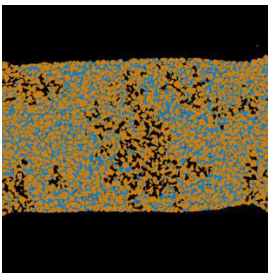
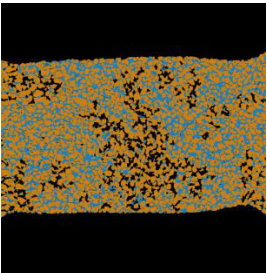
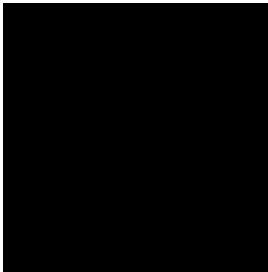
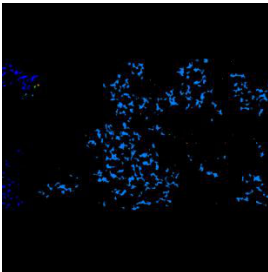
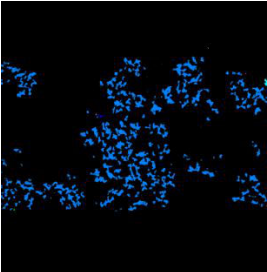
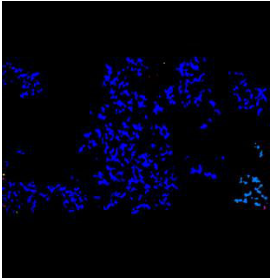
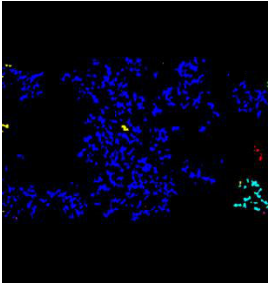
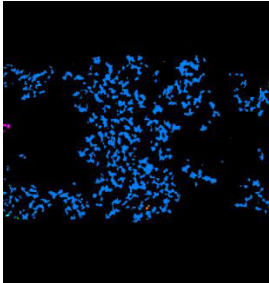
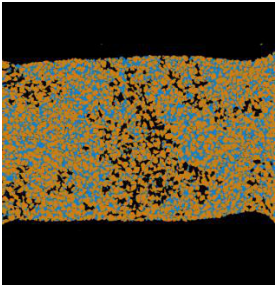
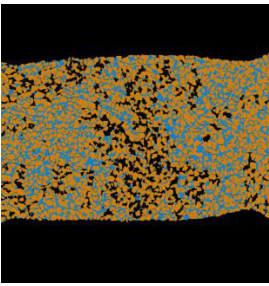
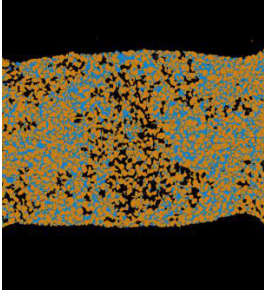
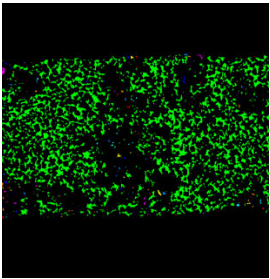
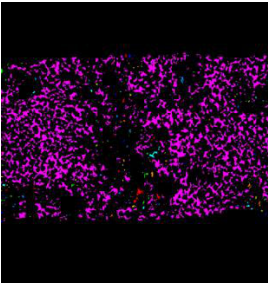
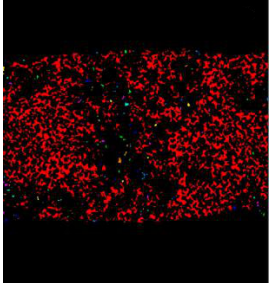
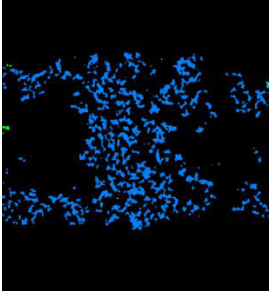
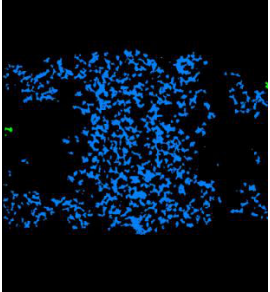
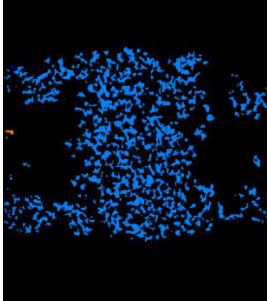
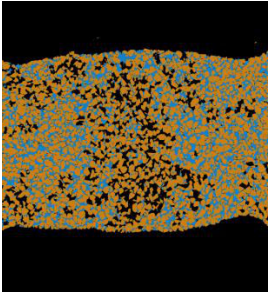
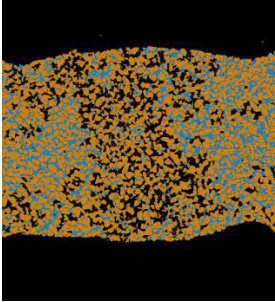
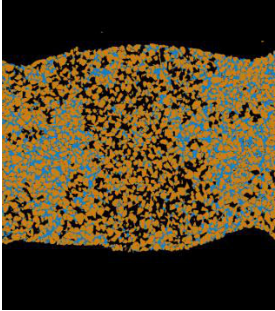
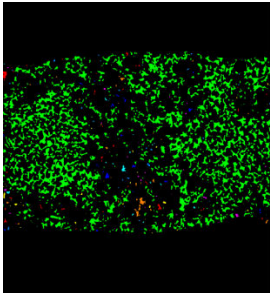
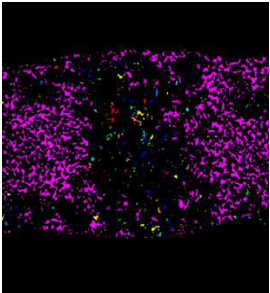
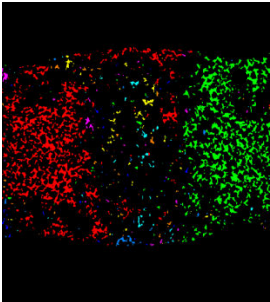


Figure E-3: a) Central vertical slices in the degree of saturation map b) Degree of saturation histogram, c) Degree of saturation vertical profile, for all loading steps in the unsaturated drained triaxial test HN02

E.4 Labelling process results

Loading step ε %	a)	b)	c)
Complete saturation $s = 0$ kPa $\varepsilon = 0$ %			
$s = 2.2$ kPa $\varepsilon = 0$ %			
$\varepsilon = 1.5$ %			

		
		
		
<p>$\epsilon = 3\%$</p>	<p>$\epsilon = 4.5\%$</p>	<p>$\epsilon = 6\%$</p>

		
		
		
<p>% 8 = 3</p>	<p>% 01 = 3</p>	<p>% 21 = 3</p>

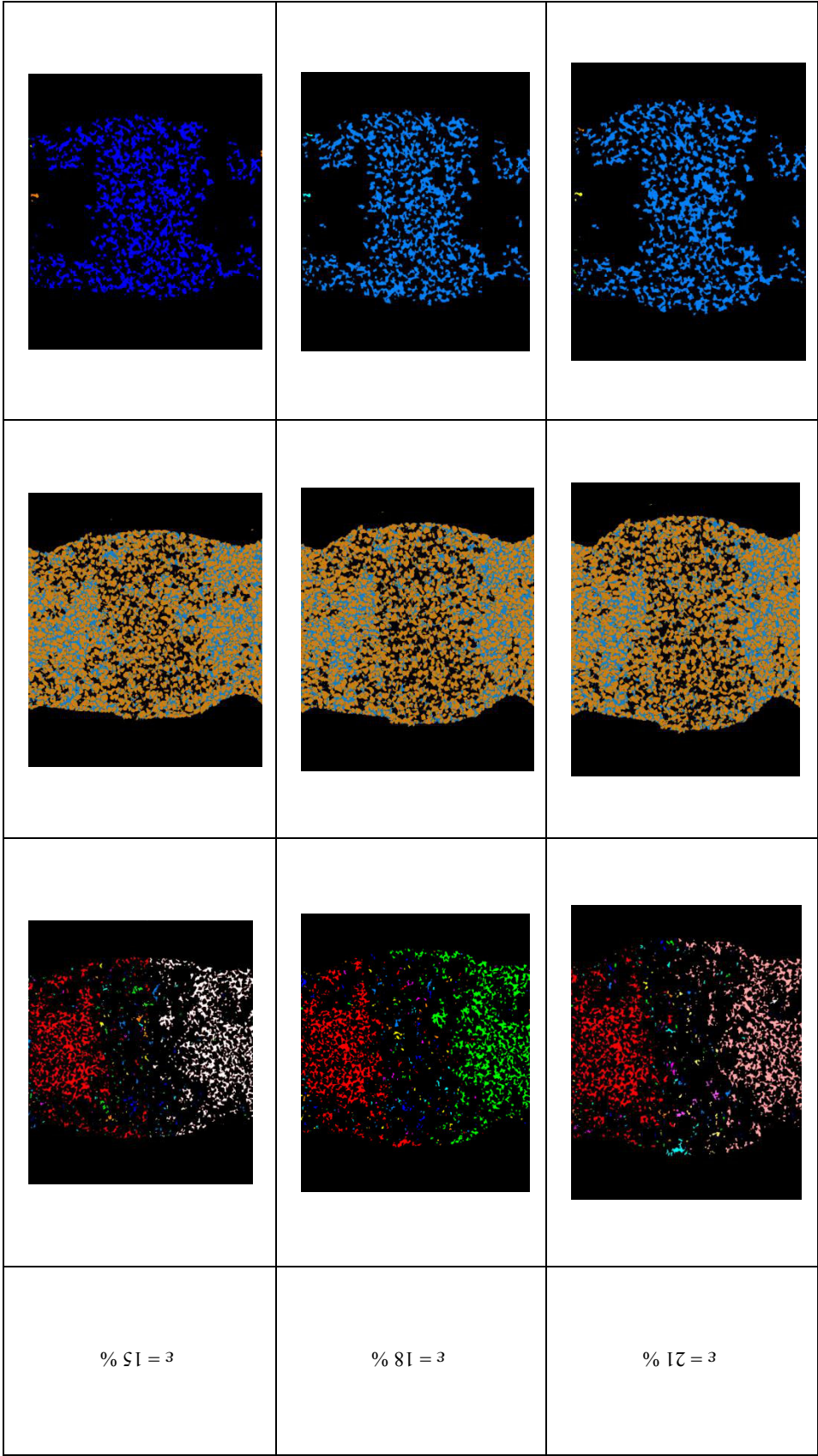


Figure E-4: a) Central vertical slices in the a) water labelled volumes b) trinarized volumes c) air labelled volumes, for all loading steps in the unsaturated drained triaxial test HN02

CURRICULUM VITAE

GENERAL INFORMATION

Ghonwa KHADDOUR

Born: 01/01/1986 in Latakia - Syria

Age: 29 years

Nationality: Syrian

Work Address: Joseph Fourier university - 3SR laboratory - Domaine Universitaire BP53 - 38041 Grenoble Cedex 9

Telephone: +33 6 20 28 46 18

Email: ghonwa.khaddour@3sr-grenoble.fr

ghonwakhaddour@hotmail.com

ACADEMIC TITLES

2012 - 2015: PhD diploma, Grenoble University-France, “*Multi-scale characterization of the hydro-mechanical behavior of unsaturated sand: water retention and triaxial response*”, defended on 13/11/2015.

2011 - 2012: Mater diploma, Grenoble University-France, “Microscopic mechanisms related to water retention in sand”, defended on 12/06/2012.

2009 - 2010: Bachelor diploma in civil engineering, Tishreen university- Syria.

RESEARCH AREAS

2004 - 2009: Hydrology and hydrogeology, Rainfall drainage systems, irrigation systems for saline soils, wells and dams loadings (stresses and strains), marine structures.

2011 - 2015: Retention behavior of granular materials, hydro-mechanical of unsaturated granular materials, x-ray tomography scanning, image processing, Strain localization in sand, continuum digital image correlation (DIC) in 3D.

TRAINING COURSES

2012 - 2013: Public lecture - Improvement of oral expression - Grenoble University - France.

2012 - 2013: Intensive French language courses - Stendhal University (CUEF) - Grenoble - France.

2012 - 2013: Synchrotron and neutron radiation (Interaction, production, absorption, diffraction and scattering) - Grenoble - France.

2013 - 2014: Team leading and assisting - Grenoble University - France.

CONFERENCES

- Khaddour, G., Ando, E., Salager, S., Bésuelle, P., Viggiani, C., Hall, S., Desrues, J. (2012). “Application of x-ray tomography to the characterization of grain-scale mechanisms in sand”, Proceedings of Advances in Multi-physical Testing of Soils and Shales, Lausanne, Switzerland.
- Khaddour, G., Salager, S., & Desrues, J. (2012). “Microscopic mechanisms related to water retention behavior of sand”, Alert Workshop, Aussois, France.
- Khaddour G., Hashemi A., Salager S., Desrues J., Massart T.J., François B. (2013). “Phase segmentation in 3D X-ray images of unsaturated granular materials”, XVI French-Polish Colloquium of Soil and Rock Mechanics, Montpellier, France.
- Khaddour, G., Hashemi, A., Salager, S., Desrues, J., Massart, T. J., & Francois, B. (2013). “Phase segmentation in 3D X-ray images of unsaturated granular materials”, XVI French-Polish Colloquium of Soil and Rock Mechanics.
- Khaddour, G., Hashemi, A., Salager, S., Desrues, J., Massart, T. J., & Francois, B. (2013) “Phase segmentation in 3D X-ray images of unsaturated granular materials”, Club Image 3D - RX solutions -Annecy, France.
- Khaddour, G., Salager, S., & Desrues, J. (2014). “3D field measurement of porosity and degree of saturation in sand using X-ray computed tomography”, Lecture to “Journées thématiques sur les techniques d'imagerie pour la caractérisation des matériaux et des structures du génie civil”, Clermont-Ferrand, France.
- Khaddour, G., Salager, S., & Desrues, J. (2015). “Advanced image analysis of X-ray tomographic images of hydro-mechanical processes in three-phase granular media”, Lecture to TC105 seminar, Tokyo, Japan.

PUBLICATIONS

- Khaddour, G., Andò, E., Salager, S., Bésuelle, P., Viggiani, G., Hall, S., Desrues, J. (2013). “Application of X-ray tomography to the characterization of grain-scale mechanisms in sand”, Multi-physical Testing of Soils and Shales, Springer Series in Geomechanics and Geoengineering, Part 4, Pages 195-200.
- Salager, S., Khaddour, G., Charrier, P., & Desrues, J. (2014). “An investigation into unsaturated states of granular media using X-ray computed tomography”, Unsaturated Soils: Research & Applications, CRC Press, Pages 703-709.
- Hashemi, M. A., Khaddour, G., François, B., Massart, T. J., & Salager, S. (2014). “A tomographic imagery segmentation methodology for three-phase geomaterials based on simultaneous region growing”, Acta Geotechnica, 9 (5), 831-846.

SKILLS

Languages: Arabic: native proficiency, English: conversational proficiency, French: elementary proficiency.

Computer skills: Microsoft OS, AutoCAD, Matlab, Watershed modeling system (WMS), Geographic information system (GIS), Water Evaluation And Planning (WEAP), GS-USA Frame program, Visual Basic (VBA), FIJI (Image J), Visilog.

WORK EXPERIENCE

2006 - 2007: Scientific agricultural research center (studies and teaching Geographic information system (GIS)).

2007 - 2009: Consulting engineering office (studies and design).

2009 - 2010: Ministry of environment (executive studies for environmental projects).

ACCOMPLISHMENTS

2007 - 2009: Winner of superiority certificate and price for three times, from the Ministry of higher education- Syria.

2011 - 2012: Winner of the Syrian government scholarship (Ministry of Higher Education) to obtain Master degree in civil engineering (Awarded to the first three top students in college).

2012 - 2015: Recipient of the French government scholarship to obtain PhD degree in civil engineering.

THÈSE

Pour obtenir le grade de

DOCTEUR DE L'UNIVERSITÉ GRENOBLE ALPES

Spécialité : **Matériaux, Mécanique, Génie Civil, Électrochimie**

Arrêté ministériel : 7 août 2006

Présentée par

Ghonwa KHADDOUR

Thèse dirigée par **Jacques DESRUES** et
codirigée par **Simon SALAGER**

préparée au sein du **Laboratoire 3SR**
dans l'**École Doctorale IMEP2**

La caractérisation multi-échelle du comportement hydro-mécanique d'un sable non saturé : la réponse de rétention d'eau et triaxial

Thèse soutenue publiquement le « **13 Novembre 2015** »,
devant le jury composé de :

Monsieur, Antonio GENS

Professeur, Université de la Catalogne, (Rapporteur)

Monsieur, Bertrand FRANCOIS

Professeur, Université libre du Bruxelles, (Membre)

Monsieur, Felix DARVE

Professeur, Université Joseph Fourier, Grenoble, (Membre)

Monsieur, Jean-michel PEREIRA

Chercheur, Ecole des Ponts ParisTech, (Membre)

Monsieur, Fabien CHERBLANC

Chercheur, Université de Montpellier 2, (Rapporteur)

Monsieur, Gioacchino VIGGIANI

Professeur, Université Joseph Fourier, Grenoble, (Membre)

Monsieur, Jacques DESRUES

Directeur de recherche, CNRS, Grenoble, (Directeur de thèse)

Monsieur, Simon SALAGER

Maitre de conférences, Université Joseph Fourier, Grenoble, (Co-Encadrant)

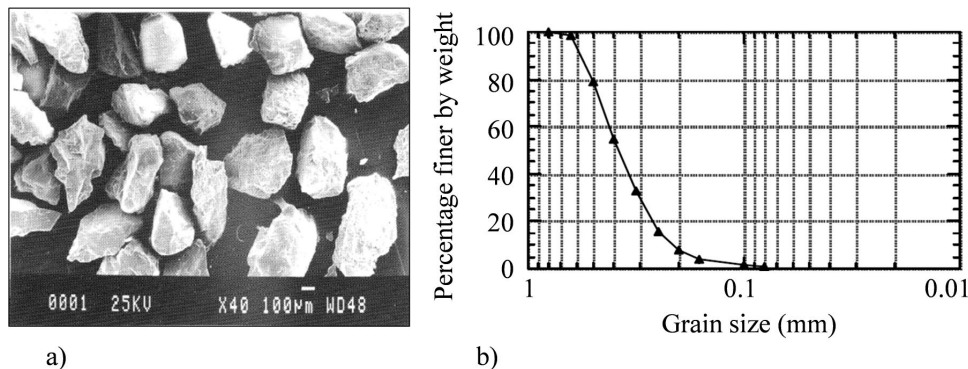


La caractérisation multi-échelle du comportement hydro-mécanique d'un sable non saturé : la réponse de rétention d'eau et triaxial

Avec les récents développements des mesures de champs, il est devenu possible de réaliser des expériences sur un échantillon de sol en effectuant des mesures simultanément aux différentes échelles pertinentes : celle de l'échantillon, celle des grains et ceci en 3D volumique. Ces progrès ont permis une meilleure compréhension des processus qui se produisent dans le sol, en les observant au cœur même des échantillons.

Cette thèse vise à caractériser les comportements de rétention d'eau et hydro-mécanique du sable d'Hostun non saturé à l'échelle du grain. Pour ce faire, des essais de rétention d'eau et des essais triaxiaux ont été effectués, qui ont nécessité le développement d'outils de traitement d'images et des montages expérimentaux spécifiques.

Le sable d'Hostun est un sable utilisé comme un matériau de référence dans différents laboratoires. Ses composants chimiques sont principalement constituées de silice ($\text{SiO}_2 > 98\%$). La forme du grain est angulaire, comme indiquée dans l'image microscope électronique de quelques grains du sable d'Hostun, sur Fig 1-a. Une analyse de la distribution de taille des particules du sable d'Hostun est représentée sur Fig 1-b.



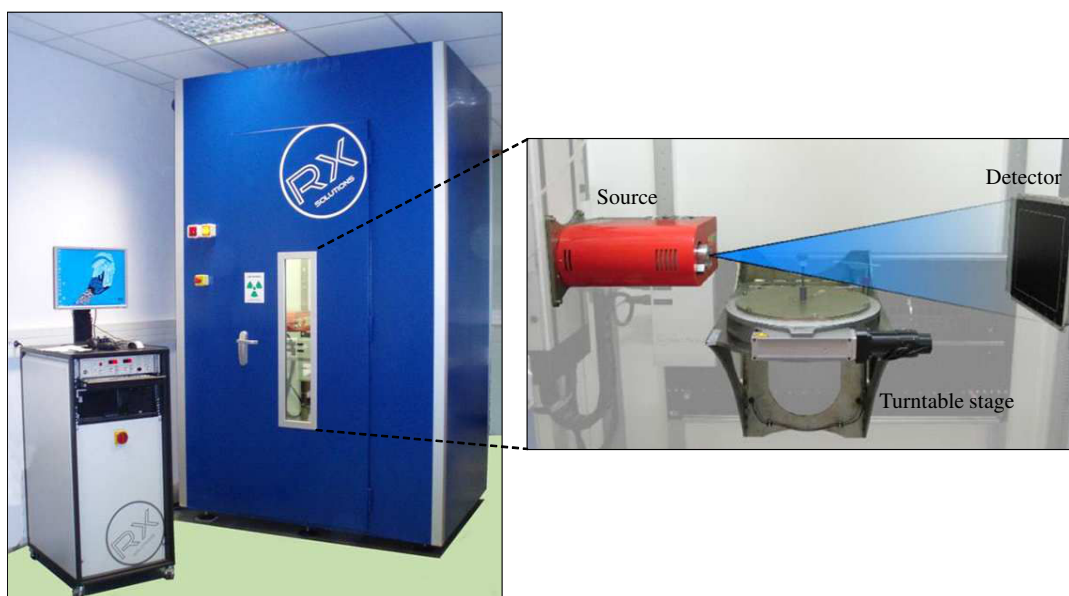


Figure 2: Le scanner à rayons x dans le laboratoire 3SR

Les radiographies à rayons x, sont reconstruites en utilisant le logiciel DigiCT, version 2.4.2. Dans Fig 3, une image 8-bits reconstruite du sable d'Hostun non saturé est présentée, avec l'histogramme, ce qui représente la répartition du nombre de voxels (pixels en 2D) en fonction de leur niveau d'intensité (valeur de gris).

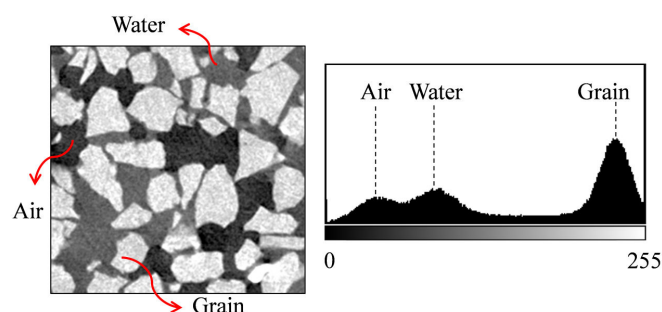


Figure 3: Le contraste des phases dans une 8-bits image reconstruite (gauche) et l'histogramme correspondant (droite)

Une technique de trinarization a été mise en œuvre pour permettre la séparation des phases (les grains, l'eau et l'air) dans les images 3D, et d'effectuer différentes mesures à l'échelle du grain. Fig 4 représente les résultats de la technique de trinarization pour les quatre étapes successives de la procédure de segmentation, appliquées pour le sable d'Hostun non saturé. Dans ces images, la couleur rouge représente les grains; la couleur verte représente l'eau; la couleur bleue représente l'air et la couleur noire pour les régions non définies.

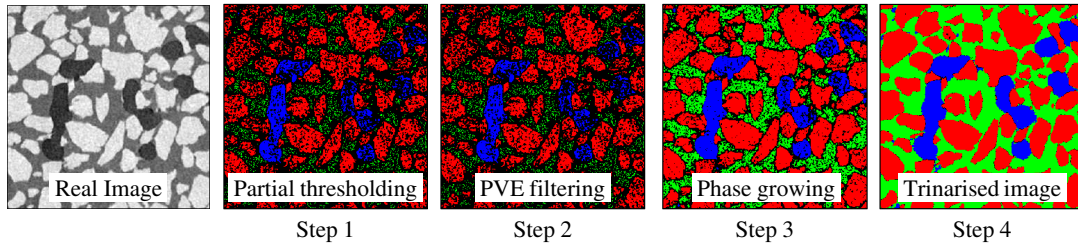


Figure 4: L'évolution du processus de segmentation des phases dans la technique de trinarization. La couleur rouge représente les grains; la couleur verte représente l'eau; la couleur bleue représente l'air et la couleur noire pour les régions non définies

La porosité et le degré de saturation ont été mesurés macroscopiquement en utilisant les images segmentées, et microscopiquement en utilisant un code de cartographie spécialement développé.

Les mesures microscopiques ont été réalisées sur un volume élémentaire représentatif (VER), dont la taille a été déterminée en utilisant une analyse développée sur la base d'outils statistiques.

Les résultats de la cartographie de la porosité et du degré de saturation est un volume (des images 3D) formé par un certain nombre de voxels, où chaque voxel est associé à un noeud. Ces résultats peuvent être manipulés et traités comme une carte de volume de porosité et du degré de saturation.

Plusieurs analyses discrètes ont été développées pour étudier l'évolution des phases fluide (l'eau et l'air) avec le chargement (suction et chargement mécanique). Les images ont ensuite été analysées en utilisant un code commercial hautement optimisé "Visilog[®]". En conséquence, le nombre d'agrégats de fluide intérieur de l'échantillon est obtenu pour chaque incrément de chargement (incrément de suction ou incrément de chargement mécanique).

La corrélation d'images numériques 3D volumique a été mise en œuvre systématiquement pour ces deux types d'essais.

1. Le comportement de rétention d'eau

Pour analyser le comportement de rétention d'eau du sable d'Hostun pendant les processus de séchage et de mouillage, des dispositifs expérimentaux spécifiques ont été développées. La suction a été appliquée en utilisant la technique de tensiométrie. L'échantillon (cylindrique $1 \times 1 \text{ cm}$) a été préparé en utilisant la technique de la pluviation sous l'eau et scanné avec une résolution de $7,5 \mu\text{m}$.

Fig 5 montre les deux dispositifs expérimentaux et leurs composants développées pour l'essai de rétention d'eau (WRT_0 et WRT_1).

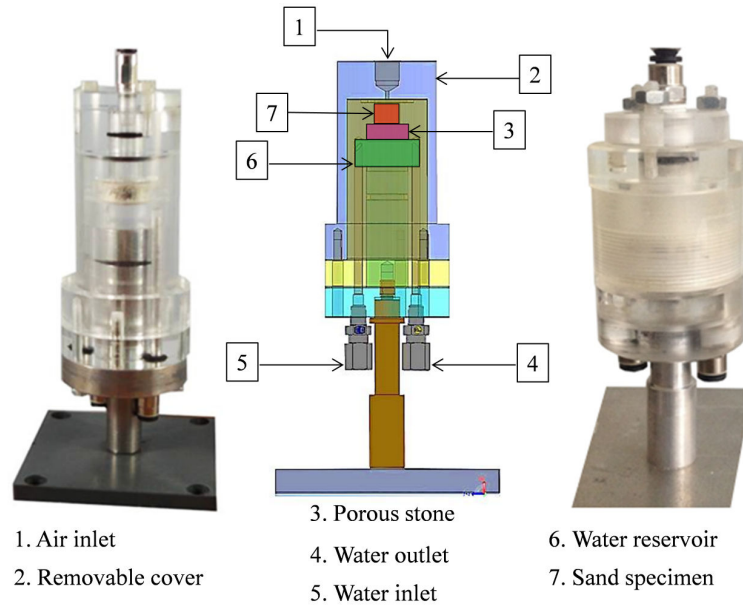


Figure 5: Les cellules de rétention d'eau pour WRT_0 et WRT_1

Fig 6 montre schématiquement la disposition complet illustre comment la succion est appliquée pour WRT_0 .

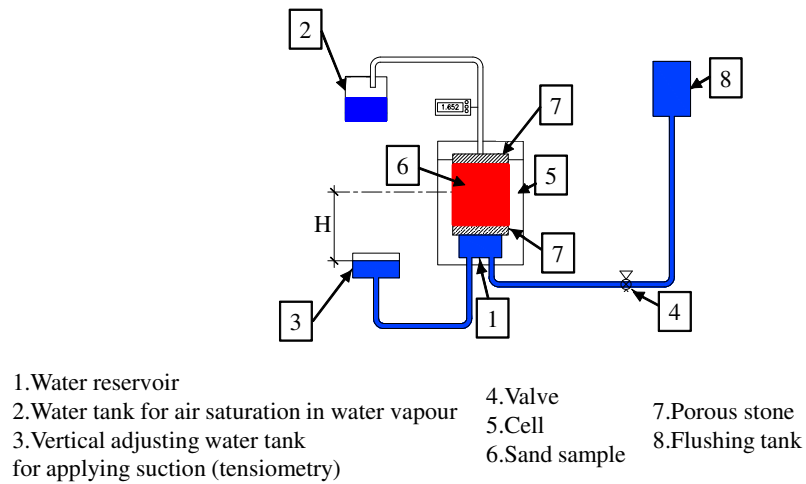


Figure 6: Un croquis du montage utilisé pour appliquer la succion pour WRT_0

la disposition complet de WRT_1 , et la technique d'application de la succion dans cet essai sont présentés dans la Fig 7.

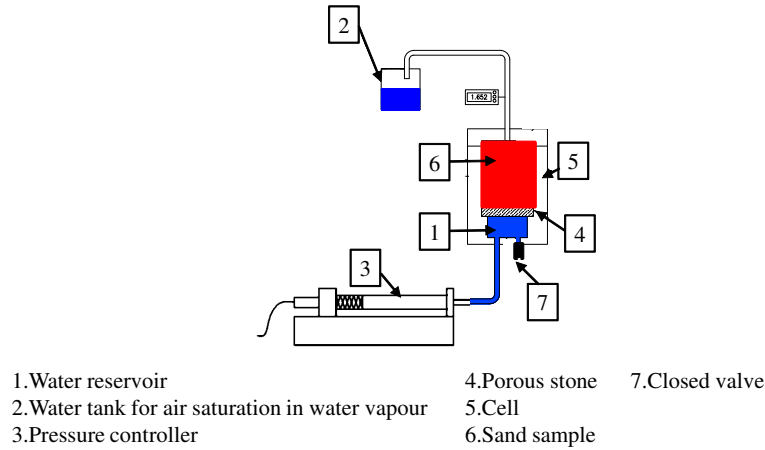


Figure 7: Un croquis du montage utilisé pour appliquer la succion pour WRT_1

Fig 8, Fig 10 et Fig 12 montrent des tranches centrales horizontales (XY) dans les volumes segmentés pour toutes les valeurs de la succion dans les chemins de séchage (D_1 et D_0) et le chemin de mouillage (W_1), respectivement. Fig 9, Fig 11 et Fig 13 montrent des tranches centrales verticales (XZ) du même azimut, dans les volumes segmentés, pour toutes les valeurs de la succion dans les chemins de séchage (D_1 et D_0) et le chemin de mouillage (W_1), respectivement.

En utilisant les images trinarisées, la porosité et le degré de saturation sont calculé macroscopiquement pour toutes les valeurs de la succion dans les chemins de séchage et de mouillage, pour l'essai de rétention d'eau. L'histogramme des images trinarisées donne le nombre de voxels qui représentent l'air (N_c), l'eau (N_w) et les grains (N_g). La porosité est calculée comme $n = V_v/V_t = (N_w + N_c)/(N_w + N_c + N_g)$ et le degré de saturation est calculé comme $S_r = V_w/V_v = N_w/(N_w + N_c)$.

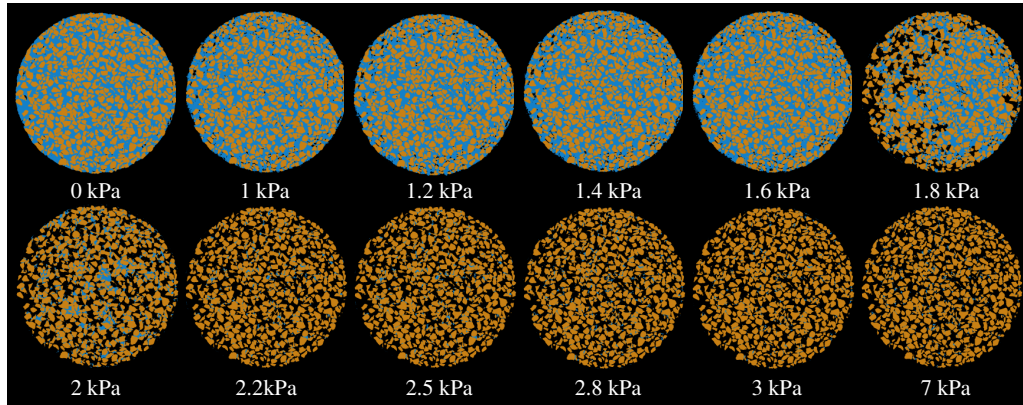


Figure 8: Des tranches centrales horizontales (XY) dans les volumes segmentés pour toutes les valeurs de la succion dans le chemin de séchage (D_1)

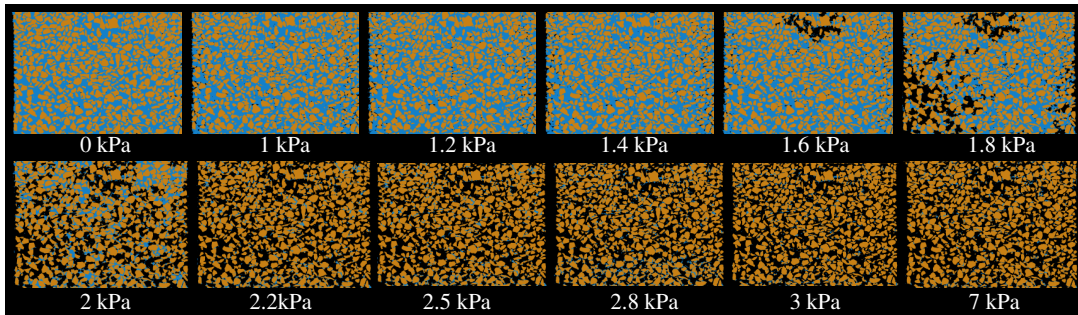


Figure 9: Des tranches centrales verticales (XZ) du même azimut, dans les volumes segmentés, pour toutes les valeurs de la succion dans les chemins de séchage (D_1)

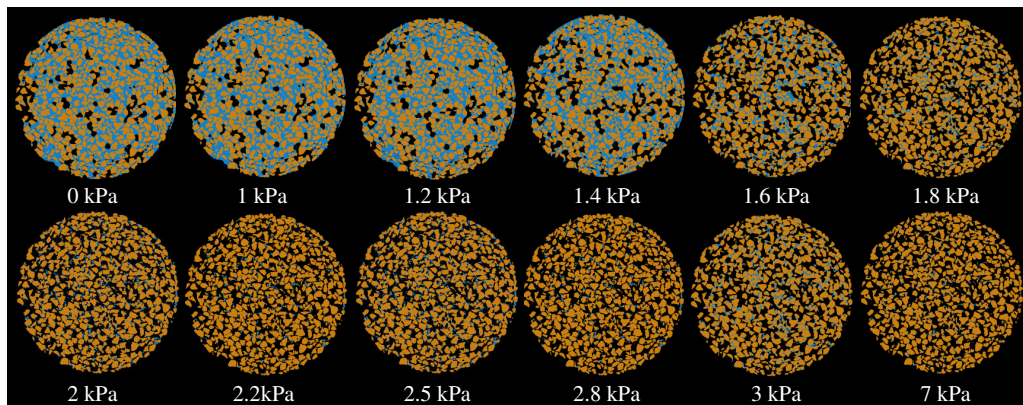


Figure 10: Des tranches centrales horizontales (XY) dans les volumes segmentés pour toutes les valeurs de la succion dans le chemin de mouillage (W_1)

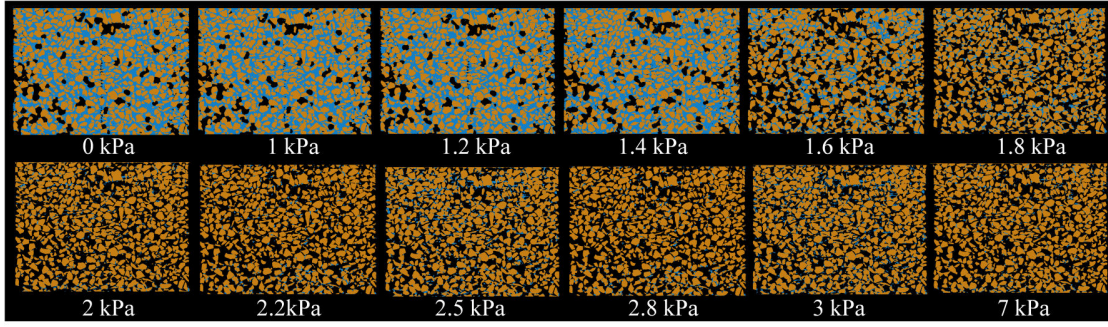


Figure 11: Des tranches centrales verticales (XZ) du même azimut, dans les volumes segmentés, pour toutes les valeurs de la succion dans les chemins de mouillage (W_1)

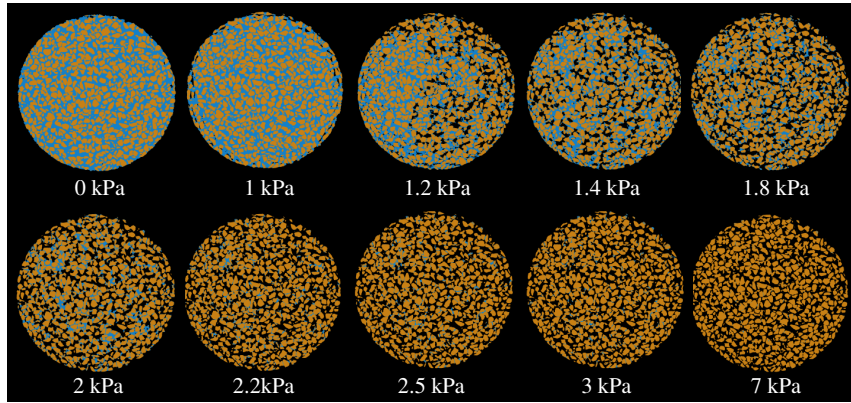


Figure 12: Des tranches centrales horizontales (XY) dans les volumes segmentés pour toutes les valeurs de la succion dans le chemin de séchage (D_0)

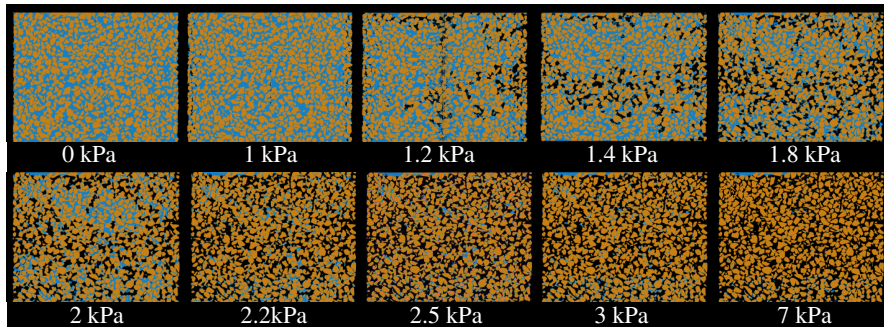


Figure 13: Des tranches centrales verticales (XZ) du même azimut, dans les volumes segmentés, pour toutes les valeurs de la succion dans les chemins de séchage (D_0)

En utilisant le degré de saturation calculé macroscopiquement, pour toutes les valeurs de la succion dans les chemins de séchage (D_0 et D_1) et de mouillage (W_1), les courbes de rétention d'eau sont établies et présentées dans Fig 14. La figure montre également la courbe référence de rétention de l'eau pour le sable d'Hostun (Ref WRC).

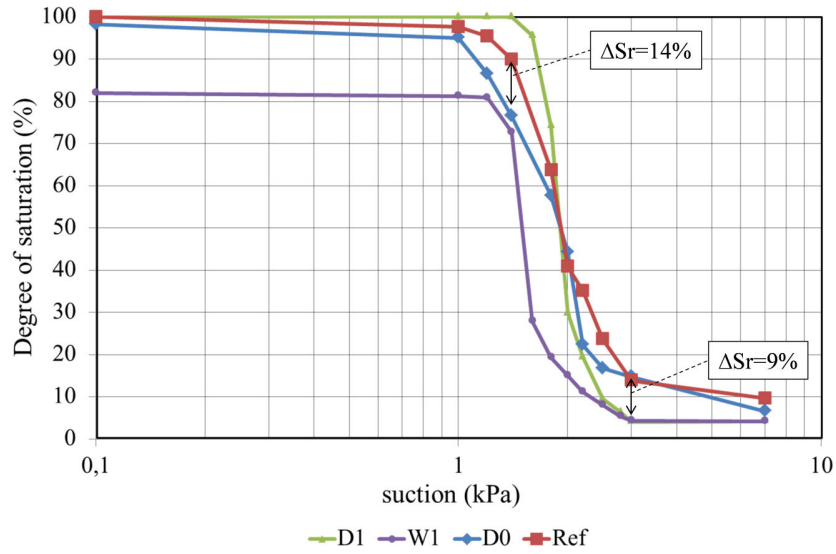


Figure 14: Les courbes de rétention d'eau (WRC) pour les chemins de séchage (D_0 , D_1), le chemin de mouillage (W_1), et Ref WRC

Le VER obtenu pour l'essai de rétention d'eau est un cube de 140 px de côté $VER=140px$ et pour l'essai triaxial de 80 px de côté. Fig 15 montre une fenêtre d'une taille égale à la taille du $VER=140px$ en 2D, par rapport à la taille des grains du sable d'Hostun. La taille du VER calculée (pour les essais rétention et triaxial) est comparable à $D_{50}=0.338mm$ du sable d'Hostun $VER \approx 3 \times D_{50}$.

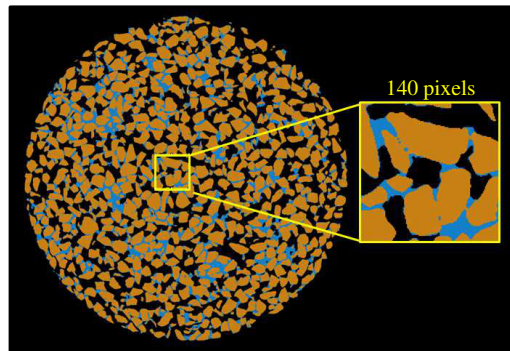


Figure 15: La taille choisie du $VER=140px$ (longueur d'un côté de la VER) par rapport à la taille des grains du sable d'Hostun pour l'essai de rétention d'eau

Fig 16, Fig 18 et Fig 20 montrent des tranches centrales horizontales (XY) dans la carte de la porosité, pour toutes les valeurs de la succion, dans les chemins de séchage et de mouillage, D_1, W_1 and D_0 , respectivement, pour l'essai de rétention d'eau. Fig 17, Fig 19 et Fig 21 montrent des tranches centrales verticales (XZ) dans la carte de la porosité, du même azimut, pour toutes les valeurs de la succion, dans les chemins de séchage et de mouillage, D_1, W_1 and D_0 , respectivement, pour l'essai de rétention d'eau. Dans ces figures, n_{\max} et n_{\min} représentent la porosité maximum et minimum, respectivement (écrit dessous la valeur de succion).

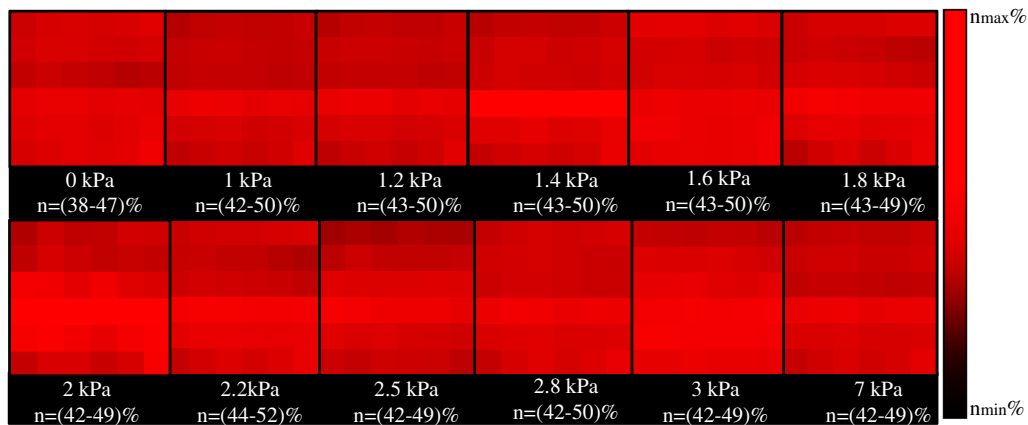


Figure 16: Des tranches centrales horizontales (XY) dans la carte de la porosité, pour toutes les valeurs de la succion, dans le chemin de séchage D_1 , pour l'essai de rétention d'eau. Dans ces figures, n_{\max} et n_{\min} représentent la porosité maximum et minimum, respectivement (écrit dessous la valeur de succion)

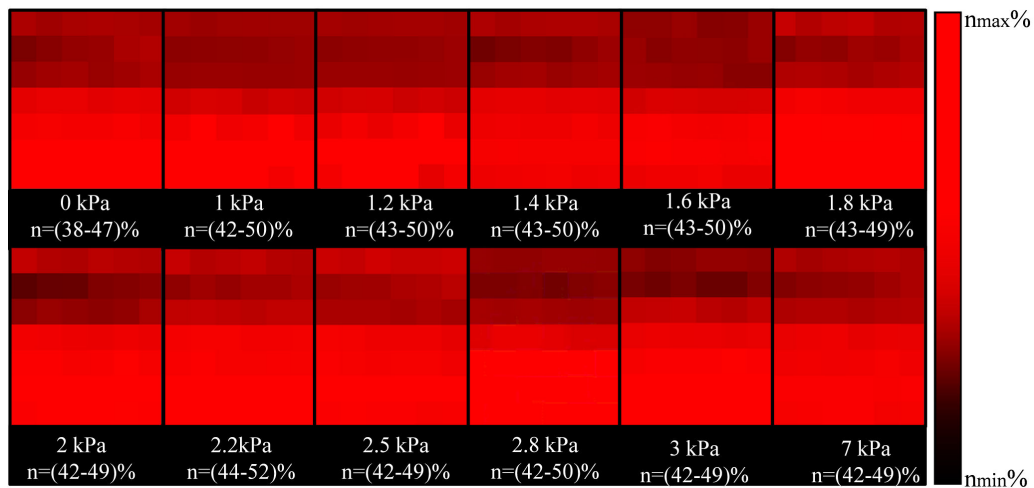


Figure 17: Des tranches centrales verticales (XZ) dans la carte de la porosité, pour toutes les valeurs de la succion, dans le chemin de séchage D_1 , pour l'essai de rétention d'eau. Dans ces figures, n_{\max} et n_{\min} représentent la porosité maximum et minimum, respectivement (écrit dessous la valeur de succion)

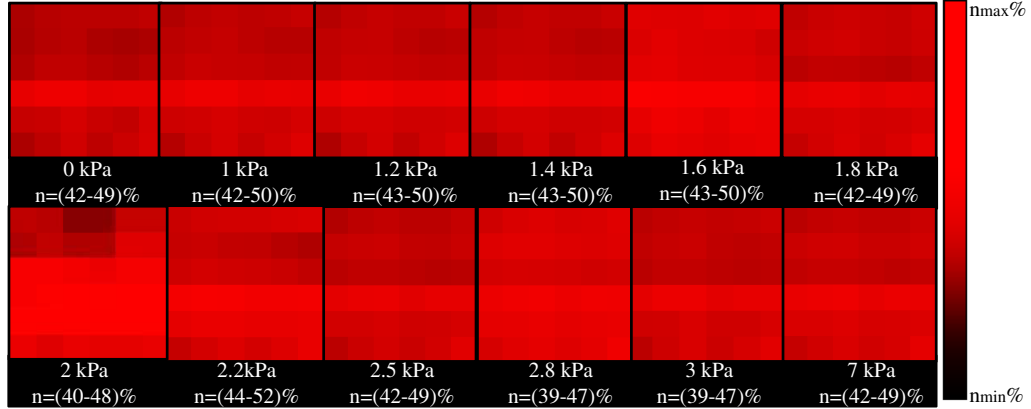


Figure 18: Des tranches centrales horizontales (XY) dans la carte de la porosité, pour toutes les valeurs de la succion, dans le chemin de mouillage W_1 , pour l'essai de rétention d'eau. Dans ces figures, n_{\max} et n_{\min} représentent la porosité maximum et minimum, respectivement (écrit dessous la valeur de succion)

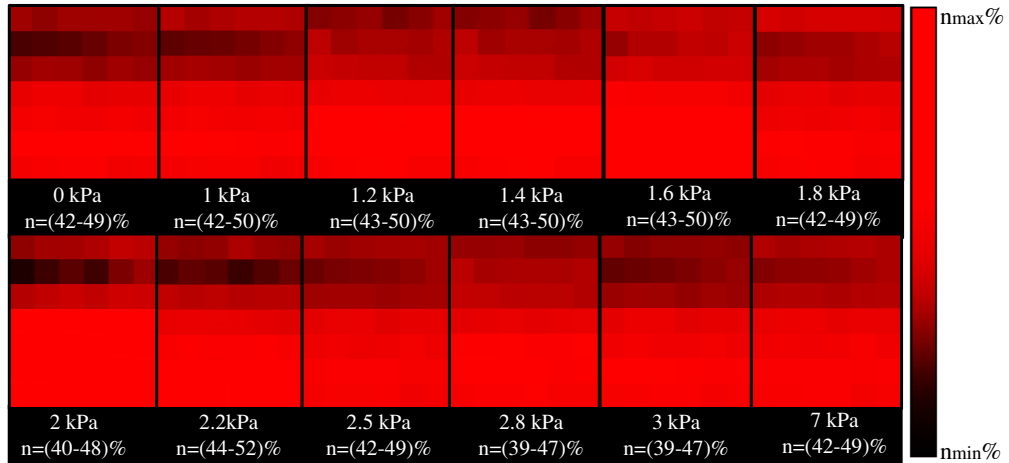


Figure 19: Des tranches centrales verticales (XZ) dans la carte de la porosité, pour toutes les valeurs de la succion, dans le chemin de mouillage W_1 , pour l'essai de rétention d'eau. Dans ces figures, n_{\max} et n_{\min} représentent la porosité maximum et minimum, respectivement (écrit dessous la valeur de succion)

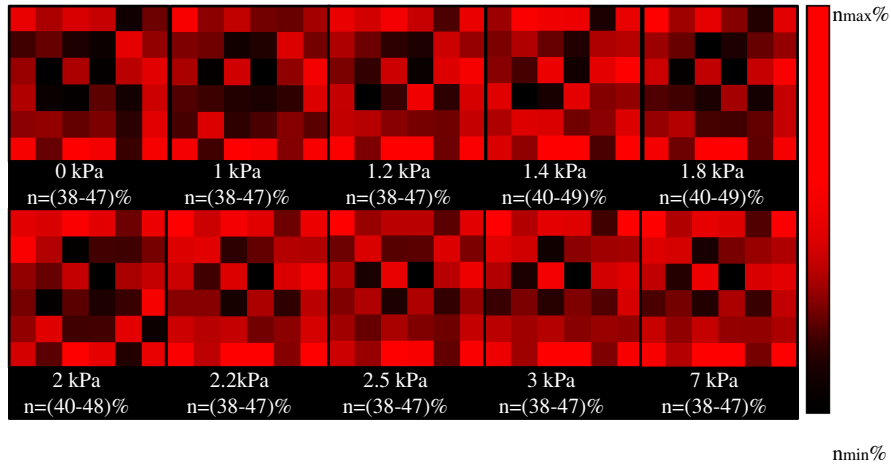


Figure 20: Des tranches centrales horizontales (XY) dans la carte de la porosité, pour toutes les valeurs de la succion, dans le chemin de séchage D_0 , pour l'essai de rétention d'eau. Dans ces figures, n_{\max} et n_{\min} représentent la porosité maximum et minimum, respectivement (écrit dessous la valeur de succion)

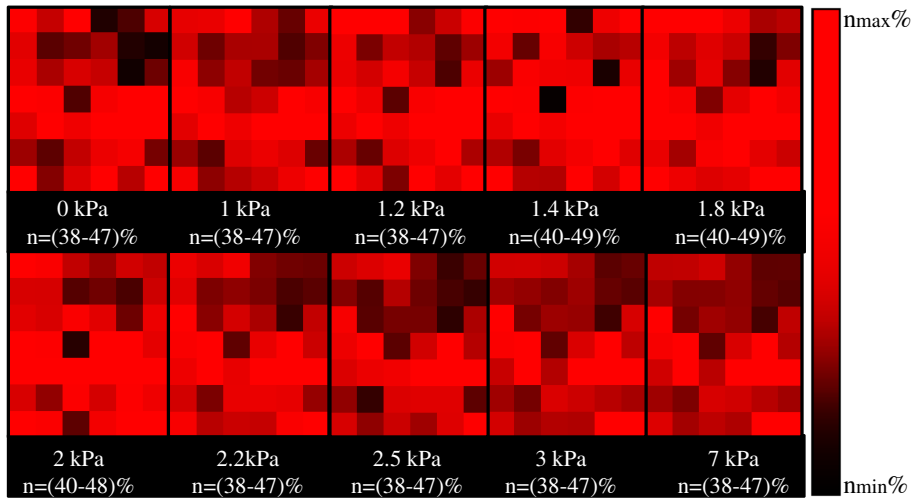


Figure 21: Des tranches centrales verticales (XZ) dans la carte de la porosité, pour toutes les valeurs de la succion, dans le chemin de séchage D_0 , pour l'essai de rétention d'eau. Dans ces figures, n_{\max} et n_{\min} représentent la porosité maximum et minimum, respectivement (écrit dessous la valeur de succion)

Fig 22, Fig 24 et Fig 26 montrent des tranches centrales horizontales (XY) de la carte du degré de saturation , pour toutes les valeurs de la succion, dans les chemins de séchage et de mouillage, D_1, W_1 and D_0 , respectivement, pour l'essai de rétention d'eau. Fig 23, Fig 25 et Fig 27 montrent des tranches centrales verticales (XZ) dans la carte du degré de saturation , du même azimut, pour toutes les valeurs de la succion, dans les chemins de séchage et de mouillage, D_1, W_1 and D_0 , respectivement, pour l'essai de rétention d'eau. Dans ces figures, Sr_{max} et Sr_{min} représentent le degré de saturation maximum et minimum, respectivement (écrit dessous la valeur de succion).

D'après Fig 28 et Fig 29 , la relation microscopique entre la porosité et le degré de saturation peut être étudiée qualitativement. L'image trinarisée dans Fig 29-milieu montre que la teneur en eau est inférieure au fond de l'échantillon par rapport au haut de l'échantillon. Ceci est cohérent avec la plus grande porosité du fond de l'échantillon, définie à partir de la cartographie de la porosité (voir Fig 28). On constate que l'augmentation de la porosité induit une diminution du degré de saturation.

Dans Fig 30, Fig 31 et Fig 32 la relation entre le nombre d'agrégats d'eau en fonction de la succion, est présentée pour l'essai de rétention d'eau, pour les chemins de séchage et de mouillage, D_1, W_1 and D_0 , respectivement.

La corrélation d'images numériques est effectuée pour WRT_1 (D_1 et W_1) afin de vérifier la présence de déformation provenant de l'application de succion. Les résultats de la DIC sont présentés dans Fig 33. les déplacements des grains dans ces essais sont considérés comme négligeables et peuvent être ignorés.

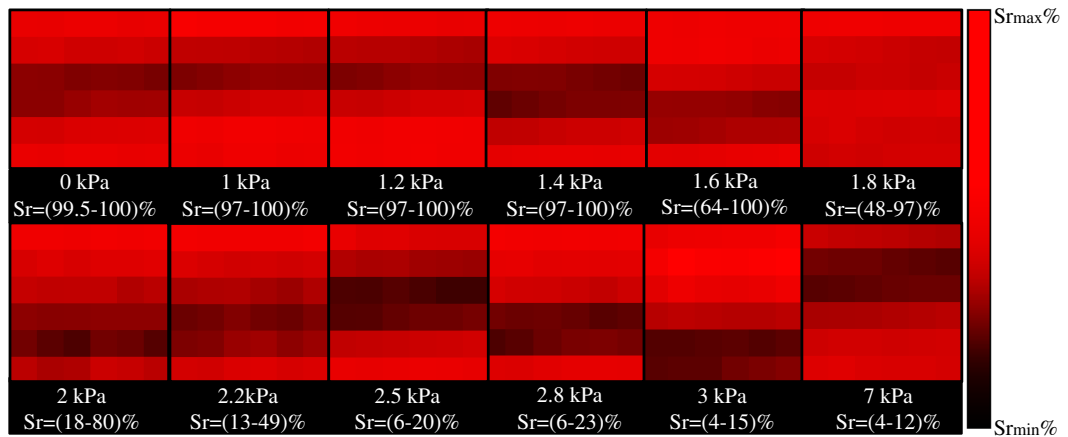


Figure 22: Des tranches centrales horizontales (XY) dans la carte du degré de saturation, pour toutes les valeurs de la succion, dans le chemin de séchage D_1 , pour l'essai de rétention d'eau. Dans ces figures, Sr_{max} et Sr_{min} représentent le degré de saturation maximum et minimum, respectivement (écrit dessous la valeur de succion)

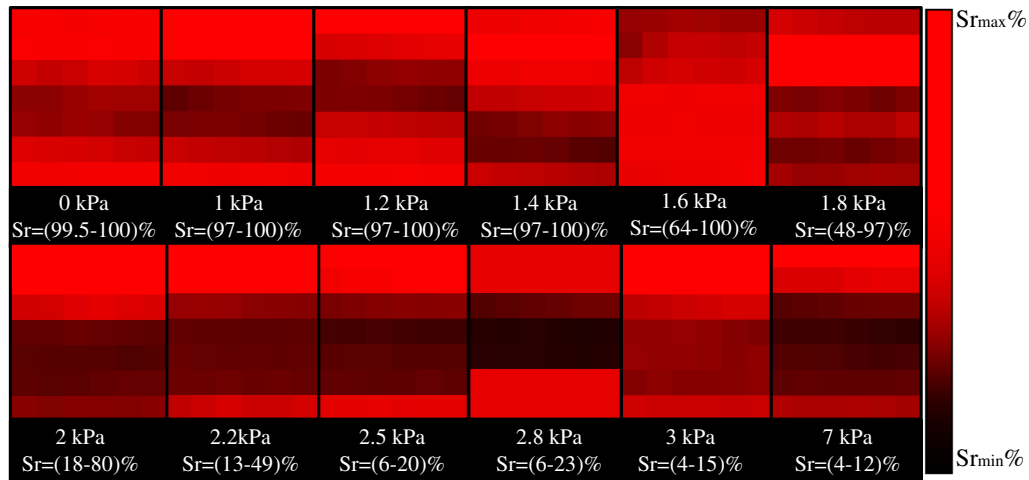


Figure 23: Des tranches centrales verticales (XZ) dans la carte du degré de saturation, pour toutes les valeurs de la succion, dans le chemin de séchage D_1 , pour l'essai de rétention d'eau. Dans ces figures, $S_{r_{max}}$ et $S_{r_{min}}$ représentent le degré de saturation maximum et minimum, respectivement (écrit dessous la valeur de succion)

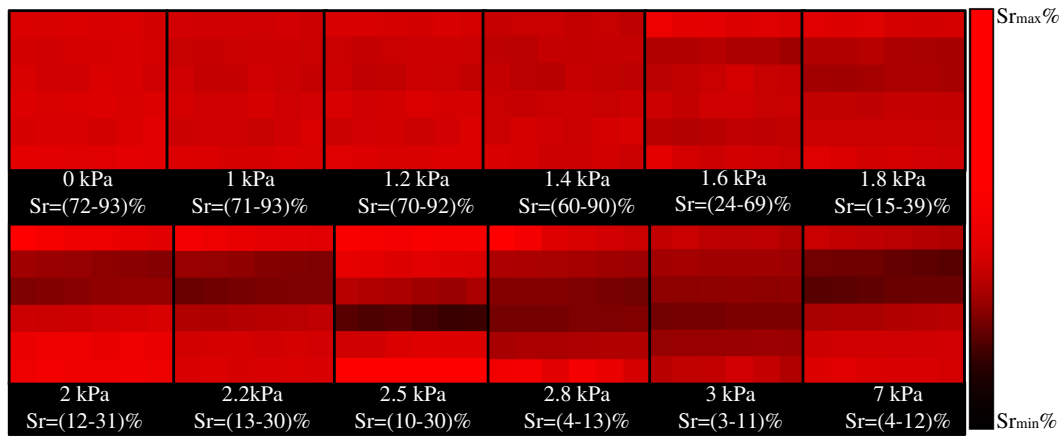


Figure 24: Des tranches centrales horizontales (XY) dans la carte du degré de saturation, pour toutes les valeurs de la succion, dans le chemin de mouillage W_1 , pour l'essai de rétention d'eau. Dans ces figures, $S_{r_{max}}$ et $S_{r_{min}}$ représentent le degré de saturation maximum et minimum, respectivement (écrit dessous la valeur de succion)

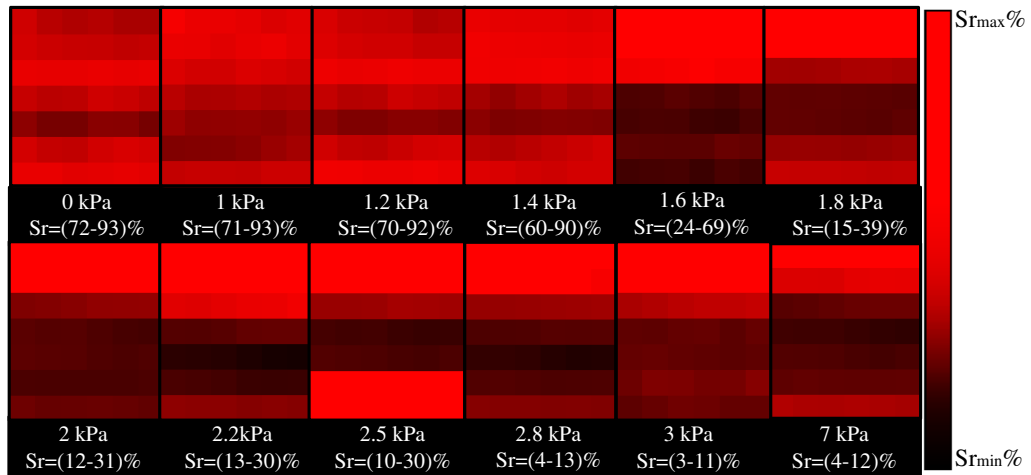


Figure 25: Des tranches centrales verticales (XZ) dans la carte du degré de saturation, pour toutes les valeurs de la succion, dans le chemin de mouillage W_1 , pour l'essai de rétention d'eau. Dans ces figures, Sr_{max} et Sr_{min} représentent le degré de saturation maximum et minimum, respectivement (écrit dessous la valeur de succion)

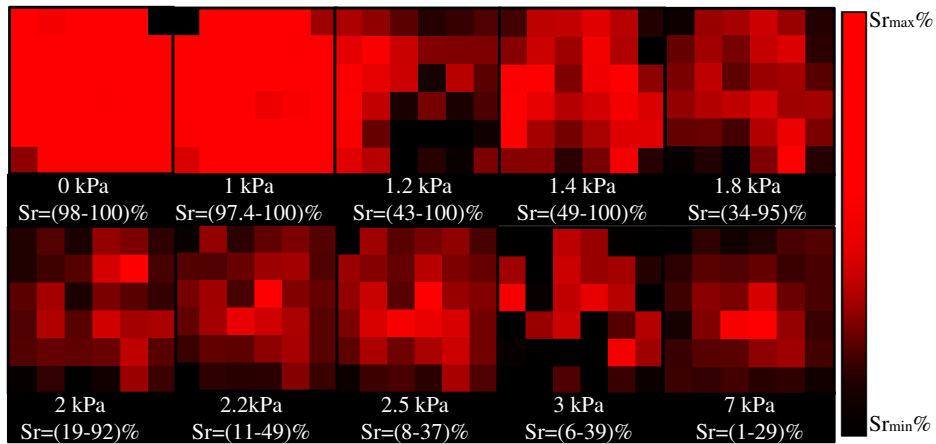


Figure 26: Des tranches centrales horizontales (XY) dans la carte du degré de saturation, pour toutes les valeurs de la succion, dans le chemin de séchage D_0 , pour l'essai de rétention d'eau. Dans ces figures, Sr_{max} et Sr_{min} représentent le degré de saturation maximum et minimum, respectivement (écrit dessous la valeur de succion)

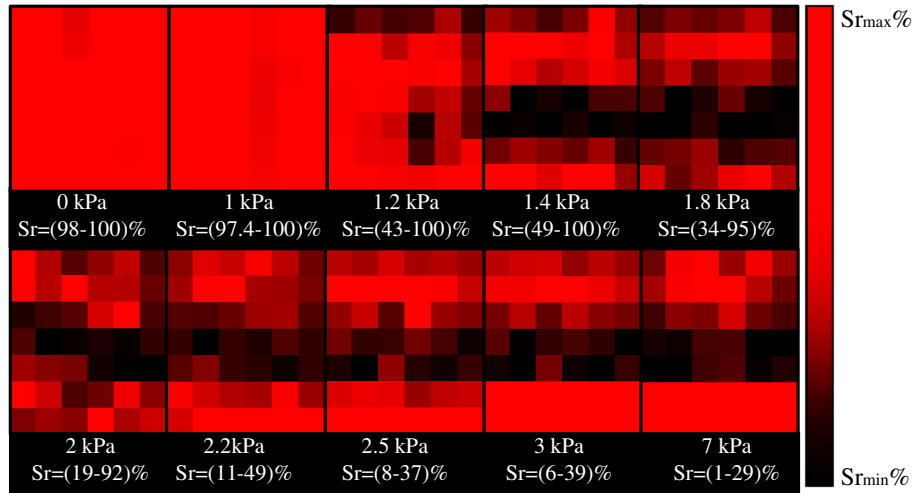


Figure 27: Des tranches centrales verticales (XZ) dans la carte du degré de saturation, pour toutes les valeurs de la succion, dans le chemin de séchage D_0 , pour l'essai de rétention d'eau. Dans ces figures, Sr_{max} et Sr_{min} représentent le degré de saturation maximum et minimum, respectivement (écrit dessous la valeur de succion)

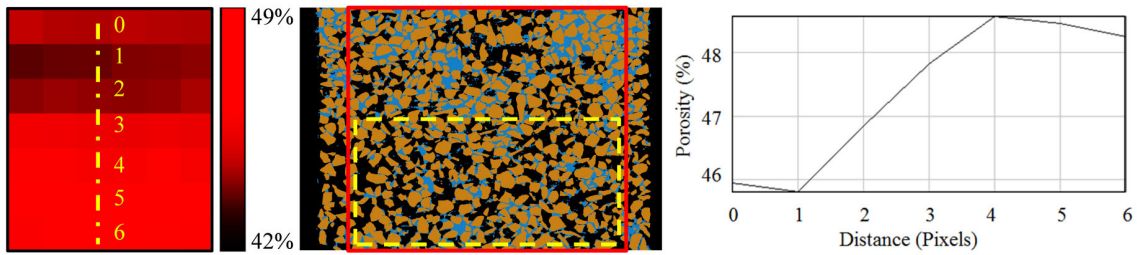


Figure 28: Une tranche centrale verticale dans la carte de la porosité (gauche), une tranche centrale verticale dans le volume trinarisé (milieu) et un profil vertical de la porosité (droite) démontré pour $s=2kPa$, dans le chemin de séchage. Le volume mappé est marquée par un rectangle rouge dans l'image trinarisée. Le rectangle en pointillé jaune correspond à la région de porosité élevée

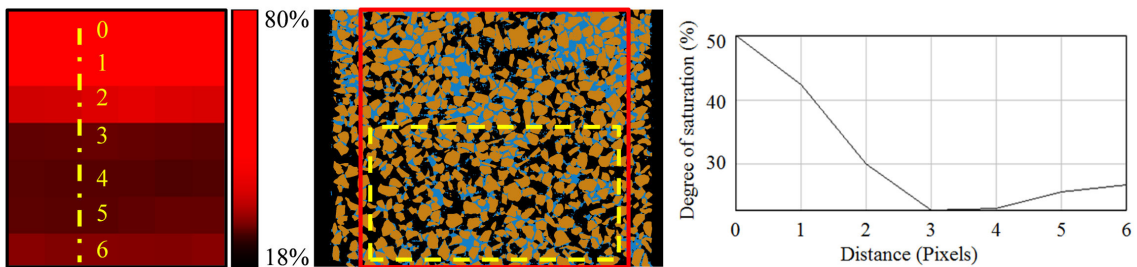


Figure 29: Une tranche centrale verticale dans la carte de degré de saturation (gauche), une tranche centrale verticale dans le volume trinarisé (milieu) et un profil vertical du degré de saturation (droite) démontré pour $s=2kPa$, dans le chemin de séchage. Le volume mappé est marquée par un rectangle rouge dans l'image trinarisée. Le rectangle en pointillé jaune correspond à la région de degré de saturation élevée

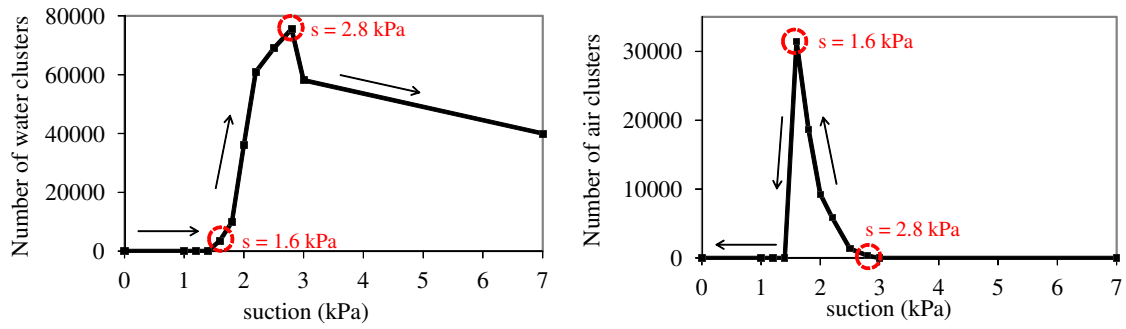


Figure 30: L'évolution du nombre d'agrégats d'eau (gauche) et d'agrégats d'air (droite) avec la suction, pour le chemin de séchage D_1

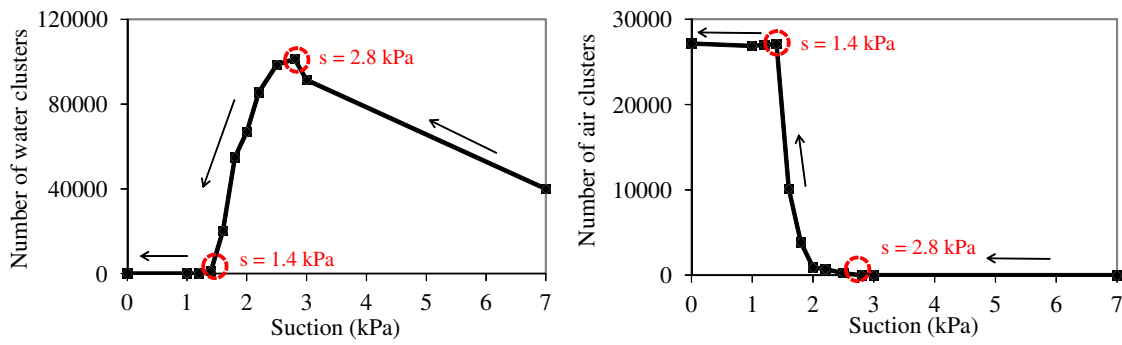


Figure 31: L'évolution du nombre d'agrégats d'eau (gauche) et d'agrégats d'air (droite) avec la suction, pour le chemin de mouillage W_1

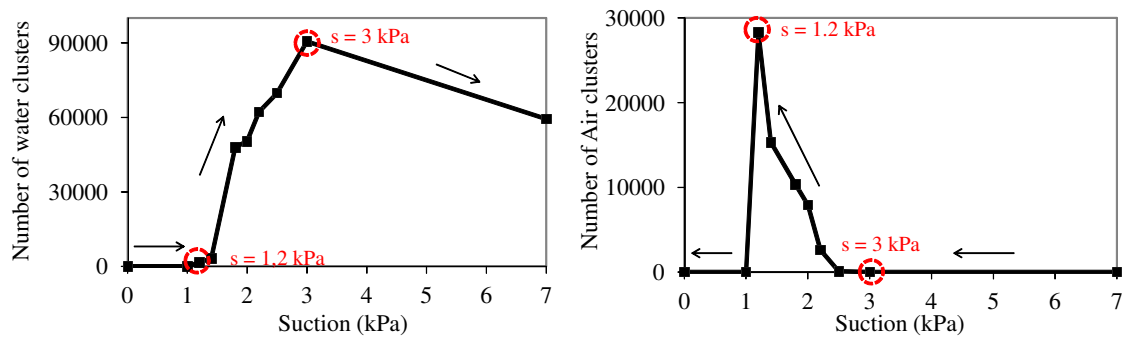


Figure 32: L'évolution du nombre d'agrégats d'eau (gauche) et d'agrégats d'air (droite) avec la suction, pour le chemin de séchage D_0

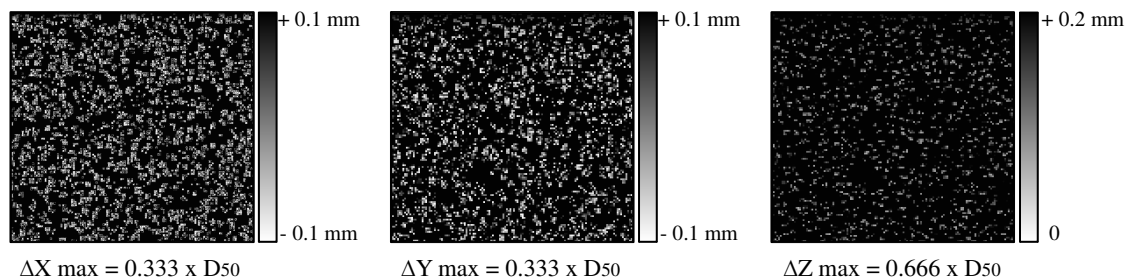


Figure 33: Les résultats de corrélation d'images pour WRT_1 (D_1 et W_1). Les deux états corrélés sont le premier état de l'échantillon dans le chemin de séchage D_1 ($s=0\text{kPa}$) et le dernier état du même spécimen dans le chemin de mouillage W_1 ($s=0\text{kPa}$)

Les résultats expérimentaux de l'essai de la rétention d'eau test a permis principalement l'obtention de la surface de rétention de l'eau et les domaines de rétention de l'eau. Fig 34 montre la surface de rétention d'eau pour le chemin de séchage.

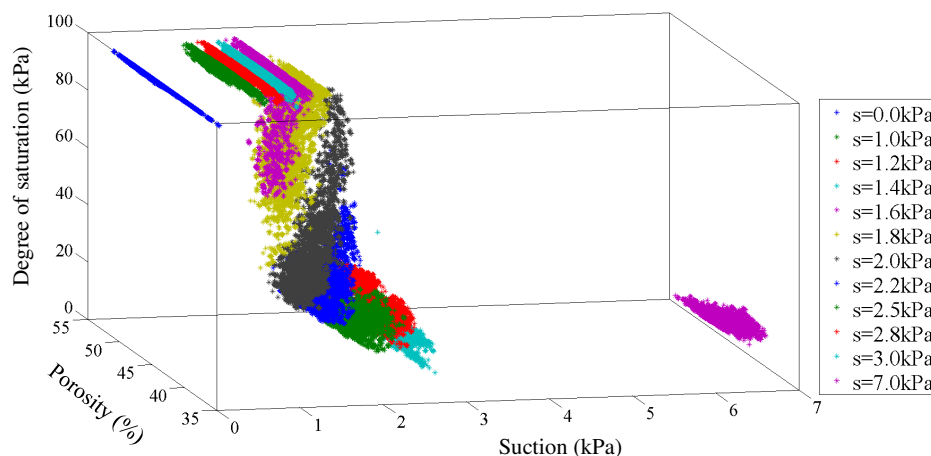


Figure 34: la surface de rétention d'eau pour le chemin de séchage

Tableau 1 montre les domaines de rétention d'eau pour D_1 .

Table 1: les domaines de rétention d'eau pour D_1

Suction (kPa)	0	1	1.2	1.4	1.6	1.8	2	2.2	2.5	2.8	3	7
Water retention domain	Saturated			Funicular			Pendular			Residual		
	Water			Water			Air			Air		
Continuous phase												

Tableau 2 montre les domaines de rétention d'eau pour W_1 .

Table 2: les domaines de rétention d'eau pour W_1

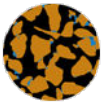
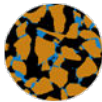
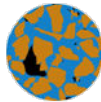
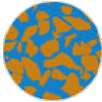
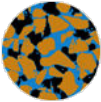
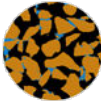

Suction (kPa)	3	2.8	2.5	2.2	2	1.8	1.6	1.4	1.2	1	0
Water retention domain	Residual		Pendular				Funicular				
Continuous phase	Air		Air				Water				
											

Tableau 3 montre les domaines de rétention d'eau pour D_0 .

Table 3: les domaines de rétention d'eau pour D_0

Suction (kPa)	0	1	1.2	1.4	1.8	2	2.2	2.5	3	7
Water retention domain	Saturated		Funicular				Pendular			Residual
Continuous phase	Water		Water				Air			Air
										

2. Le comportement hydro-mécanique

Pour le comportement hydro-mécanique des sols non saturés, des essais triaxiaux ont été effectués sous trois conditions: saturé drainé, non saturé drainé et non saturé non drainé. Un appareil triaxial que l'on peut placer à l'intérieur de la cabine du tomographe à rayons x a été développé afin de permettre le suivi des changements dans la micro-structure du sable et la distribution de l'eau lorsque l'on soumet l'échantillon à chargement mécanique. L'échantillon (cylindre de dimensions $h \times d = 2 \times 1 \text{ cm}$) a été préparé en utilisant la technique de la pluviométrie sous l'eau (complètement saturé au début des trois tests), amené ensuite au niveau de saturation désiré (dans le cas des essais non saturés), puis chargé par étapes successives avec un scanner à chaque étape avec une résolution de $13 \mu\text{m}$, jusqu'à arriver à 21% de déformation axiale pour les trois types d'essai.

Fig 35. montre tout l'arrangement de configuration triaxial intérieur de l'armoire de rayons x utilisé pour effectuer les trois essais triaxiaux.

Fig 36 montre la cellule PMMA en face de source de rayons x, avec le spécimen installés à sa place à l'intérieur de la cellule.

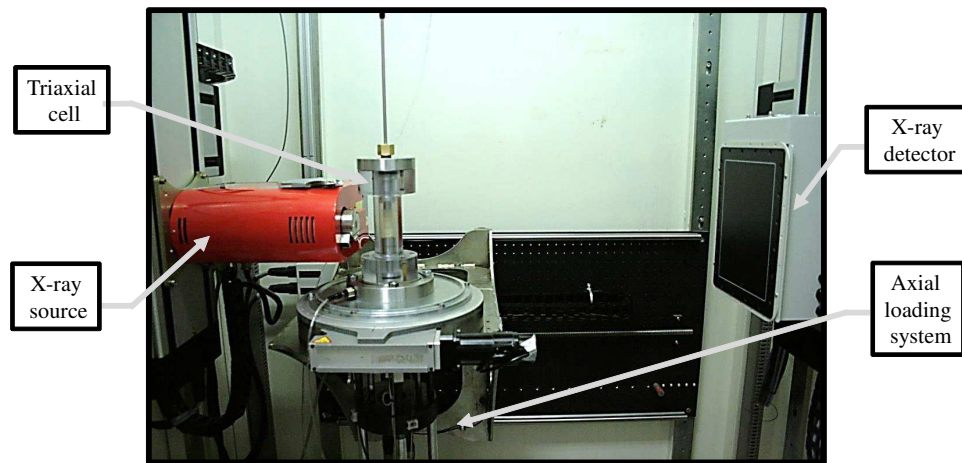


Figure 35: L'ensemble du dispositif de configuration triaxial intérieur de l'armoire de rayons x utilisé pour effectuer les trois essais triaxiaux

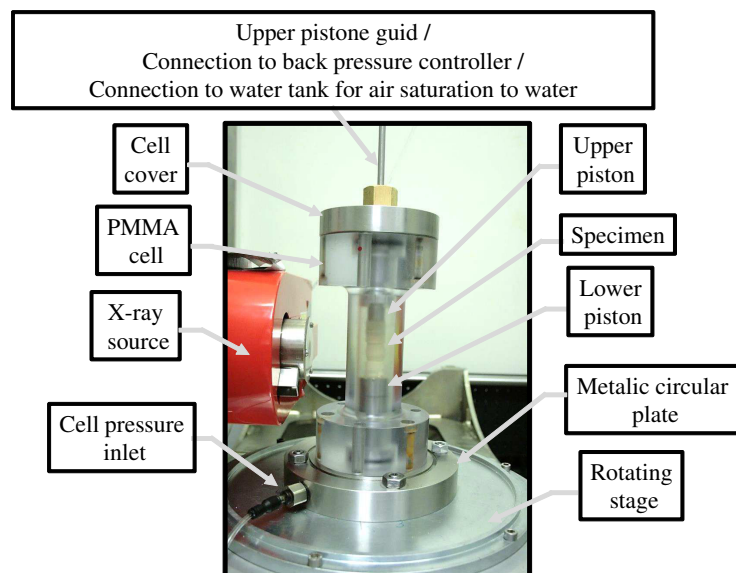


Figure 36: La cellule triaxiale en face de la source de rayons x

Fig 37 illustre la procédure par laquelle le spécimen est préparé dans ce travail, pour les trois essais triaxiaux.

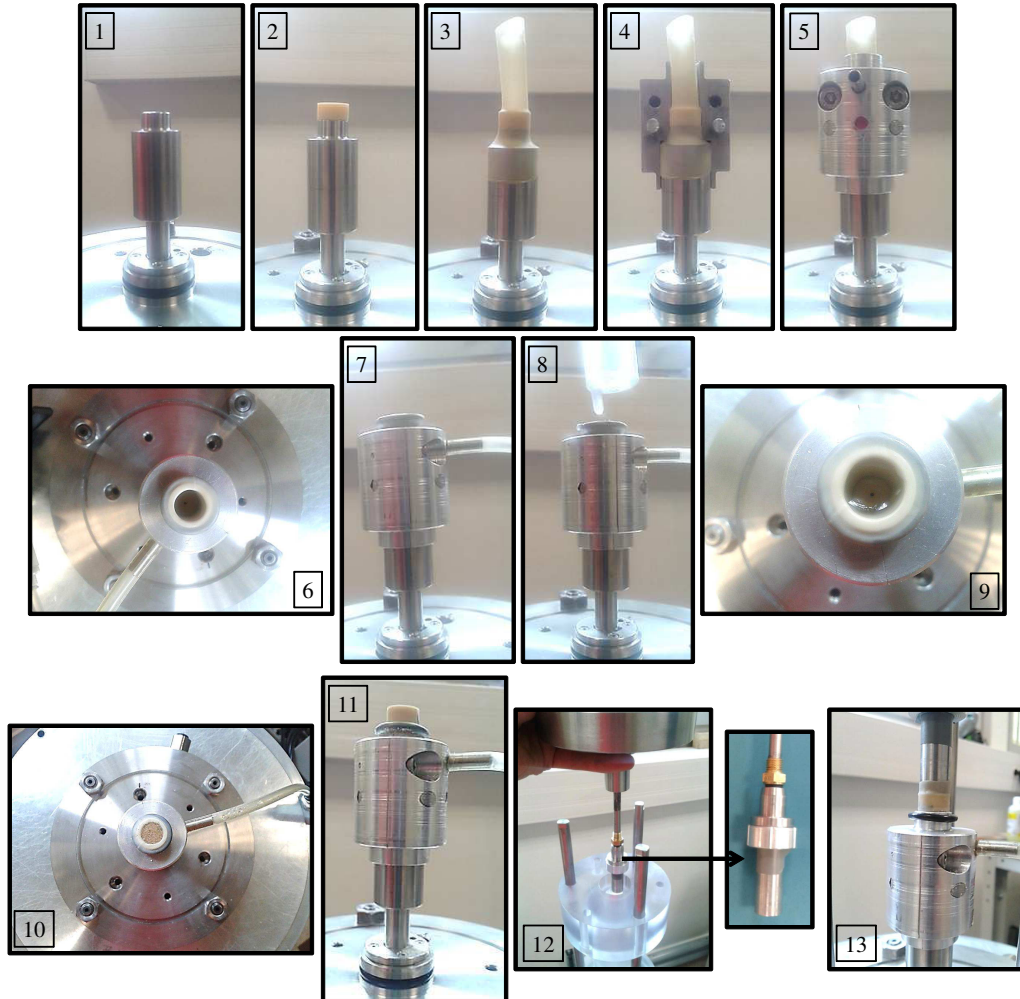


Figure 37: Une série de photographies illustrant la procédure par laquelle un spécimen est préparé dans ce travail

Les courbes contrainte-déformation pour tous les essais triaxiaux réalisés dans ce travail et pour les essais de référence sont présentés dans Fig 38. Dans Fig 38-bas, la contrainte axiale (σ_1) est normalisée par la pression de la cellule (σ_3) afin d'exclure l'influence des différentes valeurs de pression de la cellule.

Les notations dans cette figure représentent ce qui suit: SD=saturée drainé, UD=non saturé drainé, UU=nonsaturé non drainée et D=sec.

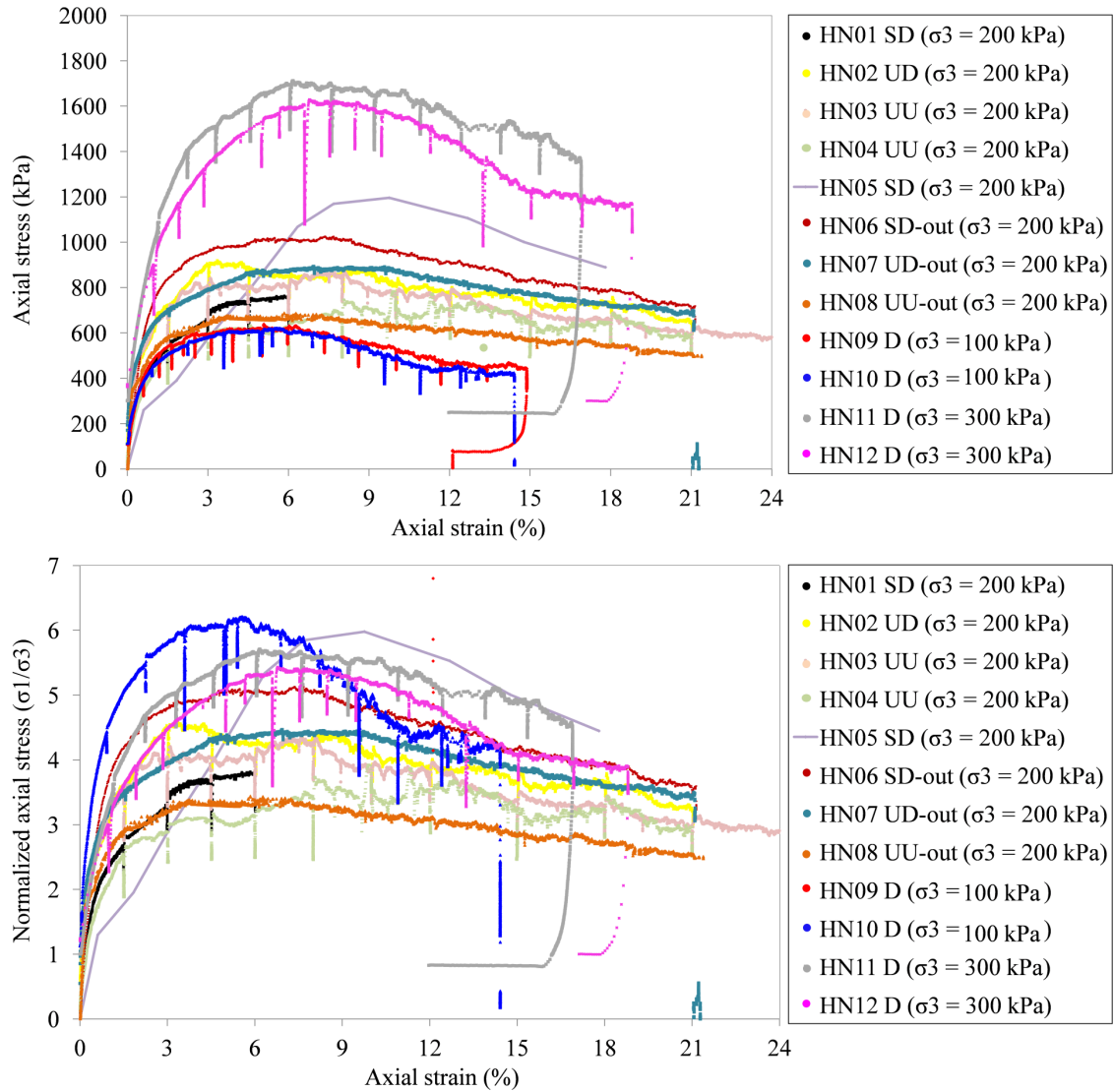


Figure 38: Les courbes contrainte-déformation pour tous les essais triaxial effectués et de référence. Dans Fig 38-bas, la contrainte axiale (σ_1) est normalisée par la pression de la cellule (σ_3) afin d'exclure l'influence de la pression de cellule différente

La porosité et le degré de saturation macroscopique sont calculés pour chaque étape de chargement dans l'essai triaxial drainé non saturé, d'une manière similaire à celle utilisée pour l'essai de rétention d'eau. Fig 39 montre l'évolution de la porosité et le degré de saturation macroscopique calculé à partir des volumes trinarisés, avec le chargement pour l'essai triaxial drainé non saturé.

Après l'application de succion sur le spécimen saturés, le degré de saturation, varie de $S_r=100\%$ à $S_r=67\%$. La porosité de l'échantillon au début de l'essai triaxial est $n=34,6\%$. Lorsque le chargement est appliqué, la porosité diminue légèrement augmente alors que le chargement augmente pour atteindre une valeur maximale à la fin de l'essai $n=40,7\%$. En

même temps, le degré de saturation diminue à mesure que de plus en plus le chargement pour atteindre une valeur minimum à la fin de l'essai $S_r=39,9\%$.

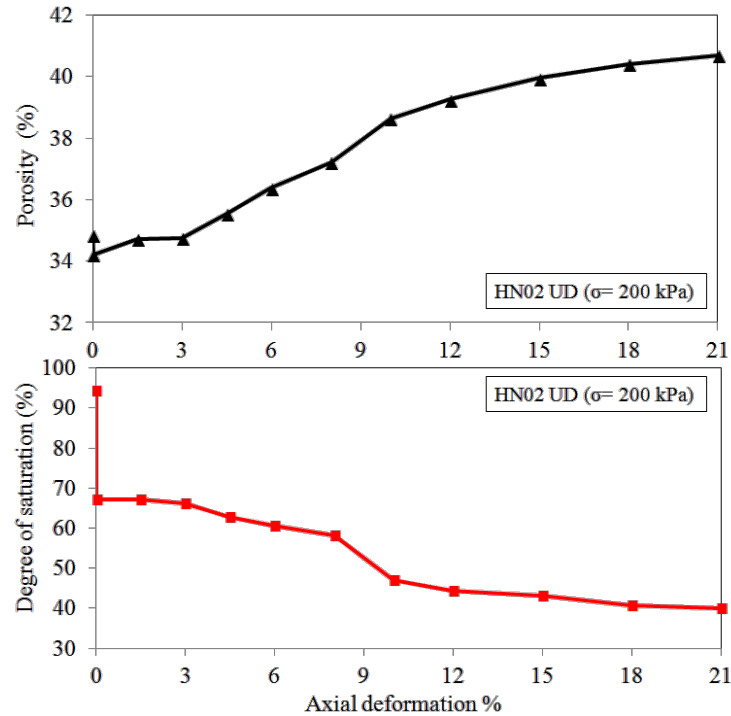


Figure 39: L'évolution de la porosité macroscopique (haut) et le degré de saturation macroscopique (bas) avec le chargement pour l'essai triaxial drainé non saturé

En utilisant l'outil de traitement d'image Fiji et les images trinarisées, le volume de l'échantillon est obtenu pour chaque étape de chargement et la déformation volumique a été calculée en conséquence, par rapport au volume initial de l'échantillon et le volume de l'échantillon après l'application de la succion ($\varepsilon=0\%$). La procédure est illustrée en 2D dans Fig 40.

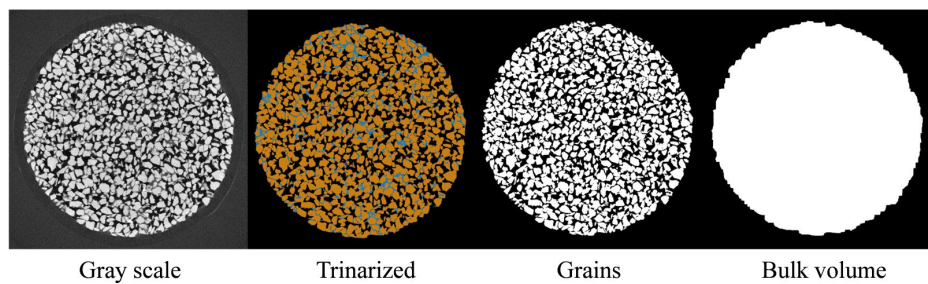


Figure 40: La procédure de mesure de volume de l'échantillon

Les graphes de contrainte volumique pour l'essai non saturé drainé triaxial (HN02 (UD)) et l'essai sec de référence (HN09 (D)) sont présentés dans Fig 41. Fig 41-haut

montre la contrainte volumique pour HN02 (UD) calculé par rapport au volume initial de l'échantillon et Fig 41-bas montre la contrainte volumique pour HN02 (UD) calculée par rapport au volume de l'échantillon après l'application de la succion (par exemple, $\varepsilon=0\%$). L'échantillon HN02 (UD) exhibe une contraction considérable lorsque la succion est appliquée (représenté par segment vertical sur l'axe Y, de 0 à 2, dans Fig 41-haut). Plus tard, au-delà de $\varepsilon=4,5\%$, la réponse volumique de l'échantillon est dilatante.

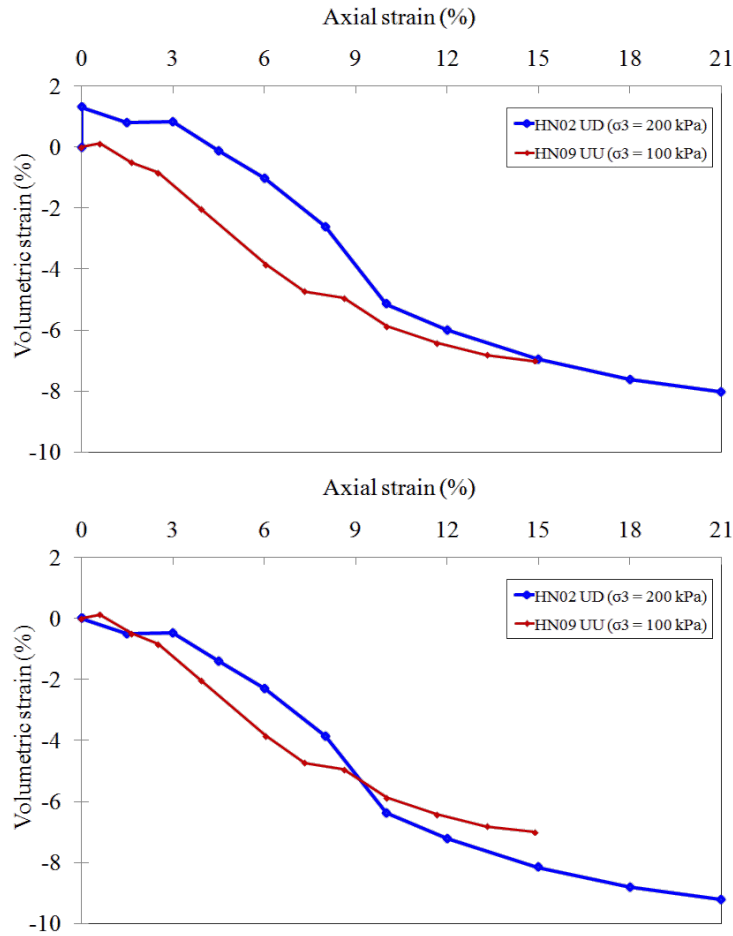


Figure 41: La contrainte volumique pour l'essai drainé non saturé HN02 (UD) et l'essai sec de référence HN09 (D). Dans le tracé du haut, le volume apparent de HN02 (UD) est calculé par rapport au volume initial de l'échantillon et la courbe du bas le volume apparent de HN02 (UD) est calculé par rapport au volume de l'échantillon après avoir appliqué la succion ($\varepsilon=0\%$)

Par rapport à HN02 (UD), l'échantillon HN09 (D) est moins contractés au début de l'essai. La pente de dilatance de HN09 (D) est plus ou moins la même que pour HN02 (UD), dans leur zone de dilatance principale (à partir de 3% à 9%), puis HN02 (UD) a une courte excès de dilatance (plus raide pente d'environ 9% comme indiqué dans Fig 41-bas) tandis HN09 (D) a une courte perte de dilatance, et enfin HN09 (D) montre plateau

dilatance globale moins de HN02 (UD).

Pour les mesures microscopiques, Fig 42 et Fig 43 montrent les cartes de la porosité et du degré de saturation, respectivement, pour chaque étape de chargement dans l'essai triaxial drainé non saturé.

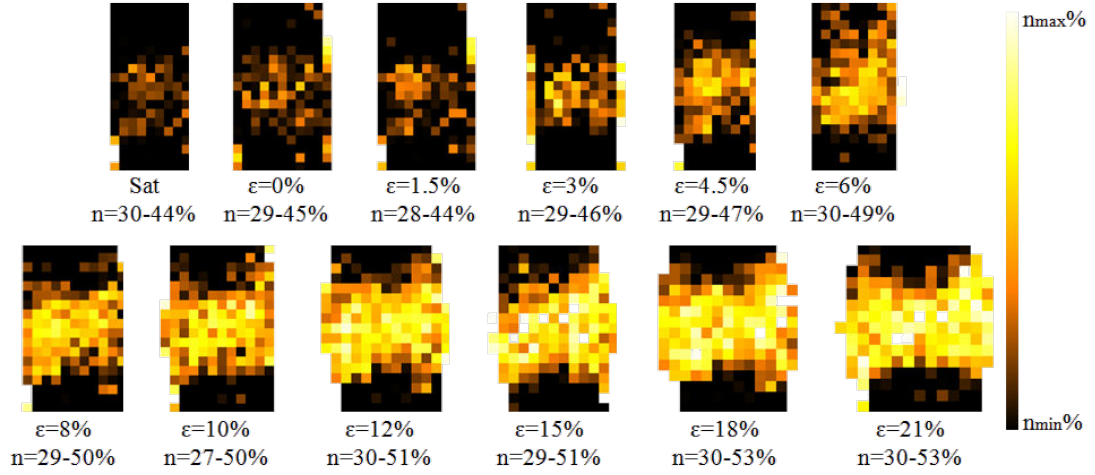


Figure 42: La carte de porosité pour chaque étape de chargement dans l'essai triaxial drainé non saturé. Dans cette figure, n_{\max} et n_{\min} représentent la porosité maximum et minimum, respectivement (écrit dessous la valeur de chargement)

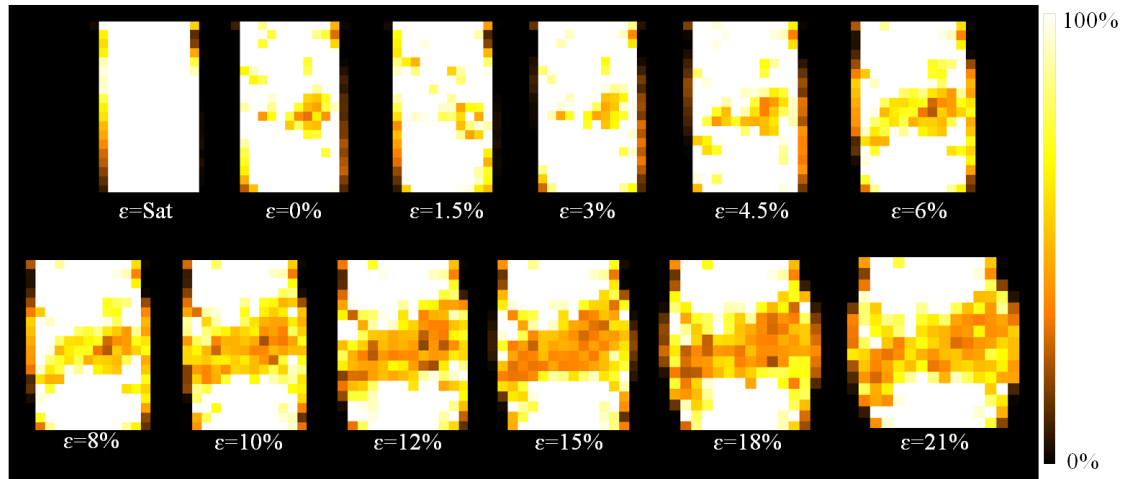


Figure 43: La carte du degré de saturation pour chaque étape de chargement dans l'essai triaxial drainé non saturé

Fig 44 montre l'évolution du nombre d'agrégats d'eau et de l'air avec la contrainte axiale, pour toutes les étapes de chargement dans l'essai triaxial HN02 (UD).

Pour l'essai triaxial HN02, Fig 45 montre le déplacement incrémental horizontal dans

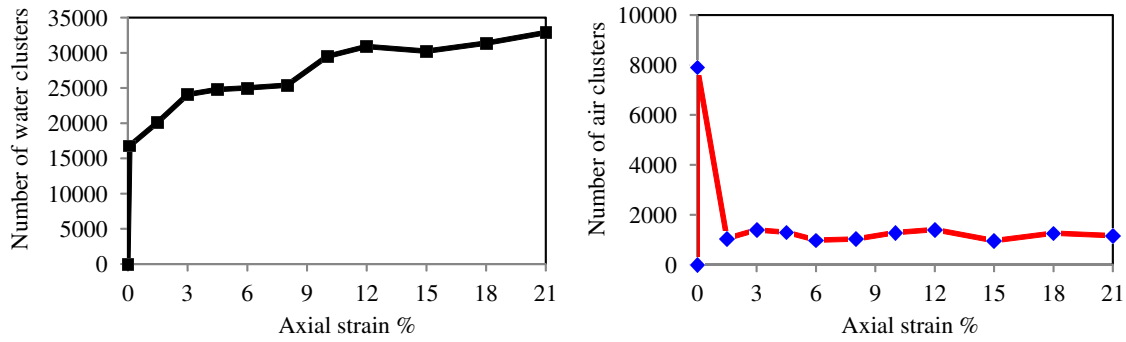


Figure 44: L'évolution du nombre d'agrégats d'eau (gauche) et d'agrégats d'air (droite) avec la suction, pour toutes les étapes de chargement dans l'essai triaxial HN02 (UD)

la direction de coordonnée X, normalisée par l'étape de déformation axiale, pour toutes les étapes de chargement dans l'essai triaxial HN02 (UD)

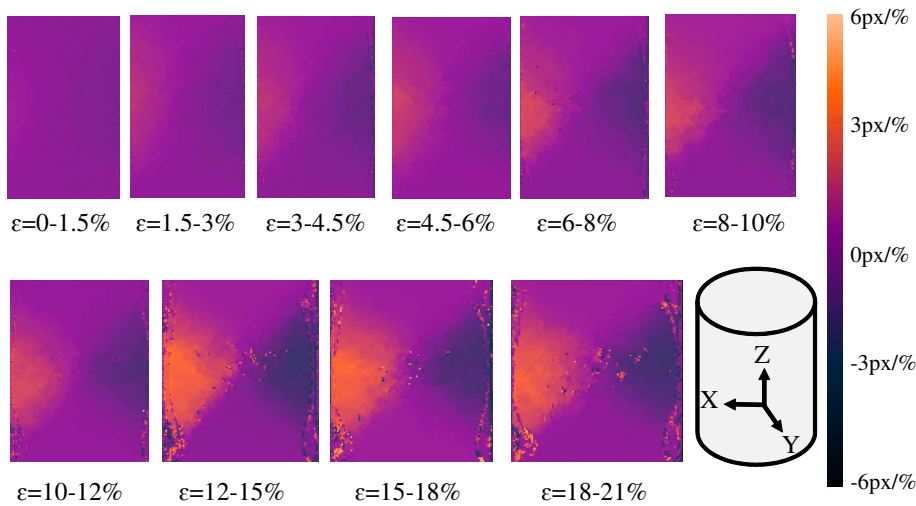


Figure 45: Le domaine du déplacement incrémental X, normalisé par l'étape de déformation axiale, pour toutes les étapes de chargement dans l'essai triaxial HN02(UD)

Le déplacement incrémental horizontal dans la direction des coordonnées Y normalisée par l'étape de déformation axiale, pour toutes les étapes de chargement dans l'essai triaxial HN02 (UD) est présentée dans Fig 46.

Le déplacement incrémental vertical dans la direction coordonnée Z normalisée par l'étape de déformation axiale, pour toutes les étapes de chargement dans l'essai triaxial HN02 (UD) est présentée dans Fig 47.

Fig 48 indique la rotation du squelette solide à l'intérieur de la fenêtre de corrélation, calculée comme la norme de rotation dans les trois directions x, y et z, pour toutes les étapes de chargement dans l'essai triaxial HN02 (UD).

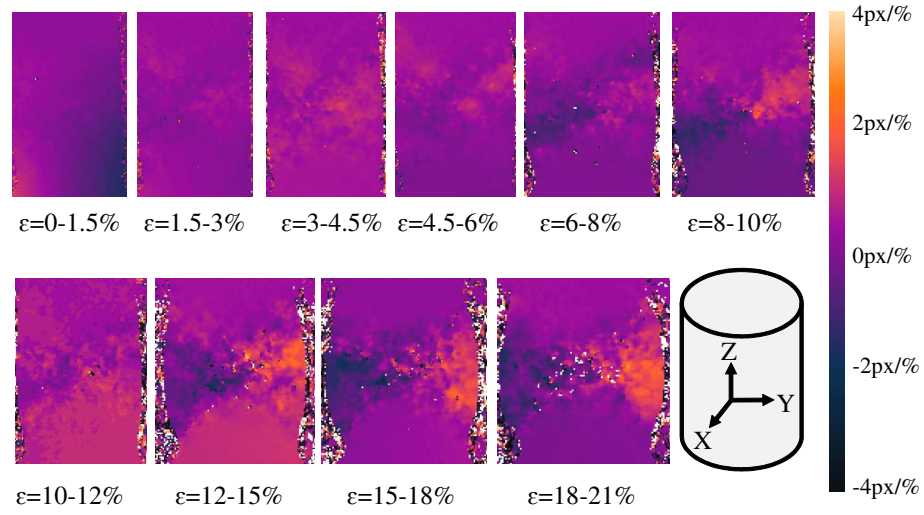


Figure 46: Le domaine du déplacement incrémental Y , normalisé par l'étape de déformation axiale, pour toutes les étapes de chargement dans l'essai triaxial HN02(UD)

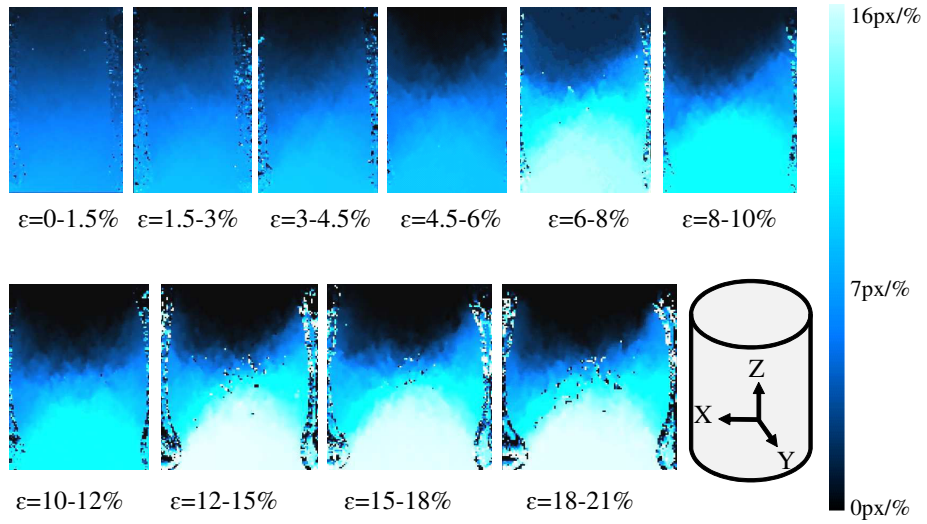


Figure 47: Le domaine du déplacement incrémental z , normalisé par l'étape de déformation axiale, pour toutes les étapes de chargement dans l'essai triaxial HN02(UD)

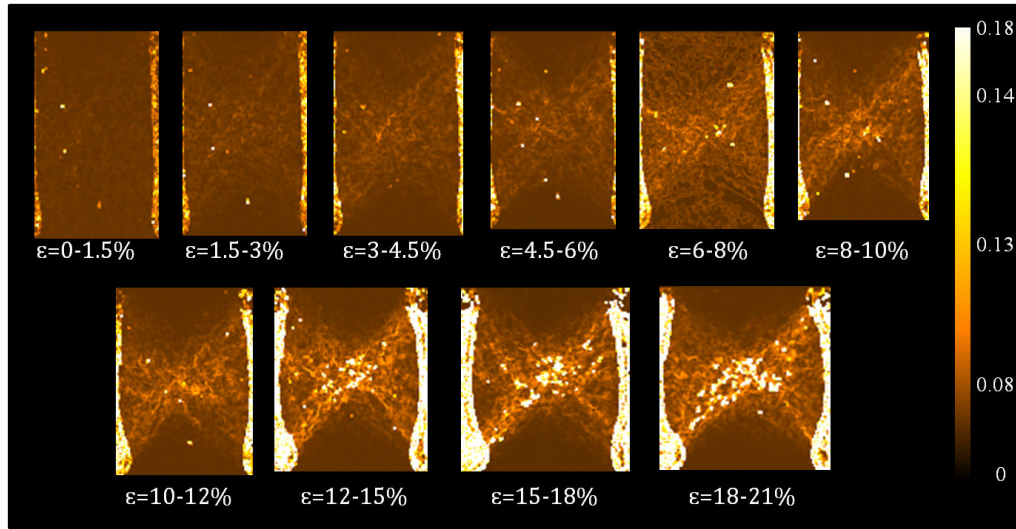


Figure 48: La rotation du squelette solide, pour toutes les étapes de chargement dans l'essai triaxial HN02 (UD)

La contrainte volumique et la contrainte déviatorique sont présentées dans Fig 49 et Fig 50, respectivement, pour toutes les étapes de chargement dans l'essai triaxial HN02 (UD).

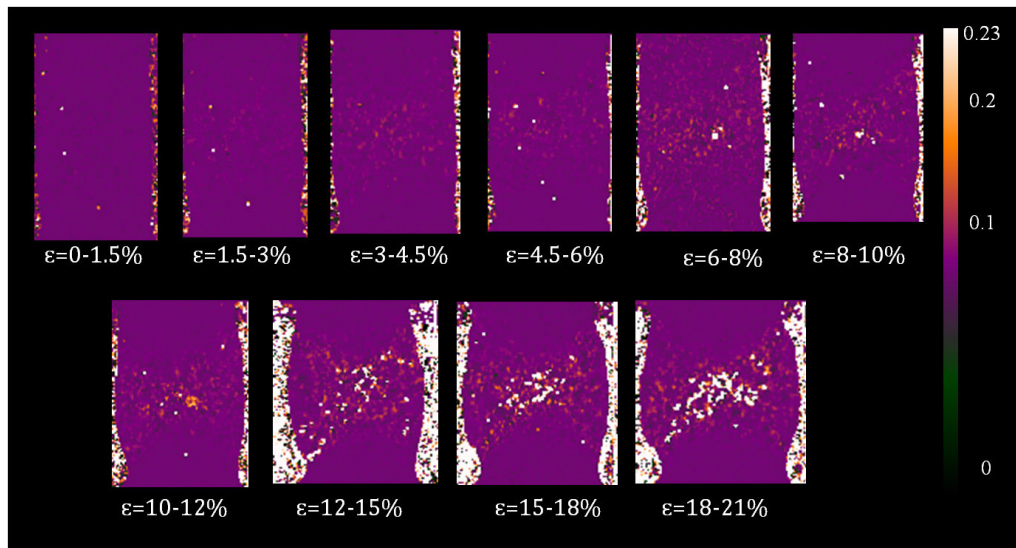


Figure 49: Le domaine de la déformation volumique pour toutes les étapes de chargement dans l'essai triaxial HN02 (UD)

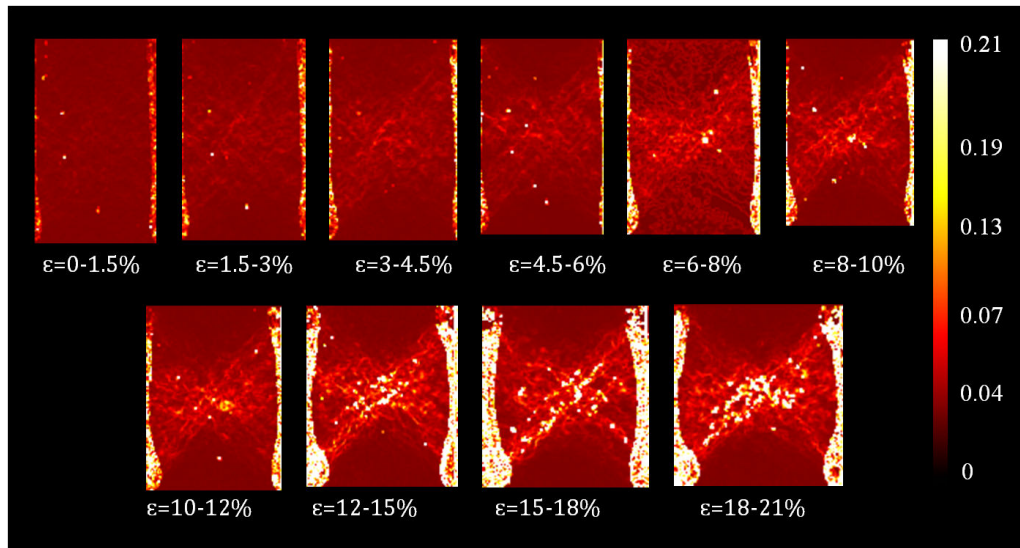


Figure 50: Le domaine de la déformation déviatorique (cisaillement maximum) pour toutes les étapes de chargement dans l'essai triaxial HN02 (UD)

Pour synthétiser, ce travail a abouti aux résultats suivants:

- Fabrication des équipements, des outils et des techniques appropriés pour l'analyse multi-échelle et la caractérisation des comportements de rétention de l'eau et hydro-mécaniques des matériaux granulaires non saturés.
- Détermination de la courbe de rétention de l'eau, la surface et les domaines hydriques (domaines de rétention d'eau) pour les matériaux granulaires non saturés, dans des conditions différentes (porosité initiale et les chemins de chargement) et analyser le phénomène d'hystérésis aux échelles microscopiques-discrètes.
- Détermination des courbes contrainte-déformation et la réponse volumique pour les matériaux granulaires non saturés, dans des conditions différentes (porosité initiale et conditions drainé-non ou drainée).
- Analyse de l'effet de la succion sur le changement de teneur en eau et sur le comportement mécanique des matériaux granulaires non saturés (par exemple, la force de cisaillement, l'homogénéité/hétérogénéité de distribution d'eau, la cohésion).
- L'évaluation de la relation entre les comportements macroscopiques et microscopiques-discrètes de matériaux granulaires non saturés.
- Définition des données expérimentales qui peut être utilisées pour la validation, l'amélioration et le développement des équations constitutives et les paramètres des modèles pour les simulations numériques des problèmes d'ingénierie.

